IntechOpen

Developments in Combustion Technology

Edited by Konstantinos G. Kyprianidis and Jan Skvaril

DEVELOPMENTS IN COMBUSTION TECHNOLOGY

Edited by **Konstantinos G. Kyprianidis** and **Jan Skvaril**

Developments in Combustion Technology
http://dx.doi.org/10.5772/61418
Edited by Konstantinos G. Kyprianidis and Jan Skvaril

Contributors

Ftwi Yohaness Hagos, Abd Rashid Abd Aziz, Shaharin Anwar Sulaiman, Bahaaddein K. M. Mahgoub, Ho Tse, Praveen Ramaprabhu, Nitesh Attal, Hilda Varshochi, Rita Branquinho, Jefrey Pilusa, Edison Muzenda, Long Liu, Ramesh K. Agarwal, Lennox Zumbe Siwale, Lukacs Kristof, Ádám Török, Akos Bereczky, Makame Mbarawa, Antal Penninger, Andrei Kolesnikov, Zhen-Yu Tian, Hong-De Xia, Guan-Fu Pan, Luis Yermán, Haixia Ma, Ningning Zhao, Jiachen Li, Rongzu Hu, Fengqi Zhao, Paweł Madejski, Tomasz Janda, Norbert Modliński, Daniel Nabagło, Odile Vekemans, Jamal Chaouki, Rudolf Pušenjak, Igor Tičar, Maks, M. Oblak, Emilia Hroncova, Juraj Ladomerský, Ján Valíček, Ladislav Dzuranda

© The Editor(s) and the Author(s) 2016
The moral rights of the and the author(s) have been asserted.
All rights to the book as a whole are reserved by INTECH. The book as a whole (compilation) cannot be reproduced, distributed or used for commercial or non-commercial purposes without INTECH's written permission.
Enquiries concerning the use of the book should be directed to INTECH rights and permissions department (permissions@intechopen.com).
Violations are liable to prosecution under the governing Copyright Law.

Individual chapters of this publication are distributed under the terms of the Creative Commons Attribution 3.0 Unported License which permits commercial use, distribution and reproduction of the individual chapters, provided the original author(s) and source publication are appropriately acknowledged. If so indicated, certain images may not be included under the Creative Commons license. In such cases users will need to obtain permission from the license holder to reproduce the material. More details and guidelines concerning content reuse and adaptation can be foundat http://www.intechopen.com/copyright-policy.html.

Notice

Statements and opinions expressed in the chapters are these of the individual contributors and not necessarily those of the editors or publisher. No responsibility is accepted for the accuracy of information contained in the published chapters. The publisher assumes no responsibility for any damage or injury to persons or property arising out of the use of any materials, instructions, methods or ideas contained in the book.

First published in Croatia, 2016 by INTECH d.o.o.
eBook (PDF) Published by IN TECH d.o.o.
Place and year of publication of eBook (PDF): Rijeka, 2019.
IntechOpen is the global imprint of IN TECH d.o.o.
Printed in Croatia

Legal deposit, Croatia: National and University Library in Zagreb

Additional hard and PDF copies can be obtained from orders@intechopen.com

Developments in Combustion Technology
Edited by Konstantinos G. Kyprianidis and Jan Skvaril
p. cm.
Print ISBN 978-953-51-2668-3
Online ISBN 978-953-51-2669-0
eBook (PDF) ISBN 978-953-51-5781-6

We are IntechOpen, the first native scientific publisher of Open Access books

3,350+
Open access books available

108,000+
International authors and editors

114M+
Downloads

151
Countries delivered to

Our authors are among the
Top 1%
most cited scientists

12.2%
Contributors from top 500 universities

WEB OF SCIENCE™

Selection of our books indexed in the Book Citation Index in Web of Science™ Core Collection (BKCI)

Interested in publishing with us?
Contact book.department@intechopen.com

Numbers displayed above are based on latest data collected.
For more information visit www.intechopen.com

Meet the editor

Dr Kyprianidis is a full-time Professor at the Energy Engineering at the Future Energy Center at Mälardalen University, Sweden, where he leads the "Smarter Modelling, Optimisation and Management" research track. He has published extensively in peer-reviewed journals and international conferences. He has been bestowed twice with the ASME "Cycle Innovations Committee Best Paper Award" and is also a past recipient of the prestigious Cranfield University School of Engineering "Arthur Lefebvre Prize". He has served as Point Contact for the ASME Aircraft Engine Committee, and since 2014, he has been a member of the organizing committee of the International Conference on Applied Energy. He lectures on Heat and Power Technology and is the coordinator for the Bachelors and Masters programs in Energy Engineering.

Jan Skvaril is a lecturer at the Future Energy Center at Mälardalen University in Sweden. He holds an M.Sc. (Ing.) degree in Power Engineering and an M.Sc. (Ing.) in Company Management and Economics, both from the Brno University of Technology in Czech Republic. His research is directed mainly on combustion in large-scale biomass-fired steam boilers, with particular focus on experimental techniques related to temperature and combustion gas distribution and online determination of fuel properties using near-infrared spectroscopy. He has authored several papers on these topics, has presented at international conferences, and also lectures on Combustion and Flue Gas Cleaning Technology at the Mälardalen University, Sweden.

Contents

Preface

Over the past few decades, exciting developments have taken place in the field of combustion technology. Pollutant emissions and environmental impact have been reduced greatly while environmental-friendly waste combustion has been made possible despite the ever-stringent environmental legislation.

Despite the fact that coal combustion remains a key player in the thermal power market, biomass and waste combustion have risen as promising alternatives. Biomass and waste combustion pose several challenges largely due to the considerable variability found in the fuel properties. A considerable amount of research has been directed towards reducing pollutant emissions with both experimental and numerical techniques at the epicenter of such efforts.

Other technological trends include combustion of biofuels in reciprocation engines, chemical looping and catalysis. In parallel with the gradual transition to renewable energy, fluidized bed boiler and reciprocating engine technology are continuously adapted to conform to new challenges such as pollutant emission legislation and the introduction of biofuels.

The present edited volume intends to cover recent developments in combustion technology and to provide a broad perspective of some of the aforementioned challenges that characterize the field. The target audience for this book includes engineers involved in combustion system design, operational planning and maintenance. Manufacturers and combustion technology researchers will also benefit from the timely and accurate information provided in this work.

The volume is organized into five main sections, comprising 15 chapters overall:

- Coal and Biofuel Combustion
- Waste Combustion
- Combustion and Biofuels in Reciprocating Engines
- Chemical Looping and Catalysis
- Fundamental and Emerging Topics in Combustion Technology

The editor is indebted to all the colleagues from across the world who have contributed to this volume with their latest research, to Jan Skvaril, for joining this effort as co-editor, to several combustion experts who volunteered as reviewers, as well as to InTech, for giving me the opportunity to work on this volume and its members of staff for their constant support during its preparation.

Prof. Konstantinos G. Kyprianidis
Future Energy Center
Department of Energy, Building and Environment
Mälardalen University, Västerås, Sweden

Jan Skvaril
Mälardalen University (MDH), Sweden

Section 1

Coal and Biofuel Combustion

Chapter 1

Combustion of Biomass Fuel and Residues: Emissions Production Perspective

Emília Hroncová, Juraj Ladomerský, Ján Valíček and Ladislav Dzurenda

Additional information is available at the end of the chapter

http://dx.doi.org/10.5772/63793

Abstract

This article provides possibilities for minimising the emissions from eight types of biomass combustion boilers given by virtue of continuous emission measurement. The measurements were carried out on various types of one- or two-stage combustion devices. In all investigated modes of combustor operation, the concentration of nitrogen oxides in the whole cycle of fuel combustion was without marked deviations and far lower than the emission limit of 650 mg/mn^3. Concentrations of carbon monoxide (CO) and total organic carbon (TOC) are extremely variable at some operating schedules of combustion boilers. The variability of these concentrations indicates that there are unstable aerodynamic conditions in the combustion device. The causes of this aerodynamic instability have been studied. The mode with stable aerodynamic conditions, for which emission concentrations of CO and TOC are relatively stable, has been determined.

Keywords: biomass, residues, combustion, emission, measurement

1. Introduction

The combustion plants, especially for the wood fuel, wood residues and other biomass combustion, are often located near residential homes and therefore they are under a direct visual control of the inhabitants. The plants take an interest in reducing their negative impact or negative impression (of the black smoke) of the inhabitants without a more distinct investment.

Wood represents one of the oldest materials used for heat and energy generation via direct or indirect burning. As fuel, wood can be evaluated similarly to any other solid fuel in accordance with the following criteria:

INTECH
open science | open minds

© 2016 The Author(s). Licensee InTech. This chapter is distributed under the terms of the Creative Commons Attribution License (http://creativecommons.org/licenses/by/3.0), which permits unrestricted use, distribution, and reproduction in any medium, provided the original work is properly cited. CC BY

1. chemical composition
2. combustion heat and calorific value
3. volatile matter content
4. ash content

The chemistry of wood combustion is a complex process. In a flame, there are many thermo-degradation and oxidation reactions accompanied by the formation and interactions of radicals. However, as a result of these reactions, in the flue gas created during the wood combustion not only carbon monoxide (CO) and NO_x are present but also some other dangerous substances: CO_2, H_2O, N_2, and unreacted surplus O_2. Moreover, in the imperfect oxidation of volatile matter products in the combustion chamber, the flue gas of wood contains different hydrocarbons, which concentration can be—from the point of view of the emission standards—expressed as total organic carbon (TOC). Wood contains more hydrogen than any other fuel which is the reason why significantly more hydrocarbons are created during its combustion. For this reason, the problem of hydrocarbon emissions from combustion can be considered to a certain degree as a specific problem related to the wood combustion process.

Other harmful substances, such as, for example, polycyclic aromatic hydrocarbons (PAU), are not represented in wood structure. Their presence in flue gases is clear evidence of synthetic reactions in a flame. The original loosely connected cyclic hydrocarbons of wood are loosened in a flame and they condense at higher temperatures. In different furnaces, these PAU can reach a significant ratio from the total hydrocarbon emissions in flue gas [1]. Combustion of wooden waste with chlorine is a particularly serious problem. Such waste comprises residues of chipwood boards on a urea–formaldehyde (UF) resin basis with a NH_4Cl catalyser as well as surface materials (polyvinyl chloride, PVC). The aforementioned catalyser until recently was almost the only hardener of UF resins used. In 1 kg of particle board is there from 1 to 3.5 g of Cl. Theoretical calculation leads to chlorine concentration values (or HCl, resp. Cl^-) in flue gas from 100 to 400 mg/m^3 [2]. These concentrations significantly exceed present emission limits.

Fuels with the compound ratio of phenol character and chlorine are the reason for a high probability of dioxin formation. Theoretically, a very low concentration of chlorine in fuel is sufficient for the formation of a trace concentration (in ng/m^3) of these toxins. Possible ways of such formation are suggested by [3].

In order to monitor the quality, optimisation and regulation of the wood combustion process, the most advantageous way is to use the measurement of CO and NO_x concentrations and the O_2 content in flue gases [4].

The quality of wood and wood waste combustion in an enclosed combustion chamber depends on the water content and chemical composition of the wood itself and on combustion parameters. Combustion parameters of particular importance include:

- temperature in the combustion chamber,
- manner in which the individual phases of burning are separated,

- the surplus of air and its distribution into primary, secondary and even tertiary combustion processes,
- the thoroughness with which flammable gas mixes with air, and
- time (retaining period) during which flammable gas components are mixed with oxygen at the required reaction temperature (homogeneous oxidation).

The impact of the above-mentioned factors influencing the combustion quality and the harmful substances formation is detailed in **Figure 1**.

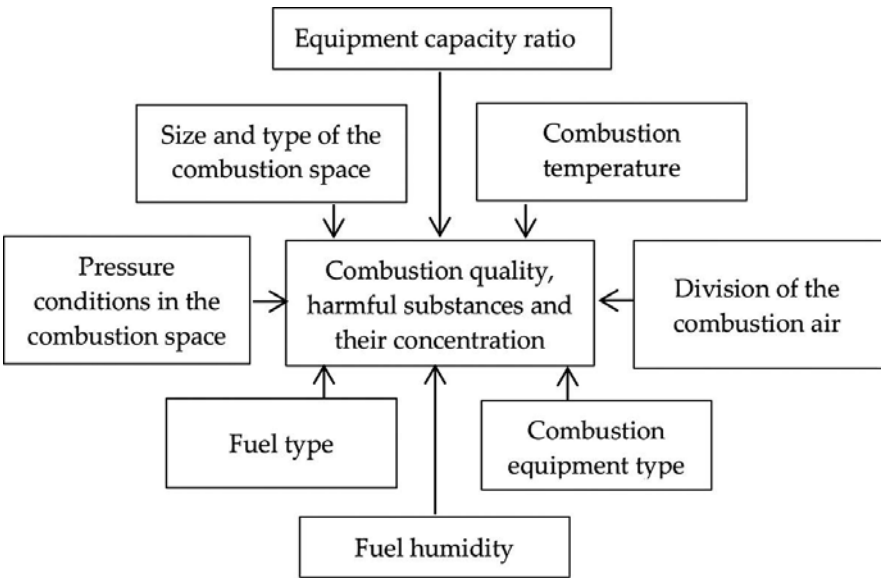

Figure 1. Impact of the factors influencing the combustion quality and the harmful substances formation (ratio of the equipment capacity in relation to the nominal capacity).

For energy generation from wood and wooden waste, different types of combustion equipment are used, which can be divided into:

- single stage
- two stage.

Single-stage combustion equipment can be characterised by one common space for the thermal decomposition and combustion of formed gaseous flammable products. According to the construction and characteristics of the burned wood, they can be divided into the combustion equipment for:

1. combustion of dry wood with humidity of $W < 30\%$, the most suitable here is grate combustion equipment;

2. combustion of wet wood with humidity of $W > 30\%$, where combustion equipment with lower fuel supply and fluid ones are mostly used.

Two-stage combustion plants burning wood and wood waste comprise a preheating firebox (first stage) and secondary combustion chamber (second stage). The wood is partially broken down by pyrolysis and gasification in the preheating firebox through oxidation. In the second stage, the gaseous products from the first stage (primarily carbon monoxide and hydrocarbons) are burned with an appropriate surplus of air. The two-stage combustion equipment is mostly suitable for combustion of dry ($W < 30\%$) pieces of wood and wooden waste or wood chips.

Experimental combustion tests are highly important for boiler operation regulation optimisation and accomplishment of the lowest emissions possible from wood and waste [5, 6]. Practical boiler regulation is varied from manual to various levels of automation and sophisticated solutions [7]. The boiler regulation demands operation optimisation and also regulation from the viewpoint of emissions [8].

From the viewpoint of minimising emissions, the request for correct biomass and varied wood waste (postconsumer wood, medium fibreboard (MDF) bound by UF resin, particleboards bound by UF resin, particleboards bound by UF resin with lamination coating on the basis of melamine-urea-formaldehyde resin) in boiler operation is particularly characteristic. Values of contaminating substance concentrations in waste gases are influenced not only by combustion technique, fuel humidity and calorific value of fuel but also by the method of fuel feeding, its dimensions, composition, etc. [9, 10]. One problem in minimising emissions is also the high percentage of volatile combustibles in biomass. In fact, there is no universal wood combustion device that can be used for every kind of biomass. Wood-based waste processing materials that have been processed with different types of adhesives, coatings and preservatives are extremely difficult to recycle as a raw material [11]. The authors of the work [12] spring harvested corn stover used for direct combustion in a 146-kW dual chamber boiler designed for wood logs. Combustion trials were conducted with corn stover and wheat straw round bales in a 176-kW boiler [13].

New combustion plants generating electricity from biomass must comply with best available techniques (BAT) requirements. Detailed knowledge of the impact of combustion parameters on the formation of emissions is critical when developing such plants and in efforts to achieve additional reductions in emissions from existing plants. Emissions are minimised over the long term by using the lessons learned from monitoring emissions across a broad range of combustion plants fuelled by various types of biomass. This chapter is focused on resolving problems related to minimising emissions from the combustion of biomass.

The aim of this chapter is to analyse the process of the biomass fuel and residues combustion and the emission production on the basis of emission measurements during the model combustion testing, and to propose solutions for minimising the emission of the investigated combustion plants.

After preliminary evaluation of the structural design of the combustion plant and analyses of the biomass fuel or residues, it was decided to analyse in detail the process of combustion on

http://dx.doi.org/10.5772/63793

the observed combustion plants. On the basis of proper measurements and in the context of the theoretical and practical knowledge of the combustion, we will:

- analyse the time behaviour for emissions from four types of wood boilers,
- specify the causes of the negative influences of operating the combustion plant on polluting the atmosphere,
- evaluate the possibilities for reducing emissions on the basis of time behaviour hereof and propose in what ways and means (the proposal of alternative solutions) it would be possible to co-ordinate outputs of the sources of the air pollution with the requirements of the Air Quality Act and belonging regulations,
- modify the usual mode of boiler operation, so that considerable reduction of ambient air burden by emissions is achieved,
- define how as much as possible to reduce the impact of the plant on the neighbouring residential area with respect to the requirement of the reasonable expenses for the implementation.

2. Experimental

The results of producing the pollutants were achieved in the different combustion plants of low and medium capacity when burning various kinds of biomass fuel or residues. The generalisation of the results will be realised on the basis of comparing the experimental results with the results of producing the pollutants in the standard wood combustion plants.

2.1. Materials

Cuttings of dry native wood, other biomass and waste from fibreboards, particleboards and other wood materials were used as fuel. The kind of combusted biomass fuel and residues during the emission experiments in combustion plants:

- residues of a Sorghum biocolor var saccharatum (L.) Mohlenber,
- residues of dry native wood with lengths up to 0.75 m,
- residues of beech and pine lumber, and cuttings after drying,
- large-surface residues of medium fibreboards (MDFs) bound by the UF resin,
- large-surface material (waste of particleboards bound by the UF resin) with lamination coating on the basis of melamine-urea-formaldehyde resin (two sorts),
- large-surface residues of particleboard bound by the UF resin with lamination coating on the basis of the melamine-urea-formaldehyde resin,
- residues of plywood bound by the UF resin,

- crushed briquettes produced from a mixture of waste from particleboards (90%) and natural wood (10%),
- the two-stage combustion equipment for wood and wood waste combustion comprise a pre-furnace chamber, where the wood pyrolyses/gasifies by partial oxidation; subsequently, in the second phase the gaseous products and the carbon monoxide are burned with the respective air surplus for gaseous fuel. The two-stage combustion equipment is mostly suitable for combustion of dry (W < 30%) pieces of wood and wooden waste or wood chips.

2.2. Methods

Boilers with discontinuous and continuous feeding were monitored. The broader characteristic of these boilers will be described in this chapter.

There were eight types of boilers used as the subject of research interest:

Boiler 1: a boiler with a stationary horizontal grate with thermal input of approximately 200 kW for heat production for a small manufactory shop. The remains of a *Sorghum biocolor var. saccharatum (L.) Mohlenber* shrub had originally been burnt in the boiler. Black smoke and unmeasurably high concentrations of CO and total organic carbon (TOC) emissions led to a boiler shutdown. An effort was made to keep this shop in a marginal zone and to verify the possibility of using another type of fuel with the aim of reducing emissions. An experiment with combustion of native wood briquettes was realised. During the experiment, manual briquette feeding was realised once per 60 min.

Boiler 2: a gasifying boiler with a nominal output of 99 kW for combustion of piece rests of dry native wood residues with lengths up to 0.75 m from furniture production. Feeding of fuel to the boiler was performed manually. The normal operator's dosage period was 40–60 min.

Boiler 3: a two-stage combustion boiler with manual regulation of primary air. The original nominal output of the grate boiler was 3.3 t/h of steam with a nominal temperature of 173°C and operational pressure of 0.75 MPa (2.5 MW). Firewood with a maximum consumption of 500 kg/h was the original nominal fuel capacity of boilers. The original boiler was adapted in such a way that a primary combustion chamber was added to it and the original combustion chamber served as a secondary combustion chamber. Types of firewood and waste wood were as follows:

- Beech and pine waste lumber, and cuttings after drying;
- Large-surface waste of medium fibreboard bound by UF resin;
- Large-surface waste of particleboards bound by UF resin;
- Large-surface material (waste of particleboards bound by the UF resin) with lamination coating on the basis of melamine-urea-formaldehyde resin.

Boiler 4: an automated warm-water boiler for waste wood combustion with a thermal input of 318.6 kW. Crushed briquettes produced from a mixture of waste from particle boards (90%) and natural wood (10%) production were combusted in the warm-water boiler. Particle boards

were produced on the basis of urea–formaldehyde resins or phenol–formaldehyde resins and were laminated with melamine resin and ABS foil. Edge-forming bands of polyvinyl chloride (PVC) were not used.

Boiler 5: a two-stage combustion boiler with capacity of 0.6 MW. In the pre-furnace chamber, the dosed fuel comes to a slope grid where it is pre-dried. Subsequently, the fuel falls to a horizontal grate where it is gasified by the substochiometric content of primary oxygen. The flammable gases formed burn out after mixing with the secondary air in the afterburning chamber under the boiler. Dosing of the fuel into the boiler can be automated or manual, therefore it is ideal for studying the operation modes.

Boiler 6: a two-stage combustion boiler with capacity of 4.1 MW with partial recirculation of flue gas. In the primary combustion chamber, there is a slope grate under which the strictly regulated primary combustion air is driven. Secondary combustion air and recirculated flue gas are driven to the entrance to the secondary combustion chamber. The boiler power and the addition of the combustion air are automatically regulated by variators on the basis of measurement of actual thermal parameters in different points of the combustion chambers and pressure.

Boilers 7 (MA 23) and 8 (PU 25) for case study: The object of power, emission and safety operational testing was hot water boiler MA 23 for gasification of wood logs with nominal heat output of 23 kW (**Figure 2(a)**), and hot water boiler PU 25 with automatic feed fuel with nominal output of 23 kW (**Figure 2(b)**).

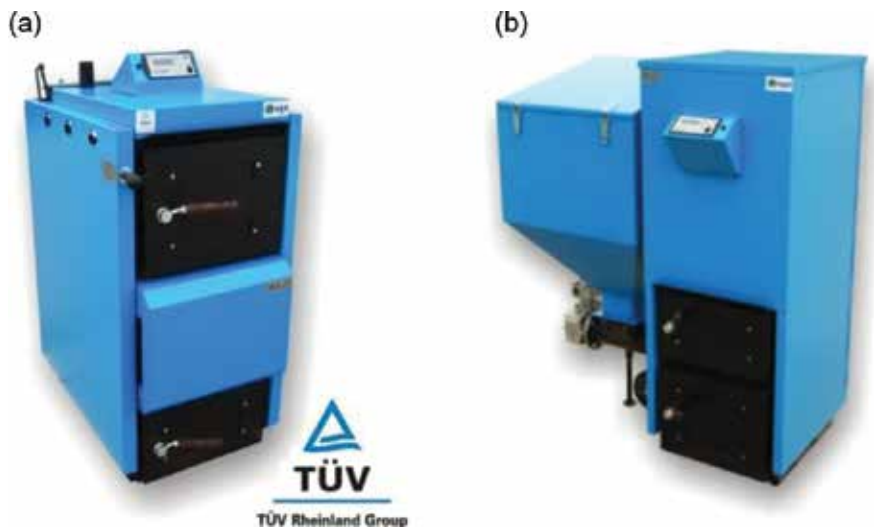

Figure 2 (a) Gasification boiler MA 23 and (b) automatic boiler PU 25.

The boilers are equipped with electronic temperature controller and a temperature safety fuse. Condition of the boiler and of its accessories was tested in accordance with the standardly supplied technical documentation. During testing, the influence of the conditions of fuel

combustion on emissions was experimentally verified, as well as resistance to thermal overloading of the boiler and of equipment for removal of excess heat. Spruce wood with a moisture content of 10% and a calorific value of 15,266 MJ/kg was used as a test fuel, and for the boiler 25 PU we used pellets with a calorific value of 16.5 MJ/kg [14–17].

2.3. Emission measurements during the wood waste combustion

Measurement of gas emissions was executed in line with standards (STN EN 15058:2007; STN EN 14789:2006; STN EN 12619:2013; STN ISO 7935:1992).

CO, NO_x and O_2 concentrations were quasicontinual measured with automatic analyser of furnace gases—ECOM SG-Plus from the RBR COMPUTERTECHNIK (Germany) on electrochemical principle and continuously measured with a HORIBA Enda 600 and Pg analyser (Japan), acting on the physical principle of non-dispersive infrared (NDIR) spectroscopy.

Organic substance emissions expressed as total organic carbon (TOC) were continuously measured with a BERNATH ATOMIC analyser (Germany), acting on the principle of flame ionization detector (FID) and ThermoFid analyser.

Calibration gases were delivered came from the delivery of the Linde Gas k.s. Slovakia.

Solid pollutant emissions were measured using a gravimetric method after a representative isokinetic sample was taken in accordance with STN EN 13284-1. Before the representative sampling process, at the measuring point, a speed profile of the air mass was measured in the piping using a Prandtl tube. The representative sample taking process at the measuring point was executed at several measuring points of the piping cross section. The measuring points were selected in order to ensure an objective sample taking from the whole piping cross section.

Smoke darkness measurements were conducted according to opacity in the Bacharach scale with a BRIGON company appliance (Germany).

3. Results and discussion

Model combustion testing and measurements of emissions have analysed the process of production of pollutants in the process of biomass fuel and residues combustion. The particularities of various kinds of biomass manifest themselves also through various thermochemical characteristics, affecting the combustion and pyrolysis processes [18, 19]. Many combustion devices are manually regulated and/or do not have regulation of biomass combustion parameters in combination with emission values of contaminating substances (°C, concentrations of CO_2, C_{CO}, C_{TOC} and C_{NOx}). The knowledge of biomass—combustion technique—combustion conditions—emissions interactions is an essential prerequisite in these cases for minimising emissions from manually regulated combustion devices.

When combusting the remains of a *Sorghum biocolor var. saccharatum (L.) Mohlenber shrub* in boiler 1 with a stationary horizontal grate, we were searching for the causes of low-quality burning. The remains of the shrub were thin and burned quite rapidly. As a consequence of

large burning velocity, no complete oxidation of burning products took place. We supposed for this reason that the CO and TOC emissions were above the measurement ranges of analysers (⊚10,000 ppm). We have not yet encountered a similar case in professional sources. Recognition of the causes of high concentrations of CO and TOC in flue gases enables the identification of solutions to minimise emissions from small boilers that currently are a long way off from the state of the art.

A reduction of burning velocity can be achieved through addition of native wood briquettes. Native wood briquettes have a high density (approximately 1.1 kg/dm^3) that is incomparably higher than the density of the shrub (approximately 0.29 kg/dm^3). When combusting native wood briquettes in this boiler, a marked reduction in black smoke and gaseous contaminating substances (**Figure 3**) was achieved. At smaller differences in the biomass density, such marked differences probably would not have become evident. Results from the combination of thermogravimetric and differential thermal analysis (TG/TGA) of six species of wood show that there is no connection between the wood density and the parameters characterising the burning process [20].

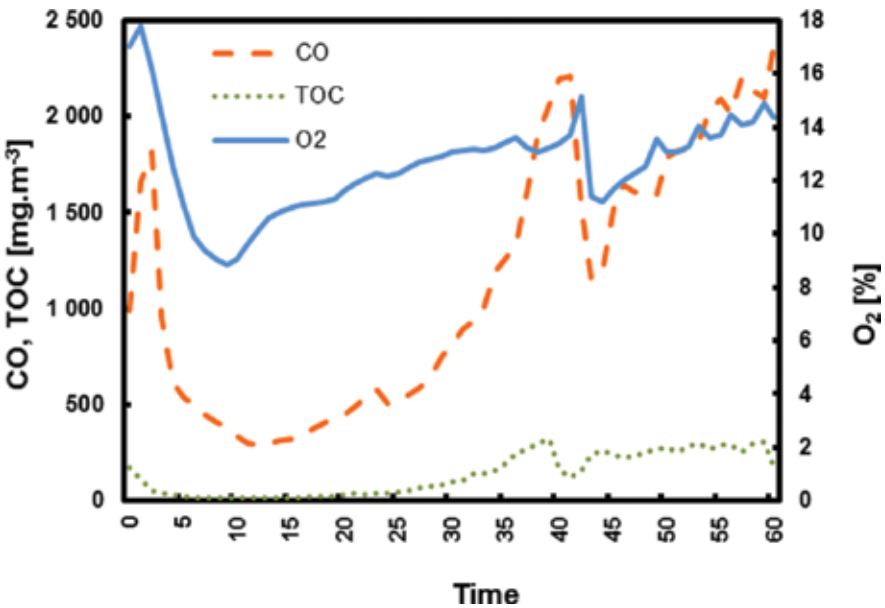

Figure 3. Trend in the emissions of CO, TOC and O_2 during combustion of wood briquettes.

The time behaviour of contaminating substance emissions (in recalculation to reference oxygen, 11% O_2) was monitored within the whole interval, starting with fuel feeding. Mean values of CO, NO_x, TOC and O_2 concentrations were recorded in 1-min intervals. The time behaviour of smoke darkness was monitored in 5-min intervals.

Measuring points were located in a vertical duct system behind a waste gas fan.

It can be seen that after briquette feeding, the CO concentration increases sharply. Then, a stable phase of briquette burning sets in at oxygen contents in waste gases of approximately 9–13%. An emission extreme at a burning time of 35–40 min can indicate unstable aerodynamic conditions in the furnace, for example, collapse of a uniform fuel layer in the furnace. Morissette et al. [13] measured average emissions of CO, NO_x and SO_2 for burning corn stover 2725, 9.8 and 2.1 mg/m^3 and average emissions of CO, NO_x and SO_2 for burning round bales 2210, 40.4 and 3.7 mg/m^3. It is interesting that changes in nitrogen oxides were correlated with changes in oxygen content (**Figure 4**) [13].

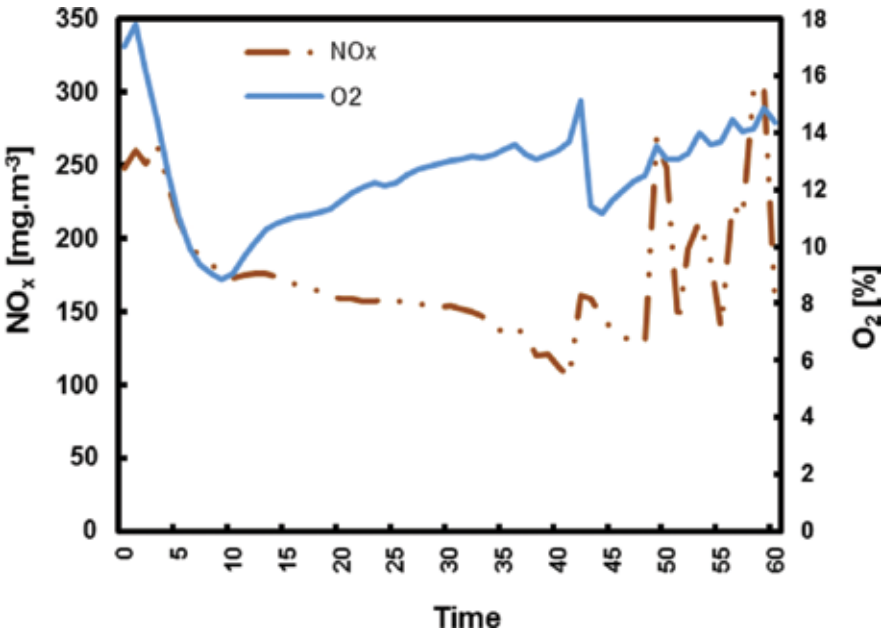

Figure 4. Trend in the emission of NO_x and O_2 during combustion of wood briquettes.

As emerged from these results, an acceptable solution could be more frequent feeding of a smaller fuel quantity at shorter intervals. This was confirmed by consequent analysis of the causes of dark smoke formation in the gasifying boiler with a nominal output of 99 kW. An experimental laboratory investigation was carried out to study the NO_x formation and reduction by primary measures for five types of biomass (straw, peat, sewage sludge, forest residues/Grot and wood pellets) and their mixtures in the work [21]. They found that NO_x emission levels were very sensitive to the primary excess air ratio and an optimum value for primary excess air ratio was seen at about 0.9. Conversion of fuel nitrogen to NO_x showed great dependency on the initial fuel-N content, where the blend with the highest nitrogen content had lowest conversion rate.

The gasifying boiler 2 with a nominal output of 99 kW often produced dark smoke. A demand was made to elaborate a proposal of technical-organisational measures for at least partial elimination of this negative aspect of power-producing use of piece rests of dry native wood

residues with lengths of up to 0.75 m from the furniture production. The boiler was expected to fulfil a single emission limit smoke darkness. The boiler operator was asked to periodically load fuel to the combustion chamber, to check temperature and pressure in the heat exchanger and to clean the device periodically. However, the regularity of feeding fuel from the viewpoint of emission minimisation was unknown. It was likewise unknown what the impact on concentrations of contaminating substances would have been for feeding dry, moist or even wet wood. The analysis of the time behaviour of emission creation on the basis of quite simple measurement of smoke darkness with proposed changes in feeding indicated possibilities for solving the problem of dark smoke creation (**Figure 5**).

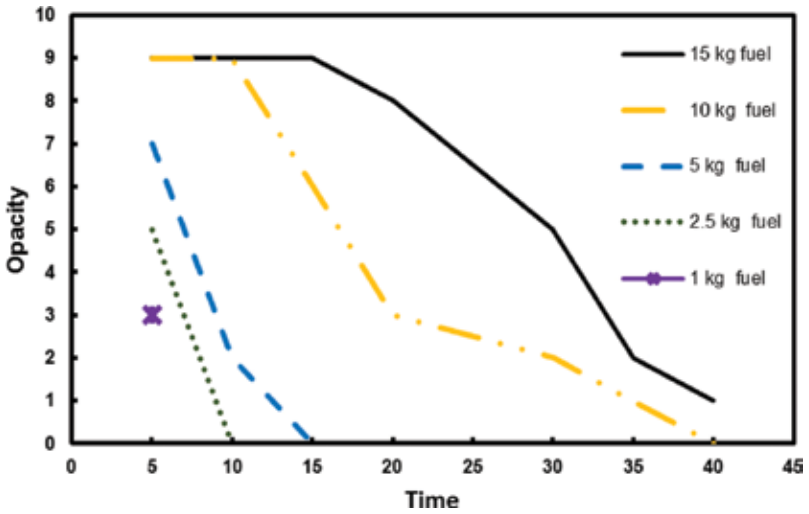

Figure 5. Trends in time behaviour of smoke darkness (opacity in the Bacharach scale) development from time of feeding of dry native wood residues with lengths of up to 0.75 m in the gasifying boiler.

By virtue of monitoring burning velocity, it can be said that this process is extremely rapid and thus highly susceptible to the formation of emission maxima. However, only dry native wood residues with lengths of up to 0.75 m are formed in operation. The combustion without emission maxima is for this reason possible only upon precise, uniform feeding at short time intervals.

The adaptation of an original one-stage combustion device with an output of 3.3 t/h of steam to a two-stage combustion device (boiler 3) did not bring an expected reduction in emissions when combusting dry fuel. In the first phase, after feeding beech and pine waste lumber and cuttings after drying into the boiler, black smoke originates even at sufficient oxygen concentration of 11.6%. During this phase, the CO concentration was approximately 30,000 mg/m^3, TOC was approximately 1300 mg/m^3 and NO_x was approximately 92 mg/m^3. Dry wood burns quite rapidly after feeding and after black smoke appeared for several minutes with extremely high CO and TOC concentrations. These are products of wood tar and non-oxidised carbon.

When combusting boards bound by UF resin, a slower burning and a smaller emission extreme are visible in comparison with combustion of beech and pine waste lumber and cuttings after drying. After combustion of large-surface waste of particleboards bound by UF resin, no production of dark smoke was observed. When combusting large-surface material (waste of particleboards bound by UF resin) with lamination coating on the basis of melamine–urea–formaldehyde resin, the entire burning process took place in a steady phase; this is seen from the course of CO and TOC concentrations (**Table 1**).

Time from fueling (min)	Oxygen content (%)	Concentration (mg/m³)		
		CO	TOC	NO_x
0–2	10.9	331	7	248
2–6	11.1	342	<5	234
6–10	11.9	292	<5	273
10–14	13.7	59	<5	316
14–18	12.4	263	9	271
18–20	15.3	28	14	312

Table 1. Concentrations of contaminating substances recalculated to oxygen content in waste gases of 11% from the combustion of particleboards with lamination coating on the basis of melamine–urea–formaldehyde resin.

N.M.	$T_{fuel\ gas}$ (°C)	Output (%)	Oxygen content (%)	Concentration (mg/m³)		
				CO	TOC	NO_x
1	145	60–63	15.34	2312	524	811
2	120	60–65	17.98	3626	781	925
3	132	65–70	17.00	2147	608	1017
4	130	70–75	18.91	4606	354	896
5	131	65–70	18.52	3301	263	985
6	135	70–75	17.49	2598	162	864
7	134	75–80	18.96	6744	298	821
8	136	8081	18.72	3852	251	923

Table 2. Summary of measured average half-hour emission values under conditions set as a standard with primary and secondary combustion air from boiler 4.

In small furniture shops, the interest in using their own waste, such as particleboards (PB), fibreboards (FB), or shaped pressed parts, for producing power has been increasing. However, securing conformity with the legal demands for air quality control is questionable. The study

of the thermo-degradation processes of adhesives and preservatives has led to useful results [22–24]. Information on thermodegradation of particleboards impregnated with various adhesives has been previously published in the works [25–27]. Our previous experiments under operational conditions showed that the impact of different binders in waste wood on CO emissions was slightly significant [4]. A similar result was obtained under laboratory conditions [26]. From a comprehensive analysis of results, it is clear that the thermal data and calorific value of biomass and biomass waste, in particular industrial wood waste, cannot be used as a basis for a regulation of the combustion process with the aim of minimising emissions.

The above-mentioned analysis results were also confirmed when examining the impacts of operational parameters of the automated warm-water boiler 4 on the concentrations of contaminating substances in waste gases. The results of the measurement of emissions under conditions of boiler operation set as a standard are given in **Table 2**.

We then optimised boiler operation precisely for the given kind of fuel. Results of emission measurements after the optimisation at the boiler output of 100% are given in **Table 3**.

N.M.	$T_{fuel\ gas}$ (°C)	Output (%)	Oxygen content (%)	Concentration (mg/m^3)		
				CO	TOC	NO_x
1	152	100	9.22	123	13	521
2	156	100	10.40	133	13	556
3	158	100	10.16	126	12	521
Stability control: average values						
4-8	159	100	9.81	97	11	508

Table 3. Summary of measured average half-hour emission values after optimisation of boiler 4's operation.

All of the results of emission measurement analyses under operational conditions show that waste combustion of particleboards in smaller wood boilers can also be optimised in such a way that the demands of emission limits are met. It arises hereafter from these results that modelling results for combustion emissions of industrial waste wood cannot be realised at the same level as they are for optimal combustion of natural, pure wood [28].

Tables 4–7 show the results of different operation regimes and **Tables 8–10** show different wood waste on two-stage combustion equipment—boiler 5. In **Tables 4–10**, the humidity means relative humidity, and harmful substances concentrations represent values calculated at 11% oxygen content in flue gas. The measured values mean the averages of at least three half-hour averages of measured concentrations.

The emission characteristics of the two-stage combustion equipment in an automated operation **Table 4** shows that even the commonly available two-stage combustion equipment is not able to keep the concentrations of harmful substances within the emission limits, which is proven by the exceeding of the emission limits CO = 850 mg/mn^3.

Parameter	Unit	Measured value
Furnace type	Two-stage—pyrolysis pre-furnace	
Nominal power	0.6 MW	
Operation regime	Automated	
Fuel type	Wood chips (spruce)	
Humidity	%	40
Fuel consumption	kg/h	192
Flue gas		
Temperature	°C	199
O_2	%	12.8
Flue gas volume	mn^3/h	1432
Emissions (at O_r = 11%): average values		
TZL	mg/mn^3	*
CO	mg/mn^3	1093
NO_x	mg/mn^3	366

Notes: *Up to 60 mg/mn^3 also in experiments with another material, thus they are not stated in further tables.

Table 4. Emission characteristics of two-stage combustion equipment in an automated operation regime: boiler 5.

In further experiments with wood and wood waste combustion, increased attention is paid to the operation of combustion equipment in a dynamic (not stable) regime. Dynamic states in operation of the combustion equipment are caused by a discontinuous dosing, or by continuous but not steady fuel dosing as well as by the regulation of incoming air. Emission characteristics measurements of the combustion equipment in a dynamic operation state were decided purposely due to the fluctuating heat take off from combustion equipment. The necessity to monitor the emission characteristics during dynamic operation of the combustion equipment is caused also by the fact that the majority of the fuel combustion processes is the power regulation. The fuel and air dosing is within the power regulation derived from the parameters of the heat transfer medium and its production.

Even the two-stage combustion equipment is not able to eliminate the unsteadiness of fuel dosing. At the jump change of the dosing (loading of the furnace with the fuel), the oxidation conditions of organic gaseous substances and carbon monoxide become worse. After loading the fuel, CO concentration immediately grows rapidly (**Table 5**). At the same time, conditions for decreased conversion of fuel nitrogen into nitrogen oxides [29] and low concentrations of nitrogen oxides are created. Probably the second stage of the combustion in this type of equipment does not meet all the construction requirements in order to achieve a high level of oxidation of organic gaseous substances. According to our calculations, this fact is caused by low temperature in the combustion chamber at the second stage (cooled by the boiler) and because flue gas remains in the chamber for a short time period.

Parameter	Unit	Measured value
Furnace type	Two-stage—pyrolysis pre-furnace	
Nominal power	0.6 MW	
Operation regime	Manual dosing—once completely filled reservoir above the grate	
Fuel type	Wood chips (spruce)	
Humidity	%	49
Fuel consumption	kg/h	204
Flue gas		
Temperature	°C	223
O_2	%	13.7
Flue gas volume	mn^3/h	1486
Emissions (at O_r = 11%)—average values at the time after fuel dosing*		
CO	mg/mn^3	27,981
NO_x	mg/mn^3	181

Notes: *In initial phase after the fuel metering were measured max. values of CO.

Table 5. Emission characteristics of two-stage combustion equipment when burning wood chips (spruce) and manual dosage in the initial phase of the fuel dosing: boiler 5.

Parameter	Unit	Measured value
Furnace type	Two-stage—pyrolysis pre-furnace	
Nominal power	0.6 MW	
Operation regime	Manual dosing—once completely filled reservoir above the grate	
Fuel type	Wood chips (spruce)	
Humidity	%	49
Fuel consumption	kg/h	204
Flue gas		
Temperature	°C	210
O_2	%	18.3
Flue gas volume	mn^3/h	1486
Emissions (at O_r = 11%)—average values at the time after fuel dosing *		
CO	mg/mn^3	480
NO_x	mg/mn^3	257

Notes: *In the phase before the burn out were measured min. values of CO.

Table 6. Emission characteristics of the two-stage combustion equipment when burning wood chips (spruce) and manual dosing in the phase before fuel burning out: boiler 5.

In manual fuel dosing, the last phase before the next dosing is the burn out phase. In this short phase, there is only the pyrolytic carbon and ashes in the primary combustion chamber. No gaseous organic substances are formed and CO concentrations are on the lowest level (**Table 6**).

In **Table 7**, average values are listed for the operation parameters and emissions during the whole fuel burning process under manual dosing—from loading until the end of continuous burning (up to 18% oxygen content in flue gas), immediately before the next fuel dose. When comparing the results of carbon monoxide and nitrogen oxides emissions measurements during the automated regime (**Table 4**) and manual regime (**Table 7**), it is evident that CO concentrations are at a higher level with manual dosing, and on the other hand, NO_x concentrations are higher with automated dosing. The automated dosing regime is stable without emission extremes of carbon monoxide concentrations. With manual fuel dosing, there are phases with high concentrations and low production of nitrogen oxides.

Parameter	Unit	Measured value
Furnace type	Two-stage—pyrolysis pre-furnace	
Nominal power	0.6 MW	
Operation regime	Manual dosing—once completely filled reservoir above the grate	
Fuel type	Wood chips (spruce)	
Humidity	%	49
Fuel consumption	kg/h	204
Flue gas		
Temperature	°C	218
O_2	%	11.6
Flue gas volume	mn^3/h	1486
Emissions (at O_r = 11%)—average values at the time after fuel dosing*		
CO	mg/mn^3	3537
NO_x	mg/mn^3	248
Phenol	mg/mn^3	6.4*
Formaldehyde	mg/mn^3	15*

Notes: *Average for the whole phase from dosage to the end of steady burning.

Table 7. Emission characteristics of the two-stage combustion equipment when burning wood chips (spruce) and manual dosing during the whole fuel burning phase: boiler 5.

In this boiler, very good results of CO concentrations were reached when burning spruce bark with steady manual dosing (**Table 8**). Higher nitrogen content in spruce bark (N^{daf} = 0.38%) in comparison to spruce wood (N^{daf} = 0.04%) was manifested in higher NO_x concentrations.

Parameter	Unit	Measured value
Furnace type	Two-stage—pyrolysis pre-furnace	
Nominal power	0.6 MW	
Operation regime	Steady manual dosing*	
Fuel type	Spruce bark	
Humidity	%	35
Fuel consumption	kg/h	100
Flue gas		
Temperature	°C	211
O_2	%	12.0
Flue gas volume	mn^3/h	1491
Emissions (at O_r = 11%)—average values in the steady combustion phase		
CO	mg/mn^3	202
NO_x	mg/mn^3	397

Notes: *In amounts approx. 15 kg each 9 min.

Table 8. Emission characteristics of the two-stage combustion equipment when burning spruce bark and steady manual dosing: boiler 5.

Parameter	Unit	Measured value
Furnace type	Two-stage—pyrolysis pre-furnace	
Nominal power	0.6 MW	
Operation regime	Steady manual dosing*	
Fuel type	Remains from PF plywood	
Humidity	%	8
Fuel consumption	kg/h	180
Flue gas		
Temperature	°C	224
O_2	%	10.4
Flue gas volume	mn^3/h	1468
Emissions (at O_r = 11%)—average values in the steady combustion phase		
CO	mg/mn^3	11
NO_x	mg/mn^3	382

Notes: *In amounts approx. 36 kg each 13 min.

Table 9. Emission characteristics of the two-stage combustion equipment when burning remains from PF plywood and steady manual dosing: boiler 5.

In **Tables 9** and **10**, CO and NO_x concentrations are listed in flue gas from waste combustion —waste from the plywood on a phenol–formaldehyde resin basis and chipwood boards on a urea formaldehyde resin basis. In both cases, low CO concentrations in flue gas were measured, which is caused by high calorific value of dry remains. The UF resin significantly increases the nitrogen content in fuel, which results in high values for NO_x concentrations.

Parameter	Unit	Measured value
Furnace type	Two-stage—pyrolysis pre-furnace	
Nominal power	0.6 MW	
Operation regime	Steady manual dosing*	
Fuel type	Remains from UF DTD	
Humidity	%	7
Fuel consumption	kg/h	140
Flue gas		
Temperature	°C	225
O_2	%	10.8
Flue gas volume	mn^3/h	1426
Emissions (at O_r = 11%)—average values in the steady combustion phase		
CO	mg/mn^3	81
NO_x	mg/mn^3	1260

Notes: *In amounts of approx. 23 kg each 10 min.

Table 10. Emission characteristics of the two-stage combustion equipment when burning UF DTD remains and steady manual dosing: boiler 5.

Boiler no.	Boiler 5 two-stage 0,6 MW	Boiler 6 two-stage 4,1 MW
Ratio of the waste from chipwood board (%)	35	50
Content of O_2 (%)	14.3	13.3
CO (mg/mn^3)	172	88
NO_x (mg/mn^3)	588	503

Table 11. The results of measurements of pollutant emissions (as averages of three half-hour values calculated for 11% O_2) in flue gas from wood waste from furniture production.

Another goal of the emission limits measurements—when burning native wood and furniture residues from chipwood boards and MDF in boilers 5 and 6—was setting the highest possible ratio of this waste in order to keep to the emission limits. The results of our measurements

(**Table 11**) show that the combustion process itself is highly efficient and there are no problems to keep to the CO emission limits. In boiler 5, it is possible to keep to the emission limit for NO_x with a ratio of the chipwood board in fuel up to 35%. In boiler 6, the emission limit for NO_x 650 mg/mn^3 is maintained with a reserve with a ratio of chipwood board in fuel up to 50%.

In the past, extensive research was conducted on emissions from various combustion plants for wood and wood waste [4]. The set of emission measurements is from 31 types of combustion plants (prevailing output range of 20 kW–10 MW and combustion plants of standard and lower technical level) and 23 types of wood fuel and industrial wood wastes.

In order to evaluate a large number of emission measurement, we used the statistical method rotation in factor analysis. Varimax rotation is a useful statistical method used to simplify and better interpret the measuring results. We can identify and describe each variable with a single factor. The results of calculated varimax rotated factor matrix (**Table 12**) enable to identify the influence of combustion conditions on the production of CO, TOC and NO_x.

From the results of cited emission measurements, the factor analysis (**Table 12**) confirms the importance of precise oxide dosing (O_2) in the combustion space (variable/factor 1) for hydrocarbon emissions (C_xH_y) and carbon monoxide (CO). On the other hand, a type of wood fuel does not influence this factor of "good burning" (when respecting suitability for the given combustion plant). With important differences in oxygen content in industrial wood fuels, it is an influence of a kind of fuel (variable/factor 2) which is very important for producing nitrogen oxides (NO_x). At the same time, in the wide spectrum of analysed data, the variable/factor 2 confirms different and mutually opposing mechanism of producing pollutants of CO, TOC and NO_x.

Varimax rotated factor matrix		
Variable/factor	**1**	**2**
CO	0.6744	−0.5340
NO_x	0.1577	0.8720
TOC	0.8365	0.1244
O_2	0.8395	0.1660
Type of combustion plant	0.3858	−0.3569
Fuel sort	0.0166	0.8374

Table 12. Factor matrix of the results of measurements on the emissions from burning wood and wood wastes in various combustion plants.

This research shows further ways and means towards the realisation of measures to minimise emissions from the combustion of wood and wood waste. From the viewpoint of emission production, the decisive prevailing influence of the technique of wood waste combustion was proven in comparison with the influence of the chemical composition of wood waste. The knowledge and respecting the mechanism of producing pollutants are usable for regulation

of emissions from atypical combustion plants or generally for minimisation of emissions in combustion plants.

4. Case study: example of minimisation of emissions by appropriate boiler regulation

Emissions of individual pollutants at combustion of solid fossil fuels (black coal and lignite) and of biomass (wood pellets) in boilers can be found by the analyses of data obtained from different experiments or commercial measurements of emissions. Data for individual pollutants are described, for example, in the study [14] which summarises the most important findings concerning the production of pollutants at combustion of various fuels.

It is possible to see from the measurement results that combustion of biomass does not always directly reduce the amount of harmful emissions generated. An important factor is particularly the manner of combustion control, which is given by the method of fuel supply, simply speaking by stoking. The next section shows the method of regulation and of other modifications of the boiler MA 23, which resulted in reduction of emissions.

4.1. Comparison of the measured evolutions with expected ones

Stoichiometric analysis of fuel samples under normal conditions, and of reference oxygen content in the flue gas O_r = 11% corresponded to the excess air in the flue gas of n = 2.1. The values of thermal emission measurement in **Table 13** contain stoichiometric calculations, as well as the average values of measurements expressed as percentage of wet flue gas.

Volumetric combustion		Unit	MA23	PU25
Oxygen for combustion	O_{min}	mn^3/kg	0.815	0.906
Theor. air, dry	O^S_{air}	mn^3/kg	3.881	4.313
Excess air	n	–	4.464	2.220
Water in flue gas	V^{SP}_{H2O}	mn^3/kg	0.794	0.744
Real flue gas, dry	$V^{SP}_{real, S}$	mn^3/kg	17.286	9.537
Real flue gas, wet	$V^{SP}_{real V}$	mn^3/kg	18.08	10.282
Nitrogen oxides	NOx	% V/V	75.756	73.724
Carbon dioxide at n = 1	CO_{2max}	% V/V	16.515	16.97
Measured carbon dioxide	CO_2	% V/V	4.28	8.271
Oxygen	O_2	% V/V	15.8	10.765
Carbon monoxide	CO	% V/V	3.815	10.219
Water vapour	H_2O	% V/V	4.394	7.239

Table 13. Stoichiometric parameters.

It is evident from the results that increased oxygen content in the flue gas increases the CO content, that is, the component, from which it is still possible to extract some heat and to reduce thus the loss of the unused fuel. This observation leads us to the fact that gas did not get enough time to react with oxygen and to transform to CO_2.

Table 13 gives the percentage composition of real wet flue gas, when it is apparent that the percentage composition of the flue gas is affected also by the amount of flue gas. **Table 13** gives for comparison also the theoretical volume concentration of carbon dioxide at stoichiometric combustion, that is, with excess air $n = 1$. This is the maximum value of the carbon dioxide for a perfect transformation of carbon in the fuel, that is, an ideal state.

4.2. Analysis of hot water boiler MA 23

The boiler works on the principle of fuel gasification. It consists of two chambers situated one above the other. The upper chamber serves as a fuel reservoir with pre-burning, while the lower chamber serves as a combustion chamber and an ash pan, which allows perfect gasification of coal and wood. The bottom of the combustion chamber contains an afterburner chamber in which the wood gas and solid residues are burned. Supply of combustion air is realised by radial fan.

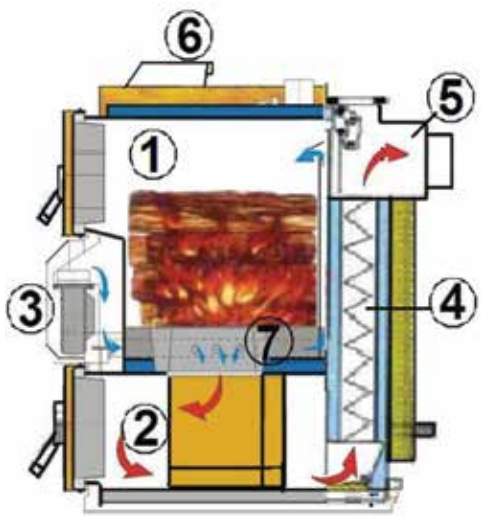

Figure 6. Hot water boiler MA 23—1. Stoking chamber, 2. Combustion chamber, 3. Fan, 4. Tube heat exchanger, 5. Chimney spout, 6. Electronic regulator, 7. Nozzle made of refractory concrete.

The boiler (**Figure 6**) provides a fuel pre-drying with subsequent gasification at higher temperatures. The primary air and secondary air are pre-heated and distributed in an ideal proportion to the centre of a fire and to the nozzle. The primary air is driven into the combustion chamber below the level of the upper door. Uniform distribution of pre-heated primary air ensures that the fuel gasification takes place gradually in small amounts of fuel. The boiler is

therefore economical and it has high combustion efficiency of 70–89% in the entire range of its power output. This arrangement allows better gasification of larger pieces of wood. The secondary air, which is fed to the gasification nozzle, is pre-heated to a higher temperature. The flame thus does not cool down and combustibles burn up completely. The lower combustion chamber is lined with refractory concrete in which the final burning of all solid particles, which fall down, takes place.

Figure 7(a) shows the original shaped piece through which the combustion air for secondary combustion was supplied by two large holes. **Figure 7(b)** shows the proposed shaped piece, which was also tested, through which the air was supplied along the longer side of the shaped piece by several holes. This resulted in a better reaction with the generated wood gas, in better burnout of gas and thus in the already mentioned reduction of emissions.

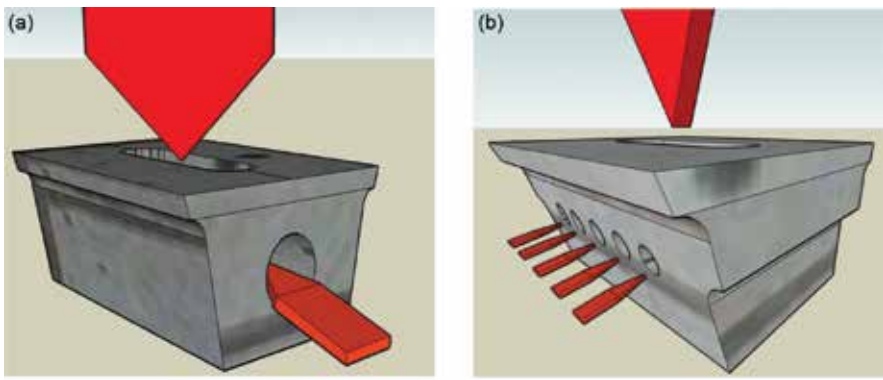

Figure 7. (a) Original shaped piece and (b) newly designed shaped piece.

Modification of combustion leads to reduction in generation of the gases we measured. The components of the produced gas have the ability to react with the incoming air to produce heat. Recording of the measured production of CO during the first test measurement (**Figure 7(a)**) of the rated heat output of the gasification boiler showed unsatisfactory results. Average value of carbon monoxide during two fuel charges without modification of the distribution of the combustion air, that is, with the initial fitting, was 2350 mg/m^3. The gasification boiler, therefore, had to undergo a modification of the combustion air and gas inlet into the space of the secondary combustion zone; this position is in **Figure 6** indicated by number 2. This newly designed fitting does not have one hole of larger diameter but five holes along the longer side for the supply of secondary combustion air and gas from the gasification chamber (see **Figure 7(b)**). Modification of combustion leads to lower productions of the gases we measured. Modification of the fitting affected the measured values of carbon monoxide, which were on an average of 830.3 mg/m^3. Such a result was expected and it was confirmed by measurements. The cause of this improvement consists in more even and planar supply of air. The air thus oxidises the active zone of the heating chamber in a wider area and greater volume. This brings a higher intensity of oxidisation and higher quality of combustion.

4.3. Verification and interpretation of the data obtained from the gasification boiler

Basic measurements by both direct and indirect methods were performed in accordance with the relevant standards and regulations for Slovak Republic, the Czech Republic and the EU. In the entire range from ignition to extinction (due to the need to compare modifications of equipment), we selected evaluation within the limits of water heated to 60°C up to 90°C, that is, within the temperature interval of the most frequently used operation. Our interest was to determine during this measurement the amount of CO (non-reacted fuel component) in dependence on the boiler output. We were also interested in the output water temperature in dependence on the flue gas temperature.

Average scatter is low due to the leap type control of the combustion air supply, when large fluctuations from the mean value are caused by the opening and closing of the air valves. **Table 14** presents the average values of the desired variables.

		Original state	New formed piece 1D	New formed piece 2D
P_{kot}	kW	19.2	19.3	18.5
CO	mg/m^3	2072.0	660.8	696.3
O_2	%	16.6	16.5	18.2
NO_x	mg/m^3	115.2	120.4	90.9
Output temperature	°C	79.6	79.3	79.4
Chimney temperature	°C	154.3	156.6	145.9
Temperature gradient	°C	17.2	17.3	16.6

Table 14. Average values of the desired variables.

Measurement of performance parameters of the hot-water boiler MA 23 was performed by erudite experts from the Department of Energy Technology, Zilina University (ZU) in Zilina, Slovak Republic. They made measurements of all the parameters cited in the paper. The records of the tests were prepared both in tabular form and in diagrams. The measurement was performed continuously beginning from the first ignition of the boiler. The total duration of measurement was 405 min with steps of 1 min. The records were evaluated by regression analysis of the measured values. The correlation coefficient for all dependencies varies from 0.9 to 0.95. On the basis of the derived regression relationship, it is possible to render flow diagrams of the main functions, such as an increase in boiler output in kilo Watt, as shown in **Figure 8**. Optimal values functions are represented on the line of optimal performance, that is, 23 kW. In **Figure 8**, the functions are extended up to the output of 90 kW for more efficient boilers. Evolution of functions can be equally well plotted in dependence on time in minutes. **Figure 8** shows very clearly that combustion occurring during the first few minutes after ignition is rather problematic and unstable until an output of at least 10 kW is achieved. Evolutions of functions are interdependent, and we used them for the proposal of regulation of the combustion quality and oxygen balance by the ventilator. The sensor for continuous

measurement of temperature is situated in the stack throat. The regulator controls in dependence on the flue gas temperatures and fluctuations of the draught in the revolutions of an auxiliary fan. The coefficient of progression is defined as a dimensionless ratio between an optimal oxygen balance and the real one in relation to the optimal boiler output and to the corresponding desired oxygen balance according to the fuel.

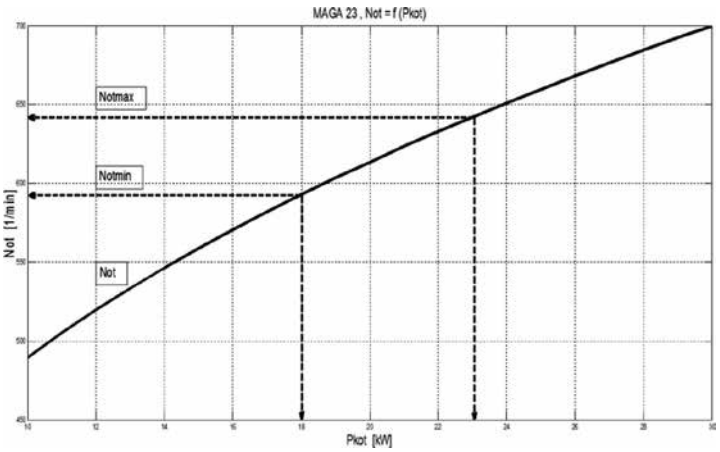

Figure 8. MA 23, fan revolutions in dependence on the power output.

A regression analysis was conducted on the basis of the data analysis in order to obtain description and prediction of the acquired dependencies and relationships between individual parameters. The analyses yielded in the following Eqs (1)–(12):

Dependence of draft in the chimney p_k on the power output P_{kot}:

$$p_k = 35.78498 + 2.0755 \cdot P_{kot} \;\; ; \;\; R^2 = 0.97 \tag{1}$$

Dependence of the chimney temperature t_k on the power output P_{ko}:

$$t_k = 124.14299 + 3.075308 \cdot P_{kot} \;\; ; \;\; R^2 = 0.93 \tag{2}$$

Progression coefficient of the oxygen balance K_{kb} to draft in the chimney p_k and optimal draft in the chimney p_{kOPT}:

$$K_{kb} = \frac{1.136 \cdot p_k}{p_{kOPT}} \tag{3}$$

Fan revolutions N_{ot} in relation to the power output P_{kot}:

http://dx.doi.org/10.5772/63793

$$N_{ot} = 10^{(2.265 + 0.325 \cdot \log(P_{kot}))} \tag{4}$$

Fan revolutions N_{ot} in dependence on the chimney temperature t_k:

$$N_{ot} = 10^{(2.265 + 0.325 \cdot \log(-1406.4927 + 49.81042 \cdot t_k - 0.69949 \cdot t_k^2 + 0.00494 \cdot t_k^3 - 1.75068 \cdot 10^{-5} \cdot t_k^4 + 2.49413 \cdot 10^{-8} \cdot t_k^5))} \tag{5}$$

Fan revolutions N_{ot} in dependence on the pressure in the chimney p_k:

$$N_{ot} = 10^{(2.365 + 0.325 \cdot \log(17.56402 + 0.4526 \cdot p_k))} \tag{6}$$

Values of emissions at the optimal power output (maximum power output) $P_{kotOPT} = P_{kotmax}$ = 23 kW. In Eqs (7)–(12), the following is valid:

$$CO_{prep} = -2912.68649 + 698.44724 \cdot P_{kot} - 55.35295 \cdot P_{kot}^2 + 1.48709 \cdot P_{kot}^3 \tag{7}$$

$$NOx_{prep} = -361.15795 + 79.64852 \cdot P_{kot} - 5.70241 \cdot P_{kot}^2 + 0.14407 \cdot P_{kot}^3 \tag{8}$$

$$CO_{ppm} = -2351.95047 + 578.63494 \cdot P_{kot} - 46.84466 \cdot P_{kot}^2 + 1.27787 \cdot P_{kot}^3 \tag{9}$$

$$CO_{cmg} = -1782.53905 + 438.61597 \cdot P_{kot} - 35.51257 \cdot P_{kot}^2 + 0.96881 \cdot P_{kot}^3 \tag{10}$$

$$NOx_{ppm} = -77.93008 + 17.32183 \cdot P_{kot} - 1.24033 \cdot P_{kot}^2 + 0.03233 \cdot P_{kot}^3 \tag{11}$$

$$NO_{ppm} = 49.76939 - 10.47717 \cdot P_{kot} + 0.47193 \cdot P_{kot}^2 \tag{12}$$

The maximum output occurs at P_{kot} = 23 kW, see Eqs (1)–(6). These values were obtained from the operational measurements p_k = 12.4475, t_k = 210.4638, K_{kb} = 1.136, N_{ot} = 642.

It follows from Eqs (7)–(12) that the values of emissions were obtained in this manner:

CO_{prep} = 1.9633 10^{+003} (value standardised at the normal conditions), NO_{xprep} = 207.0828 0828 (value standardised at the normal conditions), CO_{ppm} = $1.7237 \cdot 10^{+003}$, CO_{cmg} = $1.3070 \cdot 10^{+003}$, NO_{xppm} = 57.6966 and NO_{ppm} = 58.4455.

These values can be read on the straight line P_{kotmax}, while maintaining the maximum output. The mechanism of the combustion process in the boiler can be actively controlled and regulated by fan revolutions. The boiler operates in such a way that temperature in the chimney is measured continuously and depending on it, the fan revolutions are regulated, for example,

with use of PID controller. The fan speed will be set according to **Figure 8** at 642 rpm. Control of revolutions, that is, of the chimney draft, is an important parameter that helps to stabilise a fluctuating combustion process.

Eqs. (1)–(12), derived by analytical processing of the measured values, are used in solution for conversion of the basic combustion functions to complex mathematical model of the combustion process as it is graphically represented in **Figure 8**. This mathematical model is of interactive nature, and it helps in programming of the electronic controller.

5. Conclusions

The results of emission measurement analyses indicated that the standard practice of boiler operation with a lower level on measurement and combustion process automation that governs the combustion mode on the basis of calorific value, humidity of wood fuel and demanded boiler output is insufficient for minimising emissions. For this reason, an original task for each type of boiler with wood as a fuel is to define optimum conditions of the combustion process under which the lowest emissions possible are reached.

New lessons from our operating experiments concerning the production of pollutants during power generating using wood and wood waste are useful for reducing emissions:

- from small combustion plants,
- from unconventional combustion plants and in general to minimise emissions from other biomass combustion plants.

The results of analyses showed that the standard mode of operation for a particular wood boiler, as a result of large variability of wood fuel and waste wood properties, should be optimised by virtue of emission measurements.

The analysis of time behaviour for wood boiler emissions is a good basis for a theoretical analysis examining the possibilities for adaptation of the usual mode of boiler operation with the aim of reducing emissions.

The results of combustion mode adaptation in six types of boilers with smaller outputs show by virtue of emission measurements and according to the methodology worked out that when combusting wood of various dimensions (briquettes, cuttings) or waste wood cuttings (of fibreboards and particleboards bound by UF resin, and/or with lamination coating on the basis of melamine-urea-formaldehyde resin), it is possible to markedly reduce emissions and smoke darkness.

The purpose of design of gasification boilers consists in the most effective and most perfect combustion of volatile substances (especially carbon monoxide) in the secondary combustion zone. Insufficient amount of combustion air in the combustion nozzle leads to high emissions of carbon monoxide.

After analysis of the results of emission measurements, we proposed a new component of the boiler, that is, the shaped piece between the gasification and post-combustion chamber. This

modification reduced the values of emissions, so combustion occurred with higher efficiency and the values of the generated flue gas CO, CO_2 and other components of the flue gas got stabilised. We also proposed control of the combustion air supply.

The next modification concerns the electronic control. The tested gasification hot water boiler is equipped with a reliable microprocessor controller of the type G-403-P02, which provides control of air supply via fan on the basis of the input temperatures, which ensures a relatively wide range of boiler regulation between 30 and 100% of the rated power output of the boiler, as well as its safe operation. Combustion is then closer to the ideal, stoichiometric combustion, which manifests itself by the smallest possible air excess. This condition ensures us low production of flue gas and thus also of the resulting pollutants.

Acknowledgements

This research was supported by the Slovak Grant Agency VEGA under contract No. VEGA 1/0547/15 "Experimental measurement and modelling of fugitive emissions." This work was also supported by the Slovak Research and Development Agency under the contract No. APVV-0353-11 "A proposal and realisation of a pilot retort with reduced emissions for charcoal production in marginal zone and verification its application" and project ITMS 26210120024, the project of the Institute of Clean Technologies for Mining and Utilization of Raw Materials for Energy Use, Reg. No. LO140 and the project RMTVC No. LO1203.

Author details

Emília Hroncová[1*], Juraj Ladomerský[1], Ján Valíček[2,3,4] and Ladislav Dzurenda[5]

*Address all correspondence to: emilia.hroncova@umb.sk; emilia.hroncova@gmail.com

1 Department of Environmental Management, Faculty of Natural Sciences, Matej Bel University, Banská Bystrica, Slovakia

2 Institute of Physics, Faculty of Mining and Geology, Technical University Ostrava, Ostrava-Poruba, Czech Republic

3 Institute of Clean Technologies for Mining and Utilization of Raw Materials for Energy Use, Technical University Ostrava, Ostrava-Poruba, Czech Republic

4 RMTVC, Faculty of Metallurgy and Materials Engineering, Technical University Ostrava, Ostrava-Poruba, Czech Republic

5 Department of Woodworking, Faculty of Wood Sciences and Technology, Technical University in Zvolen, Zvolen, Slovakia

References

[1] Annon. Emissionsprobleme bei Holzfeuerungsantungen (Emission problems in wood combustion devices). Holz und Kunststoff 1986, VIII-IX:5–6

[2] Dickhäuser K. Verbrennung von Spanplattenabfällen. (Combustion of Particle Board Wastes). Holz und Kunststoff 1998, 4:388–391.

[3] Nesvadba J. Dioxins in the flue gas and residues from waste incineration plants. Air Prot. 1989, 2:103–107.

[4] Ladomerský J. Emission analysis and minimization from the wood waste combustion. Wood Res.-Slovakia 2000, 45:33–44.

[5] Horbaj P. Some notes on basic parameters, determination of empirical formula and incineration of solid municipal waste. Chem. Listy 2005, 9:694–702.

[6] Juszczak M. Experimental study of pollutant concentrations from a heat station supplied with wood pellets. Pol. J. Environ. Stud. 2011, 20:1519–1524.

[7] Prokhorenkov AM, Sovlukov AS. Fuzzy models in control systems of boiler aggregate technological processes. Comp. Stand. Inter. 2002, 2:151–159.

[8] Liang LG, Meng Y, Wu, SL. Study on combustion adjustment for optimal operation of a 1004 t/h boiler. Power Equipment 2010, 1:16–20.

[9] Horbaj P. Model of the kinetics of biomass pyrolysis. Wood Res-Slovakia 1997, 42:15–23.

[10] Dzurenda L, Geffertová J, Hecl V. Energy characteristics of the wood-chip produced from Salix viminalis – clone ULV. Drvna Industrija 2010, 61:27–31.

[11] Lin HC, Huang JC, Fujimoto Y, Murase Y. Analysis of gases emitted from particleboard combustion. Forest Prod. Ind. 2001, 20:165–174.

[12] Morissette R, Savoie P, Villeneuve J. Combustion of corn stover bales in a small 146-kW boiler. Energies 2011, 4:1102–1111. DOI: 10.3390/en4071102

[13] Morissette R, Savoie P, Villeneuve J. Corn stover and wheat straw combustion in a 176-kW boiler adapted for round bales. Energies 2013, 6:5760–5774. DOI: 10.3390/en6115760

[14] Grabic R, Danihelka P, Ocelka T, Dej M, Horák J. Emission of POPs from incineration of used oils in heat sources to 30 kW and to 233 kW power at presence of heavy metals. In. Conference proceedings "Dioxíny v prumyslu"[Dioxins in industry]. Cracow 1999.

[15] Valíček J, Müllerová J, Kuběna V, Koštial P, Harničárová M, Mikulík M. Emission distribution and regulation of local heat source. Defect and Diffusion Forum 2012, 326–328:330–334.

[16] Müllerová J, Hloch S, Valíček J. Reducing emissions from the incineration of biomass in the boiler. Chem. Listy 2010, 104:876–879.

[17] Müllerová J, Borovička A, Valíček J, Müller M, Hloch S, Lupták M. Method of power regulation of a gasification boiler. Patent CZ 302544 B6: Industrial Property Office; 26.05.2011; Czech Republic; 2011. p. 1–10.

[18] Zajemska M, Musiał D, Radomiak H, Poskart A, Wyleciał T, Urbania D. Formation of pollutants in the process of co-combustion of different biomass grades. Pol. J. Environ. Stud. 2014, 23:1445–1448.

[19] Wang Y, Wang X, Hu Z, Li Y, Deng S, Niu B, Tan H. NO emissions and combustion efficiency during biomass co-firing and air-staging. BioResources 2015, 10:3987–3998.

[20] Brostow W, Menard KP, Menard N. Combustion properties of several species of wood. Chem. Chem. Technol. 2009, 3:173–176.

[21] Houshfar E, Løvås T, Skreiberg Ø. Experimental investigation on NO_x reduction by primary measures in biomass combustion: straw, peat, sewage sludge, forest residues and wood pellets. Energies 2012, *5*:270–290. DOI: 10.3390/en5020270.

[22] Lin HC, Ohuchi T, Murase Y. Estimating thermal behavior and analyzing evolved species of adhesives through thermogravimetric analysis combined with spectrometric techniques. J. Fac. Agr. Kyushu U. 2004, 49:449–459.

[23] Lin HC, Ohuchi T, Murase Y, Tsai JT, Kao CC. CEM techniques and X-ray analytical microscope analysis for evaluating the combustion emissions and char of CCA- and ACQ-treated woods after QUV degradation. J. Fac. Agr. Kyushu U. 2008, 53:497–503.

[24] Lin HC, Murase YJ. Analysis of evolved species and estimation of the combustion emissions of PACB and AAC preservatives using TGA-IR and CEM techniques. J. Fac. Agr. Kyushu U. 2009, 54:223–229.

[25] Cichy W, Pawlowski J. Combustion of solid recovered fuels made from post-consumer wood waste in a power installation of low power. Drewno 2009, 182:25–63.

[26] Lin HC. Combustion emissions analysis of wood-based waste processing-materials. In: The Impact of Air Pollution on Health, Economy, Environment and Agricultural Sources, Mohamed K. Khallaf (ed.), InTech, Croatia 2011, 295–322.

[27] Cichy W. Combustion of plywood waste in a low-power boiler. Drewno 2012, 187:21–36.

[28] Saastamoinen J, Huttunen M, Kilpinen P, Kjaldman L, Oravainen H, Bostrom S. Emission formation during wood log combustion in fireplaces—part II: char combustion stage. Prog. Comput. Fluid Dy., An Int. J. 2006, 6:209–216.

[29] Dzurenda L, Ladomerský J, Hroncová E. Conversion factor of fuel-bound nitrogen to oxides in the process of spruce wood combustion in boiler grate furnaces. Pol. J. Environ. Stud. 2015, 24:505–509.

Chapter 2

A Combustion Process Optimization and Numerical Analysis for the Low Emission Operation of Pulverized Coal-Fired Boiler

Paweł Madejski, Tomasz Janda,
Norbert Modliński and Daniel Nabagło

Additional information is available at the end of the chapter

http://dx.doi.org/10.5772/64442

Abstract

The paper presents experimental and numerical investigation of pulverized coal combustion process analysis and optimization. The research was conducted on the front-fired pulverized coal boiler with dedicated low-NOx furnace installation. In order to find optimal boiler operating conditions the acoustic gas temperature measurement system and mass flow rate of pulverized coal measurement system was applied. The uniform temperature distribution as a result of uniform coal and air flow provides the optimal combustion process with low level of NOx emission and total organic carbon content in ash. Experimental results confirm that the monitoring and control of fuel and air flow distribution allows to optimize combustion process by increasing thermal efficiency of the boiler. In the numerical part of investigation, the complex CFD model of pulverized coal boiler was made. The calculations of turbulent, reactive, and thermal flow processes were performed at different boiler operating conditions retrieved from power plant on-line monitoring system. The results of numerical simulations enable to identify the optimal boiler operating conditions.

Keywords: pulverized coal combustion, low-NOx combustion, combustion process optimization, computational fluid dynamics, coal combustion monitoring system, acoustic pyrometry

INTECH
open science | open minds

© 2016 The Author(s). Licensee InTech. This chapter is distributed under the terms of the Creative Commons Attribution License (http://creativecommons.org/licenses/by/3.0), which permits unrestricted use, distribution, and reproduction in any medium, provided the original work is properly cited. CC BY

1. Introduction

Currently we observe an increase in natural gas utilization, deployment of renewable energy sources, and a need to improve coal plant efficiency, which tend to decrease coal consumption in OECD. In spite of the above, coal will long remain a key energy fuel for electricity generation in a number of developed countries. Performance optimization of large-scale pulverized coal (PC) utility boilers has become more and more relevant through the recent years for the utility industry. Optimization efforts are focused on increasing thermal efficiency, extending their lifetime, and lowering pollutant emissions.

The coal-fired power plants face a big challenge of improving combustion process enforced by environmental concerns. The new units designed for high steam parameters must meet strict limits for emissions of gaseous pollutants. Meeting the requirements of CO_2 emissions while maintaining highly efficient production process is still the subject of many research [1–6]. Regulations for reducing NO_x and SO_x emissions become more strict and meeting them must be achieved by both new and old production units. It is currently possible to achieve the required quality of exhaust gasses with primary and secondary measures. Primary measures of NOx reduction are used inside the boiler combustion chamber and consist of activities such as proper selection of the excess air ratio and temperature, as well as modification of combustion techniques (reburning, exhaust gas recirculation, air staging, cooling the flame, and burners redesign). Secondary measures of NOx reduction include activities and auxiliary installations located behind the combustion zone of boiler like selective non-catalytic reduction (SNCR) and selective catalytic reduction (SRC) methods. The efficiency of the NOx reduction of primary measure is about 35% (reduction from 540 to 350 mg/m^3). Secondary measures are more effective. SNCR achieve the NOx reduction efficiency of up to 50% and efficiency of SCR method can reach about 95%.

However, in the case of older units, applying these methods in the wrong way can greatly affect the quality of the combustion process and consequently reduce production efficiency. To keep the thermal efficiency of the boiler constantly at a high level, it is necessary to perform optimization work. In recent years, the increasing number of activities using optimization methods based on computer simulations is observed. The optimization activities are carried out to improve performance of coal and biomass cofiring process [7], and decrease the carbon content in ash [8]. Many investigations were devoted to the modeling and prediction of NOx emission [9–11] as well as to optimization methods for NOx reduction [12–14]. Current research on optimization methods are based on data from available measurement systems. To further optimize pulverized coal boiler performance, dedicated systems for monitoring and control of boiler operating conditions [15, 16] can be required. This optimization process can be done by optimizing the amount and distribution of fuel and air supplied to the boiler [17]. Flame shape and its symmetry is a critical factor influencing combustion process performance. Optimization of combustion process can improve thermal efficiency of boilers up to 0.84% [18]. Homogenous temperature distribution of flue-gas promotes lower emissions of NO_x, CO, and minimizes total organic carbon (TOC) content in ash. Acoustic gas temperature and mass flow rate of pulverized coal measurement systems

http://dx.doi.org/10.5772/64442

allow for online monitoring of the most important combustion parameters. A temperature measurement can also be applied to verify the results of computational fluid dynamics (CFD) modeling [19].

The next big challenge for the electricity producers will be the flexible operation with regard to increasing share of renewable sources of energy in the domestic markets. The increase of electricity produced from renewable energy sources means that coal units have to adapt to market needs and work with increased load variations during the day. Working under changing load requires constant monitoring and controlling the operating parameters of the boiler in order to maintain high efficiency and required levels of gas emissions. Conducted research also shows that the time required to load changes can be much shorter than the one that is currently used [20]. As a result, in the near future, coal-fired units will work more often in transient conditions which will require the use of new methods presented in this paper, to control and optimize the combustion process also at transient conditions.

In recent years the development of computer modeling techniques, in particular the computational fluid dynamics, has allowed for accurate analysis of coal combustion process in tangentially fired [21–26] as well as front-fired furnaces [27–29]. Results of CFD modeling [30] can be used at the stage of the combustion process optimization to provide complete information about the process. A comprehensive large-scale furnace CFD model should be capable of properly predicting trends in NO_x reduction by means of primary [31] and secondary [32] methods.

2. Coal combustion process monitoring and control

Air flow as well as fuel flow distribution in a power plant has to be measured and controlled in order to achieve optimum combustion conditions and improve the boiler efficiency. In low-NOx combustion system, the air and fuel flow has to be precisely controlled. Both the total air distribution (primary and secondary air to the boiler) and the mass flow rate through the individual burner. **Figure 1** presents dependence of the key combustion parameters (NO_x, O_2, CO, LOI, and boiler efficiency) on the air/fuel ratio. To optimize the combustion process the accurate measurements and control systems are needed.

The combustion stoichiometry can be easily controlled by air distribution. For low air-fuel ratio value the O_2 versus CO dependency is high. As long as the amount of air is not optimized in reference to fuel the CO can reach very high values. While increasing O_2 the CO declines—the combustion is getting complete. The optimum zone is defined as low CO value for the lowest possible O_2 supply, while the excess of O_2 has to be maintained for combustion stabilization. For optimum zone the NOx value also has to be as low as possible. O_2 has crucial influence on NOx generation. The NOx level is proportional to the amount of O_2, depending on NOx generation stoichiometry. If the excess of air will reach the highest values the NOx will also grow. For those conditions we start to lose the combustion efficiency. The output losses will grow rapidly according to O_2 value. This can be observed by highest FEGT.

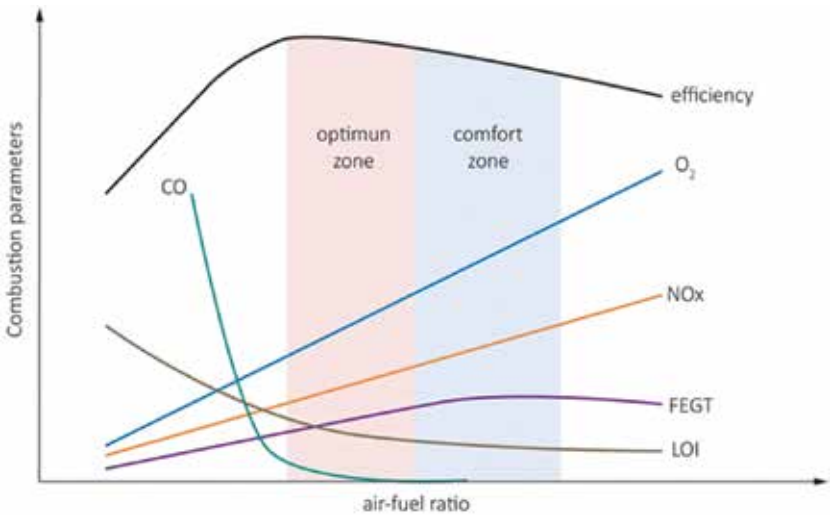

Figure 1. The key combustion parameters as a function of air-fuel ratio [33].

2.1. Low NOx emission technique of pulverized coal combustion

The purpose of improving NO_x emissions resulted in the use of low-emission combustion technology, which is characterized by staged combustion process with extended low oxygen combustion zone. In pulverized coal boiler, the low-NO_x combustion technology is most often implemented using low-emission burners and spatial distribution of air supplied to the furnace. Furnace installations can also be equipped with a system of fuel staged supply to the boiler. This process involves providing coal-air mixture with better fineness in the higher regions of furnace. General scheme of low-emission combustion system in PC boiler OP-650 (EDF Poland, Rybnik Power Plant) is presented in **Figure 2**.

OP-650 is a front wall fired, pulverized coal boiler with steam drum and natural circulation. Maximum continuous rating is 650 t/h of live steam generation (700 t/h in peak load). Boiler is equipped with six ring-ball mill units (A, B, C, D, E, and F) that supply 24 burners. Mills are equipped with static classifiers with movable blades.

Low-emission combustion system consists of two rows of main swirl burners located at the lower part of windbox (six burners in each row). Additional diluted coal-air mixture is provided through 12 drop tubes located at the upper part of windbox (**Figure 3**). Boiler also consists of two levels of overfired air nozzles (OFA) located at the front wall (6 OFA ports) and rear boiler wall (10 OFA ports). All burners are fitted in the common windbox located on the front wall of the boiler. The burners' arrangement was designed to reach the low-NO_x combustion conditions with air and fuel staging method. The first two rows of burners (low-NO_x burners) (burners I and II) are supplied with a high concentration mixture and the third row (burners III—without swirl) is supplied with low concentration mixture. Depending on load demand, the mill units operation configuration is different (some of the mills are out of operation).

http://dx.doi.org/10.5772/64442

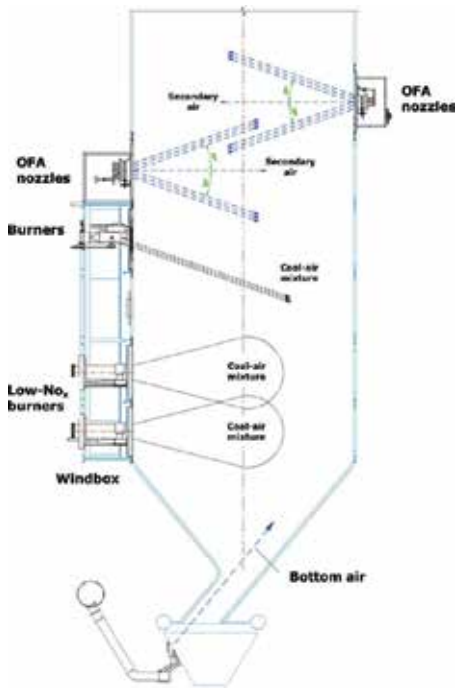

Figure 2. Low-emission combustion system in PC boiler.

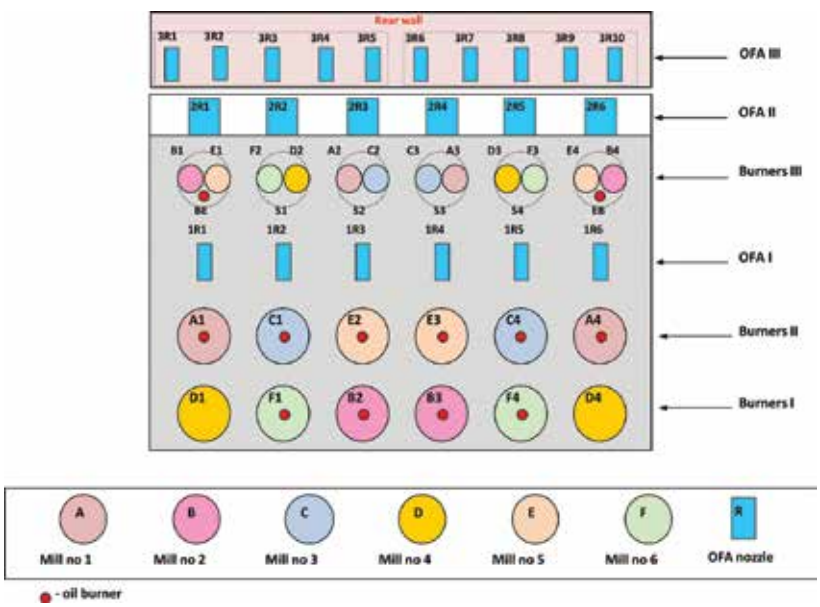

Figure 3. Fuel and air supply system in PC boiler OP-650 (EDF Poland, Rybnik Power Plant).

The main swirl burner design with marked flow zone of coal-air mixture and secondary air is presented in **Figure 4**. Combustion air is separated into core, primary, secondary, and tertiary as is shown in **Figure 4**. Additional diluted coal-air mixture is provided through 12 burners located in a single row at the upper part of windbox. These burners are made of drop tubes with additional six nozzles for optional biomass injection.

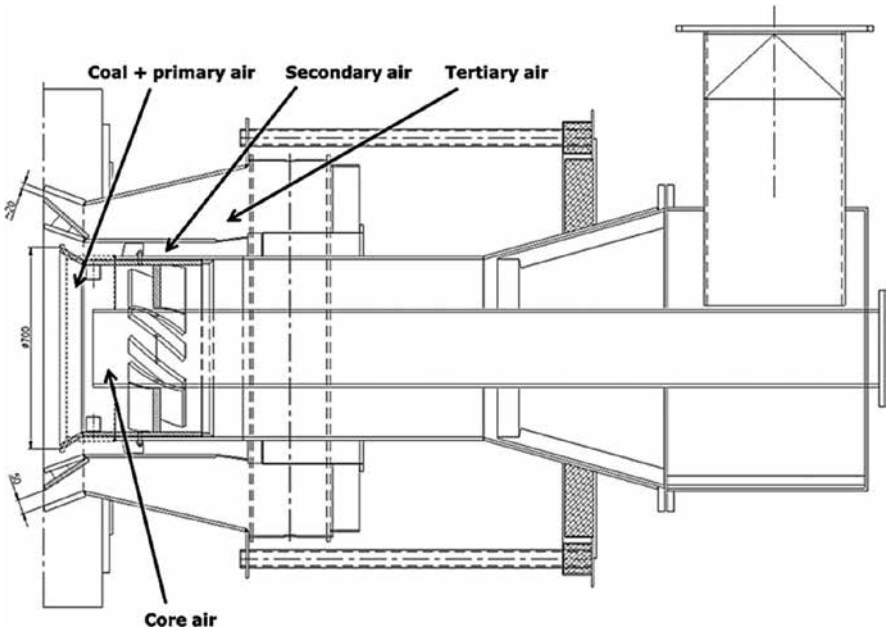

Figure 4. Low-NO_x burner and supplying scheme of fuel and air.

2.2. Monitoring and control of fuel flow rate

Pulverized coal separation into low and high concentration mixture is realized by means of louver splitters installed behind mill outlet. Each mill has two outlets (multiturret), where each outlet is equipped in splitting box. Behind each splitter there are two separate coal pipes which transport the low and high concentration mixture to the burners (**Figure 5**). The fines of high concentration mixture is approximately 30% and 5% residue for R88 and R200 mesh sieve, respectively, and low concentration mixture fineness is approximately 15% (R88) and 1% (R200).

Fuel distribution is controlled in open loop by unit operator. Each louver has individual actuator which is adjustable from distributed control system (DCS) in specific range from 0% to 100% which corresponds to 30–70% share of mixture density. **Figure 6** depicts the main idea of fuel splitter operation.

The use of louver separator allows to control the pulverized fuel (PF) distribution in share range 60–80% for high concentration mixture and 20–40% for low concentration mixture.

http://dx.doi.org/10.5772/64442

According to this PF distribution, the low emission combustion condition can be met by means of fuel staging method.

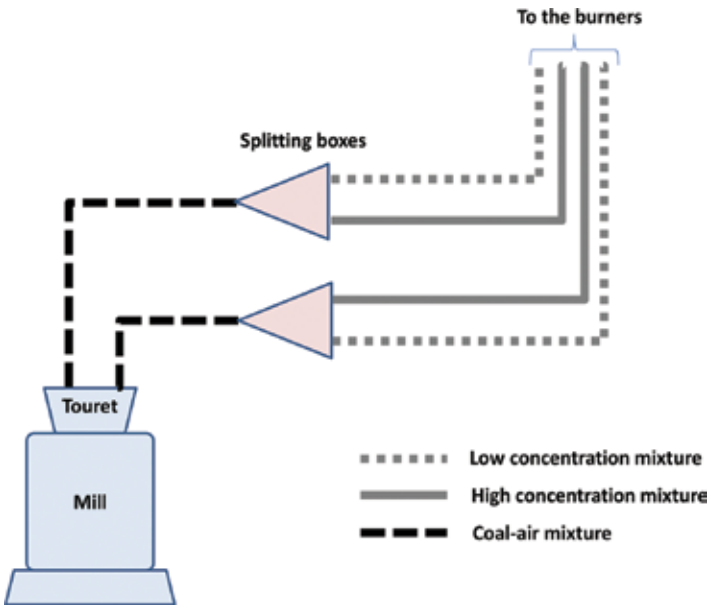

Figure 5. Fuel splitting system.

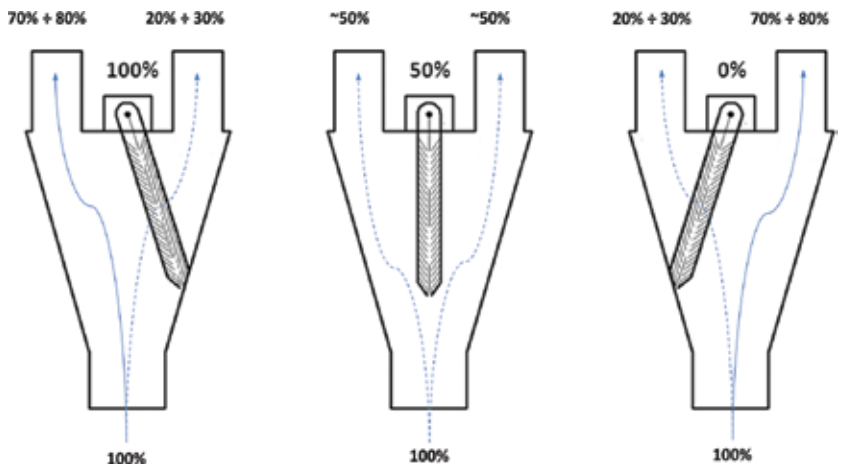

Figure 6. The principle of the fuel splitter operation.

The set point for louver position depends on current live and reheated steam temperatures and current PF distribution which is related to mill unit operation configuration. The fuel splitters settings allow to control the fire ball (flame core) location along the boiler height. This

feature is often used to achieve the nominal live and reheated steam temperature (540°C). At low unit load, where the temperature is too low, the fire ball is moved up in the combustion chamber—the high concentration mixture is driven into burners placed on third level (burners III). In case of very high temperature, the fire ball is moved down—the high concentration mixture is driven for first and second burners level (burners I and II). The more complicated situation is where the mill unit operation is changed. The PF distribution differs, which cause the imbalance between left and right side and generates nonuniformity of gas temperature. For PF distribution and velocity measurement the dedicated online measuring system is used. Each coal pipe is equipped with sensors which are connected to the measuring portable cabinets (each of four coal pipes, one for mill unit). Depending on location constraints, different section lengths (~1.2–2.4 m) of pipes with internal diameter (ID) of 0.46–0.51 m were chosen for the system installation. The general rule is to install the sensors in vertical pipes at a location of three internal diameters (3 × ID) for the inlet and one internal diameter (1 × ID) for the outlet from bends and curves. If there is no possibility to use the system for vertical pipes the horizontal sections are chosen.

Additionally, online optimization of the PF distribution is performed by unit operation, while the periodic optimization is carried out by process engineer personnel. Due to the fact that the system is portable and each mill has separate measuring cabinet, the boiler/mill group optimization is possible. The optimization strategy is simple. Initially, PF mass flow and velocities are analyzed for each mill separately to meet the following requirements: 20–40% mass flow for burners III (low concentration mixture), and 60–80% mass flow for burners I and II (high concentration mixture) for low-NOx combustion system. Next, PF flow is analyzed for boiler according to the results for each mill and consequently the symmetry between left and right sides of the furnace optimization is reached. Once satisfactory pulverized coal distribution was achieved, the system is moved to another group of mills/boiler.

2.3. Monitoring and control of air flow rate

The air distribution and flue gas systems in presented front-fired PC boiler consist mainly of three forced draft (FD) fans and three inducted draft (ID) fans (**Figure 7**). Two FD fans supply primary air to the mills and one FD fan supplies the secondary air to the boiler through the common windbox. The boiler is also equipped with two protection air fans, and one bottom air fan which supply the air to protect the boiler's evaporator (protective air) and to burn out the fuel near bottom ash hopper (bottom air).

The air distribution control process is supported by dedicated measurement systems of air temperature, mass flow rate, and pressure. These measured values are required for evaluation of set points in control system: fuel demand, combustion air demand, and steam temperatures. In addition, the boiler is also equipped with system for combustion quality monitoring, where the flue gas composition measurement subsystem (O_2, NO_X, CO, and SO_2) is the most important component.

The most commonly used air flow measurement system is based on differential pressure *dP* value. Differential pressure measurement signal is used in primary air flow measuring

http://dx.doi.org/10.5772/64442

providing the possibility to avoid the typical problems connected with air purity and thermal condition. The main disadvantage is the pressure drop in air duct which can limit the fan's maximum capacity. For different air duct profile other similar measurements are used, i.e., venturi, orifice, annubar, veribar, or pitot tubes. New advanced technologies for air flow measurement are based on electrostatic, thermal, or optical principles and are free of difficulties related to complex geometry. They are also more accurate than *dP* measurements; however, pose some limitations depending on measuring technology.

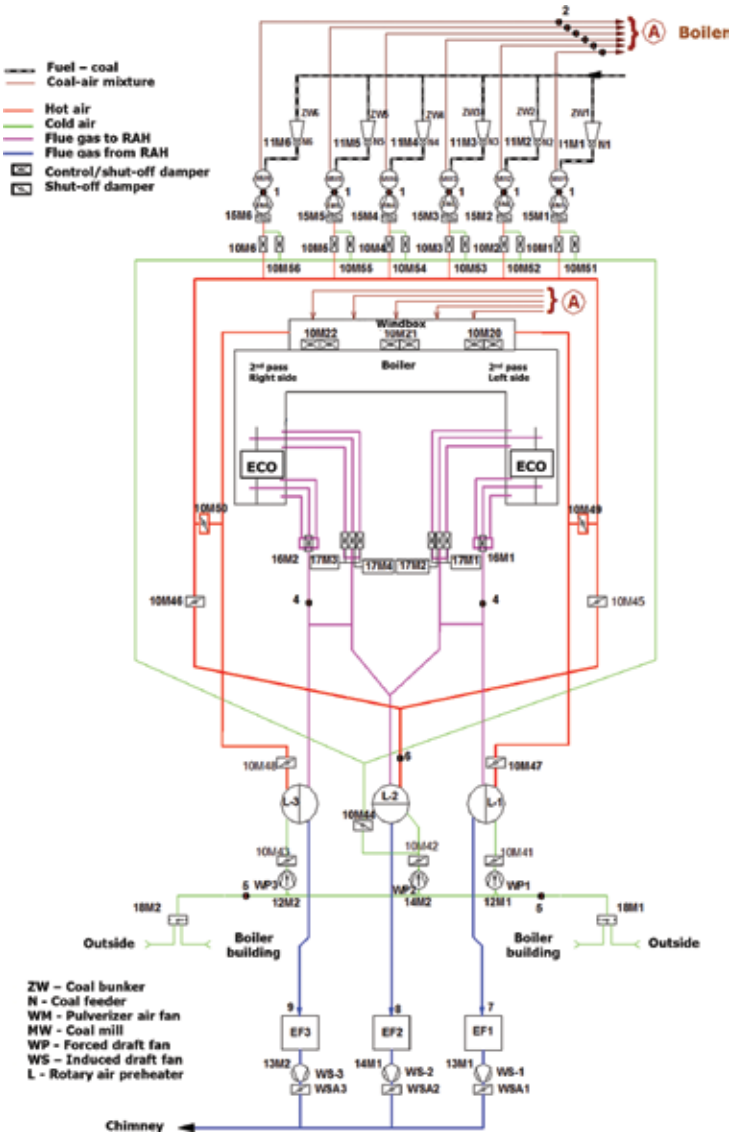

Figure 7. The main scheme of air/flue-gas distribution in PC boiler.

The boiler operation is controlled by distributed control system, in which control algorithms for fuel/air amount are implemented. The presented power unit OP-650 operates mainly in coordinated boiler follow mode. The load demand signal is applied to the turbine valves (turbine master) and combustion demand (boiler master). Boiler master is the main control signal for boiler load algorithms which acts on fuel demand control algorithm for coal feeders' capacity control. Combustion air (primary and secondary) demand is controlled according to oxygen rate in flue gases at the boiler outlet. Basing on oxygen measurement, the load of FD fans is evaluated and controlled. The air distribution system, secondary air and OFA, can be also controlled by unit operator in manual mode. In the primary and secondary air distribution optimization of advanced air balance control, some requirements have to be met. The primary/secondary air balance should be maintained in the range of 20–30%/70–80% of the total air flow.

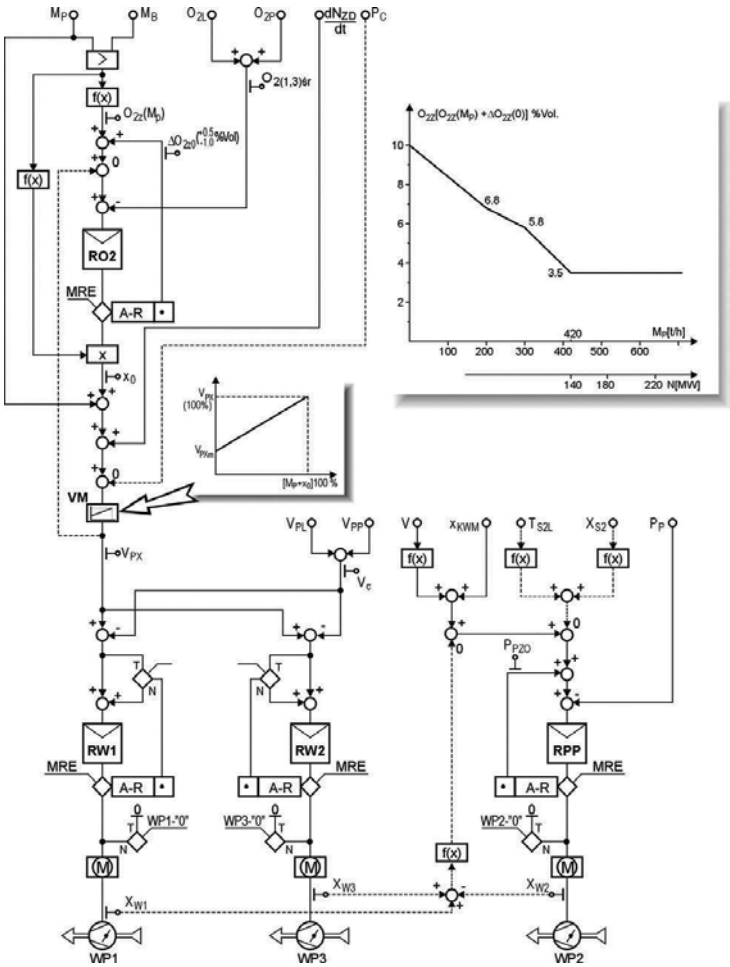

Figure 8. Total air control loop overview.

http://dx.doi.org/10.5772/64442

The amount of total air flow is measured by means of *dP* measurement on main ducts, which are common for all the three FD fans. The unit controls the load of FD1 and FD3. The FD2 is out of control in this loop. The total amount of air is controlled indirectly by amount of secondary air. For automatic total air amount control the live steam mass flow measurements have been used together with O_2 content in flue gases correction. The automatic control unit acts on two FD fans (FD1 and FD3) and on subordinate control unit responsible for primary air to the mills control (**Figure 8**), which respectively acts on FD2 load. The leading signal of live steam mass flow is added with correction signal from O_2 content in flue gas behind the boiler. The controlled O_2 content is kept on O_{2Z} set point level:

$$O_{2z} = O_{2z}\left(M_P\right) + \Delta O_{2z}\left(O\right) \tag{1}$$

where O_{2z}, $O_{2z}(M_P)$, and $\Delta O_{2z}(O)$ are oxygen set point at the boiler outlet, oxygen value as a function of steam mass flow rate M_p, and difference of oxygen content at the left and right side of boiler outlet, respectively.

The difference between those two signals is given on the input of R_{O2} (O_2 controller), which evaluate the correction signal from O_2 content. This correction is added to subordinated controller. The signal of total air flow to the boiler follows the leading signal of live steam flow recalculated in VM module (**Figure 8**). The correction from O_2 and power changes is as follows:

$$V_C = V_L + V_P \tag{2}$$

where V_C is the total air flow rate, V_P and V_L are air flow rates on the right and left side of boiler, respectively. The difference of those two signals is introduced on two controllers of secondary air (R_{W1} and R_{W2}), which controls the load of FD1 and FD3 fan.

The main controller is proportional-integral type and works accordingly to tracking control idea. The set point signal is the live steam mass flow value, the controlled variable is the total air flow to the boiler. The correction from O_2 content in flue gas is comprised in subordinated PID controller with O_2 set point value. The deviation controls directly the adjuster of steam/air share. From practical point of view, the range ±20% for steam/air share is enough to keep the set value of O_2 content at the boiler outlet.

The amount of primary air is measured by use of dedicated *dP* orifices between the mill fan and mill inlet. The primary air is dependent on the fuel mass flow rate supplied to the burner. The control process of air flow can only be achieved by modifying distribution of the secondary air supplied to both the burners and the OFA nozzles. The amount of secondary air is not measured, but is balanced by use dedicated performance calculations implemented in DCS. The secondary air is controlled by the position of the dampers presented in **Figure 9(a)**. Each burner has the ability to individually control the position of dampers, as opposed to the OFA nozzles. In the case of OFA nozzles on the front wall, the control process is carried out by changing the position of two adjacent nozzle dampers. On the rear wall of the control process

is achieved by changing the damper position of the OFA nozzle located on the left and right side of the boiler (**Figure 9b**).

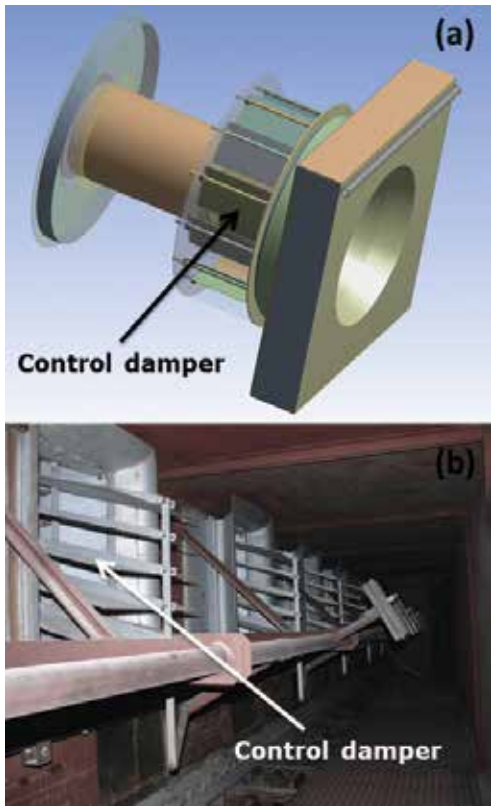

Figure 9. Air flow controlling damper of the burner (a) and OFA (b).

2.4. Protective air system

An adverse effect of low-emission combustion technology is the creation of a permanent reducing atmosphere (the reducing zone with reduced O_2 and increased share of CO) in the boundary layer of screens. If close to the screens of combustion chamber O_2 content is below 1%, and the CO content rises above 0.2%, the process of corrosion of screen tubes can occur (low-oxygen corrosion). In order to protect screen against negative effects of low-oxygen corrosion in form of intense loss of the tube material, boiler is equipped with protective air nozzles. The air supplying through nozzles located on the rear and the side walls of boiler (**Figure 10**) allows to increase the share of oxygen in the boundary layer.

The share of protective air in total amount of air supplied to the boiler can be up to 20%, and it needs be taken into account in any process related to the optimization of air distribution to the boiler.

http://dx.doi.org/10.5772/64442

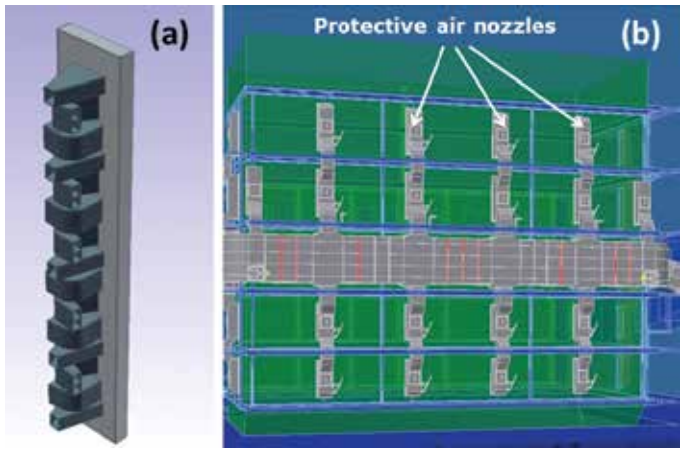

Figure 10. The single section of protective air nozzles (a) and sections arrangement on the boiler rear wall (b).

2.5. Acoustic measurement system of flue-gas temperature

The acoustic gas temperature measurement system (AGAM) allows to asses impact of operating conditions on the temperature distribution inside the combustion chamber. Measurement system is located at the level of 30.2 m and is composed of 8 heads (**Figure 11**), which form the 21 paths of measurements. Based on the 21 paths, the flue-gas temperature can be calculated in 12 zones to create maps of temperature distribution at the outlet of combustion chamber.

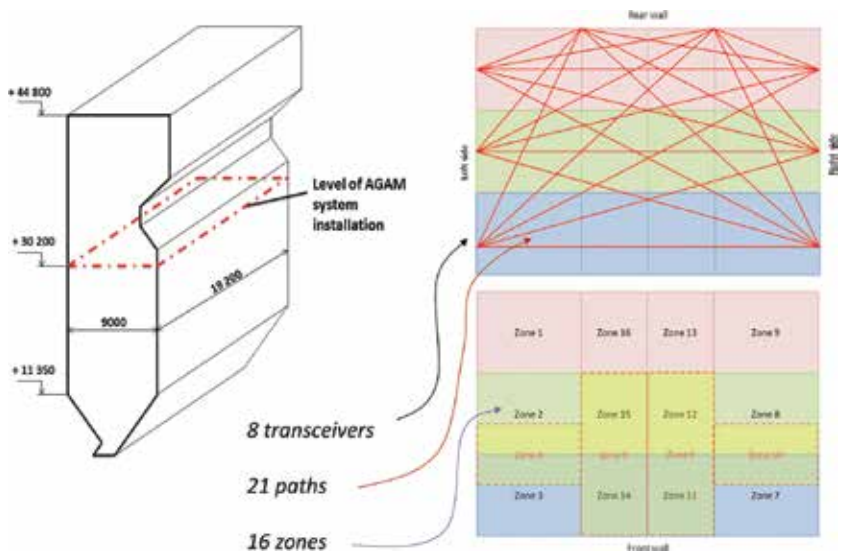

Figure 11. The level of AGAM system location (a) and the distribution of measurement paths (b).

The principle of AGAM system is based on the acoustic pyrometry, which allows to measure delay time of an acoustic wave. Time delay depends on the temperature in the environment of wave propagation and this relation is defined by the following formula:

$$v = \sqrt{\frac{\kappa \cdot R}{M} \cdot T} \tag{3}$$

where v is the speed of sound (m/s), R is the universal gas constant (kJ/(kmol·K)), M is the molar mass of gas (kg/kmol), and k is the adiabatic index.

The adiabatic index and molar mass of gas are calculated based on the typical average values of volume fraction for flue-gas in coal-fired furnaces. For analyzed boiler, the parameters are equal to: k = 1.275, N_2 = 76.5 Vol.%, O_2 = 3 Vol.%, CO_2 = 13 Vol.%, H_2O = 7.5 Vol.%.

Velocity of a wave is determined by the propagation time of an acoustic impulse between symmetrically placed transmitters and receivers. The distances between the transmitter and the receiver are constant and the temperature is calculated using the formula presented below:

$$T = \frac{l^2}{B \cdot \tau^2} \cdot 10^{-6} - 273.15 \tag{4}$$

where l is the distance between the transmitter and the receiver (m), τ is the time of delay (s), and B is the acoustic constant.

3. CFD modeling techniques in pulverized coal-fired boilers

Performance optimization of large-scale pulverized coal utility boilers has become more and more relevant through the recent years for the utility industry. CFD modeling has been extensively applied to provide information on the complex phenomena in tangentially fired [21–27] and in front wall-fired furnaces [27–29], including gas-solid flow, combustion, and heat transfer.

In [21], two tangentially fired furnaces (OP-380 and OP-430) of similar design and thermal power were numerical investigated. OP-380 was retrofitted by replacing traditional jet burners with RI–JET2 (Rapid Ignition JET-burner) swirl burners. Comparison between the boilers combustion characteristics was carried out based on the CFD simulation. In [22], different operation regimes of pulverized coal furnace have been investigated with the 3-D CFD code. Selected parameters have been compared to measurements, showing good agreement. Similar purpose was achieved in [23]. Additionally, a grid refinement study was performed. Pulverized coal ignition behavior in a 40 MW tangentially fired boiler was predicted in [24]. Ignition image was obtained from high-temperature-resistant camera and compared to simulation results. Accuracy of general simulation approach was confirmed by available operating and design

http://dx.doi.org/10.5772/64442

data. Yin et al. [25] investigated furnace and part of the rear pass in the tangentially fired boiler. The simulation has been validated with global design parameters including O_2 at the furnace outlet, heat transfer in the furnace, and furnace exit temperature. Site operation data was used to verify NO_x predictions. In [26], Euler-Lagrangian approach was incorporated to investigate numerical flow characteristics in a tangentially fired furnace. Temperature deviation has been analyzed. An example of employing a commercial code Fluent to investigate a 500 MW utility boiler firing medium volatile coal was demonstrated in [27]. Temperature profiles were calculated for different boiler loads. Calculations have been compared with measurements data. Minghou et al. [28] addresses CFD simulations of front-fired boiler for different operating conditions. The model was validated by comparing measured unburned carbon in fly ash, NOx, and total heat transfer to the walls with measured values. The combustion and wall heat flux in a 100 MW boiler under air and oxy-fuel combustion conditions was analyzed by means of computational modeling in [29]. No validation of the numerical approach was done against the experimental data.

Reducing a complex physical problem to a series of models that can be solved numerically requires a number of assumptions to be made. Specifically, for engineering problems momentum and species transport equations must be modeled. Simulations are computed using CFD code, which solves Reynolds averaged Navier-Stokes equations using a low-order finite volume formulation. In the current work, the steady-state solution is calculated using second-order discretization for all equations.

Simulation of the following processes takes place in the furnace: turbulent flow, coal combustion, gas phase combustion, particle transport, and radiative transport. The gas phase is modeled assuming an Eulerian approach, while for the solid phase both the Lagrangian as well as Euler-Euler approach is applied.

Realizable k-ε model [34] was used as a closure of turbulent Reynolds equations. The realizable k-ε model is relatively widely used for engineering applications and provides better performance in many industrial turbulent flows than the standard k-ε model. The flow near the wall is influenced by molecular viscosity rather than by turbulence. The wall function method of [35] uses algebraic formulations to link quantities at the wall to those further away. The y+ values have been kept above 20.

3.1. Coal devolatilization

The pulverized coal combustion process can be divided into two parts, devolatilization and char combustion. The most commonly used conventional devolatilization model is based on a single kinetic rate [36], which assumes that the rate of devolatilization is dependent on the amount of volatiles remaining in the particle via a first-order reaction:

$$\frac{dm_p}{dt} = k\left[m_p - \left(1 - f_{v,0}\right)m_{p,0}\right] \tag{5}$$

where k, $f_{v,0}$, and $m_{p,0}$ denote reaction rate (following Arrhenius rate), volatile fraction, and initial particle mass. These models can be extended by using network devolatilization models like FG-DVC and FLASHCHAIN [37, 38] as a preprocessor. An example of using FG-DVC model with assumed particle heating rate equal to 10^5 K/s is demonstrated below. It predicts the rate of the production and high temperature yields for the char, tar, volatiles, and the composition of key species during the devolatilization of any coal. The results as well as the proximate and ultimate analysis for the used coal are given in **Table 1**.

Proximate analysis (wt%, as received)*				
Ash	Volatile matter	Moisture	Fixed carbon	
22.34 ± 0.7	25.77 ± 3.0	12.75 ± 0.6	39.14 ± 3.0	
Ultimate analysis (wt%, daf)*				
C	H	N	S	O
84.7	5.39	1.55	1.23	7.13
FG-DVC high-temperature yield (wt%, daf)				
Volatiles	Char			
47.8	52.2			
Volatile composition from FG-DVC (wt%)				
H_2O	CO	CO_2	C_mH_n	$C_xH_yO_z$
4.8	2.3	2.08	7.12	31.5
Empirical formula for light hydrocarbons (C_mH_n) and tar ($C_xH_yO_z$)				
C_mH_n (gas)	$C_xH_yO_z$ (tar)			
$m = 1$, $n = 7.22$	$x = 7$, $y = 4.48$, $z = 0.72$			

Table 1. Coal analysis results and FG-DVC output (*analyses were performed according to the polish norm N-EN ISO/IEC 17025:2005).

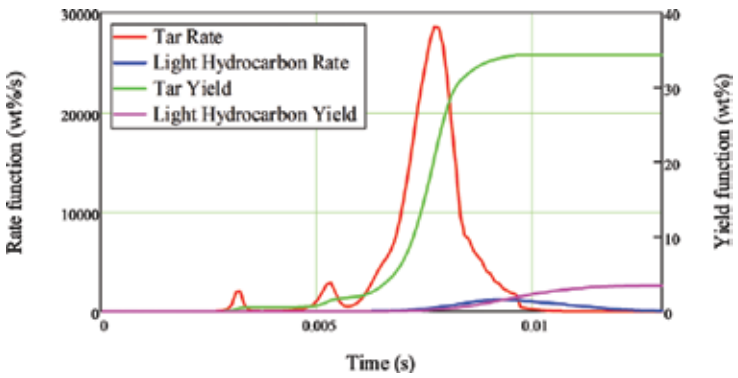

Figure 12. Comparison of tar ($C_xH_yO_z$) and light hydrocarbons (C_mH_n) devolatilization rate and yield functions.

http://dx.doi.org/10.5772/64442

During primary devolatilization each volatile species is evolved with different rate and tar undergoes secondary pyrolysis [39]. In the CFD modeling of turbulent flow with combustion it was assumed that volatiles are produced as a single compound that undergoes instantaneous breakup reaction into tar, light hydrocarbons, CO, CO_2, and H_2O. FG-DVC calculates devolatilization rate of tars and mentioned species. The most significant mass drop of fuel particle occurs when tar is evolved, which is produced in first place (**Figure 12**). For this reason tar release rate is used in devolatilization model.

Knowing the volatile fraction of dry ash free coal (f_{volatile}) and assuming that residual char is pure carbon, we can calculate lower heating value of volatiles.

$$LHV_{volatile} = \frac{LHV_{coal_{daf}} - f_{char} \cdot LHV_{char}}{f_{volatile}} \tag{6}$$

Assuming that lower heating value of light hydrocarbons is approximately equal to that of methane (LHV_{gas} = 50 MJ/kg), we can easily calculate lower heating value of tars from the instantaneous breakup reaction of volatiles:

$$LHV_{tar} = \frac{LHV_{volatile} - (y_{gas} \cdot LHV_{gas} + y_{CO} \cdot LHV_{CO})}{y_{tar}} \tag{7}$$

where y_{gas}, y_{tar}, and y_{CO} stand for mass fraction in volatiles.

A novel approach in devolatilization simulations was described as tabulated devolatilization process model (TDP) [40]. The authors indicated that in the previously mentioned modeling approach all the devolatilization parameters used in the CFD code were calculated assuming a constant heating rate for all the particles (with a typically used value of 10^5 K/s). In the TDP approach a look-up table of the devolatilization rates and yields for a set of heating rates is generated based on the FLASHCHAIN model. In the course of CFD simulations, a particular set of devolatization parameters is used based on the calculated particle heating history.

In nonpremixed reacting flows the local time-dependent mixing and chemical reaction of the species and heat transfer away from the reaction area determine the combustion process. The key gas phase combustion modeling issue is the necessity of source terms calculations in reactive species transport equations, which are the average values of strongly nonlinear reaction rates. Early combustion models have been derived on the assumption of chemical equilibrium. Taking into account detailed kinetics of reactions usually results in much higher computational effort.

3.1.1. Eddy dissipation concept (EDC)

Eddy dissipation concept [41] was used as a general concept for treating interaction between turbulence and chemistry in flames. In this model the total space is subdivided into fine

structures and the surrounding fluid. All reactions of the reactive components are assumed to react only in these spaces which are locally treated as perfectly stirred reactors (PSR) with a residence time:

$$\tau^* = 0.41 \cdot \sqrt{\frac{\nu}{\varepsilon}} \tag{8}$$

where ν is the kinematic viscosity and ε denotes turbulent kinetic energy dissipation rate. These parameters are calculated from turbulence model (k-ε). Mass fraction occupied by fine structures is modeled as:

$$\gamma^* = \left[2.13 \cdot \left(\frac{\nu\varepsilon}{k^2} \right)^{0.25} \right]^2 \tag{9}$$

The reaction rates of all species are calculated on a mass balance for the fine structure reactor. Denoting quantities with asterisk, the conservation equation of species i can be defined:

$$\frac{\rho^*}{\tau^* \left(1 - \gamma^*\right)} \left(m_i^* - \overline{m_i} \right) = M_i \cdot \varpi_i^* \tag{10}$$

where $\overline{m_i}$ is the average mass fraction of the species i, M_i is the molecular weight of the species i, and ω_i* denotes the chemical reaction rate calculated from Arrhenius equation.

The mean net mass transfer rate of species i between the fine structures and the surrounding fluid can be expressed as:

$$R_i = \frac{\bar{\rho}\gamma^*}{\tau^* \left(1 - \gamma^*\right)} \left(\overline{m_i} - m_i^* \right) \tag{11}$$

The implementation of the EDC model into CFD code is realized by solving the nonlinear system of equations for the fine structure reactor in each control volume and finding R_i, which is the source term in species i transport equation.

In most of the engineering cases implementation of the detailed reaction mechanism into 3D codes is prohibitive due to their large computational effort. For many purposes the required information can often be obtained with a less complete chemistry description. CFD simulations most often use simplified global reaction mechanism. Four-step global mechanism mainly based on the one demonstrated in [42] was employed. It contains four global reactions: hydrocarbon and tar decomposition reactions, carbon monoxide, and hydrogen oxidation:

http://dx.doi.org/10.5772/64442

$$C_mH_n + \left(\frac{m}{2} + \frac{n}{4}\right)O_2 \Rightarrow mCO + \frac{n}{2}H_2O \tag{12}$$

$$C_xH_yO_z + \left(\frac{x}{2} - \frac{z}{2}\right)O_2 \Rightarrow xCO + \frac{y}{2}H_2$$

$$CO + 0.5O_2 \Rightarrow CO_2$$

$$H_2 + 0.5O_2 \Rightarrow H_2O$$

Following the above mechanism with known heat of reactions we can further calculate enthalpies of formation of volatiles, light hydrocarbons, and tars. Enthalpy of formation of tars was calculated by assuming zero heat of volatiles instantaneous breakup reaction. Heat of pyrolysis was not included in the analysis.

3.1.2. Mixture fraction/probability density function (PDF) method

Pulverized coal combustion process is a one of example of turbulent nonpremixed combustion systems and can be modeled using the mixture fraction/PDF model. Mixture fraction f can be expressed as the local fuel mass fraction [43], where Y_F and Y_P is mass fraction of fuel and products, respectively:

$$f = \frac{Y_F}{Y_P} \tag{13}$$

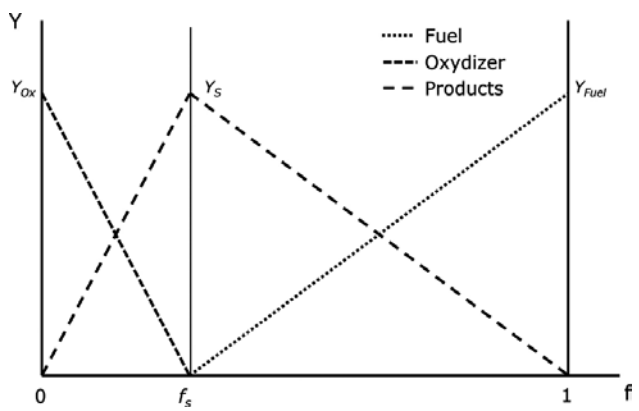

Figure 13. Mass fraction Y of fuel, oxidizer, and products as a function of mixture fraction f.

The main approach of diffusion models is that the combustion is limited only by mixing of fuel and oxidizer. The release of reaction products takes place if the fuel and oxidizer are locally mixed and does not depend on the reaction rate. In mixture fraction/PDF model transport equations for individual species are not solved. The mass fraction of oxidizer, fuel, and products is calculated based on the mixture fraction value *f*. **Figure 13** presents the graphical interpretation of mixture fraction approach.

If $0 \le f \le f_S$ fuel is deficient and the mixture is called fuel lean. The mass fraction of oxidizer and products is represented in the following form:

$$Y_i(f) = Y_{Ox} + \frac{f}{f_S}\left(Y_S - Y_{Ox}\right) \tag{14}$$

On the other side, if $f_S < f \le 1$ the mixture is called fuel rich, and the following equation can be used to calculate mass fraction of products and fuel:

$$Y_i(f) = Y_S + \frac{f - f_S}{1 - f_S}\left(Y_{Fuel} - Y_S\right) \tag{15}$$

where *f* is the mixture fraction, f_S is the stoichiometric mixture fraction, Y_S is the mass fraction of products of stoichiometric reaction at $f = f_S$, Y_i is the mass fraction linear functions (Y_O, Y_F, Y_P), Y_O is the local mass fraction of oxidizer, Y_F is the local mass fraction of fuel, Y_P is the local mass fraction of products, Y_{Ox} is the mass fraction of oxidizer at $f = 0$, and Y_{Fuel} is the mass fraction of fuel at $f = 1$.

The reaction is complete if the whole mass of fuel and oxidizer vanish ($Y_F = 0$, $Y_{Ox} = 0$) and this state is described by stoichiometric mixture fraction value f_S. The mixture fraction approach allows to calculate mass fractions at each control volume based on the one value and the modeling of combustion process is simplified to a mixing problem. The governing transport equation of mixture fraction is given by:

$$\frac{\partial}{\partial t}(\rho f) = \frac{\partial}{\partial x_i}\left(\rho D \frac{\partial f}{\partial x_i} - \left(\rho u_i f\right)\right) \tag{16}$$

where *D* is a molecular diffusion coefficient (m^2/s), u_i is the velocity in direction of *i* (m/s), x_i is the direction *i* in Cartesian coordinates system (m), and ρ is the density (kg/m^3).

Equation (14) can be applied taking into account the assumption of equal diffusivities of fuel, oxidizer, and products. In turbulent flows the turbulent convection dominates in comparison with molecular diffusion and assumption of molecular diffusion coefficient equality is acceptable.

http://dx.doi.org/10.5772/64442

When local value of mixture fraction is known, it becomes possible to calculate the local enthalpy *h* of combustion products. The enthalpy of the burnt mixture is a linear piecewise function of *f* and is presented in **Figure 14**. Therefore, the calculation of the gas temperature and an amount of heat generated (heat losses) in the combustion process becomes possible.

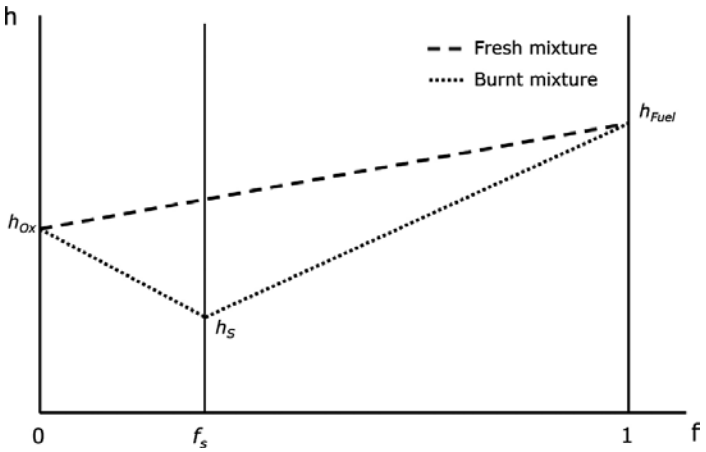

Figure 14. Enthalpy *h* of fresh and burnt mixture as a function of mixture fraction *f*.

For fuel-lean mixture and $0 \le f \le f_S$:

$$h_L = h_{Ox} + \frac{f}{f_S}\left(h_S - h_{Ox}\right) \tag{17}$$

and for fuel-rich mixture and $f_S < f \le 1$:

$$h_R = \frac{f_S \cdot h_{Fuel} - h_S}{f_S - 1} + \frac{f}{f_S - 1}\left(h_S - h_{Fuel}\right) \tag{18}$$

where h_L is the enthalpy on the lean side of f_S (kJ/kg), h_R is the enthalpy on the rich side of f_S (kJ/kg), h_{Ox} is the enthalpy of oxidizer at $f = 0$ (kJ/kg), h_{Fuel} is the enthalpy of fuel at $f = 1$ (kJ/kg), h_S is the enthalpy of products at the stoichiometric mixture fraction f_S (kJ/kg).

To determine the thermodynamical properties in turbulent flow, the probability density function of the mixture fraction is needed. The mean enthalpy $\tilde{h}$ can be computed from the following equation:

$$\tilde{h} = \int_0^1 h(f) \cdot P(f) df \tag{19}$$

The conservation equation for the mean mixture fraction $\tilde{f}$ and its variance $\widetilde{f''^2}$ (without the source term) need to be solved to fit parameters of the PDF function with already presumed shape. The most popular PDF β function [43–45] used in coal combustion modeling has a presumed shape and depends only on the mean mixture fraction $\tilde{f}$ and its variance $\widetilde{f''^2}$.:

$$P(f) = \frac{1}{B(a,b)} f^{(a-1)} \cdot (1-f)^{b-1} \tag{20}$$

where the normalization factor $B(a, b)$ and is defined as:

$$B(a,b) = \int_0^1 f^{(a-1)} \cdot (1-f)^{(b-1)} df \tag{21}$$

and the PDF parameters a and b can be determined using $\tilde{f}$ and $\widetilde{f''^2}$:

$$a = \overset{\circ}{f}\left[\frac{\overset{\circ}{f}\cdot\left(1-\overset{\circ}{f}\right)}{\tilde{f}''^2} - 1\right] \tag{22}$$

$$b = \frac{a}{\overset{\circ}{f}} - a \tag{23}$$

The β functions also have limitations and they cannot describe distributions joining an extreme peak ($f = 0$ or $f = 1$) with a maximum intermediate peak in the range of $0 < f < 1$. The different approaches can be proposed as the Dirac peak at the boundary, in order to eliminate this inconvenience.

Despite simplifications the mixture fraction/PDF method allows the determination of the basic parameters of the combustion process, also in the case of coal combustion. The mixture fraction/PDF approach is commonly used in computational fluid dynamics and particularly in modeling of the turbulent reactive flows which are the most popular cases occurring in industrial practice.

3.2. Char combustion

Char undergoes heterogeneous oxidation to CO. The reaction rate is calculated on the assumption that the process is limited by the diffusion of oxygen to the external surface of the char particle and char reactivity [46]. It is assumed that particle is spherical in shape and that surface reaction rate depends on the ratio of the reacting surface to the surface of the sphere. Diffusion phenomena with the rate:

http://dx.doi.org/10.5772/64442

$$R_{diff} = \frac{2\phi D_0 m_c}{RT_0} \frac{\left[\left(T_p + T_g\right)/2\right]^{0.75}}{d_p} \tag{24}$$

and kinetic reaction:

$$R_c = A_f \phi \cdot e^{-\left(E/RT_p\right)} \tag{25}$$

occur simultaneously. The total char combustion rate is than expressed as:

$$\frac{dm_p}{dt} = -\pi D_p^2 \rho RT \left(\frac{X_{O_2}}{M_{O_2}}\right) \frac{R_{diff} R_c}{R_{diff} + R_c} \tag{26}$$

where D_p denotes particle radius, D_0 is the diffusion coefficient, ρ is the particle density, X_{O2} is the oxygen mole fraction, M_{O2} is the oxygen mole fraction, T_p and T_g are the particle and bulk temperature, A_f is the empirical constant dependent on the fuel, and ϕ is the ratio of the reacting surface to the surface of the sphere. The particle burns out with constant diameter and variable density. It was assumed that the particle absorbs all the heat of the char burnout according to [47].

3.3. Radiative heat transfer

In case of combustion in furnace problem radiation is not only the dominant energy transport mechanism but also one of the most complex problems. The radiative transfer equation (RTE) [48] governs the radiation heat transfer in participating media. It describes the variation of radiation intensity (I) as it travels along a certain path (s) in the medium, in the direction (s, ω). Considering absorption, emission, and scattering apart from and into the direction s, the RTE can be described as follows:

$$\frac{dI(s,\omega)}{ds} = -(\kappa + \sigma) \cdot I(s,\omega) + \kappa \cdot I_b + \frac{\sigma}{4\pi} \cdot \int_{4\pi} I(s,\omega) \cdot \Phi d\omega \tag{27}$$

where k and σ denote absorption and scattering coefficients, Φ is the phase function. The spatial integration of RTE was carried out with the discrete ordinates (DO) method [49]. The number of RTE depends on the total number of gray gases and takes into account scattering of the particles. The DO method solves the RTE for a set of directions based on the concept of angular discretization scheme. Each octant of the angular space 4π is discretized into polar and azimuthal solid angle. The continuous integral over the solid angle is approximated by a numerical quadrature scheme, where the equations are solved for a series of directions.

In a typical combustion chamber H_2O and CO_2 are the main gaseous absorbers and emitters of radiant energy. The total emissivity of gas is calculated by a number of gray gases using polynomial correlations for weighing factors and absorption coefficient according to the weighted sum of gray gases method (WSGGM) [50]. Widely employed coefficients for emissivity [51], fitted from the benchmark exponential wide-band model, have been used in this work. The WSGGM represents the entire spectrum with three gray gases having uniform absorption coefficients. The total gas phase absorption coefficient is calculated from the total emissivity with the mean path length calculated from the characteristic cell size.

The gas phase absorption coefficient was corrected according to Taylor-Foster model [52], assuming uniform and constant soot concentration (10^{-3} kg/m^3) in the furnace. As noticed in [46], the main source of radiative transfer in two-phase mixture is the particle cloud. Therefore, coal particles emissivity (ε_p) treatment is crucial in coal combustion simulation. In this work the particle emissivity was assumed to be a function of unburned carbon in particle (U_c) following the relation [53]:

$$\varepsilon_p = 0.4 \cdot U_c + 0.6 \tag{28}$$

The particle reflectivity and scattering effects are also included in the calculation of heat transfer.

Thermal boundary conditions at walls have been expressed in terms of surface temperature and emissivity. It was assumed that the evaporator surface temperature is about 60° higher than the saturation temperature corresponding to the pressure of 16 MPa in the boiler drum. Calculations have been carried out for three emissivity values equal to 0.5, 0.7, and 0.9 at fixed wall temperature. All the presented figures correspond to emissivity equal 0.7, which is a typical value found in the literature [54]. We have to emphasize that during real boiler operation temperature and emissivity vary with time and spatially due to water-wall slagging and soot blowers operation. This phenomenon can be included in the simulations by implementing deposition model with thermal properties submodel [55].

4. Coal combustion process optimization

The main goal in power generation optimization is related to reduction of operational and maintenance costs. Form practical point of view it is directly dependent on two factors: first, combustion effectiveness (effectiveness in fuel consumption), and second, production effectiveness by optimal operation in steady and transient state (process performance). The combustion effectiveness depends on boiler performance and operational skills which are strictly related to the control system. To increase the combustion process performance the fuel consumption and flue gas emission (NO_X, CO, SO_2) have to be reduced.

http://dx.doi.org/10.5772/64442

4.1. Optimization method

The combustion process optimization has been performed for wall-fired pulverized coal boiler of EDF Polska S.A. in Rybnik Power Plant. The main goal was to minimize the boiler losses (maximize boiler efficiency) and to keep the environmental requirements for NO_X and exploitation requirements like live and reheat steam temperatures on optimal level.

The general optimization method used in the EDF Rybnik Power Plant was based on online calculation of manipulated variable (MV) according to controlled variable (CV) changes. The dedicated model has been created that defines the dynamic of particular values changes (CV) according to described control by MV. The defined model is adjusted in online mode, which gives good performance for boiler control units. The general description of optimization methods are presented in **Table 2**. The calculation have been performed by using dedicated software SILO [56, 57], developed and implemented by Transition Technologies Company [58]. SILO collects various data to select the best solution for defined models and for current boiler conditions.

MV (Manipulated variable)	**Control unit**	**CV (Controlled variable)**
Secondary air dumpers	Secondary air demand control	NO_x, live steam temperature, reheated steam temperature
OFA II and OFA III	OFA demand control	NO_x
Protective air dumpers	Protective air control	NO_x, CO
Coal feeders	Boiler master control	NO_x, live steam temperature, reheated steam temperature, spray water flow, CO
O_2	Total air demand control	O_2, CO, NO_x

Table 2. Control strategies for optimization process.

The main goal in boiler operating optimization was to improve the fire ball shape to achieve the nominal steam temperatures as well as low NO_x, CO, and O_2, which depend on flue gas distribution inside the furnace. The information about temperature distribution provided by the AGAM system has to be integrated with control units. Before optimal fire ball shape evaluation the dedicated tests have been performed to develop the relation between fire shape and MVs values.

The AGAM system gave the 12 independent values for 12 temperature zones in which the AGAM measuring surface was divided. The temperature values from 12 zones have been transferred into shape categories, which were described by use of three parameters listed below:

- the position of temperature hot spots indicating the maximum temperature
- intensity is evaluated as average temperature for a given temperature profile
- the dispersion is calculated as standard deviation of AGAM temperatures for each zone

During the optimization process, the boiler operation conditions and combustion process parameters were analyzed relying on standard measurements (steam temperatures, emissions, etc.). Optimization in this phase was focused on finding the highest performance and optimal fire ball shape. The different shapes were evaluated at low and high boiler load. Finally, the monitored process parameters were related to the evaluated fire ball shapes. **Figure 15** presents the evaluated fire ball shapes at low and high load where the process performance was the best.

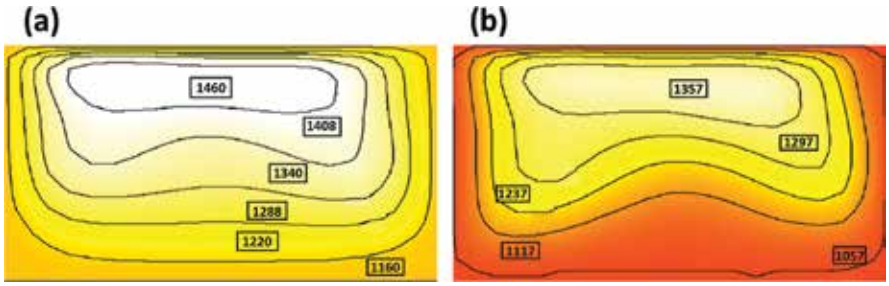

Figure 15. Example of temperature profile after optimization at high (a) and low (b) load.

4.2. Combustion process analysis using CFD modeling

To simulate the OP-650 front-fired boiler operation a commercial CFD code ANSYS Fluent was used. Furnace exit gas temperature measured by the AGAM system, located approximately 4 m under the furnace exit, was one of the key values used for verification studies. The simulation results comparison were performed using average temperature as well as temperature profile.

4.2.1. Numerical model of front-fired boiler

To create the three-dimensional geometry and the numerical mesh, ANSYS Design Modeler and ANSYS Meshing software was used [59]. Quality of mesh is one of the most important factors in the numerical simulation of the large-scale boilers [60]. A body-fitted mesh was created containing mostly hexahedral elements and mesh quality was evaluated based on the two parameters:

- Orthogonal Quality—defining to what extent the mesh is not orthogonal. The best cells are close to 1. In the generated mesh minimum orthogonal quality was 0.2, with an average value of 0.95.
- Aspect Ratio—defining the ratio of cell sizes in different dimensions. Presented mesh is characterized with maximum aspect ratio of 7 and with the average value equal to 1.4.

http://dx.doi.org/10.5772/64442

Because of the discrepancy of scale between the burner and of the larger volume of the boiler, the geometrical model was subdivided into fine-grid regions around the burners and coarser regions elsewhere. In order to facilitate the meshing process, the circular drop tubes have been replaced by rectangular ones and the platen superheaters have been modeled as zero-thickness horizontal planes. A mesh independence analysis was performed for the initial mesh consisting of 4.0 million control volumes. Reduction of cell number to about 3.3 million did not substantially change the predicted temperature field and this number of cells was selected to obtain compromise between solution accuracy and computational time. Computational domain and numerical mesh close to the swirl burners region is shown in **Figure 16**.

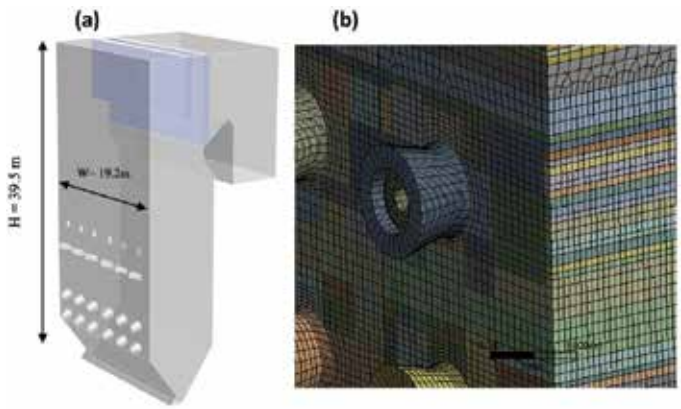

Figure 16. CFD geometrical model of a front-fired boiler (a) and the mesh in burners' region (b).

Simulations were conducted for a boiler load equal to 200 MWe (90% of nominal load). Two cases have been considered: before and after optimization process. Operating conditions have been collected from power plant online monitoring system by averaging 2-hour measurements during steady-state boiler operation. Air/fuel distribution, temperatures, and pulverizers' activity are presented in **Table 3**.

4.2.2. Results of numerical simulation

A tool being able to measure not only the average value, but also the temperature field is needed for a comprehensive CFD model validation. The aggressive environment, ash particles, high temperatures, and large dimensions of the boiler make temperature measurement a complex task [61]. Traditionally used suction pyrometry is extremely accurate and provides information of local temperatures only [62]. In order to account for a dynamic and turbulent environment in the combustion chamber, representative temperature distribution can be obtained only by performing simultaneous measurements. Number of available test ports poses a technical limitation. A turning point in accuracy assessment of CFD furnace models came with Acoustic Pyrometry [63]. This technology can provide average value in the selected cross-section. A detail validation study of the CFD model by comparison of computations against Acoustic Pyrometry measurements was demonstrated in [19].

Before optimization				
	Burner level I	**Burner level II**	**Burner level III**	**Sum:**
Not active burner/mill	All active	E2, E3	E1, E4	
Coal (kg/s)	9.17	6.55	8.46	24.18
Core air (kg/s)	0.88	0.88	0	1.76
Primary air (kg/s)	25.41	16.24	34.08	75.73
Secondary air (kg/s)	6.16	6.16	3.52	15.84
Tertiary air (kg/s)	9.02	9.02	0	18.04
OFA II (kg/s)	31.27			31.27
OFA III (kg/s)	22.99			22.99
Protective air (kg/s)	35.81			35.81
Bottom air (kg/s)	4.6			4.6
Total air (kg/s)	206.05			206.05
Total air excess	1.11			1.11
Burner belt air excess	0.6			0.6
Primary/secondary air temperature (K)	386/573			
After optimization				
	Burner level I	**Burner level II**	**Burner level III**	**Sum:**
Not active burner/mill	All active	E2, E3	E1, E4	
Coal (kg/s)	9.39	6.55	8.59	24.53
Core air (kg/s)	0.96	0.96	0	1.92
Primary air (kg/s)	24.67	16.09	33.36	74.12
Secondary air (kg/s)	6.72	6.72	3.84	17.28
Tertiary air (kg/s)	9.83	9.83	0	19.66
OFA II (kg/s)	31.92			31.92
OFA III (kg/s)	23.47			23.47
Protective air (kg/s)	35.95			35.95
Bottom air (kg/s)	4.69			4.69
Total air (kg/s)	209.01			209.01
Total air excess	1.11			1.11
Burner belt air excess	0.6			0.6
Primary/secondary air temperature (K)	386/573			

Table 3. Boundary conditions.

To show the temperature field variation over the surface, an area-based and mass-based uniformity indexes (UI_{area}, UI_{mass}) of temperature distribution were used:

http://dx.doi.org/10.5772/64442

$$UI_{area} = 1 - \frac{\sum_{i=1}^{N}\left[\left(\left|T_i - T_{average}\right|\right)\cdot A_i\right]}{2\cdot T_{average}\cdot A} \tag{29}$$

$$UI_{mass} = 1 - \frac{\sum_{i=1}^{N}\left[\left(\left|T_i - T_{average_{mass}}\right|\right)\cdot\left(\rho_i\cdot w_i\cdot A_i\right)\right]}{2\cdot T_{average_{mass}}\cdot\sum_{i=1}^{N}\left(\rho_i\cdot w_i\cdot A_i\right)} \tag{30}$$

where subscript *i* is the denoting facet defining the surface, *N* is the total number of facets (12 zones for AGAM, 2260 facets for CFD), T_{average} is the average temperature in the cross-section plane (*K*), *A* is the cross-section area (m), ρ is the density (kg/m^3), and *w* is the velocity (m/s).

The mass-based average temperature in the cross-section plane is defined as:

$$T_{average_{mass}} = \frac{\sum_{i=1}^{N}\left[T_i\cdot\left(\rho_i\cdot w_i\cdot A_i\right)\right]}{\sum_{i=1}^{N}\left(\rho_i\cdot w_i\cdot A_i\right)} \tag{31}$$

For the calculation of mass-based uniformity index, the values of average densities and velocities in 12 AGAM zones were taken from CFD results as no such measurements were available. CFD prediction of temperature distribution parameters are presented in **Figures 17** and **18**.

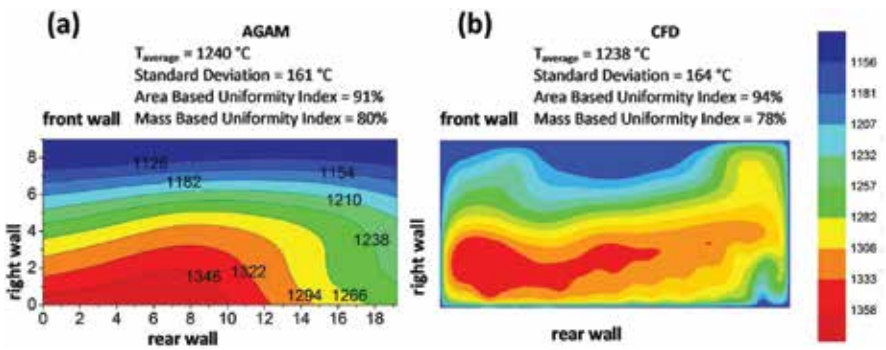

Figure 17. Comparison of temperature contours (°C) measured by acoustic gas temperature measuring system (a) with CFD simulation results (b)—before optimization.

UI values of one indicate the highest uniformity. The area-based UI calculated from measurements exceeds 90% for both cases, which means that no significant gradients exist. Measured standard deviation was 161°C and 164°C for 200 MWe before and after optimization, respectively. A conclusion is that that a more uniform temperature distribution was achieved after optimization process. The temperature homogeneity is important also for platen superheaters

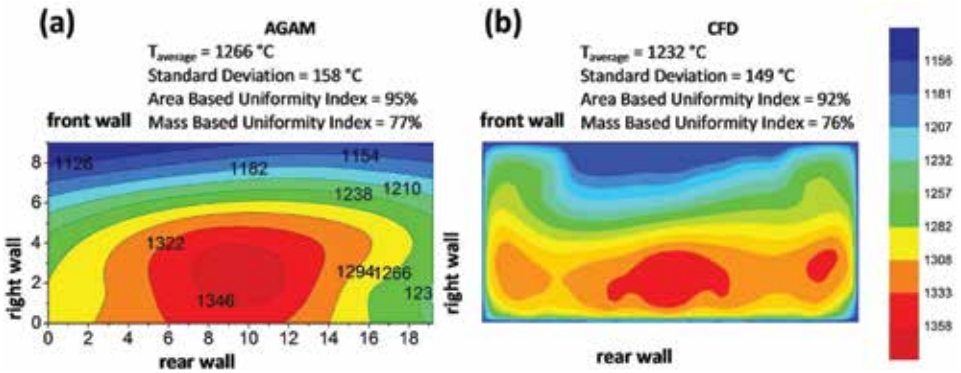

Figure 18. Comparison of temperature contours (°C) measured by acoustic gas temperature measuring system (a) with CFD simulation results (b)—after optimization.

operation, which are located above the combustion chamber. High value of area-based UI indicates relatively uniform distribution of radiative heat flux. The mass-based UI of temperature distribution can be associated with convective heat transfer. Calculated values of 77% and 79% suggest less evenly distributed convective heat flux in comparison to the radiative one. The differences of temperature distribution inside the combustion chamber are presented in **Figure 19**.

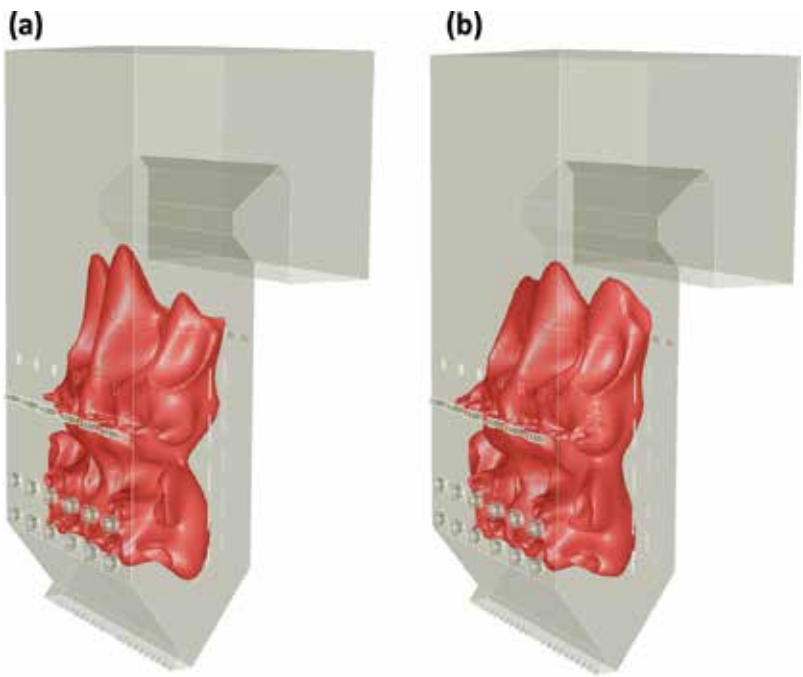

Figure 19. Iso-surface of temperature equal to 1600K before (a) and after (b) optimization.

http://dx.doi.org/10.5772/64442

After optimization the measured average temperature was 34°C higher than calculated temperature, which corresponds to 3% relative error where before optimization the difference was only about 2°C. Since the heat transfer in the furnace is highly dependent on the emissivity of the furnace wall, the choice of this value has significant influence on the calculated average temperature. All the results presented in this paper correspond to wall emissivity equal to 0.7. More detailed description of thermal wall boundary conditions can be introduced using deposition model with thermal properties submodel [55].

In addition to the verification of calculated temperature distributions, comparisons were also made of the basic values measured during boiler operation. Average values of CO, NO_x, and UBC were determined at the outlet plane of the model and compared with measured values before and after the optimization process (**Table 4**).

The results of numerical simulation and measurement confirmed the favorable effect of the combustion optimization process on the values received at the boiler outlet. By changing the operating conditions value of CO, NO_x, as well as the unburned carbon in ash was reduced.

Before optimization				
	T_{AGAM} (°C)	CO (ppm)	NO_x (mg/m^3)	UBC (%)
Calculations	1238	266	252	4.54
Measurements	1240	245	237	2.53
After optimization				
	T_{AGAM} (°C)	CO (ppm)	NO_x (mg/m^3)	UBC (%)
Calculations	1232	258	247	4.4
Measurements	1266	245	223	2.5

Table 4. Comparison of calculated and measured results.

4.3. Results of optimization process

The optimization performance evaluation was done by analyzing historical data collected from 2 months test. The method of analysis consists of results comparison before and after optimization. The results are presented as mean values of boiler efficiency (**Figure 20**) and UBC content (**Figure 21**) in function of unit load in range from low load (135 MWe) to maximum load (225 MWe). The measuring data has been prepared before analysis and only the representative data has been chosen to evaluate the results.

The results of performed tests indicate that boiler efficiency can be increased approximately by 0.2%, thanks to the optimization of boiler operation conditions. The biggest improvement of boiler performance can be achieved at high loads even by 0.6%. The lowest increase of efficiency is observed for temporary states when the time of boiler operating is shorter than at nominal load. All the effects presented above have been obtained keeping the NOx emission and total organic carbon content in ash at the correct level.

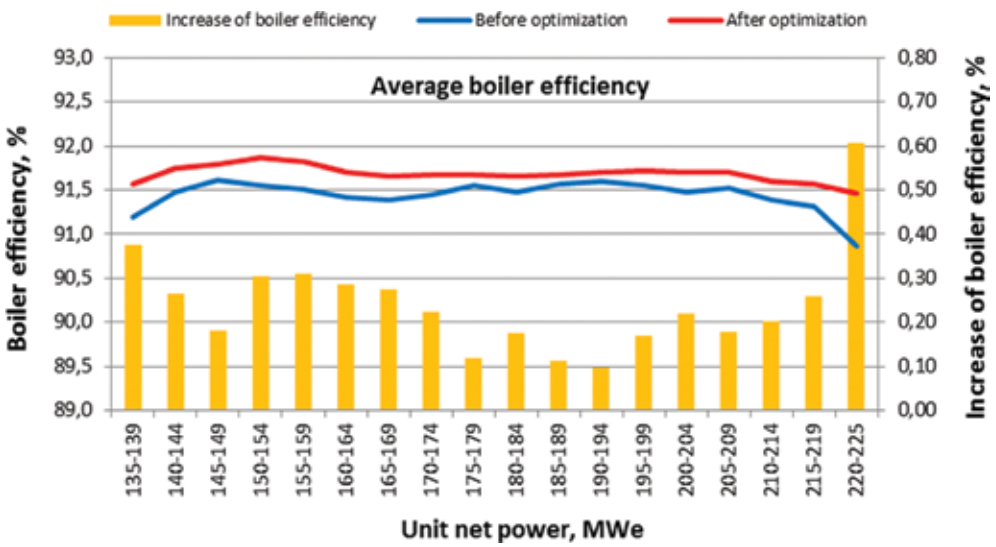

Figure 20. Boiler efficiency as a function of unit load, before and after optimization.

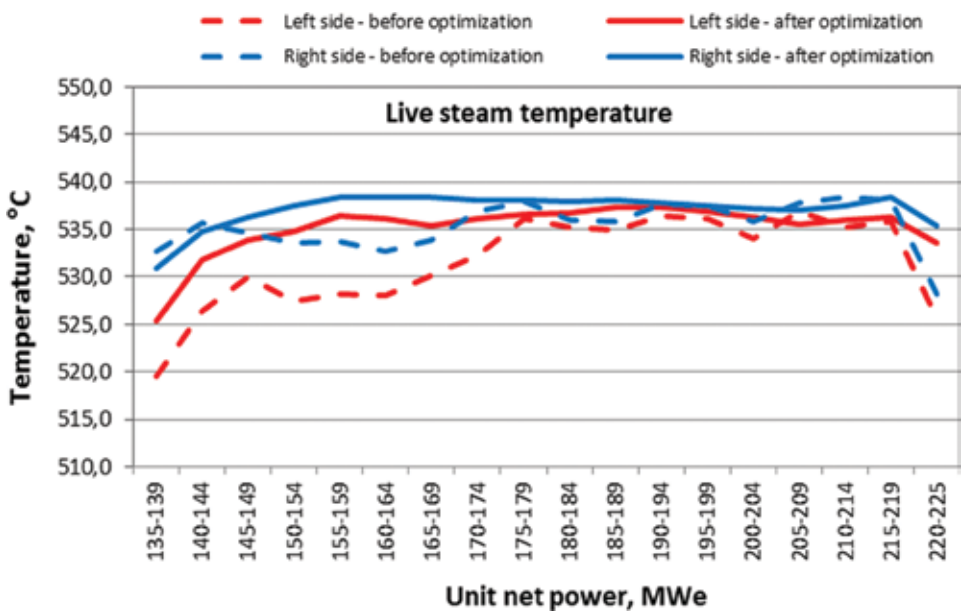

Figure 21. Live steam temperature as a function of unit load, before and after optimization.

Thermal boiler efficiency depends largely on the steam parameters at the boiler outlet. In the case of exceeding defined value, spray attemperators are launched. This process reduces the overall efficiency of the boiler and the amount of spray water has to be minimized. If the steam temperature is below the required value, parameters of the working fluid at the turbine inlet

http://dx.doi.org/10.5772/64442

are lower, reducing the overall process efficiency. The measurement results of live and reheated steam temperatures as a function of unit load are shown in **Figures 21** and **22**.

According to dynamic load changes profile and frequent change of mill unit configuration in operation those temperatures could differ from the reference value (540°C) to over 20–30°C. At low load (135 MWe) those temperatures could drop even below 520°C. At high load (225 MWe) the temperatures reach the 540°C level but with support of significant spray water flow. The results of steam temperature analysis (before and after optimization) confirm the positive effect of optimization. Temperature values of live and reheated steam are close to the required temperature 540°C in the full range of unit load. Also, the temperature variations of steam in transition states, between minimum and maximum load, were eliminated. Optimization of reheated steam temperature has a significant effect on the boiler efficiency. Due to the low pressure of reheated steam in comparison with live steam, temperature has large influence on the total energy amount generated inside the boiler.

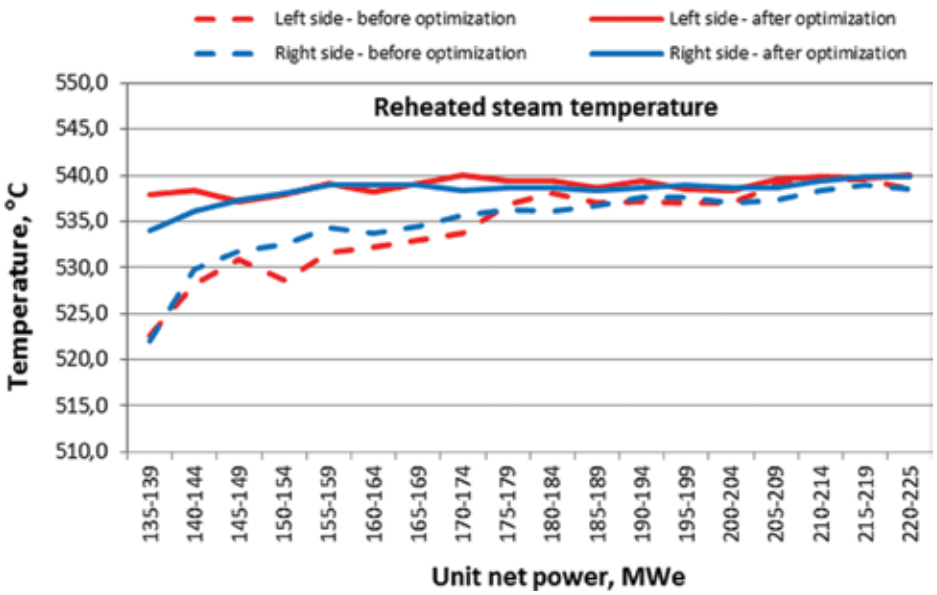

Figure 22. Reheated steam temperature as a function of unit load, before and after optimization.

The observed parameter during optimization process was temperature of live and reheated steam measured on the left and on the right side of boiler outlet, to underline that symmetry process also requires optimization. Optimization of symmetry process in practice means the minimization of differences between left and right side of the boiler in: coal flow, live and reheat steam temperatures, as well as flue gas temperature measured by AGAM and O_2, CO, and NO_X contents in flue gases. Thanks to the optimization process, the differences of steam temperature at the boiler outlet between left and right side were significantly reduced. This effect is observed for both live and reheated steam.

5. Conclusions

The results of experimental and numerical research of coal combustion process in front-fired pulverized coal boiler are presented in the paper. The experimental part was focused on coal combustion optimization to achieve better performances of electricity production process. The main goal of the work was the increase of thermal boiler efficiency based on the advanced monitoring technique of boiler operation conditions.

The experimental research was conducted on the front-fired pulverized coal boiler OP-650, located in EDF Polska Rybnik Power Plant. In the optimization process, the modern measurement systems of flue-gas temperature distribution and fuel-air distribution were used. The acoustic gas temperature measurement system allows to online monitor temperature distribution at furnace exit. The optimal combustion process was identified by uniform temperature distribution measured in online mode. To modify temperature distribution and properties of fire ball, the control system of coal and secondary air mass flow rate has been used. The comparison of results, before and after optimization process, indicates that the boiler efficiency can be increased approximately by 0.2% in the full range of unit load. The rise of boiler efficiency can reach up to even to 0.6% at the nominal load of boiler. Ensuring symmetry of the combustion process by online measuring of temperature distribution allows to reduce the differences between the outlet steam temperature at the left and right of the boiler.

To verify the impact of operating conditions on the temperature distribution as well as CO, NO_x, and TOC content in flue-gas, the numerical investigation using computational fluid dynamics modeling was done. To validate results of modeling, the acoustic gas temperature measurements in the form of temperature distribution at the furnace exit was used. The results of numerical simulations were compared with measured values. Good accuracy between numerical and experimental results was observed.

Results of numerical simulations conducted for the two states, before and after optimization, confirmed combustion process improvement by optimization of boiler operating conditions. Boundary conditions included in numerical models were based on values from power plant online monitoring system, before and after optimization process. Reduction of CO, NO_x, and TOC content in flue-gas by changing boundary conditions according to the measured values was confirmed. The numerical modeling provides also new important results of combustion process as, e.g., temperature distribution inside whole chamber of boiler.

Based on the results provided by modern measuring systems and complex CFD analysis, it becomes possible to effectively monitor the combustion process and indicate new guidelines (including changes in procedure of automatic control systems) to ensure the optimal operation of the boiler. The online monitoring systems allow to improve the combustion process through the uniform coal and air supply into the boiler. The effects of the change may increase boiler thermal efficiency keeping the NO_x emissions and TOC content at the correct level. The combination of these powerful tools can be used more often by the researchers working on the combustion process improvement as well as by the boiler manufacturers.

http://dx.doi.org/10.5772/64442

Acknowledgements

This research was partially funded from GEKON program by the National Center of Research and Development and the National Fund for Environmental Protection and Water Management under research and development project No. GEKON1/O2/213655/9/2014.

Nomenclature

Abbreviations

AGAM	Acoustic gas temperature measurement system
CFD	Computational fluid dynamics
CV	Controlled variable
DAF	Dry ash free
DCS	Distributed control system
DO method	Discrete ordinates method
EDC	Eddy dissipation concept
FD	Forced draft
FG-DVC	model Functional-group depolymerization vaporization cross-linking model
ID	Inducted draft
LHV	Low heating value
LOI	Loss on ignition
MV	Manipulated variable
OFA	Over fire air
PC boiler	Pulverized coal boiler
PF	Pulverized fuel
PID	Proportional–integral–derivative controller
PDF	Probability density function
PSR	Perfectly stirred reactors
RTE	Radiative transfer equation
SILO software	Stochastical Immunological Layer Optimizer software
TDP	Tabulated devolatilization process
TOC	Total organic carbon
UBC	Unburned carbon
VM	Main controller
WSGGM method	Weighted sum of gray gases method

Symbols

A	cross-section area, m^2
A_f	empirical constant dependent on the fuel, kg/(m^2·s·atm)
B	acoustic constant, $m^2/(s^2 \cdot K)$
D	molecular diffusion coefficient, m^2/s
D_p	particle radius, m
D_0	diffusion coefficient, m^2/s
dP	differential pressure, Pa
$f_{v,0}$	volatile fraction
f	mixture fraction
$\widetilde{f}$	mean mixture fraction
$\widetilde{f''2}$	mixture fraction variance
f_S	stoichiometric mixture fraction
h	enthalpy, kJ/kg
h_L	enthalpy on the lean side of f_S, kJ/kg
h_R	enthalpy on the rich side of f_S, kJ/kg
h_{Ox}	enthalpy of oxidizer at $f = 0$, kJ/kg
h_{Fuel}	enthalpy of fuel at f=1, kJ/kg
h_S	enthalpy of products at the stoichiometric mixture fraction f_S, kJ/kg
$\tilde{h}$	mean enthalpy, kJ/kg
I	radiation intensity, W/sr
k	devolatilization rate, 1/s
l	distance between transmitter and receiver, m
M	molar mass of gas in Eq. (3), kg/kmol
M	molecular mass
$m_{p,0}$	initial particle mass, kg
$\overline{m_i}$	average mass fraction of the species i
N	total number of facets
O_{2z}	oxygen set point at the boiler outlet
$O_{2z}(M_p)$	oxygen value as a function of steam mass flow rate
$M_p \Delta O_{2z}(O)$	difference of oxygen content at the left and right side of boiler outlet
R	universal gas constant, kJ/(kmol·K)

http://dx.doi.org/10.5772/64442

$\Re_c$	kinetic reaction rate, kg/(m²·s·atm)
$\Re_{diff}$	diffusion rate, kg/(m²·s·atm)
R_{O2}	O_2 controller
R_w	secondary air controller
T	gas temperature, K
T_p	particle temperature, K
T_g	bulk temperature, K
U_c	unburned carbon in particle
UI	uniformity index
u_i	velocity in direction of i, m/s
V_C	total air flow rate
V_P, V_L	air flow rate on the right and left side of boiler
v	speed of sound in Eq. (3), m/s
w	velocity, m/s
X_{O2}	oxygen mole fraction
x_i	direction i in Cartesian coordinates system, m
y	volatile mass fraction
Y_F	fuel mass fraction
Y_{Fuel}	mass fraction of fuel at $f = 1$
Y_O	oxidizer mass fraction
Y_{Ox}	mass fraction of oxidizer at $f = 0$
Y_P	products mass fraction
Y_S	mass fraction of products of stoichiometric reaction at $f = f_S$

Greek symbols

ε	turbulent kinetic energy dissipation rate, m²/s³
ε_p	coal particle emissivity
k	adiabatic index
k	absorption coefficient in Eq. (27), 1/m
ν	kinematic viscosity, m²/s
ω_i*	chemical reaction rate calculated from Arrhenius equation, kmol/m³/s
Φ	phase function, 1/sr
ϕ	ratio of the reacting surface to the surface of the sphere
ρ	density, kg/m³

σ scattering coefficient, 1/m

τ time of delay, s

τ^* residence time, s

Subscripts

0	initial
c	carbon
f	fuel
L	lean side
O_2	*oxygen*
Ox	oxidizer
Ox	oxidizer
p	coal particle
R	rich side
S	stoichiometric

Author details

Paweł Madejski[1*], Tomasz Janda[1], Norbert Modliński[2] and Daniel Nabagło[1]

*Address all correspondence to: Pawel.Madejski@edf.pl

1 Research and Development, EDF Polska S.A., Kraków, Poland

2 Department of Boilers, Combustion and Energy Processes, Wrocław University of Technology, Wrocław, Poland

References

[1] Fu C., Anantharaman R., Jordal K., Gundersen T.: Thermal efficiency of coal-fired power plants: From theoretical to practical assessments. Energy Conversion and Management. 2015;105:530–544. DOI:10.1016/j.enconman.2015.08.019

[2] Hagi H., Neveuxa T., Le Moullec Y.: Efficiency evaluation procedure of coal-fired power plants with CO2 capture, cogeneration and hybridization. Energy. 2015;91:306–323. DOI:10.1016/j.energy.2015.08.038

http://dx.doi.org/10.5772/64442

[3] Arias B., Criado Y.A., Sanchez-Biezma A., Abanades J.C.: Oxy-fired fluidized bed combustors with a flexible power output using circulating solids for thermal energy storage. Applied Energy. 2014;132:127–136. DOI:10.1016/j.apenergy.2014.06.074

[4] Chmielniak T., Lepszy S., Wójcik K.: Analysis of gas turbine combined heat and power system for carbon capture installation of coal-fired power plant. Energy. 2012;45:125–133. DOI:10.1016/j.energy.2012.04.055

[5] Ziółkowski P., Zakrzewski W., Kaczmarczyk O., Badur J.: Thermodynamic analysis of the double Brayton cycle with the use of oxy combustion and capture of CO2. Archives of Thermodynamics. 2013;34(2):23–28.

[6] Le Moullec Y.: Conceptual study of a high efficiency coal-fired power plant with CO_2 captures using a supercritical CO_2 Brayton cycle. Energy. 2013;32:32–46. DOI:10.1016/j.energy.2012.10.022

[7] Gao H., Runstedtler A., Majeski A., Boisvert P., Campbell D.: Optimizing a woodship and coal co-firing retrofit for a power utility boiler using CFD. Biomass and Bioenergy. 2016;88:35–42. DOI: 10.1016/j.biombioe.2016.03.006

[8] Hwang M.-Y., Kim S.-M., Kim G.-B., Lee B.-H., Song J.-H., Park M.-S., Jeon C.-H.: Simulation studies on direct ash recycling and reburning technology in a tangentially fired 500 MW pulverized coal boiler. Fuel. 2013;114:78–87. DOI: 10.1016/j.fuel.2013.05.087

[9] Belosevic S., Tomanovic I., Beljanski V., Tucakovic D., Zivanovic T.: Numerical prediction of processes for clean and efficient combustion of pulverized coal in power plants. Applied Thermal Engineering. 2015;74:102–110. DOI:10.1016/j.applthermaleng.2013.11.019

[10] Adamczyk W., Werle S., Ryfa A.: Application of the computational method for predicting NOx reduction within large scale coal-fired boiler. Applied Thermal Engineering. 2014;73:343–350. DOI: 10.1016/j.applthermaleng.2014.07.045

[11] Smrekar J., Potočnik P., Senegačnik A.: Multi-step-ahead prediction of NOx emissions for a coal-based boiler. Apllied Energy. 2013;106:89–99. DOI:10.1016/j.apenergy.2012.10.056

[12] Zhou H., Zheng L., Cen K.: Computational intelligence approach for NOx emissions minimization in a coal-fired utility boiler. Energy Conversion and Management. 2010;51:580–586. DOI:10.1016/j.enconman.2009.11.002

[13] Song J., Romero C., Yao Z., He B.: Improved artificial bee colony-based optimization of boiler combustion considering NOX emissions, heat rate and fly ash recycling for on-line applications. Fuel. 2016;172:20–28. DOI:10.1016/j.fuel.2015.12.065

[14] Zheng L.G., Zhou H., Cen K.F., Wang C.L.: A comparative study of optimization algorithms for low NOx combustion modification at a coal-fired utility boiler. Expert Systems with Applications. 2009;36:2780–2793. DOI:10.1016/j.eswa.2008.01.088

[15] Nabagło D., Janda T., Szczepanek K., Madejski P.: Evaluation of combustion process quality in boiler OP-650 using modern measurement systems (in polish). Power Machines and Devices (Eds: Łopata S., Grądziel S.), pp. 163–175, Cracow University of Technology Publishing, Kraków, 2013, ISBN 978-83-7242-720-5

[16] Deuster M., Acoustic Gas Temperature Measurement, Proceedings of VDI Forum 05F0012003 Wissenforum Temperature Measurement Technique 29-30 September 2009, Aldenhoven, Germany

[17] Nabagło D., Madejski P.: Combustion process analysis in boiler OP-650k based on acoustic gas temperature measuring system. Proceedings of 3rd International Conference on Contemporary Problems of Thermal Engineering CPOTE 2012; 18–20 September 2012, Gliwice, Poland.

[18] Campbell R.: Increasing the Efficiency of existing Coal-Fired Power Plant, Congressional Research Service Report, December 2013, R43343, www.crs.gov

[19] Modliński N., Madejski P., Janda T., Szczepanek K., Kordylewski W.: A validation of computational fluid dynamics temperature distribution prediction in a pulverized coal boiler with acoustic temperature measurement. Energy. 2015;92:77–86, DOI:10.1016/j.energy.2015.05.124

[20] Taler J., Węglowski B., Taler D., Sobota T., Dzierwa P., Trojan M., Madejski P., Pilarczyk M.: Determination of start-up curves for a boiler with natural circulation based on the analysis of stress distribution in critical pressure components. Energy. 2015;92:153–159. DOI:10.1016/j.energy.2015.03.086

[21] Modliński N.: Computational modeling of a utility boiler tangentially-fired furnace retrofitted with swirl burners. Fuel Processing Technology. 2010;91:1601–1608. DOI: 10.1016/j.fuproc.2010.06.008

[22] Belosevic S., Sijercic M., Oka S., Tucakovic D.: Three-dimensional modeling of utility boiler pulverized coal tangentially fired furnace. International Journal of Heat and Mass Transfer. 2006;49:3371–3380. DOI:10.1016/j.ijheatmasstransfer. 2006.03.022

[23] Belosevic S., Sijercic M., Tuckovic D., Crnomarkovic N.: A numerical study of a utility boiler tangentially-fired furnace under different operating conditions. Fuel. 2008;87:3331–3338. DOI:10.1016/j.fuel.2008.05.014

[24] Asotani T., Yamashita T., Tominga H., Uesugi Y., Itaya Y., Mori S.: Prediction if ignition behavior in a tangentially fired pulverized coal boiler using CFD. Fuel. 2008;87:482–490. DOI:10.1016/j.fuel.2007.04.018

[25] Yin C., Rossendahl L., Condra T.: Further study of the gas temperature deviation in large-scale tangentially-fired boilers. Fuel. 2003;82:1127–1137. DOI:10.1016/ S0016-2361(02)00418-0

http://dx.doi.org/10.5772/64442

[26] Fan J., Qian L., Ma Y., Sun P., Cen K.: Computational modeling of pulverized coal combustion processes in tangentially fired furnaces. Chemical Engineering Journal. 2001;81:261–269. DOI:10.1016/S1385-8947(00)00212-6

[27] Vuthaluru R., Vuthaluru H.B.: Modelling of a wall fired furnace for different operating conditions using FLUENT. Fuel Processing Technology. 2006;87:633–639. DOI:10.1016/j.fuproc.2006.01.004

[28] Minghou X., Azevedo J.L.T, Carvalho M.G.: Modeling of a front wall fired utility boiler for different operating conditions. Computer Methods in Applied Mechanics and Engineering. 2001;190:3581–3590. DOI:10.1016/S0045-7825(00)00287-5

[29] Sanghyun P., Jungeun A.K., Changkook R., Taeyoung C., Won Y., Young-Ju K., Ho-Young P., Hee-Chun L.: Combustion and heat transfer characteristics of oxy-coal combustion in a 100 MWe front-wall-fired furnace. Fuel. 2013;106:718–729. DOI: 10.1016/j.fuel.2012.11.001

[30] Chui E., Gao H.: Estimation of NOx emissions from coal-fired utility boilers. Fuel. 2010;89:2977–2984. DOI:10.1016/j.fuel.2010.05.008

[31] Dal Secco S., Juan O., Louis-Louisy M., Lucas Y.-V., Plion P., Porcheron L.: Using a genetic algorithm and CFD to identify low NOx configurations in an industrial boiler. Fuel. 2015;158:672–683. DOI:10.1016/j.fuel.2015.06.021

[32] Modliński N.: Numerical simulation of SNCR (selective non-catalytic reduction) process in coal fired grate boiler. Energy. 2015;92:67–76. DOI:10.1016/j.energy. 2015.03.124

[33] Wiatros-Motyka M.: Optimizing fuel flow in pulverized coal and biomass-fired boilers. 20 IEA Clean Coal Centre. 2016:28.

[34] Shih T., Liou W., Shabbir A., Yang Z., Zhu J.: A new k-ε Eddy-viscosity model for high Reynolds number turbulent flows - model development and validation. Computers Fluids. 1995:24(3):227–238.

[35] Launder B.E., Spalding D.B.: The numerical computation of turbulent flows. Computer Methods in Applied Mechanics and Engineering. 1974;3:269–289. DOI: 10.1016/0045-7825(74)90029-2.

[36] Williams A., Backreedy R., Habib R., Jones J.M., Pourkashanian M.: Modeling coal combustion: the current position. Fuel. 2002;81:605–618.

[37] Advanced Fuel Research Inc. Usurers guide for FG-DVC, East Hartford, CT, 2004.

[38] Williams A., Backreedy R., Habib R., Jones J.M., Pourkashanian M.: An extended coal combustion model. Fuel. 1999;78:1745–1754.

[39] Bradley D., Lawes M., Park H.Y., Usta N.: Modeling of laminar pulverised coal flames with speciated devolatilization and comparisons with experiments. Combustion and Flame. 2006;44:190–204.

[40] Hashimoto N., Kurose R., Hwang S., Tsuji H., Shirai H.: A numerical simulation of pulverized coal combustion employing a tabulated-devolatilization-process model (TDP model). Combustion and Flame. 2012;159:353–366.

[41] Magnussen B.F., Hjertager B.H.: On mathematical models of turbulent combustion with special emphasis on soot formation and combustion. 16th Symp. (Int'l.) on Combustion. The Combustion Institute. 1976:719–729.

[42] Hautman D., Dryer F., Schug K., Glassman I.: A multiple-step overall kinetic mechanism for the oxidation of hydrocarbons. Combustion Science and Technology. 1981;25:219–235.

[43] Code Saturne 4.0.0 Theory Guide, Fluid Dynamics, Power Generation and Environment Department, Single Phase Thermal-Hydraulics Group, EDF Lab Chatou, France, April 2015.

[44] Pope S.B.: The probability approach to the modelling of turbulent reacting flows. Combustion and Flame. 1976;27:299–312.

[45] Poinsot T., Veynante D.: Theoretical and Numerical Combustion, 2nd ed., R.T. Edwards, Inc., Philadelphia, USA, 2005.

[46] Baum M., Street P.: Predicting the combustion behavior of coal particles. Combustion Science Technology. 1971;3:231–243.

[47] Boyd R., Kent J.: Three-dimensional furnace computer modeling. 21st Symposium (international) on Combustion, Munich, West Germany, 1986:265–274.

[48] Modest M.: Radiative Heat Transfer, 2nd ed., Academic Press, Amsterdam, 2003.

[49] Jamaluddin A., Smith P.: Predicting radiative transfer in axisymmetric cylindrical enclosures using the discrete transfer method. Combustion Science Technology. 1988;62:173–186.

[50] Hottel H.C., Sarofim A.F.: Radiative Transfer, McGraw-Hill, New York, 1967.

[51] Smith T., Shen Z., Friedman J.: Evaluation of coefficients for the weighted sum of gray gases model. Transactions of the ASME. 1982;104:602–608.

[52] Taylor P., Foster P.: Some gray gas weighting coefficients for CO_2-H_2O-soot mixtures. International Journal of Heat and Mass Transfer. 1974;18:1331–1332.

[53] Lockwood F.C., Rizvi S.M., Shah N.G.: Comparative predictive experience of coal firing. Proceedings of the Institution of Mechanical Engineers. 1986;200:79–87.

[54] Karampinis E., Nikolopoulos N., Nikolopoulos A., Grammelis P., Kakaras E.: Numerical investigation Greek lignite/cardoon co-firing in a tangentially fired furnace. Applied Energy. 2012;97:514–524.

[55] Modlinski N.: Computational modeling of a tangentially fired boiler with deposit formation phenomena. Chemical and Process Engineering. 2014;35:361–368.

http://dx.doi.org/10.5772/64442

[56] Wojdan K., Świrski K., Warchoł M., Milewski J., Miller A.: A practical approach to combustion process optimization using an improved immune optimizer. Sustainable Research and Innovation Proceedings, 3, Kenya, 2011.

[57] Śladewski Ł., Nabagło D., Janda T., Chachuła J.: Combustion process optimization by using immune optimizer in power boiler. Archivum Combustionis 2015;35:52–56.

[58] www.tt.com.pl

[59] ANSYS FLUENT, www.ansys.com.

[60] Wang Z., Zhuo Y., Chen C., Xu X.: Mesh investigation about crossflow diffusion of computational flow dynamics in tangential combustion flow field. Proceedings - Chinese Society of Electrical Engineers. 2007;27:22–28.

[61] Pallares J., Arauzo I., Diez L.I.: Numerical prediction of unburned carbon levels in large pulverized coal utility boilers. Fuel. 2005;84:2364–2371.

[62] Rinaldi F., Najafi B.: Temperature measurements in WTE boilers using suction pyrometers. Sensors. 2013;13:15633–15655.

[63] Bramanti M., Salerno E., Tonazzini A., Pasini S.: A. Gray, An acoustic pyrometer system for tomographic thermal imaging in power plant boilers. IEEE Transactions on Instrumentation and Measurement. 1996;45:159–167.

Chapter 3

Bituminous Coal Combustion with New Insights

Guan-Fu Pan, Hong-De Xia and Zhen-Yu Tian

Additional information is available at the end of the chapter

http://dx.doi.org/10.5772/64136

Abstract

As one of the most important primary energy, bituminous coal has been widely applied in many fields. The combustion studies of bituminous coal have attracted a lot of attention due to the releases of hazardous emissions. This work focuses on the investigation of combustion characteristics of Shenmu bituminous pulverized coal as a representative bituminous coal in China with a combined TG-MS-FTIR system by considering the effect of particle size, heating rate, and the total flow rate. The combustion products were accurately quantified by normalization and numerical analysis of MS results. The results indicate that the decrease of the particle size, heating rate, and the total flow rate result in lower ignition and burnout temperatures. The activation energy tends to be lower with smaller particle size, faster heating rate, and lower total flow rate. The MS and FTIR results demonstrate that lower concentrations of different products, such as NO, NO_2, HCN, CH_4, and SO_2, were produced with smaller particle size, slower heating rate, and lower total flow rate. This work will guide to understand the combustion kinetics of pulverized coals and be beneficial to control the formation of pollutants.

Keywords: bituminous coal, combustion characteristics, TG-MS-FTIR technique, particle size, heating rate, flow rate

1. Introduction

Coal is one of the most important primary energy for last whole century and future decades. As the foundation of the application of coal, the research on bituminous coal combustion has never been stopped. Different kinds of bituminous coals with multitudinous research instruments and methods for the investigation of coal combustion characteristics have been carried out for

INTECH
open science | open minds

© 2016 The Author(s). Licensee InTech. This chapter is distributed under the terms of the Creative Commons Attribution License (http://creativecommons.org/licenses/by/3.0), which permits unrestricted use, distribution, and reproduction in any medium, provided the original work is properly cited. CC BY

years. Peng and Wu [1] studied the bromine release from bituminous coal during combustion. They used the sequential chemical extraction method to investigate the modes of occurrence of bromine in bituminous coal by a tube furnace. The results showed that the bromine release rate increased with the increase of temperature, and 500–900°C was the main stage of bromine release. They also concluded that water vapor can promote the Br release and the additive of SiO_2 can capture the bromine effectively in the process of the coal combustion. Tsuji et al. [2] studied the combustion emission of one bituminous coal from Australia and two high-ash coals from South Africa on different blending ratios by an advanced low NO_x burner. They concluded that the NO_x emission characteristic from bituminous coals was similar to these two high-ash coals. The combustion efficiencies on the bituminous coals were higher than those of the high-ash coals. Molina and Shaddix [3] studied the influence of enhanced oxygen levels and CO_2 bath gas on single-particle pulverized coal ignition of a U.S. eastern bituminous coal. For the ignition process observed in the experiments, the CO_2 results were explained by its higher molar specific heat and the O_2 results were explained by the effect of O_2 concentration on the local mixture reactivity. The experiments showed that a lower O_2 concentration and the presence of CO_2 increased the ignition delay time but had no measurable influence on the time of complete volatile combustion. Gao et al. [4] performed an online analysis of the soot emissions from the Inner Mongolia bituminous coal combustion and pyrolysis processes with a vacuum ultraviolet photoionization aerosol time-of-flight mass spectrometer. They concluded that at lower oven temperatures (<873 K), the soot particles generated in combustion processes contained more oxygen-containing PAHs (O-PAHs). At high temperatures, however, the soot particles from combustion contained mainly PAHs without any functional groups. Yu et al. [5] studied the characteristics of char particles and their effects on the emission of particulate matter (PM) from the combustion of a Chinese bituminous coal in a laboratory-scale drop tube furnace. The coal samples were subjected to combusted in 20 and 50% O_2 at 1373, 1523, and 1673 K, respectively. The results showed that coal particle size and pyrolysis temperature had a significant influence on the char characteristics. The influence of combustion temperature on supermicron-sized PM emission greatly depended on the oxygen concentration. Among various kinds of bituminous coals, the Shenmu bituminous coal (SBC) has been adopted as one of the most widely used bituminous coals in China [6–8] since it has the advantages of excellent thermal stability, high calorie, and huge reserves. The investigation of the combustion characteristics is essential to understand the combustion process and control the pollutant products.

In recent years, SBC has been studied in terms of its burning and gasification properties. In 2003, Sun et al. investigated the thermogravimetric (TG) characteristics of SBC and reported that vitrinite had higher volatile matter yield, maximum weight loss rate, and lower initial decomposition temperature and peak temperature than that of inertinite. Compared to pressure and heating rate, the temperature has a more important impact on the devolatilization of SBC [9]. With TG analysis, Zhao et al. studied the ignition temperature (T_{ig}), maximum reaction temperature (T_{max}), burning rate, burnout temperature (T_{burn}), and combustion features of SBC coal and coke fine mixed sample. The results showed that with the increase in the coke fine content, T_{ig} of the coal and coke fine mixture, the caloric value of the sample, and T_{max} would increase, while the burning rate would decrease [10]. Yang et al. studied the SBC ash's physicochemistry with temperature on the basis of TG-differential scanning colorimetry

(TG-DSC) methods. The results indicated that the SBC ash could convert into an eutectic at low temperatures [11]. Chang et al. investigated the formation of nitrogenous products from the gasification of SBC in a fluidized-bed/fixed-bed reactor [7]. More recently, Yang et al. investigated the SBC's characteristics of combustion and nitrogen oxide (NO_x) release in a fixed-bed reactor [12]. The composition of the flue gas was analyzed to investigate the effect of sodium acetate on the combustion process and NO_x emission. Sodium acetate was observed to reduce NO_x emissions due to their special reactions with the nitrogen-containing species [12]. Even though the maceral groups, characteristic temperature, ash's physicochemistry, and nitrogenous products of SBC have been studied, a systematic study regarding the most important conditions such as the effect of particle size, heating rate, and total flow rate on its combustion characteristics is scarcely available in the literature. Mass spectrometry (MS) and Fourier transform infrared spectroscopy (FTIR) are widely used in multicomponent analysis in energy chemical industry and are suitable to be combined with TG and the gas chromatographic method [13]. It is efficient and reliable to use the TG-MS-FTIR system for numerical analysis of the combustion characteristics of coal. In the current work, the combustion characteristic of SBC was comprehensively studied with the online TG-FTIR-MS system. The products formed in the combustion of SBC were accurately qualified and quantified by considering the electron impact ionization cross sections, ion flow intensities, and the partial pressures of different species. The condition-characteristic relationship among the particle size, heating rate and total flow rate and ignition, and burnout temperature as well as activation energy was addressed. With the comprehensive use of TG-FTIR-MS, the detailed combustion characteristics of SBC have been presented for the first time. Such strategy will supply a significant guidance for the real use of SBC and other solid fuels in the future.

2. Materials and methods

2.1. Coal samples

The SBC samples were bought from Shenmu Energy Developments Ltd Company and grinded into powder with different sizes. Before test, the sample was put into drying oven at a temperature of 105°C for 90 min. Then, the coals were sieved to a particle size of lesser than 40, 90–100, 128–180, 280–355, and 355–500 μm. To identify the phases of SBC, X-ray diffraction (XRD) patterns were recorded using Bruker D8 Focus at 40 kV and 150 mA with Cu Kα (λ = 0.154056 nm) radiation. By referring to the Joint Committee on Powder Diffraction Standards (JCPDS) database cards which have also been called power diffraction file (PDF), the crystalline phases were identified. The samples were scanned in step of 0.02° (2θ) over the range of 5–90°. By comparing with standard PDF, it was found that the coal samples are mainly composed of $CaCO_3$, SiO_2, and kaolinite as shown in **Figure 1**. The existence of carbonate could be the main reason to form the weak weight loss peak at the end of the combustion processes.

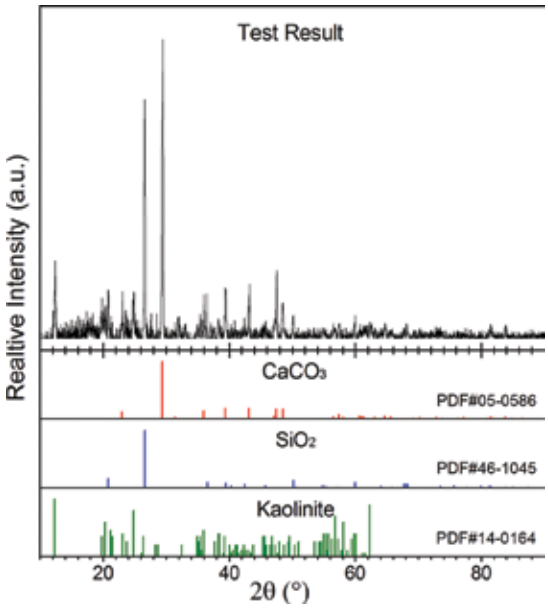

Figure 1. XRD patterns of SBC.

The elements of SBC samples were identified by the coal proximate analyzer as shown in **Table 1**. M_{ad}, A_{ad}, V_{ad}, FC_{ad}, and $Q_{ad.net}$ represent the moisture, ash, volatile, fixed carbon, and low calorific capacity in air-dried basis, respectively. C_{ad}, H_{ad}, O_{ad}, N_{ad}, and S_{ad} represent carbon, hydrogen, oxygen, nitrogen, and sulfur elements in air-dried basis, respectively.

Proximate analysis					Ultimate analysis				
M_{ad} (%)	A_{ad} (%)	V_{ad} (%)	FC_{ad} (%)	$Q_{ad.net}$ (kJ/kg)	C_{ad} (%)	H_{ad} (%)	O_{ad} (%)	N_{ad} (%)	S_{ad} (%)
6.53	10.41	32.40	50.66	26,120	66.70	4.11	10.79	1.04	0.42

Table 1. The proximate analysis and ultimate analysis results of SBC.

2.2. Comprehensive test

The tests of SBC combustion characteristics were performed with the TG-MS-FTIR system which comprises a TG analyzer (STA-449F3, Netzsch), a mass spectrometer (QMS403C, Aeolos), and an FTIR spectrometer (Tensor 27, Bruker). The combined system was controlled simultaneously and data were recorded by a computer as shown in **Figure 2**. Due to the TG's limit of highest heating temperature and heating rate, the highest heating temperature was set at 1200°C and the heating rate were set at 10, 20, 30, and 40°C/min. Considering the oxygen demand for complete combustion of 10 mg SBC samples within the limitations of TG, the total flow rates were set at 50, 100, and 150 sccm. The tests were carried out in four steps. First, an SBC sample of about 10 mg was dispersed on a circular alumina pan and the air in TG chamber

http://dx.doi.org/10.5772/64136

was replaced with a gas mixture which consists of 20% O_2 and 80% Ar. The supplied O_2 was much more than the theoretically needed for the complete oxidation of the SBC sample but was similar to the air. Second, the samples were heated with a heating rate of 10°C/min from 40 to 110°C and kept for 30 min. Third, the samples were heated to 1200°C by four heating rates, namely, 10, 20, 30 and 40°C/min, respectively. Finally, the whole temperature-rising program was finished after an isothermal process of 10 min. Three total flow rates (50, 100, and 150 sccm) containing 20% O_2 and 80% Ar were sent into the TG chamber during the whole heating processes. The detailed experimental conditions are summarized in **Table 2**.

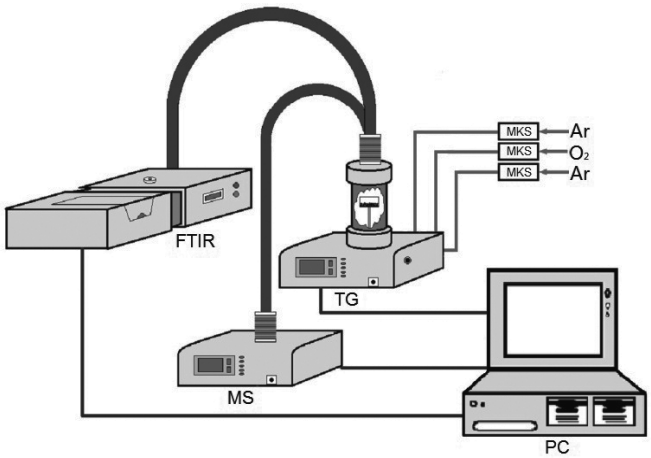

Figure 2. Scheme of the TG-MS-FTIR system.

Condition	Mass (mg)	Flow rate (sccm)			Heating rate (°C/min)	Particle size (μm)
		O_2	Ar	Ar		
1	9.411	20	60	20	20	0–40
2	10.248	20	60	20	10	90–100
3	9.788	20	60	20	20	90–100
4	9.348	20	60	20	30	90–100
5	9.589	20	60	20	40	90–100
6	9.251	20	60	20	20	125–180
7	10.246	20	60	20	20	280–355
8	9.786	20	60	20	20	355–500
9	9.341	10	20	20	20	90–100
10	9.864	30	100	20	20	90–100

Note: Protective gas of TG is 20 sccm Ar constantly.

Table 2. Experimental conditions.

2.3. Data treatment

2.3.1. Characteristic temperature

The ignition characteristic of SBC is analyzed based on T_{ig}. In the present work, T_{ig} is determined by the commonly recognized TG-DTG methods [14]. T_{burn} is defined as the temperature with 98% total weight loss. T_{max}, referring to the temperature at which combustion product own maximum volumetric flow, was also determined through numerical analysis.

2.3.2. Kinetic analysis

The combustion kinetic parameters from TG data are calculated by the Coats-Redfern method [15]:

$$n = 1,\ldots \ln[\frac{-\ln(1-\alpha)}{T^2}] = \ln\frac{AR}{\beta E}(1-\frac{2RT}{E}) - \frac{E}{RT} \tag{1}$$

$$n \neq 1,\ldots \ln[\frac{1-\ln(1-\alpha)^{1-n}}{T^2(1-n)}] = \ln[\frac{AR}{\beta E}(1-\frac{2RT}{E})] - \frac{E}{RT} \tag{2}$$

where $\alpha = (m_0 - m)/(m_0 - m_\infty)$ is the weight loss ratio; m refers to the sample mass; m_0 and m_∞ represent the initial mass and the final mass, respectively; β is heating rate, K·min^{-1}; $R$is the gas constant; E stands for activation energy, J·mol^{-1}; A is the frequency factor, min^{-1}; and n refers to the order of reaction. In general, the item $\frac{2RT}{E} << 1$ and $(1 - \frac{2RT}{E}) \approx 1$. As the first item of the right side of equations is nearly a constant, the two equations should result in a straight line of slope. E can be deduced through calculation with the slope.

2.3.3. Products analysis

To obtain the volumetric flow rates of the products during the oxidation of SBC, both MS and FIIR were used. In order to provide accurate quantitative analysis, a novel method of equivalent characteristic spectrum analysis was employed and the details of such method can be found elsewhere [16]. In the MS analysis, argon was used as a reference gas to calibrate the products by considering the electron impact ionization cross sections, ion flow intensities, and the partial pressures of different species. The characteristic spectra and relative sensitivity were deduced. The effect of initial coal weight on the formation of products was excluded by normalization of the coal weight.

Derivative thermogravimetry (DTG) curve is a very important result of SBC because DTG can reflect the change of combustion rate directly and it was related to the acquirement of ignition temperature, burnout temperature, and combustibility index. Since the mass loss of sample mainly comes from the decomposition of volatiles in the coal samples, the DTG calculated from

MS results of combustion products should be consistent with the DTG results measured by TG analyzer. As a representative, **Figure 3** compares the DTG curve calculated from MS results and measured TG results under condition 4 (see **Table 2**). The results indicate that the calculated MS results are in good agreement with the measured ones. The relative uncertainty was estimated to be ±2.6% [16].

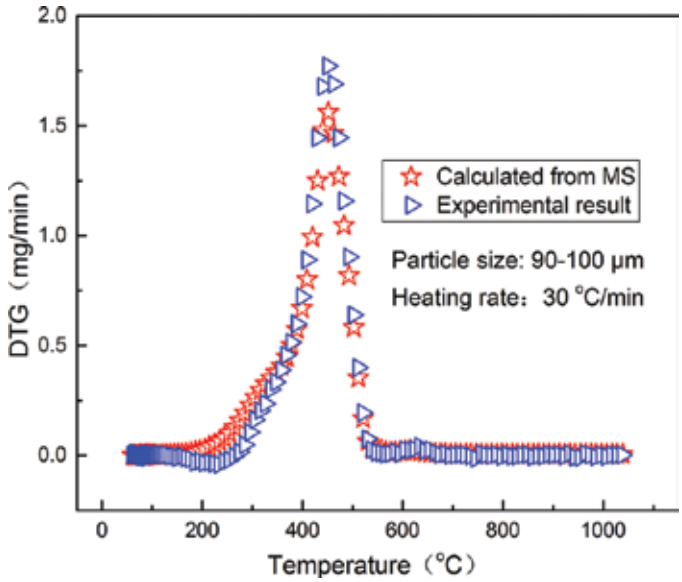

Figure 3. Comparison of DTG curves from calculation and experiment.

3. Results and discussion

3.1. TG/DTG results

Figure 4 presents the TG/DTG curves obtained in the combustion of SBC samples. As temperature increases, the coal sample could proceed with several steps, including devolatilization, coke formation, and coke combustion. The peak of maximum weight loss moves toward high temperatures gradually and the peak value decreases slightly as the particle size increases. The combustion rate depends on the diffusion and reaction ability. During the rapid combustion processes, the major factor affecting the combustion is diffusion ability. As the particle size increases, the contact surface area decreases, which would inhibit the diffusion of oxygen and make the devolatilization and combustion difficult. As a consequence, the devolatilization occurs at higher temperatures and the value of weight loss peak decreases.

Compared to particle size, heating rate has more apparent effect on the characteristics of weight loss. As the heating rate increases, the peak of weight loss moves toward high temperatures. In addition, the peak values and residues decrease as well. Since diffusion ability is the

dominant factor in affecting the combustion process, longer contact time of sample surface and oxygen could contribute to SBC conversion. Furthermore, longer time is needed to reach the same temperature at slower heating rate relative to faster one. For instance, the time needed to reach 1200°C at 10°C/min is four times as the time needed to reach 1200°C at 40 °C/min. Thus, the burnout time with low heating rate is longer. Sufficient contact of particles and oxygen is beneficial for the combustion process, and the maximum value of weight loss occurred at lower temperatures and the maximum weight loss shifted to larger values [17]. It is clear that there is a small weight loss peak within 600–700°C. This weak peak could come from the decomposition of carbonate in the coal samples. In addition, the TG/DTG results of different total flow rates are observed to be quite similar as displayed in **Figure 4c**. As the oxygen supplied is much more than that theoretically needed for the complete combustion, the weight loss characteristics are insensitive to the diverse total flow rate changed in experiments.

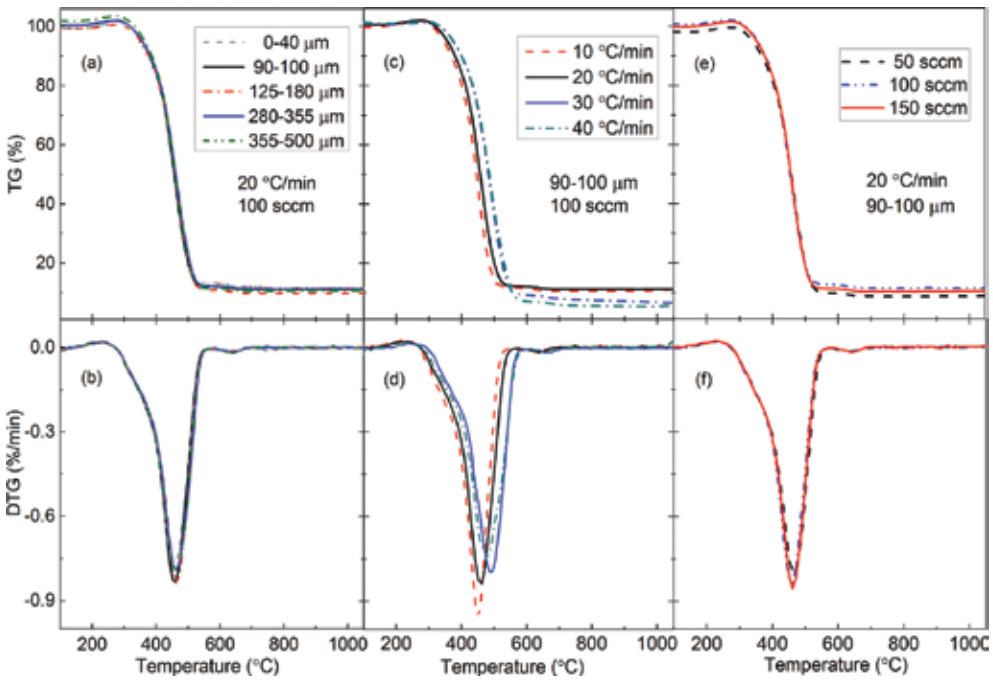

Figure 4. TG and DTG curve of SBC combustion with different particle sizes, heating rates, and total flow rates.

3.2. Characteristic temperatures

The characteristic temperatures obtained in the combustion of SBC at different particle sizes, heating rates, and total flow rates are shown in **Figure 5**. As indicated in **Figure 5a**, both T_{ig} and T_{burn} fall down as the particle size decreases, which is consistent with the results reported by Zhang et al. [18] for Yuanbaoshan and Datong coal and Zhou et al. [19] for Lengshuijiang

coal and lean coal. According to Zhang et al. and Zhou et al., the decrease of particle size could lead to larger surface area to expose to oxygen. The same behavior could occur to SBC and the larger surface area of SBC sample with smaller particle size would endow it with lower T_{ig} and T_{burn}.

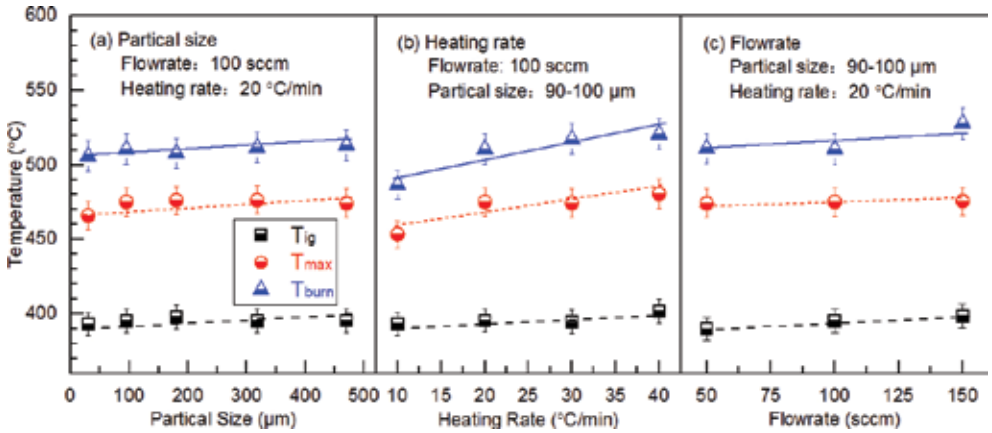

Figure 5. Characteristic temperatures of SBC combustion with different particle sizes, heating rates, and total flow rates.

Figure 5b displays the characteristic temperature as a function of heating rate. T_{ig}, T_{max}, and T_{burn} tend to decrease slightly as the heating rate decreases, which agrees well with the conclusion drawn by Lu et al. [20] for Qilianta coal. This is due to the fact that the thermal conduction in coal particle at lower heating rate is better than that at higher ones. With the increase in temperature, the diffusion becomes better, which is helpful to the devolatilization and results in lower T_{ig}. Moreover, the reaction time is more sufficient at slower heating rate. As the plugging of the surface pores is avoided, it is more difficult to form ash cladding, which could give rise to a lower T_{burn} [21].

For the total flow rate, a slight increase of T_{ig} is observed with large total flow rate (see **Figure 5c**). This slight increase mainly comes from shorter residence time of O_2 on the surface of coal particles at higher total flow rates. Even though more oxygen reached the coal surface, the higher speed of oxygen molecule makes the adsorption of oxygen more difficult. As the supplied O_2 was much more than the theoretically needed for the complete oxidation of the SBC sample, the influence of oxygen flow on the complete combustion and maximum combustion speed is not obvious. As a consequence, both T_{max} and T_{burn} exhibit similar values in the combustion of SBC at different total flow rates.

3.3. Activation energy

Figure 6 summarizes activation energy (E) of SBC with variation of particle size, heating rate, and total flow rate. E tends to be low with the increase in the heating rate, decrease in the

particle size, and the total flow rate. As the particle size decreases, the surface area increases, which would result in more contact area with oxygen and better thermal reactivity. Thus, energy transfer from outside to inside rapidly increases, and the value of E decreases. When the total flow rate increases, the contact time of oxygen and sample surface will be shortened and the value of E increases. On the other hand, the temperature will rise quickly with fast heating rate and the oxidation of coal could become easier. The lower energy barrier makes the oxidation easier [22–24]. This finding also shows good agreement with the conclusion drawn by Lu et al. [20] for different kinds of coals. Similar to the tendency of T_{ig}, E decreased when the total flow rate turned lower. The adsorbability of oxygen on the coal particle surface is better with lower total flow rate, which could be responsible for the decrease in the energy barrier.

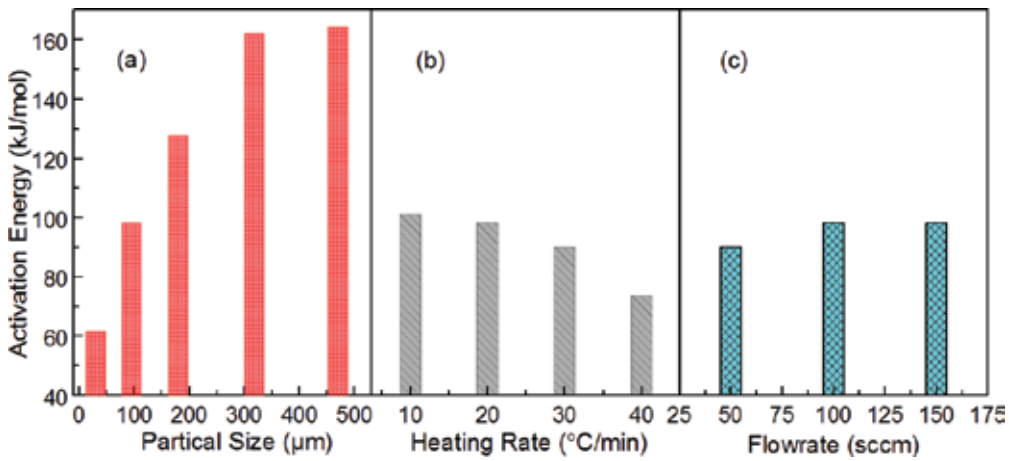

Figure 6. Activation energies of SBC combustion with different particle sizes, heating rates, and total flow rates.

3.4. MS and FTIR results

The volumetric flows of different combustion products at different temperatures can be obtained by normalization and numerical analysis of MS results. The maximum volumetric flows of different combustion products as well as the corresponded temperatures (T_m) are used to explore the formation rule of emitted pollutants. **Table 3** shows the maximum volumetric flows of CH_4, NH_3, NO, HCN, NO_2, and SO_2 as well as the corresponded T_m. By comparing the results obtained with different particle sizes, the listed species tend to be less produced with smaller particle sizes. In view of the heating rate, lower amounts of these products were measured at lower heating rate. As far as the total flow rate is concerned, the quantity of these species becomes lower when the total flow rate is smaller. In general, T_m is insensitive to the particle size. However, the increase in the total flow rate normally results in smaller T_m. With the increase in the heating rate, T_m of NO, NH_3, and HCN tends to be higher, while T_m of SO_x becomes lower. To summarize, lower concentrations of CH_4, NH_3, NO, HCN, NO_x, and SO_2 were observed at smaller particle size, slower heating rate, and higher total flow rate.

http://dx.doi.org/10.5772/64136

No.	CH_4		NH_3		NO		HCN		NO_2		SO_2	
	Value (slm)	T_m (°C)	Value (slm)	T_m (°C)	Value (slm)	T_m (°C)	Value (slm)	T_m (°C)	Value (slm)	T_m (°C)	Value (slm)	T_m (°C)
1	4.08E–05	442	3.61E–04	318	4.72E–05	493	5.05E–04	452	6.14E–05	431	6.38E–06	400
2	3.53E–05	427	2.41E–04	309	3.56E–05	458	3.68E–04	443	4.17E–05	438	4.52E–06	402
3	5.91E–05	440	2.81E–04	305	7.69E–05	492	3.09E–04	451	6.41E–05	440	7.73E–06	388
4	6.51E–05	437	2.17E–04	307	6.46E–05	494	4.94E–04	453	9.84E–05	429	8.37E–06	379
5	5.06E–05	430	3.41E–04	337	1.40E–04	507	3.97E–04	512	1.29E–04	439	1.24E–05	350
6	7.27E–05	453	4.23E–04	338	4.60E–05	494	6.74E–04	463	7.10E–05	442	4.55E–06	400
7	7.94E–05	453	4.89E–04	306	6.97E–05	504	5.19E–04	453	7.43E–05	442	6.33E–06	410
8	7.96E–05	432	3.73E–04	317	4.95E–05	503	4.52E–04	463	7.20E–05	442	6.20E–06	390
9	9.75E–05	453	7.72E–04	327	9.44E–05	504	6.53E–04	463	1.47E–04	453	1.01E–05	400
10	3.76E–05	430	1.58E–04	316	4.32E–05	482	3.03E–04	472	4.99E–05	440	5.75E–06	398

Note: T_m refers to the temperature at which the peak flow is obtained.

Table 3. Maximum volumetric flow of representative combustion products.

Figure 7 shows the volumetric flow rates of different species formed under condition 4 (see **Table 2**). In the combustion of SBC, both NH_3 and HCN exhibited two-peak shapes. The peak before T_{ig} comes from the devolatilization, whereas the peak after T_{ig} mainly results from the decomposition of nitrogen components in both coal volatile and char. Further increase in the temperature led to the conversion of the two species into NO and NO_2.

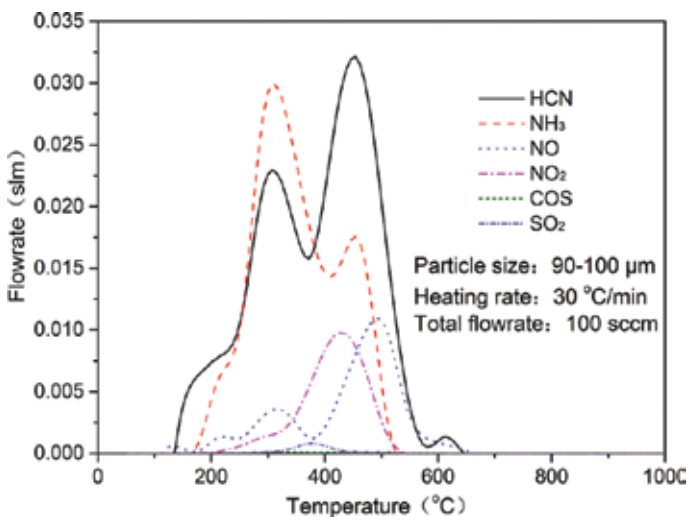

Figure 7. Flow rates of major products.

NO_2 exhibited a shoulder peak and an asymmetric single peak. The shoulder peak is due to the weak release of NO_2 during devolatilization. The asymmetric single peak could result from the conversion of nitrogen-containing heterocyclic species at the end of devolatilization and the beginning of char combustion. However, the other nitrogenous components enriched in char will release NO_2 during the rapid combustion of char. Less NO_2 emissions were observed at smaller particle size, slower heating rate, and higher total flow rate. Similarly, the emissions of SO_2 are relatively less than those formed with slower heating rate and higher total flow rate. However, the amount of SO_2 is quite similar for the investigated particle size range, indicating that it is insensitive to the particle size.

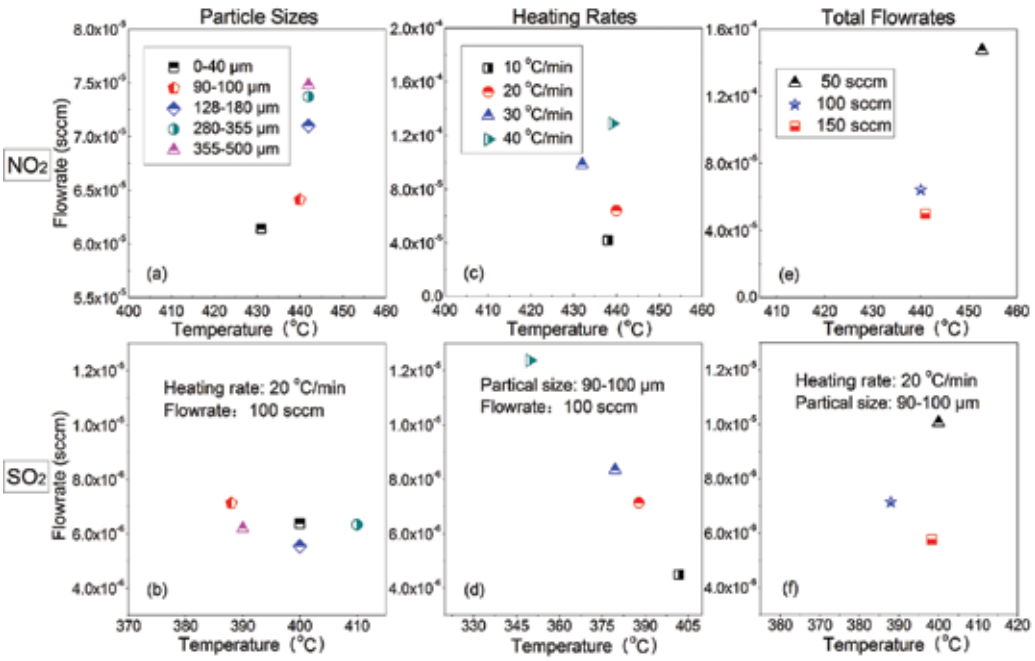

Figure 8. Production of NO_2 (a, c, e) and SO_2 (b, d, f) with different particle sizes, heating rates, and total flow rates.

By comparing the formation of NO_2 and SO_2 with different particle sizes, heating rates, and total flow rates shown in **Figure 8**, it is obvious that the amount of SO_2 production is much lower than those of NO and NO_2. To summarize, the SBC combustion with smaller particle size, slower heating rate, and higher total flow rate is beneficial to controlling the formation of pollutants. This finding is consistent with the results reported for Hegang, Tiefa, and Zhungeer coals by Wei et al. [25] and Heshan sulfur coal by Jiang et al. [23, 26].

To visualize the formation of the major species and avoid the effect of ion fragmentation in MS, FTIR with the spectral range of 500–5000 cm^{-1} was involved in the current work. **Figure 9** presents a representative three-dimensional (3D) spectrum measured with a particle size of 90–100 μm, a total flow rate of 100 sccm, and a heating rate of 20°C/min. The

http://dx.doi.org/10.5772/64136

maximum absorbance peak is located at the wave number of 2380 cm^{-1} corresponding to the anomalistic vibration of CO_2. Another obvious peak at 700 cm^{-1} belongs to the bending vibration of CO_2. The peaks at 1375 and 3600 cm^{-1} correspond to SO_2 and H_2O, respectively. By comparing the standard spectral peaks of different species, overlapped peaks were observed. For instance, the peak between 1500 and 1800 cm^{-1} should be the overlap of H_2O and NO [27, 28]. As can be seen in **Figure 9**, CO_2 becomes detectable at around 140°C. Up to 200°C, a slow increase was observed. Another turning point was measured at about 375°C, which also agrees well with the wave valley in the profiles of HCN and NH_3. Besides CO_2, the fast production of the major species was achieved within the temperature range of 400–500°C, which is consistent with the rapid combustion temperature revealed in the MS analysis. In order to show gradual change of specific species at different temperatures in **Figure 9**, **Figure 10** presents two-dimensional (2D) spectra. The peaks located at about 2380 and 3600 cm^{-1} correspond to the CO_2 and H_2O, respectively. By comparing different spectra obtained at different temperatures, it is obvious that the maximum peak values of different combustion products are located at the temperature of 450°C, corresponding to the rapid combustion temperature. The spectra obtained at temperatures higher than 450°C exhibit very weak peaks since the SBC samples were nearly burned out.

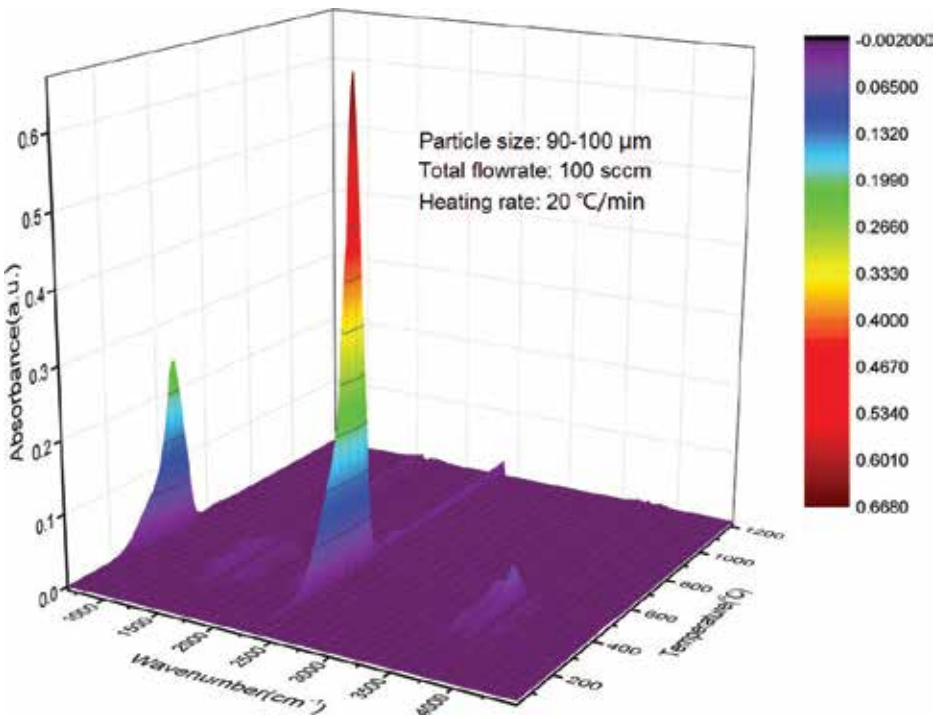

Figure 9. 3D FTIR spectra with different wave numbers and temperatures.

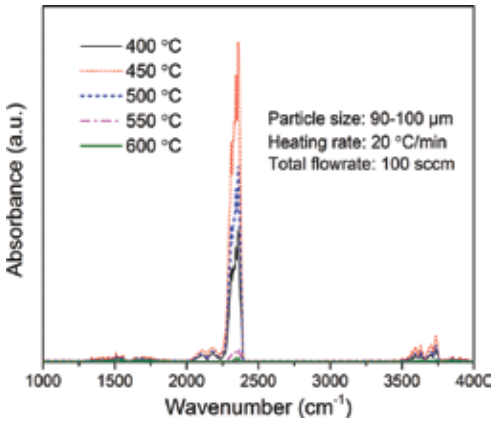

Figure 10. 2D FTIR spectra at different temperatures.

4. Conclusions

The combustion of SBC was comprehensively studied with the online TG-MS-FTIR system in terms of characteristic temperatures as well as qualitative and quantitative analyses of products. Five particle sizes ranging from 0 to 500 μm, four heating rates from 10 to 40°C/min, and three total flow rates from 50 to 150 sccm were used. To avoid the influence of overlap peaks, signal drift, and dynamic response delay in ion current spectra during MS analysis, argon was used as a reference gas to calibrate the products by considering the electron impact ionization cross sections, ion flow intensities, and the partial pressures of different species. The results indicate that the decrease in the particle size, heating rate, and flow rate lead to lower ignition and burnout temperatures, while the activation energy tends to be lower with smaller particle size, faster heating rate, and lower flow rate. The decrease in the particle size could lead to more contact area with oxygen and better thermal reactivity. Slower heating rate could provide more sufficient time for the reaction. Moreover, a higher total flow rate would reduce the oxygen adsorbability on the coal particle surface at a higher flow speed. From MS and FTIR analysis, lower concentrations of different products were observed to be formed at smaller particle size, slower heating rate, and higher total flow rate. These findings will guide to understand the combustion kinetics of SBC and be beneficial to control the formation of pollutants.

Acknowledgements

The authors thank the financial support from the Recruitment Program of Global Youth Experts and Strategic Priority Research Program of the Chinese Academy of Sciences (Grant No. XDA0703100). The authors also thank Mr. Kai Wei, Mr. Zhi-Qiang Gong, and Dr. Zhi-Cheng Liu for their help in the experiments.

http://dx.doi.org/10.5772/64136

Abbreviations

Abbreviations	Full name
A	Frequency factor
A_{ad}	Ash in air-dried basis
C_{ad}	Carbon in air-dried basis
DSC	Differential scanning colorimetry
DTG	Derivative thermogravimetry
E	Activation energy
FC_{ad}	Fixed carbon in air-dried basis
FTIR	Fourier transform infrared spectroscopy
H_{ad}	Hydrogen in air-dried basis
M	Sample mass
m_0	Initial mass
m_∞	Final mass
M_{ad}	Moisture in air-dried basis
MS	Mass spectrometry
N	Order of reaction
N_{ad}	Nitrogen in air-dried basis
O_{ad}	Oxygen in air-dried basis
PAH	Polycyclic aromatic hydrocarbons
PDF	Power diffraction file
$Q_{ad.net}$	Low calorific capacity in air-dried basis
TG	Thermogravimetric
T_m	Peak flow temperature
T_{ig}	Ignition temperature
T_{max}	Maximum reaction temperature
T_{burn}	Burnout temperature
S_{ad}	Sulfur in air-dried basis
SBC	Shenmu bituminous pulverized coal
V_{ad}	Volatile in air-dried basis
XRD	X-ray diffraction
A	Weight loss ratio
B	Heating rate
R	Gas constant

Author details

Guan-Fu Pan[1,2], Hong-De Xia[1] and Zhen-Yu Tian[1*]

*Address all correspondence to: tianzhenyu@iet.cn

1 Institute of Engineering Thermophysics, Chinese Academy of Sciences, Beijing, China

2 University of Chinese Academy of Sciences, Beijing, China

References

[1] Peng, B.X., Wu, D.S. Study on bromine release from bituminous coal during combustion. Fuel. 2015;157:82–86. DOI: 10.1016/j.fuel.2015.04.059

[2] Tsuji, H., Shirai, H. Matsuda, H. Rajoo, P. Emission characteristics of NOx and unburned carbon in fly ash on high-ash coal combustion. Fuel. 2011;90(2):850–853. DOI: 10.1016/j.fuel.2010.09.053

[3] Molina, A., Shaddix, C.R. Ignition and devolatilization of pulverized bituminous coal particles during oxygen/carbon dioxide coal combustion. Proceedings of the Combustion Institute. 2007;31:1905–1912. DOI: 10.1016/j.proci.2006.08.102

[4] Gao, S.K., Zhang, Y. Meng, J.W., Shu, J.A. Real-time analysis of soot emissions from bituminous coal pyrolysis and combustion with a vacuum ultraviolet photoionization aerosol time-of-flight mass spectrometer. Science of the Total Environment. 2009;407(3):1193–1199. DOI: 10.1016/j.scitotenv.2008.10.026

[5] Yu, Y., Xu, M.H., Yao, H., Yu, D.X., Qiao, Y., Sui, J.C., Liu, X.W., Cao, Q. Char characteristics and particulate matter formation during Chinese bituminous coal combustion. Proceedings of the Combustion Institute. 2007;31:1947–1954. DOI: 10.1016/j.proci.2006.07.116

[6] Cheng, J., Zhou, J.H., Liu, J.Z., Cao, X.Y., Cen, K.F. Transformations and affinities for sulfur of Chinese Shenmu coal ash in a pulverized coal-fired boiler. Energy Sources Part A—Recovery Utilization and Environmental Effects. 2009;31(11):956–966. DOI: 10.1080/15567030802572206

[7] Chang, L.P., Xie, K.C., Li, C.Z. Release of fuel-nitrogen during the gasification of Shenmu coal in O_2. Fuel Processing Technology. 2004;85(8):1053–1063. DOI: 10.1016/j.fuproc.2003.11.038

[8] Wang X.M., Jiao Y.Q., Wu L.Q., Rong H., Wang X.M., Song J. Rare earth element geochemistry and fractionation in Jurassic coal from Dongsheng-Shenmu area, Ordos Basin. Fuel. 2014;136:233–239.

[9] Sun, Q.l., Li, W., Chen, H.K., Li, B.Q. TG-MS study on pyrolysis behavior of Shenmu coal macerals. Journal of China University of Mining & Technology. 2003;32(6):664–669.

[10] Zhao, S.Y. Thermal gravity analysis on combined combustion features of Shenmu coal and semi coke. Coal Science and Technology. 2007;35(7):80–82.

[11] Yang, J.G., Deng, F.R., Zhao, H., Cen, K.F. Mineral conversion and microstructure change in the melting process of Shenmu coal ash. Asia-Pacific Journal of Chemical Engineering. 2007;2(3):165–170. DOI: 10.1002/Apj.036

[12] Yang, W.J., Zhou, J.H., Liu, M.S., ZHou, Z.J., Liu, J.Z., Cen, K.F. Combustion process and nitrogen oxides emission of Shenmu coal added with sodium acetate. Energy & Fuels. 2007;21:2548–2554.

[13] Dijkmans T., Djokic M.R., Van Geem K.M., Marin G.B. Comprehensive compositional analysis of sulfur and nitrogen containing compounds in shale oil using GC × GC-FID/SCD/NCD/TOF-MS. Fuel. 2015;140:398–406.

[14] Yu, Q.M., Pang, Y.J., Chen, H.G. Determination of ignition points in coal-combustion tests. North China Electric Power. 2001;(7):9–10, 50.

[15] Redfern, J.P., Coats, A.W. Kinetic parameters from thermogravimetric data. Nature Biotechnology. 1964;201(4914):68–69.

[16] Xia, H.D., Wei, K. Equivalent characteristic spectrum analysis in TG-MS system. Thermochimica Acta. 2015;602:15–21. DOI: 10.1016/j.tca.2014.12.019

[17] Wang, S.Q., Tang, Y.G., Schobert, H.H., Mitchell, G.D., Liao, F.R., Liu, Z.Z. A thermal behavior study of Chinese coals with high hydrogen content. International Journal of Coal Geology. 2010;81(1):37–44. DOI: 10.1016/j.coal.2009.10.012

[18] Zhang, C.Q., Yu, L.J., Cui, Z.G., Jiang, X.M. Experimental research and computation analysis of combustion kinetic characteristics of micro-pulverized and common-pulverized coal. Journal of Chemical Industry and Engineering. 2005;56(11):2189–2194.

[19] Zhou, Z., Liu, L., Wang, Y.L., Liu, H. Study on the influence of pulverized coal's particle size upon the combustion properties. Thermal Power Generation. 2007;3:35–38, 47.

[20] Lu, H.B., Xu, H.J., Jia, C.X., Zhang, D.L. Experimental study on combustion characteristics of coal in thermogravimetric analyzer. Power System Engineering. 2006;22:11–12, 15.

[21] Nyathi, M.S., Mastalerz, M., Kruse, R. Influence of coke particle size on pore structural determination by optical microscopy. International Journal of Coal Geology. 2013;118:8–14. DOI: 10.1016/j.coal.2013.08.004

[22] Fan, D.M., Zhu, Z.P., Na, Y.J., Lu, Q.G. Thermogravimetric analysis of gasification reactivity of coal chars with steam and CO_2 at moderate temperatures. Journal of Thermal Analysis and Calorimetry. 2012;113:599–607.

[23] Jiang, X.M., Li, J.B., Qiu, J.R. The influence of particle size on compositions analyzing and combustion characteristics of pulverized coal. Journal of China Coal Society. 1999;24:643–647.

[24] Lu, S., Lu, G.J., Jiang, X.G., Chi, Y., Yan, J.H., Cen, K.F., Yu, X.H., Liao, H.Y., Zhao, H. Pyrolysis/combustion characteristics and kinetic analysis of Indonesia lignite sludge. Journal of Coal Science & Engineering. 2014;3:554–561.

[25] Wei, L.H., Jiang, X.M., Yang, T.H., Li, Y.J., Wang, L. Influence of mineral matter on nitrogen conversion in coal during combustion. Acta Scientiae Circumstantiae. 2006;11:1780–1784.

[26] Jiang, X.M., Liu, H., Li, J.B., Zheng, C.G., Liu, D.C. Experimental investigation on sulfur emission properties of micro-pulverized coal. Environmental Science & Technology. 2002;23:126–128.

[27] Ahamad, T., Alshehri, S.M. TG-FTIR-MS (evolved gas analysis) of bidi tobacco powder during combustion and pyrolysis. Journal of Hazardous Materials. 2012;199:200–208. DOI: 10.1016/j.jhazmat.2011.10.090

[28] Silvera, S. TG-FTIR and kinetics of devolatilization of sulcis coal. Journal of Analytical and Applied Pyrolysis. 2013;104:95–102.

Section 2

Waste Combustion, Conversion and Treatment

Chapter 4

Combustion Characteristics of Waste Tyre Pyrolysis Fuel as Industrial Burner Fuel

Jefrey Pilusa and Edison Muzenda

Additional information is available at the end of the chapter

http://dx.doi.org/10.5772/63078

Abstract

This study examined the potential of using waste tyre pyrolysis fuel oil as an industrial burner fuel. The combustion characteristics of tyre-derived fuel (TDF) oil were evaluated using Cuenod NC4 forced draught oil burner equipped with a built-in fuel atomizer and an onboard control system. TDF oil obtained from a local waste tyre treatment facility was blended with petroleum diesel (DF) at TDF volumetric concentration of 40% (TDF_{40}), which was tested against pure petroleum diesel and refined modified tyre-derived fuel (TDF*). Critical combustion parameters such as thermal power output, fuel consumption, flame stability, flue gas temperature, and emissions were investigated to evaluate the performance of the combustion equipment. Using DF as a reference fuel, it was observed that TDF_{40} required high air-to-fuel ratio (AFR) in order to produce a stable flame with high flame temperature and less emissions. TDF* produced a reasonably stable flame with less sulphur dioxide emissions compared to TDF_{40}; however, its specific fuel consumption (SFC) was higher than that of DF. It was also discovered that the burner's SFC was higher when fuelled with TDF_{40}. Total contamination and viscosity of TDF oil contribute significantly to the flow characteristics of the fuel, resulting in reduced pressure and subsequently poor fuel atomization. Rapid soot formation at atomizer nozzle was also observed when the burner was fuelled with TDF_{40}. TDF oil and its derivatives (TDF*) produce SO_2, NO_2 and CO emission levels higher than the acceptable limits as prescribed by the European Air quality standard (EU2015/2193). It was concluded that TDF oil could be used as a potential industrial burner fuel if diluted with petroleum diesel fuel at TDF volumetric concentration of <40% or any ratio that could adjust the viscosity level below 5.3 cSt. Fuel preheating and multistage filtration system are also recommended to reduce total contamination and water levels in the fuel mixture. Exhaust gas scrubbing is recommended due to significantly high sulphur oxide emission in the flue gas.

Keywords: atomization, boiler, emissions, energy, flame

INTECH
open science | open minds

© 2016 The Author(s). Licensee InTech. This chapter is distributed under the terms of the Creative Commons Attribution License (http://creativecommons.org/licenses/by/3.0), which permits unrestricted use, distribution, and reproduction in any medium, provided the original work is properly cited. CC BY

1. Introduction

1.1. Background

An ongoing increased fuel demand continues to speed up depletion of fossil fuel resources such as crude oil and coal. The use of non-renewable fossil-derived fuels such as petroleum diesel for power and energy production contributes toward a large global carbon footprint compared to other cleaner renewable energy sources such as biogas, natural gas and biodiesel. Renewable energy sources and various waste-to-energy initiatives are being explored globally; however, most of these initiatives are inefficient and environmentally unfriendly. This continues to put a lot of pressure on emerging countries to find cost-effective use of sustainable alternative fuels in order to reduce dependency on fossil-derived fuels. It remains a challenge to develop economical and sustainable solutions to derive fuels from waste streams or renewable sources in order to supplement the traditional fossil-derived fuels. One of the methods is to produce low-cost alternative fuels from waste tyres and rubber products through pyrolysis technology and blend it with available commercial fuels.

There is an increasing interest in pyrolysis technology, especially for the treatment of waste automotive tyres with the aim of producing alternative liquid fuel and solid char. This fuel is traditionally used as heavy bunker fuel oil in environments where emissions control legislations are not very stringiest [1]. Previous research has shown that tyre-derived fuel (TDF) oil has similar properties to petrochemical diesel fuel; hence, it has been tested in compression ignition engines [2, 3].

TDF oil is produced through the thermal decomposition of rubber-based material in an oxygen-depleted environment followed by a condensation of the vapors to yield a liquid fuel [4–6]. In a continuous pyrolysis technology, shredded tyre chips are continuously fed into an oxygen free reactor vessel, which is heated to temperatures of 570°C in a "continuous pyrolysis reactor" as shown in **Figure 1**. The produced gases are contained and condensed into liquid TDF oil (47 wt% of feed), and the remaining solid char (35 wt% of feed) is separated from steel (10 wt% of feed) using a magnetic separator. A stream of uncondensed pyrolysis gas (5 wt% of feed) is recycled into the process to heat up the pyrolysis reactor as shown in **Figure 1**. A flue gas scrubber system is incorporated to remove toxic emissions from the flue gas stream because the process uses TDF oil and excess pyrolysis gases to heat up the reactor vessel [7]. Waste tyre pyrolysis technology has been considered as an alternative method for disposal of waste tyres while producing alternative fuel. Several studies have been carried out in the production of TDF oil by various techniques. Rodriguez et al. [8] investigated pyrolysis of tyres in a fixed-bed reactor at 500°C and reported that product oils consisted of 62 wt% aromatic compounds, 31.6 wt% aliphatic compounds, 4 wt% nitrogen-containing compounds and 18,000 ppm sulphur-containing compounds. It has also been reported that the main difference between the continuous and batch processes is in the yield of aromatics content, which is 43.5% in the continuous process described in **Figure 1** [9].

http://dx.doi.org/10.5772/63078

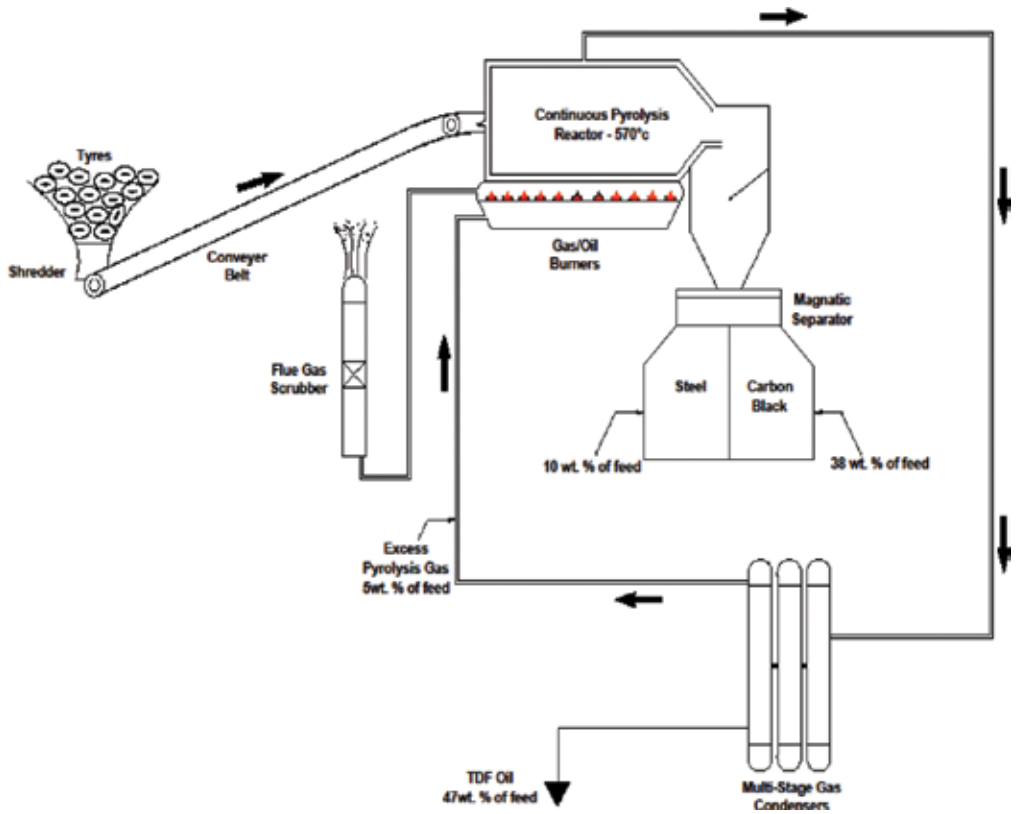

Figure 1. Continuous waste tyre pyrolysis plant.

1.2. Tyre-derived fuel oil

TDF oil has similar characteristics to diesel fuel; hence, it has been demonstrated for use in boilers, turbine and diesel engines; however, concerns with regard to its acidity, ignition characteristics, clogging tendency and gaseous emissions have limited its commercial application [10, 11]. Previous researchers have determined some properties of TDF oil such as ultimate analyses, flash point, moisture content, density and viscosity. The results showed that TDF oil had fuel properties similar to those of petroleum diesel fuel [12, 13]. Chromatographic and spectroscopic studies on TDF oil also show that it can be used as liquid fuel, with a calorific value of 43 MJ/kg [14].

TDF oil has generated significant interest as an alternative option to petroleum diesel. As a result, a number of studies compared internal combustion and emission as well as engine performance of various TDF–petroleum diesel blends [2, 9, 15–17]. External combustion characteristics of TDF oil are not fully understood because most of the research in TDF oil combustion has been demonstrative in nature. Therefore, the purpose of this research is to

develop a better understanding of TDF oil combustion with regard to the operating conditions used during combustion as well as its physical properties.

While TDF has high energy content, it requires some processing to ensure efficient use in combustion equipment. However, the results reported by [18] indicate that because of its high viscosity and low cetane number, TDF must be blended with petroleum diesel fuel or complemented by a cetane improver, such as diethyl ether, for application in most common combustion equipment. Consequently, many studies using TDF blended with petroleum diesel fuel or methyl esters for application in internal combustion engines are found in the literature [19, 20], but none of them were tested in external combustion fuel burners.

Certain properties of TDF oil such as cetane number, viscosity, and total sulphur contribute to burner performance and emission characteristics. Previous research performed some investigations on qualitative analysis of waste rubber-derived oil as an alternative diesel additive, whereby it was found that TDF oil has high viscosity, total sulphur, total contamination, water content, and flash point of 9 cSt, 9106 ppm, 143 mg/kg, 3.43 vol.% and 94°C, respectively [21].

A further study revealed that TDF oil could be refined through fractional distillation process to obtain cleaner fuel with reduced total sulphur of 1800 ppm, kinematic viscosity of 1.6 cSt, flash point of 26°C, total contamination of 29 mg/kg, water content of 0.03 vol.% and gross calorific value of 43 MJ/kg [22]. In addition, the use of refined TDF in combustion equipment results in reduction of unburned hydrocarbons, particulate matter and carbon monoxide [20]. In contrary, combustion of TDF oil results in an increased sulphur dioxide emissions, due to the presence of high sulphur levels in the fuel [23, 24].

1.3. Combustion emissions

In an ideal combustion process of a hydrocarbon liquid fuel occurring in excess oxygen, all fuel would be converted into heat, water, carbon dioxide and negligible equilibrium amounts of carbon monoxide. However, given the complexity of physiochemical interactions during the combustion process, there are other side reactions taking place, resulting in the formation of pollutants or emissions.

The most significant combustion emissions are sulphur dioxide (SO_2), nitrogen dioxide (NO_2), carbon monoxide (CO), unburned hydrocarbons (HC) and particulate matter (PM) [25]. These are among emissions regulated by the National Air quality Act No. 39 of 2004, which is in line with the European Air quality standards published under the European Union directive No 2015/2193 as summarized in **Table 1**. Some of these emissions are promoted by inefficient operation of the combustion equipment due to the quality of fuel used, for example, when large numbers of inert particles are passing through the combustion equipment pump and atomizer nozzle, cavitation occurs causing erosive wear and increasing nozzle size. This leads to larger fuel drop sizes and particles becoming trapped in the mating surfaces of the sealing areas of the injector tips, keeping them apart. Leaking and dribbling subsequently occur at injector nozzle resulting in reduced injection pressure and poor atomization. The effects of these various problems are the main cause of inefficient combustion and subsequent increased emissions levels. Pilusa et al. [26] reported that sufficient filtration of fuel ensures uniform fuel

http://dx.doi.org/10.5772/63078

flow through the precision components of the combustion equipment, resulting in efficient combustion and reduced emissions.

Pollutant	Pollutant limit	Exposure period	Test method
SO_2	300 μg/m^3 (134 ppb)	1 h	ISO 6767
NO_2	200 μg/m^3 (106 ppb)	1 h	ISO 7996
CO	30 mg/m^3 (26 ppm)	1 h	ISO 4224
	10 mg/m^3 (8.7 ppm)	8 h	
PM_{10}	120 μg/m^3 (134 ppb)	24 h	EN 12341

Table 1. Selected regulated pollutants limits as per national ambient air quality standards [27].

1.4. TDF combustion

Previous research investigated the use of oils for the operation of medium industrial boilers, whereby several atomization techniques have been employed, including pressure atomization, air atomization, steam atomization and fuel preheating in order to reduce viscosity [28]. A higher air-to-fuel (AFR) equivalent was recorded for efficient combustion of high-viscosity fuel oils. Particulate matter has arisen as one of the most challenging aspects of TDF oil combustion given its consistently high readings, particulates have been observed to collect on burner surfaces [29]. The aim of this research was to assess the combustion characteristic of TDF oil as an alternative low-cost industrial burner fuel.

2. Material and experimental procedures

2.1. Material

A sample of TDF oil produced from a continuous waste tyre pyrolysis process was obtained from a local waste tyre treatment technology. As reported in literature, TDF oil produced from a continuous pyrolysis process at temperature above 500°C has superior characteristics in terms of aromatic content as compared to the one produced from a lower temperature batch process [8, 9]. Petroleum diesel (500 ppm) was purchased from a nearby fuel filling station, and it was used as a reference test fuel and also to prepare TDF oil–diesel mixtures. An illustration of the combustion experimental setup is shown in **Figure 2**. In order to produce a chemically modified TDF (TDF*), TDF oil was distilled using an experimental setup illustrated in **Figure 3** and all chemical reagents used were purchased from Sigma Aldrich South Africa. Vinyl acetate, n-heptane, n-hexane, methacrylic anhydride, n-butanone and amyl alcohol and nitric acid were used as reagents to chemically modify some properties of

TDF*. **Tables 2** and **3** present the technical specifications of the burner and emissions analyzers used for these research.

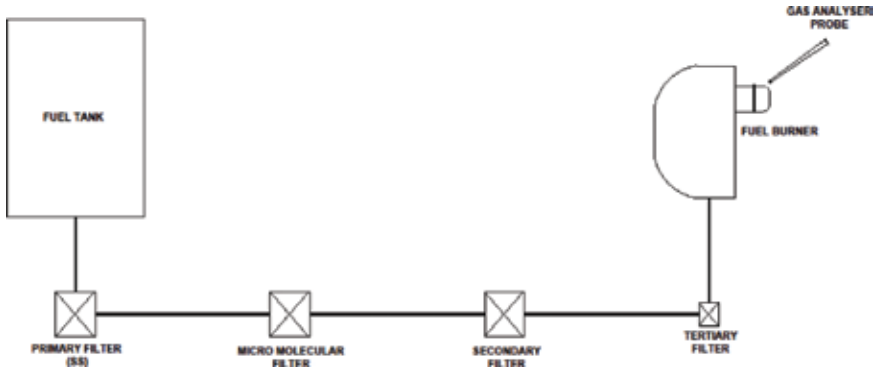

Figure 2. Experimental setup for external fuel combustion.

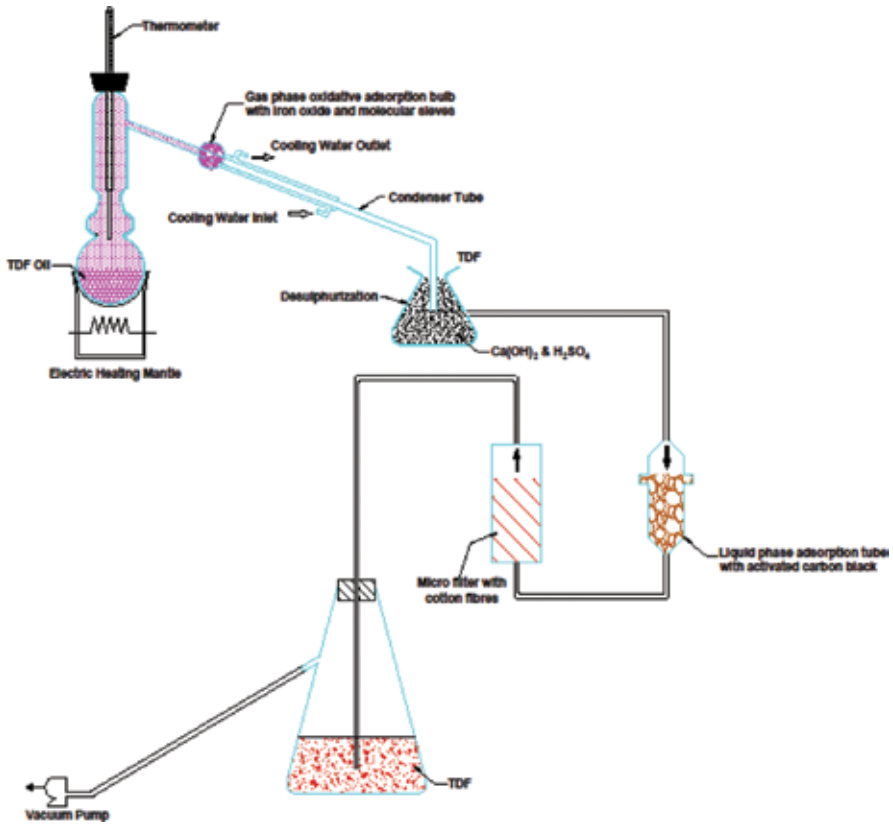

Figure 3. Experimental setup for TDF* production from TDF oil [22].

http://dx.doi.org/10.5772/63078

Fuel flow (kg/h)	1.5–3.4
Flame power (kW)	18–40
Nozzle (US gal/h)	0.5–0.85
Preheated nozzle line	Yes
Pump and fan motor	Single phase, 230 V, 50 Hz, 2800 min^{-1}, 4 μF/400 V capacitor
Electronic igniter	EBI
Blower turbine	Ø133 × 42
Air flap control	Manual
Control panel	Yes
Blast tube	Ø63/80 × 177
Fuel pump	11 bar discharge precision gear pump with solenoid valve AS47D

Table 2. Technical specification NC4 fuel burner [30].

Parameter	Sensors	Range	Resolution
Carbon monoxide	Electrochemical cell	0–10000 ppm	1 ppm
Nitrogen dioxide	Electrochemical cell	0–500 ppm	0.1 ppm
Sulphur dioxide	Electrochemical cell	0–5000 ppm	1 ppm

Table 3. Testo 350 gas analyzer technical specifications [31].

2.2. Experimental procedures

2.2.1. Fuel preparation

An experimental setup consisting of a fuel tank, in-line filtration system, and a forced draught external combustion system with emissions analyzer was developed as shown in **Figure 2**. Mixtures of TDF oil and petroleum diesel (DF) were prepared at TDF oil volumetric concentration in each sample of; 10, 20, 30, 40, 50 and 70%. To ensure that the problem of total contamination and water content is eliminated, all fuel bends were processed through a multi-stage filtration illustrated in **Figure 2** and random confirmation tests were performed to verify that the water content and total contamination were within acceptable limits. The most economical fuel blend was determined by the highest possible TDF oil volumetric concentration yielding the acceptable viscosity and flash point of the fuel mixture. Various TDF oil–

petroleum diesel blends were assessed by measuring their viscosities and flash points as per ASTM D445/D93 test methods, and the most economical mixture was selected and undergone full analysis as per test results presented in **Table 4**.

Parameter	Unit	Test method	TDF oil	DF	TDF_{40}	TDF*	SANS342
Kinematic viscosity	(cSt at 40°C)	ASTM D445	9.23	2.25	4.9	3.41	2.2–5.3
Density	(kg/m^3 at 20°C)	ASTM D4052	942	828	846	848	800–950
Flash point	(°C)	ASTM D93	96	67	63	42	>50
Cetane index		ASTM D4737	22.3	53.9	41.7	51.8	
Calorific value	(MJ/kg)	ASTM D3338	39.9	45.9	42.7	43.8	
Total sulphur	(mg/kg)	ASTM 4294	11,450	443	4,516	1,100	<500
Aromatics	(wt%)	Calculated	43.5	26.1	36.3	27.2	
Lubricity	(μm WS1.4)	CEC-F06-A-96	939	489	678	471	>460
Oxidation stability	(g/m^3)	ASTM D2274	15	20	13	17	23
Total contamination	(mg/kg)	IP440	589	12	8	14	20
Water content	(mg/kg)	ASTM 6304	33,540	160	56	98	85

Table 4. Physical properties of TDF oil, DF, TDF_{40} and TDF*.

A sample of TDF* was produced by flash distillation of TDF oil using the experimental setup shown in **Figure 3**. Other samples of TDF oil, DF and TDF* were also prepared for testing. Each sample was characterised in accordance with SANS 342 as per results presented in **Table 4**.

A bench-scale distillation setup consisting of 1 L round bottom flask, heating mantle, glass water-cooled condenser and a collecting flask as shown in **Figure 3** was used for flash distillation of TDF oil. The glass condenser was fitted with steel wool in order for the water vapour from the oil to promote oxidation of steel wool into ferric oxide, which will act as a catalyst for oxidation of sulphur compounds in gaseous phase. The temperature of the feed crude oil was monitored and initially maintained at 100°C to allow for evaporation and recovery of water, low boiling point mercaptans, sulphides and disulphides in the crude oil. The condenser bulb was filled with 13× molecular sieves supported over oxidized steel wool. This will ensure oxidation of high boiling point sulphur compound and adsorption over the active layer of micro-porous sieves in a gas phase prior to condensation. The function of 13× molecular sieve pellets is to enhance adsorption of low boiling points sulphur compounds as well as water removal from the fuel.

http://dx.doi.org/10.5772/63078

The distillation temperature of the crude oil was raised to 350°C for extraction of light and heavy fuel fractions from the crude oil, while oxidizing and capturing the sulphur compounds over the active layer of molecular sieves in the condenser bulb as shown in **Figure 3**. The system was properly sealed at each connection point to ensure that all vapours pass through the ferric oxide and molecular sieves before they are condensed into light fraction fuel. The condensed fuel was desulphurized by adding 25 wt% $Ca(OH)_2$ and 10 wt% H_2SO_4 as per treatment method reported [24]. This was followed by filtration through a series of activated carbon and micro-molecular filtration system presented in **Figure 3** for the removal of suspended and dissolved contaminants. The distillate was further chemically modified to adjust its viscosity and cetane index by adding recommended amounts of vinyl acetate and methacrylic anhydride as per IARC guideline for liquid fuel additives [32]. Chemical modifiers including 1400 ppm of vinyl acetate as viscosity modifier and 0.4 wt% methacrylic anhydride as fuel stabilizer were dosed into the distillate. A mixture of 30 vol.% n-heptane, 50 vol.% n-hexane and 20 vol.% methyl tert-butyl ether was added to the distillate at 5 vol.% to homogenize the fuel with the reagents to form modified tyre-derived fuel (TDF*).

2.2.2. Combustion tests

An NC4 Cuenod forced draught fuel burner was connected to a fuel tank through fuel piping consisting of 100 μm stainless steel mesh primary filter followed by a two-stage micro-molecular filter with packed cotton fibers and 13× molecular sieves, 5 μm paper-based secondary filter media and a 1 μm cellulose-based polishing filter. All joints and connection points were lined with thread tape to prevent leakages. The fuel tank was placed at elevated position, 1.5 m above the burner pump suction point in order to create enough net positive suction head for the pump. The burner head was mounted on a stationary frame facing an open area with sufficient ventilation.

The emission gas analyzer was also mounted on a stationary frame next to the burner head, such that its probe is in line with the burner head. The burner was switched on allowing the nozzle line to be preheated to optimum operating temperature. The test fuel was added into the tank and allowed to accumulate into the filters before firing the burner. The burner was fired, and the flame intensity was adjusted using manual air flap to select the optimum combustion air setting (CAS), while monitoring flue gas temperature using an infrared thermometer.

The burner was run for 60 min for each test fuel, and performance parameters such thermal power output, fuel consumption, flame stability, flue gas temperature and emissions were recorded. Flue gas emission was measured using Testo 350 emissions analyzer equipped with built-in electrochemical cells with an auto dilution system capable of measuring gaseous emissions of SO_2, CO and NO_2. The analyzer probe was positioned at the burner head to automatically sample the gases and measure the emissions. The tests results were stored into the analyzer memory and exported into Microsoft excel spreadsheet for analysis.

3. Results and discussions

3.1. Fuel characterisation

Based on the test results presented in **Table 4**, it was evident that pure TDF oil has some properties that do not comply with the minimum SANS 342 requirements to be use as combustion fuel in precision combustion equipment. Amongst these properties, TDF oil has significantly high concentrations of total sulphur and high viscosity compared to petroleum diesel. Its high total contamination and water content are the main reasons for its low calorific value and possibly high flash point. Although water and total contamination can be easily separated from the fuel by physical separation processes such as evaporation and filtration, some properties require distillation and chemical modification to be adjusted.

It has been reported that fractional distillation of TDF oil at temperatures of 350°C reduces total sulphur and that further chemical desulphurization and filtration produces a cleaner fuel [2, 22, 24]. However, the fuel's viscosity and flash point drops below the acceptable limits prescribed in SANS 342 standards due to some TDF oil constituent components being stripped away during distillation and chemical desulphurization process. It is believed that some of these constituent components solidify and removed from the fuel during filtration.

Addition of recommended amounts of 1400 ppm vinyl acetate (viscosity modifier) and 0.4 wt % methacrylic anhydride (fuel stabilizer) as per IARC guideline for liquid fuel additives has shown a significant improvement of the fuel's viscosity and flash point [32]. However, the flash point was found to be lower than the specified minimum limit for safe handling. Lower flash point is often associated with elevated fuel consumption and potential risks of auto-ignition during handling and storage; hence, it is expected for TDF* to be consumed faster than diesel fuel during combustion with higher flame temperature as a result of auto-ignition. A mixture of 30 vol.% n-heptane, 50 vol.% n-hexane and 20 vol.% methyl tert-butyl ether, which was added to the TDF* at 5 vol.% to homogenize the fuel, is believed to have contributed to the fuel's improvement in calorific value as well as the cetane index as reported in **Table 4**.

Ignition properties of TDF oil are typically poor as represented by a low cetane index of 22.3. This is associated with the presence of high concentrations of non-flammable components such as water and total contaminants of 3.54 vol.% and 586 mg/kg, respectively. Nonetheless, the cetane number improved to 44.8 as the TDF oil was converted to TDF* by gas phase oxidative fractional distillation process described in **Figure 3**. This number was further improved by the addition of chemical modifier. Alkyl nitrate is commonly used as ignition improvers due to their affinity for hydrocarbon chain clouding in oils and hydrocarbon liquid fuels [33]. It was observed that the addition of 800 mg/L of alkyl nitrate into TDF could effectively increase the cetane index of the fuel by 12–16%.

Previous research has shown that TDF oil is distillable at temperature range of 193–359°C, up to 10, 50 and 90 vol.% of this fuel can be recovered at distillation temperatures of 218, 289 and 335°C, respectively [22]. At this temperature range, sulphur is more easily removed because lower boiling oil fractions primarily contain sulphurous compounds that are in the form of mercaptans, sulphides, disulphides or lower member ring compounds, which are relatively

http://dx.doi.org/10.5772/63078

easier to desulphurize [34]. Typical sulphur compounds such as mercaptans, sulphides and disulphides boils below 193°C and can be easily evaporated for effective gas phase desulphurization over an active surface layer of adsorbent such as molecular sieves or activated carbon [35].

There were few TDF oil parameters not complying with SANS 342 specifications for use in precision combustion equipment. These included viscosity, total sulphur, total contamination and water content. Adequate filtration can easily eliminate the concerns associated with total contamination and water content. Parameters such as viscosity and total sulphur may be adjusted by blending TDF oil with other cleaner petroleum fuels. A blend containing 40 vol. % TDF (TDF_{40}) was found to be the optimum test mixture with an acceptable kinematic viscosity of 4.9 cSt and flash point of 63°C. This sample was taken for full analysis and was tested against TDF* and pure petroleum diesel to evaluate its combustion characteristics.

TDF oil was obtained with relatively high viscosity of 9.23 cSt; however, the viscosity dropped to 1.88 cSt after distillation. Although viscosity of liquid fuels decreases temporarily as its temperature is increased, the specifications for precision combustion equipment require the kinematic viscosity of the fuel measured at 40°C to range between 2.2 and 5.3 cSt for normal fuel flow and operation of the equipment with less emissions. The test results presented in **Table 4** show that the kinematic viscosity of TDF could be improved by the addition of 1400 ppm vinyl acetate. Additives such as vinyl acetate can reduce the thinning effect of the fuel caused by operation at high temperatures [36]. This viscosity improver has long chains and high molecular weights. Its function is to increase the relative viscosity of the fuel more at high temperatures than at low temperatures. It coils at low temperatures and uncoils as the temperature increases. Uncoiling makes the molecules larger, which increases internal resistance within the thinning oil [37].

The test data presented in **Table 4** show a 90.3% overall reduction in total sulphur from conversion of TDF oil into TDF*. This was achieved by multiple processing methods as described in **Figure 3**. Previous research has revealed that sulphur reduction in TDF oil can be achieved by chemical treatment followed by blending it with low sulphur commercial diesel fuel [38, 39]. Pilusa et al. [22] has presented that most mercaptans boils at below 100°C, explaining why they could be removed from the TDF oil via gas-phase desulphurization distillation over an adsorbent with a pore size large enough to capture all molecular size ranges.

Desulfurization remains a key driver with increasing trends to shift towards cleaner fuels. As the sulphur level in diesel fuel is reduced, the inherent lubricity characteristics of the fuel are also reduced. Sulphur level of the petroleum diesel fuel is reduced by the application of hydrotreating processes which remove sulphur- and nitrogen-containing compounds, and these compounds have good natural lubricity [35]. The process of producing low-sulphur diesel fuel also leads to a reduction in aromatic compounds, and these compounds are known to have better lubricity than aliphatic compounds [40]. Combustion fuels with poor lubricity characteristics can lead to atomizer pump wear and eventually failure, so the lubrication properties of the fuel have become an important parameter. Lubricity improvers such as 0.03 wt% phosphate ester amide restore the natural lubricity properties of the fuel [41]. There was no

need to add any lubricity modifier as the test value for TDF* was found to be within the acceptable limits after the fuel was treated with other chemicals.

3.2. Combustion tests

Uniform fuel droplets are consistently generated by the atomizer at the combustion zone allowing mixing with incoming forced air. An electric-generated spark initially ignites the mixture, while the stable flame at the burner core continues to ignite the incoming fuel air mixture as demonstrated in **Figure 4**.

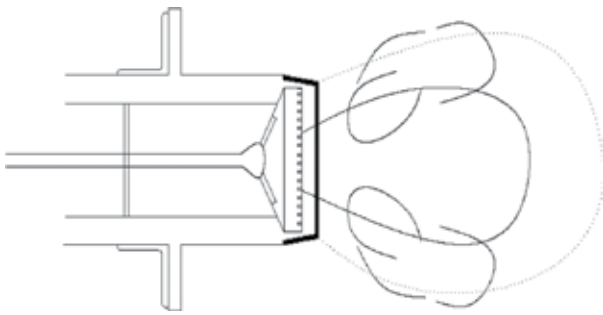

Figure 4. Cross section of the fuel burner.

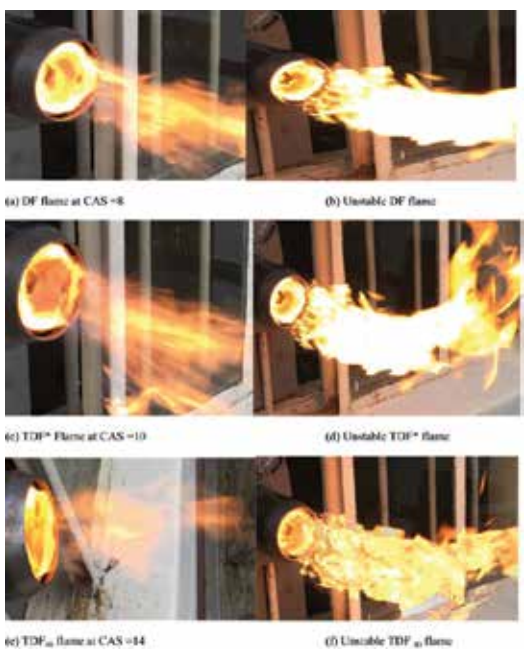

Figure 5. Images of stable and unstable burner flames produced by various fuels tested.

http://dx.doi.org/10.5772/63078

It was discovered that fuels with different physical properties attained stable flames under different AFR, which was controlled by CAS in this instance. DF flame stabilized quite quickly at CAS of 8, whereas TDF* and TDF40 stabilized at CAS of 10 and 14, respectively, as shown in **Figure 5**. This implies that stoichiometric air requirement for TDF* and TDF40 is much higher than that of diesel fuel. This could be as a result of high viscosities and flash points of both TDF* and TDF40. As reported in literature, high viscosity results in restricted fuel flow and poor atomization whereas low flash point is associated with auto ignition and higher fuel consumption [9]. **Figure 5(a, c** and **e**) show the different stable flame intensities for DF, TDF* and TDF40 with a decrease from white to dark orange core flame colors, respectively. This is also justified by the decrease in flue gas temperatures measured for each fuel.

All fuel tested were able to produce peak flame power output similar to the ones specified by the burner manufacture as stipulated in **Table 2**. The test results presented in **Figure 6** show that burner operated more efficiently with diesel fuel as it was able to reach the highest flame power output at CAS of 6 with actual fuel consumption of 2.84 kg/h. TDF* and TDF_{40} has lower fuel consumption and consequently unstable flames and low flame power as a result of high viscosity, low flash point and low calorific value.

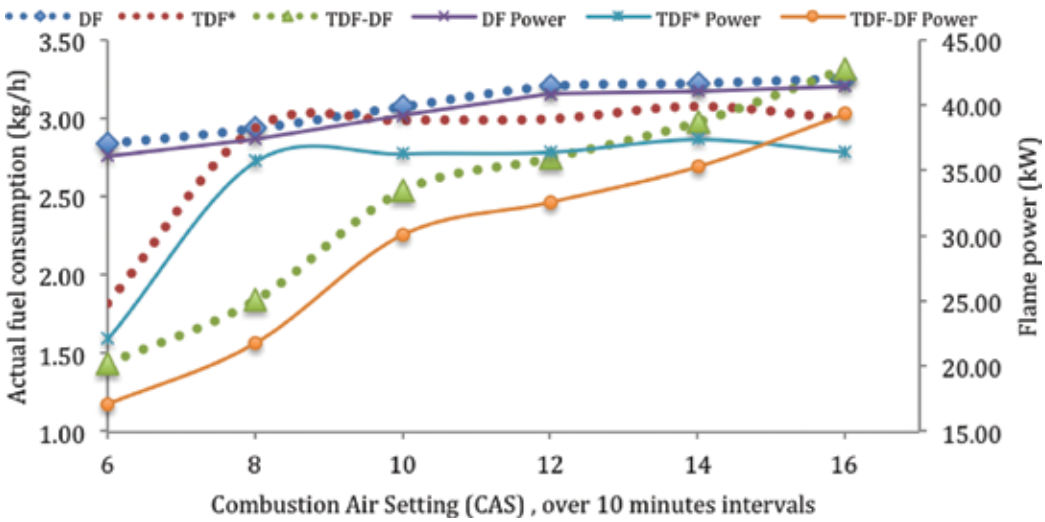

Figure 6. Performance test data of NC4 fuel burner using DF, TDF* and TDF_{40}.

The burner reached a stable flame at CAS 8 when operated with diesel fuel whereas TDF* and TDF_{40} reached their stable flames at CAS of 10 and 14, respectively. The burner specific fuel consumption (SFC), which is defined as a ratio of the actual fuel consumed and power delivered, was found to be 78.43, 82.19 and 84.37 g/kWh when operated with DF, TDF* and TDF_{40}, respectively. This implies that more efficient heat was produced by diesel fuel due to its high colorific value and good flow characteristics.

3.3. Flue gas emissions

Combustion tests were carried out for 60 min for each test fuel. Average emission data were recorded every 10 min as the combustion air setting (CAS) was adjusted to the next value. The data reported in **Figure 7** display the average test data taken at the optimum CAS value for each fuel. CAS is a measure of air-fuel ratio (AFR); selection of higher CAS value on the burner allows more air to be introduced into the combustion zone for enhanced combustion. The optimum CAS was attained when a more stable flame with highest flue gas temperature was recorded. These values were obtained as 8, 10 and 14 for DF, TDF* and TDF_{40}, respectively.

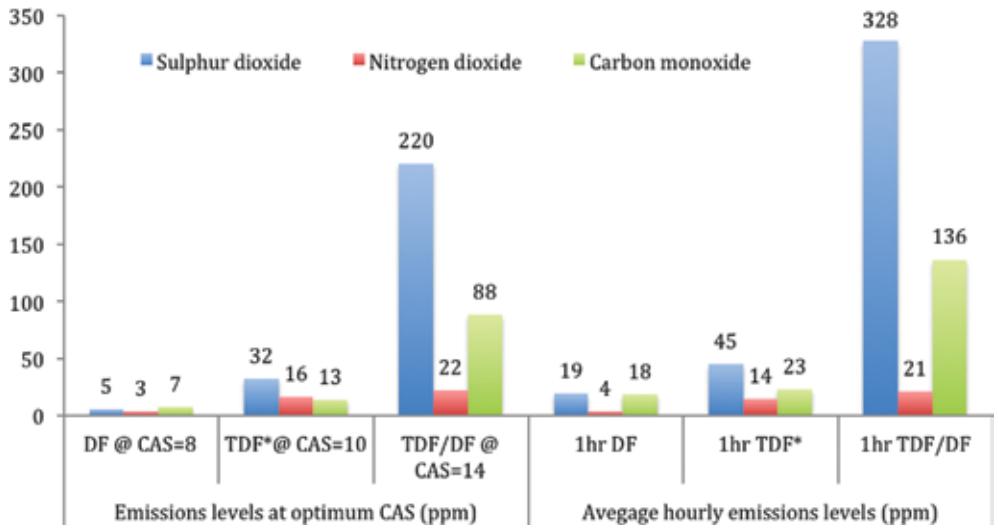

Figure 7. Selected flue gas emissions from a burner operated with various fuels.

The results show that TDF_{40} produces high emission levels compared to TDF* and DF. High sulphur emissions are attributed by the concentrations of sulphur in the fuel; TDF_{40} contains 4516 ppm total sulphur, while TDF* contains 1100 ppm total sulphur which is significantly higher than the sulphur levels in DF (443 ppm). The maximum flue gas temperatures for each fuel at optimum CAS were recorded as 546, 489 and 420°C for DF, TDF*, and TDF_{40}, respectively. Hence, the flame core color changed from white to dark orange as seen in **Figure 5** (a, c and e).

In practice, there are a number of reasons why this temperature will be lower than the adiabatic flame temperature, which has been reported to be 2102°C [42]. One of the reasons is that combustion products dissociate back into reactants or other higher reactive species accompanied by absorption of energy, hence reducing the actual flame temperature. Any excess air will increase the mass of flue gas relative to the mass of fuel, with a corresponding reduction in

http://dx.doi.org/10.5772/63078

temperature; hence, the flue gas temperature of highest CAS value (TDF_{40}) was reported to be the lowest. With sub-stoichiometric air supply, the flame temperature will also fall, as though the mass of flue gas is reduced. The effective calorific value of the fuel is also reduced by an amount equivalent to the calorific value of the CO, which is present in the flue gas.

CO emissions was found to be reasonably low and within the ambient air quality standards presented in **Table 1**, except for TDF_{40} blend which was higher. However, the formed CO molecules are oxidized if there is enough oxygen in the combustion environment. This may be as a result of high-volume fuel being introduced to the atomizer at high viscosity resulting in poor fuel atomization [43]. Larger fuel droplets are introduced into the combustion zone. These droplets are not fully oxidized due to their larger surface area and the flue gas product and also tend to contain high HC, CO and high flame temperatures promoting NO_2 formation. Under these conditions, more fuel is used due to inefficient fuel oxidation as it was observed with rapid soot formation on the burner nozzle when the TDF_{40} was tested.

4. Conclusions

TDF oil from continuous tyre pyrolysis plant has been refined by gas-phase oxidative fractional distillation including desulphurization, adsorption, filtration and chemical modification of certain physical properties in accordance with SANS 342 for use in precision combustion equipment. TDF* was produced as a test fuel to be compared with standard diesel fuel in a Cuenod NC4 fuel burner. It was concluded that TDF oil could be refined into TDF* exhibiting similar properties to standard diesel fuel. Vinyl acetate, alkyl nitrate and some combination of organic polar solvents can effectively adjust the fuel's viscosity, cetane index and calorific value. It was also concluded that TDF oil is not recommended for use in precision combustion equipment in its raw form. Pretreatment processes, such as multistage filtration, are essential for the removal of total contamination and residual moisture. Modification of the fuel's properties such as viscosity, flash point and total sulphur is essential. Purification of TDF oil through a process of oxidative desulphurization fractional distillation with chemical desulphurization and filtration has shown a great potential of using the fuel derivative (TDF*) directly in precision combustion equipment. TDF can also be blended with petroleum diesel fuel at TDF oil volumetric concentration of <40% (TDF_{40}), and the fuel mixture must undergo multistage filtration. TDF oil and its derivatives produce SO_2, NO_2 and CO emission levels higher than acceptable limits as prescribed by the European Air quality standard (EU2015/2193). It was concluded that TDF oil is a potential industrial burner fuel if diluted with petroleum diesel fuel at TDF volumetric concentration of <40% or any ratio that could adjust the viscosity level below 5.3 cSt. Multistage filtration system is highly recommended to reduce total contamination and water levels in the fuel mixture. Exhaust gas scrubbing is also recommended due to significantly high sulphur oxide emission in the flue gas.

Acknowledgements

This work was supported by the Faculty of Engineering and the Built Environment at the University of Johannesburg. The Authors would also like to acknowledge the National Research Foundation-South Africa for financial support.

Author details

Jefrey Pilusa* and Edison Muzenda

*Address all correspondence to: pilusat@webmail.co.za

Process Energy and Environmental Technology Station, University of Johannesburg, Doornfontein, Johannesburg, Republic of South Africa

References

[1] Gust S. Combustion experiences of flash pyrolysis fuel in intermediate size boilers. In: Bridgwater AV, Boocock DGB, editors. Developments in thermochemical biomass conversion. Blackie Academic and Professional. London. 1997;481–488.

[2] Murugan S, Ramaswamy MC, Nagarajan G. Performance, emission and combustion studies of a DI diesel engine using distilled tyre pyrolysis oil–diesel blends. Fuel Processing Technology. 2008;89(15):2–9.

[3] Frigo S, Seggiani M, Puccini M, Vitolo S. Liquid fuel production from waste tyre pyrolysis and its utilisation in a diesel engine. Fuel. 2014;116:399–408.

[4] Meier D, Faix O. State of the art of applied fast pyrolysis of lignocellulose materials: a review. Bioresource Technology. 1999;68:71–77.

[5] Demirbas A. Current technologies for the thermo-conversion of biomass into fuels and chemicals. Energy Sources. 2004;26:715–730.

[6] Huber GW, Iborra S, Corma A. Transportation fuels from biomass: chemistry, catalysts, and engineering. Chemical Reviews. 2006;106(9):4044–4098.

[7] Continuous waste tyre pyrolysis plant [Internet]. 2013. Available from: http://www.internationalrubberrecycling.co.za/cp/14028/irr-pyrolysis-plant. Accessed 2016-01-05.

[8] Rodriguez IM, Laresgoiti MF, Cabrero MA, Torres A, Chomon MJ, Caballero B. Pyrolysis of scrap tires. Fuel Processing Technology. 2001;72:9–22.

[9] Olazar M, Lopez G, Arabiourrutia M, Elordi G, Aguado R, Bilbao J. Kinetic modeling of tyre pyrolysis in a conical spouted bed reactor. Journal of Analytical Applied Pyrolysis. 2008;81(1):27–32.

[10] Czernik S, Bridgwater AV. Overview of applications of biomass fast pyrolysis oil. Energy and Fuels. 2004;18:590–598.

[11] Chiaramonti D, Oasmaa A, Solantausta Y. Power generation using fast pyrolysis liquids from biomass. Renewable and Sustainable Energy Reviews. 2007;11:1056–1086.

[12] Lopez G, Olazar M, Amutio M, Aguado R, Bilbao J. Influence of tire formulation on the products of continuous pyrolysis in a conical spouted bed reactor. Energy Fuels. 2009;23(5):23–31.

[13] Lah B, Klinar D, Likozar B. Pyrolysis of natural, butadiene, styrene-butadiene rubber and tyre components: modeling kinetics and transport phenomena at different heating rates and formulations. Chemical Engineering Science. 2013;8:1–13.

[14] Rofiqul IM, Haniu H, Rafiqul ABM. Liquid fuels and chemicals from pyrolysis of motorcycle tire waste: product yields, compositions and related properties. Fuel. 2008;87(31):12–22.

[15] Galvagno S, Casu S, Casabianca T, Calabrese A, Cornacchia G. Pyrolysis process for the treatment of scrap tyres: preliminary experimental results. Waste Management. 2002;22(9):17–23.

[16] Li S, Yao Q, Chi Y, Yan J, Cen K. Pilot-scale pyrolysis of scrap tires in a continuous rotary kiln reactor. Industrial Engineering Chemical Research. 2004;43(51):33–45.

[17] Onay O. Influence of pyrolysis temperature and heating rate on the production of bio-oil and char from sunflower seed by pyrolysis using a well-swept fixed-bed reactor. Fuel Processing Technology. 2007;88(5):23–31.

[18] Hariharan S, Murugan S, Nagarajan G. Effect of diethyl ether on tyre pyrolysis oil fueled diesel engine. Fuel. 2013;104:109–115.

[19] Martinez JD, Rodriguez-Fernandez J, Sanchez-Valdepenas J, Murillo R, Garcia. Performance and emissions of an automotive diesel engine using a tire pyrolysis liquid blend. Fuel. 2014;115:490–499.

[20] Koc AB, Abdullah M. Performance of a 4-cylinder diesel running on tire oil-biodiesel–diesel blend. Fuel Processing. 2014;118:264–269.

[21] Pilusa J, Muzenda E. Qualitative analysis of waste rubber-derived oil as an alternative diesel additive. In: Proceedings of the international conference on chemical and environmental engineering (ICCEE'2013); 15–16 April 2013; Johannesburg (South Africa). 2013; pp. 13–17.

[22] Pilusa T, Muzenda E, Shukla M. Reduction of sulphur in crude tyre oil by gas-liquid phase oxidative adsorption. South African Journal of Chemical Engineering. 2014;19(1): 22–30.

[23] Agrawal AK, Srivastava DK, Dhar A, Maurya RK, Shukla PC, Singh AP. Effect of fuel injection timing and pressure on combustion, emissions and performance characteristics of a single cylinder diesel engine. Fuel. 2013;111:374–383.

[24] Hüseyin A, Cumali I. Analysis of combustion, performance and emission characteristics of a diesel engine using low sulfur tire fuel. Fuel. 2015;143:373–382.

[25] Bowman CT. Chemistry of gaseous pollutant formation and destruction. In: Bartok W, Sorafin AF, editors. Fossil Fuel Combustion. New York: John Wiley & Sons, Inc.; 1991. pp. 529–652.

[26] Pilusa TJ, Mollagee MM, Muzenda E. Reduction of vehicle exhaust emissions from diesel engines using the whale concept filter. Aerosol and Air Quality Research. 2012;12:994–1006.

[27] DEA, National environmental management: air quality Act No. 39 of 2004. South African national department of environmental affairs government gazette No 32816. 2009;12:6–9.

[28] Kyto M, Martin P, Gust S. Development of combustors for pyrolysis liquids. In: Bridgwater AV, editor. Pyrolysis and gasification of biomass and waste. CPL Press. Tatcham. 2003; pp. 187–190.

[29] Preto F, Gogolek PEG, Wong JKL. Nozzle testing and development for bio-oil combustion. In: Bridgwater AV, Boocock DGB, editors. Science in thermal and chemical biomass conversion. CPL Press. London. 2006; pp. 1480–1490.

[30] Cuenod NC. Product range manual, Art Nr. 4200 1013 9301A [Internet]. 2009. Available from: http://www.manualslib.com/products/Cuenod-Nc4-3838347.html [Accessed 2015-11-22].

[31] Testo 350 instructions manual [Internet]. 2014. Available from: http://www.testo350.com/downloads/350/literature-manuals/2-%20testo%20350%20Instruction%20Manual.pdf [Accessed 2015-12-22].

[32] IARC monographs on the evaluation of carcinogenic risks to humans, 45, diesel and gasoline engine exhausts and some nitroarenes, Lyon, 2013, 45:224–227.

[33] Zajac WW. Encyclopedia of reagents for organic synthesis. John Wiley & Sons. New Jersey. 2001.

[34] Williams PT. Waste treatment and disposal. 2nd ed. John Wiley & Sons. New Jersey. 2005; p. 28.

[35] Rodríguez-Cabo B, Rodríguez H, Rodil E, Arce A, Soto A. Extractive and oxidative extractive desulfurization of fuels with ionic liquids. Fuel. 2014;117:882–889.

[36] Haider MI, Kuder JE, Long BJ, Menczel JD, Stamatoff JB, Bayer M. Thermally expandable, viscosity modified wax compositions and method of use in actuators. 1998; United States of America Patent Office: US 5772949 A.

[37] Gadvi SN, Pandya AV. Enhancement in viscosity of diesel by using chemical additives. International Journal of Modern Engineering Research. 2014;3(4):2108–2110.

[38] Murugan S, Ramaswamy MC, Nagarajan G. Assessment of pyrolysis oil as energy source for diesel engines. Fuel Processing Technology. 2009;90:67–74.

[39] Islam MR, Joardder MUH, Hasan SM, Takai K, Haniu H. Feasibility study for thermal treatment of solid tyre tastes in Bangladesh by using pyrolysis technology. Waste Management. 2011;31:2142–2149

[40] Van de Beld B, Holle E, Florijn J. The use of pyrolysis oil and pyrolysis oil derived fuels in diesel engines for CHP application. Applied Energy. 2013;102:190–197.

[41] Specifications and distribution additive HiTEC 1440A [Internet]. 2011. Available from: https://www.aftonchemical.com/…/Fuel/HiTEC-4140A_PDS.pdf [Accessed 2015-12-17].

[42] Belyea HA, Holland WJ. Flame temperature in oil-fired fuel-burning equipment and its relationship to carbonaceous particulate emissions. Journal of the Air Pollution Control Association. 1967;17:320–323.

[43] Dorri A, Lamani A, Hoxha A. Influence of hole geometry in the cavitations phenomena of diesel injector, a numerical investigation. GOMABN. 2009;47:351–371.

Chapter 5

Municipal Solid Waste Cofiring in Coal Power Plants: Combustion Performance

Odile Vekemans and Jamal Chaouki

Additional information is available at the end of the chapter

http://dx.doi.org/10.5772/63940

Abstract

The combustion of fuel derived from municipal solid waste is a promising cheap retrofitting technique for coal power plants, having the added benefit of reducing the volume of waste disposal in landfills. co-combustion of waste-derived fuel (WDF) and coal, rather than switching to WDF combustion alone in dedicated power plants, allows power plant operators to be flexible toward variations in the WDF supply. Substituting part of the coal feed by processed high calorific value waste could reduce the NO_x, SO_2, and CO_2 emissions of coal power plants. However, the alkaline content of WDF and its potentially harmful interactions with the coal ash, as well as adverse effects from the presence of chlorine in the waste, are important drawbacks to waste-derived fuel use in large-scale power plants. This chapter reviews these points and gives a centralized review of co-combustion experiments reported in the literature. Finally, this chapter underlines the importance of lab-scale experiments previous to any large-scale application and introduces the idea of combining waste and additives dedicated to the capture of targeted pollutants.

Keywords: waste, coal, power plant, emissions, RDF

1. Introduction

Worldwide, around 1.3 billion tons of MSW (municipal solid waste) are generated every year, an amount that is expected to grow to 2.2 billion tons of MSW per year by 2025 [1]. A large fraction of MSW is disposed in landfills, which may lead to groundwater contamination by leachates and atmospheric emission of biogas, a mixture of CH_4 and CO_2 generated by biological processes related to MSW decay. In order to avoid these environmental disturbances,

INTECH
open science | open minds

© 2016 The Author(s). Licensee InTech. This chapter is distributed under the terms of the Creative Commons Attribution License (http://creativecommons.org/licenses/by/3.0), which permits unrestricted use, distribution, and reproduction in any medium, provided the original work is properly cited. CC BY

governments lean toward banning landfill sites and encouraging development of alternative waste treatments.

Many of the components of MSW currently sent to landfill, such as paper, cardboard, textiles, wood, and plastics, are not hazardous and have high caloric content. For example, the composition of the MSW landfilled in 2013 in the United States is given in **Figure 1**. Instead of being disposed in a landfill, these components could be recovered and treated to produce waste-derived fuels (WDFs) for use as an energy source.

Based on financial, environmental, social, and management considerations, the waste management sector defined a "waste management hierarchy," classifying the different waste management options, presented in **Figure 2**. This concept, which appeared in the early 1970s, was formalized in the 2008 European Commission Waste Framework Directive [3]. From a sustainability point of view, waste reduction, reuse, recycling, and recovering are preferred—all these options decreasing the quantity of waste to be disposed of [1]. Unfortunately, not all waste streams can be diverted to such end and final wastes are always produced. Furthermore, even though some materials can have an increased lifetime, they generally end up degraded and in a state where their reutilization is impossible. Finally, some wastes, especially if they are made of mixed materials, are so that their recycling is really costly or is associated with a quite high energy demand or pollutant production and therefore is unrealistic [4]. For these wastes, energy recovery through co-combustion is an option of great interest.

Currently, coal combustion accounts for around 40% of the world's electricity generation [5] despite the fact that coal combustion is a major source of NO_x and SO_2 emissions. These emissions are precursors for acid rain, and therefore sensible environmental policy suggests that they be curtailed. Cheap retrofitting techniques are needed to permit existing infrastructure to continue to operate without contributing to the incidence of acid rain.

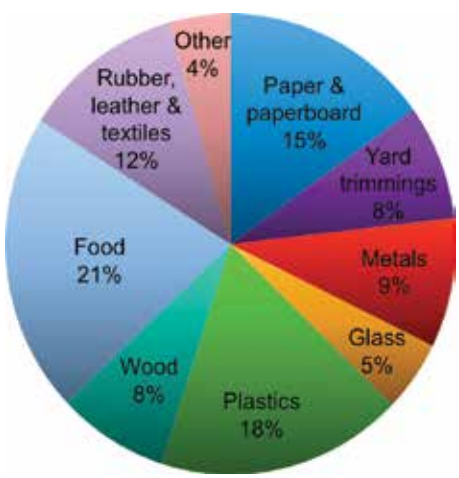

Figure 1. Total MSW discards (by material) in the United States in 2013 [2].

http://dx.doi.org/10.5772/63940

Since municipal solid waste generally has negligible sulfur content and lower nitrogen content than coal, substituting part of the coal with waste-derived fuel might be beneficial to the environmental performance of coal power plants. Furthermore, since the coal power plants electric efficiency is usually 10–20% superior to that of incinerators [6], burning MSW in coal power plants can lead to higher waste utilization efficiency than in dedicated incineration plants. Also, MSW contains a renewable fraction and can therefore helps reducing the amount of fossil CO_2 generated by coal power plants. This is somewhat mitigated by the higher chlorine and alkaline content of WDF compared with coal, which may contribute to corrosion and ash deposition issues. Consequently, the co-combustion of coal and WDF has to be studied before a large-scale utilization of WDF in power plants. This chapter will discuss the production of WDF as well as the effect of its cofiring in coal power plants in terms of CO_2, NO_x, and SO_2 emissions. The ashes behavior and the fate of chlorine in the combustors will also be covered. This chapter therefore summarizes the benefits and limitations related to WDF co-combustion in existing coal power plants.

2. Fuels derived from waste, a large ensemble

Due to their inhomogeneity, their high moisture content and fraction of incombustibles, municipal solid wastes cannot be fired in large-scale coal power plants unless they are transformed in a more homogeneous and calorific feedstock, broadly called waste derived fuels (WDFs). Unfortunately, the fuels that can be derived from MSW are almost as diversified as the MSW themselves.

Depending on the characteristics and the type of wastes used for the production of the WDF, it is common to differentiate solid recovered fuel (SRF) from refuse-derived fuel (RDF). Generally, SRF is more homogeneous, less contaminated, and have a higher calorific content than RDF that is more generic. In Europe, to overcome the ambiguous situation regarding fuel quality, the European Commission has given mandate to CEN/Technical Committee (TC) 343 to prepare a document classifying solid recovered fuels [7]. Different SRF qualities based on three criteria that are the net calorific value (serving as the economic indicator), the chlorine content (as the technological indicator), and the mercury content (as the environmental key

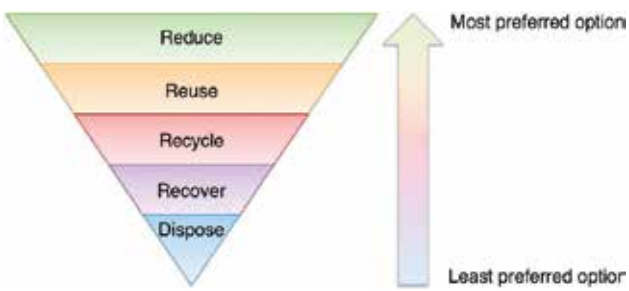

Figure 2. Waste management hierarchy.

parameter) have been defined [8]. Readers are advised to refer to the CEN/TC 343 published standards for more information.

On top of RDF and SRF, there has been mention of process engineered fuel (PEF), engineered fuel (EF), refuse plastic fuel (RPF), generally made of more than 60% of plastic waste [9], and packaging-derived fuel (PDF). These fuels are usually of higher quality than RDF and SRF as they are made of source-separated processed dry combustible fraction, which cannot be used for recycling [10, 11]. Also, they are of predictable and consistent quality, which is critical to ensure their market security. Finally, they are not considered as waste but as a marketable product that has to meet strict end-user requirements [12].

Numerous processes have been implemented to produce WDF from MSW. These processes generally consist of sorting and mechanical separation of the waste, size reduction (shredding, chipping, and milling), separation and screening, blending as well as drying and densification [13–15]. All these steps are used to increase the homogeneity and the heating value of the final WDF, improving their in-situ handling and feeding. An example of WDF production chain is given in **Figure 3**.

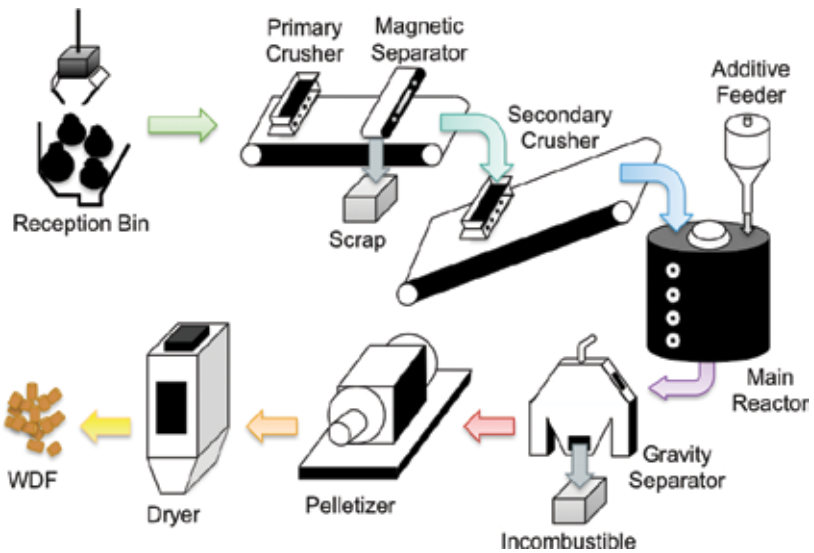

Figure 3. Production of WDF, inspired from [16].

WDF production generally involves a source-separation step where the organic fraction (food residues, yard trimmings, etc.) is removed. One of the best-established and less expensive processes is the mechanical biological treatment (MBT). In an MBT plant, the metals and inert materials are removed, the organic fraction is screened out, and the high-calorific fraction is separated. The organic fraction is further stabilized using composting processes, either with or without a digestion phase, producing compost and biogas. The high-calorific fraction, on the other hand, is further processed into waste-derived fuel, as described above [11]. Extensive mechanical treatment (MT) processes can also be used to produce WDF [7].

http://dx.doi.org/10.5772/63940

Even though the majority of the technologies involves the removal of the organic fraction some, such as the dry stabilization process, produce WDF containing the organic fraction. In this process, the residual waste, after separating out metals and inert materials, is dried through a composting process leaving the residual mass with a higher calorific value [11]. The high-calorific output of this process, developed in Germany, has the trade name of "Trockenstabilat". WDF containing the stabilized organic fraction are however not the norm, and will therefore not be studied in the rest of the chapter.

The high-calorific fraction of the waste, used as WDF, can generally be separated into a biogenic fraction and a plastic fraction. The biogenic or fibers fraction refers to the textiles, wood pieces, papers, and cardboards found in the MSW. Papers range from newspaper to glossy magazine sheets and can contain multiple chemicals as a large variety of additives are used during their fabrication, whether it is as pigment, binder, filler, or else. As an example, some of the pigments that can be used are clay (kaolin), calcium carbonate, titan oxide, satin white ($3CaO{\cdot}Al_2O_3{\cdot}3CaSO_4{\cdot}3H_2O$), barium sulfate, talc, and aluminum hydroxide [17]. Calcium carbonate can further be used as filler, and therefore may account for up to 15% of the paper content.

The plastic fraction, majorly derived from oil, also regroups a wide variety of materials. The more common plastics found in MSW are polyethylene (PE), polypropylene (PP), polystyrene (PS), and polyvinyl chloride (PVC) [14]. While the biogenic fraction has a high ash content, the plastic fraction generally contains chlorine, both raising processing and environmental concerns [18].

Finally, multimaterial pieces can also be found in the high-calorific fraction of MSW, such as cardboard drink containers or Tetrapack™, combining both paperboard and plastic, with or without aluminum foil.

Once produced, the waste-derived fuels can be used for the electricity production combined with coal or natural gas in thermal power plants, for their energetic content in industrial processes (e.g., cement kilns and blast furnace) or for their material properties also in various industrial processes (e.g., asphalt production) [19]. Due to the large number and poor environmental performance of coal power plants and the importance of developing cheap retrofitting technology to improve this performance, only the utilization of WDF in coal power plant will be studied in this chapter.

During co-combustion studies, proportions of each of the combustible can be expressed in terms of weight fraction or energetic (also called thermal) fraction [20]. Energetic fractions are evaluated according to:

$$x^{e}_{WDF} = \frac{W_{WDF}\, LHV_{WDF}}{W_{WDF}\, LHV_{WDF} + W_c\, LHV_c} \tag{1}$$

with W the mass flow (kg/h) of the WDF and of the coal (c), and LHV the lower heating value (kJ/kg). The mass fractions, on the other hand, are evaluated as follows:

$$x_{WDF}^{wt} = \frac{W_{WDF}}{W_{WDF} + W_c} \tag{2}$$

It should be mentioned that a large number of research projects currently focus on oxycombustion of coal and waste, which facilitates CO_2 sequestration from the flue gas [21–23]. However, the costs related to such technology still remain a major obstacle to any commercial application [24]. The rest of this chapter will therefore only focus on the benefits and limitations related to WDF co-combustion in existing coal power plants.

3. Effect of WDF co-combustion on CO_2 emissions

Because WDF contain products derived from biogenic sources (e.g., paper), "fossil CO_2" emissions are reduced when WDF is cocombusted with coal [25]. Indeed, biogenic sources capture the same amount of CO_2 during their lifecycle than what is emitted during their combustion [26]. Furthermore, methane being a greenhouse gas 25 times more damageable than CO_2 in terms of global warming [27], the beneficial effect of waste co-combustion in terms of greenhouse gas emission is even greater if are taken into account the avoided methane emissions associated with their disposal in landfills. Therefore, in the European Union, for example, diversion of MSW from landfilling to composting, recycling, and energy recovery could produce a reduction from 40 to over 100 Mt CO_2-equivalent per year [28].

In order to evaluate the fossil CO_2 emissions that could be avoided through WDF cocombustion, one needs to know the carbon and water content, the calorific value, and the biogenic fraction of the fuel [9]. Characteristics of varied WDF found in the literature are given in **Table 1**.

What can be seen from **Table 1** is that WDF with a wide range of carbon content (from 34 to 69%) and of heating value (from 13 to 27 MJ/kg) can be produced. As for the biogenic content, it is rarely known, especially for RDF. Furthermore, fossil CO_2 emissions avoided will depend on the coal characteristics, which also vary widely.

Anyhow, for example in [10], the authors evaluated that the emission of fossil CO_2 associated with lignite combustion is around 955 g/kg, whereas that of an SRF with a biogenic content of 67% is (1–0.67) × 1067 = 352 g/kg. Lignite and SRF having comparable calorific content, for a 15 wt% cofiring ratio, emission of 90.5 g of fossil CO_2 are avoided per kilogram of feedstock burned. Taking, for example, REW's BoA 2 and 3 boilers, which are fed with lignite at a rate of 820 t/h [29], fossil CO_2 savings of around 74.2 t/h could be obtained through WDF co-combustion, which sum up to 1781 t of fossil-CO_2 avoided per day in one boiler.

Since WDF co-utilization in existing thermal plants usually requires low additional investments and, as was described in this section, since WDF are partially renewable, co-combustion of WDF could allow the production of partly renewable electricity at low cost. Furthermore, in comparison with pure WDF combustion systems, the potential variability of the cofiring ratio allows energy producers to be adaptable toward fluctuations in WDF availability.

http://dx.doi.org/10.5772/63940

Even though CO_2 emissions are in the heart of nowadays concerns, other pollutants such as NO_x and SO_2 still remain critical in coal power plants. The effect of WDF co-combustion on their emissions is discussed in the following two sections.

Fuel name	Ref	Dp	Proximate analysis, wt%				Ultimate analysis, wt%					Trace elements, wt%			HHV	LHV	Fib. %
		mm	WC	VM	FC	Ash	C	H	N	O	S	Cl	Ca	Na	MJ/kg		
EF	[12]	1–8	6.8	67.5	10.1	15.6	39.0	5.8	0.7	37.7	0.1	–	–	–	15.9	–	30
EF	[29]	0.1–0.4	1.0	82.5	14.1	2.4	55.6	7.7	0.22	32.9	0.20	0.047	1.72	<1	23.7	–	80
EF	[29]	0.1–0.4	1.4	84.2	12.0	2.4	58.9	8.5	0.22	28.3	0.17	0.062	1.65	<1	26.6	–	70
EF	[29]	0.1–0.4	2.8	85.3	10.9	1.0	52.0	7.0	0.23	36.7	0.25	0.039	1.60	<1	22.0	–	90
SRF	[6]	0.164	5.20	72.1	7.1	5.7	58.0	6.6	1.00	27.4	0.42	0.28	0.67	0.11	–	20.9	–
SRF	[7]	18	3.0	79.6	6.3	11.1	40.5	5.3	0.03	–	0.07	0.02	–	0.025	22.7	21.4	78
SRF	[28]	–	18.3	–	–	7.5	54.9	7.6	0.79	29.1	0.15	0.46	1.78	0.196	–	18.8	–
SRF	[28]	–	18.1	–	–	7.5	55.1	7.6	0.48	29.1	0.15	0.44	1.91	0.186	–	18.8	–
SRF	[30]	0.5–1.3	28.1	56.0	6.4	9.7	60.1	8.4	0.98	30.3	0.21	–	–	–	–	14.8	75
RDF	[7]	18	30.4	46.1	8.3	16.2	28.1	3.4	0.98	–	0.32	0.25	–	0.536	14.8	13.2	–
RDF	[13]	15	5.4	71.6	10.8	12.2	40.4	5.7	0.92	36.1	0	0.85	0	–	–	–	–
RDF	[24]	0.12	2.6	80.2	2.8	14.4	44	6.8	1.0	31.1	0.06	–	–	–	26.9	25.1	–
RDF	[31]	–	3.7	67.6	9.8	18.9	61.2	8.2	1.3	26.6	0.2	2.5	–	–	22.3	20.8	–
RDF	[31]	9.5	1.7	73.6	7.0	17.7	69.1	7.4	1.9	19.6	0.3	1.7	–	–	24.6	23.3	–
RDF	[31]	–	19.7	49.1	10.8	20.4	57.4	3.8	–	36.8	0.2	1.8	–	–	13.9	12.6	–
RDF	[32]	–	3.0	70.8	13.0	13.0	49.7	7.0	0.82	25.2	0.15	1.15	–	–	–	21.1	–
RDF	[33]	3–6	1.8	75.1	9.6	13.5	49.4	6.9	0.8	28.4	0.3	0.5	–	–	–	21.1	–
RDF	[34]	–	4.5	81.2	8.0	6.4	46.0	6.4	0.25	34.6	1.08	0.85	–	–	–	23.9	–
RDF	[35]	21.5	0	67.6	9.7	22.7	59.0	9.6	0.61	30.9	0.01	–	–	–	–	12.3	–
RDF	[36]	15–50	1.6	62.3	5.1	31.0	39.2	5.1	0.11	24.0	0.08	0.79	–	–	–	17.5	–
RDF	[37]	–	7.83	70.6	12.8	8.7	41.7	5.6	0.80	35.3	0.09	0.14	1.35	–	–	16.4	–
RDF	[38]	15	0	73.5	9.4	17.2	57.2	9.1	0.21	14.4	0.26	–	–	–	–	24.1	–
RDF	[39]	–	18.8	55.3	13.5	12.4	34.0	4.2	0.54	29.7	0.22	0.123	–	–	13.0	–	–
RDF	[40]	0.1	1.48	70.7	11.2	16.6	43.5	5.8	0.9	32.6	0.6	–	–	–	–	–	–
HT MSW	[41]	1.5	0	75.2	23.8	1.09	56.9	7.3	0.97	32.6	0.08	1.09	0.1	0.67	19.1	–	–

EF, engineered fuel; SRF, solid recovered fuel; RDF, refuse derived fuel; HT MSW, hydrothermally treated municipal solid waste.

Table 1. Examples of WDF characteristics.

4. Effect of WDF co-combustion on NO_x emissions

During combustion processes, nitrogen oxides, collectively termed NO_x, are formed either from fixation of N_2 in the combustion air or from oxidation of nitrogen chemically bound in the fuel [30]. A schematic representation of the different NO formation paths is given in **Figure 4**. Thermal-NO refers to NO formed by oxidation of atmospheric nitrogen at high temperature, whereas prompt-NO is formed by reactions of atmospheric nitrogen with hydrocarbon radicals in fuel-rich regions of flames. Finally, fuel-NO refers to NO formed by oxidation of the nitrogen bound in the fuel. Due to the relatively high nitrogen content of coal, the latter is the largest source of NO_x in coal-fired systems [31]. On the other hand, NO can be reduced to N_2 by heterogeneous reaction with carbonaceous surfaces, and therefore can be reduced by reaction with char and soot particles [32]. The amount of NO_x emitted is therefore closely dependent on the combustion environment but also on the fuel composition.

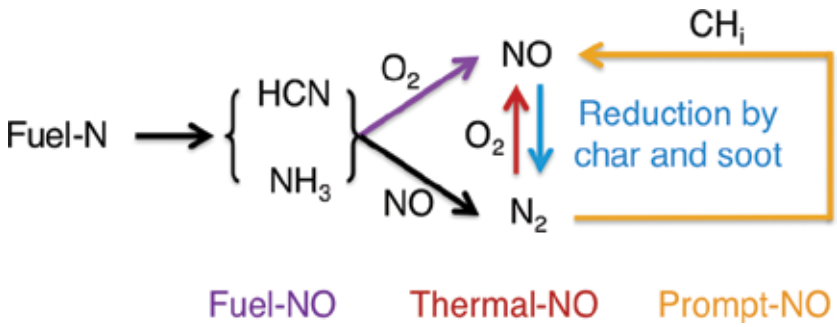

Figure 4. Schematic representation of NO formation in coal combustion system.

Largely, all combustion processes lead to the formation of NO_x, emitted mostly as nitric oxide (NO) with smaller amounts of nitrogen dioxide (NO_2). Nitrous oxide (N_2O) emissions can be significant in fluidized bed combustion, but are negligible in most combustion systems [30].

During co-combustion tests of WDF in fluidized bed combustors (FBCs), authors reported a reduction in NO_x emissions [12, 33–35]. They explain these reduced emissions by the lower nitrogen content of WDF compared with coal, up to 10 times less [30], but also by the nature of the nitrogenous groups in the waste material. Indeed, the main nitrogen compounds of WDF are simple proteins known to release NH_3, which is then decomposed to NH_2, NH radicals forming N_2 after reacting with NO [34]. However, with the increase in cofiring ratio (>30%), increases in NO_x emissions have been recorded [13, 33]. The authors suggest that since less coal is fed to the FBC, availability of unburned carbon is reduced, decreasing the extent of NO reduction by char.

Reductions in NO_x emissions was also recorded during cofiring tests in a cyclone fired combustor [36], as well as in entrained flow reactors (EFRs) [6, 37]. In EFR, contrary to FBC, increased cofiring ratio led to increasing NO_x reductions. The conversion of fuel nitrogen into NO seemed therefore to decrease with increasing share of WDF. This is likely related to the

http://dx.doi.org/10.5772/63940

high volatile content of WDF (as can be seen in **Table 1**), which might generate a reduction zone with lower excess air ratio near the burner [6]. This lower oxygen concentration may inhibit the conversion of fuel nitrogen to NO resulting in reduced NO formation. In addition, since the formation of thermal NO may not be negligible in the EFR, co-combustion of coal and WDF may result in a lower flame temperature compared with coal alone, thus leading to a reduced formation of thermal-NO.

Because NO_x emissions are closely related to the combustion environment, it is critical to maintain a stable and homogeneous solid feed-rate. However, several studies reported difficulties in achieving a steady mass flow rate of WDF to the combustor [12, 34, 36, 37]. This could be due to its inhomogeneity or its "fluffiness". Therefore, for large-scale utilization of WDF, attention should be brought to the optimization of the feeding system. Increasing the carrier gas flow rate, adding a dedicated burner, and working at low cofeeding ratio can help reduce these feeding fluctuations. Finally, producing a homogeneous WDF in terms of particle size and composition, with physical properties as close as possible to that of the injected coal, is advised in order to experience smooth operation of the boiler with reduced NO_x emissions.

5. Effect of WDF co-combustion on SO_2 emissions

Whether a fluidized bed combustor, a cyclone fired combustor, or an entrained flow reactor was used, increasing the WDF cofiring ratio led to a decrease in SO_2 emissions [6, 12, 33–36, 38]. Two main explanations can be found regarding the decrease in SO_2 emissions. The first

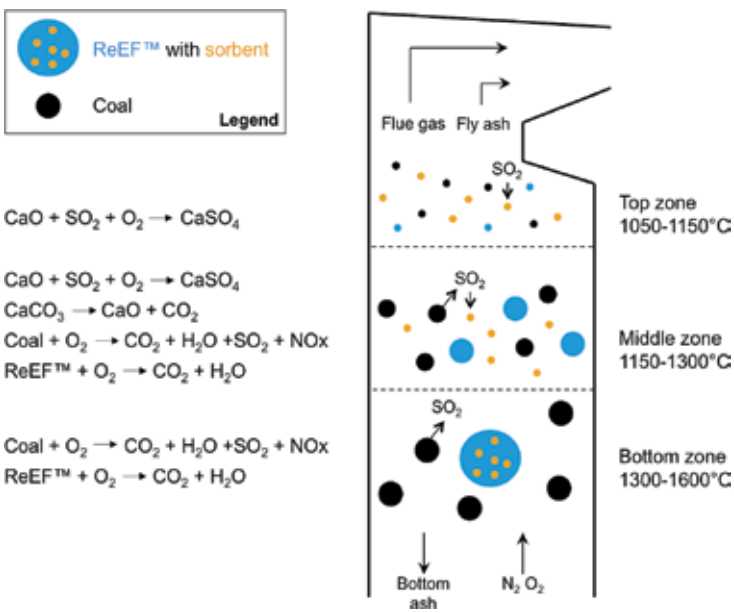

Figure 5. Expected behavior of a WDF combined with alkaline sorbent in a pulverized fuel combustion environment, inspired from [42].

one is the reduced sulfur content of the WDF compared with coal. The second one, corroborated by an increased sulfate content in the bottom and fly ash, is the absorption of SO_2 by alkaline oxides, and more precisely calcium. With the higher calcium content of the WDF compared with coal, a sulfur self-retention process can occur according to the following overall reaction [39]:

$$CaO + SO_2 + 0.5\,O_2 \rightarrow CaSO_4 + heat \tag{3}$$

i.e. decreasing the concentration of SO_2 in the flue gas.

To further take advantage of such phenomenon, Accordant Energy LLC®, formerly known as ReCommunity Inc., developed a novel WDF, called ReEF™ or ReEngineered Feedstock™, to which air-emission control sorbents (e.g., calcium-, sodium-, halide-based and DeNOx reagents) are physically bound [40, 41]. Due to the combined effect of a lower sulfur content in the solid feed, SO_2 capture by the sorbents and transport of small sorbent particles by larger waste particles, SO_2 emissions can be greatly reduced. A schematic representation of this novel technology's behavior is given in **Figure 5**.

In pulverized coal boiler, the ReEF™ is designed so that as the solid feed and the reactant gas enter the bottom of the reactor, the fibers and plastics undergo endothermic pyrolysis, and protect inorganic sorbents from exposure to high temperature, thus minimizing sintering. At this level in the reactor, the coal burns and releases SO_2. When ReEF™ fragments travel upward and are combusted, sorbents are released and can capture the SO_2 present in the flue gas. At the same time, any remaining residues continue to combust. Finally, in the top zone, also called the convection zone, sorbents desulfurize the flue gas to the point when complete burnout and conversion are achieved. This way, optimal ReEF™ design minimizes sintering of the sorbent early in the reactor while maximizing gas absorption later at lower temperatures before exiting as gas/solid products [42].

The use of this novel fuel led to SO_2 emissions reduction greater than 80% in a bubbling fluidized bed [43], up to 85% in a circulating fluidized bed [42], and up to 55% in pulverized coal boiler environment [37]. This fuel and the concept behind it open a new avenue for WDF, as they could be combined with various air-emission control sorbents and tailored to react with pollutant of interest (sulfur, nitrogen, heavy metals, etc.).

6. Effect of WDF co-combustion on ash related issues

Ash-forming elements occur in solid fuels mainly as internal or external mineral grains, as simple salts (e.g., NaCl or KCl), or associated with the organic matrix of the fuel [44]. In coal, a large fraction of the inorganics is present as minerals, mainly as Si, Al, Fe, and Mn. In biomass-derived fuels, such as WDF, on the other hand, the major part of the inorganics consists of free ions and simple salts or is associated with the organic matrix, and is rich in alkali and alkali earth metals (K, Na, Ca, and Mg) [24, 44]. Therefore, while approximately 0.5–4 wt% of the

http://dx.doi.org/10.5772/63940

inorganics in coal vaporizes during combustion, between 30 wt% and 75 wt% of the inorganics in straw, for example, is vaporized at 1200°C [44]. Alkali metals are indeed generally released to a larger extent than the other mentioned species, vaporizing at temperature under 600°C [24]. These alkali metals, once vaporize, may react with silica to form alkali silicates, sulfates, and chlorides that melt or soften at low temperature, which make the co-combustion systems candidate to deposition issues [45].

It should be noted, though, that the release of volatile inorganics depends on a large extent in the presence of more conservative inorganic elements such as silicon and aluminum in the fuel. It has been found that higher aluminosilicate content in the fuel makes alkalis significantly less volatile during combustion [46]. Furthermore, alkali earth metals decrease the retention of alkali metals on silicates leading to the formation of less adhesive compounds [24]. Mechanisms behind ash deposition are therefore rather complex, which are quite challenging as they are of vital importance for the boiler operators. Indeed, careless cofiring of difficult alternative fuels could lead to a reduction of boiler reliability and availability, and to unscheduled plant shut downs [47].

Three major interrelated problems associated with the inorganic content of alternative fuels such as WDF have been identified: bed agglomeration, fouling/slagging, and corrosion.

6.1. Bed agglomeration

Bed agglomeration is caused by interaction between alkali species and silica sand (the bed material in fluidized bed combustors) at high temperature, which can create low melting point eutectics. These eutectics can then act as binder between bed particles, which can result in a partial or complete collapse of the bed leading to defluidization and resulting in costly shut downs [48, 49]. Bed agglomeration and defluidization are influenced by various parameters, including temperature, fluidization velocity, size of bed particles, and combustor size [48]. Detection methods for agglomeration have been developed, such as monitoring of local temperature and pressure fluctuations, which can help to forewarn the onset of defluidization [49]. Anyhow, while agglomeration can be a major problem in fluidized bed combustors fired with biomass-derived fuels only, cofiring of biofuels and coal largely decreases the risk for agglomeration [50].

6.2. Slagging and fouling

While only fluidized bed combustors are affected by agglomeration, all types of furnaces are subject to ash deposition. Heat exchanger surfaces, combustion chamber walls, and cyclones are typically sensitive areas where deposits may cause extensive operational problems [51, 52]. These deposits reduce the heat transfer intensity and cause corrosion that reduces the lifetime of the equipment [53]. In order to limit these issues, many coal-fired power plants conduct sootblowing every 8–12 h [54]. Generally, two main types of deposits can be found [55–57]:

– slagging: occurs in the high-temperature radiant sections of the furnace, directly exposed to flame irradiation, usually associated with some degree of melting of the ash, forming a highly viscous liquid layer;

– fouling: happens in the lower-temperature convective sections of the combustor, generally related to condensation on the low-temperature tube surfaces of volatile species that have been vaporized in previous sections and are loosely bonded, forming an adhesive film that can cause ash particles to adhere to the surface.

Slagging and fouling are very complex phenomena, but they generally simply start with the adhesion of the ashes in suspension on the various boiler surfaces. Ashes will adhere on a surface if it is coated with a partially melted layer. This layer can either be composed of ashes previously vaporized which condensed on the surface [58], or be due to the fusion at really high temperature of the materials composing the surface itself. These mechanisms are schematized in **Figure 6**.

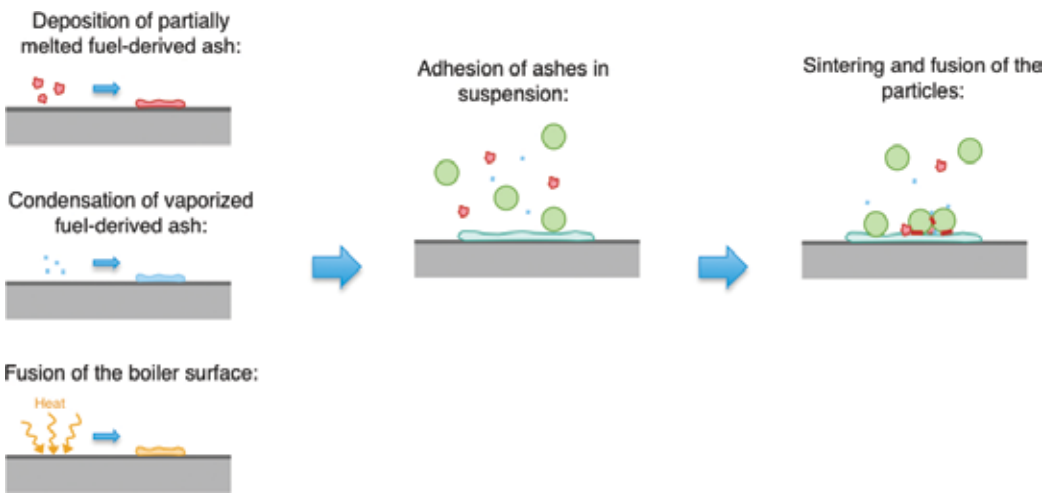

Figure 6. Schematic representation of the formation of deposits in the boilers.

Once the ashes have been deposited on the melted surface, phenomena such as sintering and fusion can produce stronger and more lasting deposits, which are therefore more problematic. These phenomena are accelerated in presence of alkali salts [59]. Therefore, the higher the ash fusion temperature, the better, so that the deposits are not melted, but are loosely bond and easy to clean with sootblowers [20]. Fusion temperature of crystals and eutectics typically present during coal and WDF co-combustion are given in **Table 2**. It can be seen that the higher the alkali content, and more precisely sodium and potassium, the lower the fusion temperature and therefore the more acute the slagging and fouling [45, 57]. At present, in purely waste-fired units, corrosive deposits and ash melting have limited their steam temperature to 420–470°C, and consequently their electric efficiency to 20–24% [28].

http://dx.doi.org/10.5772/63940

Component	Fusion temperature (°C)
$K_2S_2O_7$	325
$Na_2S_2O_7$	401
$Na_3K_3\ Fe_2\ (SO_4)_6$	552
Na_2SO_4 –NaCl	625
Na_2 S-FeS	640
$CaSO_4$ –CaS	850
Na_2SO_4	884
$K_2O.Al_2O_3\ .6SiO_2$	1150
$CaSO_4$	1450
$2CaO.Al_2O_3\ .2SiO_2$	1593
SiO_2	1700

Table 2. Switch the table to have the line as column and vice versa. Separation between the column is not clear for the first line. We read K2O.Al2O3CaSO4 for example [45, 60].

In order to understand and predict the ash deposition propensity of fuels, numerous research approaches have been undertaken. Among them is the development of a number of empirical indices and several laboratory methods to determine the ash fusion temperatures [47].

Four temperatures are used to characterize the ash melting behavior of laboratory prepared ash [61]: (1) the shrinking temperature (ST) defined as the temperature at which shrinking of the test piece occurs, (2) the deformation temperature (DT) defined as the temperature at which the first signs of rounding of the edges due to melting of the test piece occur; (3) the hemisphere temperature (HT) defined as the temperature at which the test piece's height becomes equal to half the base diameter; and (4) the flow temperature (FT) defined as the temperature at which the ash is spread out over the supporting tile in a layer, the height of which is equal to half the height of the test piece at the hemisphere temperature. These temperatures are represented in **Figure 7**. Over the ST ashes can be strongly adhesive, which can result in slagging [60].

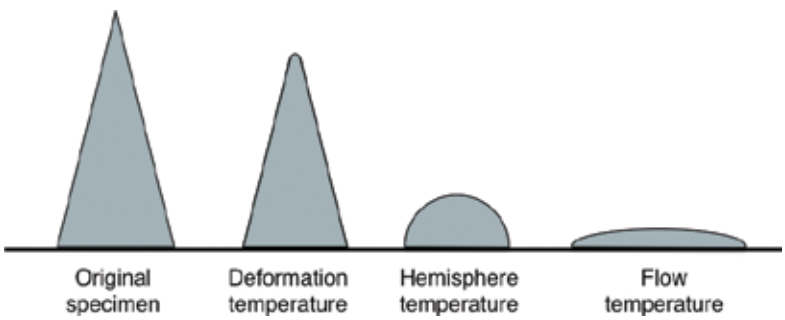

Figure 7. Ash characteristic temperatures.

From these characteristic temperatures, a slagging propensity index is evaluated as:

$$F_s = \frac{4DT + HT}{5} \tag{4}$$

with the temperatures expressed in degree Celsius. Ashes are classified as having a boiler slagging propensity medium when F_s lies between 1232 and 1342°C; high when F_s is between 1052 and 1232°C; and severe when F_s is less than 1232°C. Accordingly, MSW and paper/plastic fluff will both have a high slagging propensity [61].

Other indices are based on the finding that so-called basic compounds (or fluxing oxides) lower the deformation temperature of ashes, whereas acidic ones (also called sintering oxides) increase it [60]. This general rule of thumb, developed for coal ashes, can also be applied to WDF ashes [61]. The slagging propensity of mixes of WDF and coal ashes can therefore be correlated to the B/A ratio [60]:

$$B/A = \frac{Fe_2O_3 + CaO + MgO + Na_2O + K_2O + P_2O_5}{SiO_2 + Al_2O_3 + TiO_2} \tag{5}$$

with Fe_2O_3, CaO, MgO, Na_2O, K_2O, P_2O_5, SiO_2, Al_2O_3 and TiO_2 the weight fraction of the corresponding components in the ashes.

Intensive slagging has been observed when the index is in the 0.75–2 range. Moving away from this range in either direction has decreased the slagging intensity [47].

Finally, thermodynamic equilibrium modeling has become another tool to better understand and predict the chemical reactions of the ash-forming matter during co-combustion of coal, and WDF. Comprehensive description of thermodynamic database and model of ash-forming elements in waste combustion can be found in [62].

Such approaches can give an initial assessment of the slagging and fouling propensity of the fuels [24]. However, for a true evaluation, experimental work is greatly recommended, especially since interactions between burned coal particles and pyrolyzed WDF particles could lead to the formation of unexpected species. For example, in [47], the authors tested the co-combustion of coal and 5% RDF in a drop tube furnace and observed an unexpectedly strong effect of RDF addition, enhancing the deposition rates by a 1.5 average factor. Furthermore, they observed big molten RDF particles in the deposits. In [6], on the other hand, the authors observed in an entrained flow reactor a decrease of the ash deposition flux with the increase of the SRF share. They suggest that this decrease might be related to the relatively high calcium content of the SRF ashes, which might generate calcium components with high melting temperature. They also suggest that due to the higher char fragmentation degree of SRF particles, average ash particle size and/or density might be smaller and therefore the inertial impact efficiency decreased, resulting in reduced ash deposition rate. Another example is given in [33] where increased fouling deposits, usually composed of sulfates and chlorides, were

http://dx.doi.org/10.5772/63940

observed in a circulating fluidized bed boiler with the increase of the RDF cofiring share. Anyhow, even when increased slagging and fouling propensity was found, authors concluded that co-combustion of coal and WDF in power plant was feasible.

6.3. Corrosion

On top of the extent of the deposits, another important characteristic is their corrosiveness. The ratio between alkalis and chlorine in the fuels has been used to evaluate if the resulting deposit will be corrosive or not. For WDF, this ratio is likely to be <1, predicting that alkalis are likely to occur bounded to chlorine with little availability for alkali silicates formation [24]. Furthermore, the presence of melt in the salt deposit increased significantly the corrosion of the steel material, especially in presence of chlorine [63]. More details about the role of chlorine will be given in the next section, but catalytic effect between the deposit and the metal oxides covering the tube could lead to the enhanced oxidation of SO_2 to SO_3, which could lead to the formation of sodium and potassium pyrosulfates and trisulfates [20]. In temperature exceeding 550°C, these species can react with the tube protective layer of oxides, and molten deposit can exist even at temperature as low as 398°C, $Na_2S_2O_7$ existing in molten state at such low temperature [20].

The oxygen content in the flue gas is of primary importance for the corrosion process—in oxidizing conditions, the damaged oxides layer may be rebuilt, giving adequate anticorrosive protection [20, 64]. Therefore, the occurrence of reduction atmosphere in the area of superheaters (which can take place by low-NO_x combustion in pulverized fuel boilers) strongly increases the risk of corrosion. This can also happened when the melted deposit prevent the oxygen to reach the tube metallic surface [20].

One of the major drawbacks of the utilization of WDF is the higher propensity of their ashes to deposit on the boilers surfaces. Cofiring experiments showed that even if higher slagging and fouling occur, they were of manageable magnitude. Furthermore, combining WDF to coal greatly reduces the ash-related damages, compared with the combustion of WDF alone. Cofiring is therefore doable, but caution is needed.

7. Chlorine behavior in WDF co-combustion

The origin of chlorine in the fuels can be separated as organic and inorganic chlorine. In coal, the chlorine exists mainly as semiorganic Cl that is anion Cl^- sorbed on the coal organic surface in pores, surrounded by pore moisture [65]. In WDF, inorganic chlorine (e.g., NaCl) and organic chlorine (e.g., PVC) coexist. Furthermore, their chlorine content is largely superior to that of coal, reaching up to 1.8 wt% (see **Table 1**). Therefore, during the combustion of WDF, their chlorine content reacts and is emitted in the furnaces as vapor of hydrochloric acid or as chlorides which can condense on the surfaces of the furnaces as salts and cause their corrosion [65]. Finally, HCl can also react with organic molecules and form dioxins and furans. These three potential fates are described in this section and are illustrated in **Figure 8**.

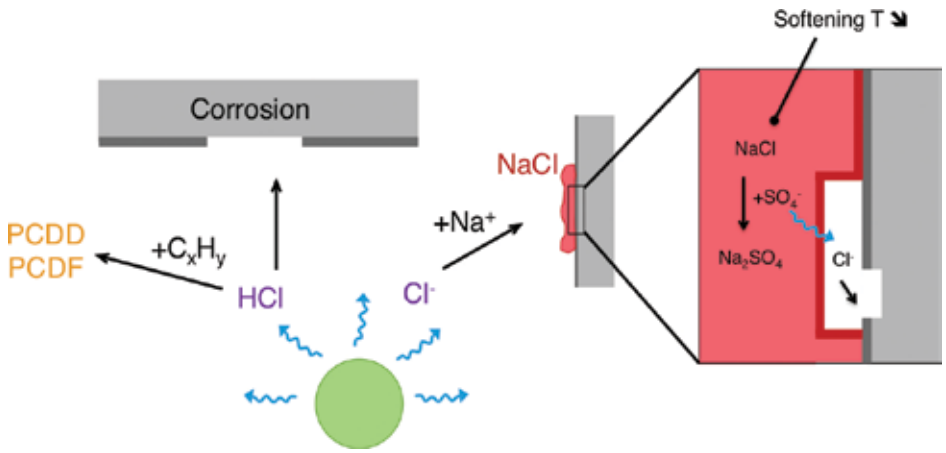

Figure 8. Illustration of the chlorine behavior in a combustion environment.

7.1. High-temperature corrosion

High-temperature corrosion in boilers is defined as the chemical attack of the metallic surfaces. In combustion units, corrosion mainly occurs when the metallic surfaces are in contact with melted salts. During combustion of coal only, the component responsible for the high-temperature corrosion is typically $(Na,K)_3Fe(SO_4)_3$, which may form a eutectic mixture at low melting temperature. Potassium, sodium, and sulfur originate from the coal, whereas the metallic surface provides the iron [59]. However, in the presence of chlorine, other corrosion mechanisms become dominant.

Chlorine in the ash deposits accelerates the corrosion by various mechanisms. First, chlorides decrease the softening temperature of the deposits, which, once melted, can damage the protective oxide layer of the metallic surfaces. Therefore, as soon as the deposits temperature exceeds the ST, the speed of corrosion increases significantly [51]. Second, the partial pressure of gaseous chlorine under the deposits containing chlorides can be significant, even at temperature lower than the ST, making chlorine available to attack the metallic surfaces through a gas phase corrosion mechanism. The presence of gaseous chlorine is mainly attributed to the sulfation of the deposited alkaline chlorides by gaseous SO_2 and to the reaction of the alkali chlorides with the metallic oxides [66]. In fact, in [63], the authors studied that when chlorine was present in the salt, corrosion could take place at temperatures clearly below any melting of the salt deposits, and only a very low amount of chlorine was needed to trigger such corrosion. These results can be explained by the presence of gaseous chlorine produced by the sulfation of the deposits.

On the other hand, other studies support that the sulfation of the alkali chlorides could reduce the deposit based corrosion [58, 67, 68]. Indeed, in [69], it was shown that a pure alkali salt, whether it contained sodium or potassium, with no chlorine did not cause any corrosion of any of the tested steels while all steel's samples showed indications of iron being volatilized

http://dx.doi.org/10.5772/63940

from the steel surface when the alkali salt contained chlorine. Furthermore, the corrosion by alkalis sulfates can be managed by reducing the tube surface temperature and by adequately using sootblowers [70].

It has, therefore, been established that when the S/Cl molar ratio is higher than 4, the fuel can be regarded as noncorrosive, whereas by S/Cl < 2 the corrosion occurs almost inevitably [20].

Based on the idea of a protective layer, one of the recent developments in the field of corrosion protection is the coating of the pipes by a dense ceramic layer of porosity under 1%. This layer avoids the contact between the chlorine species and the metal, thus avoiding its corrosion [71]. The thickness of these layers is generally around 75–90 μm.

7.2. Hydrogen chloride (HCl)

Even if in the high-temperature regions of the boiler chlorine can be found as alkali chloride, at lower temperature, and thus at the exit of the boiler, the majority of the chlorine is found in the flue gas as HCl [46, 72]. In [44], for example, it was observed that during the co-combustion of straw containing 0.55 wt% of chlorine, 98 wt% of it is found as HCl.

The major problem related with HCl is the active oxidation of the tubes at high temperature [20] (this kind of corrosion is however less aggressive than that of the melted alkali chlorides) and the attack of the joints and equipment downstream from the boiler, where the temperature and concentration allow the formation of liquid chloric acid [68].

However, presence of HCl could allow the oxidation of the mercury and therefore facilitates its capture and control. Indeed, it seems that the percentage of mercury leaving the furnace in its elementary form decreases drastically from 85 to 10% for coal containing more than 150–220 ppm of chlorine in dry basis, facilitating the mercury capture in the particle control devices [72].

Finally, HCl can also react with calcium, sodium oxides, and carbonates [68, 73]:

$$CaO + 2HCl \leftrightarrow CaCl_2 + H_2O \tag{6}$$

$$Na_2CO_3 + 2HCl \leftrightarrow 2NaCl + H_2O + CO_2 \tag{7}$$

and be retained in the ashes. This phenomenon was observed, for example, in [12], where the authors measured low levels of HCl in the flue gas and higher chlorine retention in the ashes during co-combustion of coal and EF compared with coal alone in a fluidized bed. Experiments of co-combustion of RDF and coal in a vortexing fluidized bed described in [13] also concluded in a decrease of HCl in the flue gas in the presence of $CaCO_3$, as did Kim et al. [35] with their circulating fluidized bed co-combustion experiments.

7.3. Dioxins and furans formation

Another preoccupation regarding the presence of chlorine is the formation and the control of polychlorinated dioxins and furans (PCDD and PCDF). PCDD and PCDF are chemically stable components, formed at temperature around 250–400°C [35]. Present during the combustion of MSW in dedicated incinerators, they however have not been detected during the co-combustion of coal and WDF [74]. This might be explained by one of the major difference between coal power plants and waste incinerators, that is the higher sulfur level. Typical S/Cl ratio in incinerators is around 0.2, which is one order of magnitude less than what is found during coal co-combustion.

The major chlorination agent in the formation of PCDD and PCDF is Cl_2, HCl being relatively ineffective. Cl_2 may be formed via a reaction known as the Deacon reaction, which may occur during the gas cooling process [65]:

$$2HCl + 0.5O_2 \leftrightarrow H_2O + Cl_2 \tag{8}$$

Cl_2, however, is decomposed by homogeneous reaction with SO_2:

$$Cl_2 + SO_2 + H_2O \leftrightarrow 2HCl + SO_3 \tag{9}$$

Consequently, SO_2 prevents the presence of molecular chlorine and suppresses the PCDD and PCDF formation [65, 74]. Therefore, very low concentrations (<0.03 ng-TEQ/N m^3) of PCDD and PCDF have been observed during WDF and coal co-combustion [33, 35, 36, 43].

8. Conclusion

The combustion of fuel derived from municipal solid waste is a promising cheap retrofitting technique for coal power plants, having the added benefit of reducing the volume of waste disposal in landfills. Furthermore, co-combustion of WDF and coal, rather than switching to WDF combustion alone in dedicated power plants, allows power plant operators to be flexible toward variations in the WDF supply.

Experiments show that substituting part of the coal feed by processed high-calorific value waste reduces the NO_x, SO_2, and CO_2 emissions of coal power plants. However, the alkaline content of WDF and its potentially harmful interaction with the coal ashes, as well as adverse effects from the presence of chlorine in the waste are important drawbacks to waste-derived fuel use in large-scale power plants. On the other hand, synergetic effects between the coal and the waste, such as suppression of the PCDD and PCDF formation by SO_2, or oxidation of mercury by HCl facilitating its capture in the particulate control device, are promising outlooks. Furthermore, in a world looking toward green energy production, re-

http://dx.doi.org/10.5772/63940

duction of the amount of coal used to produce energy through co-combustion of cheap partly renewable material that are the waste is of critical interest. Finally, waste-derived fuels can be combined with additives dedicated to the capture of targeted pollutants, improving even further the environmental performance of coal power plants.

Nomenclature

F_s	slagging propensity index (−)
DT	deformation temperature (°C)
HT	hemisphere temperature (°C)
LHV_i	lower heating value of *i* (kJ/kg)
W_i	mass flow of *i* (kg/h)
x_i^e	energetic fraction of *i* (−)
x_i^{wt}	mass fraction of *i* (−)

Subscripts

c	coal
WDF	waste-derived fuel

Author details

Odile Vekemans* and Jamal Chaouki

*Address all correspondence to: odile.vekemans@polymtl.ca

Department of Chemical Engineering, Polytechnic School of Montreal, Montreal, QC, Canada

References

[1] D. Hoornweg, P. Bhada-Tata, What a Waste—A Global Review of Solid Waste Management, Urban Development Series (Ed.), World Bank, 2012.

[2] US EPA, Advancing Sustainable Materials Management: 2013 Fact Sheet, US Environmental Protection Agency (Ed.), 2015.

[3] European Commission, Directive 2008/98/EC on waste (Waste Framework Directive), 2008.

[4] J.H. Schmidt, P. Holm, A. Merrild, P. Christensen, Life cycle assessment of the waste hierarchy – a Danish case study on waste paper, Waste Management, 27 (2007) 1519–1530.

[5] US EIA, International Energy Outlook, U.S. Department of Energy, 2013.

[6] H. Wu, P. Glarborg, F.J. Frandsen, K. Dam-Johansen, P.A. Jensen, B. Sander, Co-combustion of pulverized coal and solid recovered fuel in an entrained flow reactor: general combustion and ash behaviour, Fuel, 90 (2011) 1980–1991.

[7] S.T. Wagland, P. Kilgallon, R. Coveney, A. Garg, R. Smith, P.J. Longhurst, S.J.T. Pollard, N. Simms, Comparison of coal/solid recovered fuel (SRF) with coal/refuse derived fuel (RDF) in a fluidised bed reactor, Waste Management, 31 (2011) 1176–1183.

[8] J. Maier, A. Gerhardt, G. Dunnu, Experiences on co-firing solid recovered fuels in the coal power sector, in: P. Grammelis (Ed.), Solid Biofuels for Energy, Springer, London, 2011, pp. 75–94.

[9] S.K. Kim, K.W. Jang, J.H. Hong, Y.W. Jung, H.C. Kim, Estimated CO_2 emissions and analysis of solid recovered fuel (SRF) as an alternative fuel, Asian Journal of Atmospheric Environment, 7 (2013) 48–55.

[10] C.S. Psomopoulos, Residue derived fuels as an alternative fuel for the Hellenic power generation sector and their potential for emissions reduction, AIMS Energy, 2 (2014) 321–341.

[11] A. Gendebien, A. Leavens, K. Blackmore, A. Godley, K. Lewin, K.J. Whiting, R. Davis, J. Griegrich, H. Fehrenbach, U. Gromke, N. del Bufalo, D. Hogg, Refuse Derived Fuel, Current Practice and Perspectives, European Commission – Directorate General Environment, 2003.

[12] D. Boavida, P. Abelha, I. Gulyurtlu, I. Cabrita, Co-combustion of coal and non-recyclable paper and plastic waste in a fluidised bed reactor, Fuel, 82 (2003) 1931–1938.

[13] C.-S. Chyang, Y.-L. Han, L.-W. Wu, H.-P. Wan, H.-T. Lee, Y.-H. Chang, An investigation on pollutant emissions from co-firing of RDF and coal, Waste Management, 30 (2010) 1334–1340.

[14] T. Hilber, J. Maier, G. Scheffknecht, M. Agraniotis, P. Grammelis, E. Kakaras, T. Glorius, U. Becker, W. Derichs, H.-P. Schiffer, M.D. Jong, L. Torri, Advantages and possibilities of solid recovered fuel co-combustion in the European energy sector, Journal of the Air & Waste Management Association, 57 (2007) 1178–1189.

[15] M. Nasrullah, P. Vainikka, J. Hannula, M. Hurme, J. Karki, Mass, energy and material balances of SRF production process. Part 1: SRF produced from commercial and industrial waste, Waste Management, 34 (2014) 1398–1407.

http://dx.doi.org/10.5772/63940

[16] Ishikawajima-Harima Heavy Industries Co., The J-Catrel process for making refuse derived fuel, Waste Treatment Technology in Japan.

[17] L. Sørum, Task IEA, Characterisation of MSW for Combustion Systems, SINTEF Energy Research, 2001.

[18] C.A. Velis, S. Wagland, P. Longhurst, B. Robson, K. Sinfield, S. Wise, S. Pollard, Solid recovered fuel: materials flow analysis and fuel property development during the mechanical processing of biodried waste, Environmental Sciience and Technology, 47 (2013) 2957–2965.

[19] G. Dunnu, J. Maier, A. Gerhardt, Thermal utilization of solid recovered fuels in pulverized coal power plants and industrial furnaces as part of an integrated waste management concept, in: E.K. Yanful (Ed.) Appropriate Technologies for Environmental Protection in the Developing World, Springer Netherlands, 2009, pp. 83–91.

[20] M. Pronobis, The influence of biomass co-combustion on boiler fouling and efficiency, Fuel, 85 (2006) 474–480.

[21] L.P. Belo, R. Spörl, K.V. Shah, L.K. Elliott, R.J. Stanger, J. Maier, T.F. Wall, Sulfur capture by fly ash in air and oxy-fuel pulverised fuel combustion, Energy & Fuels, (2014).

[22] J. Chen, H. Yao, L. Zhang, A study on the calcination and sulphation behaviour of limestone during oxy-fuel combustion, Fuel, 102 (2012) 386–395.

[23] M. Müller, U. Schnell, G. Scheffknecht, Modelling the fate of sulphur during pulverized coal combustion under conventional and oxy-fuel conditions, Energy Procedia, 37 (2013) 1377–1388.

[24] G. Wang, R.B. Silva, J.L.T. Azevedo, S. Martins-Dias, M. Costa, Evaluation of the combustion behaviour and ash characteristics of biomass waste derived fuels, pine and coal in a drop tube furnace, Fuel, 117, Part A (2014) 809–824.

[25] S.V. Vassilev, C.G. Vassileva, V.S. Vassilev, Advantages and disadvantages of composition and properties of biomass in comparison with coal: an overview, Fuel, 158 (2015) 330–350.

[26] M. Sami, K. Annamalai, M. Wooldridge, Co-firing of coal and biomass fuel blends, Progress in Energy and Combustion Science, 27 (2001) 171–214.

[27] Environment Canada, Global Warming Potentials, www.ec.gc.ca/ges-ghg/default.asp?lang=En&n=CAD07259-1, 2015.

[28] P. Vainikka, S. Enestam, J. Silvennoinen, R. Taipale, P. Yrjas, A. Frantsi, J. Hannula, M. Hupa, Bromine as an ash forming element in a fluidised bed boiler combusting solid recovered fuel, Fuel, 90 (2011) 1101–1112.

[29] Q. Zhu, Update on lignite firing, IEA Clean Coal Centre, 2012.

[30] P. Glarborg, A.D. Jensen, J.E. Johnsson, Fuel nitrogen conversion in solid fuel fired systems, Progress in Energy and Combustion Science, 29 (2003) 89–113.

[31] S.C. Hill, L. Douglas Smoot, Modeling of nitrogen oxides formation and destruction in combustion systems, Progress in Energy and Combustion Science, 26 (2000) 417–458.

[32] D. Förtsch, F. Kluger, U. Schnell, H. Spliethoff, K.R.G. Hein, A kinetic model for the prediction of no emissions from staged combustion of pulverized coal, Symposium (International) on Combustion, 27 (1998) 3037–3044.

[33] H.-P. Wan, Y.-H. Chang, W.-C. Chien, H.-T. Lee, C.C. Huang, Emissions during co-firing of RDF-5 with bituminous coal, paper sludge and waste tires in a commercial circulating fluidized bed co-generation boiler, Fuel, 87 (2008) 761–767.

[34] Y.-q. Jin, L. Lu, X. Ma, H. Liu, Y. Chi, K. Yoshikawa, Effects of blending hydrothermally treated municipal solid waste with coal on co-combustion characteristics in a lab-scale fluidized bed reactor, Applied Energy, 102 (2013) 563–570.

[35] D.-W. Kim, J.-M. Lee, J.-S. Kim, Co-combustion of refuse derived fuel with anthracites in a CFB boiler, in: Proceedings of the 20th International Conference on Fluidized Bed Combustion, Springer, 2010, pp. 262–270.

[36] O. Ohlsson, Results of combustion and emission testing when co-firing blends of binder-enhanced densified refuse-derived fuel (d-dRDF) pellets and coal in a 440 MWe cyclone fired combustor, Vol. 1, National Technical Information Service, 1994.

[37] O. Vekemans, J.-P. Laviolette, J. Chaouki, Reduction of pulverized coal boiler's emissions through ReEngineered Feedstock™ co-combustion, Energy, 101 (2016) 471–483.

[38] O. Vekemans, J.-P. Laviolette, J. Chaouki, Co-combustion of coal and waste in pulverized coal boiler, Energy, 94 (2016) 742–754.

[39] J.A. Lasek, K. Kazalski, Sulfur self-retention during co-combustion of fossil fuels with biomass, Energy & Fuels, 28 (2014) 2780–2785.

[40] P.A. Calabrese, D. Bai, Engineered fuel feed stock useful for displacement of coal in coal firing plants, U.S. Patent, 8,349,034, United States, 2010.

[41] D. Bai, Systems and methods for producing engineered fuel feed stocks from waste material, U.S. Patent, 8,579,997, MPH Energy LLC, United States, 2013.

[42] C. Zhu, S. Chu, G.A. Tompsett, J. Yang, T. Mountziaris, P.J. Dauenhauer, Reengineered feedstocks for pulverized coal combustion emissions control, Industrial & Engineering Chemistry Research, 53 (2014) 17919–17928.

[43] P. Sauriol, A. Rakib, J. Shabanian, R. Jafari, D. Bai, J. Chaouki, Reduction of criteria air contaminants during co-combustion of coal with ReEngineered Feedstock™ (ReEF) in a bubbling fluidized bed combustor, in: Proceedings of the 22nd Fluidized Bed Conference, Turku, Finland, 2015.

http://dx.doi.org/10.5772/63940

[44] K.H. Andersen, F.J. Frandsen, P.F.B. Hansen, K. Wieck-Hansen, I. Rasmussen, P. Overgaard, K. Dam-Johansen, Deposit formation in a 150 MWe utility PF-Boiler during co-combustion of coal and straw, Energy & Fuels, 14 (2000) 765–780.

[45] T.-h. Yang, F. Lú, X.-p. Kai, Y.-g. He, R.-d. Li, Mechanism of coal and biomass co-combustion: deposition characteristics, Journal of Fuel Chemistry and Technology, 40 (2012) 273–278.

[46] K.V. Shah, M.K. Cieplik, C.I. Betrand, W.L. van de Kamp, H.B. Vuthaluru, Correlating the effects of ash elements and their association in the fuel matrix with the ash release during pulverized fuel combustion, Fuel Processing Technology, 91 (2010) 531–545.

[47] T. Kupka, M. Mancini, M. Irmer, R. Weber, Investigation of ash deposit formation during co-firing of coal with sewage sludge, saw-dust and refuse derived fuel, Fuel, 87 (2008) 2824–2837.

[48] T. Fouilland, J.R. Grace, N. Ellis, Recent advances in fluidized bed technology in biomass processes, Biofuels, 1 (2010) 409–433.

[49] J. Shabanian, P. Sauriol, A. Rakib, J. Chaouki, Characterization of gas–solid fluidization at high temperature by analysis of pressure signals, in: Proceedings of the 11th International Conference on Fluidized Bed Technology (CFB-11), Beijing, China, 2014.

[50] K. Davidsson, L.-E. Åmand, A.-L. Elled, B. Leckner, Effect of cofiring coal and biofuel with sewage sludge on alkali problems in a circulating fluidized bed boiler, Energy & Fuels, 21 (2007) 3180–3188.

[51] B.-J. Skrifvars, R. Backman, M. Hupa, G. Sfiris, T. Abyhammar, A. Lyngfelt, Ash behaviour in a CFB boiler during combustion of coal, peat or wood, Fuel, 77 (1998) 65–70.

[52] M.U. Degereji, D.B. Ingham, L. Ma, M. Pourkashanian, A. Williams, Prediction of ash slagging propensity in a pulverized coal combustion furnace, Fuel, 101 (2012) 171–178.

[53] J. Tomeczek, H. Palugniok, Kinetics of mineral matter transformation during coal combustion, Fuel, 81 (2002) 1251–1258.

[54] K. Annamalai, J. Sweeten, M. Freeman, M. Mathur, W. O'Dowd, G. Walbert, S. Jones, Co-firing of coal and cattle feedlot biomass (FB) fuels, Part III: fouling results from a 500,000 BTU/h pilot plant scale boiler burner, Fuel, 82 (2003) 1195–1200.

[55] J.-L. Fernandez-Turiel, A. Georgakopoulos, D. Gimeno, G. Papastergios, N. Kolovos, Ash deposition in a pulverized coal-fired power plant after high-calcium lignite combustion, Energy & Fuels, 18 (2004) 1512–1518.

[56] A. Magdziarz, M. Wilk, Thermogravimetric study of biomass, sewage sludge and coal combustion, Energy Conversion and Management, 75 (2013) 425–430.

[57] H.B. Vuthaluru, Remediation of ash problems in pulverised coal-fired boilers, Fuel, 78 (1999) 1789–1803.

[58] F. Moradian, A. Pettersson, T. Richards, A thermodynamic equilibrium model applied to predict the fouling tendency in a commercial fluidized-bed boiler, combusting solid waste, Energy & Fuels, 29 (2015) 3483–3494.

[59] P.F.B. Hansen, K.H. Andersen, K. Wieck-Hansen, P. Overgaard, I. Rasmussen, F.J. Frandsen, L.A. Hansen, K. Dam-Johansen, Co-firing straw and coal in a 150-MWe utility boiler: in situ measurements, Fuel Processing Technology, 54 (1998) 207–225.

[60] M. Pronobis, Evaluation of the influence of biomass co-combustion on boiler furnace slagging by means of fusibility correlations, Biomass and Bioenergy, 28 (2005) 375–383.

[61] G. Dunnu, J. Maier, G. Scheffknecht, Ash fusibility and compositional data of solid recovered fuels, Fuel, 89 (2010) 1534–1540.

[62] D. Lindberg, R. Backman, P. Chartrand, M. Hupa, Towards a comprehensive thermodynamic database for ash-forming elements in biomass and waste combustion—current situation and future developments, Fuel Processing Technology, 105 (2013) 129–141.

[63] B.J. Skrifvars, R. Backman, M. Hupa, K. Salmenoja, E. Vakkilainen, Corrosion of superheater steel materials under alkali salt deposits. Part 1: the effect of salt deposit composition and temperature, Corrosion Science, 50 (2008) 1274–1282.

[64] L. Baxter, Biomass-coal co-combustion: opportunity for affordable renewable energy, Fuel, 84 (2005) 1295–1302.

[65] X. Wei, Y. Wang, D. Liu, H. Sheng, W. Tian, Y. Xiao, Release of sulfur and chlorine during cofiring RDF and coal in an internally circulating fluidized bed, Energy & Fuels, 23 (2009) 1390–1397.

[66] M.A. Uusitalo, P.M.J. Vuoristo, T.A. Mäntylä, High temperature corrosion of coatings and boiler steels below chlorine-containing salt deposits, Corrosion Science, 46 (2004) 1311–1331.

[67] D.N. Duong, D.A. Tillman, F.W. NA, N. Clinton, Chlorine issues with biomass cofiring in pulverized coal boilers: sources, reactions, and consequences ? literature review, in: Proceedings of the 34th International Technical Conference on Coal Utilization and Fuel Systems, Clearwater, FL, USA, 2009.

[68] D.A. Tillman, D. Duong, B. Miller, Chlorine in solid fuels fired in pulverized fuel boilers-sources, forms, reactions, and consequences: a literature review, Energy & Fuels, 23 (2009) 3379–3391.

[69] B.J. Skrifvars, M. Westén-Karlsson, M. Hupa, K. Salmenoja, Corrosion of super-heater steel materials under alkali salt deposits. Part 2: SEM analyses of different steel materials, Corrosion Science, 52 (2010) 1011–1019.

http://dx.doi.org/10.5772/63940

[70] A.L. Robinson, H. Junker, S.G. Buckley, G. Sclippa, L.L. Baxter, Interactions between coal and biomass when cofiring, Symposium (International) on Combustion, 27 (1998) 1351–1359.

[71] A.P. Baskakov, The prospects for incineration of municipal solid waste in Russia in order to produce heat and electric power, Thermal Engineering, 61 (2014) 265–273.

[72] J.H. Pavlish, E.A. Sondreal, M.D. Mann, E.S. Olson, K.C. Galbreath, D.L. Laudal, S.A. Benson, Status review of mercury control options for coal-fired power plants, Fuel Processing Technology, 82 (2003) 89–165.

[73] G.-Q. Liu, Y. Itaya, R. Yamazaki, S. Mori, M. Yamaguchi, M. Kondoh, Fundamental study of the behavior of chlorine during the combustion of single RDF, Waste Management, 21 (2001) 427–433.

[74] K. Raghunathan, B.K. Gullett, Role of sulfur in reducing PCDD and PCDF formation, Environmental Science & Technology, 30 (1996) 1827–1834.

Chapter 6

Self-sustaining Smouldering Combustion as a Waste Treatment Process

Luis Yermán

Additional information is available at the end of the chapter

http://dx.doi.org/10.5772/64451

Abstract

This chapter reviews the utilization of self-sustaining smouldering combustion as a treatment for solid or liquid waste, embedded in a porous matrix. Smouldering has been identified as an attractive solution to treat waste with high moisture content. The fundamental aspects of this technology, such as the experimental setup and the ignition mechanism, are described here.

The operational parameters determine the physical properties of the media, and will dictate the self-sustainability of the process. A discussion on how the operational parameters affect the smouldering performance is also presented. The performance of smouldering is usually assessed by the peak temperatures and the velocity of propagation of the smouldering front through the material.

The potential sources for energy recovery are described. Importantly, as oxidation and pyrolysis coexist during smouldering, it was shown with potential for the recovery of pyrolysis products, such as pyrolysis oil. Finally, a brief insight on the gas emissions, and the perspectives regarding the technoeconomic viability in full-scale are also discussed.

Keywords: smouldering combustion, self-sustaining, waste treatment, energy recovery, review

1. Introduction

Smouldering is a complex process that involves heat and mass transfer in porous media, heterogeneous reactions at the solid/gas pore interface, thermochemistry and chemical kinetics [1]. It has been historically studied from a fire safety perspective because it represents a fire

INTECH
open science | open minds

© 2016 The Author(s). Licensee InTech. This chapter is distributed under the terms of the Creative Commons Attribution License (http://creativecommons.org/licenses/by/3.0), which permits unrestricted use, distribution, and reproduction in any medium, provided the original work is properly cited. CC BY

risk as the combustion can propagate slowly through the material and go undetected for long periods of time [2]. Smouldering combustion is among the leading causes of residential fires. It is also the dominant combustion phenomena in wildfires of natural deposits of peat and coal which are the largest and longest burning fires on Earth [3].

Nevertheless, the application of smouldering combustion to waste treatment is quite recent. The first paper published using self-sustaining smouldering combustion as a waste treatment alternative is from Vantelon et al. in 2005 [4]. The utilization of smouldering combustion for these purposes opens a new series of questions that needs to be answered. These questions are related, for example, to the experimental setup, the nature of the waste, the characteristics of porous medium, the possibility of energy recovery or the generation of valuable-added products.

The answer to some of these questions is known, while substantial research is required for others. This chapter reviews the state of art on how smouldering combustion can be applied for the thermal treatment of organic waste. The discussion will be almost exclusively centered on issues related to treatment process and does not aim to cover every aspect of smouldering. If the reader wants to go further in depth on the science and theory behind smouldering, the publications of Thomas J. Ohlemiller, who has been studied smouldering for more than three decades, A. Carlos Fernandez-Pello or José L. Torero are strongly recommended.

The main objective of this chapter is to provide the reader a general overview of the self-sustaining smouldering, identifying the main variables that affect the performance and applicability and understanding why smouldering combustion represents an excellent alternative to treat certain type of waste.

The chapter starts defining the concept of smouldering combustion, the mechanisms that govern its ignition and propagation and the main differences with incineration. In Section 2, the fundamental aspects of this technology, such as experimental setup, reactor configuration and ignition mechanisms are presented. Section 3 discusses the conditions necessary to achieve self-sustaining smouldering; and the operational parameters affecting the performance of the smouldering combustion. In Section 4, a description of the possible sources for energy recovery is presented. The potential fuel production from a smouldering combustion treatment is also introduced, showing some examples. Finally, Section 5 discusses the most important issues related to pollutant emissions produced during smouldering; while Section 6 presents the perspectives regarding the technoeconomic viability of smouldering in a full-scale plant.

1.1. Smouldering combustion

Smoldering combustion is a slow, low-temperature, flameless form of combustion sustained by the heat evolved when oxygen attacks the surface of a condensed phase fuel [5]. It has been studied for decades, generally from a fire safety perspective [6, 7] and for a wide range of fuels such as: polyurethane foam [8–13], biomass [14–18], peat [19–23], cotton [24–26], char [27, 28] and mining dumps [29, 30].

A familiar example of smoldering combustion is the glowing char in a barbeque or a burning cigar. Smoldering requires that a fuel be porous as this promotes a high surface area for heat

http://dx.doi.org/10.5772/64451

and mass transfer, insulates the reaction front to reduce heat losses and allows the flow of oxygen to the reaction zone. Ignition is governed primarily by heat transfer and chemical kinetics. The heat supplied during ignition initiates pyrolysis and other endothermic processes, such as evaporation, before oxidation occur. Propagation will occur when the exothermic oxidation reaction is sufficiently strong to overcome the heat required for pyrolysis and heat losses. If the energy available is not enough, the smoldering will quench and the propagation ceased.

The two limiting factors for smoldering propagation are the oxygen flow and the heat losses [1]. When the reaction is far from its quenching limits, the rate of propagation is directly related to the rate of oxidizer supply to the reaction zone [31]. Close to the quenching limits, heat losses and fuel characteristics can play a significant role. During a waste treatment application, typical heat losses are associated with the presence of water in the fuel, as part of the energy from the exothermic oxidation has to be consumed for water evaporation.

1.2. Smoldering applied as a waste treatment

Incineration is a common practice for the disposal of waste to reduce the waste volumes, especially in those countries where land occupation is undesired. The waste management hierarchy, described by United Nations, indicates an order of preference for action to reduce and manage waste. The six levels of the waste hierarchy pyramid (from most to least preferred) are: prevention, minimization, reuse, recycling, energy recovery and disposal [32]. Incineration attends the least favored option in the pyramid of waste hierarchy. In the best case scenario, energy recovery can be achieved by combustion of waste, which is the second least favorable option.

In addition, while pathogens and toxins present in certain hazardous wastes can be destroyed by the high temperatures achieved during flaming combustion (850–1200°C) it usually requires the use of supplementary fuel to maintain the flame and the high temperatures without quenching.

Before flaming ignition can occur, volatiles needs to be produced [33]. The characteristic time scales of flaming combustion are on the order of milliseconds while gasification takes on the order of seconds. This means that heat losses from the flame (radiation and convection) are significant resulting in a decrease in flame temperature that eventually leads to quenching [34]. Characteristic reaction times in the flame cannot be changed significantly therefore flame quenching can only be avoided by increasing the energy available to gasify the fuel or by eliminating energy sinks. The latter can be achieved by reducing the water content, insulating the reaction vessel or recirculating hot reaction products, while the former requires addition of supplemental fuel.

A more direct method to achieve time-scale compatibility is to increase the characteristic reaction time by using a slower combustion process, such as smoldering. During smoldering the reaction rate is usually controlled by diffusion of oxygen through the fuel [5, 31]. This means the reaction occurs on a time scale that is comparable with the diffusive transfer of heat away from the reaction zone. Enhanced energy recovery can be achieved by directing the flow

through the porous medium in a manner that allows for the oxidizer flow to be preheated and the combustion products to be used to preheat the fuel. In an idealized one-dimensional framework, this process is known as forward smoldering [8, 13].

The energy efficiency of forward smoldering allows for extended quenching limits [31], as compared to incineration. For this reason, smoldering combustion has gained attention in the last years as a thermal waste treatment for feces [35–40], used tires [4] and vegetable oils [41] and as remediation technique, by treating nonaqueous phase liquids (NAPL) contaminants in soil [41–48].

The temperatures and propagation velocities depend strongly on the operation conditions and the nature of the waste and are generally higher than those observed during fires. With some exceptions, typical peak temperatures for waste treatment processes are in the range 400–800°C and smoldering velocities between 0.1 and 4 cm/min. This temperature range is lower than that in incineration processes (usually from 850 to 1200°C, depending on the waste), but enough to eliminate pathogens and destroy certain hazardous components.

Liquid or pasty fuels can also be smoldered when they are embedded in an inert porous matrix, such as sand or soil. By mixing the fuel with an inert granular material, a porous matrix is created with the necessary heat retention and air permeability properties for smoldering combustion to be self-sustained. Sand is commonly used because it is usually inexpensive and has been identified as an effective agent for increasing the porosity of fuels for application to smoldering treatments [42]. For this reason, from now on in this chapter we will refer interchangeably to sand or porous matrix.

High levels of water content within the organic waste result in a very low effective calorific value. Incineration of this kind of waste requires pretreatment or the use of supplemental fuel to avoid quenching [49, 50]. This means that conventional incineration techniques are uneconomical for these treatments. Importantly, smoldering has been proven as an efficient mechanism for the treatment of waste with high moisture content. For example, it was demonstrated that self-sustained smoldering can be used for the treatment of biosolids with moisture content up to 80% [51].

2. Experimental configuration and procedure

The most common configuration utilized for waste treatments is generally one-dimensional, upwards, forward smoldering. Nevertheless, other configurations are possible. Probably, the most notable example of this is the smoldering combustion of contaminated soil in situ. In this process, the reaction takes place in the ground subsurface, avoiding the necessity of reactors (ex situ smoldering) [48]. However, this configuration is not always possible as the waste-soil characteristics must be suitable for smoldering without pretreatment.

Following, we present a general description of the reaction systems, the ignition procedure and the diagnostics that are generally utilized for smoldering treatment. This section will

http://dx.doi.org/10.5772/64451

restrict the discussion to *ex situ* smoldering. The reader can find a detailed description of in situ smoldering in reference [48].

2.1. Smoldering reactors

Figure 1 shows a schematic representation of a typical smoldering reactor and all its components, in upwards forward configuration. Particularly, the reaction system showed in **Figure 1** has been utilized for the smoldering combustion of feces [35–37, 40, 52]. In this case, upwards smoldering is taking place in a metallic and cylindrical column. The column is placed over a base which houses an electrical heater and air diffuser. These components are covered with layers of gravel to ensure uniformity in the airflow along the cross section of the reactor.

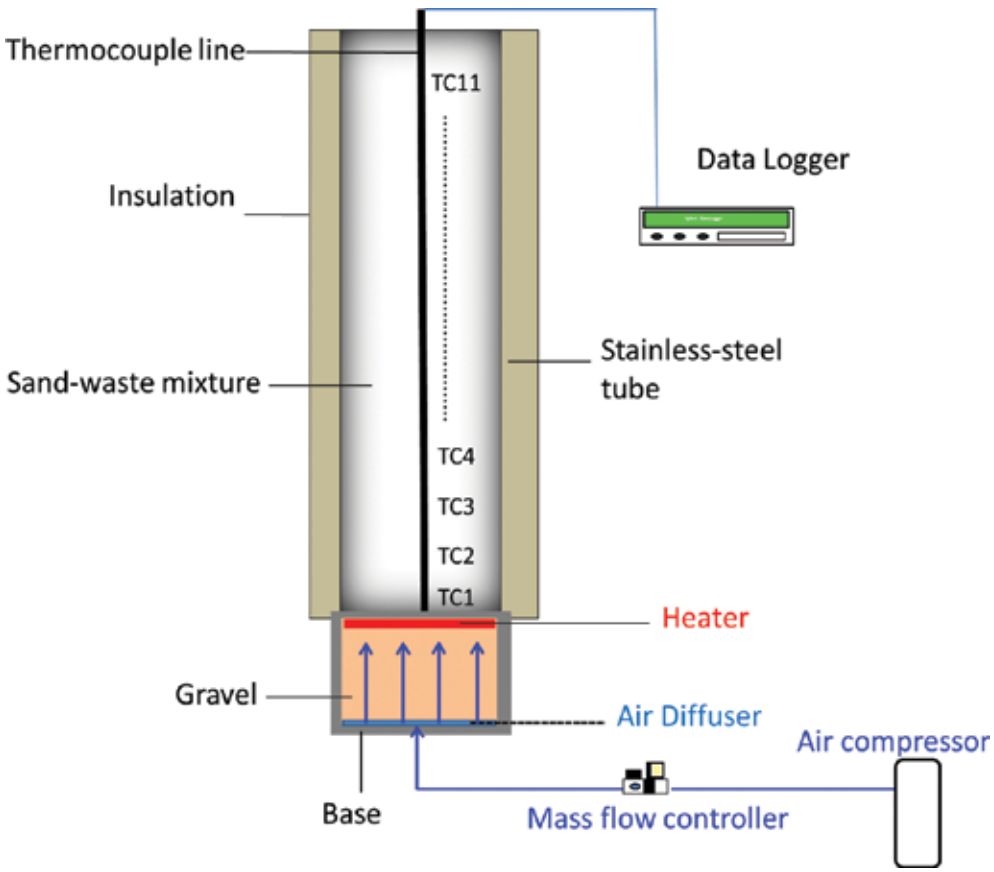

Figure 1. Schematic representation of the reaction system used in the smoldering of waste.

The propagation of the smoldering reaction through the reactor is monitored by thermocouples (TCs) positioned along the central axis of the tube. The TCs are connected to a data logger and a computer to register the temperatures as a function of time and height in the reactor.

Other reactor geometries described in the literature are drums and bins, which have been utilized for contaminated soil remediation [46]. Hasan et al. reported two-dimensional experiments and computational simulations for self-sustaining smoldering of coal tar for the remediation of contaminated sand, conducted in a metallic box-shaped reactor [47].

In general, all the smoldering reactors described in the literature are similar to the one showed in **Figure 1**. Even those with different geometries possess the same elements, albeit some components can differ. For example, an horizontal thermocouple configuration has also been used in some cases [12], and the air diffusor can vary from a wide range of configurations (disk [42], ring-shaped [35] or star-shaped tubes [46]).

Variations from the configuration showed can be also in the air supply or in the heating element. For example, the smoldering of used tires has been investigated on a reaction system that uses convective flame heating, while the airflow through the reactor is produced by a fan placed in the exhaust line [4].

The utilization of convective heating involves higher energy losses and therefore a larger energy input. The efficiency of the convective heater performance can be improved by reducing the heat capacity of the reactor base, improving the heat transfer of the system (e.g., adding insulation to the air injection system) and reducing the airflow rate during ignition [36]. However, despite the higher energy consumption, its implementation can be easier and economically competitive. It can represent an excellent alternative for off-grid applications, or in those places where electricity is expensive.

The pulling-air configuration has been also used, not only to treat used tires but also for the smoldering of feces [38]. As the air permeability of the medium is changing as the waste is being consumed, the utilization pushing-air configuration (mass flow controller) offers much more control on the airflow. However, the pulling-air configuration offers a more economical and easier solution as avoids the utilization of the mass flow controller, tubes and compressed air.

2.2. Procedure of ignition and temperature profiles

Typical plots of temperature histories obtained from a self-sustained smoldering combustion treatment can be seen in **Figure 2**. The example shown corresponds to smoldering of organic waste at 65% (wet basis) of moisture content. Initial heating of the bottom layer of waste-sand mixture is achieved by means of the heating element. Once the thermocouple closest to the heater (TC1 in **Figure 2**, at 2 cm from the heater) reaches a certain temperature (400°C in **Figure 2**) the smoldering reaction is initiated by the injection of air. From now on, we will refer to this temperature as ignition temperature or T_{ig}. It is important that the reader must not misconceive this temperature with the ignition point of the waste.

The heater is turned off once the temperature at TC1 peaks. In this way, ignition of the organic material is ensured. This procedure and configuration yields a robust, repeatable ignition across a wide range of conditions. Ignition protocols can vary depending on the fuel [53].

http://dx.doi.org/10.5772/64451

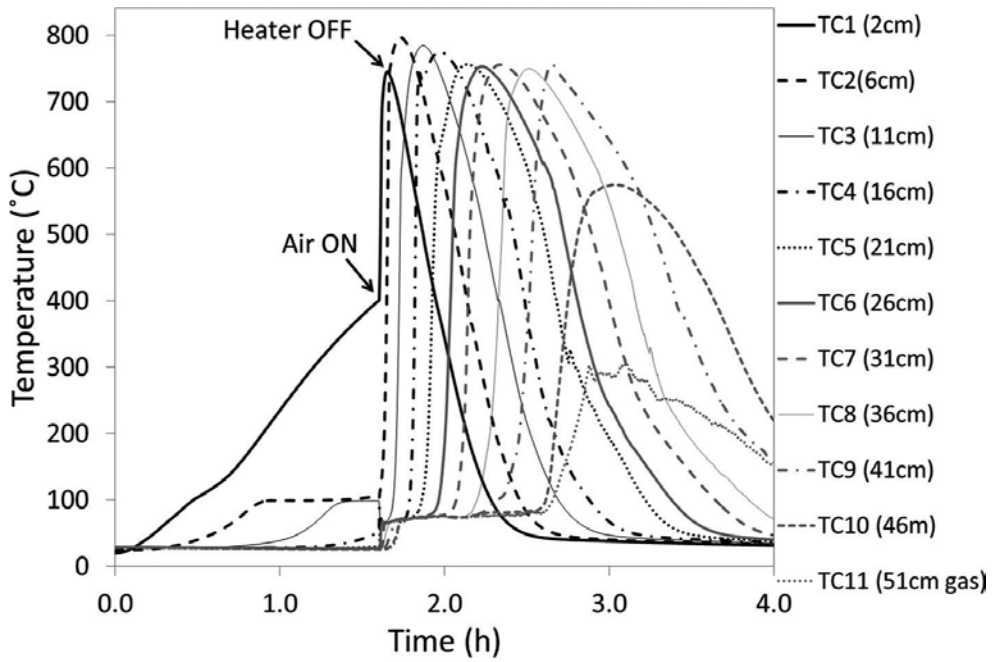

Figure 2. Typical temperature histories of a self-sustaining smoldering test.

In this example the preheating period lasts approximately 90 minutes and is characterized by a gradual increase in temperature up to the desired ignition temperature, and a plateau at 100°C which corresponds to water evaporation. Here, the dominant heat transfer mechanism is conduction due to the electric heater used. Convection and radiation mechanisms are also present at some degree. In this preheating period, as the distance from the heater increases, the duration of this plateau increases. The reason is that more energy is required to evaporate the additional water condensed in the cooler portion ahead. Hence, this plateau is more evident in the temperature profile of TC2 in **Figure 2**.

When the airflow is initiated, the location closest to the heater experiences a sharp increase in temperature up to a peak (close to 750°C in **Figure 2**) as rapid exothermic oxidation of the dried and pyrolyzed fuel occurs. At this moment, convection becomes the dominant mechanism as the hot gases move upwards. The adjacent TCs experience a temperature increase due to the convective heat transfer from the reaction zone to the virgin material ahead.

In the combustion zone, as the reaction front approaches, only a minor plateau is observed at 100°C indicating that the heat flux from the combustion zone is enough to rapidly dry the mixture ahead. In **Figure 2**, this is more evident for TC9, at 41 cm from the heater. The material is thus predried ahead of the smoldering front's arrival. As the fuel is consumed and the reaction at that location stops, the temperature falls as it is cooled by incoming air. The

succession of temperature peaks is observed throughout the mixture is indicative of a self-sustaining smoldering reaction.

Due to the high moisture content of the material, the example showed in **Figure 2** is among the most complex smoldering treatments. In the case of treating dry waste, the plateaus aforementioned are not seen as evaporation and recondensation of water do not occur.

3. Parameters affecting the smoldering performance

Several papers in the literature have systematically studied the influence of the key parameters affecting the smoldering performance, which is generally assessed in terms of self-sustainability, average smoldering velocity and average peak temperature. For example, He et al. studied the influence of the fuel characteristics on the smoldering of biomass powder [16]; Pironi et al. studied the influence of the airflow, fuel saturation and sand characteristics on the smoldering of NAPLs and coal tar; Switzer et al. addressed the scaling effects on the same reaction [46]. Regarding wastes with high moisture content, Yermán et al. investigated the influence of all these parameters on the smoldering combustion of feces [35, 40, 52, 54], while Rashwan et al. [51] mapped the parameter space for smoldering of biosolids and studied the influence of waste nature and airflow. For every operational parameter, there is a range where self-sustaining smoldering is possible. The velocity of smoldering is an important factor in waste treatment processes as it is related to the waste consumption rate and hence will determine the necessary reactor scale. The smoldering temperature is related to the possibility of energy recovery, heat losses and insulation required and gas emissions.

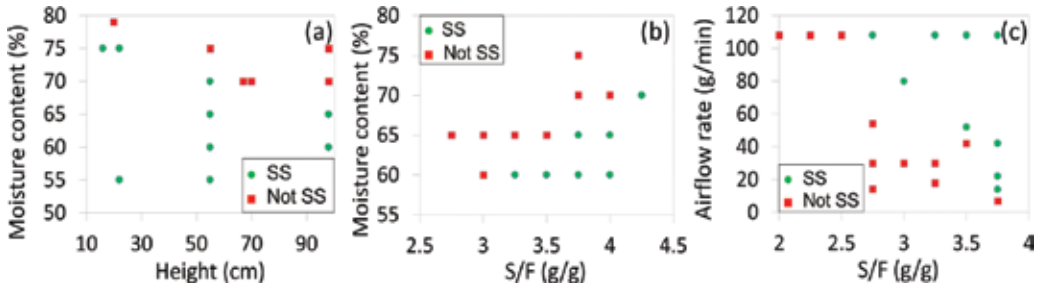

Figure 3. Parameter space outlining the range of conditions yielding self-sustaining (SS) and not self-sustaining (not SS) smoldering: (a) moisture content versus height of sand-fuel mixture, (b) moisture content versus sand-to-fuel mass ratio (S/F), (c) airflow rate versus sand-to-fuel mass ratio (from [35]).

The ranges of self-sustainability for each parameter are not independent; rather they are interdependent in a complex manner. In practice, it is necessary to identify the parameter space in which a robust self-sustaining process will operate. As an example, **Figure 3** shows the interdependency of some of these parameters for the smoldering of surrogate feces mixed with sand [35]. A parameter space has been mapped for conditions yielding to self-sustaining

http://dx.doi.org/10.5772/64451

smoldering by varying moisture content, sand-to-fuel pack height, airflow rate and sand-to-fuel ratio.

For example, these results showed that if the moisture content of the waste is increased, then the pack height of mixture in the reactor must be shortened and the sand concentration increased. A similar situation occurs with the relationship between airflow rate and sand concentration, where higher sand concentrations allow lower airflow rates. Following, the influence of these and other key parameters on the smoldering performance will be treated in more detail.

3.1. Moisture content

The moisture content of the feces is an important energy sink that affects the ignition [20], and the conditions under which sustained smoldering will occur without quenching [55]. Water evaporation during smoldering represents an important energy sink. Close to quenching limits, moisture content is a crucial parameter for the self-sustainability of the smoldering propagation.

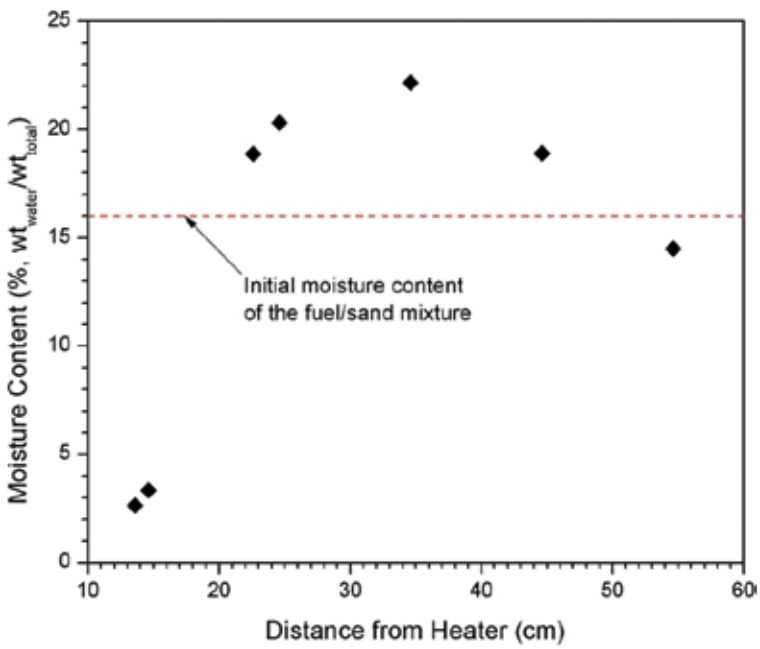

Figure 4. Moisture distribution of the sand-fuel mixture above the reaction zone for a non-self-sustaining test of feces mixed with sand at 75% moisture content (from [35]).

Additionally, studies showed that water recondensation in the layers of cooler mixture above the smoldering front can be significant [35]. This situation provokes an increment in the local moisture content levels. Moreover, free water flowing down inside the column can occur and can lead the reaction to quenching. **Figure 4** shows the moisture content at different heights

in the reactor after excavation of the mixture in a non-self-sustaining smoldering test. Water accumulation can be clearly seen above 20 cm, and is responsible for the experiment's quenching.

Reference [35] demonstrates that the limit of moisture content for a self-sustaining smoldering process depends on the pack height of mixture inside the reactor. The mixture pack height affects the time-varying distribution of moisture content. This happens in two ways: (i) from a thermal perspective, a longer pack of cool material favors increased degree of recondensation ahead of the reaction front; (ii) from a hydraulic perspective, recondensed water is unbound and a longer pack can generate a higher hydrostatic pressure at the moisture front leading to more significant drainage downwards into the front. Therefore, quenching can be avoided by using a shorter pack of sand-waste. Furthermore, other possibilities are predrying the waste or mixing it with other waste streams to increase the average calorific value. However, both alternatives require energy for implementation.

Far from quenching limits, the effect of moisture content in the performance of the smoldering experiments was studied for different types of waste [16, 40, 44]. Experimental observations showed that the velocity of smoldering propagation is not affected by the moisture content of the medium. This independence is somehow expected since the propagation of the smoldering reactions occurs on completely dried [20]. Regarding the smoldering peak temperatures, as water acts as an energy sink, a reduction in the peak temperatures can be expected when moisture content increases, as reported in [44] (up to 200°C within the range of self-sustainability). Still, variations of 10–20% in the waste moisture do not produce significant differences in the observed peak temperature [16, 40].

3.2. Porous medium

Inert porous media that have been used for waste treatment applications are: sand, soil, a mixture of both, gravel and refractory briquettes. By far, the most common inert porous medium used in waste treatment processes is sand because is inexpensive and commonly available. Agricultural waste has also been used for the smoldering of feces, however its use is only reported and there is no systematic study on the influence on smoldering performance [36]. While the nature of the porous medium may have also an influence on the smoldering performance, this is not addressed in the literature.

The effect of the porous medium on the smoldering performance can be explained because it affects the air permeability of the waste-porous medium mixture. This influence can be described through the porous medium concentration and the particle size. Both parameters have been investigated.

3.2.1. Concentration

The concentration of porous medium in the smoldering mixture determines the air permeability of the mixture matrix and hence, its self-sustainability. If the concentration is too low, the air permeability of the medium may not be sufficient for the oxygen to reach the fuel in the surface of the porous medium, and smoldering will not propagate. If the concentration is

http://dx.doi.org/10.5772/64451

too high there is a critical condition where there is not enough fuel (waste) to overcome heat losses and sustain the smoldering reaction.

As **Figure 3** shows, the operational window for sand concentration (expressed as sand-to-fuel mass ratio) is reduced if, for example, the airflow is reduced. Within the range of self-sustainability, the smoldering performance is affected by the porous medium concentration. Both smoldering temperatures and propagation velocities decrease when the sand concentration increases.

As the sand concentration increases, there is less fuel per length unit. This decreases the energy release rate and therefore the smoldering velocity. As the porous medium is generally inert and not combustible, part of the energy released from the exothermic oxidation has to be consumed on heating the porous medium and therefore, it acts as energy sink. This provokes that the smoldering temperatures also decrease when the porous medium concentration increases [40, 44].

3.2.2. Particle size

A similar situation occurs with the influence of the particle size. A window of particle size can be identified where self-sustaining smoldering is possible. At low particle sizes, the fine particles do not provide enough air permeability to the mixture. At the other extreme, when the particle size is too high, the hot gases pathway towards the end of the reactor is short, and therefore the energy is not efficiently transferred from the smoldering front to the portion of mixture ahead.

This was confirmed by some experimental observations where the temperature of the exhaust gases was higher when using gravel instead of sand as porous medium. These hotter gases leaving the reactor take away part of the energy which is required for the self-sustaining propagation.

Smoldering performance as a function of the particle size was studied for the combustion of feces [40] and coal tar [44] mixed with sand/gravel. Both the temperature and smoldering velocities decrease when the particle size increases towards the critical value. However, this parameter appears to be the one with the least impact on the peak temperatures and smoldering velocities, at least among those that were systematically studied. Those papers described a slight variation of smoldering temperatures and velocities (not more than 36%) within the range of self-sustainability. Pironi et al. [44] suggested that it might be balance between the expected increment in the smoldering velocity due to the increment in the fuel surface area per unit volume, and the decreased fuel concentration.

3.3. Airflow rate

Smoldering requires oxygen to sustain the exothermic oxidation reactions. Thus, there is a minimum oxygen concentration in the smoldering front required for propagation. This minimum concentration is mainly a function of the air permeability of the propagation medium. Above that threshold, the oxygen concentration will always be enough for

self-sustaining propagation. While there are some studies on the influence of the oxygen concentration on smoldering [56], all waste treatment processes utilize atmospheric air. On the other extreme, at very high airflows there is a critical condition that can enable transition to flaming. This transition depends on the scale, moisture content and characteristics of the fuel.

There is enough evidence that the rate of propagation is directly related to the rate of oxidizer supply to the reaction zone [31]. Switzer et al. studied the smoldering remediation of NAPL-contaminated materials [46] and found that the remediation time can be controlled by the air injection rate, with higher rates leading to higher propagation velocities. The correlation seems to be linear in experiments performed with different reactor geometries.

In another work, Yermán et al. found a clear linear relationship between the airflow and the smoldering velocity during the smoldering of feces mixed with sand. Authors reported a linear regression of 0.996 within an airflow range where the airflow is increased more than 13 times (see **Figure 5**). Airflow is the parameter with higher impact on the smoldering performance. As the example shows, just modulating the airflow, the smoldering propagation velocities can be changed by more than one order of magnitude.

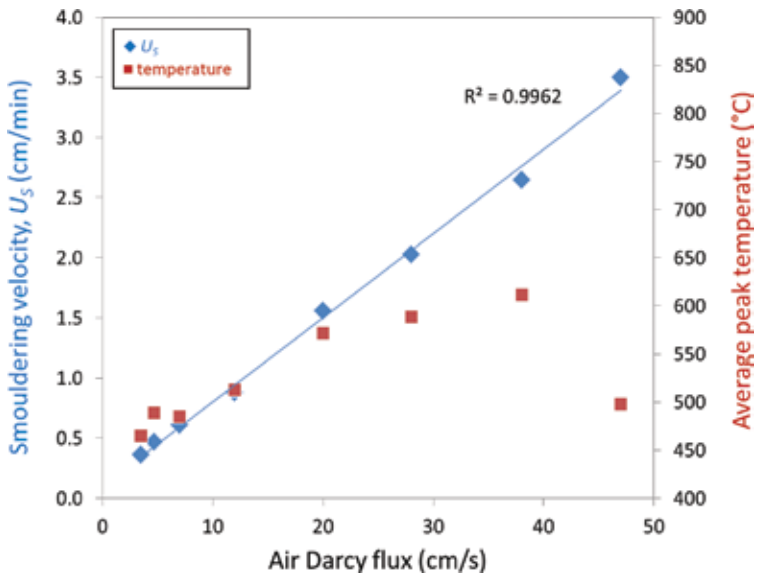

Figure 5. Average peak temperature and smoldering velocity (U_s) as a function of air Darcy flux for self-sustaining smoldering experiments of feces mixed with sand (from [40]).

Regarding the peak temperatures, these tend to increase at low airflows and decrease at high airflows, as **Figure 5** shows. This is mainly associated with the fine energy balance between heat transfer and the heat release rate from the exothermic oxidation. Increasing the airflow implies higher heat release rate, which raises the temperature inside the reactor. On the other hand, at high airflows, it was observed that the temperature of the gases leaving the reactor

http://dx.doi.org/10.5772/64451

increases with the airflow. This means part of the energy is leaving the reactor with the exhaust gases. Due to the high velocity of the gas inside the reactor, the heat from the exothermic reaction is not efficiently transferred to the mixture inside the reactor, and the observed temperatures are lower. A similar behavior was reported for the smoldering of coal tar [42].

3.4. Others

3.4.1. Scale

During smoldering, heat loses are linked to process scale. Heat losses diminish when the scale is increased due to the lower surface-to-volume ratio. Consequently, the operational window where self-sustaining smoldering can be possible is extended at larger scales (e.g., higher moisture content).

Smoldering temperatures are also usually higher at larger scale due to the reduced heat losses. However, the propagation velocities are not necessarily affected. This was observed in [52] where the smoldering of surrogate feces was studied under the same operational conditions, reactor geometry, but different scales. While the smoldering velocity does not change with scale for the same operational conditions, the waste consumption in mass per time unit increases with the size of the reactor. This is an important observation for scaling-up the smoldering technology, as the waste consumption rate can be predicted from laboratory-scale tests.

3.4.2. Ignition temperature

It is important to remind the reader that ignition temperature was defined as the temperature where the airflow is initiated. Reports showed that the airflow can be initiated at temperatures that are considerably below the spontaneous ignition of the waste, even at ambient temperature [36, 40].

Those studies also showed that there is no influence of the ignition temperature on the smoldering performance. Therefore, as it is always desired to operate this technology with the least energy consumption as possible, the situation where the energy consumed during ignition is the lowest should be chosen and determined for every case.

A higher ignition temperature is usually associated with a larger energy input from the heating element. However, this is not the case at low (close to ambient) ignition temperatures. When the airflow is initiated at low temperatures, the sand-waste mixture is then cooled by the incoming fresh airflow. Hence, more energy (and time) from the heating element will be required to achieve combustion of the organic waste.

4. Energy recovery

There are several sources for potential energy recovery from a smoldering combustion process. These are: (i) steam condensation, (ii) hot sand, (iii) hot gases and (iv) fuel production.

4.1. Steam condensation

Steam condensation represents an attractive source of energy, especially when the waste to treat has high moisture content. In some cases, the energy recovered from condensation can be as large as the energy required for ignition [36].

Another example of this is one of the prototypes presented for the Reinvent the Toilet Challenge launched by The Bill and Melinda Gates Foundation. This prototype is a sanitation mechanism for disinfection of human waste that relies on the smoldering combustion of feces. In this system, the steam generated from flash drying of the feces, before condensation, is used in a heat exchanger to pasteurize the urine and liquid waste from the toilet, maintaining the temperature between 65 and 75°C for several hours [38].

4.2. Hot sand

After the smoldering treatment, the sand obtained is clean and hot. In general, only a slight change in color is observed [35, 36, 43, 52]. This is usually attributed to the oxidation of the iron compounds in the sand [42].

The hot sand represents an important heat source than can be used, for example, to predry the next batch of waste. In the case of smoldering of feces, it was demonstrated that sand can be reutilized for at least five consecutive treatments [36] without impact on the smoldering performance. The presence of fine ashes within the inert porous matrix will decrease the air permeability of the sand-waste mixture, reaching eventually a critical condition where propagation of smoldering combustion is not possible. The ash accumulation is a function of the inorganic content in the waste, and the sand concentration used for the smoldering treatment.

4.3. Fuel production

The low temperatures of the smoldering reactions generate the potential recovery of pyrolysis products. Pyrolysis oil production from smoldering combustion processes has been assessed for used tires [4] and feces [57].

Figure 6 shows the different zones that can be distinguished during smoldering, inside the reactor and can help to understand how and where the pyrolysis products are produced. The first region (bottom) is defined as the region where the fuel has been consumed by the passing smoldering front (combustion zone). Ahead of the smoldering front heat is transferred via conduction, convection and radiation to the unreacted sand and fuel. In this region, the oxygen concentration is considerably depleted and heat is consumed in the endothermic pyrolysis of the fuel. As the available heat decreases, the temperature eventually reaches a critical point where pyrolysis cannot be sustained (usually 200–300°C).

The end of the pyrolysis zone marks the beginning of the preheating zone where heat is consumed through preheating of the unreacted zone. As the available heat decreases, the temperature eventually reaches ambient temperature, which delineates the end of the preheating zone. After that zone, only virgin sand-fuel mixture is present.

http://dx.doi.org/10.5772/64451

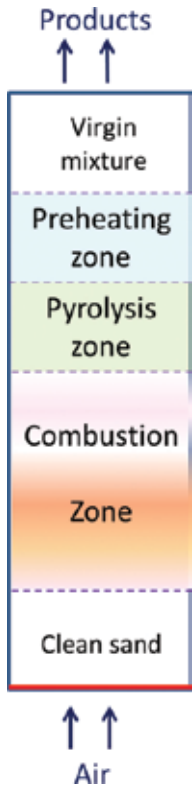

Figure 6. Zones that can be distinguished during smoldering and inside the reactor (modified from [57]).

The yield of pyrolysis products during smoldering can be maximized if pyrolysis temperatures are maintained in the zone of low oxygen concentration. In other words, the larger the pyrolysis zone is, the higher the amount of pyrolysis products obtained.

The extension of the pyrolysis zone can be increased if the fuel is dry and has a high calorific content, providing more energy available for pyrolysis and reaching higher temperatures. Comparing the two aforementioned examples, rubber tires have a calorific content about eight times higher than wet feces. That study observed that the oils exhibited a mass percentage yield of 35% relative to the tires. Maximum oil recovery was observed at the minimum smoldering velocity. On the other hand, maximum oil yield from smoldering of feces was only 7% relative to the mass of dry feces. In this case, pyrolysis oil yield seems to increase with the airflow rate, although the relationship is not completely clear.

5. Gas emissions

The potential for the formation of harmful compounds exists in every smoldering process, especially when the waste represents an environmental hazard (e.g., coal tar). As in an

incineration process, the gas emissions must be assessed and controlled or captured. In the same way, gas emissions can vary significantly depending on the waste nature, oxygen excess and other operating conditions. Nevertheless, some general features associated with the effluent gas composition can be addressed.

It is of great importance to notice that the gas emissions associated with smoldering differ significantly from those produced during flaming combustion. Yet, the same standard gas treatment practices can be applied in both cases. As pyrolysis and oxidation coexist during smoldering, smoldering produces higher amount of hydrocarbons and CO than incineration. For example, Rein et al. found that the CO/CO_2 ratio is approximately 0.4 during smoldering, while it is approximately 0.1 in flaming combustion [22, 58]. In addition, Switzer et al. report CO/CO_2 ratios of 0.1–0.7 when using smoldering for remediation of NAPL-contaminated soil [46].

Pyrolysis products, which are usually oxidized in the presense of flaming combustion, contribute significantly to the gas emissions during smoldering. These products include hydrocarbons, volatile organic compounds (VOCs) and polyaromatic hydrocarbons.

While quite a few papers on emissions during natural smoldering can be found in the literature, there are not many scientific reports on emissions during smoldering combustion applied to waste treatment. Scholes et al. report total VOCs between 47 and 88 g/L for the smoldering remediation of coal-tar-contaminated soils [48]. While these values can be higher than those during incineration, they are considerably below the VOC emissions during composting of waste [59] or from typical manufacturing industries [60].

Regarding production of NOx and SOx, Switzer et al. studied the smoldering combustion of nonaqueous phase liquids mixed with sand and soil. Nitrogen and sulfur oxides were not detected above the threshold of 1 ppm [43]. It is preassumed that this is due to the lower temperatures during smoldering as compared to incineration, although further and extensive research is needed in this matter.

6. Technoeconomic viability

As for any other technology, the technoeconomic feasibility for applying smoldering as a waste treatment process must be assessed for every particular case, and compared to other possible alternatives. Applicability scenarios can be very different, and many factors should be taken in consideration for a technical analysis, that every particular case must be considered separately. For example, the aim of the treatment (e.g., environmental hazard, volume reduction, dewatering, metal or nutrients recovery) is strongly related to the economic return. In this section, the general considerations and critical issues to take into account when performing technical and economic analyses are presented.

At present, soil remediation is the only full-scale and real application of smoldering as a waste treatment process [48]. Nevertheless, current investigations on the topic demonstrate that the

http://dx.doi.org/10.5772/64451

technology is economically feasible for other applications. In the close future, smoldering is envisaged as an alternative for the treatment of many waste streams.

As a general rule, smoldering is a suitable alternative for reduction of waste volumes, especially for waste streams with high moisture content. Furthermore, it is an attractive option to treat hazardous waste, as the high temperatures ensure pathogen destruction. In both cases, the thermal treatment should be performed on site. In the former case, this would avoid important transportation costs as highly wet waste usually comprises large volumes, and in the latter, it would elude the impracticality of handling hazardous materials.

In general, the technical feasibility can be usually assessed at laboratory scale, as the higher heat losses make this scale a conservative scenario. As the smoldering velocity does not change with the scale, the operating conditions and size of the reactor for a full-scale application can be easily extrapolated from those laboratory tests. The full-scale of this technology depends on the waste production rate and also on the type of waste. While accumulation of waste may be possible in some cases to generate adequate volumes, this is not always feasible. If the aim of the treatment is the elimination of pathogens – as can be the case of feces, animal waste or hospital residues – then the destruction has to be almost immediately, and the scales required are smaller. For example, a toilet that smolders feces should operate in the range of kilos per day, as compared with agricultural waste or contaminated soil that must operate in the range of tons per day.

For the economic analysis, the expenses to consider are: equipment, installation, operation, maintenance and reduction of fees paid for the disposal of waste. Equipment, installation and maintenance are substantially the same for every smoldering application. However, maximum temperatures and corrosiveness of the waste can determine the necessity of different reactor materials and wall thicknesses. The operation costs are mainly associated with waste pretreatment, mixing, ignition and reactor loading/unloading. Waste pretreatment can include: adaptation of the waste particle size (in the case of solid waste) or predrying (for liquid or pastry waste).

The potential sand reutilization and energy recovery must be also considered in the economic analysis, as they would reduce the operative costs. The operating conditions of smoldering should be chosen to maximize the benefit from these. There are other issues to consider that may have impact on the operating conditions. For example, heterogeneity of the waste is inevitable and because of this the smoldering must operate far from quenching conditions. Also, the possibility of mixing the waste with other waste streams should also be considered. This can have two benefits: reduce/avoid sand utilization and increase the calorific value (and/or reduce the moisture content).

Finally, additional profit can be obtained from environmental benefits. Still, environmental issues must also be carefully taken in consideration. For example, smoldering applied to soil remediation can bring massive benefits, as avoids the contamination of water resources. On the other hand, losses of nitrogen and carbon in the soil result in a poor soil for plant growth, and further soil rehabilitation is needed [61].

Acknowledgements

The author wants to thank Prof. José L. Torero for his support, knowledge and contribution to my inspiration.

Nomenclature

NAPL	nonaqueous phase liquids
S/F	sand-to-fuel mass ratio
SS	self-sustaining
TC	thermocouple
T_{ig}	ignition temperature
U_S	smoldering propagation velocity
U_S	smoldering propagation velocity
VOC	volatile organic compounds

Author details

Luis Yermán

Address all correspondence to: l.yermanmartinez@uq.edu.au

School of Civil Engineering, University of Queensland, Brisbane, Australia

References

[1] Ohlemiller TJ. Standards USNBo, Research CfF. Modeling of Smoldering Combustion Propagation: National Bureau of Standards; 1985.

[2] T'ien JS, Shih H-Y, Jiang C-B, Ross HD, Miller FJ, Fernandez-Pello AC, et al. Mechanisms of Flame Spread and Smolder Wave Propagation. In: Ross HD, editor. Microgravity Combustion: Fire in Free Fall. Cleveland, USA: Academic Press; 2001.

[3] Rein G. Smoldering Combustion. In: Hurley MJ, editor. SFPE Handbook of Fire Protection Engineering. 5th ed. Greenbelt, USA, 2016.

[4] Vantelon JP, Lodeho B, Pignoux S, Ellzey JL, Torero JL. Experimental observations on the thermal degradation of a porous bed of tires. Proceedings of the Combustion Institute. 2005;30(2):2239–2246.

[5] Rein G. Smouldering combustion phenomena in science and technology. International Review of Chemical Engineering. 2009;1:3–18.

[6] Krause U, Schmidt M, Lohrer C. A numerical model to simulate smouldering fires in bulk materials and dust deposits. Journal of Loss Prevention in the Process Industries. 2006;19(2–3):218–226.

[7] Evtyugina M, Calvo AI, Nunes T, Alves C, Fernandes AP, Tarelho L, et al. VOC emissions of smouldering combustion from Mediterranean wildfires in central Portugal. Atmospheric Environment 2013;64:339–348.

[8] Torero JL, Fernandez-Pello AC. Forward smolder of polyurethane foam in a forced air flow. Combustion and Flame. 1996;106(1–2):89–109.

[9] Rein G, Bar-Ilan A, Fernandez-Pello AC, Ellzey JL, Torero JL, Urban DL. Modeling of one-dimensional smoldering of polyurethane in microgravity conditions. Proceedings of the Combustion Institute. 2005;30(2):2327–2334.

[10] Rein G, Lautenberger C, Fernandez-Pello AC, Torero JL, Urban DL. Application of genetic algorithms and thermogravimetry to determine the kinetics of polyurethane foam in smoldering combustion. Combustion and Flame. 2006;146(1–2):95–108.

[11] Torero JL, Fernandez-Pello AC. Natural convection smolder of polyurethane foam, upward propagation. Fire Safety Journal. 1995;24(1):35–52.

[12] Torero JL, Fernandez-Pello AC, Kitano M. Opposed forced flow smoldering of polyurethane foam. Combustion Science and Technology. 1993;91(1–3):95–117.

[13] Bar-Ilan A, Rein G, Fernandez-Pello AC, Torero JL, Urban DL. Forced forward smoldering experiments in microgravity. Experimental Thermal and Fluid Science. 2004;28(7):743–751.

[14] Carvalho ER, Gurgel Veras CA, CarvalhoJr JA. Experimental investigation of smouldering in biomass. Biomass and Bioenergy. 2002;22(4):283–294.

[15] Rabelo ERC, Veras CAG, Carvalho Jr JA, Alvarado EC, Sandberg DV, Santos JC. Log smoldering after an amazonian deforestation fire. Atmospheric Environment. 2004;38(2):203–211.

[16] He F, Yi W, Li Y, Zha J, Luo B. Effects of fuel properties on the natural downward smoldering of piled biomass powder: Experimental investigation. Biomass and Bioenergy. 2014;67(0):288–296.

[17] Tissari J, Lyyränen J, Hytönen K, Sippula O, Tapper U, Frey A, et al. Fine particle and gaseous emissions from normal and smouldering wood combustion in a conventional masonry heater. Atmospheric Environment. 2008;42(34):7862–7873.

[18] McKenzie LM, Hao WM, Richards GN, Ward DE. Quantification of major components emitted from smoldering combustion of wood. Atmospheric Environment. 1994;28(20): 3285–3292.

[19] Hadden RM, Rein G, Belcher CM. Study of the competing chemical reactions in the initiation and spread of smouldering combustion in peat. Proceedings of the Combustion Institute. 2013;34(2):2547–2553.

[20] Rein G, Cleaver N, Ashton C, Pironi P, Torero JL. The severity of smouldering peat fires and damage to the forest soil. CATENA. 2008;74(3):304–309.

[21] Huang X, Rein G. Smouldering combustion of peat in wildfires: Inverse modelling of the drying and the thermal and oxidative decomposition kinetics. Combustion and Flame. 2014;161(6):1633–1644.

[22] Rein G, Cohen S, Simeoni A. Carbon emissions from smouldering peat in shallow and strong fronts. Proceedings of the Combustion Institute. 2009;32(2):2489–2496.

[23] Chen H, Rein G, Liu N. Numerical investigation of downward smoldering combustion in an organic soil column. International Journal of Heat and Mass Transfer 2015;84:253–261.

[24] Hagen BC, Frette V, Kleppe G, Arntzen BJ. Onset of smoldering in cotton: Effects of density. Fire Safety Journal. 2011;46(3):73–80.

[25] Hagen BC, Frette V, Kleppe G, Arntzen BJ. Transition from smoldering to flaming fire in short cotton samples with asymmetrical boundary conditions. Fire Safety Journal 2015;71:69–78.

[26] Hagen BC, Frette V, Kleppe G, Arntzen BJ. Effects of heat flux scenarios on smoldering in cotton. Fire Safety Journal 2013;61:144–159.

[27] He F, Behrendt F. Experimental investigation of natural smoldering of char granules in a packed bed. Fire Safety Journal. 2011;46(7):406–413.

[28] He F, Zobel N, Zha W, Behrendt F. Effects of physical properties on one-dimensional downward smoldering of char: Numerical analysis. Biomass and Bioenergy. 2009;33(8):1019–1029.

[29] Chapter 8 - Geothermal Utilization of Smoldering Mining Dumps. In: Sokol GBSPV, editor. Coal and Peat Fires: A Global Perspective. Boston: Elsevier; 2015. p. 241–261.

[30] Melody SM, Johnston FH. Coal mine fires and human health: What do we know? International Journal of Coal Geology. 2015;152, Part B:1–14.

[31] Ohlemiller TJ. Smouldering Combustion. In: DiNenno PJ, Drysdale D, Beyler CL, Walton WD, editors. SFPE Handbook of Fire Protection Engineering: National Fire Protection Association; 2008. p. 2/200-210.

[32] Programme UNE. Guidelines for National Waste Management Strategies Moving from Challenges to Opportunities. 2013.

[33] Torero JL. Flaming ignition of solids fuels. 2008.

[34] Williams FA. A review of flame extinction. Fire Safety Journal. 1981;3(3):163–175.

[35] Yermán L, Hadden RM, Pironi P, Torero JL, Gerhard JI, Carrascal J, et al. Smouldering combustion as a treatment technology for faeces: exploring the parameter space. Fuel 2015;147:108–116.

[36] Yermán L, Carrascal J, Torero JL, Fabris I, Cormier D, Gerhard JI. Smouldering combustion as a treatment for human waste. 5th International Symposium on Energy from Biomass and Waste; Venice, Italy, 2014.

[37] Wall H, Yermán L, Gerhard J, Fabris I, Cormier D, Cheng Y-L, et al. Investigation of self-sustaining smouldering of faeces: Key parameters and scaling effects. Dynamic ecolibrium: Sustainable Engineering Society Conference (SENG 2015). 2015:113.

[38] Cheng Y-L, Kortschot MT, Gerhard JI, Torero JL, Saini R, Fernandes AX, et al. A Household Sanitation Process Based on Integrated Diversion/Dewatering, Drying/ Smoldering of Solid Waste, and Pasteurization of Liquid Waste. Third International Fecal Sludge Management Conference:Hanoi, Vietnam 2015.

[39] Fishman Z, Jung YMT, Pironi P, Krajcovic M, Melamed S, Webb M, et al. A unit operations approach for rapid disinfection of human waste based ondrying/smoldering of solid and sand filtration/UV disinfection of liquid waste. International Faecal Sludge Management Conference; Durban, South Africa, 2012.

[40] Yermán L, Wall H, Torero JL, Gerhard JI, Cheng Y-L. Smoldering combustion as a treatment technology for faeces: sensitivity to key parameters. Combustion Science and Technology. 2016, in press.

[41] Salman M, Gerhard JI, Major DW, Pironi P, Hadden R. Remediation of trichloroethylene-contaminated soils by star technology using vegetable oil smoldering. Journal of Hazardous Materials 2015;285:346–355.

[42] Pironi P, Switzer C, Rein G, Fuentes A, Gerhard JI, Torero JL. Small-scale forward smouldering experiments for remediation of coal tar in inert media. Proceedings of the Combustion Institute. 2009;32(2):1957–1964.

[43] Switzer C, Pironi P, Gerhard JI, Rein G, Torero JL. Self-sustaining smoldering combustion: a novel remediation process for non-aqueous-phase liquids in porous media. Environmental Science and Technology 2009;43:5871–5877.

[44] Pironi P, Switzer C, Gerhard JI, Rein G, Torero JL. Self-sustaining smoldering combustion for NAPL remediation: Laboratory evaluation of process sensitivity to key parameters. Environnmetal Science and Technology. 2011;45:2980–2986.

[45] MacPhee SL, Gerhard JI, Rein G. A novel method for simulating smoldering propagation and its application to STAR (self-sustaining treatment for active remediation). Environmental Modelling & Software. 2012;31(0):84–98.

[46] Switzer C, Pironi P, Gerhard JI, Rein G, Torero JL. Volumetric scale-up of smouldering remediation of contaminated materials. Journal of Hazardous Materials. 2014;268(0): 51–60.

[47] Hasan T, Gerhard JI, Hadden R, Rein G. Self-sustaining smouldering combustion of coal tar for the remediation of contaminated sand: two-dimensional experiments and computational simulations. Fuel. 2015;150(0):288–297.

[48] Scholes GC, Gerhard JI, Grant GP, Major DW, Vidumsky JE, Switzer C, et al. Smoldering remediation of coal-tar-contaminated soil: Pilot Field tests of STAR. Environmental Science & Technology. 2015.

[49] McKay G. Dioxin characterisation, formation and minimisation during municipal solid waste (MSW) incineration: review. Chemical Engineering Journal. 2002;86(3):343–368.

[50] Chang YM, Kang JS, Ho CC. Circulating fluidized bed incineration of industrial solid wastes. Waste Management & Research. 1992;10(4):357–369.

[51] Rashwan TL, Gerhard JI, Grant GP. Application of self-sustaining smouldering combustion for the destruction of wastewater biosolids. Waste Management. 2016.

[52] Yermán L, Wall H, Torero JL, Gerhard JI, Fabris I, Cormier D, et al. Self-sustaining smouldering combustion of faeces as treatment and disinfection method. APCChE 2015 Congress incorporating Chemeca 2015; Melbourne, Australia, 2015

[53] Drysdale D. Spontaneous Ignition within Solids and Smouldering Combustion. An Introduction to Fire Dynamics: John Wiley & Sons, Ltd; 2011. p. 317–348.

[54] Yermán L, Wall H, Torero JL. Experimental Investigation on the Destruction Rates of Organic Waste with High Moisture Content by Means of Self-sustained Smouldering Combustion. Thirty-sixth International Symposium on Combustion, Seoul, Korea, 2016.

[55] Frandsen WH. Ignition probability of organic soils. Canadian Journal of Forest Research. 1997;27(9):1471–1477.

[56] Walther DC, Anthenien RA, Fernandez-Pello AC. Smolder ignition of polyurethane foam: effect of oxygen concentration. Fire Safety Journal. 2000;34(4):343–359.

[57] Yermán L, Cormier D, Fabris I, Carrascal J, Torero JL, Gerhard JI, et al. Potential bio-oil production from smouldering combustion of faeces. Waste Biomass Valor. 2016; DOI 10.1007/s12649-016-9586-1

[58] Chapter 1 - Smoldering-Peat Megafires: The Largest Fires on Earth. In: Rein GBSP, editor. Coal and Peat Fires: a Global Perspective. Boston: Elsevier; 2015. p. 1–11.

[59] Pagans E, Font X, Sánchez A. Emission of volatile organic compounds from composting of different solid wastes: Abatement by biofiltration. Journal of Hazardous Materials. 2006;131(1–3):179–186.

[60] Wang H, Nie L, Li J, Wang Y, Wang G, Wang J, et al. Characterization and assessment of volatile organic compounds (VOCs) emissions from typical industries. Chinese Science Bulletin. 2013;58(7):724–730.

[61] Pape A, Switzer C, McCosh N, Knapp CW. Impacts of thermal and smouldering remediation on plant growth and soil ecology. Geoderma. 2015;243–244(0):1–9.

Section 3

Combustion and Biofuels in Reciprocating Engines

Chapter 7

Combustion and Emission Characteristics of Blends: -n-Butanol-Diesel (D2); and Dual Alcohols: n-Butanol-Methanol with Gasoline in Internal Combustion Engines

Lennox Siwale , Lukacs Kristof , Torok Adam ,
Akos Bereczky , Makame Mbarawa ,
Antal Penninger and Andrei Kolesnikov

Additional information is available at the end of the chapter

http://dx.doi.org/10.5772/64747

Abstract

A study of the effects of oxygenated alcohol/gasoline/diesel fuel blends on performance, combustion, and emission characteristics in conventional reciprocating engines is reported. On the one hand, in alcohol-gasoline blends, dual alcohols-gasoline blends have not yet been sufficiently proven as suitable alternatives to single alcohol-gasoline blends in engines as far as performance is concerned. On the other hand, n-butanol-diesel, although it has a better miscibility factor in diesel than methanol or ethanol, is limited with regard to extensive application in the diesel engines due to its low cetane number. Engine performance was compared using single alcohol-gasoline and dual alcohol-gasoline blends, where the dual blends were constrained to meet the vapor issues regarding fuels and regulations. The blends were selected in terms of a combination by volume of one being higher alcohol (n-butanol) and the other, lower alcohol (methanol). The engines used for this study included a single-cylinder and a four-cylinder, naturally aspirated, four-stroke spark ignition engines and a four-cylinder, four-stroke compression ignition turbocharged diesel engine. In the n-butanol-diesel studies, a comparison was made with other studies in order to determine how suitable n-butanol-diesel blends were across the biofuel family such as the biodiesel-ethanol-diesel blends. The findings were as follows: The dual alcohols-gasoline blends performed better than the single alcohol-gasoline blends depending on certain compositional ratios of the alcohols in gasoline regardless of vapor pressure consideration. The n-butanol/diesel alcohol blend (B5, B10, and B20, where B5 represents 5% n-butanol and 95% diesel) significantly reduced the regulated emissions in a turbocharged engine compared to other studies using biodiesel-diesel blends. The significant decrease in NO_x, CO emissions, and reduction of unburned hydrocarbons content using n-butanol/diesel fuel (DF) blends were found experimentally. The use of dual alcohol /

INTECH
open science | open minds

© 2016 The Author(s). Licensee InTech. This chapter is distributed under the terms of the Creative Commons Attribution License (http://creativecommons.org/licenses/by/3.0), which permits unrestricted use, distribution, and reproduction in any medium, provided the original work is properly cited. CC BY

gasoline blends was beneficial due to their shorter combustion duration in crank angles and their higher-energy content compared with single alcohol-gasoline blends. The n-butanol/diesel blend fired in the diesel engine showed a higher brake thermal efficiency and improved brake specific fuel consumption compared to the study by others where ethanol\diesel and methanol\diesel blends were used.

Keywords: compression ignition engine-diesel, emission reduction, butanol (-n) brake-specific fuel consumption (BSFC), brake thermal efficiency, combustion and emission, bioalcohols, spark ignition engine, global climate change

1. Introduction

The efforts of researchers worldwide have been and continue to be directed toward finding fuels that are cleaner than fossil fuels in internal-combustion engines. The goal is to replace or reduce the use of petroleum oil because conventional fuels such as gasoline degrade the environment. Use of petroleum oil in transportation greatly contributes to the deterioration of the environment through the emission of regulated emissions such as nitrogen oxides (NO_x), unburned hydrocarbon (UHC), carbon monoxide (CO), particulate matter (PM), and carbon dioxide (CO_2) [1].

A very strong debate on the gradual substitution of petroleum by using renewable alternatives such as biofuels dominates the political and economic agenda worldwide [2].

In their two articles, Andersen et al. [3, 4] reported on the vapor pressures (VP) of single bioalcohol-gasoline blends. They evaluated the VP for lower alcohols, methanol, and ethanol and higher alcohols including, n-butanol and propanol. Vapor pressure is an indirect way to measure the volatility of liquid fuels, which emit fuel vapors known as evaporative emissions. Evaporative emissions will cause vapor lock on restricted spaces in the fuel lines and the pump in spark ignition (SI) engines and carburetor fuel delivery systems. Port injection is also prone to this problem [3, 4].

	Molar mass Kg/kmol	RVP (kPa)	Density at 20°C (g/mL)	Normal boiling point (°C)
Gasoline	98.5	60-62	0.741	NA
n-butanol	74.12	2.2	0.81	117.8
Methanol	32.04	32	0.791	64.6
Ethanol	46.07	16	0.789	78.3

Source: Ref. [4].

Table 1. Typical physical properties of gasoline and alcohols.

Adherence to stringent regulation of the Reid's vapor pressure (RVP) for gasoline as presented in **Table 1** is required by many countries in order to limit evaporative emissions. Depending

http://dx.doi.org/10.5772/64747

on the properties of the individual alcohols, it is possible to add another alcohol to the single alcohol-gasoline blend in order to reduce the evaporative emissions [4].

When alcohols are blended with gasoline or diesel fuel, the resulting mixture has more or fewer different properties than the conventional fuels on the basis of which the engines were designed to operate. This creates problems such as vapor lock, changes of viscosity, energy-content (low heating value), boiling point of the fuel blends, and different flame propagation hence limiting their application.

To mitigate the negative impacts caused by vapor lock of single alcohol/gasoline (SAG), Andersen et al [3] proposed the use of dual alcohols, one higher and the other lower alcohol blended in gasoline engines, as well as a method of determining the composition of dual alcohols/gasoline (DAG) blends. Based on this concept, the lower volatility of n-butanol (a higher alcohol) can be exploited by mixing n-butanol and another highly evaporative lower carbon alcohol (methanol) in gasoline. The expected net effect is to reduce problems in the fuel delivery system.

However, the researchers Andersen et al. did not formulate any list and conduct experiments using alcohol-gasoline blends, which satisfy the Reid's vapor pressure requirement for gasoline fueled engines. Thus, their performance in reciprocating engines remains unclear.

Although Andersen et al. studied VP issues of alcohol-gasoline blends in spark ignition engines only, alcohol-diesel blends also appear to be as promising as the former. Low carbon-content alcohols (C_1 and C_2) have a greater auto-ignition temperature than (C_{4-5}) ones. Therefore, methanol and ethanol have a much *higher auto-ignition* temperature than n-butanol. For this reason, C_1–C_2 alcohols may not be preferred to C_4–C_5 alcohols for blending with diesel fuel. This renders n-butanol or any other high carbon-content alcohols promising candidates for blending with diesel fuel.

This author has proposed a number of dual alcohols-gasoline blends, which were selected based upon the vapor pressure requirements as proposed by Andersen et al. The dual blends were experimentally tested in a laboratory using engines in order to determine whether they can satisfy the requirements of operation with different engine loads.

The research hypothesis is that the dual alcohols-gasoline and higher alcohol/diesel blends with the shared volume above the known limits may be applied satisfactorily to both spark and compression ignition engines, respectively. These may also comply with the most recent emission regulations as well as the engine performance requirements.

2. Objectives

The general objective of this research is to reduce the negative impacts of petroleum oil-based fuels in reciprocating engines on the environment through the use of oxygenated (alcohol) blends, while not deteriorating engine performance. The specific objectives include the following:

- To compare the performance, combustion, and emission characteristics of dual alcohol-gasoline with single alcohol-gasoline blends fired in a four cylinder naturally aspirated (NA) spark ignition (SI) engine.
- To compare the combustion and emission characteristics of dual alcohol (methanol-n-butanol-gasoline) blends with single alcohol (methanol-gasoline) blends in a single-cylinder SI engine.
- To evaluate the combustion and regulated emission characteristics of diesel fuel (DF) and n-butanol/diesel blends (B5, B10, and B20, where B5 represents 5% shared volume of n-butanol to 95% diesel fuel) fired in a high load turbocharged diesel engine and to compare the findings with a study that was conducted by others [5]. Detailed information on the advantages and disadvantages of using n-butanol, comparisons of ethanol or methanol, and heating value estimation of the blends can be found in Ref. [6].

3. Engine experimentation

The engine experiments and methodology, data collection process, and analysis software are all described in turn in Ref. [6].

3.1. Multipoint injection NA engine

3.1.1. Fuel mass flow rate

The electronic control unit (ECU) controls the fuel mass flow rate and changes the fuel delivery system. The change to the type of fuel is different from gasoline; in particular, the type of fuel (blends) affects the quantity of the mass of fuel delivered by the fuel pump.

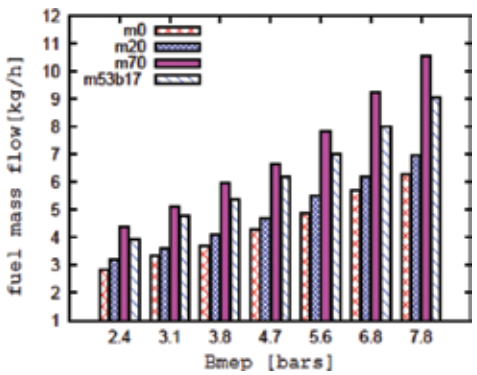

Figure 1. Effect of blends on fuel mass flow rate vs. Bmep.

http://dx.doi.org/10.5772/64747

Figure 1 depicts the increase of the fuel's mass-flow rate (m_f) for the blends with the load or brake mean effective pressure (BMEP). The raised fuel mass flow with the blends in comparison with GF is well known.

3.1.2. BSFC and BTE

Figure 2(a) demonstrates the effect of the blends on BSFC and **Figure 2(b)** on BTE. Improvement of brake thermal efficiency (BTE) as a result of the raising of the heating value and oxygen atoms of the blend is well understood (**Figure 2(b)**). A well-known relation between BTE and BSFC is such that as the BTE increases, the BSFC reduces as BMEP increases (see **Figure 2(a)** and **(b)**). It is well established that alcohol-gasoline blends indicate a higher BSFC than GF does at a given BMEP. Other factors that could contribute to the observed improvement of BTE are better atomization of the blend and effects on friction [7]. Atomization of a fuel is affected by the fuel's surface tension [7, 8]. The increased BTE when using M70 being greater than the BTE when using M53b17 indicates the improved combustion process of the single alcohol-gasoline blend in comparison with that of the dual alcohol-gasoline blend.

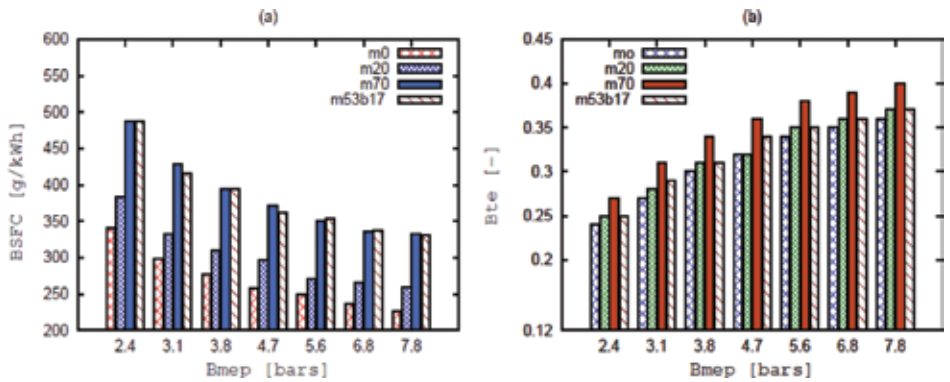

Figure 2. Effect of blends on (a) BSFC and (b) BTE.

3.2. Diesel (TDI) engine

3.2.1. BSFC and BTE

A study in which a small shared volume of ethanol to diesel (E5 and E10) was compared with methanol-diesel blends: M5, M10 (M5 represents 5% by volume of methanol in diesel fuel) was conducted [9].

The test was based upon the engine type Super Star 7710a, (age of the engine: year 2000) four-stroke, single-cylinder, naturally aspirated diesel engine, and displacement of 770 cc, with bore size of 98 mm and stroke 100 mm and compression ratio 17:1. The intake valve opens at 15° crank angle (CA) before top dead centre (BTDC), and the exhaust valve opens at 15° after top dead centre (ATDC), in the conditions of original injection timing of 27°CA BTDC, the injection

nozzle with needle valve and four holes, a nozzle-valve lifting pressure of 150±0.5 bar; a maximum torque 39.8 Nm (at 1650 rpm), and maximum power 7.4 kW at 1900 rpm.

The minimum BSFC in the study carried out by Ref. [9] was 298 g/kWh when compared with 237 g/kWh on 1500 rpm in this study. This is expected, as n-butanol has a lower fuel consumption rate than ethanol or methanol blends, due to the higher-energy content of n-butanol. In this study, however, the lower-energy content of n-butanol blends than DF resulted in an increased mass flow rate with n-butanol /diesel blend as depicted by the increased BSFC in **Figure 3(a)** and **(b)**. In the writer's study, the BSFC, on low BMEP, was higher than that on high BMEP for all the test fuels.

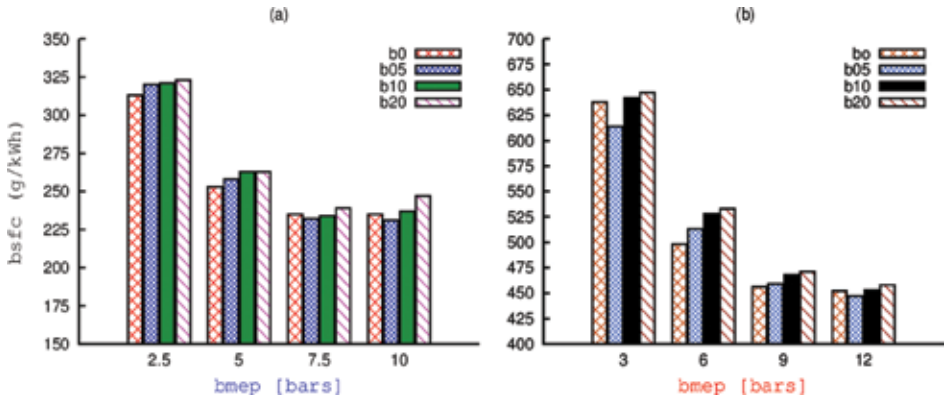

Figure 3. BSFC vs. BMEP (a) at 1500 rpm (b) at 3000 rpm.

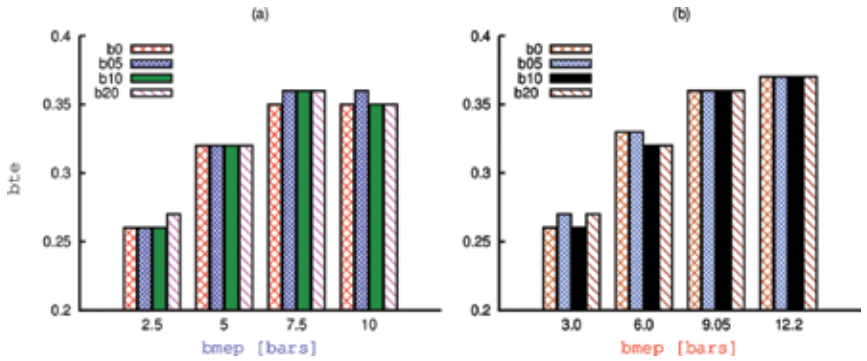

Figure 4. BTE vs. BMEP: (a) at 1500 rpm and (b) at 3000 rpm.

Figure 4(a) and **(b)** depicts the BTE at speeds 1500 and at 3000 rpm, respectively. The range of BTE in the study [9] was 0.22–0.28 in the speed range of 1000–1600 rpm. In the writer's study, the BTE fell into the range: 0.25–0.35 with 1500 rpm. The higher BTE of n-butanol/diesel blends than the ethanol/or methanol-diesel blends is attributed to the higher CN of n-butanol [10]. The energy content (LHV) of the blend decreases with the increase of the

http://dx.doi.org/10.5772/64747

shared volume of n-butanol in DF. This causes fuel mass flow to increase the BSFC. Thus, the two effects compensate each other and maintain the same BTE. The effects of atomization of the blend and friction discussed in Ref. [10] could apply here; however, the BTE is not raised as much because of the slow evaporation of the blends.

3.3. Conclusions

3.3.1. Naturally aspirated engine

The purpose of this part of the study was to compare the performance characteristics of a single alcohol (methanol)/gasoline with a dual alcohol (methanol-n-butanol)/gasoline blend relative to gasoline fuel (GF) used in a four stroke and cylinder naturally aspirated SI engine. The dual alcohol blend M53b17 was chosen according to a technique developed by Andersen et al. [4] where the VP of M53b17 was a match to the VP for gasoline fuel. The test fuels were as follows: reference fuel GF, M20, M70, and M53b17. The following conclusions can be drawn:

- Blends had higher BSFC than that of GF for the same BMEP to compensate for their lower-energy content. As the thermal efficiency increases with BMEP, the BSFC drops.
- Blend M70 indicated a higher BTE than M53b17 did.

3.3.2. Diesel (TDI)

The purpose of this work was to evaluate the performance characteristics of n-butanol-diesel blends as fuel fired in a turbocharged, direct-injection, and diesel engine and to compare the performance characteristics with those found in literature [9] using ethanol-diesel and methanol-diesel blends. The n-butanol additive is an attractive biofuel to consider because it is readily miscible with diesel fuel and has a higher CN than ethanol or methanol. The blends tested were reference fuel, DF, and blends B5, B10, and B20 (where B5 represents 5% of n-butanol by volume 95% diesel fuel).

The results reported in a study conducted by Sayin [9] (regarding the BSFC and BTE of ethanol-diesel and methanol-diesel blends) with similar parameters were compared with n-butanol-diesel blends of this study. The following conclusions can be drawn:

- The BSFC was lower and BTE higher in this study than those in the cited study. The range of BTE in the cited study was 0.22–0.28 in the speed range of 1000–1600 rpm. In this study, the BTE fell into the range 0.25–0.35 for 1500 rpm. However, due to the lower-energy content of the n-butanol blends than that of DF, the BSFC increased. On the other hand, the BSFC reduced as a result of improved BTE when increasing the brake mean effective pressure.
- Smaller shared volumes of n-butanol to diesel fuel fired in a turbocharged diesel engine is recommended instead of ethanol-or methanol-diesel blends as a result of improved brake thermal efficiency and BSFC, including the benefits not requiring any engine modification.

4. Results of and discussion on combustion and emissions characteristics

4.1. Indicated pressure, HRR and emission of NO_x,

4.1.1. Effect of blends on octane rating SI engine

By inspection of the relevant heat release rate (HRR) (see **Figure 5(a)–(d)**), blends with the same combustion duration in CADs as that in GF, it was found to be SAG blend M10 (see **Figure 5(a)**) and for DAG blends M-nB 30:20. Both blends had the same indicated peak pressure. Blends with shortened combustion duration relative to GF were M25 in the category of SAG blends and M-nB 40:20, M-nB 25:35, and M-nB 80:10 in that of the DAG blends. Blends with slightly prolonged combustion duration such as SAG blends were M15, M20, M30, and M80, while in the DAG, blends were M-nB 10:20, M-nB 15:25, and M-nB 20:30. It can therefore be deduced that in the case of DAG blends, when the blending ratios or shared volumes of both methanol and n-butanol to GF were increased, the combustion duration was shortened, whereas increasing the methanol shared volume prolonged the combustion duration in the case of the SAG blends. This could be due to the improved combustion efficiency of oxygenated fuels resulting from the higher heating value in the DAG rather than in the SAG blends. **Figure 6** illustrates the effect of blends on HRR in stoichiometric mixtures for both the DAG and the SAG blends. The combustion duration was substantially more prolonged for the SAG than the DAG blends.

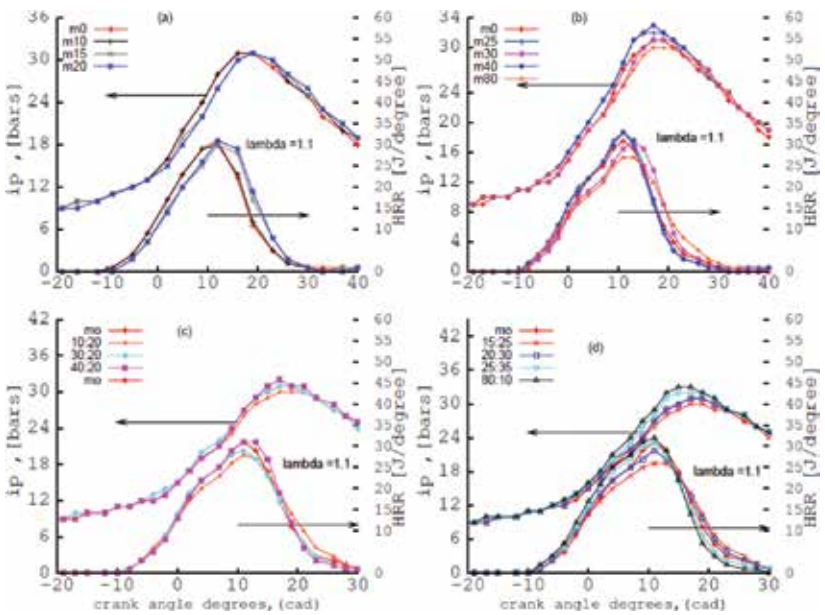

Figure 5. Effect of SAG (a, b) and effect of DAG (c, d) blends on mean indicated pressure (IP) and heat release rate (HRR) at $\lambda = 1.1$.

http://dx.doi.org/10.5772/64747

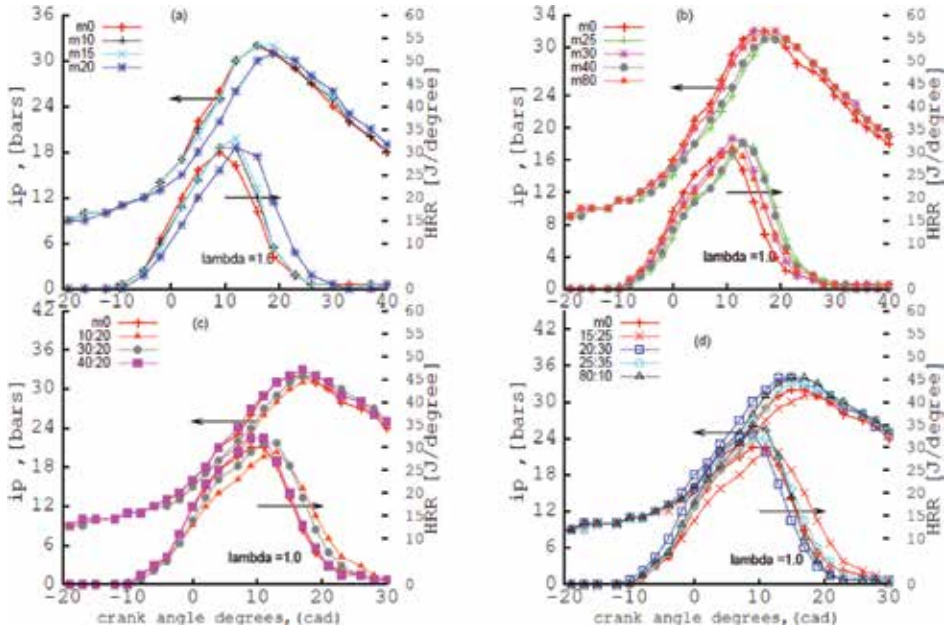

Figure 6. Effect of SAG (a, b) and DAG(c, d) blends on mean indicated pressure (IP) and heat release rate (HRR) at λ = 1.0.

Figure 7(a) and **(b)** indicates the effect of blends on the emissions of nitrogen oxides in the category of the SAG blends and **Figure 7(c)** illustrates the effect of DAG blends on the emissions of nitrogen oxides. Thermal NO_x is a by-product of combustion, and its exponential formation rate is dependent on temperature. Thermal NO_x formation, which is well studied and understood [5], depends upon the residence time and higher temperatures. The peak emission of NO_x for test fuels occurs at approximately: λ = 1.1. This means that its formation is more probable at very high temperatures as a function of heat release. **Figure 5(a)–(d)** illustrates the HRR and indicated pressure for methanol and DAG blends. The high latent heat of evaporation in alcohols results in an evaporative cooling of the mixture. Because of this any increase in the alcohol percentage of the fuel mixture causes NO_x to drop (see **Figure 7(a)** and **(b)**. For methanol blends up to M20, the maximum HRR and maximum indicated pressure at λ = 1.1 were all similar (**Figure 6(a)**); therefore, the peak NO_x emissions were also identical (see **Figure 7(a)**).

Figure 7(e) demonstrates the effect of blends on NO_x, which includes n-butanol. Blends of M30 and M-nB 10:20 both contain a total alcohol content of 30% (v/v), and by examining the relevant figures (**Figure 5(b)** and **(c)**), it is evident that the maximum HRR is lower for M-nB10:20 than for M30, although both produced about the same NO_x emission concentration. This result could be explained by the *difference in residence* time between the combustion products of the two blends, which absorb energy from the surrounding. Of the two blends, the faster burning mixture prolonged the residence time and had more time to absorb energy than the slower burning blend. So the net effect was the same.

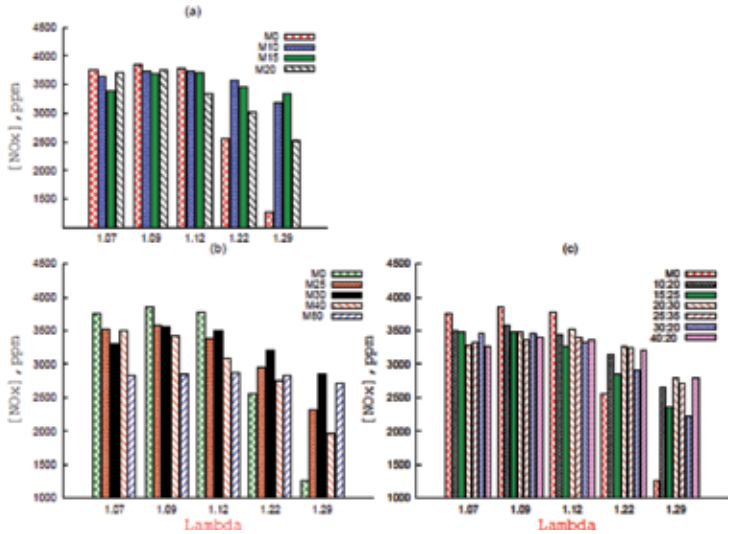

Figure 7. Effect on NOx: (a, b) single alcohol/gasoline (SAG) blends (c) dual alcohol/gasoline (DAG) blends.

4.1.2. Mean indicated pressure, HRR and effect of blends on multipoint injection NA engine

Figure 8(a) and **(b)** compares the effect of blends on combustion HRR and indicated pressure against different spark timings (STs). Both M70 and M53b17 revealed the same combustion duration at the ST of 24.5 CAD BTDC, (see **Figure 8(a)**). The blend M70 indicated a more shortened combustion duration compared with that of M53b17 when the ST (**Figure 8(b)**) was advanced, suggesting an improved combustion efficiency. The effect of knock limited how far the Injection timing of M20 could be advanced, which was 26.5 CAD BTDC. However, blend M53b17 could be advanced to 28.5 CA BTDC without any problems relating to knocking.

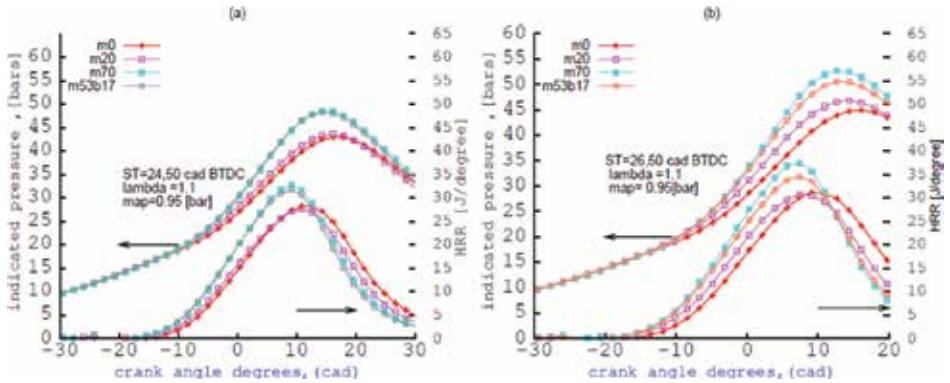

Figure 8. Effect of blends on heat release rate (HRR) and mean indicated pressure at 7.8 bars (BMEP).

http://dx.doi.org/10.5772/64747

Since the indicated peak pressure (**Figure 9(a)**) or HRR (**Figure 9(c)**) rises with an increase in the BMEP, the trend is to reduce the CAD at which these peaks occur (**Figure 9(b)** and **(d)**). The ST for M0, M20, M70, and M53b17 were suitably set to: 27.5, 28.5, 26.5, and 28.5 CAD BTDC, respectively. Therefore, blends M53b17 and M20 followed by M70 and M0, indicated early combustion, which resulted from high peak pressures or peak HRR (**Figure 9(a)** and **(c)**). Blend of M53b17 was, therefore, expected to produce the highest pressure peaks because its ST CAD BTDC was more advanced than that of M70 and GF, drawing the peak pressure and HRR closer to the top dead centre (TDC). The combustion duration is therefore, expected to shorten with the use of M53b17 when its ST is fixed at 28.5 CAD BTDC. The crank angles of the indicated peak pressure set at a medium BMEP of 5.5 bars for GF, M70, M53b17, and M20 were 17, 16, and 15 CAD after top dead centre (ATDC), respectively.

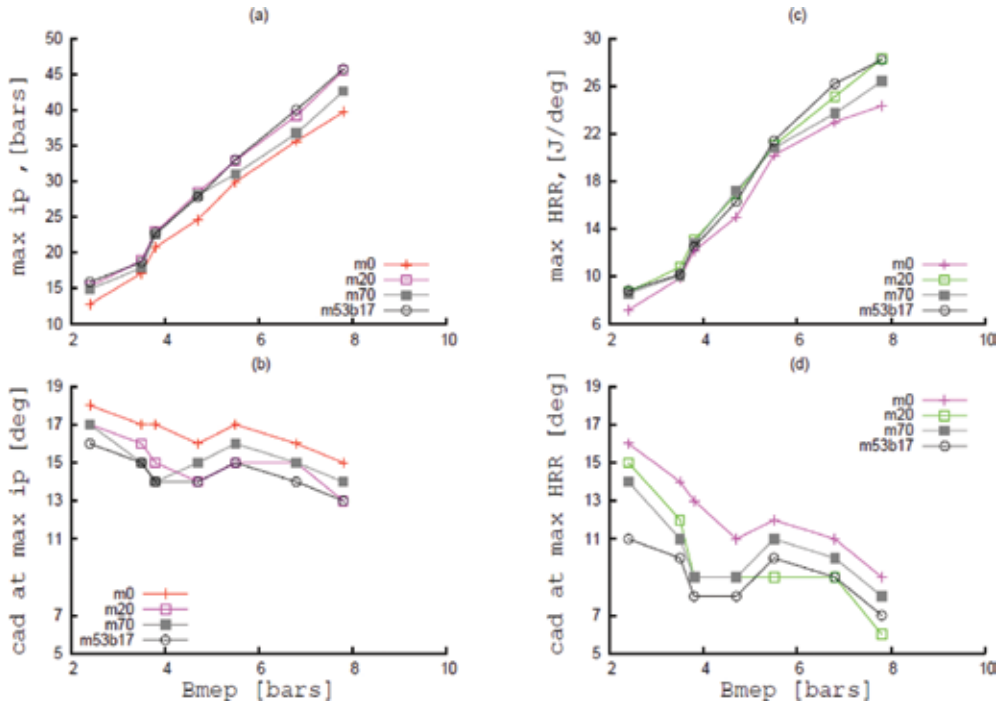

Figure 9. Relationship of cad at maximum mean indicated pressure (IP) and HRR for blends vs. BMEP.

4.2. Emission of CO

4.2.1. Effect of blends on (TDI) CI engine

The data in this section demonstrate that smaller shared volumes of n-butanol when using fuel fired in a light-duty, turbocharged, direct-injection diesel engine significantly reduce regulated emissions compared with the findings of a similar study using a naturally aspirated diesel engine using 30% biodiesel from rapeseed oil with admixes of E5 and E7.5 [5].

Researchers [5], studied multi component fuelling of a naturally aspirated diesel engine using biodiesel (BD), composed of a shared volume of 30 % (v/v) or BD30 (RMEs) from rapeseed oil and compounded with diesel fuel (DF), with properties similar to those of DF used in the current study. A third admix to BD30 that was tested in the cited study is ethanol 5 and 7.5% (E5 and E7.5). The BSFC values for the admixed blends B30 + 5E and B30 + 7.5E were similar to those of DF.

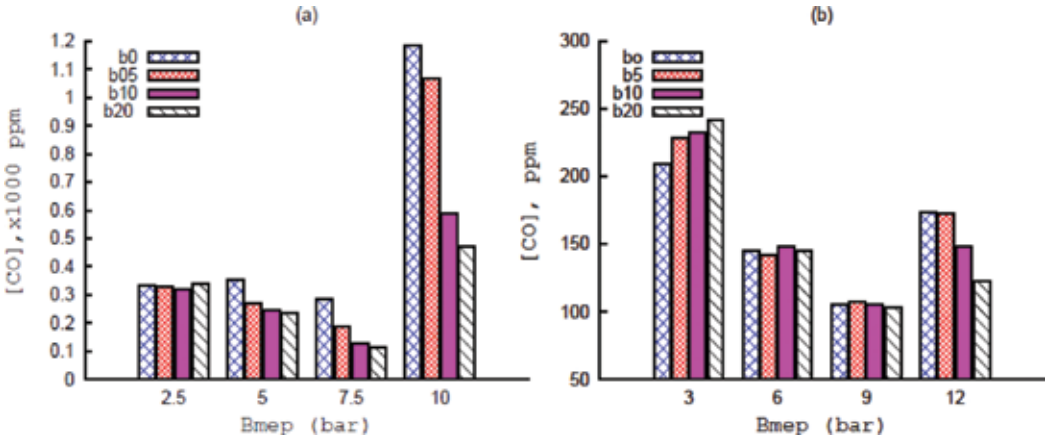

Figure 10. Carbon monoxide emissions (a) at 1500 rpm and (b) at 3000 rpm.

Figure 10 illustrates the effect of blends on the CO concentration at speeds: of 1500 and 3000 rpm. The CO measured in Ref. [5]: For DF: when the BMEP was 0.650, 0.325, or 0.1 MPa, the CO was 912, 351, and 634 ppm, respectively, while in the author's study, when the BMEP for DF was 0.751, 0.50, or 0.251 MPa, the CO was 286, 355, and 334 ppm, respectively. Furthermore, in the cited study, when the BMEP was 0.650, 0.325, or 0.100 MPa, for B30+E5-7.5%, the CO was 300, 575, and 280 ppm, respectively. On the other hand, in the author's study, when the BMEP was 0.751, 0.50, or 0.251 MPa for B20, the CO was reduced to 111, 234, and 338 ppm, respectively [10].

4.3. Emissions of UHC

In this section of the study, the emission of UHC using DAG blends is compared with the emission of UHC using SAG blends. The dual blends meet the VP requirement for GF, in internal-combustion engines. The blends do not require any engine modification.

4.3.1. Effect of blends on (TDI) diesel engine

The effect of the blends on the unburned hydrocarbon emission concentration at 1500 and 3000 rpm is illustrated in **Figure 11**. The amount of fuel injected during the ignition delay period has an influence on its concentration. For BD30, where CN was higher, the injection period was shorter, decreasing correspondingly, with the emission of UHC [5]. When the BMEP for DF was 0.650, 0.325, or 0.100 MPa, the UHC was 318, 347, and 406 ppm, respectively, while

http://dx.doi.org/10.5772/64747

the UHC emission for B30+5-7.5E was 220, 240, and 280 ppm for the same range of BMEP. Conversely, in this study, when the BMEP for DF was 0.751, 0.50, or 0.251 MPa, the UHC was 14, 20, and 30 ppm, respectively, and, the UHC emission for B20 was 30, 37, and 55 ppm, showing a significant reduction in the UHC emissions in this study [10].

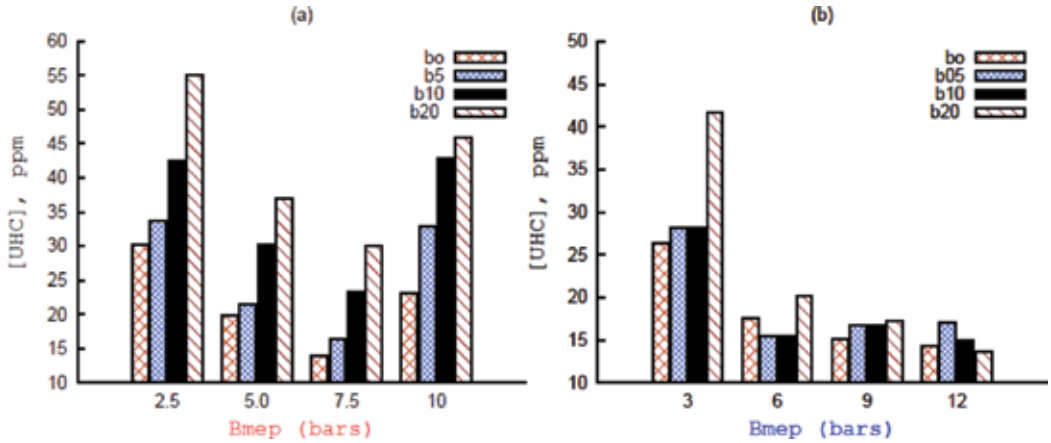

Figure 11. UHC emissions varying against BMEP (a) at 1500 rpm and (b) at 3000 rpm.

4.4. Conclusions

The combustion of the alcohol/conventional fuel blends in reciprocating engines indicate certain effects on the regulated emission and combustion characteristics as summarized later.

4.4.1. Octane engine

The experiments were conducted on a single-cylinder BASF octane rating SI engine at the constant speed of 600 rpm. The aim of this part of the study was to compare regulated emissions of DAG with SAG blends.

The combustion duration was shortened using the DAG blends as the total shared volume of methanol and n-butanol to GF was increased. However, the combustion duration was prolonged using the SAG blends as the methanol shared volume in GF was increased. The combustion duration was substantially more prolonged for the SAG blends than for the DAG blends in stoichiometric mixtures.

The SAG blends reduced the UHC emission concentration more than the DAG blends did (both with the same total alcohol content). Regarding the GF, the UHC emission was reduced by 9.2% for M-nB 10:30 and 20% for the M30 at $\lambda = 1.1$. Blend of M-nB 15:25 reduced the UHC emission by approximately 16.9% whereas M40 reduced the UHC emission by 26.9% at $\lambda = 1.1$.

Although, the SAG blends produced lower UHC emission than the DAG blends, in this study, the use of DAG blends is recommended. The combustion duration for the latter was shortened

in crank angles due to their higher-energy content than the SAG blends. By either increasing the methanol or the n-butanol shared volume to GF, the UHC emission was improved.

4.4.2. Naturally aspirated engine

The purpose of this part of the study was to compare the combustion characteristics of a single alcohol (methanol)/gasoline with a dual alcohol (methanol-n-butanol)/gasoline blend relative to gasoline fuel (GF) based on a four-stroke and four-cylinder naturally aspirated spark ignition engine. The test fuels were as follows: reference fuel: GF, blends: M20, M70, and M53b17.

The following conclusion can be drawn from the engine experiments:

The same combustion duration was attained by both M70 and M53b17 at ST of 24.5 Crank angle degree (CAD) BTDC. However, the blend M70 exhibited slightly shorter combustion duration than M53b17 at ST of 26.5 CAD BTDC. However, when the ST for M53b17 was fixed at 28.5 CAD BTDC, its combustion duration was shorter than that for M70. All the test fuels indicated an increase in both the heat release rate and the indicated pressure when the ST CAD BTDC was advanced.

Blend M53b17 was recommended as a suitable substitute for M70 in the SI engine because the heating value and the combustion duration using M53b17 improved compared with using M70 blend.

4.4.3. Diesel (TDI)

The purpose of this part of the study was to evaluate the combustion characteristics and regulated emissions of pure DF and n-butanol/diesel blends: B5, B10, and B20 fired in a high load turbocharged diesel engine. A similar study was used as a basis for comparison and attenuation of the results from the current study in order to build understanding of the impact of fuel property on combustion and regulated emission.

A comparison of regulated emissions in this study using a turbocharged diesel engine with a similar study [5] (based on a naturally aspirated diesel engine) indicated an improvement in the reduction of UHC and CO using a turbocharged engine.

Unburned hydrocarbons emissions were more significantly reduced when using n-butanol/DF blends in this study than when using 30% RME and 5–7.5% bioethanol in the other study [5]. However, in both cases, the blends produced higher UHC emission than DF. In this study, the UHC emission concentration increased by 21.4, 71.4, and 214% regarding DF on a 75% load at 1500 rpm for B5, B10, and B20 respectively. Smaller shared volumes, up to 20% (v/v) of n-butanol added to DF are highly recommended to use especially in a turbocharged engine. These blends substantially reduce the regulated emissions requiring no engine modification.

http://dx.doi.org/10.5772/64747

5. Final conclusions

5.1. Accomplishments in this study

Dual alcohol-gasoline blends, in particular, burned in internal-combustion engines that meet the VP requirements do not make them entirely good performers in spark ignition engines.

The following dual alcohol-gasoline blends were analyzed as being suitable in spark ignition engines in terms of shortened combustion duration while maintaining the same reduction of important pollutants of single alcohol-gasoline blends in a spark ignition reciprocating engine.

- M53b17 (53% methanol and 17% n-butanol in gasoline)
- M-nB 40:20, M-nB 25:35 and M-nB80:10
- The following dual alcohol gasoline blends prolonged the combustion duration
- M-nB 10:20, M-nB15:25 and M-nB 20:30.
- On the part of the diesel engine, it was demonstrated that the reduction of emissions on a turbocharged engine was greater in this study than in another study carried out by others [5] who used 30% biodiesel (rape methyl esters, RME, derived from rapeseed oil). They blended with diesel fuel and operated at similar conditions except for the type of engines (a turbocharged one was used in this author's study and a naturally aspirated engine in the other study).

5.2. Future work recommendations

- To investigate additives to the dual alcohol-gasoline blends (that prolonged the combustion duration) in order to shorten their combustion duration although they meet the VP requirement as shown throughout this study.
- To *increase* the n-butanol blend percentage in pure diesel or biodiesel/diesel blend and to investigate performance in a diesel engine. This is to be supported by firstly, increasing the biodiesel fraction (which increases the cetane number) in the biodiesel/diesel blend. The advantage of doing this is that the calorific value of n-butanol is lower than that of biodiesel.

There is evidence in this study that bioalcohols have a significant role to play in achieving the goal of the reduction of regulated emissions although partially, in the search for alternative fuels to replace the conventional fuels used in the IC engines.

Acknowledgements

Authors are grateful for the support of Bolyai Janos scholarship of Hungarian Academy of Science.

Author details

Lennox Siwale[1*], Lukacs Kristof[2], Torok Adam[2], Akos Bereczky[2], Makame Mbarawa[3], Antal Penninger[2] and Andrei Kolesnikov[4]

*Address all correspondence to: zumbe.siw@gmail.com

1 The Copperbelt University, Kitwe, Zambia

2 Department of Energy Engineering, Budapest University of Technology and Economics, Budapest, Hungary

3 Ministry of Communication, Science and Technology, Dar es Salaam, United Republic of Tanzania

4 Department of Mechanical Engineering, Tshwane University of Technology, Pretoria, South Africa

References

[1] McAllister, S., Chen, J.Y., and Fernandez-Pello, A.C., Fundamentals of combustion processes. Springer: Berkely, CA, 2011.

[2] Demain, A., Biosolutions to the energy problem. Ind Microbiol Biotechnol, 2009. 36: p. 319–332.

[3] Andersen, V.F., et al., Distillation curves for alcohols and gasoline blends. Energy Fuels, 2010. 24(4): p. 2683–2691.

[4] Andersen, V.F., et al., Vapor pressures of alcohol-gasoline blends. Energy Fuels, 2010. 24(6): p. 3647–3654.

[5] Raslavicius, L. and Bazaras, Z., Variations in oxygenated blend composition to meet energy and combustion characteristics very similar to the diesel fuel. Fuel Process Technol, 2010. 91(9): p. 1049–1054.

[6] Siwale, L., Effect of oxygenated additives in conventional fuels for reciprocating internal combustion engines on performance, combustion and emission characteristics, 2012. Accessed from: https://www.google.co.zm/search?q=EFFECT+OF+OXYGENATED+ADDITIVES+IN+CONVENTIONAL+FUELS+FOR+RECIPROCATING+INTERNAL+COMBUSTION+ENGINES+ON+PERFORMANCE%2C+COMBUSTION+AND+EMISSION+CHARACTERISTICS [accessed 8 June 2016].

http://dx.doi.org/10.5772/64747

[7] Kikuchi, T., Shinichiro, I., and Yoshinori, N., "Piston Friction Analysis Using a Direct-Injection Single Cylinder Gasoline Engine", Japan Society of Automotive Engineers, No. 1, 2003, pp. 53–58.

[8] Wu, Z., Zhu, Z., and Huang, Z., An experimental study on the spray structure of oxygenated fuel using laser-based visualization and particle image velocimetry. Fuel, 2006. 85(2006): p. 1458–1464.

[9] Sayin, C., Engine performance and exhaust gas emissions of methanol and ethanol-diesel blends. Fuel, 2010. 89(11): p. 3410–3415.

[10] Siwale, L., et al., Combustion and emission characteristics of n-butanol/diesel fuel blend in a turbo-charged compression ignition engine. Fuel, 2013. 107(2013): p. 409–418.

Chapter 8

Combustion and Emissions of a Diesel Engine Fueled with Diesel-Biodiesel-Ethanol Blends and Supplemented with Intake CO_2 Charge Dilution

Ho Tse

Additional information is available at the end of the chapter

http://dx.doi.org/10.5772/64470

Abstract

This study investigated the influence of a four-cylinder naturally aspirated direct-injection diesel engine fueled with diesel-biodiesel-ethanol blended (DBE) fuels tested at a steady state speed of 1800 rev/min under different engine loads, ethanol volume and intake carbon dioxide (CO_2) dilution ratios on engine performance, combustion characteristics, regulated gaseous emissions, and soot agglomerates. Overall, the experimental results indicate that DBE blends can in general improve brake thermal efficiency (BTE) and reduce nitrogen oxides (NO_x), carbon monoxide (CO), CO_2, volatile organic fractions, particulate mass (PM), and particulate number (PN) concentrations, while brake-specific fuel consumption (BSFC) and hydrocarbon (HC) might increase slightly. Compared with ultra-low-sulfur diesel, DBE blends can maintain a good tradeoff relationship among PM-PN-NO_x. Compared with biodiesel, the blended fuels perform better in suppressing brake-specific particle number emissions (BSPN), leading to a reduction of ultrafine and nanoparticle numbers. The combined effect of DBE blends with intake CO_2 dilution has marginal effects on BSFC and BTE, significantly reducing NO_x emission while slightly increasing particulate emissions. On particulate characteristics, DBE blends produce soots with curved, tortuous, and disorganized nanostructures with low soot burnout temperature and strong oxidation rate favoring PM-PN reduction.

Keywords: diesel-biodiesel-ethanol, combustion characteristics, gaseous emissions, particle emissions, particle morphology

INTECH
open science | open minds

© 2016 The Author(s). Licensee InTech. This chapter is distributed under the terms of the Creative Commons Attribution License (http://creativecommons.org/licenses/by/3.0), which permits unrestricted use, distribution, and reproduction in any medium, provided the original work is properly cited. CC BY

1. Introduction

1.1. Transport biofuels

The trend toward low-emission diesel fuels is growing worldwide with particular concerns from the regulated tradeoff emissions of NO_x and PM, and other air toxics. European Union (EU) mandates 10% share for biofuels in the EU total energy mix by 2020 and United States sets a total of 36 billion gallon target for biofuel production by 2022. Therefore, oxygenated-type biofuel become popular to be used and blended with diesel for producing cleaner burning fuels. Many researchers explore methods to improve fuel quality by blending with oxygenated additives as coproducts [1]. The commonly used oxygenated additives are (a) ethanol, (b) acetoacetic esters and dicarboxylic acid esters, ethylene glycol monoacetate, (c) 2-hydroxy-rhyl esters, (d) diethylene glycol dimethyl ether, (e) sorbitan monooleate and polyoxyethylene sorbitan monomethyl ether, (f) ethanol and dimethyl ether, (g) dimethyl ether (DME), (h) dimethyl carbonate (DMC), (i) 1-octylamino-3-octyloxy-2-propanol and *N*-octyl nitamine, (j) methanol, and (k) a mixture of methanol and ethanol. In fact, there are only few literatures studying the effects of oxygenated additives in CI engine experiments. Among these additives, DME, DMC, ethanol, or methanol have been studied by few researches as effective additives to be applied as coproducts in CI engines. **Table 1** lists their major advantages and limitations from literature findings on gaseous emissions and **Table 2** lists their fuel properties [1, 2].

1.2. Food, energy, and environment trilemma

Of the alternative biofuels, the most widely investigated include biodiesel and ethanol [3–5]. These two fuels have clear emission advantages over diesel. However, some studies have raised the concern of "food versus fuel" arising from plant-based biodiesel and ethanol, which might be the main hurdle for commercialization [6]. In fact, the economic consequences of these biofuel expansions are mixed and there are still some issues that will influence the actual impacts on food costs that have not been accounted for. To counter the "food, energy, and environment trilemma", the development of these biofuels from nonfood sources (i.e., biodiesel from waste cooking oil, ethanol from cellulosic nonfood crops, etc.) can show great promise in reducing food commodities being utilized for biofuel production [7].

1.3. Investigation of DBE blends

Focus of many previous researches was placed on diesel-biodiesel blends on general diesel engine performance and emissions as the fundamental investigation due to the interest of biodiesel being low cost, less polluting, renewable nature, and high energy density against diesel [8]. The dominant trend could be found in most research cases [9–13] that diesel-biodiesel blends would decrease the full-load effective power, increase brake-specific fuel consumption, and maintain thermal efficiency. As for vehicular emissions, partial regulated air parameters (viz., smoke density, particulate mass concentration, CO, and aromatic hydrocarbon) and partial unregulated air toxics (viz., formaldehyde, 1,3-butadiene, toluene, and xylene) decreased. However, other partial regulated air parameters (viz., NO_x, NO_2 and nanoparticle) and air toxics (viz., acetaldehyde and benzene) increased instead.

http://dx.doi.org/10.5772/64470

Oxygenated additives	Advantages	Limitations
Dimethyl ether (DME)	A slight decrease of NO_x emissions with % DMC in blended fuel. Strong effect on smoke reduction.	Maximum blending concentration up to 25% into diesel fuel; otherwise significantly reduce the viscosity of final mixture.
Dimethyl carbonate (DMC)	A slight decrease of NO_x emissions with % DMC in blended fuel. Most effective at 5% DMC for reducing submicro and microsized particle emissions.	Slight increase of HC and CO, but can be resolved with DOC. Obvious increase in benzene, toluene, and *m,p*-xylene (BTX) emissions. Increase in fuel consumption or decrease in engine power due to lower calorific value of DMC.
Ethanol	Effective in reducing particulate mass at high engine load. Effective in reducing unregulated emission of formaldehyde, ethane, ethene, 1,3-butadiene, and BTX.	Lower cetane number. Increase in fuel consumption or decrease in engine power. Increase of NO_2 (toxic and highly reactive gas) is associated with the use of ethanol-ULSD blends having adverse influence on human health.
Methanol	Effective at a fumigation ratio of 0.1 for reducing NO_x and particulate mass concentration. Particle emitted under methanol fumigated engine are reduced under both low and medium engine loads. No increase in the number of nanosized particles and changes in geometrical mean diameter of emitted particles under low and medium engine loads.	Maximum fumigation ratio of 0.4 for avoiding engine knock. Marginal reduction in particle emission in high engine loads. Significant increase of HC and CO with increase of fumigation ratio of methanol, but can be resolved with DOC. Increase of NO_2 (toxic and highly reactive gas) is associated with the use of methanol having adverse influence on human health.

Table 1. Advantages and limitations for four oxygenated additives.

Due to the increases in public concerns about the environmental and health impacts from diesel-biodiesel blends, further development of using additional oxygenated-type fuel additives (viz., ethanol) to improve engine and emission performance flaws from diesel-biodiesel blends is significant and viable [14]. In fact, there are very few literatures studying the effects of diesel-biodiesel-ethanol (DBE) blends in diesel engine experiments and the impacts from these new blends are still not fully understood till date. For long-term environmental and public health protection, new forms of clean and economical oxygenated diesel blends fuel must be explored to progressively replace conventional mineral diesel. Ethanol is the type of alcohol made from renewable resources such as biomass from locally grown crops and even waste products such as waste paper, grass, and tree trimmings. They are also an alternative transportation fuel since it has properties allowing its use in existing diesel engines with minor hardware. Despite this, they are only used on a limited basis to fuel diesel engines

due to their respective problems in toxicity, corrosivity, miscibility with water, or immiscibility with diesel. However, they have higher octane number enduring higher compression ratios before engine starts knocking, thus giving diesel engine an ability to deliver more power efficiently and economically and to produce lesser CO, HC, and NO_x/NO_2 with higher heat of vaporization, thereby reducing peak temperature inside combustion chamber [2, 3].

Property	Euro V diesel	Biodiesel	Ethanol	Methanol	DME	DMC
Cetane number	52	51	6	<5	55–60	35–36
Lower heating value (MJ/kg)	42.5	37.5	28.4	19.7	28.43	15.78
Density (kg/m^3) at 20°C	840	871	786	792	668	1079
Viscosity (mPa S) at 40°C	2.4	4.6	1.2	0.59	–	0.63
Heat of evaporation (kJ/kg)	250–290	300	840	1178	410	369
Carbon content (%mass)	86.6	77.1	52.2	37.5	52.2	40
Hydrogen content (%mass)	13.4	12.1	13	12.5	13	6.7
Oxygen content (%mass)	0	10.8	34.8	50	34.8	53.3
Sulfur content (%mass)	<10	<10	0	0	<10	<10

Table 2. Properties of Euro V diesel, biodiesel, ethanol, methanol, DME, and DMC.

The use of ethanol on a limited basis in diesel-biodiesel blends can compensate the decreased octane caused by the presence of biodiesel in diesel fuel and produce lesser particulates and CO_2 due to the lower carbon-to-hydrogen ratio of these alcohols. On the one hand, the presence of biodiesel can act as stabilizer to stabilize the phase stability of diesel-biodiesel-ethanol in blend fuels. Therefore, more understanding for the long-term stable diesel-biodiesel-ethanol (DBE) blends in diesel engine application with improved engine and emission performance can be achieved.

1.4. Novelty and contributions

This chapter provides the following contributions in filling the knowledge gaps on using DBE blends as potential transport biofuels that the current literatures do not cover or rarely study.

- Simultaneous reduction in NO_x and PM is a challenging issue in diesel industry. The use of DBE blends is proven to attain the reduction of both pollutants without engine modification works. The combined effect of DBE blends with intake CO_2 charge dilution can even reduce NO_x emission significantly while minimizing the adverse impact on particulate emissions.
- Correlation equations formulated through curve-fitting process for predicting percentage change in NO_x, CO, and HC emissions. The predicted percentage change has been found to agree closely with that of experimental data at the 95% confidence level.
- Correlation between combustion characteristic parameters and the particulate emissions for DBE blends over a range of ethanol contents. The soot reduction by DBE blends is associated with its lower cetane number and higher latent heat of evaporation thereby leading to longer ignition delays, shorter combustion duration, and lesser diffusion fuel mass.

http://dx.doi.org/10.5772/64470

- Correlation between particle oxidation reactivity and internal nanostructure morphology from the DBE-derived soot by the results of thermogravimetric and transmission electronic microscopic analysis. It is generally found that test fuel with higher oxygen content, larger percentage of volatile organic fractions (VOFs), and lower soot burnout temperature (low activation energy) would have stronger oxidative reactivity with particle morphology of smaller primary particle size and curved, tortuous, and disorganized nanostructures.

2. Experimental investigation

2.1. Test plan

Four sets of experimental investigations were adopted. First, a naturally, water-cooled, four-cylinder direct-injection diesel engine was tested at a steady speed of 1800 rev/min under five engine loads when fueled with diesel-biodiesel containing 15 vol% of waste-cooking-oil biodiesel while the ethanol volume varied from 0 to 20% at a step of 5%. The engine performance and gaseous emission analysis are summarized in Sections 3 and 4, respectively. Second, the correlations between combustion characteristic parameters and the particulate emissions for DBE blends are described in Section 5. Third, the combined effect of DBE blends and intake CO_2 dilution of 1.5–4.5% (at 1.5% interval) is evaluated and tested under a high engine load in Section 6. Finally, the effect of DBE blends on particulate volatility, oxidation properties, and nanostructures is investigated in Sections 7 and 8. The specifications of test engine and test fuels are shown in **Tables 3** and **4**, respectively. The test plan was based on the commonly accepted testing norms [2, 8, 11, 15–20] used in Europe, China, and Hong Kong for comparable results so as to investigate the influence of DBE blends and intake CO_2 dilution under different fuel energy substitutions and engine loads, considering combustion characteristics and emission performance.

Model	**Isuzu 4HF1**
Engine type/combustion chamber shape	Inline four-cylinder DI/Omega
Max. power	88 kW/3200 RPM
Max. torque	285 Nm/1800 RPM
Bore × stroke	112 mm × 110 mm
Displacement	4334/cc or 4.334 l
Compression ratio	19.0:1
Fuel injection timing	8° BTDC
Injection pump type	Bosch inline type
Injection nozzle	Hole type (with five orifices)
Injection nozzle diameter	0.3 mm
Injection nozzle opening pressure	18.1 MPa

Table 3. Specifications of test diesel engine.

Properties	ULSD	Biodiesel	Ethanol	
Cetane number	52	51	6	
Lower heating value (MJ/kg)	42.5	37.5	28.4	
Density (kg/m^3) at 20°C	840	871	786	
Viscosity (mPa S) at 40°C	2.4	4.6	1.2	
Heat of evaporation (kJ/kg)	250–290	300	840	
Carbon content (%mass)	86.6	77.1	52.2	
Hydrogen content (%mass)	13.4	12.1	13	
Oxygen content (%mass)	0	10.8	34.8	
Sulfur content (%mass)	<10	<10	0	
Calculated properties	**DBE0**	**DBE5**	**DBE10**	**DBE20**
Cetane number	51.9	49.6	47.3	42.7
Density (kg/m^3) at 20°C	845	842	839	833
Lower heating value (MJ/kg)	41.7	41.0	40.3	38.9
Oxygen content (%mass)	1.7	3.3	5.0	8.2

Table 4. Properties of blending stocks and test fuels.

2.2. Gaseous and particulate measurement

The schematic and photographs of the experimental system are shown in **Figures 1–3**. The gaseous species including hydrocarbon (HC), nitrogen oxides (NO_x), carbon monoxide (CO), carbon dioxide (CO_2), particulate mass and number concentration (PM and PN) and volatile organic fractions (VOF) were measured. When studying the effect of CO_2 dilution on the engine performance and exhaust emissions using DBE blends, the intake CO_2 concentration was measured at the engine intake manifold. HC was measured with a heated flame ionization detector (HFID); NO_x was measured with a heated chemiluminescence analyzer (HCLA); CO and CO_2 were measured with nondispersive infrared analyzer (NDIR). Exhaust gas temperature was measured with a K-type thermocouple. All gas analyzers were manufactured by California Analytical Instruments, Inc., and calibrated with standard gases and zero span checks before each experiment. A two-stage Dekati minidiluter was used to create a constant volume sampling to obtain a diluted exhaust gas that is representative of the average concentration while engine runs particularly in measuring low-concentration particle mass-number emissions. The primary diluted exhaust gas was delivered to a tapered element oscillating microbalance (TEOM) for measuring particulate mass concentration and then secondary diluted exhaust gas to a scanning mobility particle sizer (SMPS) for measuring the size distribution and number concentration. The dilution ratio (DR) was determined from the measured CO_2 concentrations of background air, undiluted exhaust gas, and diluted exhaust gas. The primary dilution ratio for TEOM was around 11 ± 2 whereas the secondary dilution ratio for SMPS was around 88 ± 7. The exhaust emission measuring instruments are listed in **Table 5**.

http://dx.doi.org/10.5772/64470

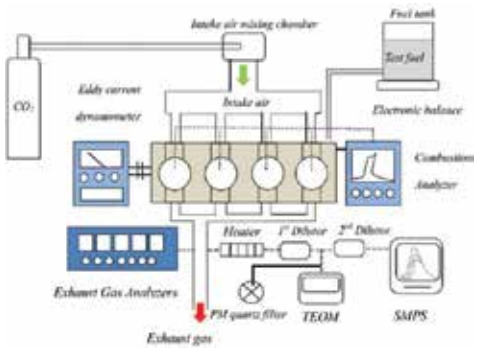

Figure 1. Schematic diagram of the experimental setup.

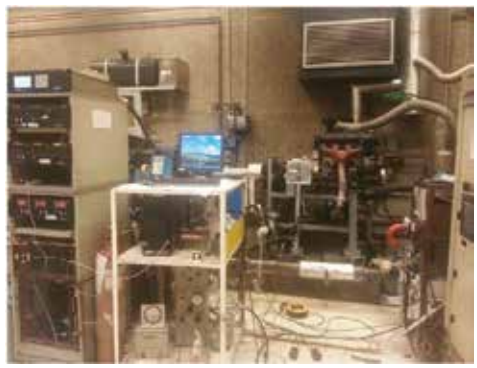

Figure 2. Photograph of the experimental setup.

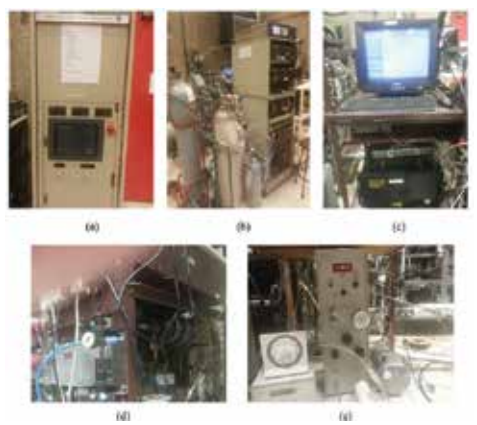

Figure 3. Photographs of (a) engine dynamometer, (b) HFID/HCLA/NDIR gas analyzers, (c) TEOM PM mass analyzer, (d) Dekati minidiluter, and (e) SMPS PM number-size distribution analyzers.

Gas species	Unit	Make/type
HC	ppm	CAI model 300
NO_x/NO	ppm	CAI model 400
CO_2/CO	ppm/%	CAI model 300
PM mass	$\mu g/m^3$	R&P TEOM 1105
PM number and size distribution	$\#/cm^3$	TSI 3934

Table 5. Exhaust emissions measuring instruments.

2.3. Combustion analysis

A Kistler type 6056A piezoelectric pressure transducer was used to measure the in-cylinder pressure at 0.5 crank-angle interval. Crankshaft position was measured by a Kistler crank-angle encoder. The cylinder pressure was averaged over 400 cycles to smooth any combustion cyclic irregularity that may appear in diesel engines fueled with low-ignition-quality biofuels [21] and was then analyzed with a commercial combustion analyzer (DEWETRON, DEWE-ORION-0816-100X) to obtain the heat release rate due to fuel combustion, which is developed under the first law of thermodynamics to obtain the heat released arising from the fuel burned per crank angle.

Figure 4. Photograph of thermogravimetric analyzer.

http://dx.doi.org/10.5772/64470

2.4. Thermogravimetric analysis

Particulate samples used for particulate oxidation property and morphology were collected on the 47 mm quartz filter paper inside a particulate collector with the same diluted condition as TEOM. The transfer line from the exhaust to the dilutor was insulated and heated at around 170°C to avoid volatile HC condensation loss. The investigation of the particulate composition and oxidation property was conducted through the thermogravimetric analysis (TGA) on the particulate sample in an Al_2O_3 crucible. TGA was conducted using the Netzsch STA 449 TGA/DSC (thermogravimetric analysis/differential scanning calorimetry) with a measurement resolution of 25 ng as shown in **Figure 4**. The heating program is listed in **Table 6**. When the TGA temperature was below 400°C, the particulate samples were heated in argon to remove the volatile substance. The samples were then oxidized in air for the investigation of particle oxidation. The total mass loss versus TGA furnace temperature is used to determine the fraction of volatile substances (VS) and nonvolatile substances (non-VS) in the diesel particulate. The volatile substances can be divided into two parts: low- and high-volatility fractions. The volatility fraction versus temperature range is defined below:

Steps	TGA heating program
Devolatilization	
1	Initial atmosphere under argon
2	Isothermal for 10 min
3	Ramp 3°C/min to 45°C
4	Ramp 10°C/min to 400°C
Oxidation	
5	Change atmosphere with air
6	Ramp 10°C/min to 800°C
7	Isothermal for 10 min

Table 6. TGA heating program.

High-volatile substances (H-VS): $50°C \leq T \leq 250°C$, under argon environment

Low-volatile substance (L-VS): $250°C \leq T \leq 400°C$, under argon environment

Nonvolatile substances (non-VS): $400°C \leq T \leq 800°C$, under air environment

2.5. Transmission electronic microscopic analysis

The investigation of particle morphology was conducted through high-resolution transmission electronic microscopy (STEM, JEOL JEM-2100F) as shown in **Figure 5**. The maximum

magnification is up to 910,000× with a measurement resolution of about 0.2 nm. The soot samples were first collected in the 47 mm diameter quartz filter paper and the paper was cut into tiny pieces and mixed with ethanol in cylinder. The particulate sample in the filter paper was extracted ultrasonically in ethanol for 15 min. Droplets of the colloidal solution were dropped on a TEM grid by tweezer and left for drying in atmosphere before arranging image processing. The above procedures shown in **Figure 6** for preparing the TEM samples follow the method suggested by Vander Wal [22].

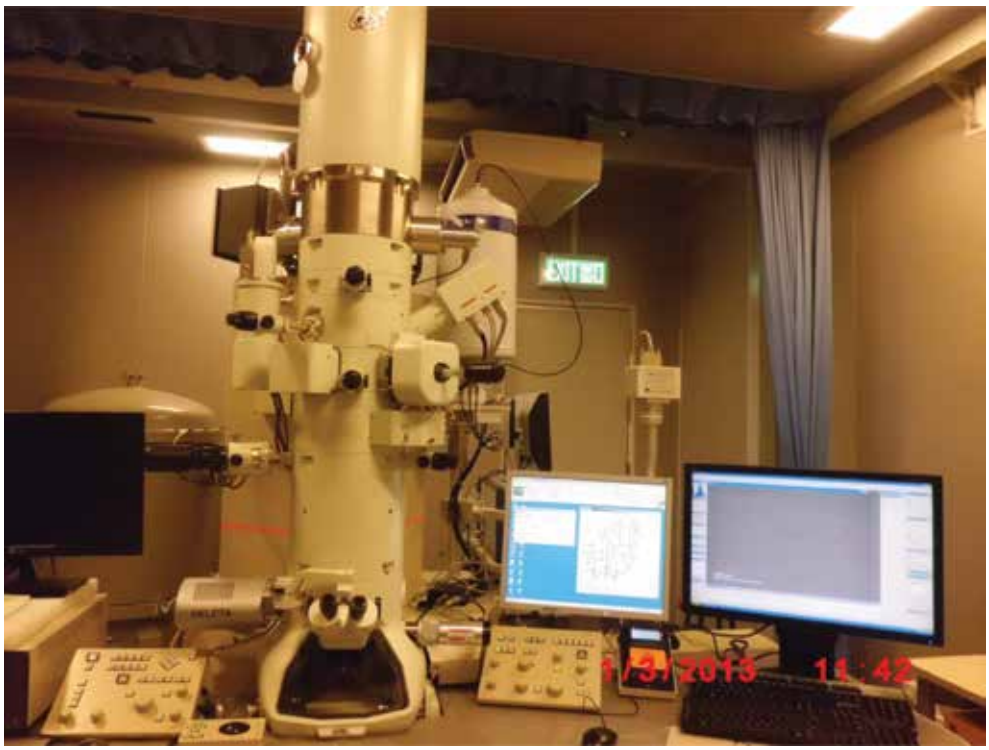

Figure 5. Photograph of high-resolution transmission electronic microscopy.

TEM images were taken from four locations with several aggregates surveyed at the same locations to maintain the consistency of examination. The commercial image processing software Image-Pro Plus 6.0 (Media Cybernetics) was used for analyzing the HRTEM images. From the images, the diameter and width of soot aggregates and primary fine particle with clear boundaries would be measured with the software. The nanostructure of primary fine particles is exhibited in the form of parallel or twisted carbon lamellae. Three parameters including fringe length, fringe separation distance, and tortuosity of the carbon lamellae could be measured and used to describe the nanostructure of particle.

http://dx.doi.org/10.5772/64470

(a) Colloidal solution is ultrasoniced for 15 minutes.

(b) Droplets are dropped on a TEM grid by tweezer.

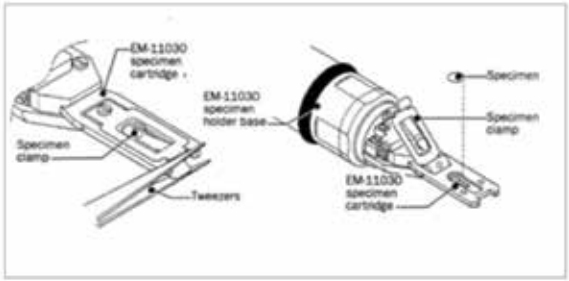

(c) Details of the specimen chamber.

(d) The TEM grid is fixed on the specimen chamber.

(e) The specimen chamber is inserted into the TEM machine for imaging

Figure 6. Procedures for preparing TEM samples. (a) Colloidal solution is ultrasoniced for 15 min; (b) droplets are dropped on a TEM grid by tweezer; (c) details of the specimen chamber; (d) the TEM grid is fixed on the specimen chamber; (e) the specimen chamber is inserted into the TEM machine for imaging.

2.6. Experimental uncertainties

Successive testing fuels will be filled in both a fuel tank and a 5 l measuring cylinder. There is a manual switch for selecting the fuel source either fed from the fuel tank or the measuring

cylinder to the engine. In order to ensure that the residual fuel from the previous test inside engine is fully consumed, a portion of around 1000 ml successive testing fuel filled in the measuring cylinder would be consumed first by the test engine running for around 5 min at each testing condition after the cooling water reached 80°C and the exhaust gas temperature become stable (±1°C). Upon consuming all the fuels in the measuring cylinder, the fuel source will then switched manually to the fuel tank for formal record of each testing case. The gaseous emissions were converted from volumetric concentrations to brake-specific emissions by employing the SAE J1088 method [23]. The steady-state tests were repeated three times to ensure that the data are repeatable within the experimental uncertainties of the measurements. The experimental uncertainty and standard errors in the measurements have been determined based on the method proposed by Moffat [24]. The measurement results obtained from different fuels were compared with baseline fuel of ultra-low-sulfur diesel (ULSD) using the two-sided Student's *t*-test to testify they are significantly different from each other at the 95% significance level.

3. Engine performance analysis

This section reports the effects of DBE blends on brake-specific fuel consumption, brake thermal efficiency, in-cylinder pressure, heat release rate, combustion duration, and diffusion fuel mass when diesel-biodiesel is blended with different ethanol contents that were tested in a diesel engine at a steady-state speed of 1800 rev/min under five engine loads of 30, 60, 120, 200, and 240 Nm corresponding to the brake mean effective pressure of 0.09, 0.17, 0.35, 0.58, and 0.70 MPa, respectively.

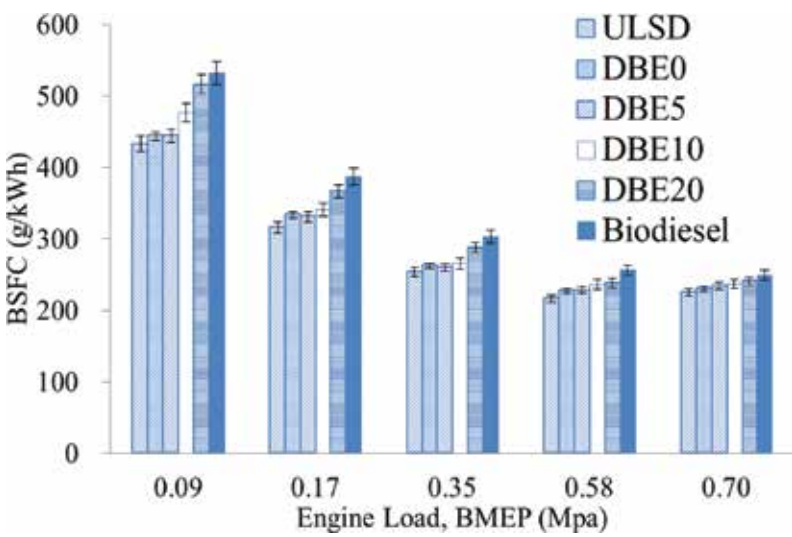

Figure 7. Comparison of BSFC.

http://dx.doi.org/10.5772/64470

3.1. Brake-specific fuel consumption

Figure 7 indicates that the brake-specific fuel consumption (BSFC) of all test fuels decreases with an increase in the engine load from 0.09 to 0.70 MPa with decreasing slope due to an increase in the brake thermal efficiency at higher engine loads. The results are similar to those reported in early works [15, 16, 25]. At each engine load, fuels having lower heating values (LHVs) require a higher fuel mass consumption rate to compensate their low-energy content for generating the same engine power. The maximum LHV (42.5 MJ/kg) belongs to neat diesel, followed by DBE5 (41.04 MJ/kg), DBE10 (40.34 MJ/kg), DBE20 (38.93 MJ/kg), and neat biodiesel (37.5 MJ/kg). At the highest test engine load of 0.70 MPa, the minimum BSFC is 225.3 g/kWh for diesel, followed by 234.8 g/kWh for DBE5, 239.1 g/kWh for DBE10, 240.5 g/kWh for DBE20, and 249.2 g/kWh for neat biodiesel. Therefore, the BSFC for neat biodiesel is the highest due to its lowest energy content while that for diesel is the least among the test fuels. The higher the proportion of ethanol in the DBE blends, the higher the BSFC is.

3.2. Brake thermal efficiency

Figure 8 indicates that the brake thermal efficiency (BTE) increases as a function of oxygen contents in the test fuels and increases with an increase in engine loads. For each engine load, the more the oxygenates are added in the fuels, the lower the heating value of the fuel blends and the higher the BSFC. However, the increase of oxygenates could provide additional lubricity, reduce fuel viscosity, improve atomization, and provide more oxygen contents for improving the combustion process in converting fuel chemical energy into useful engine work. Consequently, BTE is elevated. At the highest test engine load of 0.70 MPa, the maximum BTEs attained for biodiesel, DBE20, DBE10, DBE5, and diesel are 38.53, 37.95, 37.82, 37.36, and 37.10%, respectively. Therefore, there is no obvious variation of BTE among diesel, biodiesel,

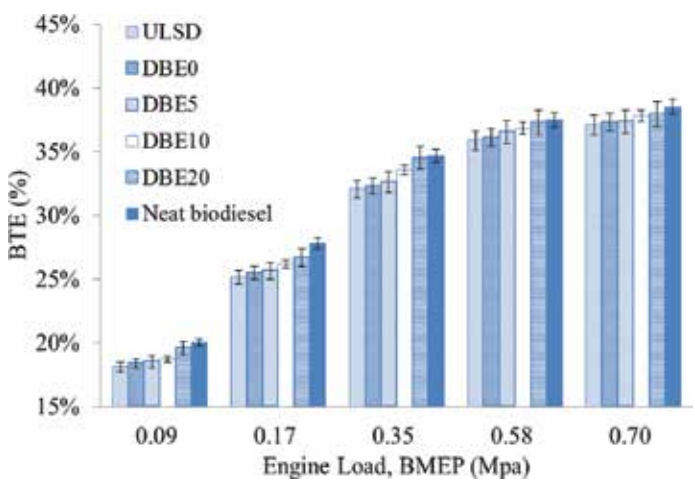

Figure 8. Comparison of BTE.

and the DBE fuels at the high engine load, which is similar to observations reported in the literature [16].

3.3. Cylinder pressure and heat release rate

The variations in the in-cylinder pressure and heat release rate are shown in **Figure 9** for different fuels at the low, medium, and high engine loads of 0.09, 0.35, and 0.70 MPa, respectively. The peak in-cylinder pressure occurs further away from the top dead center (TDC) in the expansion stroke with the increase in the engine load, which is similar to the results of Qi et al. [26]. The peak heat release rate increases with an increase in the engine load from low to the medium, but decreases at the high engine load for all test fuels, which is similar to the results of Zhu et al. [27]. The in-cylinder pressure and the peak heat release rate of DBE blends

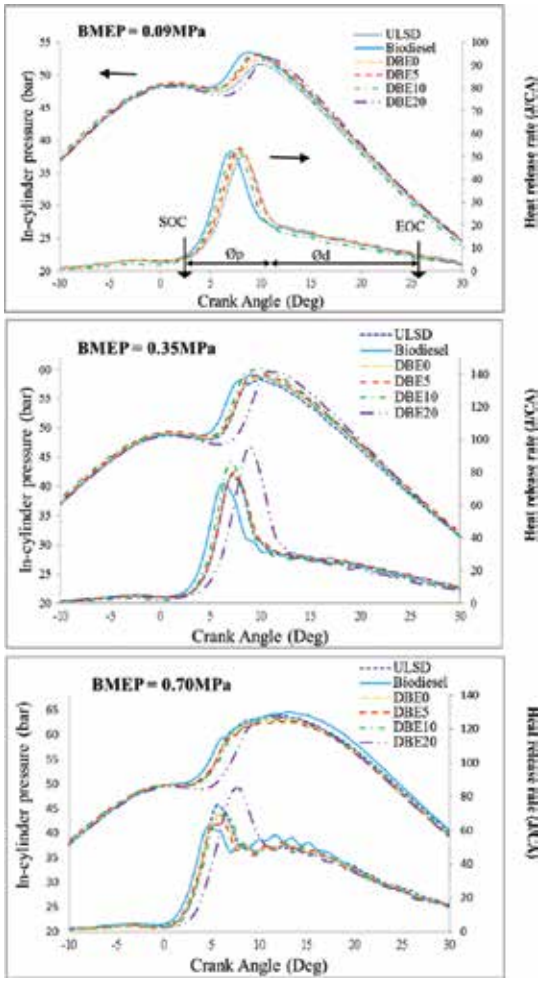

Figure 9. Variation of the in-cylinder pressure and heat release rate.

http://dx.doi.org/10.5772/64470

are comparatively higher than that of ULSD and biodiesel. With the increase of ethanol in the blended fuels, the ignition delay becomes longer. The in-cylinder pressure and peak heat release become higher and retarded due to more fuel burned in the premixed burning phase.

3.4. Start of combustion and combustion duration

The start and duration of combustion for different fuels under different engine loads are shown in **Figure 10**. It can be found that with the increase in the engine load, the start of combustion of all test fuels advances while combustion duration increases. Thus, the ignition delay decreases with the increase in the engine load. For the different fuels, the ignition delay increases in the order of biodiesel, ULSD, DBE0, DBE5, DBE10, and DBE20. The shorter ignition delay of biodiesel compared with ULSD is attributed to its higher bulk modulus of compressibility [28, 29]. Moreover, Sivalakshmi et al. [30] explained that gaseous compounds of low molecular weight, broken down from biodiesel during injection into the engine cylinder at high temperature, could ignite earlier thus reducing the ignition delay and advancing the start of combustion for biodiesel. As for the DBE blends, the increase of ethanol fractions from 0 to 20% increases the ignition delay thereby retarding the start of combustion.

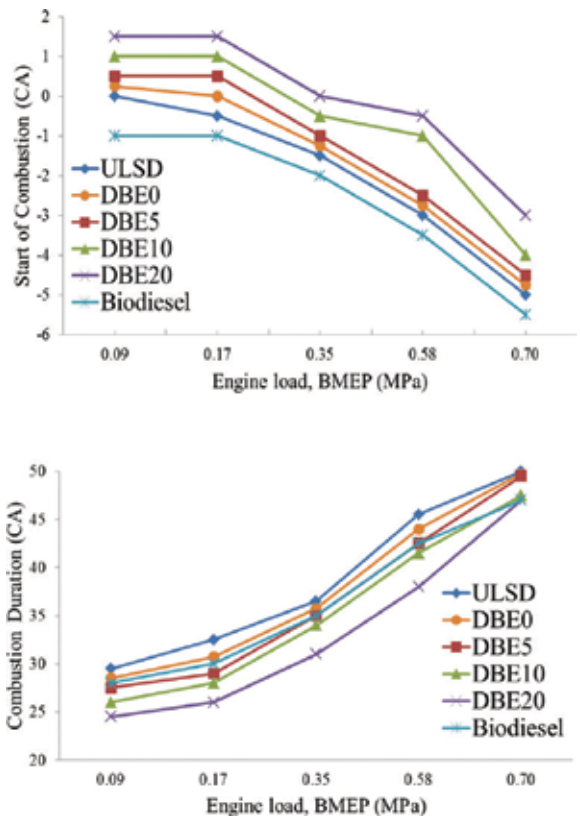

Figure 10. Variation of start of combustion and combustion duration with engine load.

The combustion duration in general increases in the order of DBE20, DBE10, DBE5, biodiesel, DBE0, and diesel. For a specific engine load, the volume of fuel consumed increases in the order of ULSD, DBE0, DBE5, DBE10, DBE20, and biodiesel due to the lower calorific values of biodiesel and ethanol compared with ULSD. DBE blends generally have longer ignition delay, larger amount of fuel burned in premixed mode, and less burned in diffusion mode, resulting in shorter combustion period when compared with biodiesel and diesel fuel for all engine loads. At high engine load, the difference in combustion duration among different fuels decreases as the ignition delay period decreases at a high engine load.

3.5. Total and diffusion fuel mass

Diesel particles are composed of soot, volatile organic fraction, and sulfate, while soot is mainly formed in the diffusion combustion mode. In order to understand the effects of combustion characteristics of different fuels on particulate emission, it is essential to examine their respective mass of fuel burnt in the diffusion mode. The variations of the total fuel mass consumption and diffusion fuel mass consumptions for different fuels with engine load are shown in **Figure 11**.

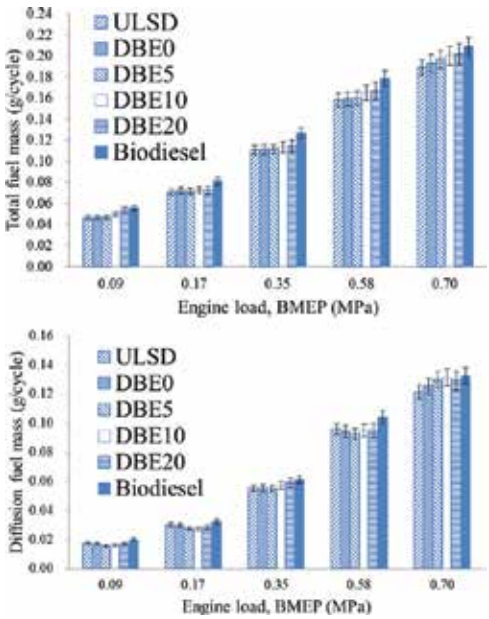

Figure 11. Variation of the total fuel mass and diffusion fuel mass with engine load.

The DBE blends retard the start of combustion and shorten the combustion duration resulting in longer premixed and shorter diffusive combustion duration when compared with biodiesel and ULSD. The higher the ethanol fraction in the blended fuel, the shorter the diffusion combustion duration and the lesser mass of fuel burned in the diffusion mode.

http://dx.doi.org/10.5772/64470

4. Regulated gaseous emission analysis

This section presents the experimental results on exhaust emissions of carbon monoxide (CO), carbon dioxide (CO_2), hydrocarbon (HC), and nitrogen oxides (NO_x) from the test diesel engine at a steady speed of 1800 rev/min under five engine loads when diesel-biodiesel blended with 0, 5, 10, and 20% ethanol. Correlation equations are formulated through a curve-fitting process for predicting percentage changes in CO, CO_2, HC, and NO_x.

4.1. Brake-specific CO and CO_2 emissions

The variations of BSCO and $BSCO_2$ emissions with engine loads are shown in **Figures 12** and **13**, respectively. BSCO decreases with the increase in the engine load. $BSCO_2$ decreases with the increase in the engine load at low engine loads and does not change much with further increase in the engine load from 0.35 to 0.70 MPa. Biodiesel has the lowest BSCO and the highest $BSCO_2$ among all the test fuels in low and medium engine loads, but at similar level with the other fuels at high loads. The BSCO emission increases with the ethanol content in the blended fuel at light and medium engine loads but at similar level at high engine loads. Compared with ULSD, BSCO emissions are increased by 2.97, 2.05, and 37.80% on arithmetic mean under the five different engine loads for DBE5, DBE10, and DBE20, respectively. The $BSCO_2$ emissions generally increase when the ethanol content is increased but the increment becomes less with increasing engine load. Compared with ULSD, $BSCO_2$ emissions are decreased by 4.41, 9.53, and 4.07% on arithmetic mean under the five different engine loads for DBE5, DBE10, and DBE20, respectively, due to a lower carbon-to-hydrogen ratio when increasing the ethanol fractions in fuels.

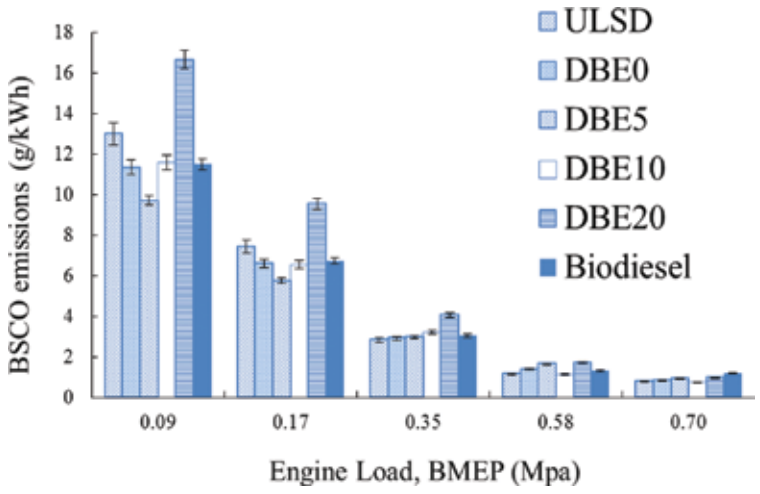

Figure 12. Variation of BSCO with engine loads.

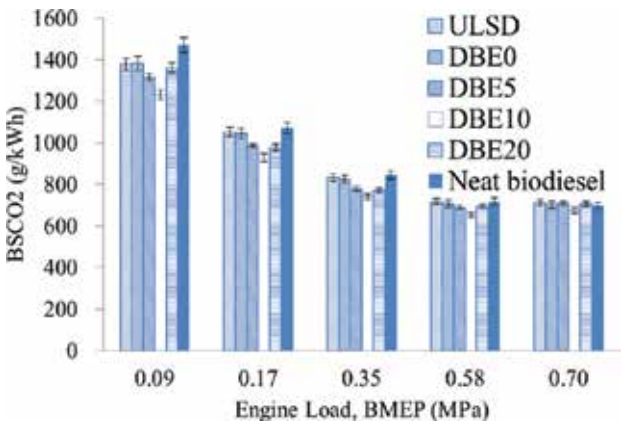

Figure 13. Variation of $BSCO_2$ with engine loads.

4.2. Brake-specific HC emissions

The variation in the brake-specific hydrocarbon (BSHC) emissions with engine load is shown in **Figure 14**. Biodiesel has the lowest BSHC emissions among the test fuels in all engine loads. The BSHC emissions of DBE blends are higher than that of ULSD in all engine loads. BSHC emission decreases with engine load but increases when the ethanol content is increased in the DBE blends at light and medium engine loads but at similar level at high engine loads. Compared with ULSD, BSHC emission decreases with engine load but increases by 45.98, 90.46, and 116.79 on arithmetic mean of the five engine loads for DBE5, DBE10, and DBE20, respectively.

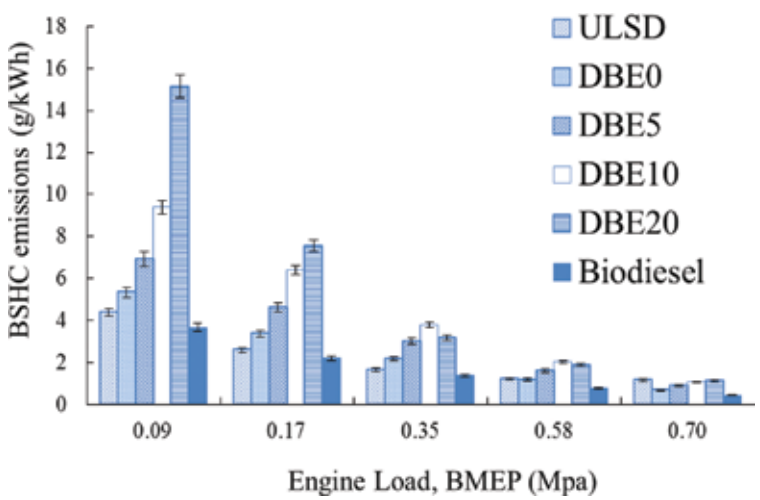

Figure 14. Variation of BSHC with engine loads.

http://dx.doi.org/10.5772/64470

4.3. Brake-specific NO_x emissions

Figure 15 shows the variation of brake-specific NO_x ($BSNO_x$) emissions with engine loads. In general, the $BSNO_x$ decreases with the increase in the engine load. Biodiesel has the highest oxygen content among the test fuels thereby having the maximum temperature during the combustion and thus the highest $BSNO_x$. The lower heating value (LHV) of ethanol is 1.3 times lower than biodiesel and 1.5 times lower than ULSD whereas the latent heat of evaporation of ethanol is about 2.8 times greater than biodiesel and ULSD, which decreases the peak temperature in the cylinder. Thus, the $BSNO_x$ decreases when the ethanol content is increased in the DBE blends from 5 to 20%. In comparison with ULSD, the $BSNO_x$ are reduced by 15–33.3, 2.9–42.4, 4.7–27.5, 4.7–21.5, and 12.5–23.2% corresponding to the five engine loads from 0.09 to 0.70 MPa under different percentages of ethanol in the DBE blends. However, some researchers observed opposite results of DBE blends on NO_x emissions [31]. Probably, in this study, the lower LHV and higher latent heat of evaporation of ethanol are more effective than the lower cetane number and higher oxygen content in influencing NO_x formation.

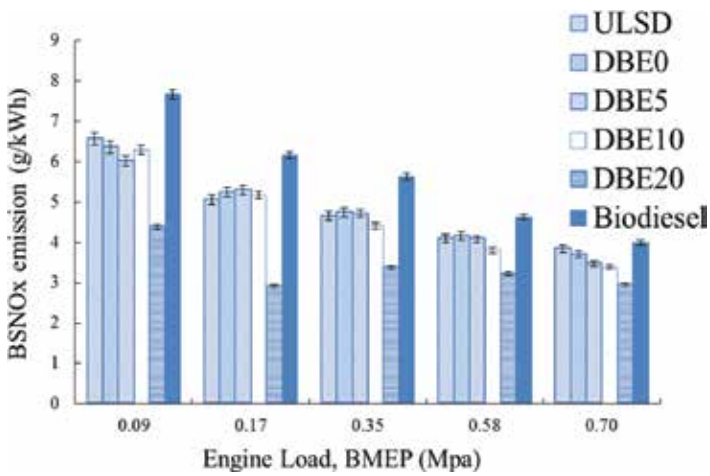

Figure 15. Variation of $BSNO_x$ with engine loads.

4.4. Emission correlation models

Statistical regression correlation is used as a method to determine how diesel engine emissions are affected by the use of DBE blends. The analysis is not intended to predict the absolute regulated emission levels, but rather the percentage change in emissions resulting from the use of DBE. The correlations are obtained by modifying the models proposed by USEPA for diesel-biodiesel blended fuels [8]. Based on the experimental data, the numerical values of the coefficients for the emission correlations obtained through statistical curve fitting are shown in **Table 7**. While for test of significance for the combination of vol% of biodiesel and ethanol, the results are shown in **Table 8**. It can be noted that the combined use of biodiesel and ethanol in DBE blends shows a significant effect in reducing the brake-specific NO_x and PM emissions

simultaneously. However, the increase of ethanol in DBE blends can increase the brake-specific CO and HC emissions due to its cooling effect on the in-cylinder gas temperature. In general, the DBE blends can reduce the above pollutants in particularly with more significant effects in reducing brake-specific CO, HC, and PM emissions. The correlation models provide engine makers or operators a tool to evaluate emissions on the use of DBE blends:

$$\%\ \text{change in BSNO}_x\ \text{emission} = (e^{[-0.0145(\text{vol\% biodiesel})]}e^{[-0.0250(\text{vol\% ethanol})]} - 1) \times 100\% \quad (1)$$

$$\%\ \text{change in BSCO emission} = (e^{[-0.0010(\text{vol\% biodiesel})]}e^{[-0.0331(\text{vol\% ethanol})]} - 1) \times 100\% \quad (2)$$

$$\%\ \text{change in BSHC emission} = (e^{[-0.0293(\text{vol\% biodiesel})]}e^{[-0.0030(\text{vol\% ethanol})]} - 1) \times 100\% \quad (3)$$

Brake-specific emission	Coefficient "a" for vol% biodiesel	Coefficient "b" for vol% ethanol
NO_x	−0.0145	−0.0250
CO	−0.0010	0.0331
HC	−0.0293	0.0030

Table 7. Coefficients for basic emission correlations.

Emission	NO_x	CO	HC
Mean square	0.0538	0.3926	1.271
Adjusted R^2	0.9796	0.9759	0.9897
Standard error	0.0271	0.0419	0.0490
F value	73.0558	223.6300	528.7205
Significance	0.0824	2.1264E−08	4.6598E−10

Table 8. Test for significance of combination of vol% biodiesel and vol% ethanol.

5. Particulate mass-number emission analysis

This section presents the experimental results on exhaust emissions of brake-specific PM emissions, combustion characteristics on PM, particle size distribution, particle number concentrations, and tradeoff relations among PM, PN, and NO_x from the test fuels.

http://dx.doi.org/10.5772/64470

5.1. Particle mass emission

Figure 16 shows that the brake-specific particulate mass (BSPM) emission of each tested fuel decreases with engine load from 0.09 to 0.35 MPa while increases from 0.58 to 0.70 MPa. At low engine loads, the fuel is burned mainly in the premixed mode and more time is available for soot oxidation, resulting in lower particulate formation. When engine load is increased, more fuel is injected into the combustion chamber and hence more fuel is burnt in the diffusion mode while less time is available for soot oxidation, leading to higher particulate formation at high engine load [16]. However, the brake thermal efficiency increases with engine load, leading to the lowest BSPM emission at the engine load of 0.35 MPa.

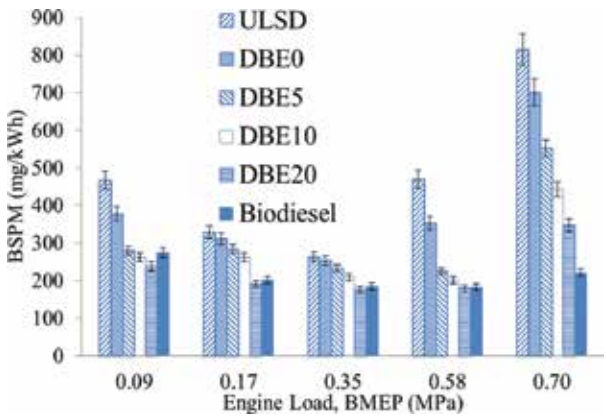

Figure 16. Variation of BSPM with engine loads.

ULSD, which has no oxygen in the fuel, has the highest BSPM among the tested fuels at all loads. When compared with ULSD, the DBE blends could effectively reduce BSPM by 19–49% at 0.09 MPa, 5–42% at 0.17 MPa, 4–33% at 0.35 MPa, 25–61% at 0.58 MPa, and 14–57% at 0.70 MPa for ethanol fractions of 0–20%. The percentage reduction increases with increase of ethanol fractions in the blended fuels. Biodiesel has the highest oxygen contents in the fuel and BSPM is always lower than that of ULSD and DBE0, but its BSPM is close to that of DBE5 at 0.09 MPa, close to that of DBE20 at 0.17–0.58 MPa, and is the lowest among all fuels at 0.79 MPa. The reduction of BSPM is resulted from the reduction of soot and sulfate in particulate. The DBE blends have oxygen concentration ranging from 1.7 to 8.2%. They are also effective in reducing BSPM emissions, compared with ULSD, due to the increasing displacement of diesel fuel by ethanol which has higher oxygen content and lower fuel aromatics and fuel sulfur, all of which are favorable for reducing soot formation.

5.2. Particle number emission

Influence of particles to the environment and human health depends not only on their mass concentration, but also on their number concentration and size distribution. It has been hypothesized that particle toxicity increases with decreasing size due to the higher specific

surface area of smaller particles [32]. It is generally believed that nanoparticles are more dangerous and hazardous to health. Therefore, the particles investigated by SMPS in this study are classified into three groups: (i) total number of particles, (ii) ultrafine particles with diameter less than 100 nm, and (iii) nanoparticles with diameter less than 50 nm. The results, including brake-specific particle number concentration (BSPN) and percentages of both ultrafine and nanoparticles evaluated based on the total particle numbers, are shown in **Table 9**.

1800 rev/min	Parameters	ULSD	Biodiesel	DBE0	DBE5	DBE10	DBE20
0.09 MPa	BSPN (#/kWh)	1.61E+15	1.96E+15	8.07E+14	1.62E+13	1.38E+13	9.84E+12
	Total number (#/cm^3)	3.05E+07	3.48E+07	1.54E+07	3.22E+05	2.65E+05	2.59E+05
	Ultrafine particle (#/cm^3)	2.74E+07 89.8%	3.35E+07 96.3%	1.35E+07 90.3%	3.02E+05 93.7%	2.51E+05 94.7%	2.46E+05 95.3%
	Nanoparticle (#/cm^3)	1.54E+07 50.5%	2.33E+07 67.0%	7.48E+06 55.2%	1.90E+05 59.0%	1.65E+05 62.3%	1.69E+05 65.2%
0.35 MPa	BSPN (#/kWh)	9.21E+14	9.96E+14	4.64E+14	8.86E+12	7.90E+12	6.46E+12
	Total number (#/cm^3)	5.15E+07	5.40E+07	2.60E+07	5.18E+05	4.67E+05	3.77E+05
	Ultrafine particle (#/cm^3)	4.39E+07 85.3%	4.97E+07 92.0%	1.96E+07 75.5%	4.09E+05 78.9%	4.16E+05 89.1%	3.43E+05 90.9%
	Nanoparticle (#/cm^3)	2.17E+07 42.1%	2.90E+07 53.7%	8.87E+06 45.2%	2.52E+05 48.6%	2.27E+05 48.6%	1.95E+05 51.7%
0.70 MPa	BSPN (#/kWh)	1.53E+15	1.49E+15	7.88E+14	1.27E+13	1.22E+13	1.33E+13
	Total number (#/cm^3)	1.25E+08	1.27E+08	6.30E+07	1.05E+06	1.03E+06	1.16E+06
	Ultrafine particle (#/cm^3)	7.99E+07 63.9%	1.16E+08 91.2%	4.36E+07 69.2%	7.39E+05 70.3%	7.47E+05 72.5%	8.46E+05 72.9%
	Nanoparticle (#/cm^3)	2.74E+07 21.9%	6.84E+07 53.8%	1.24E+07 28.5%	3.82E+05 36.3%	4.58E+05 44.5%	5.85E+05 50.4%

Table 9. Particulate emissions for different test fuels.

For each fuel, the total particle numbers, ultrafine particles, and nanoparticles increase with engine load, while BSPN is the highest at 0.09 MPa and lowest at 0.35 MPa. The increase in the aforesaid three number concentration is associated with the increasing amount of fuel with engine load and hence carbon mass with engine load. Labecki et al. [33] reported that the number concentration of nuclei mode particles (i.e., particle size < 100 nm) increased as the

http://dx.doi.org/10.5772/64470

fuel injection pressure increased at higher engine load while the number concentration of accumulation mode (i.e., 100 nm < particle size < 2500 nm) decreased with an increase in the injection pressure.

At each engine load, biodiesel is generally observed to achieve the highest in BSPN, total number, ultrafine, and nanoparticle emissions among the tested fuels although it has the lowest BSPM in most cases. Various reasons have been provided in the literature for increased particulate number concentration associated with biodiesel. Some researchers explained that biodiesel reduced soot emission due to the reduced soot surface growth rate weakening the ability of condensation and adsorption of volatile organic fractions on soot particle such that high supersaturation may lead to form more nuclei mode particles [34–36]. Tsolakis [37] reported that the higher production of smaller particles from biodiesel was due to its higher viscosity thereby increasing the fuel injection pressure for better fuel atomization and air fuel mixing. Pang [38] also found that the increased fuel injection pressure could affect particle size distribution and increase the number of nuclei mode particles during his study with a heavy-duty diesel engine.

DBE blends with ethanol could reduce BSPN, total particle numbers, ultrafine particles, and nanoparticles by 99% on average for all engine loads as compared with both biodiesel and ULSD. It is due to the combined effects of the presence of fuel-bound oxygen, reduced aromatics and sulfur compound, and the alcohol structure in ethanol which are effective on reduction of soot precursors than methyl-ester structure [39] and the subsequent reduction in particle numbers. Di et al. [17] also reported that diesel-ethanol blends gave lower total number concentrations, ultrafine particles, and nanoparticles than ULSD while diesel-biodiesel blends showed the opposite trends. Thus, besides the particulate mass reduction, DBE also plays an important role in particle number reduction.

For each fuel, the percentages of both ultrafine and nanoparticles in the total particle numbers decrease with increasing engine load, implying that the emitted particles become larger in size. Biodiesel has the highest percentage of ultrafine and nanoparticles because of its higher fuel viscosity that favors higher production of smaller particles. ULSD has the lowest percentage of ultrafine and nanoparticles, implying that larger particles are emitted than biodiesel and DBE blends.

5.3. Tradeoff relations among PM, PN, and NO_x

There is tradeoff between PM and NO_x emissions due to their contradictory responses to oxygen content in fuel. It is well known that biodiesel could reduce PM emissions but lead to an increase in NO_x emissions. Adding ethanol to a diesel fuel could reduce NO_x emissions because of the cooling effect associated with the high latent heat of evaporation of ethanol. **Figures 17** and **18** show that increasing ethanol from 0 to 20% in the DBE blends gives lower BSPM, BSPN, and $BSNO_x$ simultaneously than ULSD, weakening the PM-PN-NO_x tradeoff relationship, while compared with biodiesel, DBE blends give lower $BSNO_x$ and BSPN but higher BSPM.

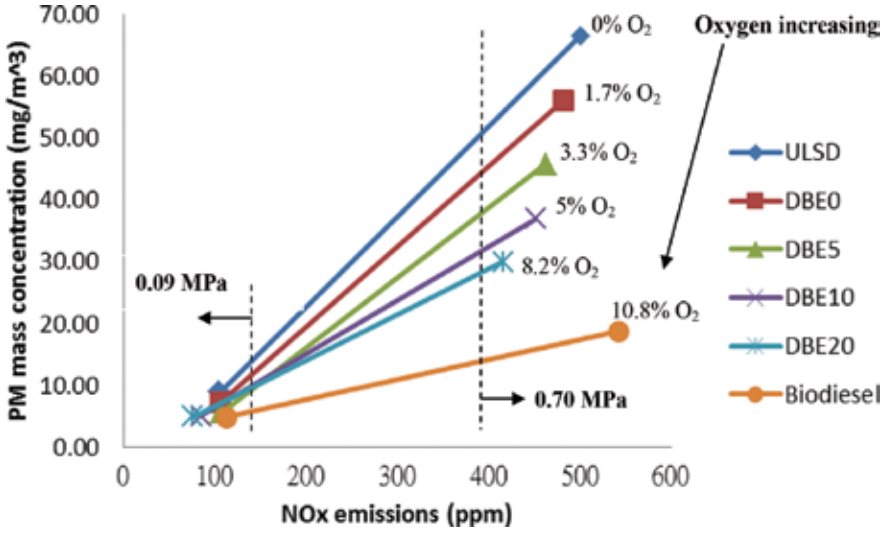

Figure 17. PM-NO_x tradeoff curves for different fuels at loads of 0.09 and 0.70 MPa.

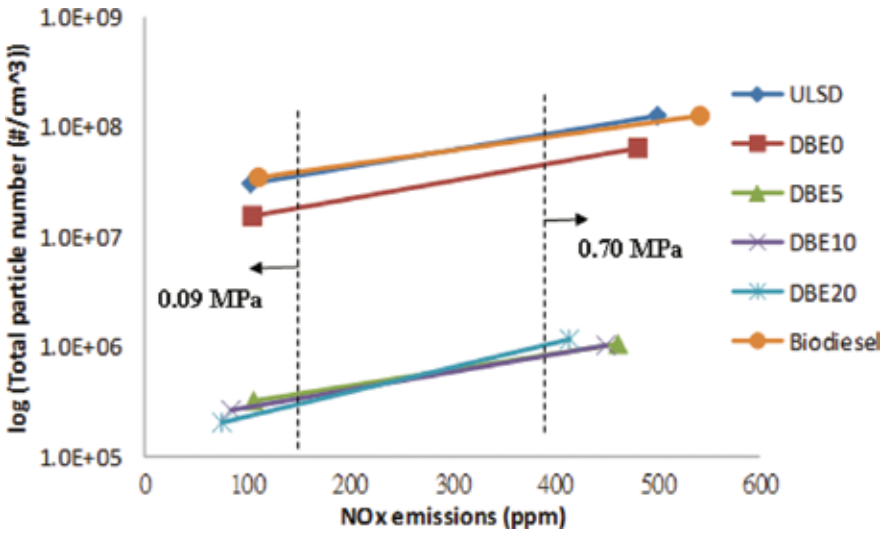

Figure 18. PN-NO_x tradeoff curves for different fuels at loads of 0.09 and 0.70 MPa.

6. Intake charge dilution

This chapter presents the experimental studies on using CO_2 to dilute the intake air of the test diesel engine to reduce NO_x while minimizing the adverse impact on particulate emissions.

http://dx.doi.org/10.5772/64470

The evaluations cover the brake-specific fuel consumption, brake thermal efficiency, combustion characteristics, brake-specific NO_x, brake-specific PM mass, and particle number emissions for diesel-biodiesel blended with 5, 10, and 20% ethanol with intake CO_2 of 1.5, 3, and 4.5% tested at a steady speed of 1800 rev/min under a high engine load of 0.58 MPa.

6.1. Brake-specific fuel consumption and thermal efficiency

At the engine load of 0.58 MPa with no intake dilution, the brake-specific fuel consumption, from the lowest to the highest, is 216.5 g/kWh for ULSD, 237.5 g/kWh for DBE5, 238.2 g/kWh for DBE10, 241.5 g/kWh for DBE20, and 255.9 g/kWh for biodiesel. The brake thermal efficiency attained for ULSD, DBE5, DBE10, DBE20, and biodiesel is 35.9, 34.2, 34.1, 33.6, and 31.6%, respectively. Increasing the ethanol fractions in DBE blends will increase the BSFC and reduce the BTE. **Figure 19** shows the effect of intake CO_2 concentration on BSFC and BTE of DBE blends at the engine load of 0.58 MPa. Increasing the intake CO_2 dilution ratio from 1.5 to 4.5% resulted in a drop in BSFCs by 0.82–1.89% for DBE5, 1.06–1.99% for DBE10, and 0.85–1.52% for DBE20, correspondingly there is an increase in BTE of 0.86–2.01% for DBE5, 1.12–2.12% for DBE10, and 0.89–2.64% for DBE20. In this particular case, CO_2 dilution leads to longer delay, resulting in higher peak pressure, higher peak heat release rate, and hence a slight improvement in BSFC and BTE.

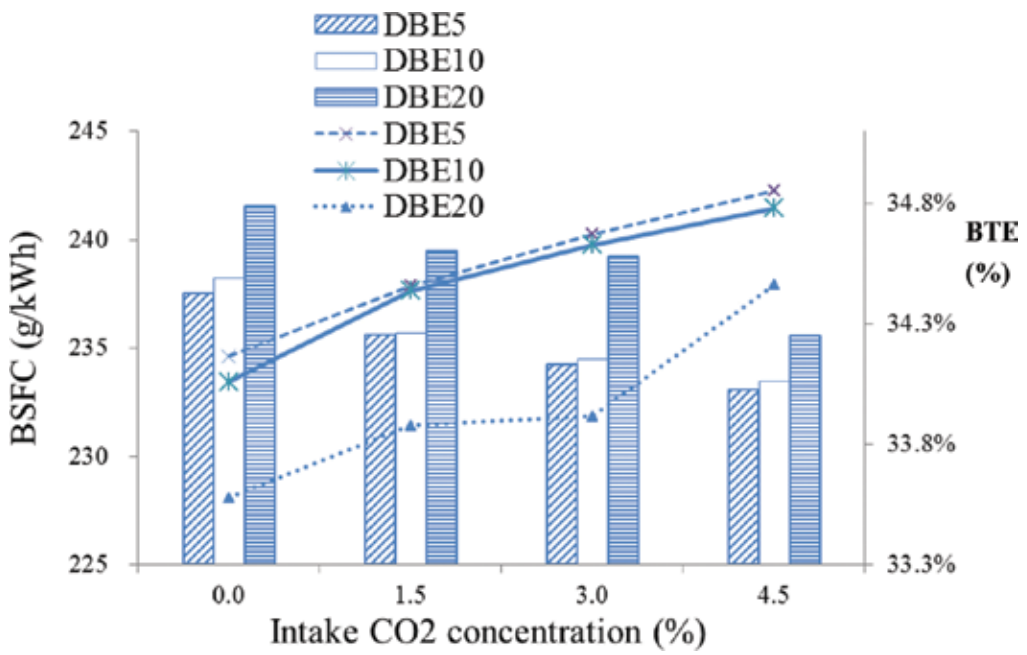

Figure 19. Effect of intake CO_2 on BSFC and BTE of DBE blends at load of 0.58 MPa.

6.2. Combustion characteristics

At the engine load of 0.58 MPa, the exhaust gas temperature of DBE5, DBE10, and DBE20 decreased from 477–467, 471–461, and 481–464°C, respectively, when CO_2 dilution was changed from 0 to 4.5%, indicating less loss in the engine exhaust. The combustion temperature reduced when CO_2 was added due to the higher specific heats of CO_2 than air. Increasing ethanol fractions in DBE blends gives higher and later peak combustion pressure and heat release rate [40]. **Figure 20** shows the in-cylinder pressure and heat release rate (averaged over 400 cycles) of DBE20 at different percentage of CO_2 dilution. Similar results are obtained for DBE5 and DBE10. In general, when intake CO_2 is applied, the maximum in-cylinder pressure increased and occurs further away from the top dead center in the expansion stroke while the peak heat release rate increased and occurs later. Increasing the CO_2 ratio from 0 to 4.5% has attained peak heat release rate of 70.7–113.3 J/°CA for DBE5, 100.1–116.8 J/°CA for DBE10, and 110.0–124.5 J/°CA for DBE20. The peak in-cylinder pressure attained for DBE5 is from 61.8 to 67.9 bar, for DBE10 is from 63.8 to 68.4 bar, and for DBE20 is from 67.6 to 68.9 bar. The in-cylinder pressure and heat release rate increased with more intake CO_2 due to the changes in thermodynamic properties of intake mixture. When intake CO_2 is applied, the ignition delay of DBE blends is further enhanced due to the reduction of oxygen and increase of specific heats of the intake charge. Therefore, a larger amount of fuel is injected into the cylinder and more fuel is prepared for combustion during the ignition delay period. When combustion starts, a greater amount of fuel is quickly consumed thereby increasing the in-cylinder pressure and heat release rate.

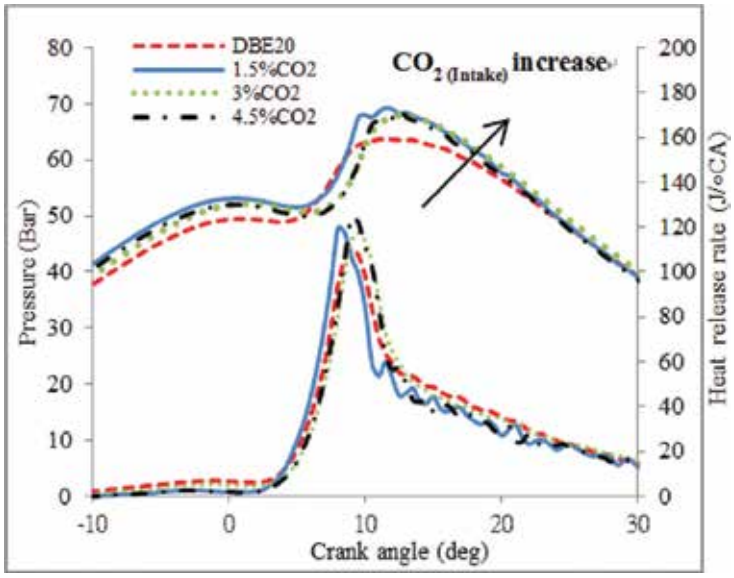

Figure 20. Effect of intake CO_2 on in-cylinder pressure and HRR of DBE20 at the engine load of 0.58 MPa.

http://dx.doi.org/10.5772/64470

6.3. Brake-specific NO_x emission

At the engine load of 0.58 MPa with no CO_2 dilution, the $BSNO_x$ is 4.75 g/kWh for biodiesel, 4.52 g/kWh for ULSD, 4.47 g/kWh for DBE5, 4.43 g/kWh for DBE10, and 3.64 g/kWh for DBE20. DBE blends could reduce NO_x emission compared with ULSD and biodiesel. When introducing CO_2 in the intake from 1.5 to 4.5% to DBE blends, the $BSNO_x$ are further reduced, leading to reductions of 9.2–70.6, 23.7–73.1, and 31.5–76.7% for DBE5, DBE10, and DBE20 respectively, as compared with ULSD as shown in **Figure 21**. There are several factors leading to the enhancement of NO_x reduction in DBE blends by CO_2 dilution. The addition of CO_2 significantly reduces the molecular oxygen and nitrogen in intake air reducing the engine-out NO_x emission. The high specific heat of CO_2 would help lowering the combustion temperature thereby suppressing the formation of NO_x from DBE blends.

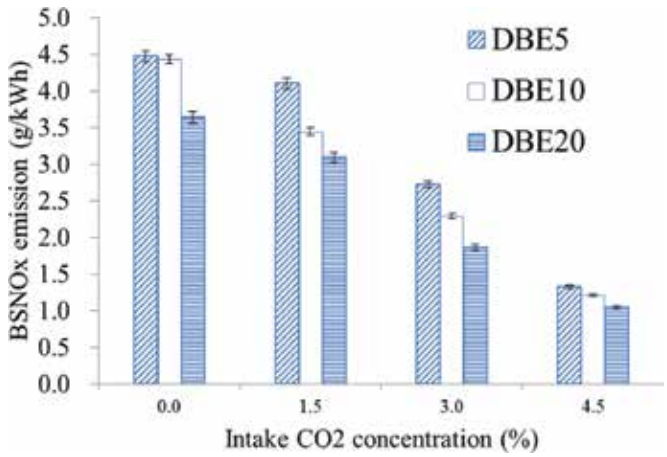

Figure 21. Effect of intake CO_2 on $BSNO_x$ of DBE blends at the engine load of 0.58 MPa.

6.4. Brake-specific PM emission

At the engine load of 0.58 MPa with no intake dilution, the maximum brake-specific particulate mass emissions (BSPM) is 469 mg/kWh for ULSD, followed by 273 mg/kWh for DBE5, 227 mg/kWh for DBE10, 207 mg/kWh for DBE20, and 184 mg/kWh for biodiesel. Increasing the ethanol fractions in DBE blends lowers the BSPM. DBE blends in general perform better than ULSD for BSPM reduction by 49.76% on average while biodiesel has attained the least BSPM emissions among the test fuels. When introducing intake CO_2 from 1.5 to 4.5%, BSPMs for the blended fuels increased but are still lower than that of ULSD but with BSPM reduction dropping from 49.76 to 36.62% on average for the three DBE blends. For individual DBE blends, the BSPM increased by 6.3–40.5% for DBE5, 2.1–29.8% for DBE10 and 0.4–47.2% for DBE20 with intake CO_2 of 1.5–4.5%. The dilution effect from CO_2 is dominant for reducing oxygen in combustion thereby increasing particulate emissions. This is because when intake air is replaced with CO_2, oxygen concentration is reduced. Besides, CO_2 would absorb some of the

released heat. Less heat will then be released during combustion to oxidize the carbon molecules [18]. With increasing CO_2 concentration, such dilution effect is greater than the chemical effect resulted from the dissociation reaction of CO_2 to nullify its soot suppression. Ladommatos et al. [41] reported that the chemical effect from CO_2 to form free radicals for soot suppression was only moderate.

6.5. Brake-specific PN emission

The use of DBE blends, compared with ULSD and biodiesel, could produce less total number of particle concentration of all sizes from low to high engine loads [40]. Increasing the ethanol fractions from DBE5 to DBE10, the carbon content of the blended fuel decreased and oxygen content increased leading to reduction of nuclei particles and total number concentration as shown in **Table 9**. **Figure 22** shows that when adding 1.5% intake CO_2 to DBE blends, there is a decrease in the brake-specific particle number concentration (BSPN). The BSPN however increased with increase of intake CO_2. This effect can also be observed from **Figure 23** which shows the size distributions for DBE20 against CO_2 intake at the engine load of 0.58 MPa. The initial decrease in BSPN with 1.5% CO_2 intake may be a consequence of the dissociation of intake CO_2 which has moderate effects on soot suppression. However, when CO_2 intake increases from 1.5 to 4.5% in the blended fuels, the size distribution curves move upward indicating an increase in the particle number concentration with larger diameter particles. The BSPNs at 4.5% CO_2 intake are higher than those obtained without CO_2 dilution. This is because the dilution effect of CO_2 becomes dominant nullifying the effect of CO_2 dissociation [41]. The reduction of oxygen concentration from the dilution effect therefore increases the particulate mass and particle number concentrations.

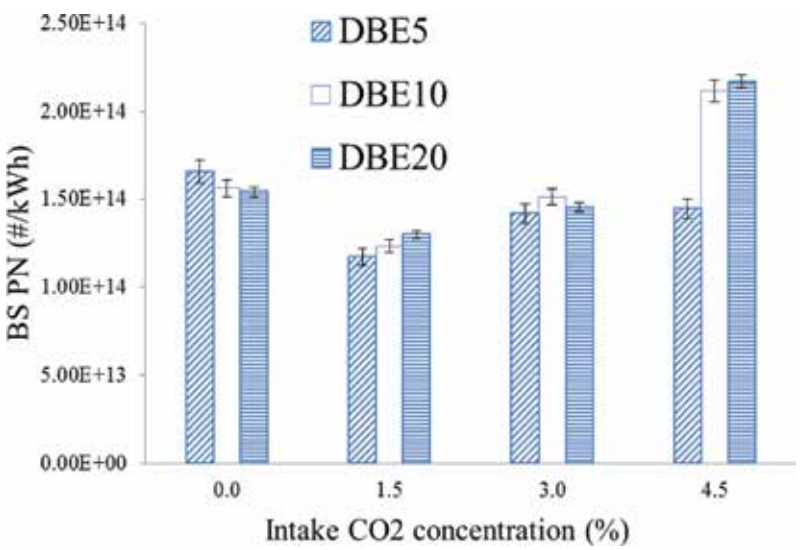

Figure 22. Effect of intake CO_2 on BSPN of DBE blends at the engine load of 0.58 MPa.

http://dx.doi.org/10.5772/64470

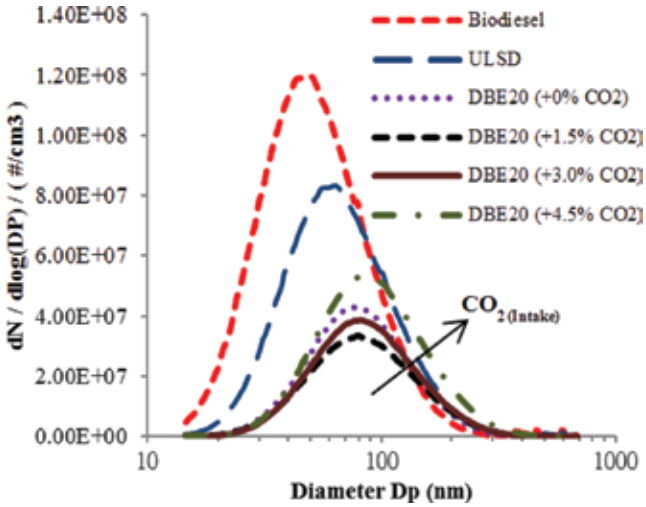

Figure 23. Effect of intake CO_2 on size distribution of DBE20 at the engine load of 0.58 MPa.

7. Thermogravimetric analysis

This section presents the experimental TGA analysis to compare the particle volatility and oxidative reactivity from DBE-derived soot under different blending compositions with those from ULSD and neat biodiesel. The reactivity of particulate samples can be related to the differences in fuel oxygen contents, percentage of VOCs, and soot burnout temperature. Hence, the evaluations would cover brake-specific VOF emissions, soot ignition temperature, activation energy, and oxidative reactivity for DBE blends tested at a steady speed of 1800 rev/min under a high engine load of 0.58 MPa.

7.1. Particle volatility

Figure 24 shows particulate mass reduction curves for different fuels at the engine load of 0.58 MPa. For each fuel, obvious carbon mass losses were found at two different temperature segments: (i) below 300°C and (ii) 550–700°C, representing loss of the volatile organic fraction and oxidation of the nonvolatile fraction, respectively. **Figure 25** shows the effect of fuel type and engine load on the volatile organic fractions (%VOF) in PM emissions. It can be seen that no matter what kind of fuel is used, %VOF decreases remarkably from 27.8 to 11.2% for ULSD, 36.6 to 14.6% for DBE0, 41.5 to 15.0% for DBE5, 46.0 to 17.7 % for DBE10, 48.7 to 19.5% for DBE20, and 73.8 to 29.5% for biodiesel with an increase in the engine load from 0.17 to 0.58 MPa. It is because VOF consisting of unburned HC is removed significantly under high combustion temperature at high load. For different fuels under each engine load, %VOF is affected and increased with increasing oxygen contents in the fuels, being the lowest for ULSD; increasing with ethanol additions in the blended fuels; and up to the highest for biodiesel, as shown in **Figure 25**. The higher %VOF in soot particles originating from oxygenated fuels like

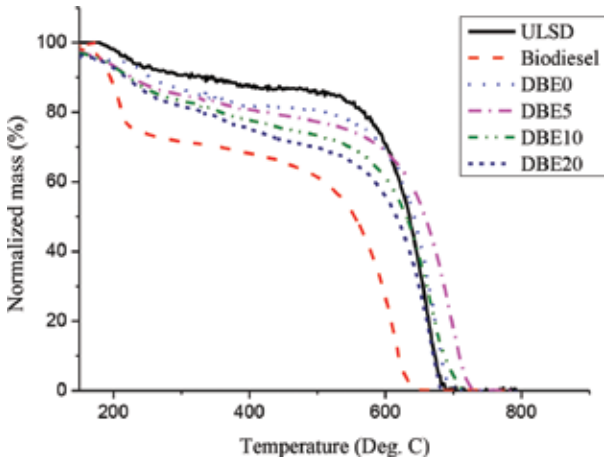

Figure 24. Particulate mass reduction curve for different fuels at a high engine load of 0.58 MPa.

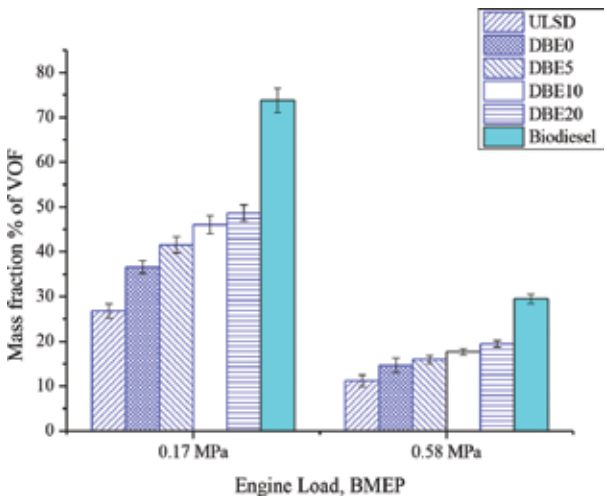

Figure 25. Mass fraction % of VOF with different fuels at two different engine loads.

biodiesel is associated with the higher surface/volume ratio of these particles, implying more pores for condensation and adsorption of unburned HC. **Figure 26** shows the brake-specific VOF emission (BSVOF). At 0.17 MPa, comparing the different fuels, the BSVOF increases with increasing oxygen content in the fuel despite there is a decrease in BSPM with increasing oxygen content in the fuel. However, at 0.58 MPa, it decreases from ULSD to DBE20 but biodiesel has the highest BSVOF. Thus, at light load, due to the higher %VOF in the PM, the blended fuel leads to a higher VOF emission, while at high load the blended fuel leads to a reduction in both PM and VOF. The effect of high combustion temperature overrides the evaporation latent heat of ethanol and the oxygen conditions surrounding the blended fuel

http://dx.doi.org/10.5772/64470

benefit of the combustion such that the VOF component tends to decrease when the % ethanol in fuel increases up to 20%. Especially, BSVOF for biodiesel is the highest and ULSD is the second highest than that for other fuels. This is because biodiesel having more active surface pores and ULSD having higher concentrations of nucleated sulfur acid particles [42] for the condensation of VOF.

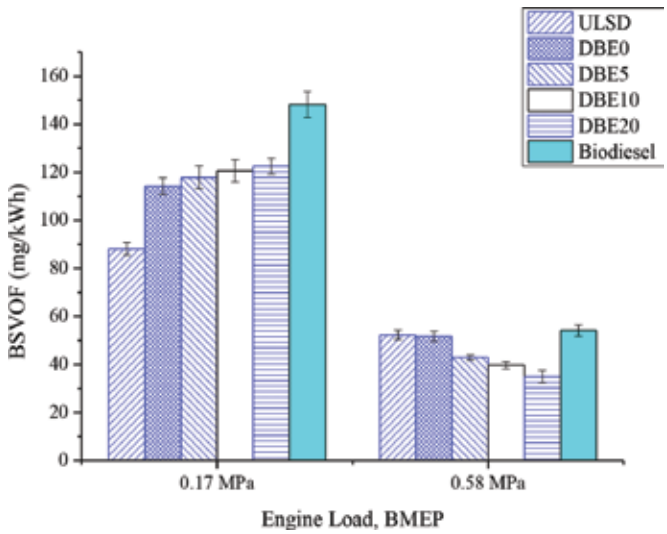

Figure 26. Variation of BSVOF with different fuels at two different engine loads.

7.2. Particle oxidative reactivity

The oxidation reactivity of combustion particles can be quantified by their soot ignition temperatures [43]. **Figure 27** shows the ignition temperature, at which the maximum heat flow rate occurs, of each fuel at the engine load of 0.58 MPa. It is the highest for ULSD (721.1°C) and the lowest for biodiesel (627.0°C), while for the blended fuels it decreases from 695.2 to 680.0°C with increased ethanol content from 0 to 20% in the fuel. In general, the ignition temperature decreases with the increase in the oxygen content in the fuel.

Based on the TGA data, a kinetic analysis was conducted on the oxidation of the nonvolatile fraction by using the Arrhenius plot of oxidation rates. **Table 10** shows the calculated kinetic parameters for particulate samples obtained from different fuels at the engine load of 0.58 MPa. The activation energy is the highest for diesel fuel and the lowest for biodiesel, while for the blended fuels it decreases with the increase in the ethanol content in the fuel. Thus, it decreases with increase in the oxygen content in the fuel. The lower the activation energy is, the higher the oxidative reactivity of the particulate sample will be [42]. Stanmore et al. [44] also reported that lower activation energy and higher reactivity could lead to lower ignition temperature. The above results indicate that the oxidative reactivity of particulates decreases in the order of biodiesel, DBE20, DBE10, DBE5, DBE0, and ULSD.

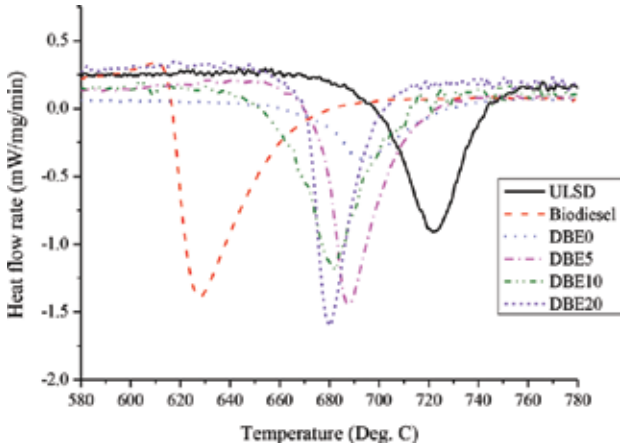

Figure 27. Heat flow rate (derivative of DSC signal) curves for different fuels at a high engine load of 0.58 MPa.

Fuels	BMEP (MPa)	Oxygen content (%)	Ignition temperature (°C)	Calculated activation energy (kJ/mol)	Calculated frequency factor (Sec^{-1})
ULSD	0.58	0.0	721.10	166.30	2.39E+08
DBE0	0.58	1.7	695.20	137.13	3.12E+07
DBE5	0.58	3.3	689.41	116.90	1.33E+07
DBE10	0.58	5.0	683.54	109.10	9.42E+06
DBE20	0.58	8.2	680.04	81.43	1.12E+06
Biodiesel	0.58	10.8	627.02	65.20	4.44E+05

Table 10. Calculated kinetic parameters of particulate samples of different fuels.

Particle volatility also affects the oxidation process. During the initial TGA thermal treatment from room temperature to 380°C, volatile fractions of test fuels filled inside the micropores of soot aggregates are removed under the argon environment. More internal particle surface areas are therefore available for subsequent soot oxidation. As such, higher %VOF would contribute higher reactivity and oxidation rate of particulates.

8. Transmission electron microscope analysis

This section is to investigate the particulate volatility and oxidation by a thermogravimetric analysis and morphology by transmission electron microscope analysis on a four-cylinder DI diesel engine using DBE blends with ethanol addition of 0, 5, 10, and 20% tested at a steady speed of 1800 rev/min under low and high engine loads of 0.17 and 0.58 MPa, respectively.

http://dx.doi.org/10.5772/64470

8.1. Properties of diesel agglomerates

The measurement of agglomerates includes maximum projected length (L) and maximum projected width normal to length (W) and projected primary particle diameter (D) and primary particle area (A). **Figures 28–33** shows the soot agglomerates produced from ULSD, biodiesel and DBE blends at the engine loads of 0.17 and 0.58 MPa, respectively. Agglomerates from different fuels at different loads were found to be composed of fine primary particles forming a mixture of chain-like structures and clusters of spherules. **Table 11** summarizes the above measurements of the soot agglomerates and their respective primary particles. For each fuel, the projected diameter and area of primary particles increase with engine load because more fuel is burned at higher load resulting in the growth of soot nuclei. The projected primary particle diameter increases in the order of DBE20 (15–18 nm), DBE10 (17–20 nm), DBE5 (19–23 nm), DBE0 (20–24 nm), biodiesel (24–31 nm), and ULSD (34–41 nm). The DBE blends, compared with biodiesel and diesel, produced smaller primary particles. Increasing the proportion of ethanol from DBE5 to DBE20, the carbon content of the blend fuels decreases and the oxygen content increases leading to the reduction of soot nuclei. The possibility of agglomeration and condensation of smaller particles to form larger ones is then reduced, leading to smaller agglomerates and primary particles. In this study, increasing ethanol from 5 to 20%, the projected length of agglomerates from DBE blends decreases from 448 to 419 nm at 0.17 MPa and 508 to 449 nm at 0.58 MPa while the projected width decreases from 562 to 387 nm at 0.17 MPa and 625 to 415 nm at 0.58 MPa.

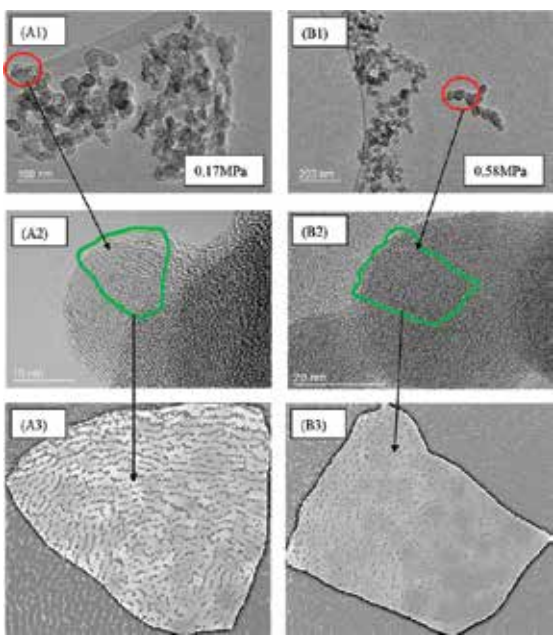

Figure 28. ULSD-derived primary particles at loads of 0.17 and 0.58 MPa: (1) TEM image, (2) high-magnified TEM image for ROIs, and (3) skeletonized ROI images.

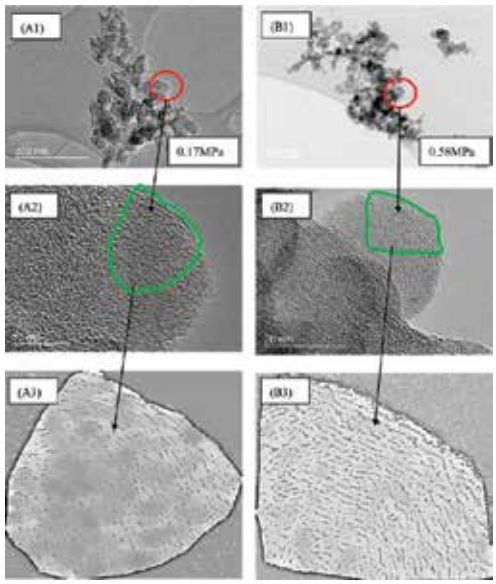

Figure 29. Biodiesel-derived primary particles at loads of 0.17 and 0.58 MPa: (1) TEM image, (2) high-magnified TEM image for ROIs, and (3) skeletonized ROI images.

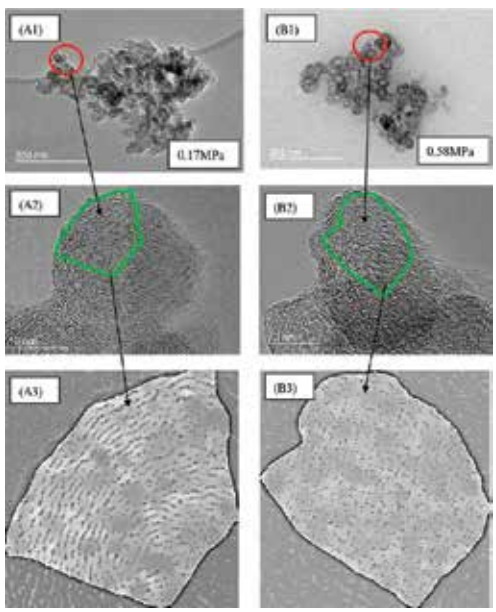

Figure 30. DBE0-derived primary particles at loads of 0.17 and 0.58 MPa: (1) TEM image, (2) high-magnified TEM image for ROIs, and (3) skeletonized ROI images.

http://dx.doi.org/10.5772/64470

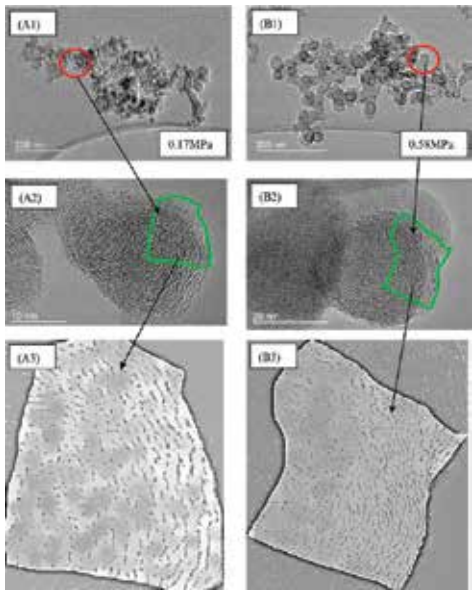

Figure 31. DBE5-derived primary particles at loads of 0.17 and 0.58 MPa: (1) TEM image, (2) high-magnified TEM image for ROIs, and (3) skeletonized ROI images.

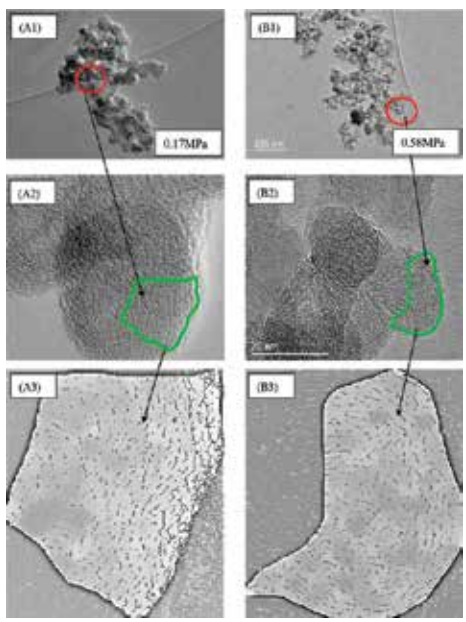

Figure 32. DBE10-derived primary particles at loads of 0.17 and 0.58 MPa: (1) TEM image, (2) high-magnified TEM image for ROIs, and (3) skeletonized ROI images.

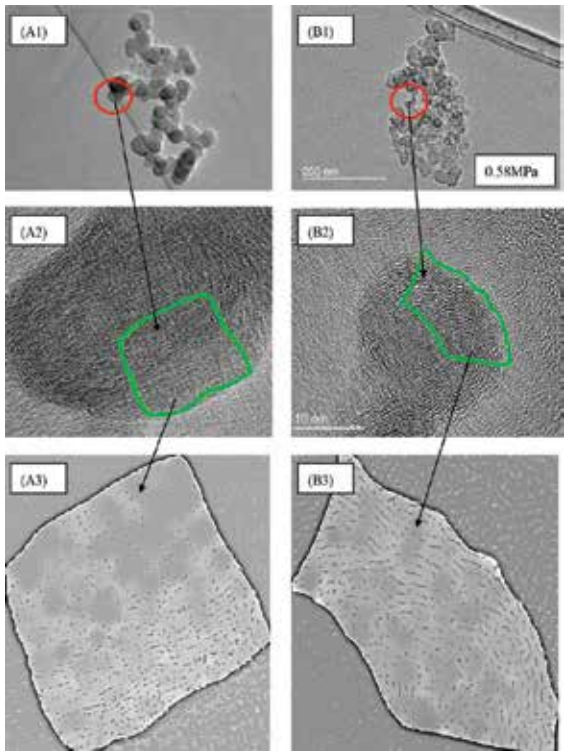

Figure 33. DBE20-derived primary particles at loads of 0.17 and 0.58 MPa: (1) TEM image, (2) high-magnified TEM image for ROIs, and (3) skeletonized ROI images.

8.2. Properties of fine particle nanostructures

For individual primary particle, the examination of its structure and distribution of graphene layers provide information about its nanostructure morphology. The classic core-shell structure of a primary particle from diesel fuel has an outer shell composed of planar-shaped crystallites oriented perpendicular to the radius of the particle and an inner core constituted by several fine spherules at the central portion. Other authors found different internal structures of diesel particles subject to different thermal exposure including (a) fullerenoid or onion-like morphology, (b) turbostratic graphite structures formed by small plates of undefined orientation, (c) purely turbostratic layers, and (d) structures formed by multiple spherical nuclei surrounded by several graphitic layers [19, 45–47]. The nanostructure can be further characterized and quantified by the fringe length, fringe separation, and tortuosity [48]. Variation in these parameters indicates different carbon nanostructures such as graphitic, fullerenic, and amorphous. HRTEM images at a high-magnification level in **Figure 28(A2)** and **(B2)** to **Figure 33(A2)** and **(B2)** show different morphology for fine primary particles from ULSD and biodiesel and DBE blends at engine loads of 0.17 and 0.58 MPa, respectively. Selected region of interest (ROI) on each image was processed and the skeletonized ROI binary images converted from **Figure 28(A1)** and **(B1)** to **Figure 33(A1)** and **(B1)** are shown in **Figure 28(A3)**

http://dx.doi.org/10.5772/64470

and **(B3)** to **Figure 33(A3)** and **(B3)**, respectively. They are further used to evaluate the nanostructure characteristics such as fringe length, fringe separation and, tortuosity. **Table 12** summarizes the measurements obtained by lattice fringe analysis, following the procedures in Vander Wal et al. [48] and Shim et al. [49].

Fuels	Load (MPa)	Figures	Numbers of agglomerates	$L_{average}$ (nm)	$W_{average}$ (nm)	$(L/W)_{average}$	Numbers of particles	$D_{average}$ (nm)	$A_{average}$ (nm^2)
ULSD	0.17	**Figure 28 (A1)**	4	241±23	303±45	0.8±0.3	39	34±4	942±29
Biodiesel	0.17	**Figure 29 (A1)**	4	488±48	424±56	1.3±0.4	35	24±4	485±32
DBE0	0.17	**Figure 30 (A1)**	4	360±23	363±20	0.9±0.3	43	20±3	332±29
DBE5	0.17	**Figure 31 (A1)**	4	448±75	562±52	0.9±0.4	52	19±3	300±24
DBE10	0.17	**Figure 32 (A1)**	4	434±54	417±23	1.0±0.2	47	17±5	224±15
DBE20	0.17	**Figure 33 (A1)**	4	419±68	387±41	1.1±0.3	46	15±4	172±17
ULSD	0.58	**Figure 28 (B1)**	4	275±50	373±33	1.0±0.4	29	41±7	1332±12
Biodiesel	0.58	**Figure 29 (B1)**	4	735±57	790±81	0.9±0.3	45	31±3	749±21
DBE0	0.58	**Figure 30 (B1)**	4	459±74	690±65	0.7±0.2	33	24±3	471±13
DBE5	0.58	**Figure 31 (B1)**	4	508±76	625±51	0.8±0.2	49	23±3	417±15
DBE10	0.58	**Figure 32 (B1)**	4	506±61	487±38	1.1±0.1	44	20±4	343±20
DBE20	0.58	**Figure 33 (B1)**	4	449±98	415±41	1.2±0.4	42	18±2	244±19

Table 11. Measurement of the soot agglomerates and their respective primary particles.

In general, the high-engine-load particulate samples for each test fuel exhibit more ordered and clear graphitic structures when compared with low-engine-load samples. At low engine load, particulate samples examined under the TEM micrographs are more amorphous and disordered due to their high content of volatile organic substances in the samples, which is in line with the findings from Lu et al. [42]. While increasing engine load with higher exhaust temperature, volatile organic substances in the samples are burnt out and the particles are then distinct and graphitic in morphology. Zhu et al. [20] in their study reported similar results that crystallite dimension of diesel particulate increases with engine load and exhaust temperature on a light-duty diesel engine.

For ULSD-derived soot, the primary particles possess typical shell-core structures and concentric ring patterns as shown in **Figure 28**. With an increase in the engine load from 0.17 to 0.58 MPa, the mean fringe length increases from 1.012 to 1.075 nm, the mean tortuosity is approximately in the range of 1.077–1.079 signifying that the fringes are not highly curved, and the mean fringe separation decreases from 0.414 to 0.336 nm. For biodiesel-derived soot, the primary particles possess long-range layers concentrically arranged along the outermost

periphery and short layers amorphously inside the inner as shown in **Figure 29**. When the engine load is increased from 0.17 to 0.58 MPa, the mean fringe length increases from 0.658 to 0.859 nm, the mean tortuosity decreases significantly from 1.117 to 1.111, indicating that the curvature of fringes slightly weakens under high load condition and the mean fringe separation is approximately in the range of 0.182–0.191 nm.

Fuels	Load (MPa)	Figures	Fringe length (nm)	Fringe separation (nm)	Tortuosity
ULSD	0.17	**Figure 28 (A3)**	1.012 ± 0.032	0.414 ± 0.012	1.079 ± 0.032
Biodiesel	0.17	**Figure 29 (A3)**	0.658 ± 0.079	0.191 ± 0.009	1.117 ± 0.040
DBE0	0.17	**Figure 30 (A3)**	0.969 ± 0.029	0.359 ± 0.023	1.107 ± 0.039
DBE5	0.17	**Figure 31 (A3)**	0.950 ± 0.020	0.350 ± 0.001	1.109 ± 0.042
DBE10	0.17	**Figure 32 (A3)**	0.903 ± 0.049	0.335 ± 0.022	1.111 ± 0.027
DBE20	0.17	**Figure 33 (A3)**	0.836 ± 0.078	0.320 ± 0.011	1.114 ± 0.009
ULSD	0.58	**Figure 28 (B3)**	1.075 ± 0.012	0.336 ± 0.014	1.077 ± 0.030
Biodiesel	0.58	**Figure 29 (B3)**	0.859 ± 0.067	0.182 ± 0.032	1.111 ± 0.038
DBE0	0.58	**Figure 30 (B3)**	1.033 ± 0.061	0.331 ± 0.019	1.068 ± 0.041
DBE5	0.58	**Figure 31 (B3)**	0.999 ± 0.041	0.345 ± 0.021	1.105 ± 0.014
DBE10	0.58	**Figure 32 (B3)**	0.987 ± 0.051	0.204 ± 0.031	1.078 ± 0.033
DBE20	0.58	**Figure 33 (B3)**	0.947 ± 0.071	0.289 ± 0.024	1.108 ± 0.037

Table 12. Measurement of the nanostructure characteristics.

For DBE-derived soot, fullerenic-like nanostructures are observed in **Figures 30–33**. The soot particles possess spherical buckyballs in center surrounded by the outer graphitic structures. For each blended fuel, increasing engine load increases the mean fringe length but decreases the tortuosity and fringe separation distance. With increasing ethanol contents in the blended fuels, the lamellae are more curved, tortuous, and disorganized. With ethanol addition from 0 to 20%, the mean fringe length reduces from 0.969 to 0.836 nm at 0.17 MPa and from 1.033 to 0.947 nm at 0.58 MPa. As compared with ULSD, DBE blends have lower mean fringe lengths reflecting more amorphous nanostructure while biodiesel has the least mean fringe lengths. The curvature of fringes for DBE blends increases with ethanol addition in particular under low load condition with mean tortuosity of 1.107–1.114 at 0.17 MPa. As for the mean fringe separation distance, ethanol addition has only mild effect and it decreases from 0.359 to 0.320 nm at low load and from 0.331 to 0.289 nm at high load.

Vander Wal et al. [22] reported that amorphous or fullerenic structured soots produced from oxygenated fuels would oxidize faster than graphitic structured soot from conventional diesel fuel thus producing less soot from tailpipe. The increase of tortuosity reflects the more amorphous structures produced from the soot. Tortuosity increases fringe separation such that adjacent carbon layer planes are more separated and more oxygen can access to the highly reactive edge-site carbon for oxidation. Song et al. [50] reported that the more amorphous arrangement within the particles reflected the more edge-site carbon density.

http://dx.doi.org/10.5772/64470

By combining the particulate emissions, and TGA and TEM results, the effects of engine load and fuel oxygenation on particle characteristics can be summarized. For the effect of engine load, it is found from all tested fuels that increasing load can lead to higher BSPM and BSPN emissions with larger primary particles formed but with lower BSVOF emissions. Under high combustion temperature at high load, the primary particles of all fuels exhibit more distinct structures as a consequence of the burnout VOFs. For all fuels, the mean fringe length decreases, and the mean fringe separation and tortuosity increase with the increase in the engine load except for the fringe length of DBE20 and tortuosity of ULSD which are not significantly influenced. Therefore, the engine load affects not only particulate mass-number emissions but also the graphitization of primary particles. For the effect of fuel oxygenation, it is generally found that with higher oxygen content in the fuel, the particulates would have larger percentage of VOF, lower soot burnout temperature (low activation energy), stronger oxidative reactivity, smaller primary particles, and more curved, tortuous, and disorganized nanostructures.

In general, the oxidative reactivity of particulates decreases in the order of biodiesel, DBE20, DBE10, DBE5, DBE0, and ULSD. Therefore, fuel oxygenation has more significant effect on reducing soot burnout temperature, lowering resistance to oxidation, and shifting toward more amorphous structures, thereby affecting particle volatility, oxidation, and morphology.

9. Conclusions

The performance of current available engine technologies is almost close to the statutory emission limits. In recent years, there has been an increase in fuel-change researches worldwide on use of transport biofuels such as biodiesel and alcohol to reduce engine emissions and fuel consumption as supplement measures without any engine modification works. In this study, engine experiments are performed with diesel-biodiesel blended with 0, 5, 10, and 20% ethanol with intake CO_2 ranging from 0 to 4.5%, at 1.5% interval, in a four-cylinder naturally aspirated DI engine tested at 1800 rev/min under different engine loads.

Engine performance, combustion characteristics, gaseous emissions, and particulate morphology are evaluated for assessing diesel-biodiesel-ethanol (DBE) blends as future fuel-change technology for using these three fuels efficiently, reducing engine emissions and minimizing reliance on diesel fuel. Each experimental test is repeated three times to ensure that the results are repeatable within the experimental uncertainties. Student's *t*-test is employed to analyze whether the difference between the results obtained from different test fuels are statistically significant at the 95% confidence level. The main conclusions from this study are drawn as follows:

1. DBE blends can effectively reduce the emissions of NO_x and C_{O2}, and PM and total particle number concentration of all sizes but lead to an increase of CO and HC emissions in low engine loads which could be resolved using diesel oxidation catalytic converter. The use of DBE facilitates the effective use of diesel-biodiesel blended fuels with improved fuel quality and reduced emissions, in particular for NO_x and PM, without the need for engine

modification. On engine performance, brake-specific fuel consumption increases with ethanol in DBE blends and the increases slightly due to improved brake thermal efficiency (BTE) at high engine loads. BTE also increases with ethanol, but again increases slightly when cooling effects of ethanol are nullified with the high in-cylinder gas temperature at high engine loads. From low to medium engine loads, the in-cylinder pressure curve of DBE blends shifts away from top dead center to the right when increasing ethanol contents. But at high loads, there is no significant change in the cylinder pressure rise with ethanol addition as a result of the shortened ignition delay period and consequently less fuel accumulates and burns in the premixed phase.

2. DBE blends have comparatively higher oxygen content, lower carbon content, and lower diffusion fuel mass than ultra-low-sulfur diesel (ULSD). Increasing ethanol fractions in DBE blends, cetane number decrease leading to longer ignition delay and shorter combustion duration. The improved combustion with more oxygen contents and lower diffusion fuel mass from DBE blends enhance the reductions of brake-specific particulate mass (BSPM) and particle number (BSPN) emissions. The application of DBE blends can attain lower BSPM and BSPN emissions in particular with lesser ultrafine and nanoparticle concentrations than ULSD. On the contrary, biodiesel led to increase of total particle, ultrafine, and nanoparticle concentrations.

3. CO_2 is used to dilute the intake air of a four-cylinder DI diesel engine fueled by DBE blends to reduce NO_x while minimizing the adverse impact on particulate emissions at high engine load. The results include brake-specific fuel consumption, brake thermal efficiency, combustion characteristics, brake-specific NO_x, brake-specific PM mass, and particle number emissions for diesel-biodiesel blended with 5, 10, and 20% ethanol with intake CO_2 of 1.5, 3, and 4.5% tested at a steady speed of 1800 rev/min under a high engine load of 0.58 MPa. It is found that combined effect of DBE blends with intake CO_2 dilution has marginal effects on brake-specific fuel consumption and brake thermal efficiency, which significantly reduces NO_x emission while slightly increases particulate emissions.

4. The test of thermogravimetric analysis shows that higher percentage of volatile organic fractions (VOF) in fuel will lead to higher reactivity and oxidation rate of particles due to more internal particle surface areas left from the lost VOF for soot oxidation. DBE blends are found oxidized faster with lower activation energy at lower ignition temperature than ULSD while oxidized slower than biodiesel. The oxidative reactivity of particles increases in order of ULSD, DBE0, DBE5, DBE10, DBE20, and biodiesel.

5. Internal nanostructure morphology of soot governs the particle oxidative reactivity. Agglomerates from different fuels are found to be composed of fine primary particles forming a mixture of chain-like structures and clusters of spherules. Increasing the fuel oxygenation leads to the increase of amorphous nanostructure characterized by smaller particle size, shorter and curved fringe-length distribution, shorter fringe separation, and higher tortuosity. Increasing the ethanol contents in DBE blends, the lamella becomes more curved, tortuous, and disorganized. The reactivity of DBE blends is generally higher than ULSD. However, the high oxygen and VOF contents in biodiesel are the major reasons

http://dx.doi.org/10.5772/64470

for its highest reactivity among the test fuels though its fringe length and tortuosity are longer and lower respectively than DBE blends.

Overall, it is concluded that the use of DBE blends can effectively reduce the NO_x, CO_2, total particle numbers with lesser ultrafine and nanoparticle concentrations than ULSD, and neat biodiesel except particulate mass concentrations a bit higher than biodiesel. By supplementing with limited intake CO_2 charge dilution, the reduction of NO_x can be further enhanced but particulate mass emissions are slightly increased.

The experimental results in this study could be applied directly in those countries with diesel engines and diesel fuel sulfur levels similar to the test Euro 2 engine and 50 ppm containing ULSD used in this study. While for those countries with newer technology-based diesel engines or lower sulfur-containing diesel fuels, the experimental results could be served as the reference data, but mapping work with revalidation test on engine performance, combustion characteristics, and emission performance is required when using DBE blends as transport biofuels.

Nomenclature

CO_2	Carbon dioxide
CO	Carbon monoxide
DBE	Diesel-biodiesel-ethanol blends
HC	Hydrocarbons
NO_2	Nitrogen dioxide
NO_x	Nitrogen oxides
PM	Particulate matters
PN	Particle number concentrations
ULSD	Ultra-low-sulfur diesel
HFID	Heated flame ionization detector
HCLA	Heated chemiluminescence analyzer
TEOM	Tapered element oscillating microbalance
NDIR	Nondispersive infrared analyzer
SMPS	Scanning mobility particle sizer
TGA	Thermogravimetric analysis
BMEP	Brake mean effective pressure
BSFC	Brake-specific fuel consumption
BTE	Brake thermal efficiency
SOC	Start of combustion

EOC	End of combustion
BSCO	Brake-specific CO emissions
$BSCO_2$	Brake-specific CO_2 emissions
BSHC	Brake-specific hydrocarbon emissions
$BSNO_x$	Brake-specific nitrogen oxide emissions
BSPM	Brake-specific particulate mass emissions
BSPN	Brake-specific particle number emissions
SOC	Start of combustion
EOC	End of combustion
TDC	Top dead center
LHV	Lower heating value
VOF	Volatile organic fraction
HRTEM	High-resolution transmission electron microscope
ROI	Region of interest
Øp	Premixed combustion phase
Ød	Diffusion combustion phase

Author details

Ho Tse

Address all correspondence to: jeff.tse@connect.polyu.hk

The Hong Kong Polytechnic University, Hong Kong, China

References

[1] Ribeiro NM, Pinto AC, Quintella CM, Rocha GO, Teixeira LSG, Guaririro LLN, Rangel MDC, Veloso MCC, Renzende MJC, Cruz RS, Oliveira AM, Torres EA, Andrade JB, "The role of additives for diesel and diesel blended (ethanol or biodiesel) fuels: a review", Energy & Fuels, 21, 2007.

[2] Cheung CS, Cheng C, Chan TL, Lee SC, Yao C, Tsang KS, "Emission characteristics of a diesel engine fuelled with biodiesel and fumigation methanol", Energy & Fuels, 22, 906–914, 2008.

[3] Agarwal AK, "Biofuels (alcohols and biodiesel) applications as fuels for internal combustion engines", Progress in Energy and Combustion Science, 33, 233–271, 2007.

http://dx.doi.org/10.5772/64470

[4] Demirbas A, "Progress and recent trends in biofuels", Progress in Energy and Combustion Science 33, 1–18, 2007.

[5] Kumar S, Cho JH, Moon Park J, Moon II, "Advances in diesel-alcohol blends and their effects on the performance and emissions of diesel engines", Renewable and Sustainable Energy Reviews, 22, 46–72, 2013.

[6] Kuchler M, Linner BO, "Challenging the food vs fuel dilemma: genealogical analysis of the biofuel discourse pursued by international organization", Food Policy, 37, 581–588, 2012.

[7] Thompson PB, "The agricultural ethics of biofuels: the food vs fuel debate", Agriculture, 2, 339–358, 2012.

[8] Lapuerta M, Agudelo JR, Armas O, "Effect of biodiesel fuels on diesel engine emissions", Progress in Energy and Combustion Science, 34, 198–223, 2008.

[9] David YC, Chang Jon H Van Gerpen, "Determination of particulate and unburned hydrocarbon emissions from diesel engines fueled with biodiesel", SAE Technical Paper Series 982527, 1998.

[10] Dorado MP, Ballesteros E, Arnal JM, Gomez J, Lopez FJ, "Exhaust emissions from a diesel engine fueled with transesterified waste olive oil", Fuel, 82, 1311–1315, 2003.

[11] Ramadhas AS, Muraleedharan C, Jayaraj S, "Performance and emission evaluation of a diesel engine fueled with methyl esters of rubber seed oil", Renewable Energy, 30, 1789–1800, 2005.

[12] Peng CY, Yang HH, Lan CH, Chien SM, "Effects of the biodiesel blend fuel on aldehyde emissions from diesel engine exhaust", Atmospheric Environment, 42, 906–915, 2008.

[13] Di Y, Cheung CS, Huang Z, "Experimental investigation on regulated and unregulated emissions of a diesel engine fueled with ULSD blended with biodiesel from waste cooking oil", Science of the Total Environment, 407, 835–846, 2009.

[14] Song KH, Nag P, Litzinger TA, "Effects of oxygenated additives on aromatic species in fuel-rich, premixed ethane combustion: a modeling study" Combustion Flame, 135, 341–349, 2003.

[15] Sayin C, "Engine performance and exhaust gas emissions of methanol and ethanol-diesel blends", Fuel, 89, 3410–3415, 2010.

[16] Zhu L, Cheung CS, Zhang WG, Huang Z, "Emission characteristics of a diesel engine operating on biodiesel and biodiesel blended with ethanol and methanol", Science of the Total Environment, 408, 914–921, 2010.

[17] Di Y, Cheung CS, Huang Z, "Experimental study on particulate emission of a diesel engine fueled with blended ethanol-dodecanol-diesel", Aerosol Science, 40, 101–112, 2009.

[18] Cinar C, Topgul T, Ciniviz M, Hasimoglu C, "Effects of injection pressure and intake CO_2 concentration on performance and emission parameters of an IDI turbocharged diesel engine", Applied Thermal Engineering, 25, 1854–1862, 2005.

[19] Chen Y, Shah N, Braun A, Huggins FE, Huffman GP, "Electron microscopy investigation of carbonaceous particulate matter generated by combustion of fossil fuels", Energy & Fuels, 19, 1644–1651, 2005.

[20] Zhu J, Lee KO, Yozgatligil A, Choi MY, "Effects of engine operating conditions on morphology, microstructure and fractal geometry of light-duty diesel engine particulates", Proceedings of the Combustion Institute, 30, 2781–2789, 2005.

[21] Rakopoulos DC, Rakopoulous CD, Giakoumis EG, Dimaratos AM, "Characteristics of performance and emissions in high-speed direct injection diesel engine fuelled with diethyl ether/diesel fuel blends", Energy, 43, 214–224, 2012.

[22] Vander Wal RL, Mueller, CJ. "Initial investigation of effects of fuel oxygenation on nanostructure of soot from a direct-injection diesel engine", Energy & Fuels, 20, 2364–2369, 2006.

[23] SAE International, "Test procedure for the measurement of gaseous exhaust emissions from small utility engines", SAE International Paper J1088, 2003.

[24] Moffat RJ, "Describing the uncertainties in experimental results", Experimental Thermal and Fluid Science, 1, 3–7, 1998.

[25] Shi X, Yu Y, He H, Shuai S, Dong H, Li R, "Combination of biodiesel-ethanol-diesel fuel blend and SCR catalyst assembly to reduce emissions from a heavy-duty diesel engine", Journal of Environment Sciences, 20, 177–182, 2008.

[26] Qi DH, Chen H, Geng LM, Bian Y ZH, Ren X CH, "Performance and combustion characteristics of biodiesel-diesel-methanol blend fuelled engine", Applied Energy, 87, 1679–1686, 2010.

[27] Zhu L, Cheung CS, Zhang WG, Huang Z, "Combustion, performance and emission characteristics of a DI diesel engine fueled with ethanol-biodiesel blends", Fuel, 90, 1743–1750, 2011.

[28] Boehman AL, Morris D, Szybist JP, Esen E, "The impact of the bulk modulus of diesel fuels on fuel injection timing", Energy & Fuels, 18, 1877–1882, 2004.

[29] Szybist JP, Song J, Alam M, Boehman AL, "Biodiesel combustion, emissions and emission control", Fuel Processing Technology, 88, 679–691, 2007.

[30] Sivalakshmi S, Balusamy T, "Effects of dimethylcarbonate-biodiesel blends on the combustion, performance and exhaust emissions of a DI diesel engine", SAE International, 2012.

http://dx.doi.org/10.5772/64470

[31] Kwanchareon P, Luengnaruemitchai A, Jai-Lin S, "Solubility of a diesel-biodiesel-ethanol blend, its fuel properties, and its emission characteristics from diesel engine", Fuel, 86, 1053–1061, 2007.

[32] Jha SK, Fernando S, Columbus E, Willcutt H, "A comparative study of exhaust emissions using diesel-biodiesel-ethanol blends in new and used engines", Transactions of the ASABE, 52, 375–381, 2009.

[33] Labecki L, Lindner A, Winklmayr W, Uitz R, Cracknell R, Ganippa L, "Effects of injection parameters and EGR on exhaust soot particle number-size distribution for diesel and RME fuels in HSDI engines", Fuel, 112, 224–235, 2013.

[34] Tree DR, Svensson KI, "Soot processes in compression ignition engines", Progress in Energy and Combustion Science, 33, 272–309, 2007.

[35] Leung DYC, Luo Y, Chan TL, "Optimization of exhaust emissions of a diesel engine fuelled with biodiesel", Energy & Fuels, 20, 1015–1023, 2006.

[36] Tan P, Lou D, Hu Z, " Nucleation mode particle emissions from a diesel engine with biodiesel and petroleum diesel fuels", SAE Technical Paper 2010-01-0787, 2010.

[37] Tsolakis A, "Effects on particle size distribution from the diesel engine operating on RME-biodiesel with EGR", Energy & Fuels 2006, 20, 1418–1424, 2006.

[38] Pang J, "Study of particle size distributions emitted by a diesel engine", SAE Technical Paper Series 1999-01-1141, 1999.

[39] Hulwan DB, Joshi SV, "Performance, emission and combustion characteristic of a multicylinder DI diesel engine running on DBE blends of high ethanol content", Applied Energy, 80, 5042–5055, 2011.

[40] Tse H, Leung CW, Cheung CS, "Engine performance and emissions of diesel-biodiesel-ethanol blend fuelled engine", International Conference on Applied Energy ICAE 2012, ICAE2012-A10789, 2012.

[41] Ladommatos N, Abdelhalim S, Zhao H, "Control of oxides of nitrogen from diesel engines using diluents while minimizing the impact on particulate pollutants", Applied Thermal Engineering, 18, 963–980, 1998.

[42] Lu T, Cheung CS, Huang Z, "Investigation on particle oxidation from a DI diesel engine fuelled with three fuels", Aerosol Science and Technology, 12, 46, 1349–1358, 2012.

[43] Stratakis GA, Stamatelos AM, "Thermogravimetric analysis of soot emitted by a modern diesel engine run on catalyst-doped fuel", Combustion and Flame, 132, 157–169, 2003.

[44] Stanmore BR, Brihac JF, Gilot P, "The oxidation of soot: a review of experiments, mechanisms and models", Carbon, 39, 2247–2268, 2001.

[45] Ishiguro T, Takatori Y, Akihama K, "Microstructure of diesel soot particles probed by electron mircroscopy: first observation of inner core and outer shell", Combustion and Flame, 108, 231–234, 1997.

[46] Wentzel M, Gorzawski H, Naumann KH, Saathoff H, Weinbrush S, "Transmission electron microscopical and aerosol dynamical characterization of soot aerosols", Journal of Aerosol Science, 34, 1347–1370, 2003.

[47] Lipkea WH, Johnson JH, Vuk CT, "The physical and chemical character of diesel particulate emissions—measurement techniques and fundamental considerations", SAE Paper 780108, 1978.

[48] Vander Wal RL, Tomasek AJ, Pamphlet MI, Taylor CD, Thompson WK, "Analysis of HRTEM images for carbon nanostructure quantification", Journal of Nanoparticle Research, 6, 555–568, 2004.

[49] Shim HS, Hurta RH, Yang NYC, "A methodology for analysis of 002 lattice fringe images and its application to combustion-derived carbons", Carbon, 38, 29–45, 2000.

[50] Song J, Alam M, Boehman AL, Kim U, "Examination of the oxidation behavior of biodiesel soot", Combustion and Flame, 146, 589–604, 2006.

Chapter 9

Low and Medium Calorific Value Gasification Gas Combustion in IC Engines

Ftwi Yohaness Hagos, Abd Rashid Abd Aziz,
Shaharin A. Sulaiman and
Bahaaddein K. M. Mahgoub

Additional information is available at the end of the chapter

http://dx.doi.org/10.5772/64459

Abstract

Higher hydrogen to carbon ratio of gasification gases produced from solid fuels has been utilized in internal combustion engines (ICE) since long ago. Advancements in the conversion technologies and the abundant availability of solid fuels added with advancements in the technology of gas engines and their fuelling system have renewed the interest and are believed to be transition fuels from carbon based to hydrogen based. Over the past 30 years, there were many trials to bring back the gasification gas technology in ICE. This study is mainly focused on the investigation of technical challenges with lower and medium calorific value gasification gases in IC engines The range of operation of these fuels is found to be influenced by available injection duration and injector pulse width in direct-injection spark-ignition engines. The lower calorific value of these gases also make them less competitive to CNG and H_2 in the dual fueling in CI engine even though they have better advantage in the emissions. Furthermore, red glow color deposit was spotted on the surface of the combustion chamber after short running on all fuels that was resulted from decomposition of iron pentacarbonyl ($Fe(CO)_5$) contaminants.

Keywords: gasification gas, fuel, combustion, IC engine, SI, CI, technical challenges

1. Introduction

The focus of utilization of gasification gases was limited in the stationary power plants since the post-World War II (WW II). The current energy statuesque is getting challenged due to the

INTECH
open science | open minds

© 2016 The Author(s). Licensee InTech. This chapter is distributed under the terms of the Creative Commons Attribution License (http://creativecommons.org/licenses/by/3.0), which permits unrestricted use, distribution, and reproduction in any medium, provided the original work is properly cited. CC BY

abundant availability of solid fuels and advancement in the solid-togas conversion technologies. This chapter intends to give the results of the study of utilization of gasification gases in internal combustion engines (ICEs) to appraise the current knowledge on the combustion, performance and emissions of both lower and medium calorific value gasification gases. Both spark ignition (SI) and compression ignition (CI) engines are considered in the study. The current energy scenario, historical background, the solid fuel potential, advancement in the conversion technologies, basic fuel properties comparison of representative gasification gases with that of CNG and hydrogen and the compositions of gasification gases from medium- and large-scale gasification plants are covered in the introduction part. The combustion, performance and emissions of gasification gases in both SI and CI are addressed in Sections 2 and 3. The safety issue of gasification gases and their overall technical challenges are discussed in Sections 4 and 5. Finally, a concluding remark and future directions in the study of these fuels is presented in Section 6.

1.1. Energy scenario

During the invention of ICEs, the energy sources were gaseous fuels and powders. In the mid of the 19th century, a French Engineer J. J. Étienne Lenoir developed a double acting SI engine, and later in 1876 [1], first gasoline-fuelled ICE was built. The first commercial vehicle in Germany was produced by Carl Benz 1886 [2], and by 1890, more than 50,000 of such commercial vehicles were sold in Europe and USA [1]. Later, the expansion of automotive production by Henry Ford in 1910 has further initiated the era of fossil fuels as an energy sources [2]. The demand for gasoline increased by fivefold in the years from 1907 to 1915 and as a result William Burton innovated the idea of thermal cracking of crude oil in 1913 [1]. Advancements in the fossil fuel extraction methods on the one hand and cheaper cost of production of cars on the other hand have had significant contribution in the growth of ICE use in transport automobiles. Thus, the fuel consumption grew sharply from 11 billion litres in 1919 to 57 billion litres in 1929 and then to 176 billion litres in 1955 [2]. World War II led to the shortage of gasoline and as a result there was a brief stagnation in the utilization of fossil fuel mainly for private use. During this period, development of wood gas vehicles expanded all over the world. More than a million of such vehicles had been produced and were functioning globally by the end of the war [3]. However, petrol domination at the end of 1940s has led to the quick exit of these types of engines out of market.

The expansion of the ICE-driven automobile transport has dramatically transformed the global economic and technological landscape. As a result, human life got more attachment with ICE and with their fuel and its consumption grew unrestrained. The negative effect of fossil fuels on the environment was not noticed for up to half century. Environmental pollution, mainly from the transportation sector, first came into attention at the end of 1940s and beginning of 1950s. During this period, it was noticed that the major contributor for the pollutant emissions of hydrocarbons (HCs), nitrogen oxide (NO_x) and carbon monoxide (CO) was the transport sector mainly automobiles. In 1960s, the state of California and later the whole nation (USA) adapted emission standard for automobile [1]. Added to this, there came a geopolitical situation in the Middle East in 1970s that resulted global energy crisis. Concern regarding the

http://dx.doi.org/10.5772/64459

long-term availability of fossil fuels started to be raised along with it. As a result, most nations started to revisit their energy policies towards fossil based fuels to address the two scenarios. Similarly, alternative source of energy became a centre of research in the scientific world.

Different fuels have been investigated as alternative fuels for ICE over the years. Natural gas, hydrogen, alcohols (ethanol and methanol) and biodiesel are the most common alternative fuels which have received greater attention over the period. Even with such extended efforts, still the transport sector is mainly dependent on the much polluting and unsustainable fossil based fuels. Energy demand in the transport sector is expected to double from the current 60 trillion passengers per tonne-km in 2050, most growth coming from passenger light-duty vehicles in developing countries [4]. This is mainly due to an increase in population and ownership of motorized vehicles in both developing and developed countries and an increased air travel as a result of urbanization in developing world. The global population is projected to reach 9.6 billion from the current 7.2 billion mark in 2050 [5]. Furthermore, developing countries will become economically stronger. As a result, the global vehicle ownership is expected to triple by 2050; up to 80% of the growth comes from the rapidly growing counties [6]. Due these concerns, solid fuels are receiving greater attention as a source of energy due to the huge burden on the conventional and other renewable fuels. Solid-to-gas fuel conversion technologies have advanced dramatically over years of research and development. The current article is focused on the investigation of the gaseous fuels processed from solid fuels employed in ICE. Even though the lower and medium calorific gasification gases are receiving more attention towards their application in ICE, more focus is still given in the area of combustion, performance and emissions in a gasifier-integrated engine where such arrangement is not practical with the current mobility demand. Therefore, the major research questions in the current article are: (i) does separation of gasifier and the engine arrangement affect the combustion, performance and emissions as compared to the gasifier-integrated engine? What are the major technical challenges designers and automotive developers should be concerned of? To address, these research gaps, lower and medium calorific value gasification gases in ICE and their technical challenges are investigated.

1.2. Solid fuel potential

Solid fuel is the oldest source of energy for mankind which has been utilized since the early Stone Age era. Our ancestors first started to use fire 250,000 year ago with solid fuels such as wood, charcoal, peat, straw and dried dung [7]. Humans first used fire for cooking and heating purposes. Due to their abundant availability and easy for collection, biomass remained as a dominant solid fuel until the beginning of the industrial revolution. It was during the industrial revolution the utilization of solid fuels expanded to other areas such as smelting of metallic ores (iron, copper, silver, etc.) and steam engine [8]. The diversification of application of solid fuels prompted the search for other types of fuels. As a result, coal has become a dominant source of energy in this era. The invention of steam engine has further facilitated the mining of coal from underground sources by pumping water from coal mining area. The higher energy density of coal gave it higher preference compared to wood and other solid biomass [8, 9].

Coal is the most abundant energy resource with an estimated reserve of 18,000 Gtoe [10]. However, the recoverable coal reserve is much lower [11]. The UK Solid Fuel Association estimated the reserves as a reserve for 118 years at its current rate of production. Even though percentage share of solid fuels in the total energy mix started to shrink since the beginning of the twentieth century, solid fuels are still the major contributors of the economy. They are the dominant energy sources for electricity and in the industrial processes (steel, cement, sugar, pulp and paper) [12]. According to the 2013 International Energy Outlook published by the US Department of Energy, electricity generation is to grow annually by 3.1% in the non-OECD countries (countries outside the Organization for Economic Cooperation and Development) while 1.1% annually in the OECD nations [13]. As a result, the global solid fuel consumption is rising annually. Coal alone is expected to rise at an annual average rate of 1.3% to 220 quadrillion Btu in 2040 [13]. The diverse application and utilization of these fuels make them preferred fuels. Besides, their abundance, their ability to convert to other form of energy and uncertainty with the gaseous and liquid fossil fuels make solid fuels the future energy supply [12]. Even though solid fuels have had such recognition in the energy sector, their direct applications as a source of heat become almost impossible these days. Beside their inconvenience in handling, there are stringent regulations at the present time due to the environmental issue. Different measures have been implemented for the improvement of pollutant emissions in the direct conversion solid fuels. However, the conversion of solid fuels to gaseous and liquid form is preferred especially in the transportation sector.

1.3. Advancements in the fuel conversion technologies

Gasification is a thermo-chemical conversion process that converts solid fuels into gaseous by increasing the hydrogen-to-carbon ratio through the breakdown of the feedstock. The process involves drying, pyrolysis combustion and reduction sub-processes. The carbon conversion efficiency of the latest gasifiers is estimated to be around 75%. The name gasification gas is a general term for any gasification product also known as syngas, town gas and producer gas [14]. Gasifying agent is the most significant parameter that affects the yield from the thermo-chemical conversion process [15]. The main gasifying agents used in the process are oxygen, steam, and air. Gasification gas produced using steam and oxygen as a gasifying agent is called medium calorific value gasification gas (simply syngas) and its heating value ranges from 10 to 28 MJ/Nm^3 [15]. On the other hand, gasification gas produced using air as a gasifying agent is called lower calorific value gasification gas or producer gas and its heating value ranges from 4 to 7 MJ/Nm^3 [16].

The current practice in the biomass use as an energy source through gasification is by coupling the gasifier to the prime mover. In this arrangement, the gasifier is sized based on the capacity of the prime mover (turbine). As a result, the gasifier operates only during the time of peak demand for electricity. Even though there is surplus of raw material (solid fuels), the gasifier cannot be operated as there is no storage system arrangement. That is why people are trying to upgrade syngas into dimethyl ether (DME) and other oxygenated hydrocarbon fuels [17, 18]. In recent years, there are some efforts to integrate a storage system in the gasification process [19–21]. If the gasifier system is separated from a prime mover, the gasifier can be sized

http://dx.doi.org/10.5772/64459

to produce extra gasification gas that can be stored for the utilization at the time of peak demand and further sourced to the market in the transport sector and chemical industry.

1.4. The history of gasification gas in the automotive sector

There are reports of the employment of various ranges of gasification gases in the IC engine over the years since the inception of the Imbert gasifier around 1920. During the World War II, there was severe shortage of gasoline globally and all private-owned cars and tracks were redesigned to operate with gasification gases by erecting an Imbert gasifier. As it is also stated in Section 1.1, the number of cars running on producer gas at the time of WW II was estimated to 7 million by Sridhar et al. [22]. After the war, petroleum distribution returned back to normal and it led to the quick exit of these engines out of market. Besides the petroleum abundance, there were operational and technical problems that prompted for the fast exist. These problems are summarized by Hagos et al. [23]. Since then, the application of gasification gases shifted into the integrated gasification combined cycle as a stationary power generation system. However, even in this period, countries did not totally give up on the use of such fuel in the mobile engine applications. The United States of America is promoting the application of this technology as a backup energy supply source in the event the country faces petroleum crisis [24].

Since the global energy crisis of the 1970s, the research on both the lower and medium calorific value gasification gases was again intensified because in one part the gasification technologies started to advance and on the other hand the price of petroleum increased. There are many results published with different success rates on the employment of these fuels on the carburetted and port-injected SI Engines [22, 25–47] and dual fuelling on the CI engines [48–54]. Gasification gases (both producer gas and syngas) in a direct-injection (DI) SI engines has never been studied except the works by the authors of this article [23, 55–60]. Their combustion behaviour and performance and emission characteristics are studied for the broader range of gasification gas species and are reported elsewhere. This chapter concentrates on the summary of the combustion, performance and emission characteristics of representative of gasification gases over a wider range of operation conditions in both the DI SI engine and dual fuelling CI engine. Besides, the technical challenges observed during the study of these gases in ICEs will be emphasized in the current work. Unlike to the conventional fuels, there is no suitable predictive tool (Kiva, Forte, and GT Power) for the effect of property of such fuels on the optimization of combustion, performance and emissions. The current work will provide additional information for the development of alternative fuels.

1.5. Properties of gasification gas and their scope in IC engines

Engine output is mainly dependent on the chemical energy released as a result of combustion of the fuel inducted. Combustion in ICE is influenced by the nature of the fuel, the oxidizer and the geometry of the chamber among others. Depending up on the mode of gasification, gasifying agent and the solid fuel used, the constituent gases (H_2, CO, CH_4, N_2 and CH_4) of gasification gas are varied. Not all gasification gases serve as fuels for ICEs. Analysis of different properties of fuels such as energy content, flammability limit, laminar flame speed

Properties		Gasification Gases		CNG	H_2
		50% H_2-50% CO [55]	19.2% H_2, 29.6% CO, 5.3% CH_4, 5.4% CO_2 and 40.5% N_2 [57]		
Composition, weight %	Carbon	40.0	21.15	75.0	0.0
	Hydrogen	6.67	2.56	25.0	100
	Oxygen	53.33	28.27	0.0	0.0
	Nitrogen	0.0	48.5	0.0	0.0
Molecular weight (g/mol)		15.0	23.2	16.04	2.02
Density at 0°C and 1 atm (kg/m³)		0.67	1.04	0.75	0.09
Specific gravity at 0°C and 1 atm		0.52	0.8	0.58	0.07
Stoichiometric air-fuel ratio	Molar Basis	2.38	1.66	9.7	2.38
	Mass Basis	4.58	2.07	17.2	34.3
Stoichiometric volume occupation in cylinder, %		29.6	37.6	9.35	29.6
Lower calorific value	MJ/Nm³	11.65	7.67	38.0	10.7
	MJ/kg	17.54	7.47	47.1	120.2
Stoichiometric Mixture Energy density (MJ/Nm³)	Mixture aspirated	3.3	2.73	2.9	3.2
	Air Aspirated	4.45	4.19	3.60	4.54
Flammability Limit, % vol. of fuel in air	Lower	6.06	13.4	5.3	4.0
	Higher	74.2	57.9	15.0	74.2
Laminar Flame Velocity (cm/s)		180	50	30	210
Adiabatic Flame Temperature, K		2385	2200	2220	2383
Auto-ignition Temperature, K		873-923	898	813	858

Table 1. Summary of the properties of different gasification gases and their comparison to CNG and H_2.

and flame temperature helps to classify those gasification gases that can be used in ICEs. The comparison of CNG with the conventional fuel in IC engines is widely available in the literature. On the other hand, fuel characteristic requirements of liquid and gaseous fuels are different. Therefore, CNG representing the hydrocarbon-based fuels and H_2 that represent the renewable and zero emission fuels are taken for comparison in the current work. Generally, gasification gases are broadly classified into lower and medium calorific values depending on the type of gasifying agent and thereby with the nitrogen content. For air as a gasifying agent, roughly up to 50% of the constituent gases is nitrogen. If oxygen or steam is used as a gasifying agent, the constituent gases of the gasification gas are without nitrogen. **Table 1** shows the detailed comparison of properties of two gasification gases that represent typical medium and lower calorific value fuels from biomass gasification, CNG and hydrogen. The summary of the fuel characteristics of these fuels could help in the understanding of combustion, performance and emissions behaviour in ICE [55]. All gasification gases are oxygenated fuels with the

medium calorific value gasification gas having the highest oxygen content at 53.33 wt%. The density of gasification gases are in the range of the density of the CNG with higher density observed in the lower calorific value gasification gases. The main concern with the gasification gases is the weight-based stoichiometric air-fuel ratio with 2.07 and 4.58 for lower and medium calorific value gasification gases, respectively, as compared to 17.2 for CNG and 34.3 for H_2. On the other hand, gasification gases have better mixture energy density at stoichiometric condition for the air aspirating engine (DI) as compared to CNG and even at par with H_2. All gasification gases have the upper hand in both the flammability limit and laminar flame velocity as compared to CNG. Similarly, they have higher auto-ignition temperature as compared to both CNG and H_2.

1.6. Typical gas compositions from practical large-scale gasification processes

Improvements in technology have increased the confidence among investors on large-scale commercial biomass gasification plants. In this chapter, large-scale gasification plants shall be referred to those with thermal capacity of above 10 MW_{th} [61]. Since the 1980s, the number of successful large-scale biomass gasification plants has increased. Currently, the largest planned biomass gasification plant is located in Vaasa, Finland. The plant, which is owned by Metso [62], uses wood-based biomass, is expected to deliver 140 MWe of electricity. Most of the gasification plants are intended for electrical power generation, resulting electricity that is usually injected into the main grid. In one of the latest biomass gasification plants in Gothenburg, Sweden, which uses forest residues as feedstock, the resulting syngas is fed into the natural gas grid [63]. Known as the GoBiGas project, the plant utilizes a 32 MW dual fluidized bed gasifier to produce about 20 MW of substitute natural gas.

The composition of syngas mainly depends on the feedstock, due to diversity in the key characteristics of different feedstocks vis-à-vis physical and chemical properties, lignocellulosic composition, energy content, morphological characteristics, ash content, bulk density, and a few other properties [64]. Apart from feedstock, the type of gasifier [65] and the operating conditions also play important roles in determining the composition of syngas [66] because the complex heterogeneous solid-gas and homogenous gas-gas chemical reactions taking place during gasification are highly dependent on the operating conditions such as equivalence ratio of gasification, reactor temperature, moisture content [67] and the gasifying medium used. The heating value of the syngas depends on its composition.

Table 2 shows a range of selected large-scale biomass gasification plants, their capacities and gas compositions. Clearly, most of the plants are located in Europe, where strong interest on clean energy is present, and supports from the government and investors are high. Because of its superiority in technology and market, circulating fluidized bed (CFB) is shown in the table as the most preferred type of gasifier used for large-scale gasification plants. On feedstock, **Table 2** shows that wood-based materials are preferred due to their availability in developed countries. The authors recognize the existence of other similar large-scale biomass gasification plants. However, detailed information about their operating conditions and their gas compositions is presently not available. The gas compositions, in volume percentage, listed in **Table 2** are CO_2, N_2, CO, H_2 and CH_4. There are also other kinds of gases reported for the plants such

as ethane, but their amounts are negligible. Of all the gases listed in **Table 2**, only CO, H_2 and CH_4 can be used as fuel. Overall, CO constitutes the largest fuel gas component in most of the plants listed, with the exception of the Viking DTU [68] plant in Denmark, which was aimed to produce more H_2. The highest generation of CO occurs at the Vermont SilvaGas plant [69] in the USA at 44% although the composition of N_2 was never revealed in their report.

Plant	Technology	Feedstock	Fuel capacity	Electric output capacity	Gas composition (vol%)				
			(MW)	(MW_e)	CO_2	N_2	CO	H_2	CH_4
Greve-in-Chianti, Italy [68]	CFB	RDF	2 × 15	6.7	15.65	45.83	8.79	8.61	6.51
Kymiarvi, Finland [72]	CFB cofiring	Recycled fuel mixture (wood, board, paper, plastic, RDF etc.)	70	20	12.3	33.1	9.6	6.7	3.3
Värnamo, Sweden [68]	– Integrated gasification combined cycle (IGCC)	Woodchips, pelletised wood, bark, straw, RDF	18	6	15.95	50	18	10.75	6.65
Vermont SilvaGas, USA [69]	Indirect CFB	Whole tree chips, residue wood, reconstituted wood pellets, forest thinning	44	9	12.2		44.4	22	15.6
Viking DTU, Denmark [68]	Two-stage fixed bed	Woodchips (45% moisture)	70	0.0175 (39 MW_{th})	15.4	33.3	19.6	30.5	1.2

Table 2. Selected large-scale gasification plants and their gas compositions.

On H_2, it is quite obvious that the Viking DTU [68] and Vermont SilvaGas [69] plants produce more than typical plants, at 30.5 and 22%, respectively. Most other plants listed in **Table 2** produce H_2 at around 6–10%. With advanced technology, more H_2 can be produced though more costly; but high H_2 may be preferred for several reasons: cleaner, high energy content (141.8 MJ/kg for H_2 as compared to 10.2 MJ/kg for CO), and it is sold in the market at relatively higher price for various industrial applications. As in most gasification processes, CH_4 tends to be in the lowest amount among the three production fuel gases. According to **Table 2**, they are typically less than 7% except for the Vermont SilvaGas [69] plant, for which the composition reported was 15.6%. Like H_2, CH_4 is also regarded as valuable a gas; but the amount produced from gasification is usually low.

http://dx.doi.org/10.5772/64459

Though not combustible, the amount of CO_2 generated is also an interest because it is a greenhouse gas that contributes to global warming. Typically, the CO_2 amount shown in **Table 2** is consistent within 12–16% for all plants. More importantly, the CO_2 released to the environment from biomass gasification could be offset by the amount absorbed by plants; presently this is the constant affirmation on why biomass is regarded as a source of renewable energy. Finally, it is worth noting that the Vermont SilvaGas [69] plant was developed based the outcome from a pilot plant, which was far smaller in scale. Interestingly, it was found that the gas compositions from the large-scale plant were almost the same with those of the pilot-scale plant. The energy content dropped 6% from 18.5 MJ/Nm^3 (pilot) to 17.3 MJ/Nm^3. The H_2 composition increased in the large-scale plant by 11%, while CO decreased by 26%; and there was almost no change for CH_4. This implies that scaling up of biomass gasification plant may result in small impact on the gas composition and energy content.

2. Gasification gas in CI engines

Amongst the options for energy conversion, only those that produce gasification gas suitable for use in a CI engine are the main focus of this part. Fluctuation of the gasification gas constituents makes it not suitable for stable combustion in SI engine at high load cases. Gasification gases can be utilized as diesel replacement in CI engine in the dual-fuelling mode. However, not all types of diesel engines can be operated on the dual-fuel mode. For example, the use of gasification gas in compression ratios of ante-chamber and turbulence chamber CI engines prospects to knocking and ignition delay caused by too high pressures [70]. The conversion of DI CI engines can normally be done due to their lower compression ratios. The conversion of an engine to operate on dual-fuel mode of operation will generally prospect to lower power output. In order to minimize the power loss, the heating value of air-gas mixture should be increased. In addition, the amount of combustible mixture should be increased by applying a supercharging or a turbocharging technique on the engine. Furthermore, adjusting some operating parameters including increasing of compression ratio and advancing the injection timing might be another solution to minimize the power loss. The limitation of dual fuelling in CI engines is that without having a supply of ignition source like diesel fuel, it cannot be run. Furthermore, overheating of the pilot fuel injection jet might be occurred when the flow of diesel fuel reach a lower level of up to 10 or 15% of its normal flow. Therefore, the injector nozzle should be checked regularly after 500 hours of dual-fuelling operation as recommended by Von Mitzlaff [71].

2.1. Fuelling strategy

In dual-fuel operation, the supply of pilot fuel (diesel) from injection system is similar to the ordinary diesel mode of operation. An air-gas mixture prepared outside the combustion chamber in an external mixing chamber in the intake system is then sucked, compressed and ignited into the engine with the diesel fuel sprayed. The mixing device should have the capacity to provide a homogeneous air-gas mixture. There are several options for mixing devices as

classified by Von Mitzlaff [71]. The type of mixers and their properties are summarized in **Table 3**.

According to the Turner and Weaver [74] the best and economic way to introduce gasification gas into dual-fuel engine is the central point mixing system.

Simple Mixing Chambers			
Designs	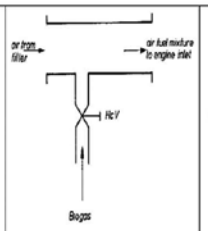 T-joint mixer	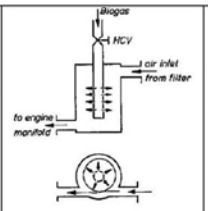 Mixing chamber with hand - controlled valve	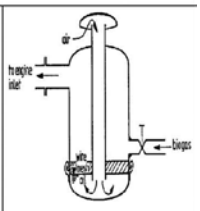 Mixing chamber with modified air filter
Properties	There is no possibility for gas fuel oversupply because the gas flow is managed by valve before entering the mixing device. Chambers having bigger volume offer much more homogeneous mixture due to the longer time of retention for air-fuel mixture within the chamber. Individual air/fuel mixture can be supplied, depending on the mixer design and/or setting of the gas flow control valve.		
Venturi Mixers			
Designs	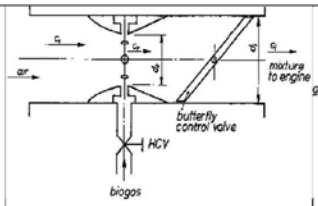 Venturi mixer with numerous number of bores	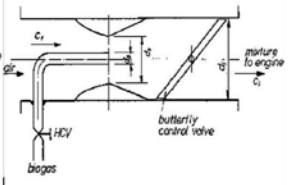 Venturi mixer with a single gas inlet nozzle	
Properties	Air-gas homogeneous mixture can be obtained by way of gas through numerous bores close to the circumference with the "bottleneck".		
Mixers with the protruding pipe inside the mixer			
Designs	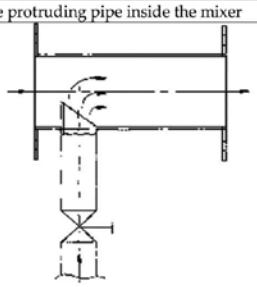 T-joint with oblique gas pipe protruding into the mixer	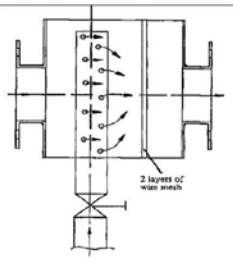 Mixing chamber with gas distribution pipe and wire mesh for intensive mixing	
Properties	The mixing performance is superior to that of a blunt T-joint	Distributes the gas via a number of holes. A number of wire mesh at short distance between each facilitates further the flows mixing	

Table 3. The list of different mixer designs and their respective properties [73].

http://dx.doi.org/10.5772/64459

2.2. Comparison of gasification gas and other renewable fuels in duel fuelling

Different types of gaseous fuels were investigated with the intention of transiting from the fossil-dominated energy to biobased energy in both the CI and SI engines. Dual-fuel engines typically use either gasification gas, H_2, CNG, liquefied petroleum gas (LPG) or sometimes biogases as the primary fuel [75–79]. Gasification gases from different sources have been used in dual-fuel engines in order to investigate the impact of their composition and some operating parameters including load, injection timing and the air intake condition on dual-fuel combustion. A study was conducted by Ramadhas et al. [80] on dual-fuelling combustion with rubber seed oil and coir-pith producer gas at distinctive load conditions and compared the performance results with normal diesel. Higher particular energy consumption at all load conditions was reported. A simulated gasification gas containing 49% N_2, 12% CO_2, 25% CO, 10% H_2 and 4% CH_4 was used in dual-fuel CI engine at a speed of 2000 rpm. The result has indicated poor combustion efficiency of gasification gas dual fuelling compared to normal diesel operation. The poor combustion was due to the lower heating value of used gasification gas (7444.13 kJ/kg) compared to diesel, or either due to a too lean mixture or a too rich mixture [81]. Sahoo et al. [51] have made an attempt to improve dual-fuelling combustion by varying the engine load. Substandard engine performance was revealed at light loads for dual-fuel operation. However, an improvement on the thermal efficiency was recorded over half load for dual-fuel mode of operation. In order to improve the poor combustion efficiency with the gasification gas fuelling in dual-fuelling strategy, Roy et al. [82] have investigated the influence of intake pressure (101–200 kPa) in order to improve dual-fuel combustion by supercharging a pyrolysis gas engine with micro-pilot ignition. It was concluded that greatest indicated mean effective pressure (IMEP) was attained with an intake pressure of 200 kPa, and the thermal efficiency was also improved.

Numerous investigations were conducted by the researchers as to provide information on the effect of composition of gasification gas on dual-fuel combustion when combusted in CI engines [82, 83]. Most of them concluded that increased hydrogen content of the gasification gas affects positively on the combustion efficiency. In the study by Roy et al. [82], higher thermal efficiency of 37–38% was attained with the use of the 20% H_2 content gasification gas rather than the 13.7% H_2 content. The dual-fuel engine was able to work with wider window of fuel-air equivalence ratio (0.42–0.79). The 20% H_2 content producer gas also shorten the combustion duration by 4 to 5°CA. The engine used by Tomita et al. [83] has functioned steadily with stable combustion and enhanced efficiency with the increase of hydrogen content in syngas, even at an equivalence ratio of $\varphi = 0.45$ because the more hydrogen content enhances the limit of lean mixture. Further, 12% greater power was attained when higher hydrogen content gasification gas was used by Roy et al. [82] in dual-fuel engine with the application of exhaust gas recirculation (EGR) in syngas emitted from hydrogen-rich coke-oven gas.

Besides the gasification gas, there are many reports on research regarding dual fuelling in CI engine with other renewable fuels. The usage of port fuel–injected natural gas and DI diesel generally results in a significantly increased fuel consumption compared to the conventional diesel operation as reported in the work by Papagiannakis and Hountalas [84]. Saleh, and many others, revealed that duel-fuel combustion with LPG (port fuel injection [PFI]) and diesel does

not have a significant influence on the efficiency of an engine [85]. For hydrogen dual fuelling, the efficiency of a dual-fuel engine tends to increase while running on hydrogen and diesel as revealed from different studies by Saravanan et al. [86–88]. An increased efficiency was also observed when dual-fuel engine was operated by Azimov et al. [89] with natural gas and syngas under premixed mixture ignition in the end-gas region (PREMIER) combustion mode and supercharging condition. However, the research carried out by Bika et al. [90] shows reduced efficiencies in dual-fuel mode.

In summary, a complete replacement of diesel fuel with gasification gas could not be possible. Besides, the performance of such dual fuelling of gasification gas and diesel was poorer as compared to dual fuelling of other renewables. However, a compromise among improved efficiency and reduced exhaust emissions might be achieved if gasification gas with increased hydrogen content is used in dual-fuel engines with maintained operating conditions. Moreover, it can be used as a supplementary fuel to reduce cost and emissions of NO_x and particulate matter. In comparison between different renewable gases, hydrogen and natural gas seem to show slight increase on the engine efficiency when compared to syngas and natural gas. Natural gas and synthesis gas seem to be used for greener options to replace fossil fuels in internal combustion engines [91–93].

2.3. Combustion process of dual fuelling

The typical dual-fuel combustion consists of three stages, premixed combustion with the direct-injected diesel fuel in addition to a minor portion of the gasification gas entrained within the diesel spray. The second stage is characterized by the premixed combustion of the major portion of the gasification gas in addition to tiny amounts of the diesel. Finally, the diffusion combustion of the rest of the two fuels represents the third stage. **Figure 1** shows the main three phases of dual-fuel combustion.

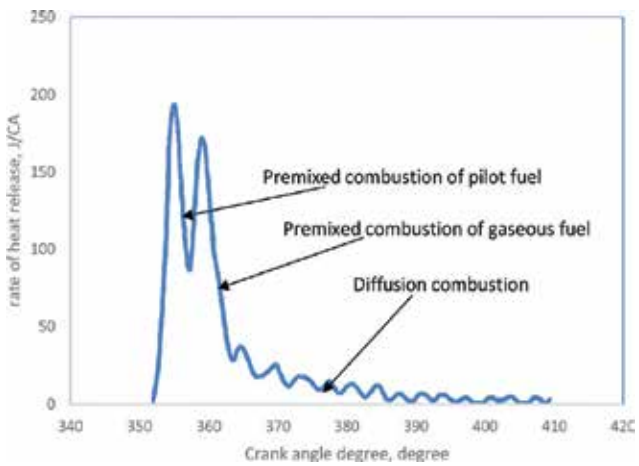

Figure 1. Rate of heat release (ROHR) for "conventional" dual fuel combustion [94].

http://dx.doi.org/10.5772/64459

The amount of diesel substituted by gasification gas is very important in order to characterize the first two stages. However, the amount of pilot fuel that can be burned during this stage has significant effect on the peak rate of heat release (ROHR). The importance of this phase decreases only once the level of pilot fuel is decreased under this specific limit. The significance of the second phase alternatively is determined through the quantity of diesel substitution. The advantage of this concept is that it makes use of the difference in flammability of the used fuels. When leaving out the gaseous fuel, the engine operates as a normal diesel engine. However, since the liquid diesel is necessary for ignition, it is not possible to run it exclusively on the gaseous fuel.

2.4. Changes in pollutant emissions as a result of using gasification gas

A number of researchers have concluded that gasification gas dual fuelling is considered a promising technique for controlling NO_x emissions and smoke [95–97]. Lower particulate matter (PM) might be achieved by utilizing a lean air-gas mixture in dual-fuel engine rather than normal ordinary diesel only. Existing dual-fuel conversions endure from significant increases in CO and unburned hydrocarbon (UHC) emissions at low engine loads due to the very lean combustion at light loads. As the combustion gets leaner, the combustion directly degrades, leaving massive quantities of partial reaction items during the exhaust. **Figure 2** shows that the gasification gas used by Mahgoub et al. [81] has the possibility of reducing the level of CO_2 and NO_x emissions compared with diesel fuel when operated on a naturally aspirated, two stroke, single cylinder, diesel engine at a speed of 2000 rpm.

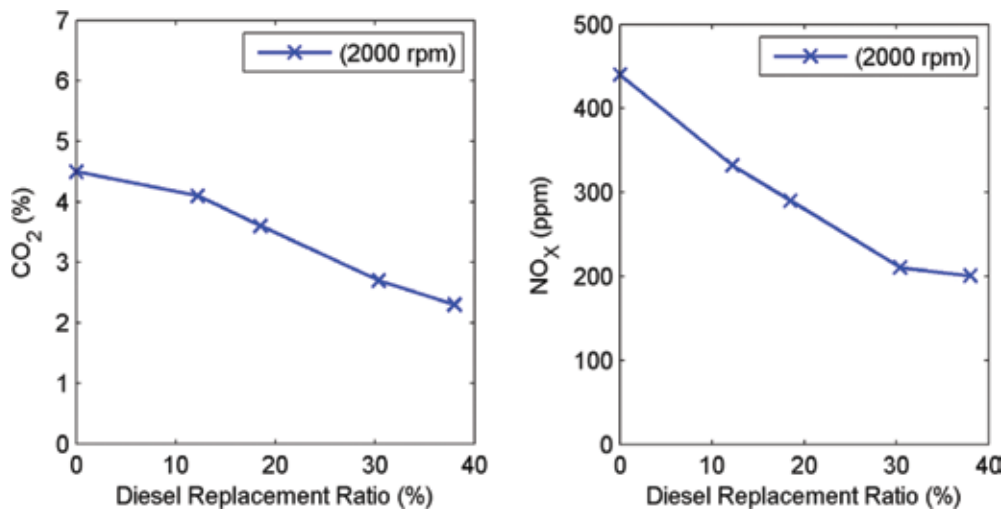

Figure 2. CO_2 and NO_x concentration versus diesel replacement ratio (syngas dual fuelling) [81].

3. Gasification gas in spark ignition engines

3.1. Fuelling strategy

As it is explained in Section 1, the history of gasification gas in the automotive engines is associated with the naturally aspirated SI-carburettor–type engines. Carburetted and port-injection engines mix the fuel and air prior to the combustion chamber and the volumetric efficiency of the engine drops at the cost of the voluminous gasification gas displacing air. Furthermore, they have higher pumping and heat losses as compared to DI SI engines, resulting in high fuel consumption [98]. Consequently, the theoretical power output of gasification gases fuelled carburetted and port-injection engines is lower than those of their DI engine counterparts and gasoline and CNG fuelled in the same arrangement.

With the emergence of DI application in SI engines, lean combustion strategy has become a means for the reduction of greenhouse gas emissions and in increasing thermal efficiency. This strategy is mainly accompanied with fuel stratification so that variable air-fuel ratio occurred around the combustion chamber. The stratification provides a relatively rich mixture near the igniter and a uniformly mixed ultra-lean mixture all over the cylinder. Engine performance reduction due to volumetric efficiency drop can also be overcome by injecting the fuel very late after inlet valve close (IVC). However, this may lead to insufficient time for fuel-air mixing and slow combustion rate. For the fast burning type fuels, this is the type of fuel injection strategy that has been adopted and it has attracted much attention these days. The H_2 component of the gasification gases, mainly the medium calorific value gasification gases, is grouped in the fast-burning–type fuels. Therefore, irrespective of the other engine operating parameters, gasification gas fuelled engine with a DI system is expected to have better engine power output. Similar hypothesis is implied by other researchers too [99]. In this section, a DI SI engine under the stratified charge strategy is preferred as a fuelling system for a two typical gasification gas representative mixtures from both the lower and medium calorific value fuels. The detailed characteristics of these two mixtures are presented in **Table 1**. The experiment was conducted in a single cylinder engine with a compression ratio of 14 and a displacement volume of 399.25 cc. Detailed engine specification can be referred from [55, 56]. The two representative gasification gases are premixed from their respective constituent gases based on their molar ratio and stored in bottles at a pressure of 140 bar.

3.2. Combustion process of gasification gases in SI engines

Investigation of the in-cylinder combustion by monitoring the pressure data with the help of a pressure sensor was performed. A piezoelectric pressure transducer was used to collect the pressure data. Pressure reading of up to 100 power cycles was recorded and a macro code is developed to analyze the combustion characteristics from the data and further to select the most representative cycle of the average cycle. Further analysis of the pressure data resulted in mean effective pressure (IMEP), rate of pressure rise, heat release rate and mass fraction burn (MFB). The performance and emissions of the gases fuelled in DI SI engine was also investigated. The fact that the gas composition, calorific value and the stoichiometric air-fuel

http://dx.doi.org/10.5772/64459

ratio of the gases are different, comparison of the two gases at the same operation conditions is impossible.

3.2.1. Lower calorific value gasification gas combustion

Figure 3 shows the variation of pressure, heat release rate and MFB with engine crank angle (CA) at different speeds ranging from 1800 to 2400 rev/min for the lower calorific value gasification gas. These combustion characteristics are presented for IMEP of 2.7 bar attained at λ = 4.93, 4.97 and 5.46 for engine speeds 1800, 2100 and 2400 rev/min, respectively. **Table 4** shows the air-fuel ratio, ignition advance and combustion durations of different engine speeds of the lower calorific value gasification gas operation at IMEP = 2.7 bar.

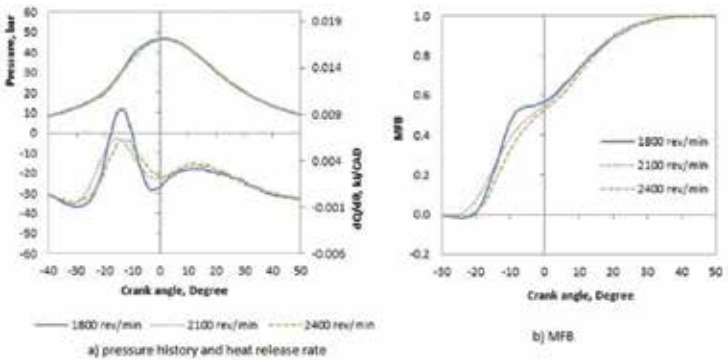

Figure 3. Combustion characteristics versus crank angle for 1800, 2100, and 2400 rev/min at IMEP = 2.7 bar.

Speed (rev/min)	1800	2100	2400
λ	2.42	2.60	2.61
Ignition advance (°BTDC)	31	31	31
Flamed development stage duration (°CA)	13	12	15
Rapid burning stage duration (°CA)	38	39	37
Overall combustion duration (°CA)	51	51	52

Table 4. λ, ignition advance and combustion durations of different speeds and IMEP = 2.7 bar.

The pressure profile presented the same curve for all speeds with its peak value of 47 bar at TDC. However, the heat release rate was shown to experience different trend for all the speeds mentioned. The fastest and shortest heat release rate was observed with the lowest engine speed. Both engine speeds at 2100 and 2400 rev/min were shown to experience similar heat release rate profile except for the position of the peak heat release rate. The position of the peak heat release rate was shown to retard with the highest speed. Both engine speeds experienced decreasing trend of heat release rate at around 5°CA before top dead centre (BTDC) and then

started increasing until another peak was observed at 12°CA after top dead centre (ATDC) as shown **Figure 3(a)**. This was attributed to heat transfer to the cylinder walls as the result of increased heat transfer area. Majority of the chemical energy was converted to heat before the piston reached its TDC. However, the surface area of the chamber is larger than that of at TDC at this position. The MFB curve in **Figure 3(b)** was observed to deviate from the well-known S-shaped curve, where there was a plateau shape of around 50–70% of MFB for all operation speeds. The ignition advance was set to be at the maximum brake torque (MBT) attained at 31°CA BTDC in both conditions as shown in **Table 4**. As a result, the maximum rate of pressure rise was recorded at around 15°CA BTDC on average for all operation conditions. Similarly, the heat release rate was also maximum in this crank angle position. However, the surface area of the chamber was higher at this crank angle position compared to TDC. Due to this, there was higher heat loss through the chamber walls and this could be witnessed from the heat release rate curves as shown in **Figure 3(a)**. In addition, the fuel produced a very low IMEP. The shape could also be due to a very weak mixture energy density in the cylinder. The flame generated through the combustion of this fuel was very weak in all operational conditions. Even though the flame was sustained throughout the cycle, there could be a chance of flame quenching during the period of high heat loss and high turbulence in the combustion chamber during the compression stage. A detailed analysis of the behaviour of such double-Wiebe of the MFB is presented in the article by Hagos and Aziz [56].

As such low calorific value fuels have not been studied in DI SI engine, and the results of this research could not be compared with previous works. However, the MFB curve shown in **Figure 3(b)** was different from the ones reported for carburetted SI engine elsewhere [44, 100], where a low calorific value gas (producer gas) of similar composition was fuelled in a carburetted naturally aspirated SI engine. This could be due to the reason that the previous works operated the engine at homogeneous mixture condition. This fuel was shown to experience technical difficulties in DI engine due to the injection duration limitation. The performance and emission gains thought from the DI fuelling were much overshadowed by the restriction of injection duration. However, the unique nature of the combustion parameters of this fuel attracted more attention. The double-Wiebe function of the MFB of this fuel could be an input in the study of in-cylinder combustion of other multi-species fuels.

3.2.2. Medium calorific value gasification gas combustion (50% H_2–50% CO)

The medium calorific value gasification gas was investigated in the DI SI engine for the combustion, performance and emissions for the engine speed ranging from 1500 to 2400 rev/min. The operation parameters studied are the effect of engine speed and injection timing and further the combustion, performance and emissions was compared with that of CNG. The two injection timings investigated are 120° BTDC that represent the direction injection where fuel is started to be injected after the inlet valve closes and 180° BTDC representing partial direct injection where fuel is started to be injected before the inlet valve closes. Late injection timings below 120° BTDC and early injection above 180° BTDC was found not suitable for such fuels due to longer injection duration demand and volumetric efficiency concerns, respectively. Both the two injection timings have their advantages with the late injection suitable for lower engine

http://dx.doi.org/10.5772/64459

speed and the early injection suiting the high engine operation speed. Details of the study are presented elsewhere [101].

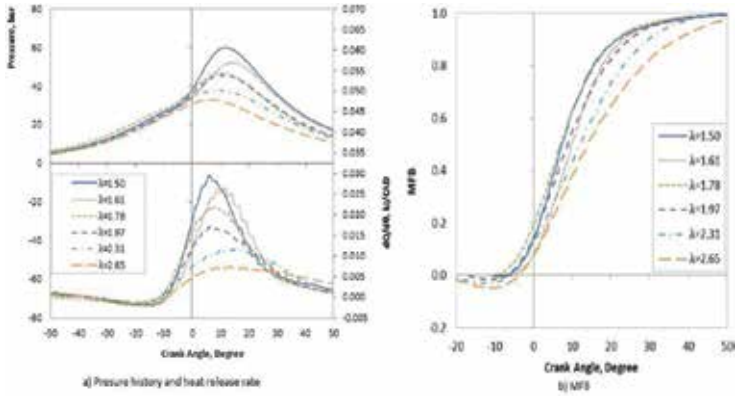

Figure 4. Cylinder pressure heat release rate and MFB versus crank angle for different λ and at 180° BTDC and 2100 rev/min.

Figure 4 shows the effect of the air-fuel ratio on the pressure profile, heat release rate and MFB for different λ at 2100 rev/min. The ignition advance was set at MBT and the injection timing at 180°CA BTDC. **Figure 4(a)** shows the variation of pressure profile and heat release rate with crank angle for various λ at 2100 rev/min. The peak in-cylinder pressure was shown to decrease with an increase in λ. The crank angle corresponding to the peak in-cylinder pressure was observed to advance except at $\lambda = 1.61$. The fastest and shortest heat release rate was presented at the lowest λ. The slowest and longest heat release rate was observed with the highest λ. The combustion phenomenon in **Figure 4(a)** could be further discussed with the cumulative heat release curve (MFB) as shown in **Figure 4(b)**. The overall combustion angle was shown to increase with an increase in λ. This was attributed to the mixture energy density in the chamber. Higher energy density generated more heat leading to higher in-cylinder temperature and thereby fast combustion. The effect of change in the air-fuel ratio on MFB was more evident at the initial stage of combustion for the lower speeds (1500 rev/min) while at the rapid burning stage for the higher speed (2100 rev/min). However, at 2100 rev/min the effect of air-fuel ratio on MFB was visible on the rapid burning stage. This is due to an increase in turbulence as a result of increased speed. This would speed up the combustion rate mainly at the rapid burning stage [58].

On the analysis of the variation of ignition advance with the air-fuel ratio, it was observed that the start of ignition for maximum brake torque was advanced with an increase in λ at all operation speeds. Similarly, the trend of flame development, rapid burning stage and overall combustion durations were shown to increase with an increase in λ. The combustion duration is also observed to increase with an increase in the engine speed. Details about the effect of the air-fuel ratio and the engine speed on the combustion characteristics in the DI SI engine are reported in Hagos et al. [58].

3.3. Comparison of gasification gas and other renewable fuels

Comparison of the combustion and performance of the medium calorific value gasification gas with CNG was conducted under the same engine atmosphere and the study is presented in a separate article [55]. The gasification gas was shown to have a higher peak cylinder pressure, higher heat release rate and faster combustion duration than CNG at all operation speeds and loads. This was attributed to the fast flame propagation of the hydrogen species in the syngas fuel. On the other hand, the ignition advance for MBT was retarded with the gasification gas compared to CNG. This was because of the longer injection duration with gasification gas compared to that with CNG. The fast flame-propagation nature of the H_2 species in the gasification gas resulted in a shorter ignition delay and also contributed in the retardation of the ignition onset of the syngas. The performance comparison of the two fuels, however, has resulted in lower brake thermal efficiency and higher brake-specific fuel consumption (BSFC) of the gasification was reported which was more pronounced at lower engine loads. With increasing speed, the difference was decreased. This was mainly attributed to the low calorific value nature of the gasification gas [55].

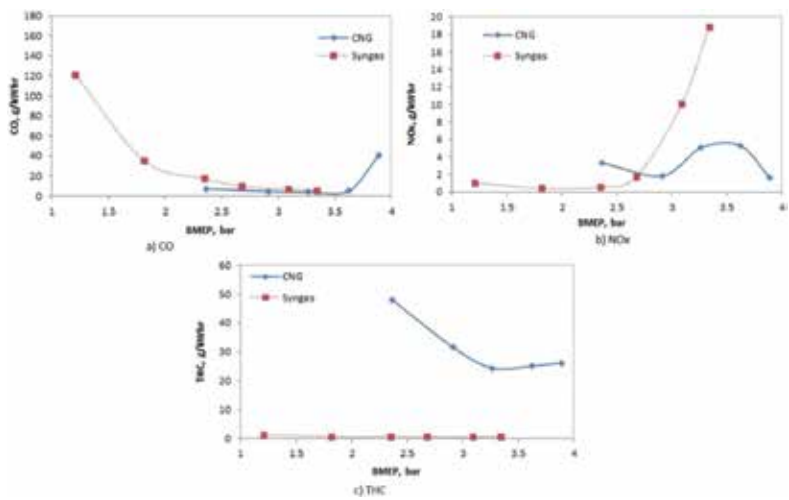

Figure 5. Brake-specific emissions versus BMEP for medium calorific value gasification gas and CNG at 2100 rev/min [55].

3.4. Changes in pollutant emissions as a result of using gasification gas

The major combustible components of the gasification gases are H_2, CO and CH_4. Due to this fact, the emission trends of such fuels in the direct-injection spark ignition engines are different as compared to that of fossil-based fuels. **Figure 5** shows the brake-specific emissions of CO, NO_x and total hydrocarbons (THC) versus the brake mean effective pressure (BMEP) of the medium calorific value gasification gas (syngas). Only the engine speed of 2100 rev/min is considered for the comparison of the gasification gas with that of CNG. The fact that heavy hydrocarbons are absent in the gasification gases indicates that the total hydrocarbon emis-

http://dx.doi.org/10.5772/64459

sions are insignificant in the combustion of gasification gases in IC engines. On the other hand, the presence of H_2 in the gasification gas leads to rapid combustion and higher peak in cylinder pressure. As a result, the NO_x emission was observed to be higher with the gasification gases even if the fuelling strategy is at lean and stratified charge. Similarly, the CO emissions with gasification gases were slightly higher with gasification gases as compared to CNG at lean operation. This is attributed to the incomplete combustion due to lower mixture energy density with lean mixture and escaping of the natural CO of the fuels unburnt from the combustion chamber.

4. Safety of gasification gases

Gasification gases are flammable fuels similar to any other fuels. **Table 1** shows the range of flammability limits of gasification gases, CNG and H_2. Flammability limit is very important characteristics in the safety of fuels in IC engines. Liquid and some gaseous fuels that are commonly used in the automotive engines have been through safety tests during their refuelling, recharging and in crash conditions. Based on the extensive tests, these common fuels are supported with safety codes. For gaseous automotive fuels such as CNG, Vehicular Gaseous Fuel Systems Code (NFPA52) is a code used to govern for their fuelling facility [102]. Alternative fuels that are aimed to replace or take part in the fuelling of automotive engines need to undergo similar safety tests. For the gasification gas fuels, there is limited research towards safety. Besides the flammability issue, the CO content of the gasification gas needs to be taken into consideration. The fact that CO is toxic gas indicates that the utilization of such fuels needs to be under a very tight condition to avoid CO contamination. On the other hand, to compensate the calorific value and increase the mileage at once charging, gasification gas needs to be compressed at high pressure in the range of 200–300 bar. This will require different safety issues that need further consideration. Similar to CNG, these gasification gases are colourless, odourless and tasteless. Therefore, their leakage may not be easily detected. Therefore, odorants should be intentionally added for the easy detection. In general, fire safety issue of gasification gases in IC engines should be adequately addressed in the development and research stage.

5. Technical challenges

The main technical challenge in the fuelling of gasification gas in ICE is the tar deposition in the combustion chamber. Even though ICE is more tolerant towards contaminants compared to gas turbines, the level of tar in the gasification if proper cleaning system is not installed would lead to frequent breakdown. Such challenge could be even worst in the direct-injection engines as injection nozzle hole diameter is too small. The deposition of contaminants and thereby blockage of injector nozzle is imminent in such engines. The molar fraction of the constituent gases varies depending on the variation of the operation conditions for syngas produced from gasification. Maintaining its consistency is huge challenge. The molar fraction

is responsible for the most of fuel properties of the gasification gas, mainly the calorific value, air-fuel ratio, laminar flame speed, auto ignition temperature and the flammability limit. The parameters on the other hand affect the combustion behaviour of the fuel. Similar concern is also present on the fuelling and/or blending of gasification gas in gas turbine plants. Similar feedback system developed for the gas turbine plants may be customized for ICE fuelled by varying molar fraction gasification gases.

The lower calorific value of gasification gas as compared to other gaseous and liquid fuels is another technical challenge that requires precise emphasis in the ICE fuelling. Fuelling of lower calorific value gaseous fuels in the direct-injection spark ignition engine leads for the demand of longer injection duration for the fuels to be fully inducted into the combustion chamber. This is difficult especially during operation at near stoichiometric operation and when the engine speed is higher than 1800 rev/min. Therefore, the utilization of such lower calorific value gaseous fuels in the direct-injection spark ignition engines is possible at lean fuelling strategy. On the other hand, the application of such fuels leads to higher BSFC in the ICE. This has its own consequence on the fuel storage system requiring high-pressure storage system. Methane enrichment of such fuels was used to tackle the challenge in the direct-injection spark ignition engine. As per preliminary study, improvements on the BSFC and on the limitation of the injection duration are observed [103]. Further study on the percentage of the enrichment is undergoing. Parallel to this, the safety issue of the utilization of these fuels in ICE needs to be studied as there is limited information. The CO content of the gasification gas is toxic and extra care need to be given mainly in the fuelling such gases in the carburetted and port-injected spark ignition engine and the dual-fuelling compression ignition engine.

The main motivation in using gasification gases and other gaseous fuels in diesel engine is for a possible substitution of diesel by gaseous fuel, thereby reducing cost, minimizing pollutant emissions such as NO_x and particulate matter, and further to increase the performance of the engine. The performance of a dual-fuel mode compression ignition engine running with gasification gas with composition of 10% H_2, 25% CO, 4% CH_4, 12% CO_2 and 49% N_2 and diesel as pilot fuel was compared with methane in the same duel fuel arrangement [48]. In both the fuels, a shift from diffusion flame combustion to propagation flame combustion was reported with the reduction of the pilot diesel fuel. Overall, methane was shown to perform better as compared to gasification gas in the duel fuelling mode for diesel substitution.

The production and storage process of gasification gases leads to the exposition of the gases to metals such as iron and nickel on the walls of the gasifier and storage tanks [14, 104, 105]. The contact of CO with these metals at higher pressure and temperature leads to the formation of metallic carbonyl contaminants such as iron pentacarbonyl ($Fe(CO)_5$) and nickel tetracarbonyl ($Ni(CO)_4$). At high temperature combustion, the metallic carbonyls, iron pentacarbonyl in particular, decomposes into metal oxide particles in the combustion chamber [106]. **Figure 6** shows the deposits in the combustion chamber of the DI SI engine fuelled with gasification gas. Apart from the deposit formation and its physical effect on the engine components, these metallic carbonyls could also contribute on the formation of particulate matter emissions and flame inhibition [14, 104]. Therefore, extra care should be given to the material in the design of syngas production and storage system.

http://dx.doi.org/10.5772/64459

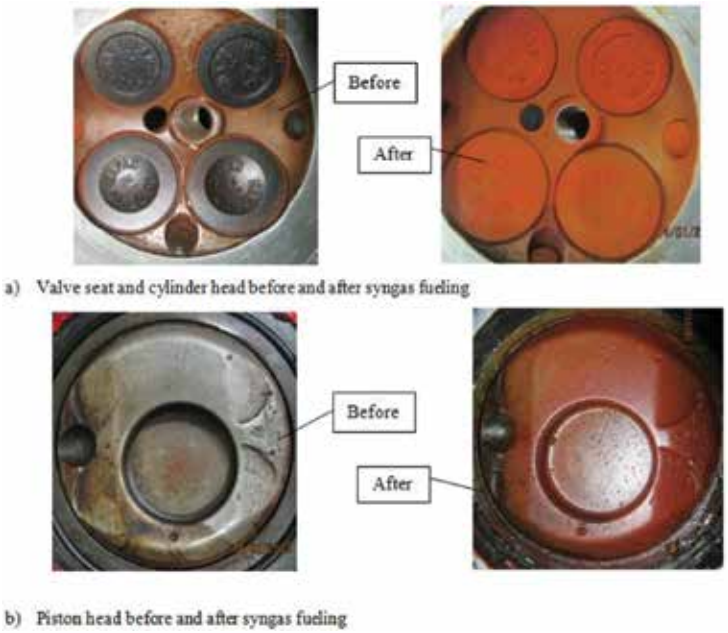

Figure 6. (a and b) Deposits of iron oxides in the combustion chamber of the SI DI engine fuelled with syngas [106].

6. Conclusions and future research directions

The prospect of gasification gas in the IC engines (both SI and CI) has been investigated by taking both the lower and medium calorific value gases into consideration. Due to the higher auto-ignition temperature of gasification gases, they are not suitable to utilize in the CI engine as lone fuels. Both lower and medium calorific value gasification gases have been utilized in a dual-fuelling CI engine with diesel as a pilot fuel for the initiation of the ignition. The amount of diesel as a pilot fuel not only affects the performance but also the combustion phenomenon in the dual fuelling, thereby the emissions of major pollutant gases. The fuelling system design influences the fuel mixing and the overall combustion process in the dual fuelling. The main fuel should be premixed and homogenized during the induction into the combustion chamber. Among the fuelling system designs, the central point mixing system is found compatible to gasification gas induction in the dual-fuelling mode operation. While the gasification gases have shown improvements in the emissions reduction, the higher calorific value gases such as CNG and H_2 have better benefit in the diesel substitution and combustion stability under wider engine operation.

During the era of World War II, where aesthetic value and space conditioning were not an issue at all, gasification gases were utilized in the carburetted SI engine by directly coupling the gasifier with the engine in the vehicle. This design has served its purpose during the severe shortage of gasoline during the war. After the war, however, gasoline distribution came to

normal and the development of vehicle designs channelled to gasoline's advantage. The major discouragements of the gasification gases were start ability, design complexity and inertia, power drop and operation problems. The advancements in the solid fuel conversion technologies and the development of large-scale power plants operating with gasification gases prompted for the application of storage system and thereby the separation of gasification plant from the power plant. This has further initiated the idea of utilizing the gasification gas in the SI DI engine. The medium calorific value gasification gases have shown promising result on the combustion stability and emissions reduction as compared to CNG with some limitations on the longer injection duration demand and higher BSFC. On the other hand, lower calorific value gasification gas is not found suitable for DI SI application. However, the combustion phenomenon observed with this fuel in the DI SI engine is unique and can be an interest to researchers to further investigate the combustion kinetics.

As a future direction, the two limitations stated in the previous paragraph for the medium calorific value gasification gas are found to have minimum effect with an enrichment of methane, thereby boasting the calorific value. However, the optimum percentage of methane enrichment has not been researched so far. The double-Wiebe function of the mass fraction burn of the combustion of lower calorific value gasification gas is another interest for further research. Finally, the safety concerns, the complete system energy balance and the potential to control the formation of deposits of metallic pentacarbonyls need to be further investigated.

Nomenclature

ATDC	after top dead centre
BMEP	brake mean effective pressure
BSFC	brake specific fuel consumption
BTDC	before top dead centre
CA	crank angle
CFB	Circulating fluidized bed
CI	compression ignition
CNG	compressed natural gas
CO	carbon monoxide
DI	direct injection
DME	Dimethyle ether
EGR	Exhaust gas recirculation
HC	hydrocarbon
ICE	internal combustion engine
IMEP	indicated mean effective pressure
IVC	inlet valve close

http://dx.doi.org/10.5772/64459

LPG	liquefied petroleum gas
MBT	maximum brake torque
MFB	mass fraction burn
NOx	nitrogen oxides
OECD	Organization for Economic Cooperation and Development
PFI	port fuel injection
PREMIER	premixed mixture ignition in the end-gas region
RDF	Refuse-derived fuel
ROHR	rate of heat release
rpm	revolutions per minute
SI	spark ignition
TDC	top dead centre
THC	total hydrocarbon
UHC	unburned hydrocarbon
λ	relative air fuel ratio

Author details

Ftwi Yohaness Hagos[1,2*], Abd Rashid Abd Aziz[3,4], Shaharin A. Sulaiman[3,4] and Bahaaddein K. M. Mahgoub[4]

*Address all correspondence to: ftwi@ump.edu.my

1 Faculty of Mechanical Engineering, University of Malaysia Pahang, Pekan, Pahang, Malaysia

2 Automotive Engineering Center, University of Malaysia Pahang, Pekan, Pahang, Malaysia

3 Centre for Automotive Research and Electric Mobility (CAREM), Universiti Teknologi PETRONAS, Bandar Seri Iskandar, Tronoh, Perak, Malaysia

4 Department of Mechanical Engineering, Universiti Teknologi PETRONAS, Bandar Seri Iskandar, Tronoh, Perak, Malaysia

References

[1] J. B. Heywood, *Internal Combustion Engine Fundamentals*. New York: McGraw Hill International, 1988.

[2] M. V. Melosi. "The automobile and the environment in American History", *Automobile in American Life and Society,* 2010 (August 12, 2014). Available at: http://www.autolife.umd.umich.edu/Environment/E_Overview/E_Overview3.htm

[3] K. D. Decker. *Wood Gas Vehicles: Firewood in the Fuel Tank*, 2010 (October 15). Available at: http://www.lowtechmagazine.com/2010/01/wood-gas-cars.html

[4] J. Dulac, "Global transport outlook to 2050: Targets and scenarios for a low-carbon transport sector", ed. EGRD, OECD/IEA, International Energy Agency, 2012.

[5] D. o. E. a. S. Affairs, "World population projected to reach 9.6 billion by 2050", in *UN News*, New York: United Nations, 2013.

[6] S. Watson, L. Fulton, S. Perkins, and R. de Jong, "50 by 50: Global Fuel Economy Initiative", 2009. Available at: http://www.fiafoundation.org/50by50/documents/50BY50_report.pdf

[7] S. R. James, "Hominid use of fire in the lower and middle Pleistocene: a review of the evidence", *Curr. Anthropol.,* vol. 30, pp. 1–26, 1989.

[8] D. Tillman, *The Combustion of Solid Fuels and Wastes*. London, UK: Academic Press, 1991.

[9] R. Kandiyoti, A. Herod, and K. Bartle, *Solid Fuels and Heavy Hydrocarbons Liquids: Thermal Characterization and Analysis*. Amsterdam, The Netherlands: Elsevier, 2006.

[10] M. Lackner, Á. Palotás, and F. Winter, *Combustion: From Basics to Applications*. Weinheim, Germany: Wiley Publisher, 2013.

[11] WEC. *World Energy Resources: 2013 Survey* [Online]. Available: http://www.worldenergy.org/data/resources/resource/coal/

[12] B. Miller and D. Tillman, *Combustion Engineering Issues for Solid Fuel Systems*. Amsterdam, The Netherlands: Elsevier, 2008.

[13] EIA, *International Energy Outlook*, Washington, DC: US Department of Energy, 2013.

[14] G. A. Richards and K. H. Casleton, "Gasification technology to produce synthesis gas", in *Synthesis Gas Combustion Fundamentals and Applications*, T. Lieuwen, V. Yang, and R. Yetter, Eds., New York: CRC Press Taylor and Francis Group, 2010.

[15] P. Basu, *Biomass Gasification and Pyrolysis: Practical Design and Theory*. United States: Elsevier; 2010.

[16] Anon, "Wood gas as engine fuel", *FAO Forestry Paper,* vol. 72, p. 133, 1986.

[17] M. Talmadge, M. Biddy, A. Dutta, S. Jones, and A. Meyer, "*Syngas Upgrading to Hydrocarbon Fuels Technology Pathway*", Denver, Colorado: U.S. Department of Energy Bioenergy Technologies Office, 2013.

[18] D. M. Alonso, J. Q. Bond, and J. A. Dumesic, "Catalytic conversion of biomass to biofuels", *Green Chem.*, vol. 12, pp. 1493–1513, 2010.

[19] S. Hassan, Z. A. Zainal, and M. A. Miskam, "A preliminary investigation of compressed producer gas from downdraft biomass gasifier", *J. Appl. Sci.,* vol. 10, pp. 406–412, 2010.

[20] J. Apt, A. Newcomer, L. B. Lave, S. Douglas, and L. M. Dunn, "*An Engineering-Economic Analysis of Syngas Storage*", Pittsburgh: National Energy Technology Laboratory, 2008.

[21] A. Newcomer and J. Apt, "Storing syngas lowers the carbon price for profitable coal gasification", *Environ. Sci. Technol.*, vol. 41, pp. 7974–7979, 2007.

[22] G. Sridhar, P. J. Paul, and H. S. Mukunda, "Biomass derived producer gas as a reciprocating engine fuel—an experimental analysis", *Biomass Bioenerg.,* vol. 21, pp. 61–72, 2001.

[23] F. Y. Hagos, A. R. A. Aziz, and S. A. Sulaiman, "Trends of syngas as a fuel in internal combustion engines", *Adv. Mech. Eng.*, vol. 2014, pp. 1–10, 2014.

[24] H. LaFontaine and G. P. Zimmerman, *Construction of a Simplified Wood Gas Generator for Fueling Internal Combustion Engines in a Petroleum Emergency*, Washington, DC: Federal Emergency Management Agency; 1989.

[25] E. Galloni and M. Minutillo, "Performance of a spark ignition engine fuelled with reformate gas produced on-board vehicle", *Int. J. Hydrogen Energ.,* vol. 32, pp. 2532–2538, 2007.

[26] B. Gamiño and J. Aguillón, "Numerical simulation of syngas combustion with a multi-spark ignition system in a diesel engine adapted to work at the Otto Cycle", *Fuel,* vol. 89, pp. 581–591, 2010.

[27] N. N. Mustafi, Y. C. Miraglia, R. R. Raine, P. K. Bansal, and S. T. Elder, "Spark-ignition engine performance with 'powergas' fuel (Mixture of CO/H_2): a comparison with gasoline and natural gas", *Fuel,* vol. 85, pp. 1605–1612, 2006.

[28] R. G. Papagiannakis, C. D. Rakopoulos, D. T. Hountalas, and E. G. Giakoumis, "Study of the performance and exhaust emissions of a spark-ignited engine operating on syngas fuel", *Int. J. Altern. Propul.,* vol. 1, pp. 190–215, 2007.

[29] C. D. Rakopoulos and C. N. Michos, "Development and validation of a multi-zone combustion model for performance and nitric oxide formation in syngas fueled spark ignition engine", *Energy Convers. Manage.,* vol. 49, pp. 2924–2938, 2008.

[30] C. D. Rakopoulos, C. N. Michos, and E. G. Giakoumis, "Availability analysis of a syngas fueled spark ignition engine using a multi-zone combustion model", *Energy,* vol. 33, pp. 1378–1398, 2008.

[31] A. Shah, R. Srinivasan, S. D. F. To, and E. P. Columbus, "Performance and emissions of a spark-ignited engine driven generator on biomass based syngas", *Bioresour. Technol.,* vol. 101, pp. 4656–4661, 2010.

[32] A. K. Sharma, "Experimental study on 75 kW_{th} downdraft (biomass) gasifier system", *Renew. Energ.,* vol. 34, pp. 1726–1733, 2009.

[33] J. A. Smith and G. J. J. Bartley, "Stoichiometric operation of a gas engine utilizing synthesis gas and EGR for NO_x control", *J. Eng. Gas Turbines Power,* vol. 122, pp. 617–623, 2000.

[34] G. Sridhar, "Experimental and modeling aspects of producer gas engine", in *Sustainable Energy Technologies (ICSET 2008) International Conference*, Singapore, 2008, pp. 995–1000.

[35] A. K. Rajvanshi, "Biomass gasification", in *Alternative Energy in Agriculture*. vol. 2, D. Y. Goswami, Ed., New York: CRC Press, 1986, pp. 83–102.

[36] S. Dasappa, P. J. Paul, H. S. Mukunda, N. K. S. Rajan, G. Sridhar, and H. V. Sridhar, "Biomass gasification technology—a route to meet energy needs", *Curr. Sci. India,* vol. 87, pp. 908–916, 2004.

[37] J. Ahrenfeldt, E. V. Foged, R. Strand, and U. B. Henriksen, *Development and Test of a New Concept for Biomass Producer Gas Engines*, Risø National Laboratory for Sustainable Energy, Technical University of Denmark, Roskilde ISBN 978-87-550-3811-0, 2010.

[38] J. Ahrenfeldt, T. K. Jensen, U. Henriksen, J. Schramm, and B. Gøbel, "CO emissions from gas engines operating on biomass producer gas", presented at the World Conference and Technology Exhibition on Biomass for Energy and Industry Florence, Italy, 2004.

[39] V. Belgiorno, G. D. Feo, C. D. Rocca, and R. M. A. Napoli, "Energy from gasification of solid wastes", *Waste Manage. (Oxford),* vol. 23, pp. 1–15, 2003.

[40] V. B. Kovács and A. Meggyes, "Investigation of utilization of low heating value gaseous fuels in gas engine", in *4th European Combustion Meeting*, Vienna University of Technology, Vienna, Austria, 2009.

[41] F. V. Tinaut, A. Melgar, A. Horrillo, and A. D. de la Rosa, "Method for predicting the performance of an internal combustion engine fuelled by producer gas and other low heating value gases", *Fuel Process Technol.,* vol. 87, pp. 135–142, 2006.

[42] S.S.Vinay, S.D.Ravi, G. PremaKumar, and N.K.S. Rajan, "Numerical and experimental modeling of producer gas carburettor", in *Advances in Mechanical Engineering*, S.V. National Institute of Technology, Surat, Gujarat, India, 2008.

[43] G. Przybyla, L. Ziolkowski, and A. Szlek, "Performance of SI engine fuelled with LCV gas", presented at the Second International Workshop on Biomass Gasification Technologies (BIOGASTECH) Gebze, Turkey, 2008.

[44] Y. Ando, K. Yoshikawa, M. Beck, and H. Endo, "Research and development of a low-BTU gas-driven engine for waste gasification and power generation", *Energy,* vol. 30, pp. 2206–2218, 2005.

[45] V. Sadykov, V. Sobyanin, V. Kirillov, V. Kuzmin, N. Kuzin, Z. Vostrikov, et al., "Syngas as a fuel for IC and diesel engines: efficiency and harmful emissions cut-off", presented

at the International Hydrogen Energy Congress and Exhibition (IHEC 2005), Istanbul, Turkey, 2005.

[46] E. Toulson, H. Watson, and W. Attard, "The lean limit and emissions of a gasoline HAJI system that employs syngas in place of hydrogen as the prechamber fuel", in *International Federation of Automotive Engineering Societies (FISITA) World Automotive Congress*, Munich, Germany, 2008.

[47] A. S. Bika, *Synthesis Gas Use in Internal Combustion Engines*, PhD, Faculty of Graduate School, University of Minnesota, Minnesota, 2010.

[48] C. T. Spaeth, *Performance Characteristics of a Diesel Fuel Piloted Syngas Compression Ignition Engine*, Master of Applied Science, Department of Mechanical and Materials Engineering, Queen's University, 2012.

[49] F. Konigsson, *Advancing the Limits of Dual Fuel Combustion*, Licentiate, Department of Machine Design, Stockholm, Sweden: Royal Institute of Technology (KTH), 2012.

[50] U. Azimov, E. Tomita, N. Kawahara, and Y. Harada, "Effect of syngas composition on combustion and exhaust emission characteristics in a pilot-ignited dual-fuel engine operated in PREMIER combustion mode", *Int. J. Hydrogen Energ.*, vol. 36, pp. 11985–11996, 2011.

[51] B. B. Sahoo, N. Sahoo, and U. K. Saha, "Effect of H_2:CO ratio in syngas on the performance of a dual fuel diesel engine operation", *Appl. Therm. Eng.*, vol. 49, pp. 139–146, 2012.

[52] B. B. Sahoo, U. K. Saha, and N. Sahoo, "Theoretical performance limits of a syngas-diesel fueled compression ignition engine from second law analysis", *Energy*, vol. 36, pp. 760–769, 2011.

[53] A. M. L. M. Wagemakers and C. A. J. Leermakers, "Review on the effects of dual-fuel operation, using diesel and gaseous fuels, on emissions and performance", *SAE Paper 2012-01-0869*, 2012, doi:10.4271/2012-01-0869.

[54] S. Hassan, Z. A. Zainal, and M. A. Miskam, "Performance and emission characteristics of supercharged biomass producer gas-diesel dual fuel engine", *J. Appl. Sci.*, vol. 11, pp. 1606–1611, 2011.

[55] F. Y. Hagos, A. R. A. Aziz, and S. A. Sulaiman, "Syngas (H_2/CO) in a spark-ignition direct-injection engine. Part 1: Combustion, performance and emissions comparison with CNG", *Int. J. Hydrogen Energ.*, vol. 39, pp. 17884–17895, 2014.

[56] F. Y. Hagos and A. R. A. Aziz, "Mass fraction burn investigation of lean burn low BTU gasification gas in direct-injection spark-ignition engine", *SAE Technical Paper 2014-01-1336*, 2014, doi:10.4271/2014-01-1336.

[57] F. Y. Hagos, A. R. A. Aziz, and S. A. Sulaiman, "Combustion characteristics of direct-injection spark-ignition engine fuelled with producer gas", *Energy Educ. Sci. Technol. Part A: Energy Sci. Res.,* vol. 31, pp. 1683–1698, 2013.

[58] F. Y. Hagos, A. R. A. Aziz, and S. A. Sulaiman, "Effect of air-fuel ratio on the combustion characteristics of syngas (H_2:CO) in direct-injection spark-ignition engine", *Energy Procedia,* vol. 61, pp. 2567–2571, 2014.

[59] F. Y. Hagos, A. R. A. Aziz, and S. A. Sulaiman, "Early flame development image comparison of low calorific value syngas and CNG in DI SI gas engine", in *IOP Conference Series: Earth and Environmental Science*, Putrajaya, Malaysia, 2013, p. 012070.

[60] F. Y. Hagos, A. A. A. Rashid, and S. A. Sulaiman, "Study of syngas combustion parameters effect on internal combustion engines", *Asian J. Sci. Res.,* vol. 6, pp. 187–196, 2013.

[61] M. Morri, L. Waldheim, A. Faaij, and K. Stahl. "Status of large-scale biomass gasification and prospects", in *Handbook Biomass Gasification*, H. Knoef and J. Ahrenfeldt, Eds., Enschede, The Netherlands: Biomass Technology Group (BTG), 2005.

[62] J. Holmala J. Isaksson, and Metso, "Metso-supplied world's largest biomass gasification plant inaugurated in Finland", Helsinki, Finland: Metso Corporation, 2013.

[63] C. Erdalen, GoBiGas, "Göteborg Energi's biogas plant GoBiGas is now fully operational", Göteborg, Sweden: Göteborg Energi AB, 2014.

[64] P. McKendry, "Energy production from biomass (part 1): overview of biomass", *Bioresource Technol.,* vol. 83, pp. 37–46, 2002.

[65] R. Konda, S. Sulaiman, and B. Ariwahjoedi, "Syngas production from gasification of oil palm fronds with an updraft gasifier", *J. Appl. Sci.,* vol. 12, p. 2555, 2012.

[66] S. M. Atnaw, S. A. Sulaiman, and S. Yusup, "Syngas production from downdraft gasification of oil palm fronds", *Energy,* vol. 61, pp. 491–501, 2013.

[67] S. M. Atnaw, S. A. Sulaiman, and S. Yusup, "Influence of fuel moisture content and reactor temperature on the calorific value of syngas resulted from gasification of oil palm fronds", *Sci. World J.,* vol. 2014, pp. 1–9, 2014.

[68] H. Hofbauer and H. Knoef, "Success stories on biomass gasification", in *Handbook Biomass Gasification*, H. Knoef and J. Ahrenfeldt, Eds., Enschede, The Netherlands: Biomass Technology Group (BTG), 2005.

[69] M. Paisley and R. Overend, "Verification of the performance of future energy resources' SilvaGas (R) biomass gasifier—operating experience in the vermont gasifier", in *Pittsburgh Coal Conference,* Pittsburgh, PA, 2002.

[70] A. Kaupp and J. Goss, *State-of-the-Art Report for Small Scale (to 50 kw) Gas Producer-engine Systems*, Department of Agricultural Engineering: California University, Davis (USA); 1981.

[71] K. Von Mitzlaff, "Engines for biogas", *German Appropriate Technology Exchange (GATE), Deutsche Gesellschaft fÃ¼r Technische Zusammenarbeit (GTZ),* 1988.

[72] D. Granatstein, *Case Study on Lahden Lämpövoima Gasification Project, Kymijärvi Power Station, Lahti, Finland*, Varennes, QC, Canada: Natural Resources Canada/CANMET Energy Technology Centre (CETC) 2002.

[73] K. Von Mitzlaff, "Engines for biogas", *German Appropriate Technology Exchange (GATE), Deutsche Gesellschaft für Technische Zusammenarbeit (GTZ),* 1988.

[74] C. S. Weaver and S. H. Turner, "Dual fuel natural gas/diesel engines: technology, performance, and emissions", *SAE Technical Paper 0148-7191*, 1994, doi:10.4271/940548.

[75] G. Karim and M. Khan, "Examination of effective rates of combustion heat release in a dual-fuel engine", *J. Mech. Eng. Sci.,* vol. 10, pp. 13–23, 1968.

[76] G. A. Karim, "A review of combustion processes in the dual fuel engine—the gas diesel engine", *Prog. Energy Combust. Sci.,* vol. 6, pp. 277–285, 1980.

[77] C. Rakopoulos and D. Kyritsis, "Comparative second-law analysis of internal combustion engine operation for methane, methanol, and dodecane fuels", *Energy,* vol. 26, pp. 705–722, 2001.

[78] C. Rakopoulos and D. Kyritsis, "Hydrogen enrichment effects on the second law analysis of natural and landfill gas combustion in engine cylinders", *Int. J. Hydrogen Energy,* vol. 31, pp. 1384–1393, 2006.

[79] C. Rakopoulos and C. Michos, "Generation of combustion irreversibilities in a spark ignition engine under biogas—hydrogen mixtures fueling", *Int. J. Hydrogen Energ.,* vol. 34, pp. 4422–4437, 2009.

[80] A. S. Ramadhas, S. Jayaraj, and C. Muraleedharan, "Dual fuel mode operation in diesel engines using renewable fuels: rubber seed oil and coir-pith producer gas", *Renewable Energ.,* vol. 33, pp. 2077–2083, 2008.

[81] B. K. Mahgoub, S. Sulaiman, and Z. Abdul Karim, "Performance study of imitated syngas in a dual-fuel compression ignition diesel engine", *Int. J. Automotive Mech. Eng.,* vol. 11, pp. 2282–2293, 2015.

[82] M. M. Roy, E. Tomita, N. Kawahara, Y. Harada, and A. Sakane, "Performance and emission comparison of a supercharged dual-fuel engine fueled by producer gases with varying hydrogen content", *Int. J. Hydrogen Energ.,* vol. 34, pp. 7811–7822, 2009.

[83] E. Tomita, N. Fukatani, N. Kawahara, K. Maruyama, and T. Komoda, "Combustion characteristics and performance of supercharged pyrolysis gas engine with micro-pilot ignition", in *CIMAC Congress*, Vienna, Austria, 2007.

[84] R. Papagiannakis and D. Hountalas, "Combustion and exhaust emission characteristics of a dual fuel compression ignition engine operated with pilot diesel fuel and natural gas", *Energy Convers. Manage.,* vol. 45, pp. 2971–2987, 2004.

[85] H. E. Saleh, "Effect of variation in LPG composition on emissions and performance in a dual fuel diesel engine", *Fuel,* vol. 87, pp. 3031–3039, 2008.

[86] N. Saravanan and G. Nagarajan, "Experimental investigation in optimizing the hydrogen fuel on a hydrogen diesel dual-fuel engine", *Energy Fuels,* vol. 23, pp. 2646–2657, 2009.

[87] N. Saravanan and G. Nagarajan, "Experimental investigation on performance and emission characteristics of dual fuel DI diesel engine with hydrogen fuel", *SAE Technical Paper,* 2009, doi:10.4271/2009-26-0032.

[88] N. Saravanan, G. Nagarajan, K. Kalaiselvan, and C. Dhanasekaran, "An experimental investigation on hydrogen as a dual fuel for diesel engine system with exhaust gas recirculation technique", *Renewable Energy,* vol. 33, pp. 422–427, 2008.

[89] U. Azimov, E. Tomita, N. Kawahara, and S. S. Dol, "Combustion characteristics of syngas and natural gas in micro-pilot ignited dual-fuel engine", *World Academy of Science, Engineering and Technology*, vol. 72, pp. 1614–1621, 2012.

[90] A. S. Bika, L. M. Franklin, and D. B. Kittelson, "Emissions effects of hydrogen as a supplemental fuel with diesel and biodiesel", *SAE Int. J. Fuels Lubric.*, vol. 1, pp. 283–292, 2008.

[91] T. Lieuwen, V. Yang, and R. Yetter, *Synthesis Gas Combustion: Fundamentals and Applications*. New York: CRC Press, 2009.

[92] R. J. Nichols, "Challenges of change in the auto industry: why alternative fuels?", in *The 15 th Annual Fall Technical Conference of the ASME Internal Combustion Engine Division, Morgantown, WV, USA, 09/26-29/93*, 1993, pp. 3–10.

[93] C. S. Weaver, "Natural gas vehicles—a review of the state of the art", *SAE Technical Paper, 892133* 1989, doi:10.4271/892133.

[94] A. Bilcan, O. Le Corre, M. Tazerout, A. Ramesh, and S. Ganesan, "Characterization of the LPG-diesel dual fuel combustion", *SAE Technical Paper, 2001-28-0036* 2001, doi: 10.4271/2001-28-0036.

[95] D. Gera, M. P. Mathur, M. C. Freeman, and A. Robinson, "Effect of large aspect ratio of biomass particles on carbon burnout in a utility boiler", *Energy Fuels,* vol. 16, pp. 1523–1532, 2002.

[96] B. K. M. Mahgoub, S. A. Sulaiman, and Z. A. B. A. Karim, "Emission of a compression ignition engine fuelled by diesel and imitated syngas", in *AIP Conference Proceedings*, 2012, p. 964.

[97] G. Sridhar, S. Dasappa, H. V. Sridhar, P. J. Paul, and N. K. S. Rajan, "Gaseous emissions using producer gas as fuel in reciprocating engines", *SAE Technical Paper 10.4271/2005-01-1732*, 2005, doi:10.4271/2005-01-1732.

[98] H. M. Cho and B.-Q. He, "Spark ignition natural gas engines—a review", *Energy Convers. Manage.,* vol. 48, pp. 608–618, 2007.

[99] E. Monteiro, M. Bellenoue, J. Sottton, and A. Rouboa, "Syngas application to spark ignition engine working simulations by use of rapid compression machine", in *Internal Combustion Engines*, K. Lejda and P. Wos, Eds., Rijeka, Croatia: InTech, 2012, pp. 51–74.

[100] J. Ahrenfeldt, *Characterization of Biomass Producer Gas as Fuel for Stationary Gas Engines in Combined Heat and Power Production*, Degree for Doctor of Philosophy, Technical University of Denmark: Department of Mechanical Engineering; 2007.

[101] F. Y. Hagos, A. R. A. Aziz, and S. A. Sulaiman, "Effect of injection timing on combustion, performance and emissions of lean-burn syngas (H2/CO) in spark-ignition direct-injection engine", *Int. J. Engine Res.,* 2015, doi: 10.1177/1468087415623910.

[102] NFPA, *The Vehicular Gaseous Fuel Systems Code*, Quincy, Massachusetts: National Fire Protection Association, 2010.

[103] F. Y. Hagos, A. R. A. Aziz, and S. A. Sulaiman, "Methane enrichment of syngas (H_2/CO) in a spark-ignition direct-injection engine: combustion, performance and emissions comparison with syngas and compressed natural gas", *Energy,* vol. 90, pp. 2006-2015, 2015.

[104] T. C. Williams and C. R. Shaddix, "Contamination of carbon monoxide with metal carbonyl: implications for combustion research", *Combust. Sci. Technol.,* vol. 179, pp. 1225–1230, 2007.

[105] C. Wyse, J. Vininski, and T. Watanabe, "Cylinder, purifier technologies for controlling contamination in CO", *Solid State Technol.,* vol. 45, pp. 125–129, 2002.

[106] F. Hagos, A. Aziz, and S. Sulaiman, "Investigation of deposit formation in direct-injection spark-ignition engine powered on syngas", *Int. J. Automotive Technol.,* vol. 16, pp. 479–485, 2015

Chapter 10

Phenomenological Modeling of Combustion Process in Diesel Engines Based on Stochastic Method

Long Liu

Additional information is available at the end of the chapter

http://dx.doi.org/10.5772/64749

Abstract

In order to satisfy the growing demand for the reduction of fuel consumption and pollutant emissions, various technologies have been employed in diesel engines. Consequently, to determine the optimal combustion control strategy, many parameters such as injection pressure, nozzle diameter, injection timing, injection quantity, and exhaust gas recirculation (EGR) rate should be selected properly corresponding to the engine operating conditions. It is difficult to obtain the appropriate strategies without understanding the change in combustion process when varying these parameters. To realize parametric studies on combustion control strategy of modern diesel engines, a phenomenological combustion model based on stochastic method was developed. In this model, the modeling of the spray tip and tail penetration after the end of injection, and interaction between the sprays of sequent injection stages were focused on to modify the stochastic combustion model for combustion simulation with multiple injection. The effects of swirl, wall impingement, and adjacent spray interaction are formulated simply to make the combustion model more accurate and computationally efficient. The simulation results were compared with experimental data from a single-cylinder test engine for pilot/main two-stage injection. The results reveal that the model has capability to accurately predict the combustion characteristics and emissions of diesel engine with pilot/main two-stage injection.

Keywords: diesel engine, combustion modeling, phenomenological model, possibility density function

1. Introduction

Recently, continuous reduction of the oxides of nitrogen (NOx) and PM emissions for confronting increasingly stringent emission standards becomes a significant task for combus-

INTECH
open science | open minds

© 2016 The Author(s). Licensee InTech. This chapter is distributed under the terms of the Creative Commons Attribution License (http://creativecommons.org/licenses/by/3.0), which permits unrestricted use, distribution, and reproduction in any medium, provided the original work is properly cited. CC BY

tion improvement of diesel engines; especially the reduction of NOx emissions is quite difficult for aftertreatment for low-load operating conditions due to low exhaust gas temperature. Hence, in-cylinder combustion improvement is required for low-load operation, subsequently the advanced combustion concepts have been proposed for dealing with this situation, such as premixed charge compression ignition (PCCI) and low-temperature combustion (LTC). No matter whether it is PCCI or LTC, the main aim is to obtain more homogeneous mixture and suppress locally high combustion temperature. This aim is typically achieved with injection timing adjustment with high exhaust gas recirculation (EGR) rate. However, accompanying with reduction of NOx and PM, the CO and HC emissions are observed to increase and even exceed the emission standards [1–4]. Meanwhile, long ignition delay promotes the fuel-air mixing before ignition; it leads to the strong dependence of ignition timing on chemical reaction, which makes the ignition timing control difficult. And fast combustion of the mixture premixed before ignition increases the combustion noise associated with rapid rise of in-cylinder pressure. Because of these barriers, the advanced combustion concepts are limited in low-load operation.

To extend the advanced combustion concepts to high-load operation and obtain the best reduction of emissions, many technologies, including high-injection pressure, small nozzle diameter, multistage injection, EGR, and high-intake boost, have to be integrated to realize in-cylinder combustion improvement. Consequently, to determine the optimal combustion control strategy, many parameters such as injection pressure, nozzle diameter, injection timing, injection quantity, and EGR rate should be selected properly corresponding to the engine operating conditions. It brings a heavy work and high cost on experiments, moreover it is difficult to obtain the appropriate strategies without understanding the change in combustion process when varying these parameters. Thus, an accurate and computationally efficient combustion model is needed for these parameters study. Considering the trade-off between accuracy and computational efficiency, the phenomenological combustion models are often adopted for the parametric study [5].

In phenomenological combustion models, the combustion process is mimicked mathematically based on the results of observed phenomena with focus on predominant and rate-determining processes in combustion. To describe the heterogeneous distribution of fuel concentration and temperature and low-temperature combustion phenomena, some detailed phenomenological diesel combustion models are developed based on the spray behavior, which incorporate the calculation of chemical reaction in the spray region. According to the method for description of fuel concentration distribution, these models can be divided into two types. One type is to divide the spray into different zones based on the spray structure [6–8]. In the other type, fuel concentration distribution is represented by probability density function (PDF) of fuel mass fraction [9, 10]. PDF method is dominant to couple the turbulent mixing and chemical kinetics to calculate the turbulent combustion process in diesel engines, and it is easy to blend with the emission models, such as NOx and soot models. Whence the pollutants production process can be predicted and analyzed with varying relevant parameters.

http://dx.doi.org/10.5772/64749

In modern diesel engines, multiple-injection has played a significant role in the latest engines to reduce NOx, smoke emissions, and combustion noise simultaneously [11–13]. Proper selection of injection strategy from numerous injection parameters satisfying different operating conditions is a challenging work. Thus, to estimate the modern diesel engines combustion, the combustion process with multiple injections needs to be included in the phenomenological combustion model. Recently, some models had been proposed based on PDF method to calculate the combustion with multiple-injection [14–16]. In these models, each injection is customarily treated to form a spray region, and relevant calculations including spray propagation, fuel evaporation, turbulent mixing, ignition, and chemical reaction are performed in each spray. According to the sprays propagation phenomena under multiple-injection situation, the combustion of the latter spray is significantly dependent on the thermodynamic states of the former spray. Therefore, the interaction between former spray and latter spray has to be considered in the model. Normally, the latter injection starts after the end of the former injection, so that the evolution of the spray after the end of injection (EOI) has to be imitated. In fact, the spray behaviors after EOI are indicated quite different from that during injection by the fundamental studies on turbulent gas and diesel jets [17–21]. However, there is no simple model available in phenomenological models to describe the spray development and air entrainment after EOI. Currently, frequently used models of spray propagation are Wakuri's model, Siebers's model, and Hiroyasu's model that only satisfy the spray propagation during injection with steady state and do not involve any information for that after EOI.

According to the modeling concept from the developed models [14–16], the latter spray is assumed to be injected into the former spray region, so that the entrained gas of the latter spray only comes from the former spray zone. It should be noted that all of these interaction treatments assume that later spray entrains the gas from the former spray zone immediately when the later injection starts, whereas some fundamental studies discover that the mixture near the injector tip is diluted very fast after EOI [20, 22]. This implies that the gas near the injector tip should be very lean when the later injection starts, particularly for the early pilot injection case. Thereby, it is necessary to consider this phenomenon in appropriate form to imitate the interaction between sprays from the sequent injections. Meanwhile, the swirl flow deflects the spray from the initial injection direction [23]. In multiple-injection case, the magnitudes of deflection are different for former and latter sprays, which results in that the swirl effects has to be involved for spray-to spray interaction modeling.

In addition, the phenomenological combustion models usually do not consider the spatial information. However, the early injection is a typical strategy for advanced combustion concepts, especially quite early pilot injection for multiple-injection strategy. The early injection causes the wall impingement, consequently the effects of different impinging positions and the spray flames propagation along the cylinder wall on fuel-air mixing need to be involved in the model.

Thus, in this study, a phenomenological combustion model was developed based on a stochastic mixing model. The heterogeneity of fuel concentration and temperature is described using the PDF. Evolution of the mixing and combustion is represented by the temporal change of PDF due to the mixing, fuel injection, fuel evaporation, air entrainment into a spray, heat

loss to the combustion chamber walls, and chemical reactions. To focus on the simulation of new combustion concepts, such as LTC and PCCI, the effects of EGR and multiple-injection was involved in the model. The model employs a quasi-global chemical kinetics model combined with stochastic mixing model to describe the low-combustion process caused by EGR effect. The key points of the study concentrated on are as follows: (1) Spray model developing to describe the spray evolution after end of injection (EOI). (2) Defining and calculating the presumed spray tail to consider the quite lean mixture near the nozzle exit after EOI. (3) Modeling spray-to-spray interaction between sequent injections and the swirl flow effects on it. (4) Introducing the effects of spray-wall interaction on fuel-air mixing. Finally, the simulations are performed in pilot/main two-stage injection cases, and are validated by experimental data from a single-cylinder diesel engine, including in-cylinder pressures, heat release rates, and NOx and PM emissions.

2. Stochastic combustion model

The stochastic combustion model in this study was first proposed in [10] for conventional combustion with single-stage injection in DI diesel engines. And then this model was modified in [24–26] to analyze the PCCI combustion process. Up to Ref. [26], this model has employed a stochastic turbulent mixing model coupled with a quasi-global chemical kinetic model to describe the heterogeneous combustion process in diesel sprays, and the specific submodels includes air entrainment, turbulent mixing, fuel vaporization, heat loss, and chemical kinetic model.

2.1. Model description

The essential of the stochastic combustion model focus on the turbulence controlled fuel-air mixing process. In this model, the heterogeneity in fuel concentration and temperature is described using probability density functions $f(x, t)$, where $x = (h, y_1, y_2, \ldots, y_n)$, h denotes the specific enthalpy and $y_1, y_2, \ldots, y_n$ the mass fraction of chemical species. Based on considering the in-cylinder pressure as uniform distribution over the entire cylinder, the time evolution of $f(x, t)$ is expressed as Eq. (1)

$$\frac{\partial f}{\partial t} + \frac{\partial \dot{y} f}{\partial y} + \dot{p}\frac{\partial v f}{\partial h} = \omega m(x,t) \tag{1}$$

where $(\cdot)$ expresses the time derivative, p the in-cylinder pressure, v the specific volume, $m(x, t)$ represents the mixing caused by turbulence, and ω the mixing rate. To calculate the $f(x, t)$, the pressure Eq. (2) was derived in [5] to simultaneously solve with Eq. (1)

http://dx.doi.org/10.5772/64749

$$\langle \dot{v} \rangle = \int v\omega m(x,t)\, dx + \int \dot{y}\, \frac{\partial v}{\partial y}\, f dx + \dot{p} \int \left(\frac{\partial v}{\partial p} + v \frac{\partial v}{\partial h} \right) f dx, \tag{2}$$

where $\langle \dot{v} \rangle$ is the average specific volume variation rate corresponding to engine speed. However, these two differential equations are too complicated to obtain the analytical solution for $f(x, t)$. Therefore, the Monte Carlo method is adopted to solve the equations. This is realized by treating numerous Monte Carlo elements as the fluid particles. The injected fuel and charged air in cylinder are assumed to be sufficiently small fluid particles compared to the microscale of turbulence, and the fluid particles are considered to have identical mass. In this process, the change of fluid particle's thermodynamic states due to turbulent mixing is described by the random collision and dispersion process occurred between fluid particles. It is calculated by modified Curl's model [27] in which a randomly selected pair of fluid particles in the spray collides and disperses with exchange of their thermodynamic states as expressed in Eq. (3)

$$\begin{aligned} f\left(x_1, t+\Delta t\right) &= \frac{X}{2} f(x_2, t) + \frac{(1-X)}{2} f\left(x_1, t\right) \\ f(x_2, t+\Delta t) &= \frac{X}{2} f(x_1, t) + \frac{(1-X)}{2} f(x_2, t) \end{aligned} \tag{3}$$

The x_1 and x_2 represent the thermodynamic states of two fluid particles, and X is a random number uniformly distributed in (0, 1). The mixing rate is represented by collision frequency that is estimated by turbulence kinetic energy in the spray.

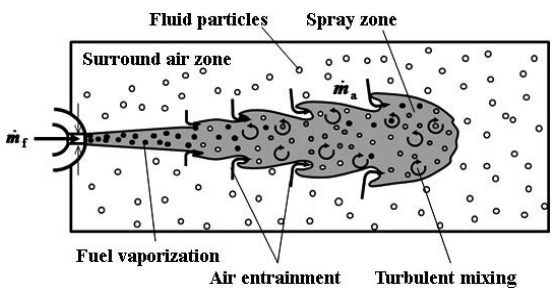

Figure 1. Stochastic combustion model diagram.

Based on this concept, the combustion process of diesel spray is described as shown in **Figure 1**. In this process, the combustion chamber is divided into spray zone and surrounding air zone after the injection start. The spray zone is formed by injected fuel particles and entrained air particles whose amount is determined by momentum theory [28]. In the spray zone, the fuel-air mixing is taken into account with modified Curl's collision and dispersion model [27]. The mixing rate is controlled by stochastic collision frequency that is dependent

on turbulence kinetic energy in spray. Meanwhile, liquid fuel contained in each fluid particle is vaporized according to an average evaporation rate, sequentially chemical reaction calculation using Schreiber's model [29] is performed in each fluid particles for combustion calculation. In addition, the heat loss from wall is also considered using Woschni's equation [30]. Thus, in the stochastic combustion model, fuel-air mixing and chemical reactions are simultaneously calculated.

3. Spray model

Figure 2 shows the shadowgraph images of two-stage injection in a constant volume combustion chamber. In **Figure 2**, the part "A" is the first spray flame region. After the second injection starts, the first spray flame region and the second spray region are separated at first as shown in the left graph. Once the second spray tip penetration is long enough to overtake the boundary of the first spray flame region, the second spray subsequently penetrates into the first spray flame region and causes the interaction between the first spray flame and the second spray as shown in the right graph.

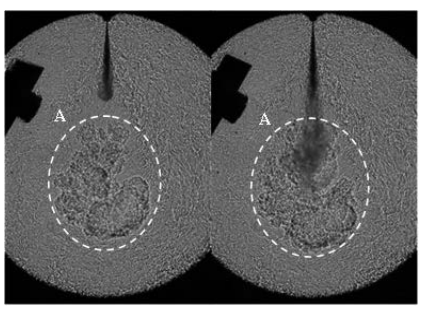

Figure 2. Shadowgraph images of two-stage injection in constant volume combustion chamber.

To simulate the combustion with multiple-injection, the situations shown in **Figure 2** can be abstracted as that shown in **Figure 3**. The volume in the cylinder is divided into three zones to represent the sprays and ambient gas for two-stage injection situation, including the first spray zone, the second spray zone, and the ambient air zone. Before injection, the air and EGR gas in the cylinder is treated as ambient air zone that is presumed to be composed of a great number of fluid elements. Then after the start of the first injection, the fuel is injected into the cylinder as fluid elements, and entrained fluid elements from ambient air zone to form the first spray zone. After the end of the injection, the first spray tail is assumed to depart from nozzle exit to the downstream. When the second injection starts, the first and second spray zones exist in the cylinder and the fluid elements of ambient air zone are entrained into these two spray zones, respectively. Once the second spray tip overtakes the first spray tail, both of the fluid elements from the ambient air zone and the first spray zone are entrained into the second spray zone. Finally, these two spray zones are combined into one spray zone after all

http://dx.doi.org/10.5772/64749

of the fluid elements of the first spray zone are entrained into the second spray zone. Obviously, the spray tip and tail penetration and air entrainment rate are primary parts to carry out the concept, and the spray tip penetration should include the spray evolution after EOI as the discussion in Section 1. Thereby, a new zero-dimensional spray penetration calculation was developed, and the air entrainment was calculated based on the developed model.

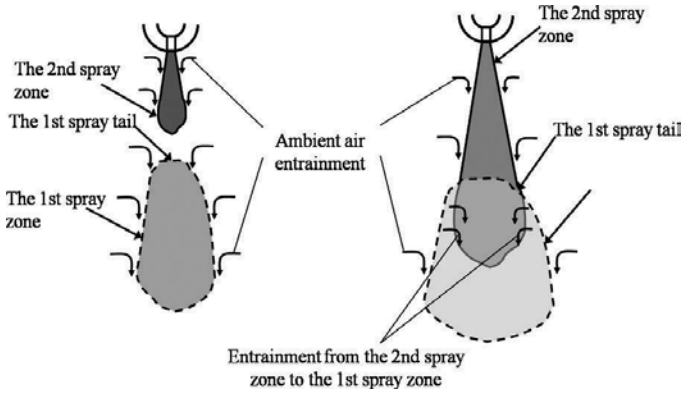

Figure 3. Model's concept diagram for multiple injection.

3.1. Spray penetration including the spray evolution after EOI

Indeed, because of the termination of injection, the spray is transformed from steady state into deceleration state that leads to the spray propagation different from that in the steady state. Recently, entrainment wave theory was proposed by Musculus [18] based on analytical research on the turbulent jets behaviors during the deceleration state. This theory describes the propagation of the increased entrainment region from nozzle exit to jet downstream after EOI, which also presents the propagation of information of the fuel injection termination. Once the entrainment wave arrives at the tip of the jet, the jet penetration shifts from a relation of square root dependence on time to a relation of fourth root dependence on time, the former relation is widely proved in steady jet and the later relation is same as the result from the experimental research on unsteady turbulent jets [17]. The entrainment wave was also observed in diesel jets, and a one-dimensional discrete model derived in [19] was successful to predict the entrainment wave in diesel jets and the penetration of diesel jets even after the entrainment wave reaches the jet tip. These indicate that the one-dimensional discrete spray model in [19] has potential to predict the diesel spray propagation after EOI. Thus, a zero-dimensional model of diesel spray propagation was developed referring to this one-dimensional discrete spray model to involve the spray information of penetration and air entrainment rate after EOI in this study. To conduct this work, the modeling method of the one-dimensional discrete model is only used for the treatment of the spray tip part, and the same assumptions as in the one-dimensional discrete spray model were employed for the zero-dimensional spray model. To simplify the spray modeling, the spray is treated to be formed with a constant injection rate.

According to the entrainment wave phenomenon, the spray propagation process can be divided into two stages. As shown in **Figure 4**, the time when the entrainment wave front arrives at the spray tip is defined as transition timing, and the diesel spray tip penetration calculation is separated in two stages by the transition timing. During injection, the spray is in steady state; after the EOI, the entrainment wave propagates from nozzle exit to the spray tip, and the spray tip keeps in the steady state before the transition timing. After the transition timing, the total spray transforms into decelerating state. In this spray propagation process, the spray tip maintains in steady state before transition timing and then decelerates from the steady state after transition timing. Thus, the spray tip penetration is calculated in two stages, before and after transition timing. In the case of constant injection rate, the transition timing is twice of injection duration.

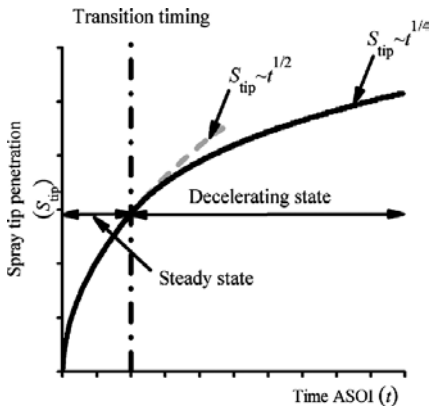

Figure 4. Spray propagation diagram.

The spray tip penetration (S_{tip}) can be expressed as

$$\frac{dS_{tip}}{dt} = u_{tip}, \tag{4}$$

where u_{tip} is the spray tip velocity. Based on the momentum theory, the spray tip velocity is equal to the ratio of the momentum flux integrated over the tip cross-sectional area ($\dot{M}_{tip}$) to the mixture mass flow rate integrated over the tip cross-sectional area ($\dot{m}_{tip}$) as Eq. (19):

$$u_{tip} = \frac{\dot{M}_{tip}}{\dot{m}_{tip}}. \tag{5}$$

$\dot{M}_{tip}$ is expressed as follows:

http://dx.doi.org/10.5772/64749

$$\dot{M}_{\text{tip}} = \rho_{\text{tip}} \beta A_{\text{tip}} \bar{u}_{\text{tip}}^{\,2}, \tag{6}$$

where ρ_{tip} is the average density in the tip cross-section, A_{tip} is the tip cross-sectional area, $\bar{u}_{\text{tip}}$ is the average velocity over the tip cross-section, and β is a factor that is introduced to consider the effects of axial velocity and fuel volume fraction profiles over the spray tip cross-sectional area on the momentum flux and fuel mass flow rate integrated over the spray tip cross-sectional area, the specific derivation of β can be found in the reference [19]. The value of β is ranged from 1.0 for a uniform profile to 2.0 for a fully developed spray.

Meanwhile $\overline{m}_{\text{tip}}^{\dot{m}_{\text{tip}}}$ is obtained as

$$\dot{m}_{\text{tip}} = \rho_{\text{tip}} A_{\text{tip}} \bar{u}_{\text{tip}}. \tag{7}$$

Substituting Eqs. (19) and (20) into (21), the spray tip velocity is represented as follows:

$$u_{\text{tip}} = \beta \bar{u}_{\text{tip}}. \tag{8}$$

Before the transition timing, the spray tip is in steady state, so that the momentum flux and fuel mass flow rate integrated over the tip cross-sectional area ($\dot{M}_{\text{tip}}$ and $\dot{m}_{\text{f, tip}}$) are constant, and the ratio of them is equal to the fuel velocity at the nozzle exit (u_f) due to the constant injection rate.

$$\frac{\dot{M}_{\text{tip}}}{\dot{m}_{\text{f,tip}}} = u_f, \tag{9}$$

where $\dot{m}_{\text{f, tip}}$ is equal to the injection rate of fuel mass ($\dot{m}_{\text{f}}$).

Therefore, after substituting Eq. (6) into (9), the $\bar{u}_{\text{tip}}$ can be derived as

$$\bar{u}_{\text{tip}} = \frac{\rho_f \bar{X}_{\text{f,tip}} u_f}{\rho_{\text{tip}}}, \tag{10}$$

where $\bar{X}_{\text{f, tip}}$ is the average fuel volume fraction over cross-section at the spray tip, as well as the average density in the tip cross-section (ρ_{tip}) can be calculated by the following equation according to [29],

$$\rho_{\text{tip}} = \rho_{\text{f}} \bar{X}_{\text{f,tip}} + \rho_{\text{a}}(1 - \bar{X}_{\text{f,tip}}). \tag{11}$$

So far the spray tip penetration (S_{tip}) can be obtained by

$$\frac{dS_{\text{tip}}}{dt} = \beta \frac{\rho_f \bar{X}_{\text{f,tip}} u_f}{\rho_{\text{tip}}}. \tag{12}$$

Eq. (12) cannot be solved as a continuous equation. Thus, the discrete method is used to calculate the spray tip penetration. The spray tip penetration at any time of t is obtained based on the spray tip penetration and the average velocity over the tip cross-section at the last time step ($t - \Delta t$) as Eq. (13)

$$S_{tip}(t) = S_{tip}(t - \Delta t) + \beta \bar{u}_{tip}(t - \Delta t)\Delta t. \tag{13}$$

And the average velocity over the tip cross-section at time t is obtained as

$$\bar{u}_{tip}(t) = \frac{\rho_f \bar{X}_{f,tip}(t) u_f}{\rho_{tip}(t)}. \tag{14}$$

After the transition timing, the total momentum flux and fuel mass flow rate over the tip cross-section decelerate from the values of steady state because the information of fuel injection termination already arrived at the spray tip [18]. However, Eq. (9) is valid also for the period after the transition timing, which had been demonstrated in [31]. Thus, the same form as Eq. (10) are available for the average velocity over the tip cross-section, where $\bar{X}_{\text{f, tip}}$ and ρ_{tip} are replaced by those after the transition timing, $\bar{X}_{\text{f, tip, atr}}$ and $\rho_{\text{tip, atr}}$.

$$u_{\text{tip,atr}} = \frac{\rho_f \overline{X}_{\text{f,tip,atr}} u_f}{\rho_{\text{tip,atr}}}, \tag{15}$$

where $\rho_{\text{tip, atr}}$ is calculated by Eq. (11), in which $\bar{X}_{\text{f, tip}}$ is replaced by $\bar{X}_{\text{f, tip, atr}}$. The spray tip penetration after transition timing can be calculated as

$$\frac{dS_{\text{tip}}}{dt} = \beta \frac{\rho_{\text{f}} \bar{X}_{\text{f,tip,atr}} u_f}{\rho_{\text{tip,atr}}} \quad (t > t_{tr}), \tag{16}$$

http://dx.doi.org/10.5772/64749

where t_{tr} is the transition timing.

To obtain $\bar{X}_{f,tip,atr}$, air volume and fuel volume in spray can be treated as separate regions as "air" region and "fuel" region shown in the figure, respectively. Before the transition timing, the fuel mass flow rate at the tip is constant, and the volumetric flow rate at the tip, $\dot{m}_f / \rho_f$, is equal to that at the nozzle exit. However, after the transition timing, the fuel volumetric flow rate decreases from its initial value in the steady state because the information of fuel injection termination already arrived at the spray tip [19]. To describe this process, the volumetric flow rate, $\dot{m}_f / \rho_f$, was assumed to be shared by fuel and air for the period after the transition timing. Based on this assumption, part of air flows into "fuel" region from "air" region and mixes with fuel, so that the "fuel" region for the steady state is replaced by the "fuel + air" region after transition timing, and then the mixture of "fuel + air" region flows out through the tip with the volumetric flow rate of $\dot{m}_f / \rho_f$. Considering the "fuel + air" region at time "t" as the control volume, the mixture flows out of the control volume from tip cross-section with the volumetric flow rate of $\dot{m}_f / \rho_f$. Because of the fluid continuity, air will flow into the control volume with the same volumetric flow rate as compensation. Therefore, at any time "t" after transition timing, the total volume of air flow into "fuel + air" region is $(\dot{m}_f / \rho_f) \cdot (t - t_{tr})$. For simplicity, it is assumed that the air and fuel mix with each other immediately in the "fuel + air" region. Then, the fuel volume fraction in the fluid flowing out of the tip is calculated by the following equation

$$X_{f,fm} = \frac{m_f(t) / \rho_f}{m_f(t) / \rho_f + C_d(\dot{m}_f / \rho_f) \cdot (t - t_{tr})}, \tag{17}$$

where $m_f(t)$ is mass of fuel in the spray, t is the time from injection start, and C_d is a model constant. Finally, $X_{f,tip,atr}$ is derived as

$$X_{f,tip,atr} = \frac{X_{f,fm}\, \dot{m}_f / \rho_f}{\dot{V}_{spray}}. \tag{18}$$

Whence the spray tip penetration after the transition timing is able to be obtained, and the method for solving Eq. (16) is same as that before transition timing.

3.2. Spray tail penetration

After EOI, the mixture near the nozzle becomes very lean due to the termination of the fuel supply. Therefore, it is assumed that the part of the spray near the nozzle acts as ambient air zone and a spray tail exists. Knowing the position of the spray tail, the start time of the interaction with the subsequent spray can be determined.

In this study, the spray tail position is determined as a cross-section of a spray where 10% of total fuel is contained up to the nozzle. It can be imagined that the tip of the spray formed by

this 10% fuel equates the total spray tail. In other words, the tail penetration of the spray containing total injected fuel can be calculated by the tip penetration of the spray formed by an injection whose quantity is equal to 10% of total injection quantity. **Figure 5** shows the examples of calculated tail penetrations compared to the tip penetrations for the injection quantity of 2.5 and 25 mg cases.

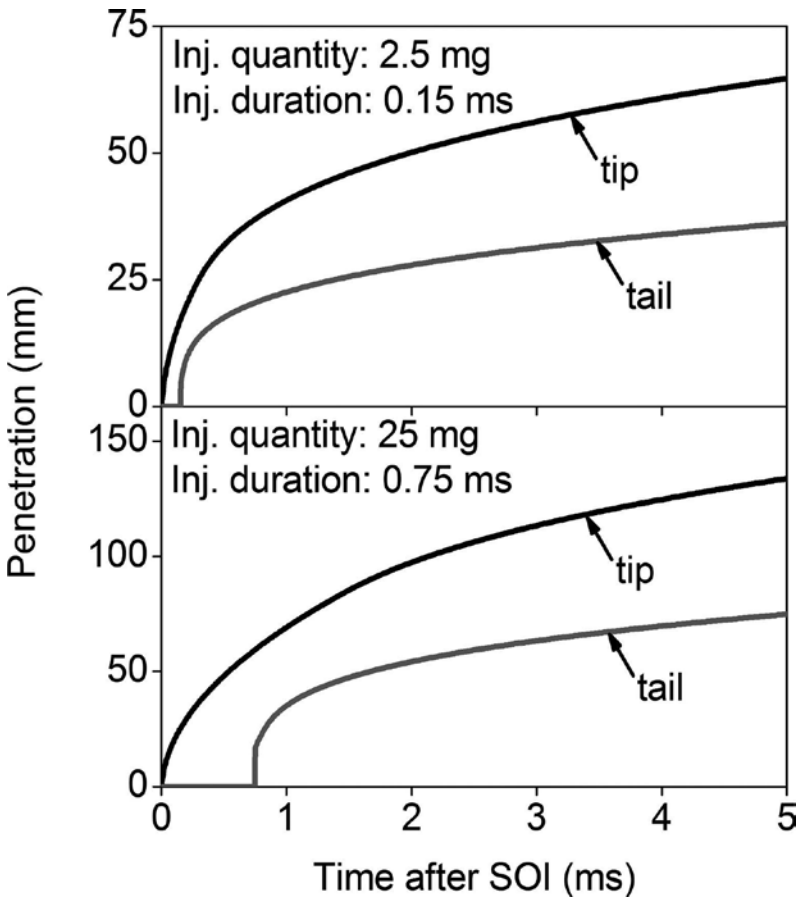

Figure 5. Calculated spray tip and tail penetrations for the injection quantity of 2.5 and 25 mg cases.

4. Spray-to-spray interaction modeling

Another primary respect of simulation for diesel combustion with multiple-injection is to describe the interaction between the sprays from sequent injections. **Figure 6** shows the spray-to-spray interaction, the interaction occurs after the arrival of the second spray tip at the first spray tail, and the entrainment from the first spray to the second spray is involved to represent the interaction.

http://dx.doi.org/10.5772/64749

The entrainment behavior can be considered as that the spray entrains the ambient gas through the spray boundary that has a conical surface, therefore the entrainment rate can be represent as the product of air density, entrainment velocity over the spray boundary surface, and the area of spray boundary surface. After the second spray tip touches the first spray tail, the entrainment area of the second spray is divided into two parts by the first spray tail as shown in **Figure 6**. The ratio of the entrainment rate of these two parts (R_e) can be obtained as Eq. (19) with assumptions as the air and the first spray have the same density and the entrainment velocity uniformly distribute over the spray boundary surface in the ambient air zone and the first spray zone, respectively:

$$R_e = C_e \frac{A_{\text{air}}}{A_{\text{spray}}}, \tag{19}$$

where A_{air} and A_{spray} are the areas of the spray boundary surface in the ambient air zone and the first spray zone, respectively. C_e is a coefficient given to describe the difference between the entrainment velocity over the spray boundary surface in the ambient air zone and the first spray zone. Based on Eq. (19) and the total entrainment rate of the second spray, it is able to obtain the amount of the first spray mixture entrained into the second spray.

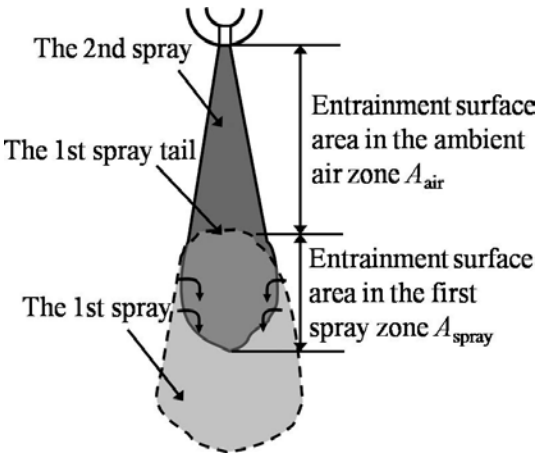

Figure 6. Spray interaction diagram.

Meanwhile, the swirl effects on the spray-to-spray interaction cannot be ignored. The swirl flow does not only decrease the spray penetration [32] but also deviates the spray path [23]. As that shown in **Figure 7**, the swirl effects causes the second spray tip to overtake the first spray tail and tip earlier than the case without swirl flow effects, and reduce the overlap region between the first and second sprays. Thus, based on the assumption that the entrainment rate is proportional to the spray surface area, the ratio (R_e) of the entrainment rate from the ambient gas and that from the first spray have to be recalculated as follows:

$$R_e = \frac{A_{upt} + (1 - R_{SA}) A_{blt}}{R_{SA} A_{blt}} \tag{20}$$

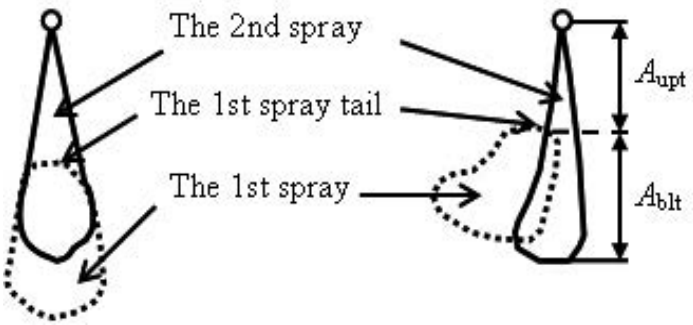

Figure 7. Diagram of sprays interaction [34].

where A_{upt} and A_{blt} are the spray boundary surface areas up and below the first spray tail, respectively, and R_{SA} is the ratio of surface area of the second spray in the first spray over A_{blt}.

To calculate A_{upt} and A_{blt}, the reduction of spray penetration in injection direction by swirl flow are considered to determine the position at which the second spray tip touches the first spray tail. The ratio (R_{MJ}) between the momentum from injected fuel (M_j) and total momentum in the spray, which includes the momentums from the injected fuel (M_j) and the entrained gas (M_s), is introduced as a factor for the penetration. The specific expressions are as follows:

$$R_{MJ} = \frac{M_j}{\sqrt{M_j^2 + M_s^2}}, \tag{21}$$

$$M_j = \int_0^t \dot{m}_f u_j dt, \tag{22}$$

$$M_s = \int_0^t \dot{m}_{as} \bar{u}_s dt, \tag{23}$$

where $\dot{m}_f$ and u_j are the mass flow rate and the velocity of fuel at the nozzle exit, $\dot{m}_{as}$ is the entrainment rate with swirl flow effect, which is calculated according to the equation proposed by Kau et al. [33], and $\bar{u}_s$ is the average swirl velocity over the total spray penetration. The spray penetration (S_{SE}) in the injection direction with swirl flow effect can be represented as $R_{MJ}S_{tip}$, where S_{tip} is the penetration without swirl flow effect. When the S_{SE} of the second spray tip is larger than that of the first spray tail, the second spray tip is treated to arrive at the first spray tail.

http://dx.doi.org/10.5772/64749

To calculate R_{SA}, the spray deflection by swirl flow was considered in a simple manner as shown in **Figure 8**. The shadow part expresses the overlap between the two sprays. The deviation angles θ_1 and θ_2, and the spray spreading angles α_1 and α_2 are assumed to have small values for this simplification. In this way, R_{SA} is approximately proportional to the ratio of the angle between the first spray windward and the second spray leeward over the second spray spreading angle as in Eq. (24)

$$R_{SA} \propto \frac{(\theta_2 + \frac{\alpha_2}{2}) - (\theta_1 - \frac{\alpha_1}{2})}{\alpha_2}. \tag{24}$$

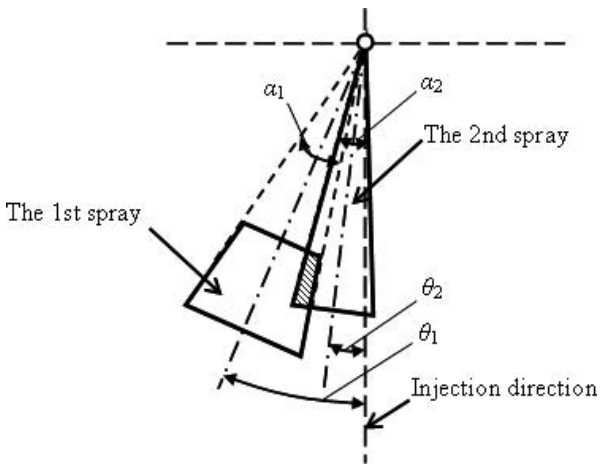

Figure 8. Simplification of sprays interaction with swirl flow effect [34].

The ratio (R_{MS}) of the momentum from entrained gas over the total momentum in the spray, which is calculated by Eq. (25), is assumed to represent the degree of spray deflection instead of θ_1 and θ_2 in Eq. (24).

$$R_{MS} = \frac{M_s}{\sqrt{M_j^2 + M_s^2}}. \tag{25}$$

5. Wall impingement effects introduced in stochastic combustion model

5.1. Wall impingement effects on the turbulent mixing

Adjusting the injection time earlier than top dead center (TDC) is often used to realize the PCCI or LTC, especially for the multiple-injection case in which the pilot injection time is usually

advanced to the middle even at the early stage of compression stroke. The early injection timing makes the spray flow into the squish region and impinges on the cylinder liner or piston top as shown in **Figure 9**. Due to the low temperature of the walls and/or the adherence of fuel on the piston top surface, oxidation reaction and mixing in the mixture are attenuated [35]. To involve such effects in the stochastic combustion model, the reduction of fuel-air turbulent mixing rate was considered according to the volume ratio of the spray flowed into the squish area and total spray. The temperature effect mentioned above was not considered; however, the overall oxidation reaction rate is lowered as a result of reduced mixing rate.

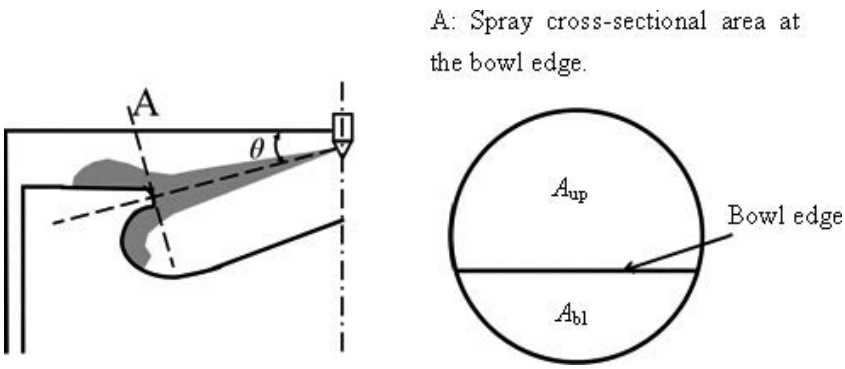

Figure 9. Wall impingement diagram.

As shown in **Figure 9**, if the spray tip cross-section impinges on the bowl lip edge, the spray can be divided into two parts, squish part and bowl part. Thus the volume ratio between squish part and incremental spray ($R_{sq,\,inc}$) can be calculated as follows:

$$R_{sq,inc} = \frac{C(\theta)A_{up}}{C(\theta)A_{up} + A_{bl}}, \tag{26}$$

where A_{up} and A_{bl} are the areas of the cross-sectional area at impinging timing over and below the bowl lip edge, respectively, and the $C(\theta)$ is a function of the angle between the spray central line and cylinder head, and it is used to describe the ratio between spray spreading velocity in squish region and bowl region. This function is selected as cot θ in this study, because it represents the ratio of the horizontal and vertical components of average spray tip velocity when the piston top is treated as a horizontal area. Sequentially, the volume ratio of spray flowed into squish region and total spray (R_{sq}) can be obtained as follows

$$R_{sq} = \frac{\int_{t_{im}}^{t} R_{sq,inc}\dot{V}_{spray}dt}{V_{spray}}, \tag{27}$$

http://dx.doi.org/10.5772/64749

where t_{im} is the impinging timing and V_{spray} is the total spray volume. And the stochastic collision frequency (ω) that represents the turbulent mixing rate is calculated as follows:

$$\omega = \omega_0(1 - C_m R_{sq} G_j^x), \tag{28}$$

where C_m is a constant, ω_0 is the collision frequency of free spray, and G_j is the total turbulence energy generated by injection. G_j is used with minus power (x), because the larger turbulence energy generated by injection causes the stronger mixing (larger ω). C_m and x were selected as 6.2 and –0.2 respectively, which are calibrated by experimental heat release rates under different injection time cases.

5.2. Wall impingement effects on the air entrainment

Figure 10 shows abstracted diagram of the situation of spray impinging on the wall in the cylinder. The upper spray represents the initial stage of wall impingement. In this stage, it is reasonable to consider that the air entrainment is enhanced because the surface area of spray is enlarged by wall impingement [36–38]. Thus, to improve the stochastic combustion model, a constant (C_{ETRM}) is given to multiply the entrainment rate of free spray after the wall impinging. In addition, the interaction between adjacent sprays is an important factor on air entrainment decrease, the primary reason can be considered that the adjacent sprays overlap after wall impingement as shown in **Figure 10** (below sprays) decreases the entrainment area of spray, thereby the entrainment rate is suppressed. In order to involve these effects in a simple way, the ratio of the total spray volume and the chamber volume was used to represent the intensity of the interaction between adjacent sprays, and the interaction effect on entrainment rate is introduced as follows:

$$\dot{m}_a = \dot{m}_{a0}\left(1 - C_{vr}\frac{V_{spray} \times n_{hole}}{V_{cyl}}\right), \tag{29}$$

where $\dot{m}_a$ is the air entrainment rate affected by spray-volume increase, $\dot{m}_{a0}$ is the original air entrainment rate, n_{hole} is the number of nozzle holes, V_{cyl} is the volume in cylinder, and C_{vr} is a constant to fit the experiment data.

C_{ETRM} and C_{vr} are set as 1.5 and 0.8, respectively, based on the comparison between calculated and experimental heat release rates.

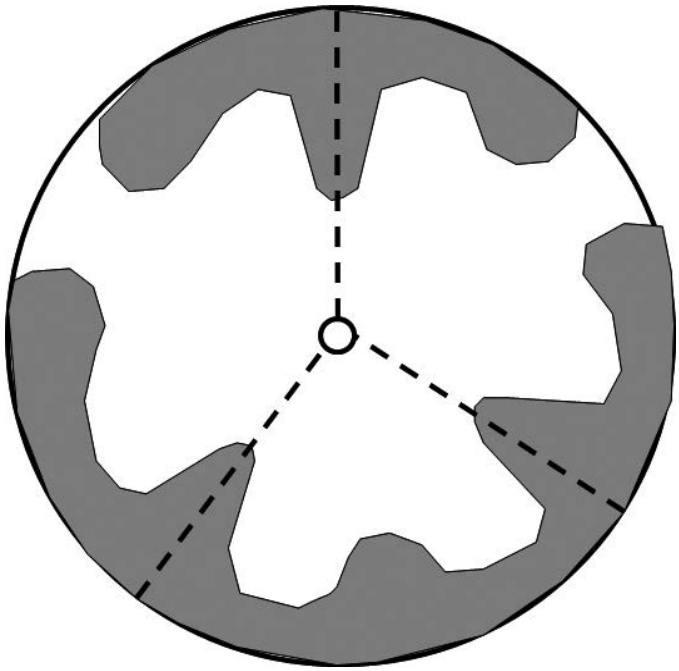

Figure 10. Spray propagation along the wall.

6. Emission models

6.1. NOx model

Based on the assumption that most of the NOx is NO, the production of NO during combustion process is computed by the extended Zeldovich mechanism [39]. Meanwhile, the NO normally produces at a high rate in the mixture with equivalence ratio around 1.0 accompanying with high temperature. Thus, the NO concentration is estimated in the fluid elements whose temperature is over 1200 K with the equilibrium species including C, CO, CO_2, O_2, O, OH, H_2, H, H_2O, N_2, and NO.

6.2. Soot model

The soot model refers to the Moss's soot model [40]. Moss's soot model is a semi-empirical soot model derived based on laminar diffusion flame. The soot particles inception and coagulation are considered for the calculation of soot particles number density, and the soot particles surface growth and oxidation are calculated to obtain the soot volume fraction. The soot oxidation rates per unit area by O_2 and hydroxyl radical (OH) are introduced to calculate the soot oxidation rate in this model. The soot oxidation rate per unit area by O_2 (R_{SO}) is calculated

http://dx.doi.org/10.5772/64749

using the Nagle and Strickland-Constable (NSC) model [41]. The soot oxidation rate per unit area by OH (R_{SOH}) is considered by referring Neoh's equation [42].

7. Validation of the developed combustion model

7.1. Test engine

The test engine is a water-cooled single-cylinder four-stroke-cycle direct-injection diesel engine equipped common-rail injection system. The standard specifications are given in **Table 1**.

Engine type	Single-cylinder, DI-diesel engine
Bore × Stroke	85 mm × 96.9 mm
Displacement	550 cc
Compression ratio	16.3
Combustion chamber	Reentrant type (ϕ 51.6 cavity)
Injection system	Common-rail system 0.125 mm × 7 holes nozzle

Table 1. Standard specifications of test engine.

All of the experiments were performed at thermally steady states of the engine at a fixed speed of 1500 rpm, an inlet coolant temperature of 80°C, and a lubricating oil temperature of 80°C. The intake pressure was 0.1 MPa and the intake temperature was 35°C. Exhaust back pressure valve was fully open. The fuel was JIS No. 2 diesel fuel (density at 15°C = 820.2 kg/m^3 and cetane index = 54.7). The averaged in-cylinder pressure of 50 cycles was used to calculate the heat release rate, which was measured using a piezoelectric pressure transducer (Kistler 6052A).

7.2. Calculation conditions

With the aim for validating the simulation of combustion with multistage injection, at first, the pilot/main two-stage injection strategies were conducted in experiment and calculation, and the calculation ran from intake valve closure (IVC) of –145°ATDC to exhaust valve open (EVO) of 125°ATDC. Since the start of main injection is normally set near TDC in the pilot/main injection strategy, the main injection timing (θ_{main}) was fixed at 1°ATDC, and pilot injection timing and quantity were varied. And the engine operating condition was selected as high load, for which the indicated mean effective pressure (IMEP) was set to 1.01 MPa, in order to observe the variation of combustion phases including premixed combustion and mixing-controlled combustion affected by pilot injection condition. The main experimental conditions are listed in **Table 2**.

Injection pressure	125 MPa
Total injection quantity	32 mm^3 per cycle
Pilot injection quantity ($q_{f\text{pilot}}$)	2, 4, and 6 mm^3 per cycle
Pilot injection timing (s_{pilot})	–9, –19, and –24°ATDC
Main injection timing	1°ATDC
EGR ratio	20%
Swirl ratio	2.0

Table 2. Experimental conditions.

7.3. Pressure and heat release rate

To valid the combustion model, the in-cylinder pressures and the heat release rates were calculated and compared to the experimental data at first. **Figures 11–13** show the in-cylinder pressures and heat release rates for different pilot injection timings and quantities. The simulation results obtain the similar levels of pressures and heat release rates to those of the experiments. It is also observed that the model is able to capture the tendencies of the pressure and heat release rate when varying the pilot injection timing and injection quantity.

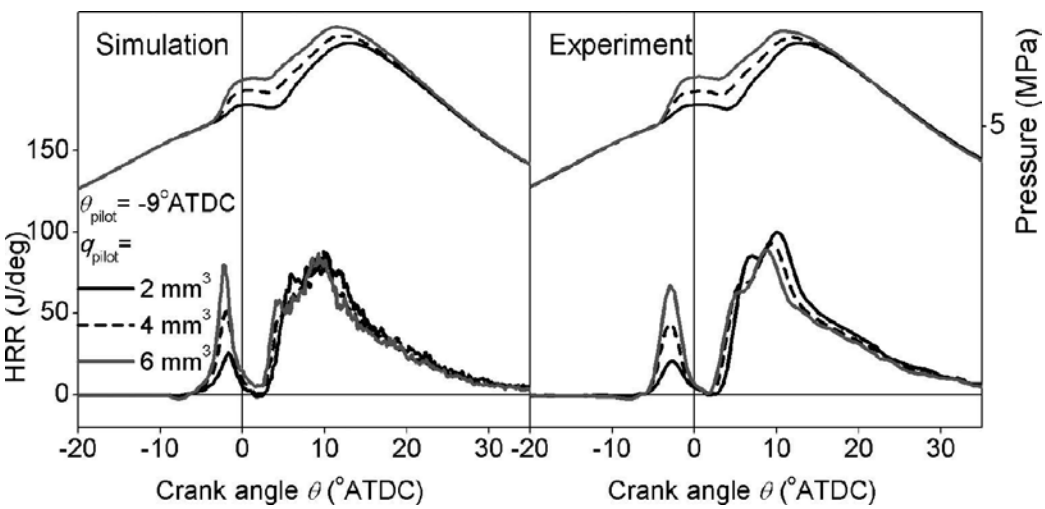

Figure 11. Effects of pilot injection quantity on the in-cylinder pressure and the heat release rate (θ_{pilot} = –9°ATDC).

http://dx.doi.org/10.5772/64749

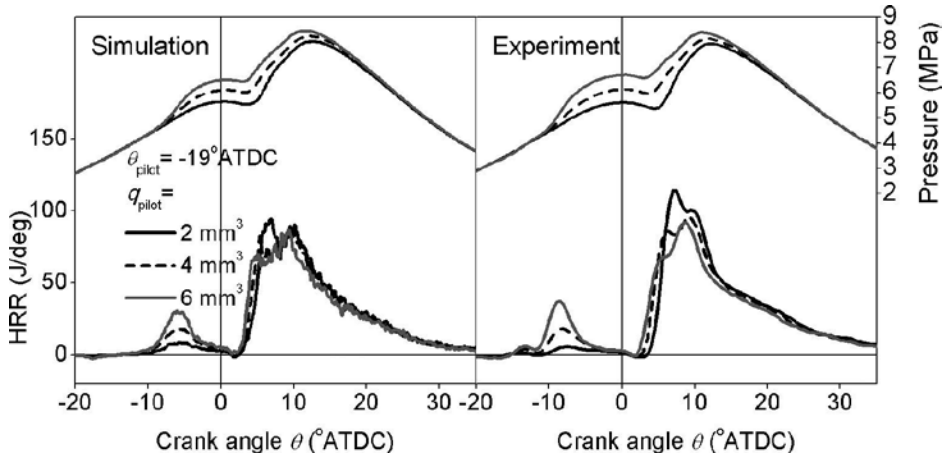

Figure 12. Effects of pilot injection quantity on the in-cylinder pressure and the heat release rate (θ_{pilot} = –19°ATDC).

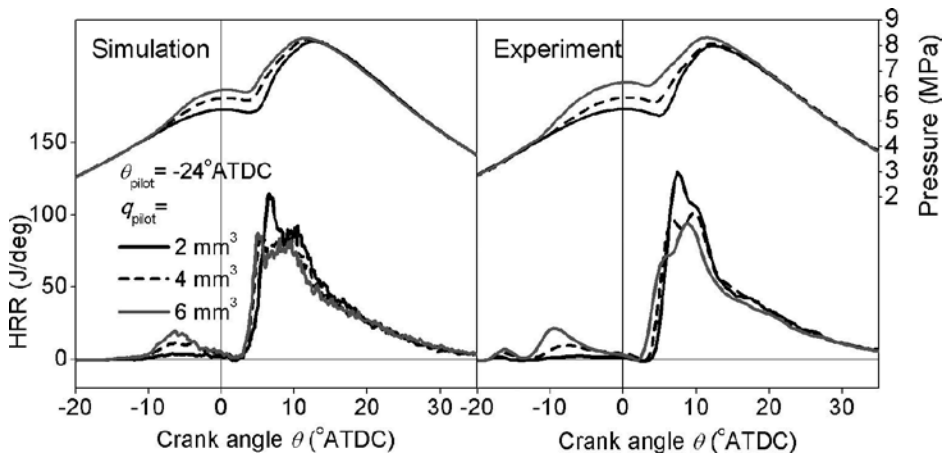

Figure 13. Effects of pilot injection quantity on the in-cylinder pressure and the heat release rate (θ_{pilot} = –24°ATDC).

7.4. Emissions calculation

Based on the good agreement in the pressures and the heat release rates, the NOx and soot emissions were calculated. **Figure 14** shows the NOx (left) and soot (right) emissions against the pilot injection timing. The results reveal that the NOx calculation obtains the similar emission level and the variation caused by pilot injection conditions changing with the measured data. Regarding to the soot emission, the soot emissions level obtained by the model is comparable with the measured data, and the calculated soot emissions are able to reproduce the increase with the increase in pilot injection quantity at fixed pilot injection timings, which is observed in the experimental data. Although the tendency of soot emissions variation with

pilot injection timing retarded does not completely coincide with that of every experiment with different pilot injection quantity, the general tendency can be captured correctly.

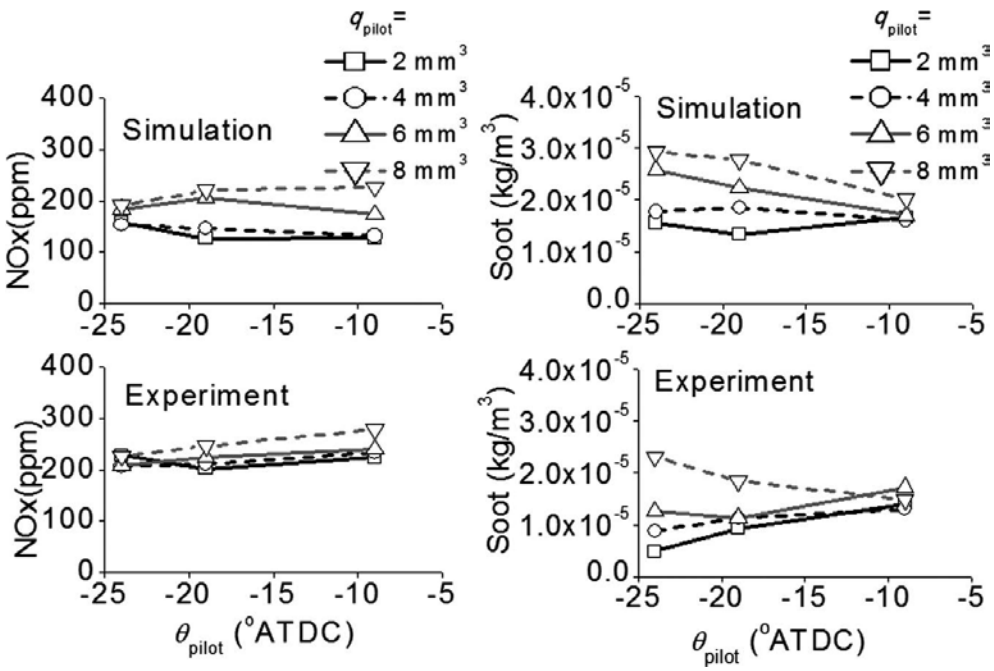

Figure 14. NOx and soot emissions.

8. Conclusion

In this study, a stochastic combustion model was introduced to develop a phenomenological combustion model for modern diesel engines. In order to be able to describe the combustion process of advanced combustion mode, the spray propagations after EOI, spray-to-spray interaction, swirl effects, and wall impingement effects were modeled based on their physical phenomena in appropriate ways for the stochastic combustion model. Then, the developed combustion model was validated based on the experimental data from a single-cylinder diesel engine with pilot/main two-stage injection. The results revealed that the model is able to accurately predict the combustion of the diesel engine with pilot/main two-stage injection, and reasonable prediction of NOx and soot emissions can be obtained by this model. Specific conclusions are as follows:

(1) A zero-dimensional spray propagation model was derived. The spray model is able to predict the spray evolution including spray tip penetration and overall air entrainment after EOI. It is capable to catch the spray propagation tendency after EOI as that well recognized by the fundamental study. Thus, based on introducing this model, the accuracy of the combustion

http://dx.doi.org/10.5772/64749

model can be improved especially for the short injection duration case in which the ignition is later than the EOI. As for the multiple-injection case, the thermodynamic states of the gas in the cylinder before the later injection start can be predict more realistically.

(2) Presumed spray tail was proposed for zero-dimensional spray model, which allows to take account of the fast dilution of the mixture near the injector tip after EOI, which resulted by the terminated fuel supply and increased air entrainment rate near the injector tip after EOI. And thanks to the presumed spray tail, the interaction between sprays from sequent injections was formulated by the rate of entrainment into the later spray from the former spray and/or the surrounding gas. Meanwhile, spray deflection by swirl flow cannot be neglected when imitating the interaction between sprays from sequent injection. And the interaction with swirl flow effect was described based on a simple geometrical consideration and formulated using the momentum from injected fuel and entrained gas. In this way, the stochastic combustion model can be used for simulation of combustion with multistage injection.

(3) To consider the wall impingement effect in early injection timing case, after wall impinging, the volume ratio of the spray flowed into the squish area, and total spray was introduced to reduce the fuel-air mixing rate that can involve the combustion chamber shape effects in the phenomenological combustion model.

(4) Air entrainment rate enhancement caused by wall impingement was considered by a factor with air entrainment rate of free spray during initial stage of wall impingement. And the reduction of main spray entrainment rate by interaction between adjacent sprays was formulated by the ratio between spray volume and chamber volume to balance the effect of enhanced air entrainment rate in the late combustion period. According to the results, effects of wall impingement and adjacent spray interactions on the entrainment rate are helpful to well predict the heat release rate in initial and late combustion periods, respectively.

Acknowledgements

The experiments and modeling work presented here had been performed in Combustion and Power Engineering Laboratory at Kyoto University. The research is supported by National Natural Science Foundation of China (Grant No. 51509051) and Natural Science Foundation of Heilongjiang Province of China (Grant No. LC2015017).

Author details

Long Liu

Address all correspondence to: liulong@hrbeu.edu.cn

College of Power and Energy Engineering University, Harbin Engineering University, Harbin, China

References

[1] Colban, W. F., Miles, P. C., and Oh, S. Effect of intake pressure on emissions from an automotive diesel engine operating in low temperature combustion regimes, SAE Paper 2007-01-4063, 2007.

[2] Lee, S. and Reitz, R. D. Spray targeting to minimize soot and CO formation in premixed charge compression ignition (PCCI) combustion with a HSDI diesel engine, SAE Paper 2006-01-0918, 2006.

[3] Cho, K., Han, M., Sluder, C. S., Wagner, R. M., and Lilik, G. K. Experimental investigation of the effects of fuel characteristics on high efficiency clean combustion in a light-duty diesel engine, SAE Paper 2009-01-2669, 2009.

[4] Ojeda, W., Zoldak, P., Espinosa, R., and Kumar, R. Development of a fuel injection strategy for diesel LTC, SAE Paper 2008-01-0057, 2008.

[5] Lakshminarayanan, P. A. and Aghav, Y. V. Modeling diesel combustion, Springer, Dordrecht/Heidelberg/London/New York, 2009.

[6] Shahed, S. M., Chiu, W. S., and Yumlu, V. S. A preliminary model for the formation of nitric oxides in DI diesel engine and its application in parametric studies, SAE Paper 730083, 1973.

[7] Dent, J. C. and Mehta, P. S. Phenomenological combustion model for a quiescent chamber diesel engine, SAE Paper 811235, 1981.

[8] Hiroyasu, H., Kadota, T., and Arai, M. Development and use of a spray combustion modeling to predict diesel engine efficiency and pollutant emissions: Part 1. Combustion modeling, Bulletin of JSME, 26 (1983), pp. 569–575.

[9] Kaminoto, T., Chang, Y. J., and Kobayashi, H. Rate of heat release and its prediction of a diesel flame in a rapid compression machine, SAE Paper 841076, 1984.

[10] Ikegami, M., Shioji, M., and Koike, M. A stochastic approach to model the combustion process in direct-injection diesel engines. In: Twentieth International Symposium on Combustion, (1984), pp. 217–224.

[11] Hotta, Y., Inayoshi, M., Nakakita, K., Fujiwara, K., and Sakata, I. Achieving lower exhaust emissions and better performance in an HSDI diesel engine with multiple injection, SAE Paper 2005-01-0928, 2005.

[12] Badami, M., Mallamo, F., Millo, F., and Rossi, E. E. Influence of multiple injection strategies on emissions, combustion noise and BSFC of a DI common rail diesel engine, SAE Paper 2002-01-0503, 2002.

[13] Vanegas, A., Won, H., Felsch, C., et al. Experimental investigation of the effect of multiple injections on pollutant formation in a common-rail DI diesel engine, SAE Paper 2008-01-1911, 2008.

http://dx.doi.org/10.5772/64749

[14] Inagaki, K., Ueda, M., Mizuta, J., et al. Universal diesel engine simulator (UniDES): 1st report: Phenomenological multi-zone PDF model for predicting the transient behavior of diesel engine combustion, SAE Paper 2008-01-0843, 2008.

[15] Dulbecco, A. and Lafossas, F. A. A 0D phenomenological approach to model diesel HCCI combustion with multi-injection strategies using probability density functions and detailed tabulated chemistry, SAE Paper 2009-01-0678, 2009.

[16] Nicolas, B., Christian, C., and Pascal, H. A physical 0D combustion model using tabulated chemistry with presumed probability density function approach for multi-injection diesel engines, SAE Paper 2010-01-1493, 2010.

[17] Sangras, R., Kwon, O. C., and Faeth, G. M. Self-preserving properties of unsteady round nonbuoyant turbulent starting jets and puffs in still fluids. Journal of Heat Transfer, 124 (2002), pp. 460–469.

[18] Musculus, M.P.B. Entrainment waves in decelerating transient turbulent jets, Journal of Fluid Mechanics, 638 (2009), pp. 117–140.

[19] Musculus, M.P.B. and Kattke, K. Entrainment waves in diesel jets, SAE Paper 2009-01-1355, 2009.

[20] Musculus, M. P. B., Lachaux, T., Pickett, L. M., et al. End-of-injection over-mixing and unburned hydrocarbon emissions in low-temperature-combustion diesel engines, SAE Paper 2007-01-0907, 2007.

[21] Moon, S., Matsumoto, Y., and Nishida, K. Entrainment evaporation and mixing characteristics of diesel sprays around end-of-injection, SAE Paper 2009-01-0849, 2009.

[22] Kastengren, A., Powell, C. F., Tilocco, F. Z., et al. End-of-injection behavior of diesel sprays measured with X-ray radiography, Journal of Engineering for Gas Turbines and Power, 134 (2012), 094501 (1–4).

[23] Yamane, K., Ikegami, M., and Shioji, M. Fuel injection pressure and nozzle orifice diameter in direct-injection diesel engine, Proceedings of International Symposium COMODIA, 94 (1994), pp. 225–230.

[24] Ishiyama, T., Shioji, M., and Ihara, T. Analysis of ignition processes in a fuel spray using an ignition model including turbulent mixing and reduced chemical kinetics, International Journal of Engine Research, 4 (2003), pp. 155–162.

[25] Ishiyama, T., Kee, S. S., and Kitamura, Y. Modeling and experiment of NOx formation in DI-PCCI combustion, SAE Paper 2007-01-0194, 2007.

[26] Horibe, N. and Ishiyama, T. Study on selection of injection conditions for diesel PCCI combustion: Numerical investigation using an ignition-combustion model based on stochastic approach. Transactions of JSME(B), 76 (2010), pp. 699–706, (In Japanese).

[27] Janicka, J., Kolbe, W., and Kollmann, W. Closure of the transport equation for the probability density function of turbulent scalar fields, Journal of Non-Equilibrium Thermodynamics, 4 (1979), pp. 47–66.

[28] Wakuri, Y., Fujii, M., Amitani, T., and Tsuneya, R. Studies on the penetration of fuel spray in a diesel engine, Bulletin of JSME, 3 (1960), pp. 123–130.

[29] Schreiber, M., Sakak, A. S., and Lingens, A. A reduced thermokinetic model for the autoignition of fuels with variable octane ratings, In: Twenty-fifth Symposium. (International) on Combustion, (1994), pp. 933–940.

[30] Woschni, G. Universally applicable equation for the instantaneous heat transfer coefficient in the internal combustion engine, SAE Paper 670931, 1967.

[31] Long Liu, Naoto Horibe, and Takuji Ishiyama, Combustion Modeling for a Diesel Engine with Multi-Stage Injection Using a Stochastic Combustion Model, Procs. IMech. E., Part D: J. Auto. Eng., 228 (5), pp. 516–532, 2014.

[32] Hiroyasu, H., Kadota, T., Arai, M. Supplementary Comments: Fuel spray characterization in diesel engines. In: James N. Mattavi and Charles A. Amann (eds) Combustion modeling in reciprocating engines. Plenum Press., New York, (1980), pp. 369–408.

[33] Kau, C. J., Heap, M. P., Tyson, T. J., and Wilson, R. P. The prediction of nitric oxide formation in a direct injection diesel engine, Proceedings of 16th Symposium (Internatinal) on Combustion, (1977), pp.337–350.

[34] Long Liu, Naoto Horibe, Issei Tamura, Tatsuya Komizo, and Takuji Ishiyama, Study on NOx and Soot Emissions in Diesel Engines with Multi-Stage Injection Based on a Stochastic Combustion Model, International Journal of Automotive Engineering, Vol. 5(1), pp. 7–13, 2014.

[35] Liu, L., Horibe, N., and Ishiyama, T. Combustion modeling for a diesel engine with multi-stage injection using a stochastic combustion model, Proceedings of the Institution of Mechanical Engineers, Part D: Journal of Automobile Engineering, 228 (5), (2014), pp. 516–532.

[36] Hiroyasu, H., Kadota, T., and Arai, M. Supplementary comments: Fuel spray characterization in diesel engines. In: Mattavi, J.N., and Amann, C.A. (eds), Combustion Modeling in Reciprocating Engines, Plenum Press., New York, (1980), pp. 369–408.

[37] Kook, S., Park, S., and Bae, C. Influence of early fuel injection timings on premixing and combustion in a diesel engine, Energy & Fuel, 22 (2008), pp. 331–337.

[38] Hiroyasu, H., Kadota, T., and Arai, M. Development and use of a spray combustion modeling to predict diesel engine efficiency and pollutant emissions (Part 1 Combustion Modeling), Bulletin of the JSME, 26(1983), pp.569-575.

http://dx.doi.org/10.5772/64749

[39] Bruneaux, G. Mixing process in high pressure diesel jets by normalized laser induced exciplex fluorescence. Part II: Wall impinging versus free jet, SAE Paper 2005-01-2097, 2005.

[40] Bruneaux, G. and Causse, M. Air entrainment in diesel-like gas jet by simultaneous flow velocity and fuel concentration measurements, comparison of free and wall impinging jet configurations, SAE Paper 2011-01-1828, 2011.

[41] Lavoie, G. A., Heywood, J. B., and Keck, J.C. Experimental and theoretical investigation of nitric oxide formation in internal combustion engines, Combustion Science and Technology, 1 (1970), pp. 313–326.

[42] Moss, J. B., Stewart, C. D., and Young, K. J. Modeling soot formation and burnout in a high-temperature laminar diffusion flame burning under oxygen-enriched conditions, Combustion and Flame, 101 (1995), pp. 491–500.

[43] Nagle, J. and Strickland-Constable, R. F. Oxidation of carbon between 1000–2000°C, Proceedings of 5th Carbon Conference, 1 (1962), pp. 154–164.

[44] Neoh, K.G. Soot burnout in flames, Ph.D. Thesis, Massachusetts Institute of Technology, (1980).

Section 4

Chemical Looping, Catalysis and Dust Combustion

Chapter 11

Numerical Simulation of Chemical Looping and Calcium Looping Combustion Processes for Carbon Capture

Subhodeep Banerjee and Ramesh K. Agarwal

Additional information is available at the end of the chapter

http://dx.doi.org/10.5772/62811

Abstract

Efficient carbon capture and storage (CCS) technologies are needed to address the rising carbon emissions from power generation using fossil fuels that have been linked to global warming and climate change. Chemical looping combustion (CLC) is one such technology that has shown great promise due to its potential for high-purity carbon capture at low cost. Another CCS technology that has garnered interest in recent years is calcium looping (CaL), which utilizes calcium oxide and the carbonation-calcination equilibrium reactions to capture CO_2 from the flue stream of fossil fuel power plants. Computational fluid dynamics (CFD) simulations of two CLC reactors are presented in this chapter, along with system level simulations of CaL for postcombustion carbon capture. CFD simulation of a CLC reactor based on a dual fluidized bed reactor is developed using the Eulerian approach to characterize the chemical reactions in the system. The solid phase consists of a Fe-based oxygen carrier while the gaseous fuel used is syngas. Later, the detailed hydrodynamics in a CLC system designed for solid coal fuel is presented based on a cold flow experimental setup at National Energy Technology Laboratory using the Lagrangian particle-tracking method. The process simulation of CaL using Aspen Plus shows an increasing marginal energy penalty associated with an increase in the CO_2 capture efficiency, which suggests a limit on the maximum carbon capture efficiency in practical applications of CaL before the energy penalty becomes too large.

Keywords: CFD simulation, chemical looping combustion, fluidized bed, chemical reactions, calcium looping

INTECH
open science | open minds

© 2016 The Author(s). Licensee InTech. This chapter is distributed under the terms of the Creative Commons Attribution License (http://creativecommons.org/licenses/by/3.0), which permits unrestricted use, distribution, and reproduction in any medium, provided the original work is properly cited. CC BY

1. Introduction

The relationship between the global surface temperature of the Earth and the concentration of CO_2 was identified by Arrhenius as early as 1896 [1]. Since then, the concentration of CO_2 in the atmosphere has risen from 280 ppm to around 400 ppm today, largely due to carbon emissions from fossil fueled power plants and other anthropogenic sources. As such, there is an imminent need for high-efficiency carbon capture and storage (CCS) technologies to avoid the "unequivocal warming of the global climate system" [2]. Chemical looping combustion (CLC) is one such CCS technology that is well-suited for high-efficiency, low-cost carbon capture. In the CLC process, fuel combustion takes place in the fuel reactor using oxygen supplied by a metal oxide oxygen carrier. The reduced oxygen carrier is pneumatically transported to the air reactor where it is reoxidized in air; it then circulates back into the fuel reactor to complete the loop. The typical CLC setup employing two dual fluidized bed reactors is shown in **Figure 1(a)** [3]. Alternatively, a single packed bed reactor can be swapped between fuel reactor and air reactor configurations through a high temperature gas switching system as shown in **Figure 1(b)** [3].

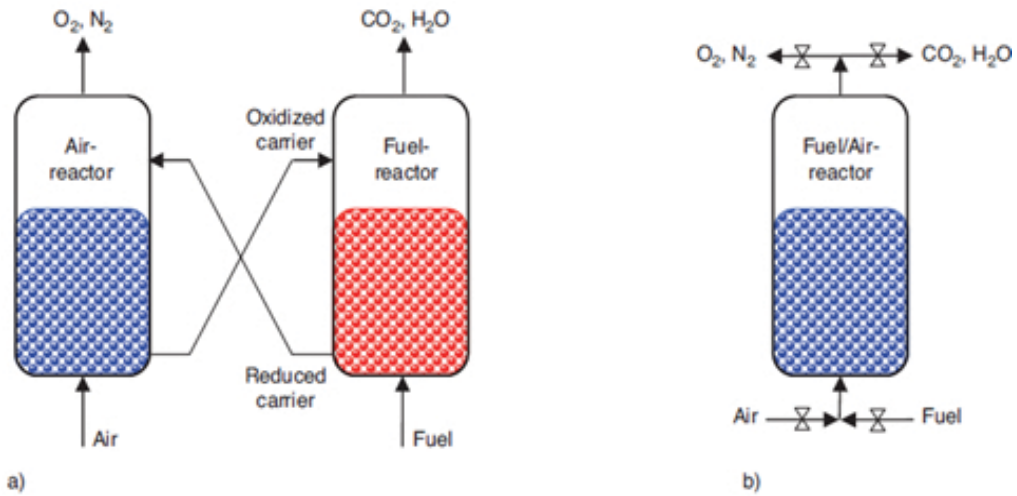

Figure 1. Schematic representation of a chemical looping combustion system with (a) dual interconnected fluidized beds and (b) packed bed with alternating flow [3].

Since the fuel combustion in a CLC system takes place in the absence of air, the flue stream from the fuel reactor is not diluted or contaminated by other gases such as nitrogen. Hence, CLC can produce a high-purity stream of CO_2 available for capture at the fuel reactor without the need for the energy expensive gas separation process required by other CCS technologies such as oxy-fuel combustion. The only energy cost of separation associated with CLC is the cost of solid recirculation. Previous works based on energy and exergy analysis have demonstrated that CLC systems can achieve power efficiencies greater than 50% along with nearly complete CO_2 capture [4–8]. The low-cost carbon capture associated with CLC has a direct bearing on the cost of electricity, as confirmed by a techno-economic study published recently

http://dx.doi.org/10.5772/62811

by the National Energy Technology Laboratory (NETL) that reported that the cost of electricity for a CLC plant using Fe_2O_3 oxygen carrier is $115.1 per MWh compared with $137.3 per MWh for a conventional pulverized coal power plant with a postcombustion amine-based CO_2 absorption system [9].

Unlike CLC where the combustion process is altered to facilitate carbon capture, CCS technologies can also be retrofitted into existing power plants postcombustion setting. The use of calcium oxide (CaO) as the sorbent to capture CO_2 from the flue stream of a power plant has been proposed in several studies [10–13]. The calcium looping (CaL) process consists of two interconnected reactors called the carbonator and the calciner in which the carbonation and calcination reactions take place respectively. The overall carbonation-calcination equilibrium reaction is given by

$$CaO_{(s)} + CO_{2(g)} \leftrightharpoons CaCO_{3(s)} \tag{1}$$

The carbonation reaction entraps the CO_2 from the flue gas stream using the CaO sorbent to form calcium carbonate ($CaCO_3$). The flue stream exiting the carbonator is CO_2-lean and can be exhausted into the atmosphere. The solid $CaCO_3$ from the carbonator is transported to the calciner where it is heated to decompose into CaO and CO_2. The calciner produces a stream of pure CO_2 that is sent for pressurized storage for subsequent sequestration or use. The CaO is transported back into the carbonator to complete the loop. The typical setup for calcium looping (CaL) mirrors that of a chemical looping combustion plant, with the carbonator and calciner analogous to the air and fuel reactors in CLC and the $CaO/CaCO_3$ equivalent to the oxidized/reduced metal oxide oxygen carrier. A schematic representation of the CaL process is shown in **Figure 2**. The make-up CaO flow and solids disposal are required to maintain reactivity of the sorbent; if the CaO was not replenished, the reaction rates would degenerate over time as the loop ran its course. It is noted that CaL can also be employed to remove carbon from the fuel prior to combustion and generate a stream of H_2 for clean burning. However, the precombustion CaL scenario requires significant alteration to the combustion process and loses the advantage of being able to be retrofitted into existing power plants; it also has a higher energy penalty compared with the postcombustion CaL process considered in this chapter.

Computational fluid dynamics (CFD) simulations of chemical looping combustion provide an efficient means to analyze the performance and characterize the fluidization behavior and chemical kinetics in the system. Past CFD simulations of CLC have primarily focused on the single reactor setup similar to **Figure 1(b)**, such as the work of Mahalatkar et al. [14, 15] demonstrating the capability of CFD to match the reaction mechanics inside a CLC fuel reactor. However, the single reactor setup cannot be operated with solid fuels since there is no way to remove the coal from the system prior to switching to the air reactor configuration. Given that coal is projected to remain the dominant fossil fuel in the near future [16], it is necessary to establish a credible CFD simulation for CLC based on the dual fluidized bed setup shown in **Figure 1(a)**.

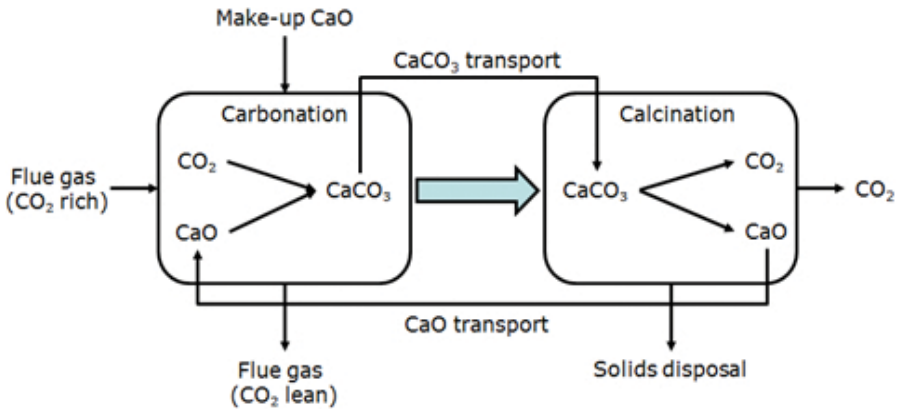

Figure 2. Schematic representation of a calcium looping system with interconnected reactors.

A detailed three-dimensional CFD simulation of the experimental CLC reactor of Abad et al. [17] is presented in this chapter employing the Eulerian or continuum approach to model the solid phase. Later, the cold flow behavior of the fully-looped CLC system at NETL is modeled employing the Lagrangian discrete element method (DEM) as a follow up to the CFD simulation conducted for this case previously by Parker [18]. The CFD simulations discussed in this work are among the very few present in the current literature of the complete circulating dual fluidized bed setup for CLC. Finally, a system level simulation of postcombustion CaL in Aspen Plus is presented to evaluate the energy penalty associated with the carbon capture. The estimation of the energy penalty in CaL is of great interest in the field of CCS; the goal of an ideal carbon capture process is to consume the least amount of energy while achieving a high CO_2 capture efficiency.

2. Eulerian simulation of the experimental CLC reactor of Abad et al.

In this section, the laboratory scale experiment of Abad et al. [17] is used as a basis to perform a detailed CFD simulation of a CLC system using the Eulerian multifluid approach. It is one of the few CFD models in the literature of a complete circulating dual fluidized bed setup with chemical reactions. The fluidization behavior in both air and fuel reactor beds and the circulation of the oxygen carrier between the beds is investigated and compared with the experiment. The simulation results of the chemical reactions in the fuel reactor are evaluated against the outlet concentrations of the flue gases in the experiment.

The experiment uses the two-compartment fluidized bed design proposed by Chong et al. [19] and further investigated by Fang et al. [20]. The experimental reactor setup is illustrated in **Figure 3**. Dimensions and additional details can be found in the work of Abad et al. [17]. The experiment used a Fe-based oxygen carrier consisting of 60% Fe_2O_3 by mass and 40% Al_2O_3 designated as F6A1100. The gaseous fuels used in the experiment are natural gas, consisting of primarily CH_4 and syngas consisting of a mixture of 50% CO and 50% H_2. The fluidization

http://dx.doi.org/10.5772/62811

velocity in the air reactor is greater than the terminal velocity of the oxygen carrier particles and carries the particles upward. The flow then undergoes a sudden expansion (i.e., a reduction in velocity) in the particle separator at the top of the reactor, which causes the particles to fall into the down-comer and enter the fuel reactor. The fuel reactor constitutes a bubbling fluidized bed given the fluidization velocity is smaller than the terminal velocity of the particles. The flue streams from both the reactors are connected to a gas analyzer to measure the concentrations of the outlet gases.

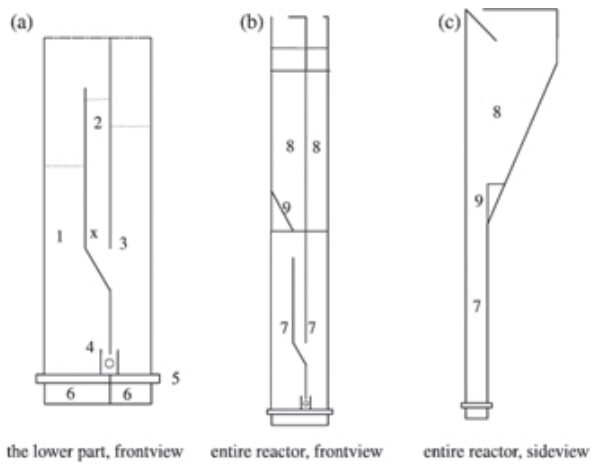

Figure 3. Sketch of experimental reactor [17]: (1) air reactor, (2) down-comer, (3) fuel reactor, (4) slot, (5) gas distributor plate, (6) wind box, (7) reactor part, (8) particle separator, and (9) leaning wall. The symbols (×) and (o) indicate fluidization in the down-comer and slot.

2.1. Numerical solution procedure

A numerical model of the experimental CLC reactor of Abad et al. [17] is developed using the commercial CFD software ANSYS Fluent, release version 14.5 [21, 22]. The complete Navier-Stokes equations of fluid dynamics are solved to account for the chemical active multiphase flow with heat transfer. The Eulerian two-fluid model is used to approximate the solid phase as a secondary fluid phase by averaging particle variables such as mass, velocity, temperature, etc. over a region that is large compared with the particle size. Interactions between the solid and gas phases are included in the model via constitutive equations for solid phase pressure and viscosity that are provided by the kinetic theory of granular flow, an extension of the classical kinetic gas theory that includes inelastic interparticle interactions [23, 24].

2.1.1. Eulerian two-fluid model equations

For multiphase simulations, the Navier-Stokes equations are modified by including the phase volume fraction α to account for the presence of other phases [22]. The continuity equation for phase q is given as

$$\frac{\partial}{\partial t}(\alpha_q \rho_q) + \nabla \cdot (\alpha_q \rho_q \boldsymbol{u}_q) = \sum (\dot{m}_{pq} - \dot{m}_{qp}) \tag{2}$$

where $\dot{m}_{pq}$ is the mass transfer rate from the pth phase to the qth phase. The current simulation contains one gas phase comprising six species (CO, CO_2, H_2, H_2O, O_2, and N_2) and one solid phase comprising two species (Fe_2O_3 and Fe_3O_4). The species transport equation is given as

$$\frac{\partial}{\partial t}(\alpha_q \rho_q Y_{iq}) + \nabla \cdot (\alpha_q \rho_q \boldsymbol{u}_q Y_{iq}) = \sum (\dot{m}_{ij}^{qp} - \dot{m}_{ji}^{pq}) \tag{3}$$

where Y_{iq} is the mass fraction of the species i in the qth phase and $\dot{m}_{ij}^{qp}$ is the mass transfer rate from the jth species of the pth phase to the ith species in the qth phase.

The momentum equation for the gas phase is given as

$$\frac{\partial}{\partial t}(\alpha_g \rho_g \boldsymbol{u}_g) + \nabla \cdot (\alpha_g \rho_g \boldsymbol{u}_g \boldsymbol{u}_g) = -\alpha_g \nabla p + \nabla \cdot \bar{\bar{\tau}}_g + \alpha_g \rho_g \boldsymbol{g} + \sum (\boldsymbol{R}_{sg} + \dot{m}_{sg} \boldsymbol{u}_{sg} - \dot{m}_{gs} \boldsymbol{u}_{gs}) \tag{4}$$

where the terms in the summation are source terms added to the standard form of the Navier-Stokes momentum equations to account for the momentum transfer between the solid phase and the gas phase. Specifically, $\boldsymbol{R}_{sg} = \beta_{sg}(\boldsymbol{u}_s - \boldsymbol{u}_g)$ is the momentum transfer due to interphase drag and the other terms are due to the transfer of mass. The momentum equation for the solid phase follows from the momentum equation for the gas phase with the source term for interphase drag being equal but opposite.

$$\frac{\partial}{\partial t}(\alpha_s \rho_s \boldsymbol{u}_s) + \nabla \cdot (\alpha_s \rho_s \boldsymbol{u}_s \boldsymbol{u}_s) = -\alpha_s \nabla p + \nabla \cdot \bar{\bar{\tau}}_s + \alpha_s \rho_s \boldsymbol{g} + \sum (\boldsymbol{R}_{rs} + \dot{m}_{rs} \boldsymbol{u}_{rs} - \dot{m}_{sr} \boldsymbol{u}_{sr}) \tag{5}$$

The gas inside a CLC reactor can be considered as an incompressible fluid. As such, the fluid stress tensor $\bar{\bar{\tau}}_g$ is simply

For the flow conditions in a fuel reactor, the gas can be considered as an incompressible fluid. The fluid stress tensor is simply the Cauchy stress tensor with zero bulk viscosity.

$$\bar{\bar{\tau}}_g = \alpha_g \mu_g (\nabla \boldsymbol{u}_g + \nabla \boldsymbol{u}_g^T). \tag{6}$$

On the other hand, the granular solid stress tensor considers all terms in the Cauchy stress tensor,

http://dx.doi.org/10.5772/62811

$$\bar{\bar{\tau}}_s = -p_s \bar{\bar{I}} + \alpha_s \mu_s (\nabla \boldsymbol{u}_s + \nabla \boldsymbol{u}_s^T) + \alpha_s \lambda_s (\nabla \cdot \boldsymbol{u}_s) \bar{\bar{I}} \tag{7}$$

where p_s is the solids pressure, μ_s is the granular viscosity, and λ_s is the granular bulk viscosity. The definition of these terms and the interphase exchange coefficient β_s provide the basis for the Eulerian approach for multiphase flow simulation. The solids pressure and granular bulk viscosity used in the present work are according to Lun et al. [25]; the granular viscosity is according to Gidaspow [26].

The experimental reactor of Abad et al. [17] includes a wide range of solid loadings, from the densely-packed loop-seal and down-comer, the bubbling fluidized bed in the fuel reactor, and the dilute regions in the particle separator. The Gidaspow drag model [26] is selected to model the solid-gas interaction because it accounts for the differences in the behavior in dilute and dense regions by switching between the drag prediction of the Ergun equation [27] and the drag model of Wen and Yu [28] based on the solids volume fraction α_s. For $\alpha_s > 0.8$, the Gidaspow model for the exchange coefficient β_s gives

$$\beta_{sg} = \frac{3}{4} C_D \frac{\alpha_s \alpha_g \rho_g |\boldsymbol{u}_s - \boldsymbol{u}_g|}{d_s} \alpha_g^{-2.65}; C_D = \frac{24}{\alpha_g \mathrm{Re}_s} [1 + 0.15(\alpha_g \mathrm{Re}_s)^{0.687}] \tag{8}$$

Conversely, for $\alpha_s \leq 0.8$,

$$\beta_{sg} = 150 \frac{\alpha_s (1 - \alpha_g) \mu_g}{\alpha_g d_s^2} + 1.75 \frac{\rho_g \alpha_s |\boldsymbol{u}_s - \boldsymbol{u}_g|}{d_s} \tag{9}$$

where d_s is the particle diameter and Re_s is the Reynolds number based on d_s.

Finally, the energy equation for phase q is expressed in terms of the enthalpy as

$$\frac{\partial}{\partial t}(\alpha_q \rho_q h_q) + \nabla \cdot (\alpha_q \boldsymbol{u}_q h_q) = \alpha_q \frac{\partial p}{\partial t} + \nabla \cdot (\bar{\bar{\tau}}_q \cdot \boldsymbol{u}_q) - \nabla \cdot \boldsymbol{q}_q + S_q + \sum Q_{pq} \tag{10}$$

where h_q and $\boldsymbol{q}_q$ are the specific enthalpy and heat flux of phase q respectively. As with the continuity and momentum equations, the source terms S_q and $\boldsymbol{Q}_{pq}$ are included in Eq. (10) to account for the transfer of enthalpy between the solid and gas phases. S_q is the enthalpy source due to chemical reaction and Q_{pq} is the heat transfer as a function of the temperature difference between the pth phase and the qth phase, given in terms of the interphase heat transfer coefficient h_{pq} as

$$Q_{pq} = h_{pq}(T_p - T_q) \tag{11}$$

The interphase heat transfer coefficient is based on the Nusselt number, Nu, the ratio of convective to conductive heat transfer across a boundary.

$$h_{pq} = \frac{6\kappa_q \alpha_p \alpha_q Nu_p}{d_p^2} \tag{12}$$

where κ_q is the thermal conductivity of phase q. In the current simulation, the Nusselt number for the solid phase is obtained using the empirical relation of Gunn [29] given in terms of the Prandtl number Pr as

$$\mathrm{Nu}_s = (7 - 10\alpha_q + 5\alpha_q^2)(1 + 0.7\,\mathrm{Re}_s^{0.2}\,\mathrm{Pr}^{1/3}) + (1.33 - 2.4\alpha_q + 1.2\alpha_q^2)\,\mathrm{Re}_s^{0.7}\,\mathrm{Pr}^{1/3} \tag{13}$$

2.1.2. Chemical reaction scheme and rates

The oxygen carrier used in the numerical simulation is F6A1100, consisting of 60% Fe_2O_3 and 40% inert Al_2O_3 by mass, following the experiment of Abad et al. [17]. Of the two gaseous fuels used in the experiment, only syngas has been considered in the current work because the chemical kinetics for the reaction of Fe_2O_3 with the nonmethane components of natural gas is not available. The metal oxide reduction reactions that are used in the simulation are

$$3\mathrm{Fe_2O_3} + \mathrm{CO} \rightarrow 2\mathrm{Fe_3O_4} + \mathrm{CO_2} \tag{14}$$

$$3\mathrm{Fe_2O_3} + \mathrm{H_2} \rightarrow 2\mathrm{Fe_3O_4} + \mathrm{H_2O} \tag{15}$$

Exact reaction rates for the reduction of F6A1100 with CO and H_2 are not available in the literature; the reaction rates for the reduction of hematite (Fe_2O_3) with CO and H_2 obtained from the work of Mattisson et al. [30] and further developed by Mahalatkar et al. [14] are used as an approximation. Based on these papers, the reaction rates $\dot{m}$ (in kg/s per cell volume or kg/(m^3 s)) of the fuel gases with Fe_2O_3 are given by

$$\dot{m}_{H_2} = \frac{k_{H_2} R_o}{2MW_{O_2}} \rho_{avg} \alpha_s \left(Y_{Fe_2O_3} + Y_{Fe_3O_4} \frac{\nu_{Fe_2O_3} MW_{Fe_2O_3}}{\nu_{Fe_3O_4} MW_{Fe_3O_4}}\right)(1 - X)^{2/3} MW_{H_2} \tag{16}$$

And

$$\dot{m}_{CO} = \frac{k_{CO} R_o}{2MW_{O_2}} \rho_{avg} \alpha_s \left(Y_{Fe_2O_3} + Y_{Fe_3O_4} \frac{\nu_{Fe_2O_3} MW_{Fe_2O_3}}{\nu_{Fe_3O_4} MW_{Fe_3O_4}}\right)(1 - X)^{2/3} MW_{CO} \tag{17}$$

http://dx.doi.org/10.5772/62811

where k is the nominal reaction rate based on the Arrhenius rate, R_o is the oxygen carrying capacity, MW is the molecular weight (in kg/kmol), Y is the mass fraction, v is the stoichiometric coefficient, and X is the conversion fraction based on the fully reduced state; in each case, the subscript identifies the species under consideration. More details of the reaction rate derivation can be found in the work of Mahalatkar et al. [14]. The reaction rates identified in Eqs. (16) (17) are implemented into the numerical simulation through separate user-defined functions.

2.2. Three-dimensional simulation of Abad et al. experiment

The results of a two-dimensional simulation of the experiment of Abad et al. [17] can be found in the authors' previous work [31]. Although the two-dimensional model successfully captured the salient features of the fluidization behavior in the dual fluidized bed system, it was unable to produce the expected concentrations of CO_2 and H_2O in the fuel reactor because of the inadequacy of the two-dimensional simulation in modeling the gaseous diffusion, which is an inherently three-dimensional process. Therefore, a three-dimensional simulation of Abad et al.'s experiment [17] is performed to produce a more accurate match for the chemical reactions between the simulation and experiment. The computational domain is an exact representation of the experimental reactor shown in **Figure 3**. A structured mesh with around 45,000 elements is used to model the geometry; the grid is relatively fine in the lower part of the reactor where the solids loading is densely-packed (minimum cell volume of around 10^{-8} m) and coarser in the dilute upper part (cell volume of around 10^{-7} m). The mesh is shown in **Figure 4**.

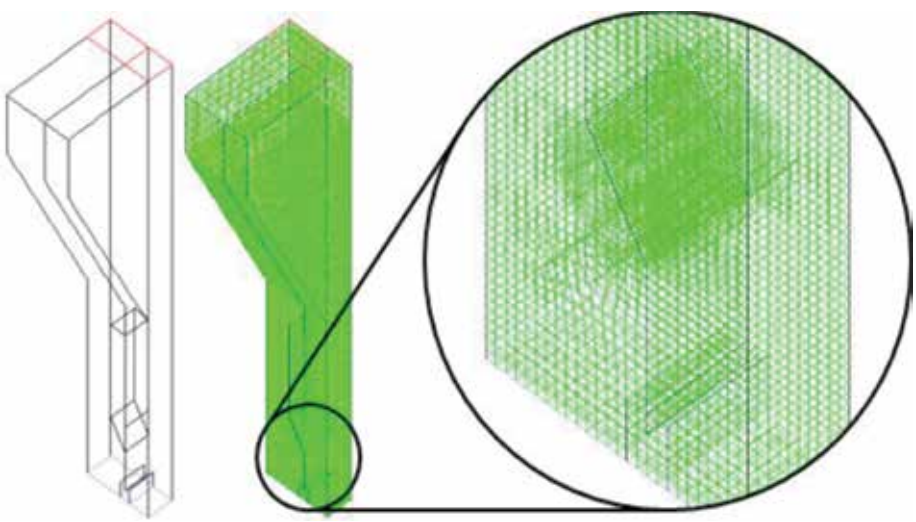

Figure 4. Computational domain and grid for three-dimensional CFD simulation with detailed view of lower part.

The oxygen carrier used by Abad et al. [17] has a density of 2150 kg/m^3 with a diameter of 90–212 μm; the average value of 150 μm is used in the simulation. The batch processing results of Abad et al. [17] are used as a basis for the simulation. The initial solids loading in the bed is

about 300 g, of which 110 g is in the fuel reactor, in line with the experiment. The temperature in the system is set at 850°C or 1123 K based on the experimental conditions. It is expected that the densely-packed solids in the down-comer and slot regions will be enough to keep the leakage to a minimum without the need for an active pressure differential between the reactors. As such, both reactors are set at atmospheric pressure. The initial oxygen carrier mass in the fuel reactor is sufficient to react with all the injected fuel, so the fuel conversion is not affected by reoxidation in the air reactor. The CFD simulation is thus considerably simplified by setting the fluidization gas in the air reactor to an inert gas (in this case, nitrogen). The secondary phase mass fraction is set to zero at both fuel and air reactor inlets because no new oxygen carrier is added. The numerical parameters used in the CFD simulation are summarized in **Table 1**. The simulation was run on a Dell workstation with a quad-core Intel Xeon CPU for around four days to complete 30 s of simulation. The contours of the mass fraction of CO_2 are shown in **Figure 5**.

Primary phase	**Fuel-gas mixture**
Secondary phase	Oxygen carrier (F6AL1100)
Average particle diameter	150 μm
Average particle density	2150 kg/m^3
Initial bed mass	~180 g
Fluidizing gas composition in fuel reactor	50% CO, 50% H_2
Fluidizing gas composition in air reactor	100% N_2
Inlet boundary condition in fuel reactor	Velocity inlet with velocity 0.1 m/s
Inlet boundary condition in air reactor	Velocity inlet with velocity 0.5 m/s
Outlet boundary condition in fuel reactor	Pressure outlet at atmospheric pressure
Outlet boundary condition in air reactor	Pressure outlet at atmospheric pressure
Operating temperature	1123 K
Solids pressure	Lun et al. [25]
Granular bulk viscosity	Lun et al. [25]
Granular viscosity	Gidaspow [26]
Drag law	Gidaspow [26]
Heat transfer coefficient	Gunn [29]
Numerical scheme	Phase-coupled SIMPLE
Time step size	0.0005 s
Iterations per time step	20

Table 1. Modeling parameters for three-dimensional CFD simulation of the Abad et al. experiment.

http://dx.doi.org/10.5772/62811

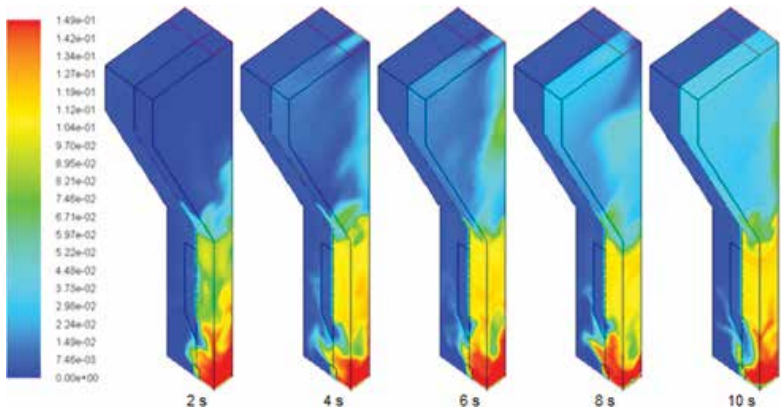

Figure 5. Contours of CO_2 mass fraction for the first 10 seconds of three-dimensional simulation showing the increased diffusion and absence of the vortex pattern compared with the two-dimensional case.

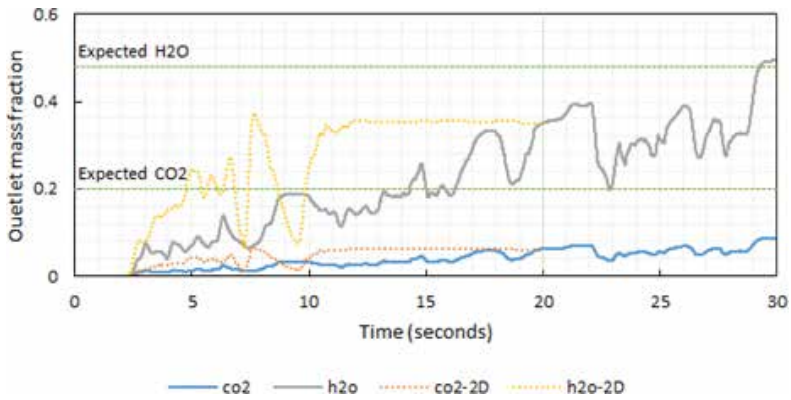

Figure 6. Mass fractions of CO_2 and H_2O at the fuel reactor outlet for the three-dimensional simulation of the CLC reactor of Abad et al. [17].

As expected, the three-dimensional simulation exhibits greater diffusion compared with the two-dimensional case presented in reference [31]. The local mass fraction of CO_2 at the base of the bed where the injected CO first comes into contact with the oxygen carrier and begins to react is around 15%. From there, the CO_2 diffuses through the fuel reactor more homogeneously as it travels toward the outlet; the vortex patterns observed in the two-dimensional case [31] are notably absent. The absence of the vortex pattern can be quantitatively confirmed by the plots of the mass fractions of CO_2 and H_2O at the fuel reactor outlet as shown in **Figure 6**, which also includes the two-dimensional results from reference [31]. The outlet mass fractions of both gases are initially lower because the gases have to diffuse through the existing N_2 in the fuel reactor instead of displacing it. The large fluctuations in the outlet mass fraction caused by pockets of reversed flow are also eliminated. The outlet mass fractions of both gases keep increasing as the fuel reaction produces more and more; by 20 s, both CO_2 and H_2O have

exceeded their stagnation values from the two-dimensional simulation. The outlet mass fraction of H_2O reaches the expected value from Abad et al.'s experiment around 30 s [17].

The three-dimensional simulation shows a significant increase in the mass fraction of the flue gases at the fuel reactor outlet. However, despite the improvement, the mass fraction of CO_2 still shows a significant discrepancy from the experimental value, which may be due to various external factors. It is known that significant apparent diffusion can occur in gases when they travel through pipes [32]. In the experiment [17], the gas streams from the reactors were pipelined to an electric cooler and then to the gas analyzer. Hence, it is reasonable to expect that the concentrations measured at the gas analyzer may be different from the concentrations present right at the fuel reactor outlet. It should also be noted that the reaction rate kinetics used in the simulation were based on the experimental study of Mattisson et al. [30] using hematite (Fe_2O_3), while the oxygen carrier used by Abad et al. [17] was F6A1100 comprising 60% Fe_2O_3 and 40% Al_2O_3. One of the reasons F6A1100 is preferred over hematite as the oxygen carrier for CLC operation is its improved reactivity owing to an increased apparent surface area due to the presence of the porous Al_2O_3[33]. Thus, it stands to reason that the experiment would show a higher concentration of the reaction products compared with the current simulation. Similar discrepancies between experiment and simulation have been previously noted in the work of Mahalatkar et al. [15] where the reaction rates obtained from experiment for the char gasification reaction had to be doubled in the simulation in order to match the result. Further research is required to determine more accurate empirical formulas for the reduction of F6A1100 specifically to improve the accuracy of the results of the CFD simulation.

3. Lagrangian simulation of complete CLC reactor at NETL

The Eulerian two-fluid model can accurately capture the bulk behavior of the solid phase in the dual fluidized bed reactor for CLC using gaseous fuels. However, given coal is projected to remain one of the dominant fossil fuels in the near future, the concept of coal-direct chemical looping combustion (CD-CLC) with in situ gasification has garnered significant interest in recent years. In the CD-CLC process, the oxygen carrier needs to be formed into particles with a relatively larger diameter compared with pulverized coal for easier separation. The work of Gryczka et al. [34] with larger particles has suggested that accurate numerical representation of particle dynamics is not likely to be achieved using the granular solid phase approximation due to "the inadequacies of the continuum model." The inaccuracy arises from the nonphysical closure terms used in the Eulerian model such as the frictional solids viscosity or the solids pressure based on the kinetic theory of granular flow. Thus, for a more detailed understanding of the hydrodynamics in a multiphase system inside a CLC reactor, the Lagrangian particle-based approach is employed to study the CD-CLC reactor system at NETL, previously investigated by Parker [18].

The geometry of the CD-CLC system used at NETL comprises an air reactor, cyclone, loop-seal, and fuel reactor, as shown in **Figure 7(a)**. In the cold flow experiment, the oxygen carrier particles start from the bottom of the air reactor and move up along the riser and into the

http://dx.doi.org/10.5772/62811

cyclone. In the cyclone, the particles are separated from the air stream and drop into the loop-seal due to the gravity. After passing through the slightly fluidized loop-seal, the particles move into the fuel reactor. The oxygen carrier particles exit the fuel reactor and return to the air reactor through an L-valve. The reactor dimensions and additional descriptions of the various components of the CD-CLC setup at NETL can be found in the work of Parker [18]. The computational grid, shown in **Figure 7(b)**, is an exact representation of the geometry. The oxygen carrier particles in the cold flow experiment are primarily ilmenite ($FeTiO_3$) with some uncombined TiO_2 and Fe_2O_3 as well. The ilmenite particles used in the experiment had a size distribution of 13-320 μm. The particle size used in the numerical simulation corresponds to the median particle size of 150 μm with the average density of ilmenite of 4450 kg/m^3.

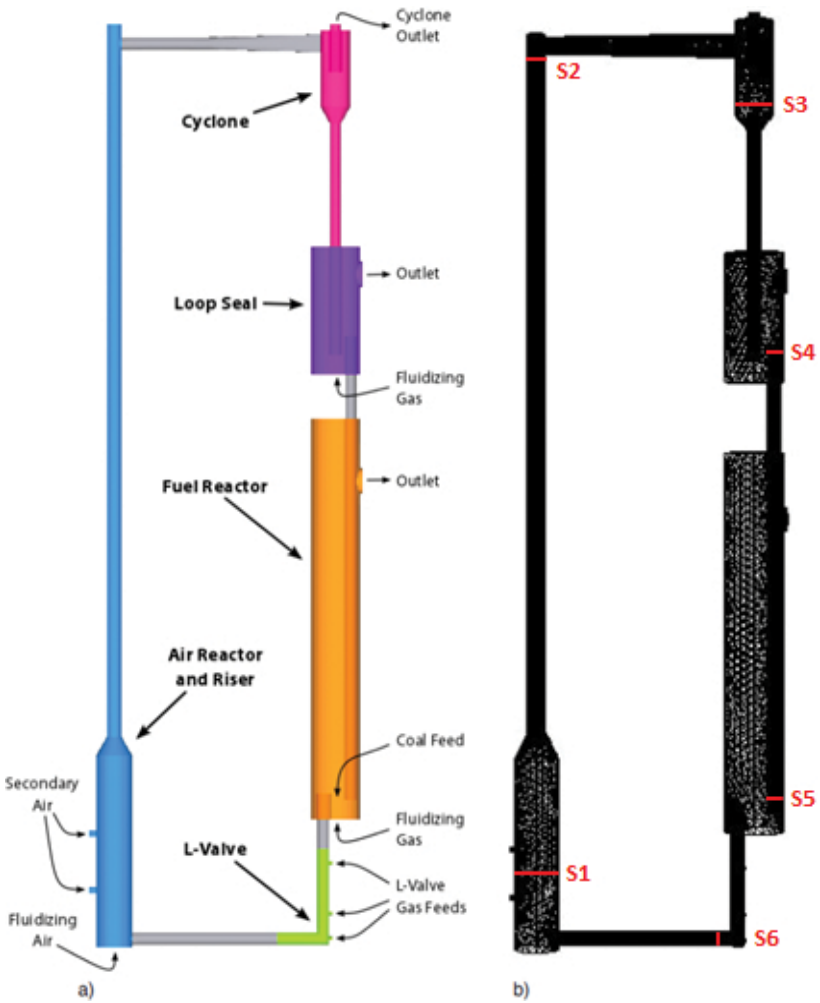

Figure 7. (a) Geometry of the coal-direct chemical-looping combustion system at NETL [18], and (b) computational grid with static pressure measurement locations marked S1–S6.

3.1. Numerical solution procedure

The equations for mass and momentum conservation for the fluid phase are identical to those used in the Eulerian model given in Eqs. (2) and (4) with the exception that the source term in Eq. (4) for the solid-gas momentum exchange term, $\boldsymbol{R}_{sg}$, is obtained from the average of the drag forces acting on all the discrete particles in a given computational cell. The shear stress term in the momentum equation is given in Eq. (6). Since the current simulation considers a cold flow with no species transport, the energy and species conservation equations are not applicable in this case.

3.1.1. Particle equations

In the Lagrangian approach, the motion of each solid particle is calculated by summing the forces acting on the particle and applying Newton's second law of motion. The force balance equation is given by

$$m_s \frac{\partial \boldsymbol{u}_s}{\partial t} = \sum \boldsymbol{F}_i = \boldsymbol{F}_{gra} + \boldsymbol{F}_{buo} + \boldsymbol{F}_{drag} + \boldsymbol{F}_{pre} + \boldsymbol{F}_{Saf} + \boldsymbol{F}_{Mag} + \boldsymbol{F}_{con} \tag{18}$$

The individual force terms in Eq. (18) are, in order, the bulk forces due to gravity and buoyancy, the hydrodynamic force due to drag, the pressure force due to the pressure gradient, the Saffman lift force due to fluid shear, and the Magnus force due to particle spin, and the contact force due to particle-particle or particle-wall collision. Given the large difference between the particle and fluid density, the pressure force can be dropped from Eq. (18) without loss of accuracy; the Magnus force can also be dropped because of negligible particle rotation. In this work, this contact force $\boldsymbol{F}_{con}$ is computed using the soft-sphere model, which decouples its normal and tangential components [22]. The normal force is given by

$$\boldsymbol{F}_{con}^{n} = (k\delta + \gamma(\boldsymbol{u}_{12}\boldsymbol{e}))\boldsymbol{e} \tag{19}$$

where k is the spring constant of the particle, δ is the overlap between the particle pair involved in the collision as illustrated in **Figure 8**, γ is the damping coefficient, $\boldsymbol{u}_{12}$ is the relative velocity vector of the colliding pair, and $\boldsymbol{e}$ is the unit vector. For large values of k, the results of the soft-sphere model are interchangeable with those obtained using a hard-sphere model [35]. The tangential contact force is calculated based on the normal force as $\boldsymbol{F}_{con}^{t} = \mu \boldsymbol{F}_{con}^{n}$ where the coefficient of friction μ is given as a function of the relative tangential velocity v_r by

$$\mu(v_r) = \begin{cases} \mu_{stick} + (\mu_{stick} - \mu_{glide})(v_r / v_{glide} - 2)(v_r / v_{glide}) & if\ v_r < v_{glide} \\ \mu_{glide} & if\ v_r \geq v_{glide} \end{cases} \tag{20}$$

http://dx.doi.org/10.5772/62811

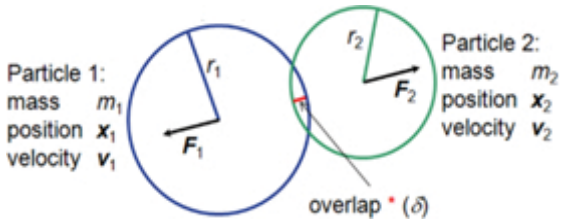

Figure 8. Schematic of particle collision model for DEM.

3.1.2. Solid-gas momentum exchange

The momentum exchange between the solid and fluid phase is a crucial element for modeling multiphase flow using the coupled CFD/DEM solver. The transfer of momentum from the fluid to a solid particle as it moves through each cell in the computational domain is attributed to the drag force given by

$$\boldsymbol{F}_{drag} = F_D(\boldsymbol{u}_f - \boldsymbol{u}_p) \tag{21}$$

where $\boldsymbol{u}_f$ is the fluid velocity, $\boldsymbol{u}_p$ is the particle velocity, and $\boldsymbol{F}_D$ is the net drag coefficient,

$$F_D = \frac{18\mu}{\rho_p d_p^2}\frac{C_D Re_p}{24} \tag{22}$$

where μ, ρ, and d_p are the viscosity of the gas and the density and diameter of the solid particle, respectively. C_D and Re_p are the particle drag coefficient for a sphere and the relative Reynolds number based on the particle diameter respectively. Re_p is defined as

$$Re_p = \frac{\rho_f d_p |\boldsymbol{u}_f - \boldsymbol{u}_p|}{\mu} \tag{23}$$

The drag coefficient can be modeled using various empirical relations. The spherical or Stokes drag law is chosen in this work for its simplicity.

3.1.3. Parcel conceptcel concept

The computational cost of the DEM approach is driven by the number of collisions between particles; to track each individual particle in a CLC system using the DEM approach is extremely computationally demanding since the total number of particles increases drastically as the particle size becomes smaller. Hence, the parcel methodology first proposed by Patankar and Joseph [36] is employed in this work to overcome the high computational cost.

According to Patankar and Joseph [36], one parcel can represent a group of particles with the same properties such as density and size. The mass used in collisions is that of the whole parcel rather than a single particle. By summing the mass and volume of each individual particle in the parcel, the total mass m_p and volume V_p of the parcel can be obtained. The radius of the parcel is then determined by the mass of the entire parcel and the particle density. For a given point in the fluid flow, the driving force of a parcel due to fluid forces is assumed to be the same as the sum of the fluid force acting on the group of particles it represents.

$$\boldsymbol{F}_{f,p} = \sum_{i=1}^{N_p} \boldsymbol{F}_{f,i} \tag{24}$$

where N_p is the number of particles in the parcel, and $\boldsymbol{F}_f$ is the net fluid force acting on a parcel p or particle i depending on the subscript. The acceleration due to inter-particle collision forces and particle-wall collisions forces is computed based on the mass properties of the parcel.

3.2. Cold flow simulation of NETL CD-CLC reactor system

The boundary conditions for the cold flow simulation are obtained from Parker [18] and are summarized in **Table 2**. Given the high gas velocity required in the air reactor to carry the particles to the top of the reactor and into the cyclone, the flow is turbulent. However, it is well-established that for gas-solid flows, the effect of turbulence is increasingly negligible compared with the effect of the solids for solid volume fractions above 0.001 [37]. For the present simulation of a fluidized bed with densely packed regions, the effect of turbulence can be ignored without loss of accuracy, in line with the work of Parker [18]. The particles are injected into the air reactor, loop-seal, and air reactor and are allowed to settle prior to the start of the simulation. A total of 717,879 particles in total are injected into the system—73,360 particles in the air reactor, 365,057 in the fuel reactor, and 279,462 in the loop-seal. After the particles are settled in each bed, the CFD/DEM model is run to simulate 360 ms of cold flow operation. The development of particle movement is shown in **Figure 9** at 10 ms intervals with the particles colored by velocity magnitude.

Unit	Boundary	Gas	Flow rate (m/s)
Air reactor	Fluidizing air	Air	20.0
Fuel reactor	Fluidizing gas	N_2	4.0
Loop-seal	Fluidizing gas	N_2	2.0
L-valve	Stripper (upper)	N_2	0.5
	Aeration (middle)	N_2	1.0
	Eductor (lower)	N_2	1.0

Table 2. Boundary conditions for cold flow simulation.

http://dx.doi.org/10.5772/62811

As shown in **Figure 9**, the particles in the air reactor reach the top of the riser at around 190 ms, and then travel horizontally along the pipe toward the cyclone aided by two secondary gas injections on the side of the air reactor. After another 40 ms, the particles enter the cyclone and start to drop down to the loop-seal. Due to an erroneously high gas velocity in the loop-seal and fuel reactor during the initial startup, the particles in these chambers are also shot up to the top. Once the gas injections are reduced to their correct values of 2 m/s and 4 m/s, respectively at 210 ms, the particles settle down again. From this point onward, it is expected that the particles in the loop-seal will drop into the fuel reactor and the L-valve, and finally be pushed back into the air reactor by the gas injection in the L-valve.

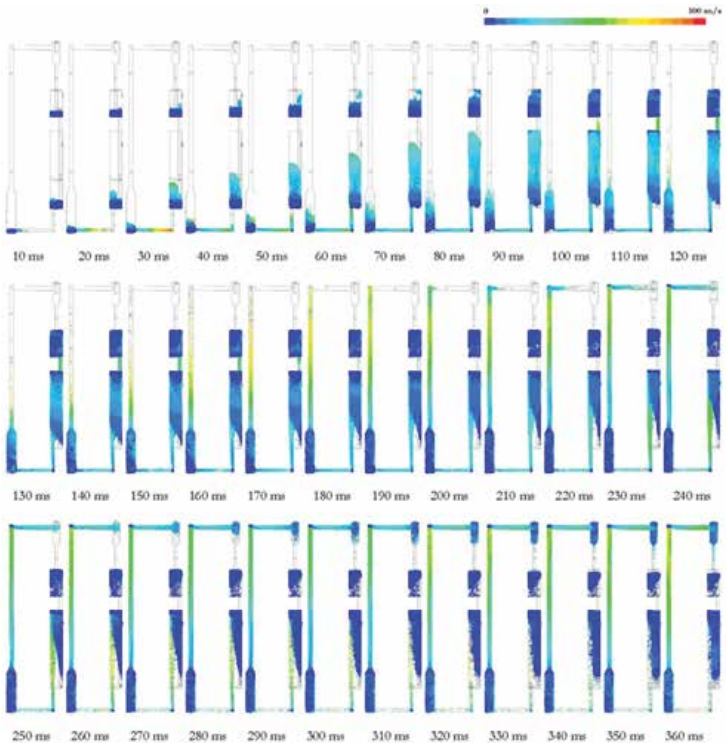

Figure 9. Particle tracks colored by velocity magnitude for the first 360 ms of cold flow simulation.

Three hundred sixty millisecond is not sufficient time to see the complete particle recirculation; however, the pressure contours in **Figure 10** indicate the development of favorable pressure gradients for particle recirculation as the simulation time increases. The static pressure in the system is evaluated at surfaces S-1 to S-6 shown in **Figure 7(b)** to quantify the pressure gradients observed in **Figure 10**; the static pressures variation at 360 ms is presented in **Figure 11**. The arrows indicate the particle movement direction. It can be observed from **Figure 11** that there is a consistent positive pressure differential between surface S-1 (air reactor bed) through to S-5 (fuel reactor bed), which confirms that particle continuous recirculation can occur between these surfaces. It is noted that the pressure gradient between S-5 and S-1

via S-6 (L-valve) is an adverse gradient, which explains why the L-valve gas injection feeds seen in **Figure 7(a)** are required to ensure particle circulation around the loop.

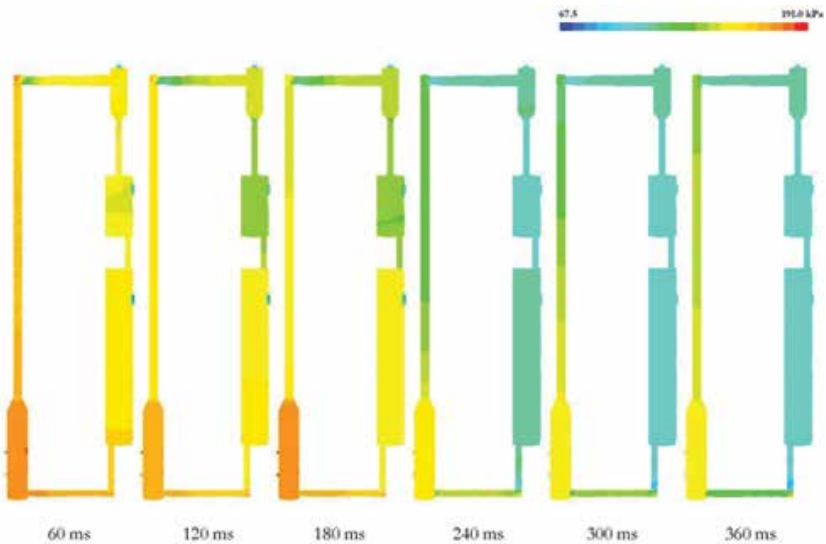

Figure 10. Pressure contours for cold flow inside the CLC apparatus.

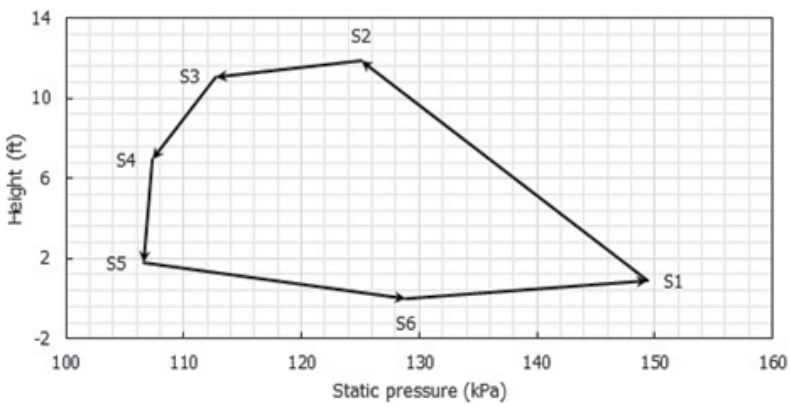

Figure 11. Static pressure at surfaces S1–S6 in the CD-CLC system shown in Figure 7 at t = 360 ms.

4. Process simulation of calcium looping

The calcium looping process offers a solution for capturing CO_2 from existing power plants. In this section, CaL is modeled at the system level using the process simulation software Aspen

Plus. In order to investigate the energy penalty associated with a CaL system, the overall heat production from a power plant without and with calcium looping is determined.

4.1. Simulation of calcium looping with postcombustion capture

In the postcombustion capture scenario, the carbonator and calciner are included downstream of the combustion process to capture CO_2 from the flue gases generated by the combustion of coal. The materials used in the process simulation include conventional and non-conventional components. Pure materials, including all possible chemical compounds comprising the elements C, N, O, H, S, and Cl that might be produced during the chemical reactions, are designated as conventional. Properties for conventional materials are obtained from the Aspen Plus data bank. Mixtures such as coal and ash are designated as non-conventional solids.

4.1.1. Process simulation setupcess simulation setup

The doctoral work of Sivalingam [38] is used as a basis for the process simulation of calcium looping presented in this chapter. Illinois #6 coal is used in the simulation in line with the work of Sivalingam [38]. The RYIELD reactor block is employed in Aspen Plus to decompose the nonconventional material coal into its constituent conventional materials—ash, H_2O, C, H_2, N_2, Cl_2, S, and O_2. Mass percentages for the component yields are set based on the proximate and ultimate analysis of the Illinois #6 coal given in **Table 3**.

Proximate analysis (wt.%)			**Ultimate analysis (wt.%)**						
Moisture	**Volatile matter**	**Fixed carbon**	**Ash**	**C**	**H**	**N**	**Cl**	**S**	**O**
11.12	34.99	44.19	9.70	80.51	5.68	1.58	0.37	3.17	8.69

Table 3. Physical and chemical properties of Illinois #6 coal [38].

The outlet stream from the RYIELD reactor goes into a burner, modeled as a RGIBBS reactor, along with air for combustion. The RGIBBS reactor automatically calculates the combustion products at equilibrium such that the Gibbs free energy is minimized. The air flow rate into the RGIBBS reactor is set at the minimum value where the carbon is completely combusted. The calculation for the proper amount of air is discussed in Section 4.1.2. The CO_2-rich flue gas after combustion then undergoes the calcium looping process. The temperature of the flue stream is maintained at 150°C in accordance with the lower limits on power plant flue gas temperatures provided by Feron [39].

The carbonator refers to the reactor where the carbonation reaction takes place. The RSTOIC reactor block is used in Aspen Plus to model the carbonator. The pressure is set at 1 bar and the temperature is set at 650°C. The RSTOIC is a reactor in which the user can define the specific reaction that occurs. The carbonation reaction is given by

$$CaO_{(s)} + CO_{2(g)} \rightarrow CaCO_{3(s)} \tag{25}$$

In real situations, CaO and CO_2 do not react completely with each other. The amount of CaO that can react with CO_2 is constrained by the surface area of CaO particles and by the extent of the solid-gas mixing as a result of the fluidization behavior in the reactor. These effects are incorporated into Aspen Plus by defining the conversion fraction for one of the reactants, CaO. The dependence of the CO_2 capture efficiency of the carbonator on the sorbent flow ratios is based on the work of Abanades et al. [40]; the data were converted into a table by Sivalingam [38] and is presented in **Table 4**. F_{CO_2} is the mole flow rate of CO_2, F_R is the mole flow rate of recycled (or looped) CaO, and F_0 refers to the make-up flow of CaO.

F_0/F_{CO_2}	$F_R/F_{CO_2} = 3$	$F_R/F_{CO_2} = 4$	$F_R/F_{CO_2} = 5$
0.05	0.63	0.81	0.99
0.10	0.76	0.95	0.99

Table 4. CO_2 capture efficiency for different flow ratios of CaO and CO_2 [38].

It is not possible to model the make-up flow of CaO as a variable in Aspen Plus. Instead, a fixed of $F_0/F_{CO_2} = 0.1$ is chosen with three values of $F_R/F_{CO_2} = 0.1$ to model three values of CO_2 capture efficiency in the range of 50–100%. Multiple cases are run in Aspen Plus using different values for the CaO conversion fraction until the correct CO_2 capture efficiency is achieved. As shown in **Table 5**, each specified CaO conversion fraction corresponds to a range of CO_2 capture efficiencies. The simulation results for the various CaO conversion fractions are plotted in **Figure 12**. The large symbols in **Figure 12** refer to those cases whose results fit the data of Sivalingam [38] exactly; these are denoted as the results obtained from experimental data in the following discussion. The small symbols represent all the trial cases conducted in Aspen Plus and are denoted as extrapolated results.

$F_R/F_{CO_2} = 3$	**CaO conversion fraction**	**CO_2 capture efficiency**
3	0.33	0.66–0.86
4	0.25	0.86–0.97
5	0.20	0.97–0.99

Table 5. Range of CO_2 capture efficiencies for each CaO conversion fraction.

Downstream of the carbonator, the solids mixture (primarily $CaCO_3$ with some CaO depending on the inlet flow rate of CaO) and the CO_2-lean flue gas is cooled back to the 150°C and sent to the calciner to regenerate the CaO. Similar to the carbonator, the RSTOIC reactor block

is employed for calciner in ASPEN Plus. The calcination reaction that takes place in the calciner is given by

$$CaCO_{3(s)} \rightarrow CaO_{(s)} + CO_{2(g)} \tag{26}$$

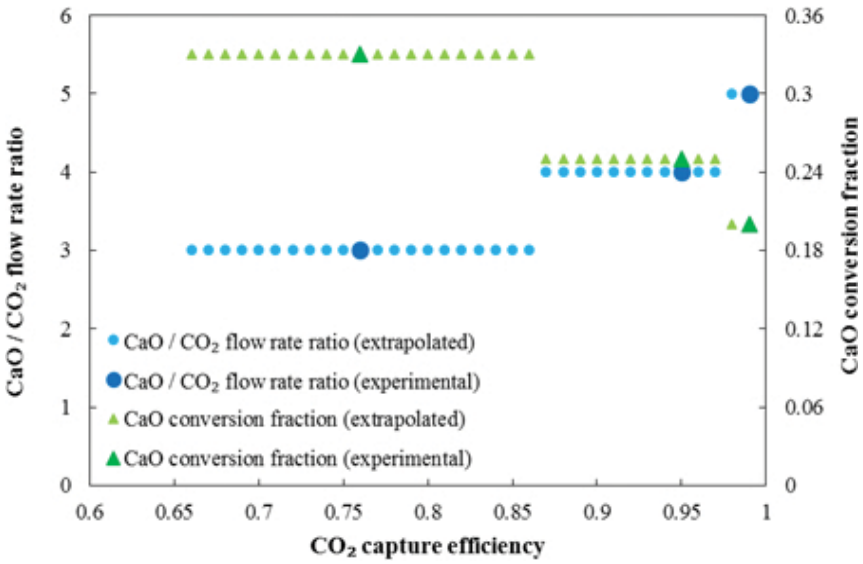

Figure 12. Range of CO_2 capture efficiencies for various CaO conversion fractions.

The temperature in the calciner is 900°C and the pressure is 1 bar in accordance with Sivalingam [38]. The calcination reaction is a complete reaction, so the conversion fraction of $CaCO_3$ is set at 1. The reactor blocks used in Aspen Plus for calcium looping with postcombustion capture are summarized in **Table 6** along with their functions and reactions; the final flow sheet is shown in **Figure 13**.

Name	Reactor	Function	Reaction formula
DECOMP	RYIELD	Converts nonconventional solids into conventional	Coal → char + volatiles
BURN	RGIBBS	Burns coal with air	Char + volatiles + O_2 → CO_2 + H_2O
CARBONAT	RSTOIC	Carbonation	CaO + CO_2 → $CaCO_3$
CALCINER	RSTOIC	Calcination	$CaCO_3$ → CaO + CO_2

Table 6. Process models used for calcium looping with postcombustion capture setup in Aspen Plus.

The heat of the combustion process (without CaL) is obtained by adding the heat from the decomposer, burner, and heat exchangers for ash and flue gas. The heat from the carbonator, and calciner is the heat of the CaL process. These values of heat and the corresponding CO_2

fraction in the final outlet flow are indicative of the performance of the CaL system with postcombustion capture.

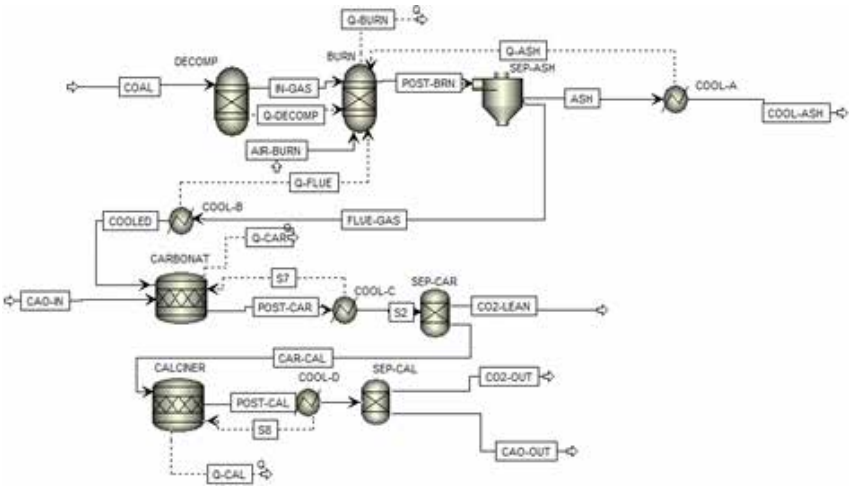

Figure 13. Aspen Plus flow sheet for calcium looping with postcombustion capture.

4.1.2. Results and discussion

The air stream is simulated as a mixture of 79% N_2 and 21% O_2. The other components of air such as Ar and CO_2 are present in such small fractions that they can be ignored with negligible effect on the results. The optimization module in Aspen Plus is employed to find the flow rates of the O_2 and N_2 flow rates such that the burner heat is maximized. The optimized flow rates of O_2 and N_2 are 4.2 kmol/s and 15.8 kmol/s, respectively for 50 kg/s of Illinois #6 coal. The sum of the flow rates of around 20 kmol/s indicates the total air flow in the burner.

The energy penalty of CaL is the sum of the net gain and loss from the carbonation and calcination processes. For each CaO conversion fraction, there is a corresponding CO_2 capture efficiency from the work of Sivalingam [38]. For a defined CaO conversion fraction in Aspen Plus, the experimental value of the CO_2 capture efficiency is matched by adjusting the CaO flow rate into the carbonator, which changes the heat duty of both the carbonator and calciner. Hence, each experimental data point corresponds to one heat duty value for the carbonator and calciner. Additional data points are obtained by considering the extrapolated data from **Figure 12** as well, providing to a range of CO_2 capture efficiencies for each CaO conversion fraction due to the varying CaO flow rates instead of just one value that matches the result of Sivalingam [38]. The heat duty of the carbonator and calciner are plotted in **Figure 14**. It is noted that the heat duty of the calciner from Aspen Plus is negative since the calcination reaction is endothermic. **Figure 14** plots the absolute value of the calciner heat absorption for direct comparison with the heat production in the carbonator. For each capture efficiency, the heat absorbed by the calciner is greater than the heat produced in the carbonator, which confirms that there is a net energy penalty associated with the calcium looping process.

http://dx.doi.org/10.5772/62811

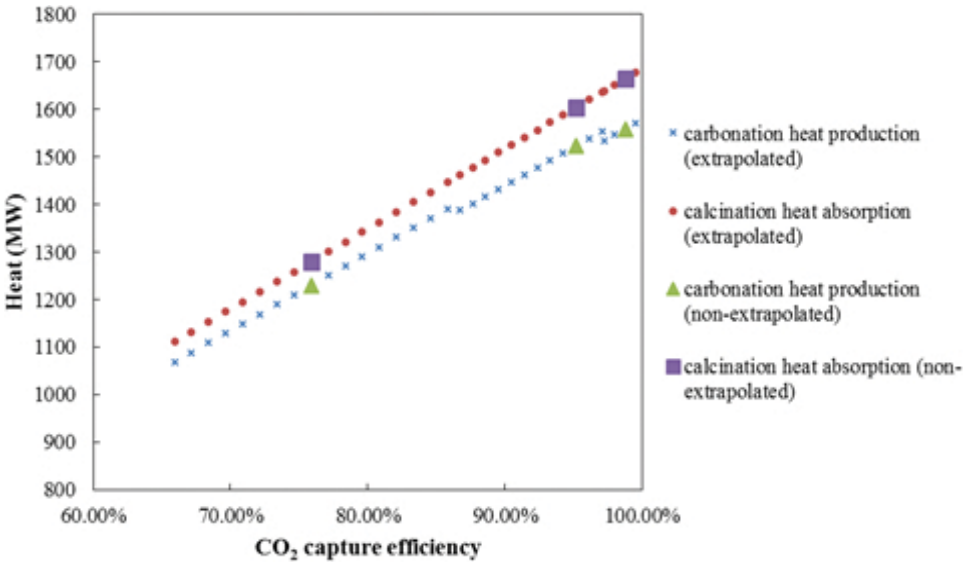

Figure 14. Heat duty of carbonator and calciner for original experimental data and extrapolated data.

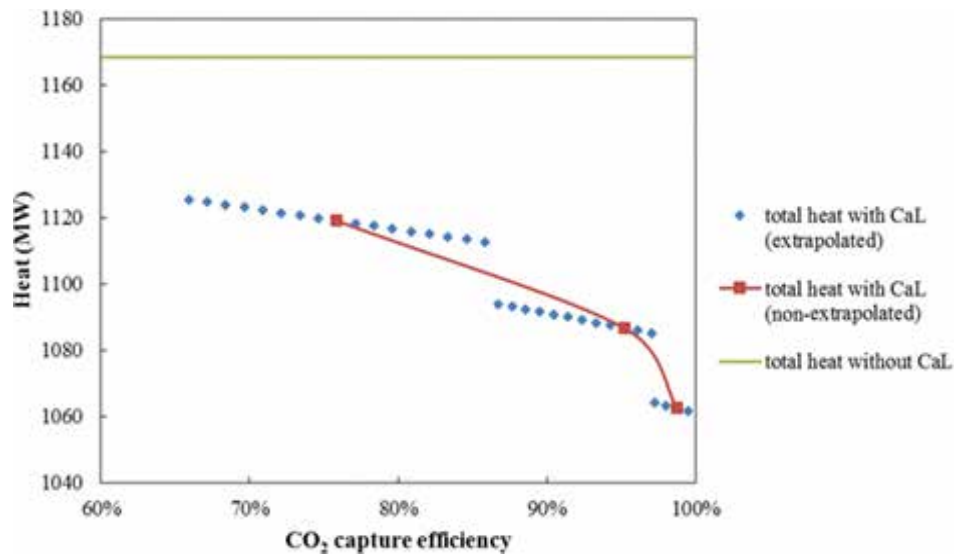

Figure 15. Plot of total energy output vs. CO_2 capture efficiency without CaL and with postcombustion CaL.

It can be observed from **Figure 14** that the calcination results fall on a straight line. This is expected since the calculation is based on a stoichiometric relation: the heat produced is proportional to the inflow rate of the reactant, $CaCO_3$. The CaO conversion fraction does not affect the heat absorbed by the calciner because the calciner has the same temperature for both

the inlet and outlet streams (150°C). Any excess CaO that passes through the carbonator and into the calciner has no effect on the heat duty of the calciner. For the carbonator, the extrapolated data around each of the three experimental data points are linear but the lines segments do not coincide. Each straight line segment corresponding to a range of extrapolated data has a reduced *y*-intercept compared with the previous section and has a more gradual slope compared with the calciner. From the modeling point of view, the only difference between these two reactors, beside the chemical reaction, is the inlet stream temperature. Since the CaO stream entering the carbonator is an external input, the inlet stream has a temperature of 25°C compared with 150°C for the calciner (internal input from the carbonator outlet stream). Thus, some heat is consumed in the carbonator for heating up the inlet stream to the temperature of the outlet. The heat production of the carbonator decreases as the CO_2 capture efficiency is increased since more heat is consumed to heat the higher CaO flow that is required for the increased capture.

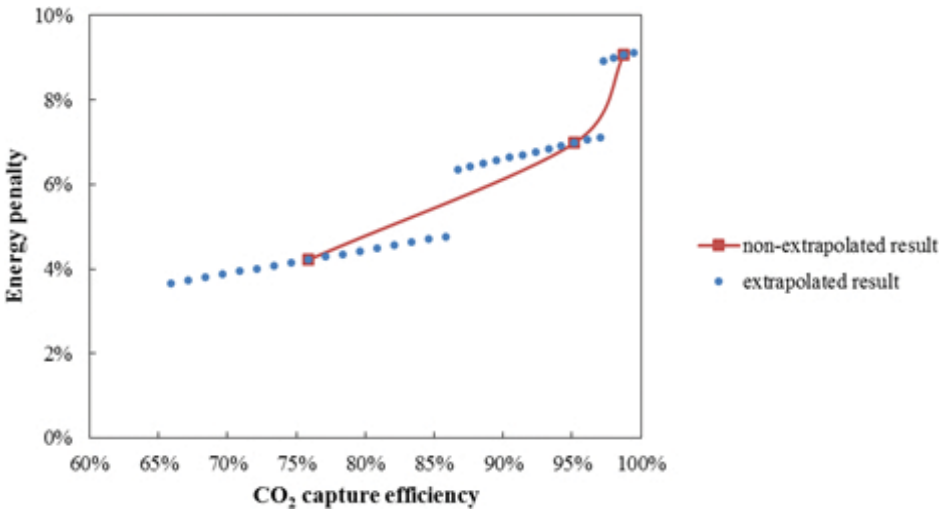

Figure 16. Plot of energy penalty vs. CO_2 capture efficiency for CaL with postcombustion capture.

For a coal feed of 50 kg/s, the heat of combustion is calculated to be 1168 MW without calcium looping. When the net heat from the carbonator and calciner is added, the total heat of the power plant with calcium looping ranges from 1060 to 1130 MW, as shown in **Figure 15**.

The energy penalty for CaL refers to the fraction of energy produced by a power station that must be dedicated to the carbonation and calcination process in order to capture CO_2. The energy penalty can be defined as

$$\text{Energy penalty} = \frac{|Q_{\text{looping}}|}{Q_{\text{total}} - |Q_{\text{looping}}|} \tag{27}$$

where Q_{total} is the total heat produced by the power plant and $Q_{looping}$ is the heat for the CaL process. The energy penalty for CaL with postcombustion capture calculated using Eq. (27) is shown in **Figure 16**. From the figure, the energy penalty ranges from 3.5% to 9.0% over the corresponding range of CO_2 capture efficiencies from 65% to 99%. These results are in line with the work of Cormos and Petrescu [41] that found energy penalties ranging from 5to 10% for capture efficiencies between 92% and 93% for various power plants. More recently, a study by BP Alternative Energy [42] showed that the marginal energy penalty associated with increasing carbon capture efficiency past 98% increases drastically, which further validates the results of the current work. It is noted that only the heat output of the combustion process and the calcium looping setup is assessed in the results presented above; the steam cycle has not been considered. The energy penalty calculated in this work should be considered as a lower bound for any investigation on calcium looping.

5. Summary and conclusion

This chapter presents numerical simulations of the chemical looping combustion and calcium looping processes used for carbon capture from fossil fuel power plants. A three-dimensional CFD simulation for a complete circulating dual fluidized bed system is developed for chemical looping combustion based on the 300 W laboratory-scale experiments of Abad et al. [17]. The oxygen carrier is modeled as an Eulerian fluid phase based on the kinetic theory of granular flow. The results of this study highlight the importance of capturing the diffusion of gases in a CLC reactor in ensuring that accurate results are obtained for the chemical reactions; the results of the three-dimensional simulation are a better match for the outlet concentrations of the gases recorded in the experiment than a two-dimensional simulation previously conducted. It is expected that the simulation accuracy can be increased further if empirical reaction rate data becomes available for the specific oxygen carrier and fuel used in the experiment.

The detailed particle hydrodynamics in a complete circulating CLC system for solid fuels is investigated using the Lagrangian particle-tracking approach known as DEM based on the CD-CLC reactor at NETL [18]. The development of particle flow is investigated as well as the pressure contours in the reactor. Although the simulation time was not sufficient to see the complete particle recirculation in the system, the static pressure contours and gradients showed evidence of favorable conditions for particle recirculation. The cold flow simulation in this work provides a foundation for more detailed simulations of CD-CLC systems in future work where the coal particles and the associated chemical reactions can be taken into account.

The energy penalty associated with the calcium looping process for postcombustion capture of CO_2 is investigated using Aspen Plus; the results indicate that the energy penalty depends on the flow rate of CaO into the carbonator. An important finding from this work is that for CO_2 capture efficiencies above 90%, the marginal energy penalty associated with any further increase in efficiency increases drastically. This suggests that there is a limit on the maximum CO_2 efficiency possible from calcium looping beyond which the process becomes impractical due to the energy consumption.

Author details

Subhodeep Banerjee and Ramesh K. Agarwal*

*Address all correspondence to: rka@wustl.edu

Department of Mechanical Engineering and Materials Science, Washington University in St. Louis, St. Louis, MO, USA

References

[1] S. Arrhenius, "On the influence of carbonic acid in the air upon the temperature of the ground," *Philos. Mag.,* vol. 41, pp. 237–277, 1896.

[2] IPCC, "Climate Change 2007: Synthesis Report. Contribution of Working Groups I, II and III to the Fourth Assessment Report of the Intergovernmental Panel on Climate Change [Core Writing Team, Pachauri, R.K., and Reisinger, A. (eds.)]," Geneva, Switzerland, 2007.

[3] H. Kruggel-Emden, F. Stepanek and A. Munjiza, "A study on the role of reaction modeling in multi-phase CFD-based simulations of chemical looping combustion," *Oil Gas Sci. Tech.,* vol. 66, no. 2, pp. 313–331, 2011.

[4] M. Ishida, D. Zheng and T. Akehata, "Evaluation of a chemical-looping-combustion power-generation system by graphic exergy analysis," *Energy,* vol. 12, no. 2, pp. 147–154, 1987.

[5] M. Ishida, H. Jin and T. Okamoto, "A fundamental study of a new kind of medium material for chemical-looping combustion," *Energy Fuels,* vol. 10, no. 4, pp. 958–963, 1996.

[6] J. Wolf, M. Anheden and J. Yan, "Performance analysis of combined cycles with chemical looping combustion for CO_2 capture," in *Proceedings of the 18th International Pittsburgh Coal Conference*, Pittsburgh, PA, 2001.

[7] J.L. Marion, "Technology options for controlling CO_2 emissions from fossil fueled power plants," in *Proceedings of the 5th Annual Conference on Carbon Capture and Sequestration*, Alexandria, VA, 2006.

[8] H.E. Andrus, G. Burns, J.H. Chiu, G.N. Liljedahl, P.T. Stromberg and P.R. Thibeault, "Hybrid Combustion-Gasification Chemical Looping Coal Power Technology Development, Phase III – Final Report," Windsor, CT, Report No. PPL-08-CT-25, 2008.

[9] U.S. Department of Energy (DOE), National Energy Technology Laboratory (NETL), "Guidance for NETL's Oxy-combustion R&D Program: Chemical Looping Combustion

Reference Plant Designs and Sensitivity Studies," Pittsburgh, PA, Report No. DOE/NETL-2010/1643, 2010.

[10] T. Shimizu, T. Hirama, H. Hosoda, K. Kitano, M. Inagaki and K. Tejima, "A twin fluid-bed reactor for removal of CO_2 from combustion processes," *Trans IChemE*, vol. 77, no. 1, pp. 62–68, 1999.

[11] S.Y. Lin, Y. Suzuki, H. Hatano and M. Harada, "Developing an innovative method, HyPr-RING, to produce hydrogen from hydrocarbons," *Energy Convers. Manage.*, vol. 43, no. 9–12, pp. 1283–1290, 2002.

[12] A. Bandi, M. Specht, P. Sichler and N. Nicoloso, "In situ gas conditioning in fuel reforming for hydrogen generation," in *Proceedings of the 5th International Symposium on Gas Cleaning at High Temperature*, Morgantown, WV, 2002.

[13] N. Nsakala, G. Liljedahl, J. Marion, C. Bozzuto, H. Andrus and R. Chamberland, "Greenhouse gas emissions control by oxygen firing in circulating fluidized bed boilers," in *Proceedings of the 2nd Annual National Conference on Carbon Sequestration*, Alexandria, VA, 2003.

[14] K. Mahalatkar, J. Kuhlman, E. D. Huckaby and T. O'Brien, "Computational fluid dynamic simulations of chemical looping fuel reactors utilizing gaseous fuels," *Chem. Eng. Sci.*, vol. 66, no. 3, pp. 469–479, 2011.

[15] K. Mahalatkar, J. Kuhlman, E.D. Huckaby and T. O'Brien, "CFD simulation of a chemical-looping fuel reactor utilizing solid fuel," *Chem. Eng. Sci.*, vol. 66, no. 16, pp. 3617–3627, 2011.

[16] U.S. Department of Energy (DOE), U.S. Energy Information Administration (EIA), "International Energy Outlook 2010," Washington, DC, Report No. DOE/EIA-0484(2010), 2010.

[17] A. Abad, T. Mattisson, A. Lyngfelt and M. Johansson, "The use of iron oxide as oxygen carrier in a chemical-looping reactor," *Fuel*, vol. 86, no. 7–8, pp. 1021–1035, 2007.

[18] J. Parker, "CFD model for the simulation of chemical looping combustion," *Powder Technol.*, vol. 265, pp. 47–53, 2014.

[19] Y.O. Chong, D.J. Nicklin and P.J. Tait, "Solid exchange between adjacent fluid beds without gas mixing," *Powder Technol.*, vol. 47, pp. 151–156, 1986.

[20] M. Fang, C. Yu, Z. Shi, Q. Wang, Z. Luo and K. Cen, "Experimental research on solid circulation in a twin fluidized bed system," *Chem. Eng. J.*, vol. 94, pp. 171–178, 2003.

[21] ANSYS, "ANSYS Fluent User's Guide," ANSYS, Inc., Canonsburg, PA, 2012.

[22] ANSYS, "ANSYS Fluent Theory Guide," ANSYS, Inc., Canonsburg, PA, 2012.

[23] D.J. Patil, M.V. Annaland and J.A.M. Kuipers, "Critical comparison of hydro-dynamic models for gas–solid fluidized beds. Part I: Bubbling gas–solid fluidized beds operated with a jet," *Chem. Eng. Sci.,* vol. 60, no. 1, pp. 57–72, 2004.

[24] D.J. Patil, M.V. Annaland and J.A.M. Kuipers, "Critical comparison of hydro-dynamic models for gas–solid fluidized beds. Part II: Freely bubbling gas–solid fluidized beds," *Chem. Eng. Sci.,* vol. 60, no. 1, pp. 73–84, 2004.

[25] C.K.K. Lun, S.B. Savage, D.J. Jeffrey and N. Chepurniy, "Kinetic theories for granular flow: inelastic particles in Couette flow and slightly inelastic particles in general flow field," *J. Fluid Mech.,* vol. 140, pp. 223–256, 1984.

[26] D. Gidaspow, Multiphase Flow and Fluidization, San Diego, CA: Academic Press, 1992.

[27] S. Ergun, "Fluid flow through packed columns," *Chem. Eng. Prog.,* vol. 48, pp. 89–94, 1952.

[28] C.Y. Wen and H.Y. Yu, "Mechanics of fluidization," *Chem. Eng. Prog. Symp. Ser.,* vol. 62, pp. 100–111, 1966.

[29] D. Gunn, "Transfer of heat or mass to particles in fixed and fluidized beds," *Int. J. Heat Mass Transfer,* vol. 21, pp. 467–476, 1978.

[30] T. Mattisson, J.C. Abanades, A. Lyngfelt, A. Abad, M. Johansson, J. Adanez, F. Garcia-Labiano, L.F. de Diego, P. Gayan, B. Kronberger, H. Hofbauer, M. Luisser, J.M. Palacios, D. Alvares, G. Grasa, J. Oakey, B. Arias, M. Orjala and V.-P. Heiskanen, "Capture of CO_2 in Coal Combustion. ECSC Coal RTD Programme Final Report," Göteborg, Sweden, Report No. ECSC-7220-PR125, 2005.

[31] S. Banerjee and R. K. Agarwal, "An Eulerian approach to computational fluid dynamics simulation of a chemical-looping combustion reactor with chemical reactions," *J. Energy Resour. Technol.,* vol. 138, no. 4, pp. 04421, 2016.

[32] G.I. Taylor, "The dispersion of matter in turbulent flow through pipes," *Proc. R. Soc. London. Ser. A, Math. Phys. Sci.,* pp. 446–448, 1954.

[33] M. Johansson, "Screening of oxygen-carrier particles based on iron-, manganese-, copper- and nickel oxides for use in chemical-looping technologies," Ph.D. dissertation, Chalmers University of Technology, Göteborg, Sweden, 2007.

[34] O. Gryczka, S. Heinrich, N.G. Deen, A.M. van Sint, J.A.M. Kuipers, M. Jacob and L. Mörl, "Characterization and CFD modeling of the hydrodynamics of a prismatic spouted bed apparatus," *Chem. Eng. Sci.,* vol. 64, p. 3352–3375, 2009.

[35] J.M. Link, "Development and validation of a discrete particle model of a spout-fluid bed granulator," Ph.D. dissertation, University of Twente, Enschede, The Netherlands, 1975.

http://dx.doi.org/10.5772/62811

[36] N.A. Patankar and D.D. Joseph, "Modeling and numerical simulation of particulate flows by the Eulerian–Lagrangian approach," *Int. J. Multiphase Flow*, vol. 27, no. 10, pp. 1659–1684, 2001.

[37] S.E. Elgobashi, "On predicting particle-laden turbulent flows," *Appl. Sci. Res.*, vol. 52, p. 309–329, 1994.

[38] S. Sivalingam, "CO_2 separation by calcium looping from full and partial oxidation processes," Ph.D. Dissertation, Technische Universität München, Munich, Germany, 2013.

[39] P.H.M. Feron, "Post-combustion capture (PCC) R&D and pilot plant operation in Australia," in *IEA GHG 11th Post Combustion CO2 Capture Meeting*, Vienna, Austria, 2008.

[40] J.C. Abanades, E.J. Anthony, J. Wang and J. E. Oakey, "Fluidized bed combustion systems integrating CO_2 capture with CaO," *Environ. Sci. Technol.*, vol. 39, no. 8, pp. 2861–2866, 2005.

[41] C.C. Cormos and L. Petrescu, "Evaluation of calcium looping as carbon capture option for combustion and gasification power plants," *Energy Procedia*, vol. 51, pp. 154–160, 2014.

[42] M. Crombie, "The results from the CO_2 capture project – carbon dioxide capture for storage in deep geological formations, Volume 4," in *Proc. 14th Annual Carbon Capture, Utilization & Storage Conference*, Pittsburgh, PA, 2015.

Chapter 12

Combustion Catalyst: Nano-Fe_2O_3 and Nano-Thermite Al/Fe_2O_3 with Different Shapes

Ningning Zhao, Jiachen Li, Fengqi Zhao, Ting An,
Rongzu Hu and Haixia Ma

Additional information is available at the end of the chapter

http://dx.doi.org/10.5772/64748

Abstract

In order to enable the energetic materials to possess a more powerful performance, adding combustion catalysts is a quite effective method. Granular, oval, and polyhedral Fe_2O_3 particles have been prepared by the hydrothermal method and used to fabricate Al/Fe_2O_3 thermites. All the Fe_2O_3 and Al/Fe_2O_3 thermite samples were characterized using a combination of experimental techniques including scanning electron microscopy (SEM), energy dispersive spectrometer (EDS), X-ray diffraction (XRD), Fourier transform infrared spectroscopy (FTIR), transmission electron microscope (TEM), and high-resolution TEM (HRTEM). The non-isothermal decomposition kinetics of the composites and nitrocellulose (NC) can be modeled by the Avrami-Erofeev equation $f(\alpha)=3(1-\alpha)[-\ln(1-\alpha)]^{1/3}/2$ in differential form. Through the thermogravimetric analysis infrared (TG-IR) analysis of decomposition processes and products, it is speculated that Fe_2O_3 and Al/Fe_2O_3 can effectively accelerate the thermal decomposition reaction rate of NC by promoting the O-NO_2 bond cleavage. Adding oxides or thermites can distinctly increase the burning rate, decrease the burning rate pressure exponent, increase the flame temperature, and improve the combustion wave structures of the ammonium perchlorate/hydroxyl-terminated polybutadiene (AP/HTPB) propellants. Among the three studied, different shapes of Fe_2O_3, the granular Fe_2O_3, and its corresponding thermites (Al/Fe_2O_3(H)) exhibit the highest burning rate due to larger surface area associated with smaller particle size. Moreover, Al/Fe_2O_3(H) thermites have more effective combustion-supporting ability for AP/HTPB propellants than Fe_2O_3 structures and the other two as-prepared Al/Fe_2O_3 thermites.

Keywords: combustion catalyst, thermal decomposition mechanism, combustion wave structure

INTECH
open science | open minds

© 2016 The Author(s). Licensee InTech. This chapter is distributed under the terms of the Creative Commons Attribution License (http://creativecommons.org/licenses/by/3.0), which permits unrestricted use, distribution, and reproduction in any medium, provided the original work is properly cited. CC BY

1. Introduction

Energetic materials (explosives, propellants, and pyrotechnics) are necessary material bases of high-performance weapons and ammunition, which are used extensively for both civil, military, and space applications. In order to enable the energetic materials to possess a more powerful performance, such as the high quantity of heat release, the high combustion temperature, the fast burning rate, and so on, adding combustion catalysts is a quite effective method.

In recent years, researchers pay much attention to the preparation and application of the combustion catalysis of nanoscale. Many studies reported that catalysts in nanoscale exhibit the absolute advantages both in accelerating the thermal decomposition process of the main energetic materials such as cyclotrimethylene trinitramine (RDX), nitrocellulose (NC), cyclotetramethylene tetranitramine (HMX), 2,4,6,8,10,12-hexanitro-2,4,6,8,10,12-hexanitro hexaazaisowurtzitane (CL-20), and 3-nitro-1,2,4-triazol-5-one (NTO), and in enhancing the ignition and combustion performances of the solid. For instance, the nano-sized Cr_2O_3 particles decrease the ignition delay time by a factor 3.5 (16 ± 2 vs 54 ± 4 ms) and accelerate the combustion rate (340 ± 10 mm s^{-1}) of the Al/Cr_2O_3 thermite, which is fabricated by Cr_2O_3 micro- or NPs (Φ ≈20 nm) and Al NPs (Φ ≈50 nm) [1]. Pantoya [2] reported that nanocomposite thermites (Al/MoO_3) can significantly reduce the ignition delay time compared with micron-composite thermites. Nitrocellulose nanofiber-based thermite textiles were studied and compared with the pure nitrocellulose and nano-aluminum incorporated nanofiber; the result indicates that the burning rates were enhanced by adding the Al/CuO thermite [3].

The abovementioned nanothermite contains two parts: metal fuel (Al, used due to its low cost, high density, and the efficient catalytic property [4]) and metal oxides (Fe_2O_3, CuO, MnO_2, MoO_3, PbO [5], Bi_2O_3, etc.). The nanothermite system, as the metastable intermolecular composites (MICs) [6], can enhance the reactivity [7–9] through the oxidation-reduction reactions, which lead to high burning rate [10], high heat production [11], and negligible gas generation. The traditional thermite, Al/Fe_2O_3, is prepared in various nanoparticle size, shape, and composition [12] in order to be better applied in free-standing heat sources, airbag ignition materials, hardware destruction devices, welding torches [13], and energetic material field. Both Al and Fe_2O_3 particles have been used as catalysts not only in the thermal decomposition process of the main energetic components but also in composite solid propellants [14–17]. However, the effects of Al/Fe_2O_3 nanoparticles on the thermal behavior and non-isothermal decomposition kinetics of NC are barely investigated. And, to the best of our knowledge, there has been no report about the dependence of catalytic properties of Al/Fe_2O_3 thermites on the morphology of Fe_2O_3 particles in combustion reactions to date.

Nitrocellulose (NC) is extensively applied as a main component in gun, blasting gelatin, dynamites, and rocket propellants [18–21] owing to its high flammability and explosiveness. In order to obtain more information about NC, the thermal decomposition mechanism of NC has been investigated. It is shown that the fission of oxygen-nitrogen bond is the first and rate-determining step during the decomposition process [22–25]. Quantities of

http://dx.doi.org/10.5772/64748

NO_2 gases, derived from the O-NO_2 bond cleavage, could stagnate in the polymer skeleton and lead to promote the secondary autocatalytic reactions (i.e., the heterogeneous reactions in condensed phase) [26]. Furthermore, Mahajan et al. [27] reported that copper oxide influences the combustion/thermal decomposition of NC in a way so as to retard the breaking of O-NO_2 bonds in solid phase. With the excellent characteristics of nanomaterials, we study the influence of Fe_2O_3 particles and Al/Fe_2O_3 thermites on thermal behavior and non-isothermal decomposition kinetics of NC in order to provide basic data for establishing the combustion model and studying the combustion process.

In this contribution, granular, oval, and polyhedral Fe_2O_3 particles have been prepared by the hydrothermal method and used to fabricate Al/Fe_2O_3 thermites by integrating Al nanopowders with Fe_2O_3 at a stoichiometric ratio of Fe_2O_3:Al (71.1wt%:28.9wt%). All the Fe_2O_3 and Al/Fe_2O_3 thermite samples were characterized using a combination of experimental techniques including scanning electron microscopy (SEM), energy dispersive spectrometer (EDS), X-ray diffraction (XRD), Fourier transform infrared spectroscopy (FTIR), transmission electron microscope (TEM) and high-resolution TEM. The effects of Fe_2O_3 nanoparticles and Al/Fe_2O_3 on the thermal decomposition of NC have been investigated by the differential scanning calorimetry (DSC) method and the thermogravimetry with Fourier transform infrared analysis (TG-IR). The influences of Fe_2O_3 and the corresponding thermite on the combustion properties of the ammonium perchlorate/hydroxyl-terminated polybutadiene (AP/HTPB) composite propellant were investigated and compared. Moreover, the combustion wave structures and the flame temperatures of AP/HTPB composite propellants containing thermites Al/Fe_2O_3 are obtained at 4 MPa.

2. Experimental section

2.1. Synthesis of Fe_2O_3 particles and Al/Fe_2O_3 thermites

The granular, oval, and polyhedral Fe_2O_3 particles were prepared following the procedures developed from our reports [28, 29], and denoted as Fe_2O_3(H), Fe_2O_3(o), and Fe_2O_3(p), respectively. Three corresponding thermites Al/Fe_2O_3(H), Al/Fe_2O_3(o), and Al/Fe_2O_3(p) were prepared [29] with a stoichiometric ratio of Fe_2O_3:Al (71.1wt%:28.9wt%) based on the calculation [30].

2.2. Preparation of Fe_2O_3-NC and Al/Fe_2O_3-NC

The Fe_2O_3 particles or Al/Fe_2O_3 thermite was evenly mixed with NC via grinding to obtain the composite materials, respectively. For the Fe_2O_3-NC composites, the Fe_2O_3:NC mass ratio was 1:1, while for the Al/Fe_2O_3-NC composites it was 1:1, too. The grinding process was maintained for 30 min to obtain light red or dark gray composite materials. The products were used for differential scanning calorimetry experiment, in order to assess the thermal behavior and the effects of Fe_2O_3 particles or Al/Fe_2O_3 on NC.

2.3. Preparation of AP/HTPB propellant formulations

The as-prepared Fe_2O_3(H), Fe_2O_3(o), Fe_2O_3(p), and their corresponding thermites are used as the burning rate modifiers in the preliminary AP/HTPB propellant formulation [29] as shown in **Table 1**.

No.	HTPB system/%	Al/%	Coarse AP/%	Superfine AP/%	Additives	Additives/%
N0	14.3	15.3	18.4	52.0	none	0.0
F1	14.3	15.3	18.4	52.0	Fe_2O_3(H)	2.0
F2	14.3	15.3	18.4	52.0	Fe_2O_3(o)	2.0
F3	14.3	15.3	18.4	52.0	Fe_2O_3(p)	2.0
S1	14.3	14.5	18.4	52.0	Al/Fe_2O_3(H)	2.8
S2	14.3	14.5	18.4	52.0	Al/Fe_2O_3(o)	2.8
S3	14.3	14.5	18.4	52.0	Al/Fe_2O_3(p)	2.8

Table 1. The composition and content of composite propellant.

2.4. Samples characterization

The physical phase, composition, morphology, and structure of materials were characterized by SEM-EDS, TEM, XRD, and FT-IR. X-ray diffractograms were recorded on a D/MAX-3C (Japan) instrument using Cu Kα_1 radiation (λ = 0.15406 nm) at 40-kV voltage and a 40-mA current ranging from 10° to 80°. SEM observations were carried out on a Quanta 400 FE-SEM (FEI Co., USA) at an acceleration voltage of 30 kV. EDS was measured using an INCAIE350 testing device from OXFORD Instruments INC (UK) with a discharge voltage of 4–10 kV and a distance of exactly 1 mm between the electrodes. The morphology and size of as-obtained products were investigated with a transmission electron microscope and high-resolution TEM on a Libra 200FE (Carl Zeiss SMT Pte Ltd., Germany). The sample structure and composition were characterized using Bruker Tensor 27 infrared spectrometer.

The specific surface area was determined with Brunauer-Emmett-Teller (BET) Procedure (Autosorb-1C-TCD, American Quantachrome Instruments).

The thermal behavior of the samples was investigated using DSC (Q2000, TA Co.) at a heating rate of 10°C min^{-1} from room temperature to 300°C in an N_2 atmosphere at a flow rate of 50 mL min^{-1} under ambient atmospheric pressure. To explore the reaction mechanism of the intense exothermic decomposition processes of NC and Fe_2O_3-NC and to obtain the corresponding kinetic parameters (apparent activation energy (E_a/kJ mol^{-1}), pre-exponential constant (A/s^{-1})) and the most probable kinetic model function, the DSC curves at the heating rates of 5.0, 10.0, 15.0, 20.0, 25.0, and 30.0°C min^{-1} were dealt by mathematic means.

The thermal decomposition studies of NC and Fe_2O_3-NC were also performed by the thermogravimetry (Netzsch STA409) with Fourier transform infrared (Brucker V70) analysis technique under nitrogen environment at the heating rate of 10°C min^{-1}.

The thermal behavior of the prepared thermites was carried out on a TA Instrument (Q600) device with a 10°C min^{-1} heating rate, using N_2 with a flow rate of 100 mL min^{-1}.

Burning parameters of AP/HTPB propellant including the rate and the pressure exponent were obtained by acoustic emission method by the AE/BX-2006 multifunction system [29].

3. Structure characterization

3.1. Morphological characterization

The microstructure characterizations of the Fe_2O_3 particles and Al/Fe_2O_3 thermites are determined by analytical SEM as well as TEM.

Figure 1 shows the SEM images of the granular, oval, and polyhedral Fe_2O_3 particles and the corresponding Al/Fe_2O_3 thermite. From **Figure 1(a)**, it can be found that Fe_2O_3(H) particles are granular in shape with a relatively small size (average 200 nm) and seem somewhat aggregated. Fe_2O_3(o) particles (**Figure 1(c)**) have an oval shape and a rough surface morphology due to the adhesion of scrap irons. The shape of Fe_2O_3(p) (**Figure 1(e)**) particles is polyhedral, which is quite different from the other two samples. A closer examination of the SEM images indicates that Fe_2O_3(p) particles are not very uniform in size, agglomerated, and have larger surface-area-to-volume (S/V) ratio than that of Fe_2O_3(o) particles. **Figure 1(b)**, **(d)**, and **(f)** show the SEM images of Al/Fe_2O_3(H), Al/Fe_2O_3(o), and Al/Fe_2O_3(p), respectively. Some degree of aggregation can be found in the three thermite systems. Also, there seems to be favorable interfacial between Al and Fe_2O_3 particles.

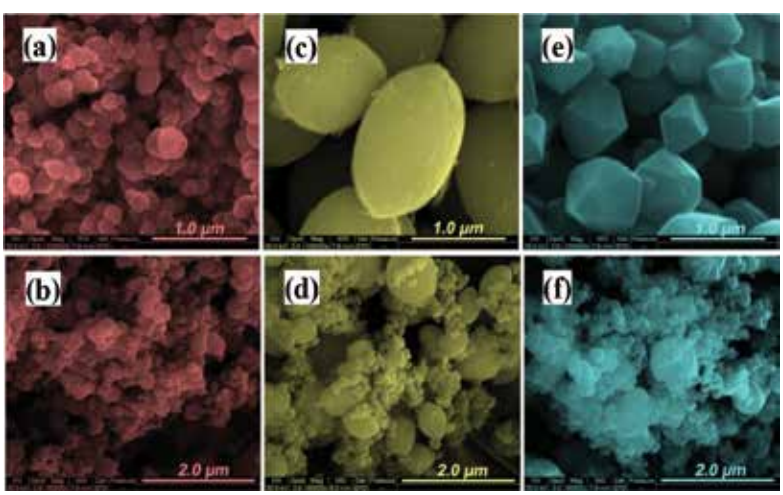

Figure 1. SEM images of Fe_2O_3 (×100,000 magnification) and thermites Al/Fe_2O_3 (×60,000 magnification). (a) Fe_2O_3(H), (b) Al/Fe_2O_3(H), (c) Fe_2O_3(o), (d) Al/Fe_2O_3(o), (e) Fe_2O_3(p), and (f) Al/Fe_2O_3(p).

Investigations of the low-magnification TEM image (**Figure 2(b)**) of Fe_2O_3(H) nanoparticles indicate that most of the particles have an irregular sphere geometrical structure, and usually possess rough surfaces. Typical HRTEM images of the small part of Fe_2O_3(H) nanoparticles were obtained and are shown in **Figure 2(b)**, **(c)**, and **(d)**. Just one set of clear lattice fringes with the interplanar distance of 0.25 nm could be seen in **Figure 2(b)**, **(d)**, inset (i), and (v), which can be indexed to the (110) plane of rhombohedral Fe_2O_3(H) structure. Excellent crystallinity is also confirmed by corresponding fast Fourier-transform (FFT) transformation (inset in **Figure 2**(iii)).

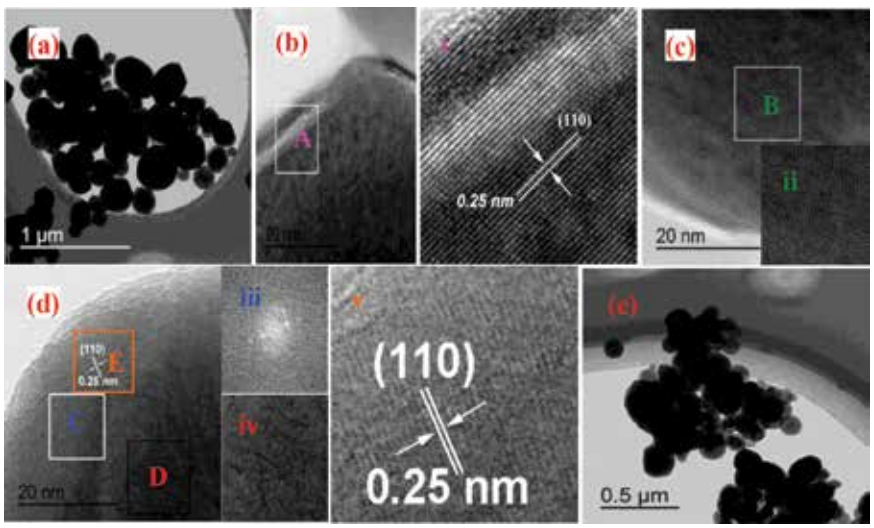

Figure 2. (a) and (e) show TEM images of Fe_2O_3(H) and Al/Fe_2O_3(H), respectively; (b, c, d) HRTEM images of Fe_2O_3(H) nanoparticles. Insets i and v are the high-resolution images of Fe_2O_3(H) nanoparticles, insets ii and iv show a high-resolution image of Fe_2O_3(H) nanoparticles containing stacking faults and dislocation tangles/networks on the surface, respectively, and inset iii shows the corresponding fast Fourier-transform (FFT) pattern of Fe_2O_3(H) nanoparticles.

Particles containing a certain extent of lattice defects such as dislocation and stacking fault caused by the high pressure, temperature, and concentration through the hydrothermal treatment have also been found. **Figure 2(c)** gives an example of a series of diagonal and straight-stacking faults within a particle throughout most of the surface. It can be seen more clearly in an enlargement of a local region (inset ii). **Figure 2(d)**, the area "D" marked black pane and the corresponding inset (iv), shows a high-resolution image of the Fe_2O_3(H) nanoparticles containing dislocation tangles/networks on the surface. These linear and plane defects mentioned above have profound effects on the growth and property of the Fe_2O_3(H) nanoparticles [31, 32].

Figure 3 shows the oval Fe_2O_3(o) particles with the length-to-diameter ratio (L/D ratio) of 1.47–1.59. From **Figure 4(b)**, it is really easy to find out the rough surface of Fe_2O_3(o) particle, which is consistent with the SEM measurement. In the TEM image of Al/Fe_2O_3(o) thermites, the small spherical Al nanoparticles stick together, and also with the Fe_2O_3(o) particles.

http://dx.doi.org/10.5772/64748

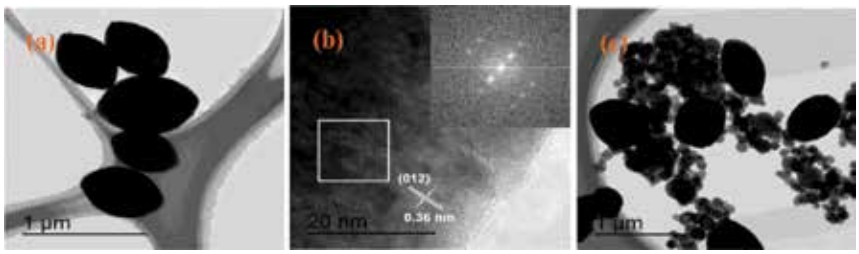

Figure 3. (a) and (c) show TEM images of Fe_2O_3(o) and Al/Fe_2O_3(o), respectively; (b) HRTEM image of Fe_2O_3(o) and the corresponding fast FFT pattern (inset).

Figure 4(a) and **(c)** show the TEM images of the Fe_2O_3(p) and Al/Fe_2O_3(p), respectively. It is obvious to see that almost all of the Fe_2O_3(p) particles are polyhedral in shape, which adhere to the Al particles as seen in **Figure 4(c)**. The corresponding selected area electron diffraction (SAED) pattern shown in **Figure 4(b)** indicates that the Fe_2O_3(p) particles are single crystals. **Figure 4(d)** shows the fringes with the interplanar distance of 0.25 nm in a typical HRTEM image of a Fe_2O_3(p) particle, which agree well with the (110) lattice spacing of the rhombohedral hematite.

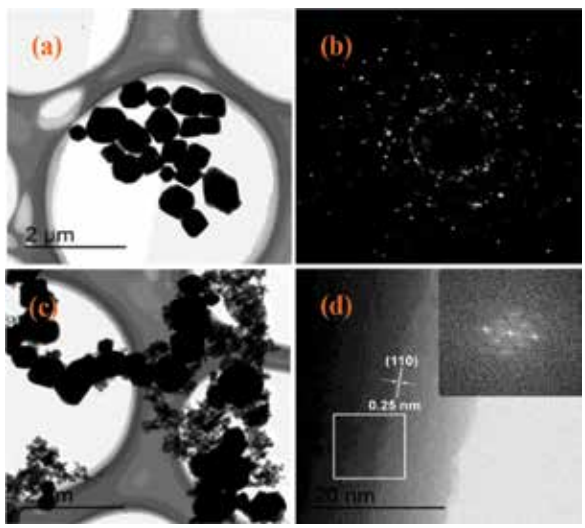

Figure 4. (a) and (c) show TEM images of Fe_2O_3(p) and Al/Fe_2O_3(p), respectively, (b) Selected area electron diffraction (SAED) pattern of Fe_2O_3(p) and (d) HRTEM image of Fe_2O_3(p) and the corresponding fast FFT pattern (inset).

Figures 5–7 show the SEM images of Fe_2O_3(H), Fe_2O_3(p), Fe_2O_3(o), and the corresponding Al/Fe_2O_3, respectively. Take **Figure 5**, for instance. The SEM observation of Fe_2O_3(H)-NC and Al/Fe_2O_3(H)-NC in **Figure 5** shows that the two composites have rough, irregular surface morphology under low magnification, probably due to the agglomeration of Fe_2O_3(H) nanoparticles or Al/Fe_2O_3(H). From **Figure 5(a)** and **(c)**, it can be found that the vast majority

of Fe_2O_3(H) particles or Al/Fe_2O_3(H) adhered on the surfaces of NC short fibers. Also, some small Fe_2O_3(H) (or Al/Fe_2O_3(H)) agglomeration and NC fragments can be observed. The enlargement of a local region on the surface of Fe_2O_3-NC and Al/Fe_2O_3(H)-NC in **Figure 2(b)** and **(d)** indicates that the mechanical-grinding treatment has not changed the basic shape and particle size of Fe_2O_3 and Al.

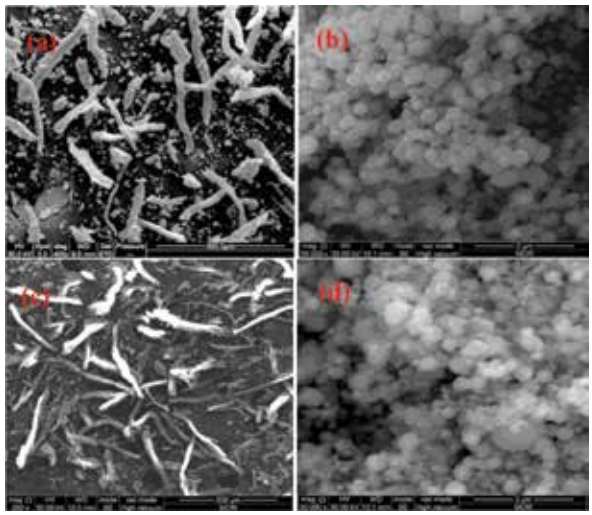

Figure 5. SEM images of Fe_2O_3(H)-NC and Al/Fe_2O_3(H)-NC. (a) Fe_2O_3(H)-NC (×400 magnification), (b) Fe_2O_3(H)-NC (×50,000 magnification), (c) Al/Fe_2O_3(H)-NC (×200 magnification), and (d) Al/Fe_2O_3(H)-NC (×50,000 magnification).

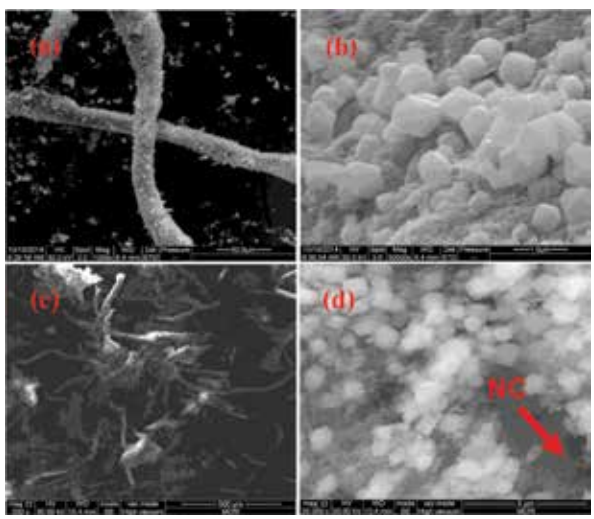

Figure 6. SEM images of Fe_2O_3(p)-NC and Al/Fe_2O_3(p)-NC. (a) Fe_2O_3(p)-NC (×1000 magnification), (b) Fe_2O_3(p)-NC (×50,000 magnification), (c) Al/Fe_2O_3(p)-NC (×200 magnification), and (d) Al/Fe_2O_3(p)-NC (×25,000 magnification).

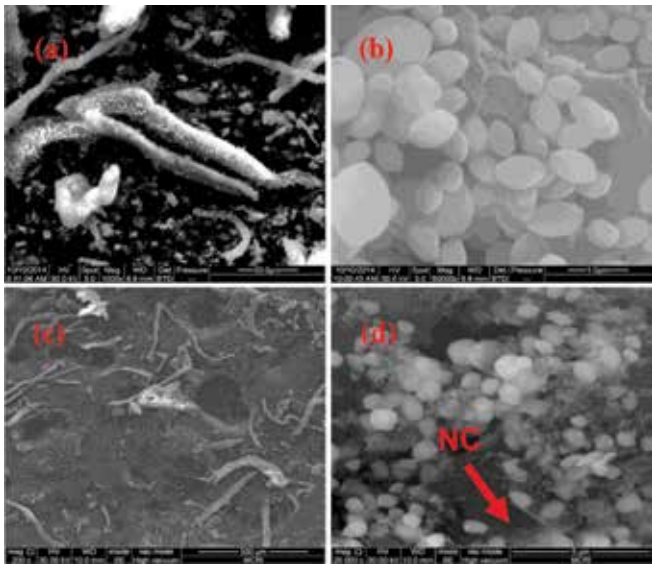

Figure 7. SEM images of Fe_2O_3(o)-NC and Al/Fe_2O_3(o)-NC. (a) Fe_2O_3(o)-NC (×1000 magnification), (b) Fe_2O_3(o)-NC (×50,000 magnification), (c) Al/Fe_2O_3(o)-NC (×200 magnification), and (d) Al/Fe_2O_3(o)-NC (×25,000 magnification).

3.2. Structure and composition

Structure and composition of Fe_2O_3 and thermite were characterized using EDS, XRD, and FTIR techniques. The results [29] show that the three prepared iron oxides are Fe_2O_3 with a stoichiometric ratio of O:Fe (3:2), because their typical XRD patterns coincided with JCPDS: 33-0664, and the hematite lattice vibration is identified at 480 and 571 cm^{-1} [33]. The EDS data show that the thermite samples contain Al element. XRD patterns of thermites reveal no reaction between Al (JCPDS: 65-2869) and Fe_2O_3. It can be found that the presence of water peaks in FTIR spectra of thermites, which is a common phenomenon in the nanomaterials [34–38] especially with the presence of Al particles.

4. Thermal analysis

To explore the reaction mechanism of the intense exothermic decomposition process of NC, Fe_2O_3(H)-NC, and Al/Fe_2O_3(H)-NC and to obtain the corresponding kinetic parameters (apparent activation energy (E_a/kJ mol^{-1}), pre-exponential constant (A/s^{-1})) and the most probable kinetic model functions, the DSC curves at six heating rates of 5.0, 10.0, 15.0, 20.0, 25.0, and 30.0°C min^{-1} were dealt by mathematic means, and the temperature data corresponding to the conversion degrees (α) were found. The values of E_α were obtained by Ozawa's method from the iso-conversional DSC curves at the heating rates of 5.0, 10.0, 15.0, 20.0, 25.0, and 30.0°C min^{-1}, and the E_α-α relation is shown in **Figure 8**. From **Figure 8**, one can see that

the activation energy slightly changes in the section of 0.10–0.80 (α), and the ranges were selected to calculate the non-isothermal reaction kinetics parameters.

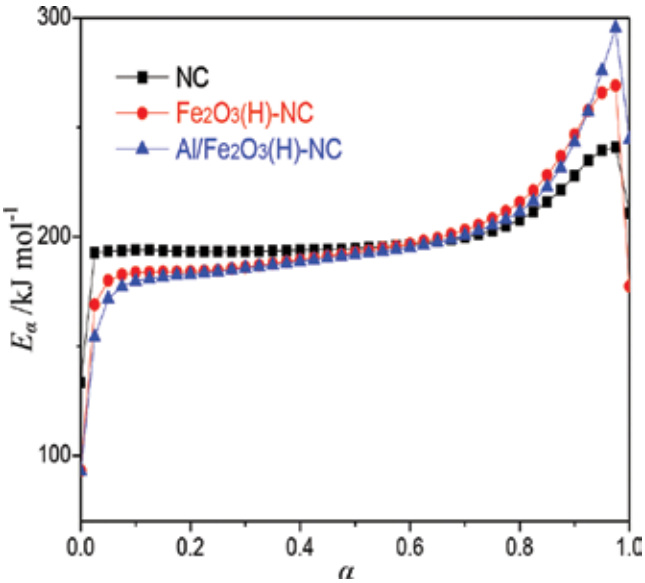

Figure 8. E_α versus α curve of NC, Fe_2O_3(H)-NC, and Al/Fe_2O_3(H)-NC by Flynn-Wall-Ozawa's method.

Six integral methods (MacCallum-Tanner, Šatava-Šesták, Agrawal, general integral, universal integral, and Flynn-Wall-Ozawa) and one differential method (Kissinger) were employed [39–43]. Forty-one types of kinetic model functions and the basic data were put into the integral and differential equations for calculation. The kinetic parameters and the probable kinetic model function were selected by the logical choice method and satisfying the ordinary range of the thermal decomposition kinetic parameters for energetic materials (E_a = 80–250 kJ mol^{-1}, log$A$ = 7–30 s^{-1}). These data together with their appropriate values of linear correlation coefficient (r), standard mean square deviation (Q), and believable factor (d, where $d = (1–r)Q$) are presented in **Tables 2–4**. The values of E_a and log$A$ obtained from each single non-isothermal DSC curve are in good agreement with the calculated values obtained by Kissinger's method and Ozawa's method. We consider the Fe_2O_3-NC composites as an example, and conclude that the reaction mechanism of the intense exothermic decomposition process of Fe_2O_3-NC is classified as Avrami-Erofeev equation $G(\alpha)$=[–ln(1–α)]$^{2/3}$. Substituting $f(\alpha)$ with 3(1–α)[–ln(1–α)]$^{1/3}$/2, E_a with 192.11 kJ mol^{-1}, and A with $10^{18.54}$ s^{-1} in Eq. (1),

$$\frac{\mathrm{d}\alpha}{\mathrm{d}T} = \frac{A}{\beta} f(\alpha) e^{-E/RT} \tag{1}$$

where $f(\alpha)$ and dα/dT are the differential model function and the rate of conversion, respectively.

http://dx.doi.org/10.5772/64748

Method	β/°C min^{-1}	E_a/kJ mol^{-1}	log (A/s^{-1})	r	S	d
MacCallum-Tanner	5	207.98	20.55	0.9983	4.45×10^{-4}	7.50×10^{-7}
	10	205.40	20.25	0.9984	4.11×10^{-4}	6.38×10^{-7}
	15	209.33	20.68	0.9988	3.25×10^{-4}	3.98×10^{-7}
	20	209.34	20.67	0.9987	3.49×10^{-4}	4.61×10^{-7}
	25	211.75	20.91	0.9990	2.56×10^{-4}	2.48×10^{-7}
	30	210.10	20.76	0.9982	4.69×10^{-4}	8.30×10^{-7}
Šatava-Šesták	5	204.55	20.23	0.9983	4.45×10^{-4}	7.50×10^{-7}
	10	202.12	19.94	0.9984	4.11×10^{-4}	6.38×10^{-7}
	15	205.83	20.35	0.9988	3.25×10^{-4}	3.98×10^{-7}
	20	205.83	20.33	0.9987	3.49×10^{-4}	4.61×10^{-7}
	25	208.11	20.56	0.9990	2.56×10^{-4}	2.48×10^{-7}
	30	206.56	20.42	0.9982	4.69×10^{-4}	8.30×10^{-7}
Agrawal	5	207.20	20.49	0.9982	2.37×10^{-3}	4.30×10^{-6}
	10	204.54	20.18	0.9983	2.19×10^{-3}	3.67×10^{-6}
	15	208.37	20.60	0.9987	1.73×10^{-3}	2.29×10^{-6}
	20	208.33	20.58	0.9986	1.86×10^{-3}	2.65×10^{-6}
	25	210.68	20.81	0.9990	1.36×10^{-3}	4.43×10^{-6}
	30	209.03	20.66	0.9981	2.49×10^{-3}	4.77×10^{-6}
General integral	5	205.81	18.98	0.9985	2.36×10^{-3}	4.33×10^{-6}
	10	203.30	18.69	0.9983	2.18×10^{-3}	3.69×10^{-6}
	15	207.22	19.10	0.9987	1.72×10^{-3}	2.30×10^{-6}
	20	207.24	19.09	0.9986	1.85×10^{-3}	2.66×10^{-6}
	25	209.64	19.33	0.9989	1.36×10^{-3}	4.43×10^{-6}
	30	208.02	19.18	0.9981	2.48×10^{-3}	4.79×10^{-6}
Universal integral	5	207.20	20.49	0.9982	2.37×10^{-3}	4.30×10^{-6}
	10	204.54	20.19	0.9983	2.19×10^{-3}	3.67×10^{-6}
	15	208.37	20.60	0.9987	1.73×10^{-3}	2.29×10^{-6}
	20	208.33	20.58	0.9986	1.86×10^{-3}	2.65×10^{-6}
	25	210.68	20.82	0.9990	1.36×10^{-3}	4.43×10^{-6}
	30	209.03	20.66	0.9981	2.49×10^{-3}	4.77×10^{-6}
Mean		207.48	20.22			
Flynn-Wall-Ozawa		185.68 (E_{eo})		0.9998		
		197.56 (E_{po})		0.9979		
Kissinger		199.68 (E_K)	19.82	0.9977		
Mean (E_{eO}, E_{pO}, E_K)		194.31				

Note: E with the subscript of eo and po is the apparent activation energy obtained from the onset temperature (T_e) and the peak temperature (T_p) by Ozawa's method, E with the subscript of K is the apparent activation energy obtained from the peak temperature (T_p) by Kissinger's method.

Table 2. Calculated values of kinetic parameters of decomposition reaction for NC.

Method	β/°C min^{-1}	E_a/kJ mol^{-1}	log(A/s^{-1})	r	Q	d
MacCallum-Tanner	5.0	182.76	17.71	0.9888	4.32×10^{-2}	4.82×10^{-4}
	10.0	190.67	18.63	0.9913	3.36×10^{-2}	2.92×10^{-4}
	15.0	178.17	17.25	0.9949	1.97×10^{-2}	1.00×10^{-4}
	20.0	196.93	19.31	0.9934	2.58×10^{-2}	1.72×10^{-4}
	25.0	203.11	19.97	0.9940	2.32×10^{-2}	1.38×10^{-4}
	30.0	208.59	20.60	0.9946	2.08×10^{-2}	1.11×10^{-4}
Šatava-Šesták	5.0	180.74	17.53	0.9888	4.32×10^{-2}	4.82×10^{-4}
	10.0	188.21	18.40	0.9913	3.36×10^{-2}	2.92×10^{-4}
	15.0	176.41	17.10	0.9949	1.97×10^{-2}	1.00×10^{-4}
	20.0	194.12	19.04	0.9934	2.58×10^{-2}	1.72×10^{-4}
	25.0	199.95	19.67	0.9940	2.32×10^{-2}	1.38×10^{-4}
	30.0	205.38	20.27	0.9946	2.08×10^{-2}	1.11×10^{-4}
Agrawal	5.0	182.16	17.69	0.9878	2.30×10^{-1}	2.80×10^{-3}
	10.0	189.92	18.58	0.9906	1.79×10^{-1}	1.69×10^{-3}
	15.0	177.45	17.22	0.9944	1.05×10^{-2}	5.88×10^{-4}
	20.0	196.02	19.24	0.9928	1.37×10^{-1}	9.95×10^{-4}
	25.0	202.11	19.89	0.9935	1.23×10^{-1}	7.90×10^{-4}
	30.0	206.79	20.51	0.9942	1.11×10^{-1}	6.44×10^{-4}
General integral	5.0	180.77	16.22	0.9877	2.29×10^{-1}	2.81×10^{-3}
	10.0	188.67	17.11	0.9905	1.78×10^{-1}	1.70×10^{-3}
	15.0	176.27	15.79	0.9944	1.05×10^{-1}	5.87×10^{-4}
	20.0	194.91	17.78	0.9927	1.37×10^{-1}	9.95×10^{-4}
	25.0	201.06	18.42	0.9935	1.23×10^{-1}	7.98×10^{-4}
	30	206.78	19.03	0.9942	1.10×10^{-1}	6.43×10^{-4}
Universal integral	5.0	182.16	17.69	0.9878	2.30×10^{-1}	2.80×10^{-3}
	10.0	189.92	18.58	0.9906	1.79×10^{-1}	1.69×10^{-3}
	15.0	177.45	17.22	0.9944	1.53×10^{-1}	4.88×10^{-4}
	20.0	196.02	19.24	0.9928	1.37×10^{-1}	9.95×10^{-4}
	25.0	202.11	19.89	0.9935	1.23×10^{-1}	7.99×10^{-4}
	30.0	207.79	20.51	0.9942	1.11×10^{-1}	6.44×10^{-4}
Mean		192.11	18.54			
Flynn-Wall-Ozawa		188.33 (E_{po})		0.9993		
Kissinger		189.98 (E_K)	18.76	0.9992		
Mean (E_{eO},E_{pO}, E_K)		189.16				

Note: E with the subscript of eo and po is the apparent activation energy obtained from the onset temperature (T_e) and the peak temperature (T_p) by Ozawa's method, E with the subscript of K is the apparent activation energy obtained from the peak temperature (T_p) by Kissinger's method.

Table 3. Calculated values of kinetic parameters of decomposition reaction for Fe_2O_3(H)-NC.

http://dx.doi.org/10.5772/64748

Method	β/°C min^{-1}	E_a/kJ mol^{-1}	log(A/s^{-1})	r	S	d
MacCallum-Tanner	5	174.56	16.81	0.9958	2.84×10^{-3}	1.21×10^{-5}
	10	178.30	17.27	0.9967	2.22×10^{-3}	7.36×10^{-6}
	15	185.26	18.04	0.9971	1.94×10^{-3}	5.61×10^{-6}
	20	183.79	17.87	0.9969	2.10×10^{-3}	6.59×10^{-6}
	25	207.72	20.50	0.9965	2.33×10^{-3}	8.11×10^{-6}
	30	195.50	19.15	0.9962	2.53×10^{-3}	9.56×10^{-6}
Šatava-Šesták	5	173.00	16.67	0.9958	2.84×10^{-3}	1.21×10^{-5}
	10	176.53	17.11	0.9967	2.22×10^{-3}	7.36×10^{-6}
	15	183.10	17.84	0.9971	1.94×10^{-3}	5.61×10^{-6}
	20	181.71	17.68	0.9969	2.10×10^{-3}	6.59×10^{-6}
	25	204.31	20.18	0.9965	2.33×10^{-3}	8.11×10^{-6}
	30	192.76	18.89	0.9962	2.53×10^{-3}	9.56×10^{-6}
Agrawal	5	174.00	16.79	0.9953	1.51×10^{-2}	7.04×10^{-5}
	10	177.61	17.24	0.9964	1.18×10^{-2}	4.29×10^{-5}
	15	184.45	17.99	0.9968	1.03×10^{-2}	3.26×10^{-5}
	20	182.94	17.82	0.9966	1.12×10^{-2}	3.84×10^{-5}
	25	206.67	20.42	0.9962	1.24×10^{-2}	4.67×10^{-5}
	30	194.49	19.07	0.9959	1.34×10^{-2}	5.53×10^{-5}
General integral	5	174.00	16.79	0.9953	1.51×10^{-2}	7.04×10^{-5}
	10	177.61	17.24	0.9964	1.18×10^{-2}	4.29×10^{-5}
	15	184.45	17.99	0.9968	1.03×10^{-2}	3.26×10^{-5}
	20	182.94	17.82	0.9966	1.12×10^{-2}	3.84×10^{-5}
	25	206.67	20.42	0.9962	1.24×10^{-2}	4.67×10^{-5}
	30	194.49	19.07	0.9959	1.34×10^{-2}	5.53×10^{-5}
Universal integral	5	172.64	15.35	0.9953	1.51×10^{-2}	7.09×10^{-5}
	10	176.39	15.80	0.9963	1.17×10^{-2}	4.31×10^{-5}
	15	183.32	16.55	0.9968	1.03×10^{-2}	3.27×10^{-5}
	20	181.88	16.39	0.9965	1.11×10^{-2}	3.85×10^{-5}
	25	205.65	18.94	0.9962	1.23×10^{-2}	4.68×10^{-5}
	30	193.52	17.63	0.9959	1.34×10^{-2}	5.53×10^{-5}
Mean		186.34	17.91			
Flynn-Wall-Ozawa		172.66(E_{eo})		0.9941	4.87×10^{-3}	
		194.23(E_{po})		0.9990	8.60×10^{-4}	
Kissinger		196.18(E_K)	19.44	0.9989	4.56×10^{-3}	
Mean(E_{eO},E_{pO}, E_K)		187.69				

Note: E with the subscript of eo and po is the apparent activation energy obtained from the onset temperature (T_e) and the peak temperature (T_p) by Ozawa's method, E with the subscript of K is the apparent activation energy obtained from the peak temperature (T_p) by Kissinger's method.

Table 4. Calculated values of kinetic parameters of decomposition reaction for Al/Fe_2O_3(H)-NC.

The kinetic equation of the exothermic decomposition reaction may be described as

$$\frac{\mathrm{d}\alpha}{\mathrm{d}T} = \frac{10^{18.71}}{\beta}(1-\alpha)\left[-\ln(1-\alpha)\right]^{1/3}\exp\left(-2.31\times10^{4}/T\right) \tag{2}$$

The values (T_{e0} and T_{p0}) of the onset temperature (T_e) and peak temperature (T_p) corresponding to $\beta\rightarrow0$ were obtained by Eq. (3), and the self-accelerating decomposition temperature (T_{SADT}) was obtained by Eq. (5) [39–43]. The values (T_{SADT} and T_{p0}) are 182.03 and 194.10°C, respectively.

$$T_{e(\text{or p})} = T_{e0(\text{or p})} + a\beta_i + b\beta_i^2 + c\beta_i^3 \; i=1-4 \tag{3}$$

where *a*, *b*, and *c* are coefficients.

$$T_{SADT} = T_{e0} \tag{4}$$

The thermal ignition temperature (T_{be0} or T_{TIT}) was obtained by substituting E_{eo} and T_{e0} into the equation of Zhang et al. (Eq. (5)) [44], and the critical temperatures of thermal explosion (T_{bp0} or T_b) were obtained by substituting E_{po} and T_{p0} in Eq. (5). The values (T_{TIT} and T_b) are 191.44 and 204.16°C, respectively,

$$T_{be0(\text{or bp0})} = \frac{E_o - \sqrt{E_o^2 - 4E_oRT_{e0(\text{or p0})}}}{2R} \tag{5}$$

The thermal behaviors of NC are also analyzed with the same method using the data in **Figure 8**. The results show that the reaction mechanism of the intense exothermic decomposition process of them is classified as reaction order $f(\alpha) = 3(1-\alpha)[-\ln(1-\alpha)]^{1/3}/2$, $G(a) = [-\ln(1-\alpha)]^{2/3}$. The DSC curves of Fe_2O_3(p)-NC, Al/Fe_2O_3(p)-NC, Fe_2O_3(o)-NC, and Al/Fe_2O_3(o)-NC at a heating rate of 10°C min^{-1} are listed in Figures S1 and S3 (Supplementary data), respectively. The E_α-α relations of Fe_2O_3(p)-NC, Al/Fe_2O_3(p)-NC, Fe_2O_3(o)-NC, and Al/Fe_2O_3(o)-NC are shown in Figures S2 and S4 (Supplementary data). **Table 5** and the supplementary data (Tables S1–S4) show the calculated values of kinetic parameters of decomposition reaction for NC, Fe_2O_3(H)-NC, Al/Fe_2O_3(H)-NC, Fe_2O_3(p)-NC, Al/Fe_2O_3(p)-NC, Fe_2O_3(o)-NC, and Al/Fe_2O_3(o)-NC. From **Table 5**, it can be found that (1) the E_a values of NC-based composites containing Fe_2O_3 and Al/Fe_2O_3 are less than that of NC; (2) the E_a value of NC-based composites containing Al/Fe_2O_3 is less than that of NC-based composites containing the corresponding Fe_2O_3; (3) among the three Fe_2O_3 particles, Fe_2O_3(H) is the best catalyst because E_a of Fe_2O_3(H)-NC is the lowest; (4) the E_a value of Al/Fe_2O_3(o)-NC is 0.16 and 5.57 kJ mol^{-1} lower than that of Al/Fe_2O_3(H)-NC and Al/Fe_2O_3(p)-NC, respectively, but the thermal ignition temperature and the critical temperature of thermal explosion of Al/Fe_2O_3(o)-NC are so high. Therefore, the

http://dx.doi.org/10.5772/64748

prepared Fe_2O_3(H) and Al/Fe_2O_3(H) are the two kinds of promising catalysts developed in accelerating the decomposition rate or the process of NC.

Sample	E_a/kJ mol^{-1}	log(A/s^{-1})	T_{e0}/°C	T_{p0}/°C	T_{be0}/°C	T_{bp0}/°C	$\Delta S^{\neq}$/J·mol^{-1}·K^{-1}	$\Delta H^{\neq}$/kJ·mol^{-1}	$\Delta G^{\neq}$/kJ·mol^{-1}
NC	207.48	20.22	181.76	197.00	191.42	206.69	138.40	199.68	134.61
Fe_2O_3(H)-NC	192.11	18.54	182.03	194.10	191.44	204.16	106.21	189.98	140.35
Al/Fe_2O_3(H)-NC	186.34	17.91	175.57	190.02	185.71	199.59	94.31	196.18	152.46
Fe_2O_3(p)-NC	200.67	19.45	176.38	196.42	185.53	206.82	123.72	185.65	127.56
Al/Fe_2O_3(p)-NC	191.75	18.51	180.29	195.55	190.25	205.52	106.31	185.39	135.56
Fe_2O_3(o)-NC	202.69	19.68	178.87	187.64	187.93	197.14	128.29	195.50	136.39
Al/Fe_2O_3(o)-NC	186.18	17.87	179.82	191.87	189.39	201.97	93.50	187.43	143.95

Table 5. Calculated values of kinetic parameters of decomposition reaction for NC, Fe_2O_3(H)-NC, Al/Fe_2O_3(H)-NC, Fe_2O_3(p)-NC, Al/Fe_2O_3(p)-NC, Fe_2O_3(o)-NC, and Al/Fe_2O_3(o)-NC.

By thermal analysis, the addition of Fe_2O_3(H) and Al/Fe_2O_3(H) did not change the kinetic model function of NC, reduced the value of $E_{a,}$ and the critical temperature of thermal explosion, thus Fe_2O_3(H) nanoparticles and Al/Fe_2O_3(H) thermites could accelerate the decomposition rate or process of NC. Furthermore, the effects of Fe_2O_3(H) nanoparticles and Al/Fe_2O_3(H) on the thermal decomposition of NC have been investigated by the thermogravimetry with Fourier transform infrared analysis (TG-IR).

The TG-IR-hyphenated technique is a highly preferred approach for investigating the thermal degradation of energetic materials. The TG-thermogravimetric derivative (TG-DTG) curves of NC, Fe_2O_3(H)-NC, and Al/Fe_2O_3(H)-NC at a heating rate of 10°C/min are presented in **Figure 9**. Just one stage of the total mass loss can be found from the decomposition processes of NC, Fe_2O_3(H)-NC, and Al/Fe_2O_3(H)-NC. The total weight loss of NC is 68.41%, while that of Fe_2O_3(H)-NC and Al/Fe_2O_3(H)-NC are about 34.77 and 31.12%, respectively, which is lower than that of NC due to the remaining Fe_2O_3 and some residues.

A series of temperature values of typical points including the initial decomposition temperature (T_i), the extrapolated onset temperature (T_e), the peak temperature (T_L), the extrapolated end temperature (T_c), and the final temperature (T_f) deserve special attention. Compared with the degradation process of NC, these typical temperature values of Fe_2O_3(H)-NC and Al/Fe_2O_3(H)-NC obviously are reduced under the influence of Fe_2O_3(H) nanoparticles and Al/Fe_2O_3(H) as seen in **Figure 9(b)** and **(c)**. The peak temperatures of NC, Fe_2O_3(H)-NC, and Al/Fe_2O_3(H)-NC are 209.43, 208.59, and 210.24°C, respectively.

The apparent variation of IR characteristic absorption peaks of the gaseous decomposition products of NC, Fe_2O_3(H)-NC, and Al/Fe_2O_3(H)-NC corresponding to the thermal decomposition process at the typical temperature points (T_i, T_e, T_L, T_c, and T_f) is shown in **Figure 10** and **Table 6**. It can be found that the gaseous products detected include CO, NO_2, NO, N_2O, HCHO,

and HCOOH during the decomposition process of NC with and without the Fe_2O_3(H) nanoparticles or Al/Fe_2O_3(H).

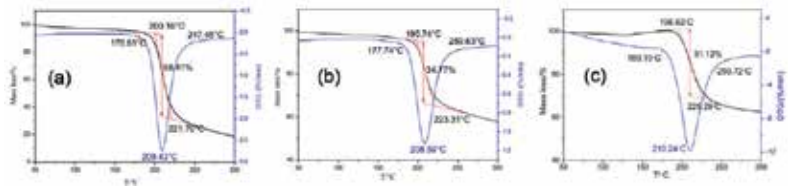

Figure 9. TG-DTG curves of NC (a), Fe_2O_3(H)-NC (b), and Al/Fe_2O_3(H)-NC (c).

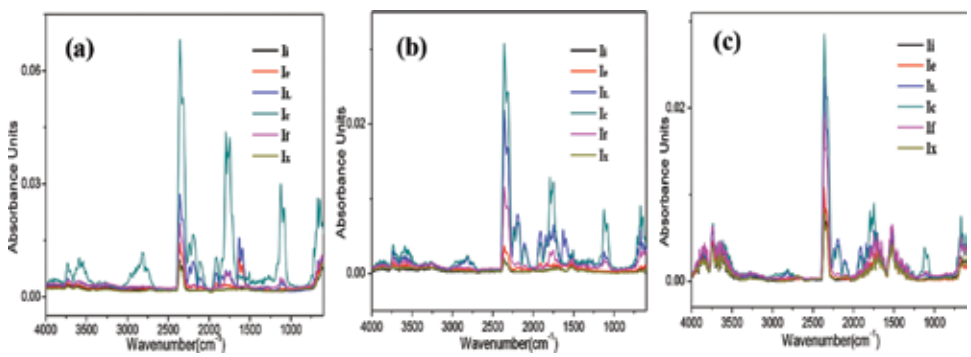

Figure 10. IR spectra of the gases evolved from the degradation of NC (a), Fe_2O_3(H)-NC (b), and Al/Fe_2O_3(H)-NC (c).

NC		Fe_2O_3(H)-NC		Al/Fe_2O_3(H)-NC	
***T*/°C**	**Gaseous products**	***T*/°C**	**Gaseous products**	***T*/°C**	**Gaseous products**
164.92 (T_x)	H_2O, CO_2	160.47 (T_{x1})	H_2O, CO_2, NO_2	164.40 (T_{x2})	H_2O, CO_2, NO_2, NO
178.81 (T_i)	H_2O, CO_2, NO_2	177.74 (T_{i1})	H_2O, CO_2, NO_2	180.19 (T_{i2})	H_2O, CO_2, NO_2, NO
200.16 (T_e)	H_2O, CO_2, NO_2, NO	195.74 (T_e)	H_2O, CO_2, NO_2, NO	196.76 (T_e)	H_2O, CO_2, NO_2, NO
209.43 (T_L)	H_2O, CO_2, NO_2, NO, N_2O, HCHO, HCOOH	208.59(T_L)	H_2O, CO_2, CO, NO_2, NO, N_2O, HCHO, HCOOH	210.24 (T_L)	H_2O, CO_2, CO, NO_2, NO, N_2O, HCHO, HCOOH
221.70 (T_c)	H_2O, CO_2, CO, NO_2, NO, HCHO, HCOOH	223.31 (T_c)	H_2O, CO_2, CO, NO_2, NO, N_2O, HCHO, HCOOH	225.47 (T_c)	H_2O, CO_2, CO, NO_2, NO, N_2O, HCOOH
247.45 (T_f)	H_2O, CO_2, NO	259.63 (T_f)	H_2O, CO_2, CO, NO, HCOOH	259.72 (T_f)	H_2O, CO_2, NO_2, NO

Note: T_x, some temperature below the initial decomposition temperature; T_{x1}(T_{x2}), some temperature below T_{i1}(T_{i2}); T_i, the initial decomposition temperature; T_{i1}, the initial decomposition temperature of the obvious exothermic peak of Fe_2O_3(H)-NC; T_{i2}, the initial decomposition temperature of the obvious exothermic peak of AL/Fe_2O_3(H)-NC; T_e, the extrapolated onset temperature; T_L, the peak temperature; T_c, the extrapolated end temperature; T_f, the final temperature.

Table 6. Gaseous products generated during the decomposition processes of NC, Fe_2O_3(H)-NC, and Al/Fe_2O_3(H)-NC at different temperatures.

http://dx.doi.org/10.5772/64748

Table 6 lists the gaseous products generated during the decomposition processes of NC, Fe_2O_3(H)-NC, and Al/Fe_2O_3(H)-NC at the typical temperature points. At the initial decomposition temperature (T_i), the IR absorption peaks of H_2O (3600–3740 cm^{-1}), CO_2 (2360, 670 cm^{-1}), and NO_2 (1593–1635 cm^{-1}) [45, 46] are easily identifiable (**Figure 10**(a, I_i) and (b, I_i)). During the whole testing process, the existence of H_2O and CO_2 from the ambience is the outside disruptive factor, which cannot be ignored. In order to prove that H_2O and CO_2 gas detected at 178.81°C are not the products of NC decomposition, the variation of IR absorption peaks at 164.92°C is obtained, which is shown in **Figure 10**(a, I_x). The TG-DTG curves of NC in **Figure 9(a)** show that the decomposition of NC has not occurred at 164.92°C and begins from 178.81°C. By comparing the curves I_x (164.92°C) and I_i (178.81°C) in **Figure 10(a)**, the bands at 3600–3740 cm^{-1} are assigned to O-H-bonding-stretching vibrational modes for water as an impurity because of the extremely similar absorptive intensities. Apart from the impurity peaks of H_2O, it can be concluded that CO_2 gas is not the initial degradation product because the intensities of the detected CO_2 gas are basically unchanged at both 164.92 and 178.81°C shown in **Figure 10**(a, I_x, and I_i). Furthermore, the noticeable IR bands of NO_2 are found in the region of 1593–1635 cm^{-1} at the beginning of the decomposition of NC shown in the curve I_i (**Figure 10(a)**) [46], which means that the NO_2 gas is an initial degradation product. The above results concur with those of several previous studies [22, 23, 47, 48] in which the O-NO_2 bond is deemed to be the first step leading to the release of NO_2

$$RO{-}NO_2 \rightarrow RO\cdot + {-}NO_2 \tag{6}$$

The NO_2 stagnates in the polymer skeleton and then reacts with the RO• radical or its degradation products. It is particularly necessary to point out that the signal of NO_2 was present as shown in the IR spectrum in **Figure 10**(b, I_x) at 160.47°C (T_{x1}). The intensities of NO_2 peaks increase with temperature, which is very different from the decomposition of NC. It is a fact that NC could be slowly decomposed as the temperature increases further, which has been enhanced by Fe_2O_3(H) nanoparticles due to their catalysis. That is, the Fe_2O_3(H) nanoparticles could accelerate the O-NO_2 bond cleavage and the release of NO_2. For this reason, the absorption peaks of H_2O and CO_2 exist not only from the environment but also from the degradation of Fe_2O_3(H)-NC at 160.47°C (T_{x1}). Moreover, both NO_2 and NO are detected besides the H_2O and CO_2 gases, which indicates that Al/Fe_2O_3(H) can make NC decompose faster than Fe_2O_3(H) does.

Figure 11 shows the 3D-IR spectra of gas products of NC, Fe_2O_3(H)-NC, and Al/Fe_2O_3(H)-NC at a heating rate of 10°C min^{-1}. At the initial decomposition temperature, the IR absorption peaks of H_2O (3600–3740 cm^{-1}), CO_2 (2360, 670 cm^{-1}), and NO_2 (1593–1635 cm^{-1}) [46, 47] are easily identifiable (**Figure 11**). With the progress of the thermal decomposition process, the gas productions such as NO (1762–1965 cm^{-1}), CO (2194 cm^{-1}), N_2O (2241 cm^{-1}), HCHO (2814 and 1746 cm^{-1}), and HCOOH (1080–1128 cm^{-1}) are detected [26, 47]. By comparing the gaseous products generated during the decomposition processes of NC, Fe_2O_3(H)-NC, and Al/Fe_2O_3(H)-NC at different temperatures, it can be concluded that Fe_2O_3(H) and Al/Fe_2O_3(H) can accelerate the O-NO_2 bond cleavage and the release of NO_2 gas. The evolution of HCOOH

gases is the products of the secondary autocatalytic reactions of NC [24, 26]. From **Figure 11**, the intensities of all these gas products are very strong, which can be taken as an important signal of identifying the faster decomposition rate of Fe_2O_3(H)-NC and Al/Fe_2O_3(H)-NC composites than that of NC. One of the reasons for generating quantities of gases is that the condensed phases break down fast with the presence of Fe_2O_3(H) nanoparticles and Al/Fe_2O_3(H). It has to be pointed out that Al/Fe_2O_3(H) thermite is a better catalyst than Fe_2O_3(H) nanoparticles for reducing the activation energy and accelerating to break the O-NO_2 bond during the thermal decomposition process of NC.

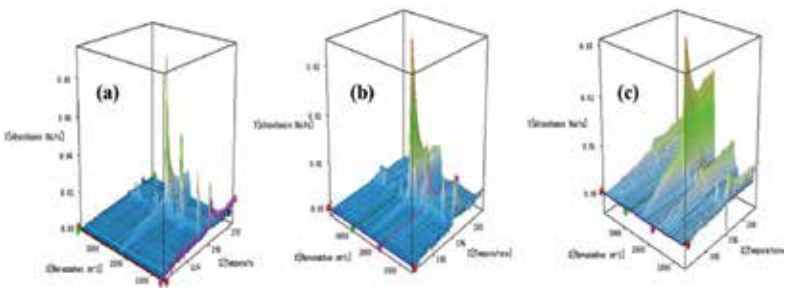

Figure 11. 3D-IR spectra of gas products of NC (a), Fe_2O_3(H)-NC (b), and Al/Fe_2O_3(H)-NC (c) at a heating rate of 10°C min^{-1}.

5. Combustion catalysts used in AP/HTPB propellants

Figure 12 shows the burning rate (u) versus pressure (p) curves of AP/HTPB propellants. Based on the experimental data, the pressure exponent (n) can be calculated [29, 49]. The catalytic efficiency is another evaluation index of the combustion catalyst [29], which is shown in **Figure 13**.

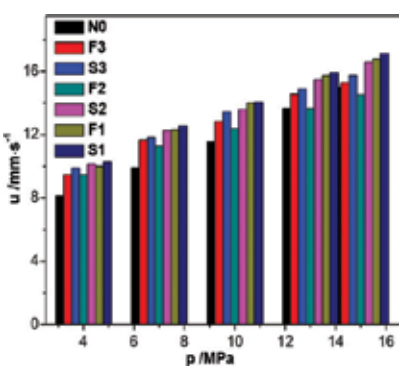

Figure 12. Burning rate (u) versus pressure (p) curves of AP/HTPB composite propellants.

http://dx.doi.org/10.5772/64748

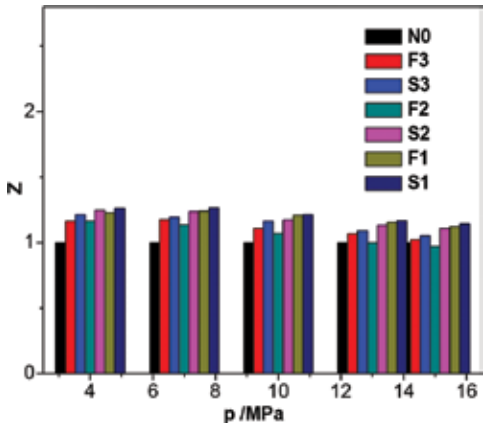

Figure 13. Efficiency of AP/HTPB composite propellants.

The burning rate of all the formulations increases as the pressure rises within 4–15 MPa. For the formulations containing Fe_2O_3, the burning rate is in the order: F2<F3<F1. For the formulations with thermite, that order is S1>S2>S3. The BET-specific surface areas of Fe_2O_3(H), Fe_2O_3(o), and Fe_2O_3(p) are 5.3, 3.1, and 6.9 m^2/g, respectively. Possibly due to the aggregation of Fe_2O_3(H), its specific surface area is smaller than that of Fe_2O_3(p), which is opposite to what we expected simply based on the particle size. However, when the particles are dispersed to the formulations, Fe_2O_3(H) particles are believed to have a larger surface area than Fe_2O_3(p) based on the particle size. Therefore, the superior combustion performance can be ascribed to the dominant role of the surface area of the Fe_2O_3 particles. From **Figures 12** and **13**, the formulations containing thermites all have better burning rate and combustion-supporting ability than the formulations containing the corresponding Fe_2O_3. And thermite with a smaller size of Fe_2O_3 (H) particles has a higher burning rate.

A good formulation is considered to have a high burning rate with a low pressure exponent. From **Table 7**, it can be found that Fe_2O_3 can take effect on decreasing the pressure exponent of the propellant. Considering the role of Al nanopowders and the thermite reaction in enhancing the burning rate, thermites Al/Fe_2O_3 are the better burning rate modifiers in improving the combustion performances of AP/HTPB composite propellants. Overall, the Al/Fe_2O_3(H) is the best combustion catalyst.

p/MPa	n_{N0}	n_{F1}	n_{F2}	n_{F3}	n_{S1}	n_{S2}	n_{S3}
4–7	0.35	0.37	0.31	0.37	0.36	0.34	0.32
7–10	0.42	0.36	0.26	0.27	0.31	0.29	0.36
10–13	0.63	0.45	0.37	0.48	0.48	0.50	0.39
13–15	0.65	0.45	0.43	0.35	0.51	0.49	0.39

Table 7. The burning rate pressure exponent of formulations under different pressure.

Moreover, the combustion wave structures of AP/HTPB composite propellants containing Al/Fe_2O_3 thermite obtained at 4 MPa are shown in **Figure 14**. The flames of the three composites (**Figure 14**) are entirely yellowish that is caused by the fuel-rich diffusion flame generated by the decomposed gases of the binder and the AP particles [50]. There is no obvious dark zone, which is different from the double-base propellants. Above the burning surface, both the AP flame and the diffusion flame produced by the decomposed gases exist simultaneously, leading to major heat release of the combustion process. High flame temperature up to 2700 K was generated at the center of the luminous flame as in the case of Al/Fe_2O_3(H) catalyst. Thick gray smoke was formed surrounding the yellowish flame of the formulation S2, due to the incomplete burning. When adding Al/Fe_2O_3(p) thermite to the AP/HTPB propellants, the front luminous flame of formulation S3 was blown down to the downstream and numerous Fe_2O_3 and Al particles were ejected from the burning surface. The results of the combustion wave structures and flame temperature characteristics indicate that the Al/Fe_2O_3(H)-containing propellant formulation is the best formulation among the tested samples.

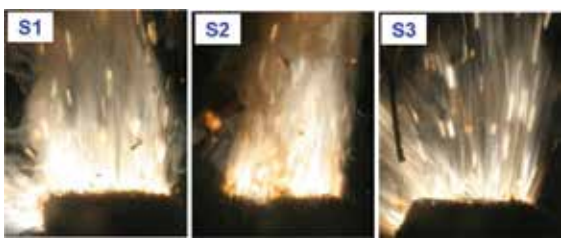

Figure 14. Combustion wave structures of AP/HTPB composite propellants contain thermites Al/Fe_2O_3: (S1) Al/Fe_2O_3(H), (S2) Al/Fe_2O_3(o), and (S3) Al/Fe_2O_3(p).

6. Conclusion

In summary, the structural effect of different sizes and shaped Fe_2O_3 particles on the performance as enhancers, with or without Al, in the thermal decomposition process of NC and the combustion of AP/HTPB has been studied and compared. The as-prepared Fe_2O_3 particles and Al/Fe_2O_3 have good compatibility with NC from DSC thermal analysis, suggesting the safely use of Fe_2O_3-NC and Al/Fe_2O_3-NC composites. The non-isothermal decomposition kinetics of the composites and NC can be modeled by the Avrami-Erofeev equation $f(\alpha)=3(1-\alpha)[-\ln(1-\alpha)]^{1/3}/2$ in differential form. Through the TG-IR analysis of decomposition processes and products of the composites and NC, it is speculated that the as-prepared Fe_2O_3 particles and Al/Fe_2O_3 can effectively accelerate the thermal decomposition reaction rate of NC by promoting the O-NO_2 bond cleavage. Among the three studied different shapes of Fe_2O_3, the granular Fe_2O_3 and its corresponding thermite (Al/Fe_2O_3(H)) exhibit the highest burning rate due to the larger surface area associated with a smaller particle size. Moreover, the Al/Fe_2O_3(H) thermites have more effective combustion-supporting ability for AP/HTPB composite propellants than Fe_2O_3 and the other two as-prepared Al/Fe_2O_3 thermites. Moreover, adding the thermites to

the composite propellants could contribute to increasing the flame temperature and improving the combustion wave structures of the formulations. In all, the addition of the prepared oxides or thermites can distinctly increase the burning rate, enhance the flame temperature, and decrease the burning rate pressure exponent of the AP/HTPB composite propellants.

Acknowledgements

This work was supported by the Program for the National Natural Science Foundation of China (No. 21373161), Research Fund for the Doctoral Program of Higher Education of China (RFDP, No. 20126101110009), and the New Century Excellent Talents in the University of Ministry of Education of China (NCET-12-1047).

Author details

Ningning Zhao[1], Jiachen Li[1], Fengqi Zhao[2], Ting An[2], Rongzu Hu[2] and Haixia Ma[1*]

*Address all correspondence to: mahx@nwu.edu.cn

1 School of Chemical Engineering, Northwest University, Shaanxi Xi'an, P.R. China

2 Science and Technology on Combustion and Explosion Laboratory, Xi'an Modern Chemistry Research Institute, Shaanxi Xi'an, P.R. China

References

[1] Gibot P, Comet M, Eichhorn A, Schnell F, Muller O, Ciszek F, Boehrer Y, Spitzer D. Highly insensitive/reactive thermite prepared from Cr_2O_3 nanoparticles. Propellants, Explosives, Pyrotechnics, 2011, 36(1): 80–87. DOI: 10.1002/prep.201000080.

[2] Pantoya ML, Granier JJ. Combustion behavior of highly energetic thermites: nano versus micron composites. Propellants Explosives Pyrotechnics, 2005, 30(1): 53–62. DOI: 10.1002/prep.200400085.

[3] Shi Y, Guo QJ, Zachariah MR. Electrospun nanofiber based thermite textiles and their reactive properties. ACS Applied Materials & Interfaces, 2012, 4(12): 6432–6435.DOI: 10.1021/am3021125.

[4] Li Y, Song WL, Xie CS, Zeng DW, Wang AH, Hu ML. Influence of humidity on the thermal behavior of aluminum nanopowders. Materials Chemistry and Physics, 2006, 97(1): 127–131. DOI: 10.1016/j.matchemphys.2005.07.064.

[5] An T, Zhao FQ, Hao HX, Ma HX, Yao EG, Yang Y, Tan Y. Effect of thermites on laser ignition characteristics of double base propellants. Chinese Journal of Explosives & Propellants, 2011, 34(1): 67–72. DOI: 1007-7812(2011)01-0067-06.

[6] Martirosyan KS. Nanoenergetic gas-generators: principles and applications. Journal of Materials Chemistry, 2011, 21(26): 9400–9405. DOI: 10.1039/C1JM11300C.

[7] Armstrong RW, Baschung B, Booth DW, Samirant M. Enhanced propellant combustion with nanoparticles. Nano Letters, 2003, 3(2): 253–255. DOI: 10.1021/nl025905k.

[8] Bockmon BS, Pantoya ML, Son SF, Asay BW, Mang JT. Combustion velocities and propagation mechanisms of metastable interstitial composites. Journal of Applied Physics, 2005, 98(6): 064903–064903-7. DOI: 10.1063/1.2058175.

[9] Sullivan K, Young G, Zachariah MR. Enhanced reactivity of nano-B/Al/CuO MIC's. Combustion & Flame, 2009, 156(2): 302–309. DOI: 10.1016/j.combustflame.2008.09.011.

[10] Granier JJ, Plantier KB, Pantoya ML. The role of the Al_2O_3 passivation shell surrounding nano-Al particles in the combustion synthesis of NiAl. Journal of Materials Science, 2004, 39(39): 6421–6431. DOI: 10.1023/B:JMSC.000004.

[11] Wang LL, Munir ZA, Maximov YM. Thermite reactions: their utilization in the synthesis and processing of materials. Journal of Materials Science, 1993, 28(14): 3693–3708. DOI: 10.1007/BF00353167.

[12] Zhou L, Piekiel N, Chowdhury S, Zachariah MR. Time-resolved mass spectrometry of the exothermic reaction between nanoaluminum and metal oxides: the role of oxygen. Journal of Physical Chemistry C, 2010, 114(33): 14269–14275. DOI: 10.1021/jp101146a.

[13] Ulrich T. Energetic Materials: Particle Processing and Characterization. Printed in the Federal Republic of Germany. Wiley-VCH Verlag GmbH & Co. KGaA, Weinheim, 2005: i–xxii. DOI: 10.1002/3527603921.

[14] Jayaraman K, Anand KV, Chakravarthy SR, Sarathi R. Effect of nano-aluminium in plateau-burning and catalyzed composite solid propellant combustion. Combustion & Flame, 2009, 156(8): 1662–1673. DOI: 10.1016/j.combustflame.2009.03.014.

[15] Galfetti L, De Luca LT, Severini F, Meda L, Marra G, Marchetti M, Regi M, Bellucci S. Nanoparticles for solid rocket propulsion. Journal of Physics Condensed Matter, 2006, 18(33): S1991–S2005(15). DOI: 10.1088/0953-8984/18/33/S15.

[16] Patil PR, Krishnamurthy VN, Joshi SS. Differential scanning calorimetric study of HTPB based composite propellants in presence of nano ferric oxide. Propellants Explosives Pyrotechnics, 2006, 31(31): 442–446. DOI: 10.1002/prep.200600059.

[17] Meda L, Marra G, Galfetti L, Severini F, De Luca L. Nano-aluminum as energetic material for rocket propellants. Materials Science & Engineering C, 2007, 27(5): 1393–1396. DOI: 10.1016/j.msec.2006.09.030.

[18] Sun DP, Ma B, Zhu CL, Liu CS, Yang JZ. Novel nitrocellulose made from bacterial cellulose. Journal of Energetic Materials, 2010, 28(28): 85–97. DOI: 10.1080/07370650903222551.

[19] Liu S, Ye M, Han A, Chen X. Preparation and characterization of energetic materials coated superfine aluminum particles. Applied Surface Science, 2014, 288(7): 349–355. DOI: 10.1016/j.apsusc.2013.10.031.

[20] Yi JH, Zhao FQ, Hu RZ, Xue L, Xu SY. Thermal safety study on TEGDN/NG/NC gun propellant. Journal of Energetic Materials, 2010, 28(4): 285–298. DOI: 10.1080/07370651003785695.

[21] López-López M, Ferrando JL, García-Ruiz C. Dynamite analysis by Raman spectroscopy as a unique analytical tool. Analytical chemistry, 2013, 85(5): 2595–2600. DOI: 10.1021/ac302774w.

[22] Konkin AL, Ershov BG, Kargin YM, Chichirov AA, Agafonov MN. Study of the radical products of the thermal decomposition of nitrocellulose. Russian Chemical Bulletin, 1989, 38(11): 2426–2428. DOI: 10.1007/BF01168105.

[23] Makashir PS, Mahajan RR, Agrawal JP. Studies on kinetics and mechanism of initial thermal decomposition of nitrocellulose. Journal of Thermal Analysis, 1995, 45(3): 501–509. DOI: 10.1007/BF02548782.

[24] Shehata AB, Hassan MA, Nour MA. Effect of new poly 2-acryloyl-N, N′-bis (4-nitrophenyl) propandiamide and poly 2-acryloyl-N, N′-bis (4-methylphenyl) propandiamide and their synergistic action on the stability of nitrocellulose. Journal of Hazardous Materials, 2003, 102(2): 121–136.

[25] Katoh K, Higashi E, Nakano K, Ito S, Wada Y, Kasamatsu J, Miya H, Yamamoto M, Wada Y, Thermal behavior of nitrocellulose with inorganic salts and their mechanistic action. Propellants Explosives Pyrotechnics, 2010, 35: 461–467. DOI: 10.1016/S0304-3894(03)00138-9.

[26] Chen JK, Brill TB. Thermal decomposition of energetic materials 50. Kinetics and mechanism of nitrate ester polymers at high heating rates by SMATCH/FTIR spectroscopy. Combustion & Flame, 1991, 85(s3–4): 479–488. DOI: 10.1016/0010-2180(91)90149-6.

[27] Mahajan RR, Makashir PS, Agrawal JP. Combustion behaviour of nitrocellulose and its complexes with copper oxide. hot stage microscopic studies. Journal of Thermal Analysis & Calorimetry, 2001, 65(3): 935–942. DOI: 10.1023/A:1011905021880.

[28] Yang Y, Ma HX, Zhuang J, Wang X. Morphology-controlled synthesis of hematite nanocrystals and their facet effects on gas-sensing properties. Inorganic Chemistry, 2011, 50(20): 10143–10151. DOI: 10.1021/ic201104w.

[29] Zhao NN, He CC, Liu JB, Gong HJ, An T, Xu HX, Zhao FQ, Hu RZ, Ma HX, Zhang JZ. Dependence of catalytic properties of Al/Fe_2O_3 thermites on morphology of Fe_2O_3

particles in combustion reactions. Journal of Solid State Chemistry, 2014, 219: 67–73. DOI: 10.1016/j.jssc.2014.06.039.

[30] Daniel P, Pantoya ML, Clapsaddle BJ. Effect of nanocomposite synthesis on the combustion performance of a ternary thermite. Journal of Physical Chemistry B, 2005, 109(43): 20180–20185.

[31] Fu YY, Wang RM, Xu J, Chen J, Yan Y, Narlikar AV, Zhang H. Synthesis of large arrays of aligned α-Fe_2O_3 nanowires. Chemical Physics Letters, 2003, 379(3): 373–379. DOI: 10.1016/j.cplett.2003.08.061.

[32] Zhu D, Chen YL, Miller RA. Defect clustering and nano-phase structure characterization of multi-component rare earth oxide doped zirconia-yttria thermal barrier coatings. Ceramic Engineering & Science Proceedings, 1990, 24(3): 525–534. DOI: 10.1002/9780470294802.ch75.

[33] Gotić M, Dražić G, Musić S. Hydrothermal synthesis of α-Fe_2O_3 nanorings with the help of divalent metal cations, Mn^{2+}, Cu^{2+}, Zn^{2+} and Ni^{2+}. Journal of Molecular Structure, 2011, 993(1): 167–176. DOI: 10.1016/j.molstruc.2010.12.063.

[34] Apte SK, Naik SD, Sonawane RS, Kale BB, Baeg JO. Synthesis of nanosize-necked structure α- and γ-Fe_2O_3 and its photocatalytic activity. Journal of the American Ceramic Society, 2007, 90(90): 412–414. DOI: 10.1111/j.1551-2916.2006.01424.x.

[35] Woo K, Lee HJ, Ahn JP, Park YS. Sol–gel mediated synthesis of Fe_2O_3 nanorods. Advanced Materials, 2003, 15(20): 1761–1764. DOI: 10.1002/adma.200305561.

[36] Khan SB, Faisal M, Rahman MM, Abdel-Latif IA, Ismail AA, Akhtar K, Al-Hajry A, Asiri AM, Alamry KA. Highly sensitive and stable phenyl hydrazine chemical sensors based on CuO flower shapes and hollow spheres. New Journal of Chemistry, 2013, 37(4): 1098–1104. DOI: 10.1039/C3NJ40928G.

[37] Aghaie-Khafri M, Lafdani MHK. A novel method to synthesize Cr_2O_3 nanopowders using EDTA as a chelating agent. Powder Technology, 2012, 222: 152–159. DOI: 10.1016/j.powtec.2012.02.024.

[38] Pei Z, Zhang Y. A novel method to prepare Cr_2O_3 nanoparticles. Materials Letters, 2008, 62(3): 504–506. DOI: 10.1016/j.matlet.2007.05.073.

[39] Ma HX, Yan B, Ren YH, Guan YL, Zhao FQ, Song JR, Hu RZ. Thermal behavior and thermal safety on 3,3-dinitroazetidinium salt of perchloric acid. Journal of Thermal Analysis and Calorimetry, 2011, 103(2): 569–575. DOI: 10.1007/s10973-010-0950-2.

[40] Ma HX, Zhao NN, Yan B, Guan YL, Li JF, Song JR. Molecular structure, quantum chemical investigation, and thermal behavior of $(DNAZ\text{-}CO)_2$. Journal of Structural Chemistry, 2012, 53(3): 534–541. DOI: 10.1134/S0022476612030171.

[41] Ma HX, Yan B, Li ZN, Song JR, Hu RZ. Synthesis, molecular structure, non-isothermal decomposition kinetics and adiabatic time to explosion of 3,

3-dinitroazetidinium 3, 5-dinitrosalicylate. Journal of Thermal Analysis and Calorimetry, 2009, 95(2): 437–444. DOI: 10.1007/s10973-008-9255-0.

[42] Ma HX, Yan B, Li ZN, Guan YL, Song JR, Xu KZ, Hu RZ. Preparation, non-isothermal decomposition kinetics, heat capacity and adiabatic time-to-explosion of NTO DNAZ. Journal of Hazardous Materials, 2009, 169(1): 1068–1073. DOI: 10.1016/j.jhazmat.2009.04.057.

[43] Ma HX, Song JR, Zhao FQ, Hu RZ, Xiao HM. Nonisothermal decomposition kinetics and computational studies on the properties of 2,4,6,8-tetranitro-2,4,6,8-tetraazabicyclo [3,3,1] onan-3,7-dione (TNPDU). Journal of Physical Chemistry A, 2007, 111(35): 8642–8649. DOI: 10.1021/jp073092o.

[44] Zhang TL, Hu RZ, Xie Y, Li FP. The estimation of critical temperatures of thermal explosion for energetic materials using non-isothermal DSC. Thermochimica Acta, 1994, 244: 171–176. DOI: 10.1016/0040-6031(94)80216-5.

[45] Li Y, Chenxia K, Huang C, Chen Y. Effect of MnC_2O_4 nanoparticles on the thermal decomposition of TEGDN/NC propellant. Journal of Thermal Analysis and Calorimetry, 2011, 109(1): 171–176. DOI: 10.1007/s10973-011-1694-3.

[46] Dong Q. Infrared Spectrometry. Beijing: Petroleum Chemical Industry Press; 1977. p. 165–170.

[47] Gratien A, Nilsson E, Doussin JF, Johnson MS, Nielsen CJ, Stenstrom Y, Picquet-Varrault B. UV and IR absorption cross-sections of HCHO, HCDO, and DCDO. Journal of Physical Chemistry A, 2007, 111(45): 11506–11513. DOI: 10.1021/jp074288r.

[48] Fan RH, Lü HL, Sun KN, Wang WX, Yi XB. Kinetics of thermite reaction in Al-Fe_2O_3 system. Thermochimica Acta, 2006, 440(2): 129–131. DOI: 10.1016/j.tca.2005.10.020.

[49] Stephens MA, Petersen EL, Carro R, Reid DL, Seal S. Multi-parameter study of nanoscale TiO_2 and CeO_2 additives in composite AP/HTPB solid propellants. Propellants, Explosives, Pyrotechnics, 2010, 35(2): 143–152. DOI: 10.1002/prep.200800104.

[50] Kubota TKN. Low pressure burning of ammonium perchlorate composite propellants. Combustion Science & Technology, 1986, 47(1): 81–91. DOI: 10.1080/00102208608923866.

Section 5

Fundamental and Emerging Topics in Combustion Technology

Chapter 13

Combustion Processes in Interfacial Instabilities

Praveen Ramaprabhu, Nitesh Attal and
Hilda Varshochi

Additional information is available at the end of the chapter

http://dx.doi.org/10.5772/64746

Abstract

Fluid instabilities, particularly interfacial instabilities, have proven to be a powerful mechanism in driving and sustaining combustion processes in several devices of practical interest. Modern combustors are in fact designed to exploit the mixing and combustion characteristics associated with a broad class of canonical, interfacial instabilities. In spite of their relevance to combustor design, a detailed understanding of such flows has been elusive. While much progress has been made in gaining insights into the dynamics of shear-driven flows, an understanding of the interaction between combustion processes and other interfacial instabilities remains preliminary. In this chapter, we review recent results on Rayleigh-Taylor (RT) instability and the shock-driven Richtmyer-Meshkov (RM) instability in the context of combustion. The vast catalogue of research on non-reacting RT and RM flows has demonstrated these instabilities can be manipulated to achieve more efficient and aggressive mixing in comparison with the canonical Kelvin-Helmholtz (KH) problem. This has motivated recent efforts to understand RT/RM instability development in the presence of chemical reactions, leading to combustion and heat release – we present a review of these results and identify opportunities and challenges in this chapter.

Keywords: interfacial instabilities, Rayleigh-Taylor instability, Kelvin-Helmholtz instability, Richtmyer-Meshkov instability, non-premixed combustion modelling

1. Introduction and background

Turbulent mixing triggered by interfacial instabilities [1–4] is a fundamental process that dominates several engineering applications and natural phenomena. In many instances, the turbulence is profoundly modified by heat release at low or high energy densities, and product

INTECH
open science | open minds

© 2016 The Author(s). Licensee InTech. This chapter is distributed under the terms of the Creative Commons Attribution License (http://creativecommons.org/licenses/by/3.0), which permits unrestricted use, distribution, and reproduction in any medium, provided the original work is properly cited. CC BY

formation from chemical or nuclear reactions. Furthermore, when the mixing occurs across an interface that initially separates a fuel from an oxidizer medium in a non-premixed configuration, the turbulent mixing is a rate-limiting step that dictates the progress of the reactions at the flame site. Thus, the flow affects the flame and vice-versa. In a recent, comprehensive review of turbulent mixing, Dimotakis [5] proposed a hierarchy of mixing phenomena extending from passive scalar mixing (Level-1) to the so-called Level-3 mixing where the active coupling described above is dominant. While such complex interactions are important in describing flow conditions as they exist in engineering applications, the vast majority of turbulence models that seek to obtain reduced order descriptions of the flow assume [6] self-similar, statistically steady, universal behaviour. Thus, reliable data from experiments and simulations is in great demand to verify the validity of these hypotheses, but has not been forthcoming due to challenges in accurately diagnosing these complex flows. The research described herein attempts to break this impasse by performing systematic, high resolution simulations of a new class of idealized flow problems and developing an understanding of the mixing processes based on the data available.

The Kelvin-Helmholtz (KH) instability occurs at a sharp or diffuse interface separating two streams at different velocities, so that the velocity differential ΔU serves to drive the growth of imposed perturbations at the interface. Much of the research on KH instabilities has been motivated by its central role in mixing fuel and oxidizer in several commonly used combustor designs. KH instabilities, whether they occur in a mixing layer, a planar or cylindrical jet, have provided a useful canonical framework for understanding non-premixed combustion. In fact, the design of many modern day combustor devices is acutely informed by the desire to exploit the dynamics of KH-driven mixing between fuel and oxidizer streams. However, there exist alternate combustor designs that exploit the mixing characteristics of other interfacial instabilities such as the RT and shock-driven RM flows. In spite of the importance of these flows in recent combustor designs [7–10], a detailed and comprehensive understanding has not emerged. This is especially true when these flows occur in non-premixed configurations.

We will describe our recent work that addresses a few of the above issues in the areas of reacting RM and RT flows. When a shock wave interacts with a contact discontinuity separating different gases, the material interface is susceptible to the development of the Richtmyer-Meshkov (RM) instability [11–13]. The instability is driven by the deposition by the shock of baroclinic vorticity [14–16] due to locally misaligned density and pressure gradients ($\sim \nabla \rho \times \nabla p$) at the interface. Perturbations present initially at the interface can thus be amplified, first through a phase of linear growth [11, 17], followed by non-linear saturation [18, 19], and eventually turbulent mixing [20]. The non-reacting RM flow has been extensively studied using theory [11, 17–19], simulations [20–25] and experiments [12, 26–30]. However, if the initial sharp interface separates a fuel and oxidizer at elevated temperatures, the turbulent mixing will enable, and in some cases limit, chemical reactions between the reactants resulting in a non-premixed combustion process. Thus, this coupled physics problem provides an idealized test bed for developing a fundamental understanding of turbulent phenomena in the presence of heat addition and product formation due to combustion.

http://dx.doi.org/10.5772/64746

Turbulent mixing and combustion enhanced by RM plays a central role in the performance of scramjets. In most scramjet designs, the interface between the fuel jet and air co-flow is repeatedly shocked by a stationary shock train, so that the misaligned density and pressure gradients result in the deposition of baroclinic vorticity. The induced velocity from the baroclinic vorticity deposition drives much of the subsequent instability development. As a result, the instability growth rate, heat release rate from combustion and combustion efficiency may all be manipulated through the incident shock strength, density ratio between the fuel and oxidizer and initial conditions that seed the interface prior to shock impact.

The dynamics of the shock-interface interaction has been investigated extensively in an idealized framework through a class of shock-bubble problems, which represent the simplest RM configuration. The study of shock interaction with a spherical flame bubble was first undertaken experimentally by Markstein [31] who observed the emergence of an eventual chaotic flame from the deposited baroclinic vorticity. The shock-bubble problem was also investigated theoretically by Picone and Boris [16], who examined the flow resulting from the interaction of a planar shock with a cylindrical flame region. Several numerical studies have also addressed this problem including investigations of shock-flamelet interactions [32, 33], shock interactions with cylindrical jet flames [34] and DDT phenomena in shock-bubble flame interaction [35]. Recently, Haehn et al. [36] performed shock tube experiments in which a focused, spherically converging shock interacted with a spherical bubble consisting of a premixed combination of H_2, O_2 and Xe, so that the high temperatures from the shock heating resulted in combustion and heat release. In **Figure 1(a)**, we show the schematic of an ideal shock-bubble configuration, which we have investigated using careful numerical simulations described in Section 2.

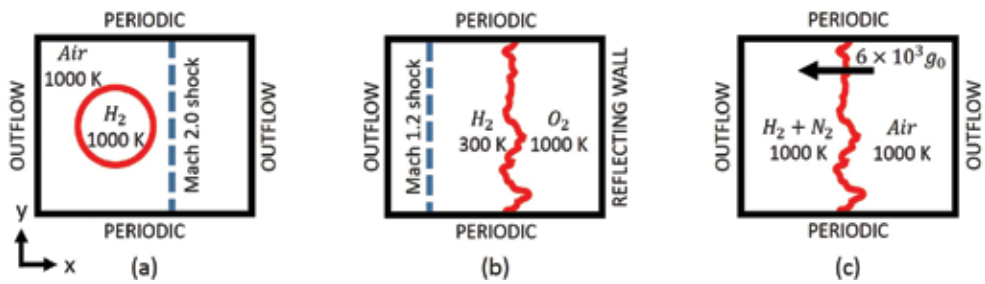

Figure 1. Schematic of (a) shock-bubble (b) Richtmyer-Meshkov and (c) Rayleigh-Taylor instabilities.

While the shock-bubble problem has illustrated certain key aspects of RM behaviour relevant to flames, the requirement to model controlled initial perturbations has led to recent numerical simulation studies in which shocks accelerate planar (premixed) flames subjected to well-defined (often sinusoidal) initial perturbations. For instance, Khokhlov et al. [37] investigated the growth of a *sinusoidally* perturbed premixed flame upon shock impingement and found the energy release from combustion varied in direct relation to the interfacial surface growth from the RM instability. These results are consistent with and follow from earlier numerical investigations of non-reacting RM interfaces [38] that found the interface surface area increased

in proportion to the baroclinic circulation deposition at the interface, according to the scaling relationship,

$$V \sim \Gamma_0 \left[c_1 \left(\frac{a_0}{\lambda} \right) + \frac{c_2}{\lambda} \right], \tag{1}$$

where V is the growth rate of the interfacial area, Γ_0 is the initial circulation, a_0 and λ are the perturbation amplitude and wavelength and c_1 and c_2 are non-dimensional coefficients. Eq. (1) points to a significant and thus far unrealized potential for mixing enhancement and improvements in combustion efficiency, particularly in a non-premixed configuration where the RM instability growth may be used to control and enhance the product formation at the interface. Thus, a configuration in which the shock impinges on an interface separating the fuel and oxidizer leading to a non-premixed flame that is controlled by turbulence and mixing at the interface (according to Eq. (1)) represents a significant departure from the earlier RM efforts described above. In Section 3, we describe results from our simulations involving a planar shock interacting with a planar, perturbed interface between fuel and oxidizer resulting in shock-induced non-premixed combustion. The details of the problem schematic are shown in **Figure 1(b)**.

The RM configurations discussed above are relevant to several applications in engineering and to a multitude of combustion phenomena occurring in nature. Shocks generated inside the combustion chamber of an internal combustion engine interact with flame or fuel/air interfaces of various thicknesses, and can result in the phenomenon of engine *knocking*, necessitating the use of expensive, higher octane fuels. In scramjet propulsion, mixing between fuel jets and co-flowing supersonic air can be impacted by the presence of oblique shocks and is thus central to the design of the injectors [39]. The baroclinic vorticity from the interaction has also been observed to play a crucial role in lifting the jet away from the combustor wall, thus decreasing wall heating effects [39]. The importance of accurately capturing such flow physics in realistic conditions was demonstrated recently in a proof-of-principle design and experimental study [40] of a shock-induced combustion ramjet (Schramjet). Our results (Section 3) below indicate a marked increase in the heat release rate and combustion efficiency immediately following shock impact, pointing the way towards high-performance combustion devices that can be manipulated by strategically structured shock trains.

We also discuss non-premixed combustion occurring at the site of a Rayleigh-Taylor unstable interface between fuel and oxidizer. The Rayleigh-Taylor instability occurs at a perturbed interface between fluids of different densities when the light fluid is accelerated into the heavier fluid (**Figure 1(c)**). Infinitesimal perturbations on the interface can still grow first exponentially (linear stage), and then secularly with a constant velocity (non-linear stage). When multiple modes are present, non-linear interactions are possible yielding an eventual turbulent, mixed state. RT-driven mixing afflicts a wide range of physical phenomena including energy yield in inertial confinement fusion [41], type Ia supernovae detonation [42–44], geophysical flows [45–47] and mixing in centrifugal combustors [8, 9, 48]. Although RT

http://dx.doi.org/10.5772/64746

instability in such flows is often intimately coupled with chemical/nuclear reactions and heat release, most studies have focused on the inert flow configuration. Recently, RT instability development in premixed flames [49, 50] has been investigated theoretically and numerically, although the corresponding non-premixed reacting configuration has never been studied before. Owing to its significance in a wide range of applications, the non-reacting RT instability has been extensively investigated over the last five decades [1, 21, 51–54]. From this body of work, a consensus has emerged on the dynamics of the turbulent RT mixing layer. When initialized with a broad spectrum of modes, the resulting flow has been observed to be self-similar, with the width of the mixing layer evolving quadratically in time according to [2, 3, 54–56]

$$h_{b/s} = aAgt^2, \tag{2}$$

where the subscripts b(s) refers to the advancing bubble(spike) front, respectively, g is the acceleration due to gravity, A is the Atwood number,

$$A = \frac{\rho_h - \rho_l}{\rho_h + \rho_l} \tag{3}$$

and α is the growth rate of the mixing layer.

Recently, RT dynamics has been recognized to play a central role in the performance of combustors that rely primarily on centrifugal loading. Recent innovations in gas turbine design include a shift towards the use of ultra-compact combustors (UCC) [8, 9] that operate at high g-loading. UCCs greatly reduce the weight of the gas turbine engine, thus increasing the thrust to weight ratio. In addition, the compact size allows for the inclusion of a reheat cycle between turbines, thus increasing the efficiency of the system. Most common UCC designs involve the admission of fuel and oxidizer streams tangentially into the combustor chamber, while the g-loading is provided centrifugally through high-speed rotation. Such a configuration in which a non-premixed fuel and oxidizer interface is subjected to high g-loading (~ 10^4 g_0) is susceptible to the development of the Rayleigh-Taylor (RT) instability [51, 52] at the flame site. In spite of this central role, the nature of the interaction between the RT instability and the flame surface has been poorly understood. RT-dominated flames provide unique opportunities in the design and operation of modern combustors that cannot be realized through device designs that rely primarily on shear-driven mixing to enhance combustion. For instance, in the unstable regime, RT growth will eventually outpace corresponding Kelvin-Helmholtz (KH) growth leading to greater mixing and more efficient burning. Thus, while RT grows self-similarly as ~ t^2, the shear-driven KH flows evolve as ~ t (but with a decaying centerline velocity). Correspondingly, the outer scale Reynolds number associated with RT mix (defined as $Re \equiv \frac{h\dot{h}}{\nu}$, where h(t) is the mixing layer width, $\dot{h}$ is its growth rate and ν is the mixture viscosity) will evolve as $\mathbf{t^3}$, while

remaining constant for KH flows [56]. This can allow for more compact designs of combustors, but also render unnecessary, several commonly used active and passive mixing augmenters. Furthermore, the faster growth of *Re* in RT ensures the flame does not undergo relaminarization upon ignition due to the increased viscosities, a common affliction that impacts several reacting flows. In addition, we have also discovered from preliminary numerical simulations that when the fuel stream is suitably diluted, the flame region can act as a stabilizing layer that can partially suppress the growth of the instability. This effect can be exploited in practical combustors to anchor the flame when necessary or to increase the time for the fuel to burn allowing for cleaner combustion with lesser unburnt fuel.

We describe detailed direct numerical simulations of non-premixed flames that evolve under the influence of mixing from RT or RM instabilities. Thus, the flow configurations studied here provide a simple, yet powerful framework in which to understand a wide class of non-premixed flames. The flame is initiated and sustained by the mixing process resulting directly from RT and RM instabilities, so that the combustion efficiency is directly dependent on the performance of these hydrodynamic instabilities. Similarly, RM/RT instability development is affected by heat release and the dynamics associated with the flame. Such a two-way coupling between flame and flow has been labelled Level III mixing, and anticipated in [5], but the non-premixed problems studied here provide a simple and idealized framework to examine such interactions.

2. Numerical methods and simulation details

The simulations reported in this chapter were performed using the FLASH code developed by the FLASH Center for Computational Sciences at the University of Chicago [57, 58]. FLASH is a multi-physics, finite-volume, Eulerian code with a broad range of capabilities including adaptive mesh refinement (AMR) on a block-structured mesh, state-of-the-art hydrodynamics solvers, implicit solvers for diffusion that include thermal conduction, mass diffusion and viscosity [57–59]. FLASH is also capable of operating in both ILES [60] (implicit large eddy simulation) and DNS [61] (direct numerical simulation) modes, where the former approach is suited to handle shocks and sharp interfaces [57, 58], while the latter approach is preferred in describing small-scale features in turbulence [61]. Recent modifications [62, 63] to the FLASH code by the authors have rendered it capable of describing a wide range of chemically reacting flows of relevance to combustion phenomena as they occur in realistic applications, and are summarized below, while additional details are available in refs. [57, 58, 62].

FLASH solves the compressible Euler equations (2)–(4), written in conservative form [57]

$$\frac{d\rho}{dt} + \nabla.\left(\rho V\right) = 0, \tag{4}$$

http://dx.doi.org/10.5772/64746

$$\frac{d\rho V}{dt} + \nabla.\left(\rho VV\right) + \nabla P = \rho g, \tag{5}$$

$$\frac{d\rho E}{dt} + \nabla.\left[\left(\rho E + P\right)V\right] = \rho V.g \tag{6}$$

where g, ρ, V, P and E are the gravitational acceleration, density, velocity, pressure and the total energy per unit mass, respectively. The internal energy (e) is obtained independently from the following equation:

$$\frac{d\rho e}{dt} + \nabla.\left[\left(\rho e + P\right)V\right] - V.\nabla P = 0. \tag{7}$$

Finally, pressure is updated using an ideal gas equation of state (EOS) for γ-law fluids. Reacting flows involving multiple species are handled through a separate advection equation for each species 'i' in the system given by,

$$\frac{\partial \rho Y_i}{\partial t} + \nabla.\left(\rho Y_i V\right) = 0 \tag{8}$$

where Y_i is the mass fraction of species 'i'. The hydro solver embedded in FLASH solves the governing equations using a second order PPM or fifth order WENO schemes. Diffusive transport of mass, momentum and heat are implemented through a dedicated diffuse unit that (a) implicitly updates the primary variable or (b) enforces the diffusion effects through the so-called "flux-based" infrastructure which updated the fluxes of primary variables.

Special care is given to the treatment of sharp interfaces and fronts to avoid spreading due to numerical diffusion. The details of the flame front thickness relative to the turbulent length scales are important in determining product formation in reacting flows. FLASH uses a multi-step approach to modify the underlying PPM/WENO methods in regions of large gradients in the primary field variables (density or temperature) to guard against the numerical diffusion of such features. The strategy involves artificial contact steepening [57, 58] using high-order polynomials of the zone-averaged primary variable in regions identified by the algorithm as having large third derivatives.

To enable FLASH to handle chemically reacting flows with heat addition, the EOS unit has been expanded to incorporate multiple species with temperature-dependent properties. The updated EOS covers a temperature range of 298 K to 5000 K and calculates thermodynamic properties by applying 10 coefficients for each species in the mixture. The 9 species 19 step reversible reaction mechanism of Mueller et al. [64] has been implemented to describe H_2-O_2

combustion. Viscosity and thermal conductivity were calculated using combination averaging formulas given in ref. [65].

Thus, the computational tools employed here are capable of handling a variety of physics including gas-phase chemical kinetics, diffusive transport of mass, momentum, and heat, shocks, presence of sharp interfaces, multi-species mixtures and thermal radiation. The results of an extensive validation and convergence study were reported in ref. [62] for several flows through comparison with analytical solutions, and published numerical and experimental data. Our validation cases included advection of reacting and non-reacting fronts in 1D and 2D [66], comparison with experimental data of laminar premixed flames in a Bunsen burner configuration [67, 68] and comparison with DNS of shock-driven combustion of a spherical bubble [69].

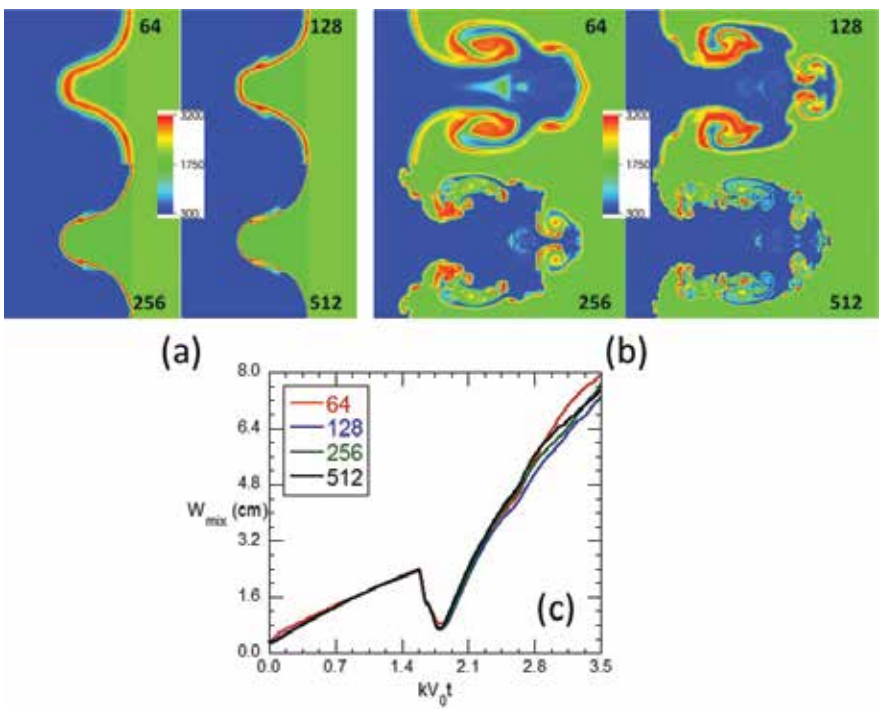

Figure 2. Temperature contours from simulations of a single-mode Richtmyer-Meshkov instability at a scaled time kV_0t = (a) 1.6 and (b) 3.0, at grid resolutions of 64 zones/λ, 128 zones/λ, 256 zones/λ and 512 zones/λ. (c) The corresponding width of the mixing zone is plotted against scaled time.

For all simulations reported here, detailed and systematic grid independence studies were performed. We summarize the results from one such study for the shock-accelerated RM problem described in Section 3. A sinusoidally perturbed (wavelength, $\lambda = 6$ cm), single-mode interface separating hydrogen (300 K) and oxygen (1625 K) was accelerated by a Mach 1.2 shock traversing from the light (H_2) to heavy (O_2) fluid (Atwood number = 0.5) in an aspect ratio 6 numerical shock tube (see [62] for details). The impulsive acceleration of the interface (ΔU)

triggers RM instability and the perturbed interface with initial amplitude (h_0 = 0.2/k, where $k = 2\pi/\lambda$) grows at a rate [11], $V_0 = \frac{dh}{dt} = kAh_0\Delta U$. The transmitted shock is reflected back from the end wall of the shock tube and interacts with the growing flame but this time processes a heavy-light interface at a scaled time kV_0t =1.6 (**Figure 2(a)**). Subsequently the interface undergoes a phase inversion followed by enhanced mixing due to the activation of higher harmonics and small-scale corrugations. **Figure 2** is a plot of temperature contours (a) before (kV_0t = 1.6) and (b) after (kV_0t = 3.0) reshock for grid resolutions of 64 zones/λ, 128 zones/λ, 256 zones/λ and 512 zones/λ. Simulations with zoning in excess of 64/λ are converged in terms of the gross features such as perturbation amplitude while the small-scale features retain some grid dependence as expected. In **Figure 2(c)** we plot the evolution of mixing width against scaled time for the four resolutions employed. Slight variations are observed at late times (kV_0t > 3), due to the appearance of small-scale, secondary instabilities which retain some grid dependence, while the amplitudes of penetration of the mixing layer have converged with respect to the grid resolution.

Finally, **Table 1** provides simulation details of the shock-bubble interaction problem, RM and RT instabilities.

	Domain size (cm)	Resolution	Mass diffusion	Thermal diffusion	Viscous diffusion
Shock-Bubble	3.0x1.5 ($x \times y$)	Uniform grid: 1280 × 640	Binary: $H_2 - O_2$	Combination averaging	Combination averaging
Richtmyer-Meshkov	36 × 6 × 6 ($x \times y \times z$)	Adaptive mesh: 1536 × 256 × 256	Numerical	Numerical	Numerical
Rayleigh-Taylor	24 × 8 × 8 ($x \times y \times z$)	Uniform grid: 768 × 256 × 256	Schmidt number = 0.75	Prandtl number = 0.75	Combination averaging

Table 1. Details of numerical simulations.

3. Results and discussion

An example of a typical configuration to investigate the interaction of a shockwave with a fuel bubble is shown in **Figure 1(a)**. In the numerical setup, a spherical hydrogen bubble moves towards and interacts with a stationary planar Mach 2 shock wave. The configuration for this 2D problem consists of a rectangular domain of dimensions 3 cm by 1.5 cm. The H_2 bubble diameter is 0.5 cm, while the stationary shock wave is located at x = 0.7. The hydrogen bubble approaches the shock with an ambient velocity U = 1.24e5 cm/s. The initial distance between the bubble surface and the shock is 0.2 mm, while the preshock temperature and pressure were specified to be 1000 K and 1 atm, respectively, for both air and hydrogen bubbles. The shocked

air on the left side of the domain is initialized with ambient velocity of $U_{shocked}$ = 4.3e4 cm/s, temperature of 1565 K and pressure of 4.4 atm. The mass fraction of the H_2 bubble as a function of radius is specified by [69]:

$$Y_{H_2} = \frac{1}{2}\left[1 + \tanh\left(\frac{r_c - r}{S}\right)\right] \tag{9}$$

$$r = \sqrt{\left(\left(x - x_0\right)^2 + \left(y - y_0\right)^2\right)} \tag{10}$$

where S represents the sharpness of the interface, r_c is the bubble radius and (x_0, y_0) determine the location of the bubble centre. As stated in ref. [62], S was chosen to be 3, which yields a value of 2.5e-2 cm for the initial interface thickness. As a result of the interaction between the shock wave and the bubble, shock waves travel towards the right outlet boundary at x=3 cm.

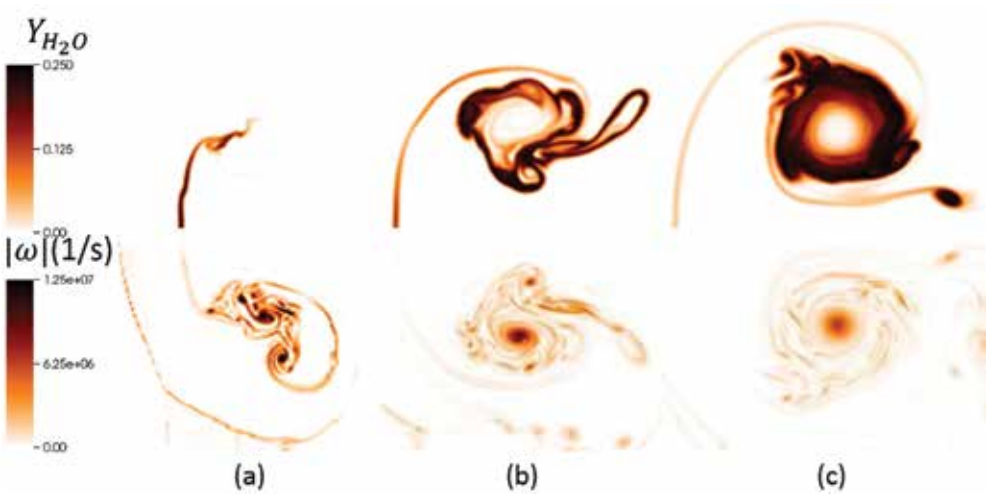

Figure 3. Time evolution of H_2O mass fraction (top panel) and magnitude of vorticity (bottom panel) from 2D simulations of a shock-bubble flame. Images are realized at t = (a) 10 μs, (b) 20 μs and (c) 40 μs.

Figure 3 shows contours of product (H_2O) mass fraction and magnitude of vorticity at different times in the evolution of the shocked fuel bubble. **Figure 3(a)** corresponds to 10 μs since shock impact and shows the onset of combustion has resulted in early product formation along the stem of the bubble. Vorticity contours reveal an organized vortex roll resulting from the baroclinic vorticity deposition from the shock interaction, and a counter-rotating counterpart (not shown). Thus, the bubble traverses under the induced velocity from the vortex ring. By t = 20 μs (**Figure 3(b)**), product formation is concentrated in a large reaction zone that is co-located with the vortex. The vorticity contour at this time shows the vorticity associated

http://dx.doi.org/10.5772/64746

with the primary rollup is now more organized in to a coherent structure. An interesting observation is that the product mass fraction appears to be concentrated along the rolled up vortex sheet, while the peaks of the vorticity are dominant within the core of the vortex structure. Thus, the reaction zones are concentrated along the rolled-up layers of vortex sheet that bring fuel and oxidizer surfaces into close contact, precipitating reaction and combustion. In contrast, the bulk of vorticity is concentrated in the vortex core and spreads from its peak value at this location due to diffusion. The images in **Figure 3(c)** correspond to t = 40 μs and show the distribution of vorticity has further diffused away from its peak value at the core. Contours of product mass fraction show the presence of H_2O has intensified within the outer layers of the vortex and is being sustained through a balance between production due to combustion and smearing due to mass diffusion.

We have investigated a variant of the RM instability, in which a planar shock interacts with a planar interface initially separating fuel and oxidizer streams. The advantage of this configuration is manifold and includes the ability to impose carefully formulated perturbations at the interface to control the progress of the turbulent mixing and the attendant flame dynamics. Furthermore, the simple geometry employed (absence of curvature effects found in the shock-bubble problem) implies that the flow is statistically isotropic and homogeneous in the two directions perpendicular to shock propagation. Thus, planar-averaged turbulent quantities may be represented as 1D functions in space and can be modelled using reduced-order 1D turbulence models.

We characterize the progress of the turbulent mixing in our simulations using the mixture fraction variable defined using [70]

$$Z = \frac{\left(\frac{Z_H}{2W_H} + \frac{Z_{O_a} - Z_O}{W_O}\right)}{\left(\frac{Z_{H_f}}{2W_H} + \frac{Z_{O_a}}{W_O}\right)}, \tag{11}$$

$$Z_H = W_H\left(\frac{2Y_{H_2}}{W_{H_2}} + \frac{Y_H}{W_H} + \frac{2Y_{H_2O}}{W_{H_2O}} + \frac{Y_{OH}}{W_{OH}} + \frac{Y_{HO_2}}{W_{HO_2}} + \frac{2Y_{H_2O_2}}{W_{H_2O_2}}\right),$$

$$Z_O = W_O\left(\frac{2Y_{O_2}}{W_{O_2}} + \frac{Y_O}{W_O} + \frac{Y_{H_2O}}{W_{H_2O}} + \frac{Y_{OH}}{W_{OH}} + \frac{2Y_{HO_2}}{W_{HO_2}} + \frac{2Y_{H_2O_2}}{W_{H_2O_2}}\right)$$

where Z_i, W_i and Y_i are the mixture fraction, molecular weight and mass fraction of species 'i', while Z_{O_a} and Z_{H_f} are the atomic mixture fraction of O and H evaluated in the air and fuel streams, respectively.

The mixture fraction defined from Eq. (11) is a conserved quantity in our reacting flow simulations and also remains monotonic across the mixing layer enabling a direct comparison

between the reacting and non-reacting flow simulations (quantities such as mass fractions are non-monotonic in reacting flows and cannot be used for this purpose). For instance, the *x*-locations of the 1 and 99% levels of the planar-averaged mixture fraction <Z> can be indicative of the extents of the mixing layer width and can be tracked in time to evaluate the growth rate of the turbulent mixing layer in both reacting and non-reacting flows. The initial interface is seeded by perturbations dominated by short wavelengths [3] and given by

$$h(y,z,t=0)=\sum_{k_y,k_z}\begin{bmatrix} a_k\cos(k_y y)\cos(k_z z)+ \\ b_k\sin(k_y y)\cos(k_z z)+ \\ c_k\cos(k_y y)\sin(k_z z)+ \\ d_k\sin(k_y y)\sin(k_z z) \end{bmatrix} \tag{12}$$

In our simulations, we evaluate Eq. (12) for an annular spectrum of wavenumbers (k_y, k_z) ranging from modes 16–32. We scale time according to $\tau = t\frac{A^+U}{\lambda_{min}}$, where $\lambda_{\min}$ is the shortest wavelength in the initial condition packet, U is the jump velocity acquired by the initially stationary interface as a result of shock impact (obtained from Rankine-Hugoniot jump conditions) and A^+ is the Atwood number across the mixing layer corresponding to post-shock conditions. The schematic details for the multimode RM problem are shown in **Figure 1(b)** and show the variegated interface separating fuel (H_2 at 300 K) and oxidizer (O_2 at 1000 K). The planar shock is initialized in the fuel stream, with a shock strength corresponding to Ma 1.2. Thus, the shock proceeds from a light to heavy fluid, so that the Atwood number is positive and is ~ 0.66. The impedance mismatch of the fluids involved in such an interaction is expected to result in reflected and transmitted shocks, which are processed by the outflow and reflecting boundary conditions, respectively. Thus, the transmitted shock from the first interaction is reflected from the endwall and is incident on the interface a second time. However, during this 'reshock' event, the 'incident' shock proceeds now from the heavy fluid (shocked O_2) to a light fluid (shocked H_2), so that the Atwood number for this interaction is −0.72. The heavy-to-light interaction produces a second transmitted shock in the H_2 stream, and a reflected rarefaction wave in the O_2 stream.

In **Figure 4(a,b)**, we show iso-surfaces of mixture fraction ranging from 1 to 99% at two critical instances in the evolution of the RM flame: early time following the first shock interaction (**Figure 4(a)**) and late time following the reshock event (**Figure 4(b)**). The iso-surfaces are coloured to indicate temperature variations across the mixing layer. At early time (τ = 16), dominant structures on the flamefront appear to be shorter in wavelength and are driven primarily by the baroclinic vorticity from the shock impact. The growth of these modes is also enhanced by a combustion wave that is generated during ignition, which accelerates the mixing front, while the pressure gradient associated with the expansion wave drives mode growth consistent with a short-lived variable-g RT phase. Across the mixing layer, regions of high temperature are visible and are predominantly organized as bubble and spike structures penetrating through the flame region. The maximum temperature is observed closer to the

http://dx.doi.org/10.5772/64746

stoichiometric surface and approaches ~3200 K, the expected adiabatic flame temperature for H_2–O_2 combustion.

At the late time ($\tau = 160$) shown in **Figure 4(b)**, the mixing region has been subjected to a second shock (the reshock event from the reflected shock) and shows the second shock has significantly transferred energy to large-scale structures. The initial condition for this second shock event is comprised of modes (structures) that are already non-linear and thus have saturated amplitudes. Thus the reshock event constitutes a finite-amplitude initialization of the RM instability, resulting in aggressive growth of already mature modes. This outcome is of consequence to the performance of scramjet engines which can be designed to expose the flame/mixing layer to multiple shock events, strategically positioned to maximize mixing and combustion efficiency, with the growth of the instability becoming more aggressive with each shock event. Temperature variations across the mixing layer at $\tau = 160$ are consistent with the presence of large-scale structures and are found to be organized with the dominant bubble and spike structures that penetrate the mixing layer and flame regions.

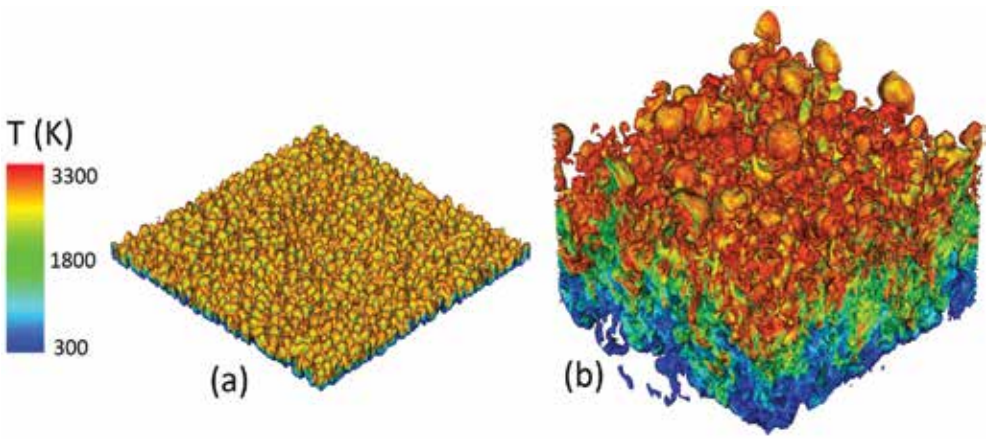

Figure 4. Time evolution of iso-surfaces of Z and the temperature distribution in the RM-driven flame (a) shortly after incident shock (τ= 16) and (b) at late time after the reshock (τ= 160).

We provide quantitative data from our reshocked RM simulation in **Figure 5**. The flame surface area was computed using a 3D numerical surface computation algorithm in the VisIt-2.9 software [71, 72] and is shown in **Figure 5** as a function of the non-dimensional RM time τ. When scaled with the square of the lateral shock tube dimension (L), the flame surface area shows significant increases shortly after the shock events at $\tau \approx 0$ and $\tau \approx 80$. In between these events, the surface area growth is gradual and consistent with the underlying power-law behaviour of the mixing layer width. Note that the surface area of the mixing layer is affected not just by the large scales (which develop as t^{θ}), but significantly by the presence of small-scale features which can be affected by diffusion and flame polishing. We

intend to examine these effects in detail in follow-up articles. In **Figure 5**, we also show the time evolution of the integrated heat release rate defined according to

$$\int_0^{L_x} < \dot{e}_{comb.} > dx, \tag{13}$$

where L_x and $\dot{e}_{comb}$ are length of computational domain in x-direction and heat release rate while the operator $< \bullet >$ indicates planar averaging in y-z direction. Peaks in the heat release rate correspond to significant ignition events that follow both the first and second shocks. Comparatively very little heat release is observed between such events.

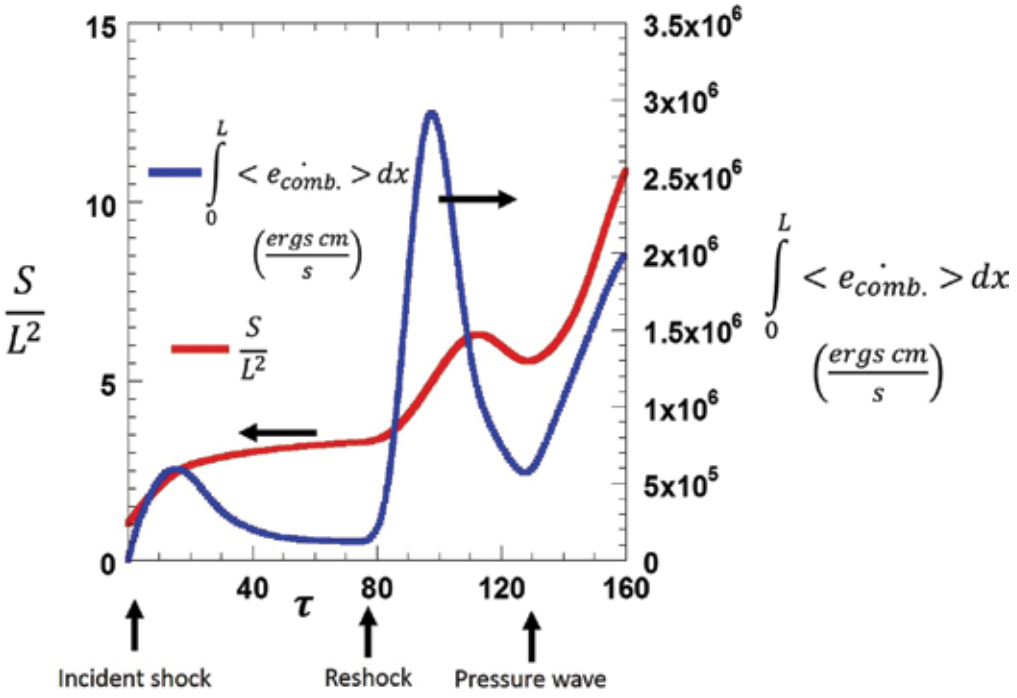

Figure 5. Evolution of flame surface area and integral heat release rate versus scaled time $\tau = t\frac{A^+U}{\lambda_{min}}$ from RM simulation.

We also discuss our recent results of the reacting Rayleigh-Taylor instability in a non-premixed flame setting. We present results from high resolution, Navier-Stokes simulations of a chemically reacting RT unstable interface separating hydrogen (fuel) and air under strong acceleration ($g = 6 \times 10^3 g_0$, where $g_0 = -981\ cm/s^2$), representative of conditions in ultra-compact combustion devices [8, 9]. The density ratio across the interface corresponds to an Atwood number of 0.6, while the temperature on the fuel and air side were specified uniformly to be 1000 K. Note that in our simulations, the fuel stream (H_2) was diluted with N_2, so that the

http://dx.doi.org/10.5772/64746

Atwood number and hence the density contrast driving the instability could be easily varied by adjusting the concentration of N_2. The simulations were initialized with a narrow spectrum of perturbation modes imposed at the interface, leading eventually to self-similarity and turbulence. A uniform grid (256 zones/L) was employed such that $\Delta x \sim \eta$ (Kolmogorov length scale) is sufficient to resolve [73, 74] late time turbulent flow field.

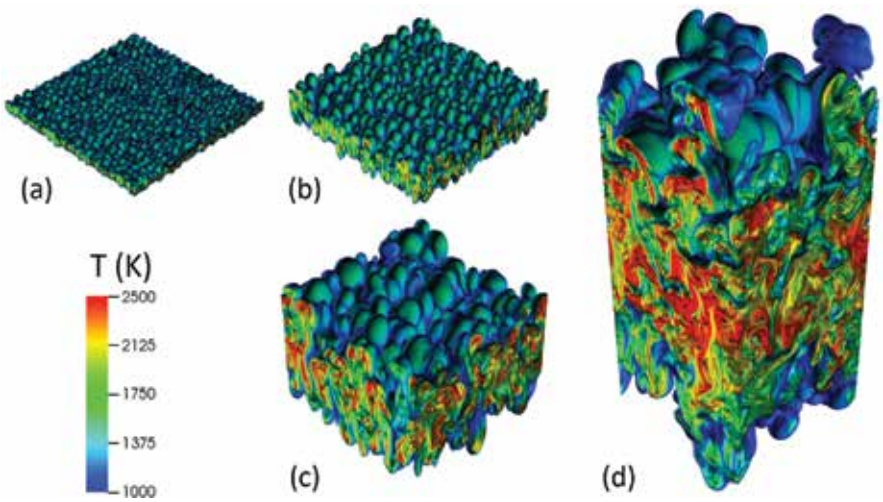

Figure 6. Time evolution of reacting RT instability at Agt^2/L = (a) 0.3, (b) 1.2, (c) 4.8 and (d) 19.2.

In **Figure 6**(**a–d**), we plot qualitative images from different stages of our reacting RT simulation, in a non-premixed configuration. The images show iso-surfaces of the mixture fraction Z (defined according to Eq. (11)), coloured by temperature. Note that for this fuel-oxidizer combination, and conditions investigated here, the flame sheet corresponds to Z ~ 12%, the stoichiometric iso-surface of mixture fraction. The timestamps are identified in terms of the RT-characteristic non-dimensional timescale Agt^2/L, where L is the spanwise extent of the computational domain. Through **Figure 6**(**a–d**), there is a clear progression in the development of RT to larger scales at the bubble and spike front. This is accompanied by ignition and combustion that results from the turbulent mixing process, and in turn affects it. The appearance of high temperature regions is visible within the internal layers of the turbulent mixing region, so that at late times, the flame sheet appears highly convoluted at both the large and small scales. The peak temperature within the RT mixing layer consistently reaches ~ 2500 K, approaching the adiabatic flame temperature for H_2-air combustion of ~2600.

In **Figure 7**, we plot quantitative data corresponding to the integral heat release rate and the total flame sheet surface area from our turbulent RT flame simulations. Interestingly, we find both quantities to scale with the characteristic non-dimensional timescale of the problem Agt^2/L. The heat release rate displays an early spike, corresponding to the first instance of ignition, likely caused due to diffusion across the initial interface. This is followed by a short-lived period during which both the heat release rate and the surface area grow rapidly in

response to the linear growth of perturbation modes imposed on the surface. However, following non-linear saturation and the onset of self-similarity (Agt^2/L ~ 3–5), an asymptotic growth rate is observed which appears to scale quadratically in time. We expect the surface area to be influenced by the square of the dominant wavelength $<\lambda>$ that deform the interface at any time, but also by intermediate scales such as the square of the Taylor microscales [1].

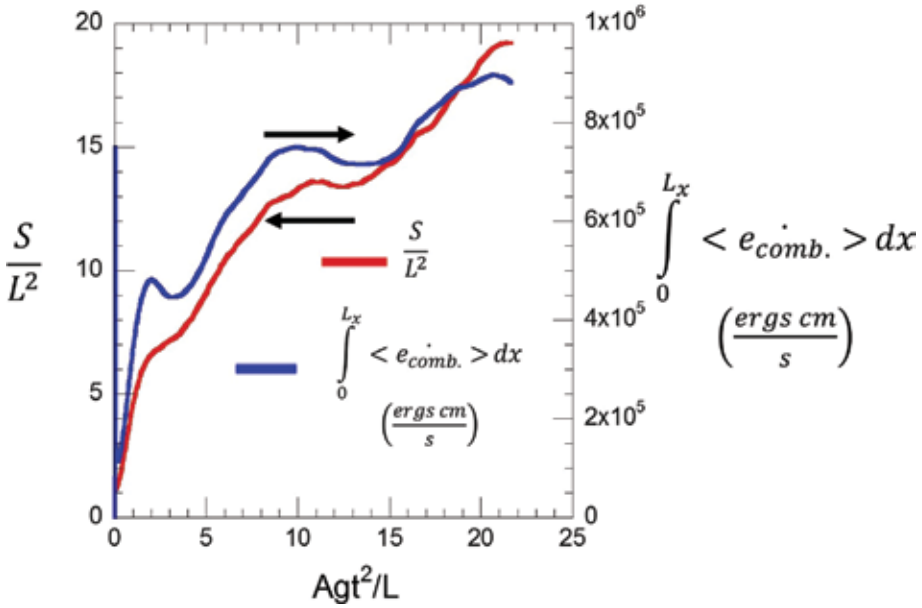

Figure 7. Evolution of flame surface area and integral heat release rate against Agt^2/L from reacting RT simulation.

4. Summary

In this chapter, we have reviewed historical progress and recent results in the area of combustion processes occurring in interfacial instabilities. While earlier efforts have focused on combustion associated with shear-driven instabilities (KH), the significance of baroclinically driven RM and buoyancy-driven RT instabilities to several combustor designs is gaining recognition. We have investigated these flows in a non-premixed setting using direct numerical simulations. Both RM and RT instabilities allow for aggressive growth and control of the combustion process through the turbulent mixing they engender between the fuel and oxidizer layers. In RM, the mixing can be controlled through several factors including the Atwood number, initial perturbations imposed at the interface and most significantly by reshocking the mixing layer at strategically chosen times. Similarly, the RT mixing and combustion can be manipulated through the Atwood number by modifying the level of N_2 dilution in the fuel stream. This is an effective strategy, since the N_2 is inert and does not affect the reaction kinetics, but can significantly alter the hydrodynamic mixing dynamics through the Atwood number.

The aggressive mixing and turbulence associated with these flows is beneficial since it can act to counter/delay the relaminarization process commonly observed in shear-driven flames due to increased viscosity following ignition. To address some of the above issues, we have defined novel formulations of RT and RM non-premixed combustion that can serve as canonical problems for this class of flows. The statistical isotropy and homogeneity in the plane of the interface implies the planar-averaged quantities associated with these flows can be represented as 1D functions, and thus can be used readily in reduced order turbulent combustion models. Our simulations also track quantities of interest to the turbulent combustion community such as the heat release rate and flame surface area, revealing a rich and complex array of phenomena associated with those quantities.

Acknowledgements

FLASH was developed by the DOE-sponsored ASC/Alliance Center for Astrophysical Thermonuclear Flashes at the University of Chicago. This research used resources of the Argonne Leadership Computing Facility, which is a DOE Office of Science User Facility supported under Contract DE-AC02-06CH11357.

Author details

Praveen Ramaprabhu*, Nitesh Attal and Hilda Varshochi

*Address all correspondence to: pramapra@uncc.edu

University of North Carolina at Charlotte, Charlotte, NC, USA

References

[1] W. H. Cabot and A. W. Cook, Nat. Phys. 2, 562 (2006).

[2] P. Ramaprabhu, V. Karkhanis, and A. G. W. Lawrie, Phys. Fluids 25, 115104 (2013).

[3] G. Dimonte *et al.*, Phys. Fluids 16, 1668 (2004).

[4] A. A. Gowardhan and F. F. Grinstein, J. Turbulence 12, 1 (2011).

[5] P. E. Dimotakis, Annu. Rev. Fluid Mech. 37, 329 (2005).

[6] S. B. Pope, *Turbulent flows* (Cambridge University Press, Cambridge, England, 2000).

[7] M. K. Smart, N. E. Hass, and A. Paull, AIAA J. 44, 2366 (2006).

[8] J. Zelina, D. T. Shouse, and R. D. Hancock, *ASME Turbo Expo 2004: Power Land, Sea, and Air* (ASME, Vienna, Austria, 2004), p. 53.

[9] D. Blunck *et al.*, *ASME Turbo Expo 2013: Turbine Tech. Conf. Exposition* (ASME, San Antonio, Texas, 2013), p. V01AT04A026.

[10] K. R. McManus, U. Vandsburger, and C. T. Bowman, Combust. Flame 82, 75 (1990).

[11] R. D. Richtmyer, Commun. Pure Appl. Math. 13, 297 (1960).

[12] E. E. Meshkov, Izv. Acad. Sci. USSR Fluid Dynamics 4, 101 (1969).

[13] M. Brouillette, Annu. Rev. Fluid Mech. 34, 445 (2002).

[14] N. J. Zabusky, Annu. Rev. Fluid Mech. 31, 495 (1999).

[15] S. Zhang, G. Peng, and N. J. Zabusky, J. Turbulence 6, 1 (2005).

[16] J. M. Picone and J. P. Boris, J. Fluid Mech. 189, 23 (1988).

[17] J. G. Wouchuk and K. Nishihara, Phys. Plasmas 4, 1028 (1997).

[18] S.-I. Sohn, Phys. Rev. E 67, 026301 (2003).

[19] V. N. Goncharov, Phys. Rev. Lett. 88, 134502 (2002).

[20] B. Thornber, D. Drikakis, and D. Youngs, Comput. Fluids 37, 867 (2008).

[21] D. L. Youngs, Laser Part. Beams 12, 725 (1994).

[22] S. K. Shankar, S. Kawai, and S. K. Lele, Phys. Fluids 23, 024102 (2011).

[23] B. Thornber, D. Drikakis, D. L. Youngs, and R. J. R. Williams, J. Fluid Mech. 654, 99 (2010).

[24] F. F. Grinstein, A. A. Gowardhan, and A. J. Wachtor, Phys. Fluids 23, 034106 (2011).

[25] G. Dimonte, G. Terrones, F. J. Cherne, and P. Ramaprabhu, J. Appl. Phys. 113, 024905 (2013).

[26] D. Ranjan, J. Niederhaus, B. Motl, M. Anderson, J. Oakley, and R. Bonazza, Phys. Rev. Lett. 98, 024502 (2007).

[27] B. J. Balakumar, G. C. Orlicz, C. D. Tomkins, and K. P. Prestridge, Phys. Scr. 2008, 014013 (2008).

[28] J. Kane, D. Arnett, B. A. Remington, S. G. Glendinning, G. Bazan, R. P. Drake, and B. A. Fryxell, Astrophys. J. Suppl. Ser. 127, 365 (2000).

[29] B. D. Collins and J. W. Jacobs, J. Fluid Mech. 464, 113 (2002).

[30] C. Tomkins, S. Kumar, G. Orlicz, and K. Prestridge, J. Fluid Mech. 611, 131 (2008).

[31] G. H. Markstein, *Nonsteady Flame Propagation* (Pergamon, Oxford, 1964).

[32] M. Gui, B. Fan, G. Dong, and J. Ye, Shock Waves 18, 487 (2009).

[33] Y. Ju, A. Shimano, and O. Inoue, in *Symp. (Int.) Combust*. (Elsevier, Boulder, Colorado, USA, 1998), pp. 735.

[34] G. A. Batley, A. C. McIntosh, and J. Brindley, Proc. R. Soc. London Ser. A 452, 199 (1996).

[35] H. H. Teng, Z. L. Jiang, and Z. M. Hu, Acta Mech. Sin. 23, 343 (2007).

[36] N. Haehn, D. Ranjan, C. Weber, J. Oakley, D. Rothamer, and R. Bonazza, Combust. Flame 159, 1339 (2012).

[37] A. M. Khokhlov, E. S. Oran, A. Y. Chtchelkanova, and J. C. Wheeler, Combust. Flame 117, 99 (1999).

[38] V. Kilchyk, R. Nalim, and C. Merkle, J. Fluids Eng. 135, 031203 (2013).

[39] J. Yang, T. Kubota, and E. E. Zukoski, AIAA J. 31, 854 (1993).

[40] R. G. Veraar, A. E. H. J. Mayer, J. Verreault, R. A. Stowe, R. Farinaccio, and P. G. Harris, *16th AIAA/DLR/DGLR Int. Space Planes Hypersonic Syst. Technol. Conf.* (Bremen, Germany, 2009), p. 8.

[41] J. D. Lindl, *Inertial Confinement Fusion: The Quest for Ignition and Energy Gain Using Indirect Drive* (Springer-Verlag, New York, 1998).

[42] M. Zingale, S. E. Woosley, C. A. Rendleman, M. S. Day, and J. B. Bell, Astrophys. J. 632, 1021 (2005).

[43] M. Herant, W. Benz, W. R. Hix, C. L. Fryer, and S. A. Colgate, Astrophys. J. 435, 339 (1994).

[44] C.-Y. Wang and R. A. Chevalier, Astrophys. J. 549, 1119 (2001).

[45] S. Zhong and M. T. Zuber, Earth Planet. Sci. Lett. 189, 75 (2001).

[46] B. D. Marsh and I. S. E. Carmichael, J. Geophys. Res. 79, 1196 (1974).

[47] C. S. Huang, M. C. Kelley, and D. L. Hysell, J. Geophys. Res. 98, 15631 (1993).

[48] W. A. Sirignano, D. Dunn-Rankin, F. Liu, B. Colcord, and S. Puranam, AIAA J. 50, 1645 (2012).

[49] A. Petchenko, V. Bychkov, V. Akkerman, and L.-E. Eriksson, Phys. Rev. Lett. 97, 164501 (2006).

[50] M. Chertkov, V. Lebedev, and N. Vladimirova, J. Fluid Mech. 633, 1 (2009).

[51] L. Rayleigh, *Scientific Papers II* (Cambridge University Press, Cambridge, England, 1900).

[52] G.I.Taylor, Proc. R. Soc. London, Ser. A 201, 192 (1950).

[53] G. Dimonte and M. Schneider, Phys. Rev. E 54, 3740 (1996).

[54] S. B. Dalziel, P. F. Linden, and D. L. Youngs, J. Fluid Mech. 399, 1 (1999).

[55] P. Ramaprabhu, G. Dimonte, and M. J. Andrews, J. Fluid Mech. 536, 285 (2005).

[56] P. Ramaprabhu and M. J. Andrews, J. Fluid Mech. 502, 233 (2004).

[57] B. Fryxell *et al*., Astrophys. J. Suppl. Ser. 131, 273 (2000).

[58] Flash User's Guide (University of Chicago) http://flash.uchicago.edu/site/flashcode/user_support/.

[59] A. Dubey, K. Antypas, M. K. Ganapathy, L. B. Reid, K. Riley, D. Sheeler, A. Siegel, and K. Weide, Parallel Comput. 35, 512 (2009).

[60] F. F. Grinstein, L. G. Margolin, and W. J. Rider, *Implicit Large Eddy Simulation: Computing Turbulent Fluid Dynamics* (Cambridge University Press, New York, 2010).

[61] P. Moin and K. Mahesh, Annu. Rev. Fluid Mech. 30, 539 (1998).

[62] N. Attal, P. Ramaprabhu, J. Hossain, V. Karkhanis, M. Uddin, J. R. Gord, and S. Roy, Comput. Fluids 107, 59 (2015).

[63] N. Attal and P. Ramaprabhu, Shock Waves 25, 307 (2015).

[64] M. A. Mueller, T. J. Kim, R. A. Yetter, and F. L. Dryer, Int. J. Chem. Kinet. 31, 113 (1999).

[65] S. Mathur, P. K. Tondon, and S. C. Saxena, Mol. Phys. 12, 569 (1967).

[66] G. Billet and R. Abgrall, Comput Fluids 32, 1473 (2003).

[67] X. Zhou, G. Brenner, T. Weber, and F. Durst, Int. J. Heat Mass Transfer 42, 1757 (1999).

[68] Q. V. Nguyen, R. W. Dibble, C. D. Carter, G. J. Fiechtner, and R. S. Barlow, Combust. Flame 105, 499 (1996).

[69] G. Billet, V. Giovangigli, and G. de Gassowski, Combust. Theor. Model. 12, 221 (2008).

[70] R. W. Bilger, in *Symp. (Int.) Combust*. (Elsevier, Pittsburgh, Pennsylvania, USA, 1989), pp. 475.

[71] E. W. Bethel, H. Childs, and C. Hansen, *High Performance Visualization: Enabling Extreme-Scale Scientific Insight* (CRC Press, Boca Raton, Florida, USA, 2012).

[72] VisIt, (Lawrence Livermore National Laboratory) http://www.llnl.gov/visit.

[73] J. H. Chen, Proc. Combust. Inst. 33, 99 (2011).

[74] R. Yu, X.-S. Bai, and A. N. Lipatnikov, J. Fluid Mech. 772, 127 (2015).

Chapter 14

Combustion Processes with External Harmonic Excitation using Extended Lindstedt-Poincare Method with Multiple Time Scales

Rudolf R. Pušenjak and Igor Tičar

Additional information is available at the end of the chapter

http://dx.doi.org/10.5772/63220

Abstract

This work treats the control of nonstationary pressure oscillations of combustion processes subject to external harmonic excitation. The low-order van der Pol model of nonstationary combustion processes with two degrees of freedom and a multiplicative feedback control function is considered. Nonstationary oscillations of the combustion process with asynchronous and synchronous excitation, respectively, are analyzed by means of the extended Lindstedt-Poincare (EL-P) method with multiple time scales. The steady-state amplitudes of competitive quenching with asynchronous excitation are not so much affected in comparison with steady-state amplitudes of an autonomous system, opposite to the synchronous excited system. The influence of control parameters on the quenching of the externally excited oscillations is investigated in details.

Keywords: combustion processes, pressure oscillations, external harmonic excitation, van der Pol model, EL-P method with multiple time scales, control

1. Introduction

The phenomenon of the instability of the combustion process is commonly explained by the nonstationary flame causing an acoustic wave, which reflects from the walls of the combustion chamber back to the combustion process. The thermoacoustic coupling between acoustic waves and unsteady heat release using a generalized energy equation, followed by feedback

INTECH
open science | open minds

© 2016 The Author(s). Licensee InTech. This chapter is distributed under the terms of the Creative Commons Attribution License (http://creativecommons.org/licenses/by/3.0), which permits unrestricted use, distribution, and reproduction in any medium, provided the original work is properly cited. CC BY

control concepts is presented by Dowling and Morgans [1]. Using theory of systems, this coupling can be explained alternatively by means of a feedback with a negative damping between the heat release process and acoustic wave propagation in the combustion chamber. The recent researches in the area of combustion process attempt to eliminate the unstable combustion and reduce the emission pollution, especially the emission of nitrogen-oxygen compounds at the same time. The reduction of pollution can be achieved by decreasing the fuel-to-air ratio; however, this causes the instability in the form of self-excited oscillations, which in general contain incommensurate frequencies. The problem of instability can be solved by the control of the fuel influx into combustion chamber, which can be realized by introduction of multiplicative control function performing the desired modulation of heat release rate. In order to obtain an efficient model of active control in this chapter, the reduced-order model of combustion instability process is proposed in the form of generalized, coupled van der Pol differential equations [2]. This model is built using a grey-box system approach [3], which is based on combination of physical knowledge determining the structure and identification of unknown parameter values, which are fitted to the measured input/output data of the system. In the proposed low-order model, the physics is present only in a feedback coupling between acoustic wave propagation and heat release giving rise to a negative damping as the cause of the combustion instability. The presented model of combustion instability is based on the linear acoustics and propagation of standing acoustic waves in the combustion chamber. Due to the presented nonlinear coupling between linear acoustics and nonlinear heat release rate, theoretically an infinite number of acoustic modes exist. Based on experimental results of Sterling [4] and Dunstan [3], the following analysis is considering the temporal variations of first two acoustic modes with corresponding natural frequencies. Unlike the models of Peracchio and Proscia [5], Dunstan and Murray et al. [6], respectively, natural frequencies in the present model can be incommensurate in general. From the system point of view, acoustic waves are modeled as pure linear oscillators and the heat release rate is modeled as the static nonlinearity, which can be accurately adapted to the real situation by identification of system parameters. On this basis, the model can be stated as a set of partial differential equations (PDEs) in terms of time scales, which are ideally suited to be attacked by the extended Lindstedt-Poincare (EL-P) method. The spatial scales are not present in the model, because it is assumed that all heat is released into the fluid at a point [5].

This chapter is organized as follows. In Section 2, the control structure and the governing coupled van der Pol equations of controlled combustion process with external harmonic excitation are presented. Section 3 applies the EL-P method with multiple time scales [7] to control problems of combustion process with asynchronous external harmonic excitation. Section 4 deals with control problems of combustion process with synchronous external harmonic force. Section 5 focuses on results and discussions of competitive quenching phenomenon. Section 6 discusses the validation of the proposed van der Pol model of combustion processes, and Section 7 outlines practical aspects of the model implementation. Section 8 contains conclusions.

http://dx.doi.org/10.5772/63220

2. Van der Pol model of combustion process with external harmonic excitation

In this section, the phenomenon of instability of the combustion process due to the feedback with negative damping is described by means of the low-order model, which consists of generalized two degrees of freedom (2-DOF) van der Pol oscillator with external harmonic excitation. The coupled van der Pol oscillator model is experimentally verified and it is possible to analyze the appearance of excited oscillations, which can evolve to limit cycles in accordance with experimental observations [8]. The dynamics of the generalized 2-DOF coupled nonautonomous van der Pol oscillator is governed by the following equation:

$$\frac{\mathrm{d}^2 y_i}{\mathrm{d}t^2} + {\omega_{ni}}^2 y_i = \varepsilon \frac{\mathrm{d}}{\mathrm{d}t}\left[\varphi_0 + \varphi_1\left(y_1 + y_2\right) - \frac{1}{3}\varphi_3\left(y_1 + y_2\right)^3\right] + F\cos\omega t, \quad \left(i = 1,2\right) \tag{1}$$

where the left-hand side of Eq. (1) models the linear acoustics of the combustion chamber represented by two harmonic oscillators with ω_{n1} and ω_{n2} being the natural frequencies of first two temporal pressure oscillation modes y_1 and y_2, respectively. The first term on the right-hand side of Eq. (1) models the nonlinear heat release process, where the sum y_1+y_2 denotes the temporal variations of the downstream pressure p at the burning plane and function $q = \varphi_0 + \varphi_1(y_1 + y_2) - \frac{1}{3}\varphi_3(y_1 + y_2)^3$ represents the flame heat release rate in dependence on pressure $p = y_1 + y_2$. Parameters φ_0, φ_1 and φ_3 are determined experimentally through system identification. The parameter φ_0 stands for a drift, which is different from zero, so that φ_0 is an arbitrary (positive or negative) constant. The parameter φ_1 is a slope of function q about origin, which corresponds to a positive constant. The term $-\frac{1}{3}\varphi_3(y_1 + y_2)^3$of the heat release rate static characteristic describes saturation phenomenon, where parameter $\varphi_3$determines the level of saturation. This level is also defined by a positive constant. The parameter ε is the gain of the heat release process. To justify the use of EL-P method in the analysis of combustion process, the feedback nonlinearity is assumed to be small. This requirement is achieved by multiplication of the time derivative of heat release rate by a small positive number ε>0. Note, that derivative term $\frac{\mathrm{d}q}{\mathrm{d}t} = \mathrm{d}\left[\varphi_0 + \varphi_1(y_1 + y_2) - \frac{1}{3}\varphi_3(y_1 + y_2)^3\right]/\mathrm{d}t$ on right-hand side of Eq. (1) represents a negative damping, which in the absence of external excitation can drive self-excited oscillations. Although temporal acoustic oscillations remain linear, nonlinearity occurs in the heat release rate, which affects the initial growth of excited oscillations until a limit cycle is reached due to the heat release saturation. The second term $F\cos\omega t$ on the right-hand side of Eq. (1) models the external harmonic excitation, where F is the excitation amplitude and ω is the excitation angular frequency. This term can be seen as a disturbance, which allows analyzing the system subjected to the noise. The proximity of excitation frequency ω to natural

frequencies ω_{n1} and ω_{n2}decides whether an interconnection between these frequencies exists. If the excitation frequency is far away of natural frequencies, all three frequencies are not interconnected and the system is driven by asynchronous force. On the other hand, when ω is close to one of two natural frequencies, there exists an interconnection between both frequencies and the system is driven by synchronous force. The thermoacoustic model of the combustion process is depicted in **Figure 2a**, where harmonic oscillators modeling acoustics are placed in two parallel forward branches and the heat release process is modeled in a feedback loop. On the basis of assumption about the spatial coherence, the proposed model captures the temporal variations of pressures and heat release rate, while the spatial distributions are omitted.

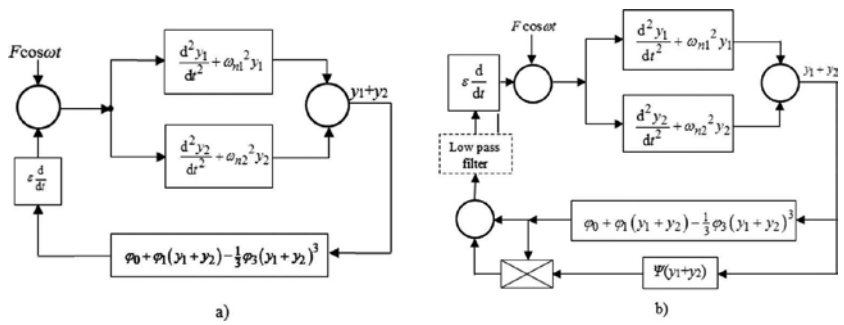

Figure 1. Van der Pol model of the combustion process with external harmonic excitation. (a) Model without control, (b) Model with control.

The coupled van der Pol oscillator in Eq. (1) can be represented by the control structure, shown on **Figure 1a**, where the control plant consists of two harmonic oscillators in forward branches, which are harmonically excited and the feedback consists of derivative of the flame heat release rate multiplied by ε. By expanding the derivative of the flame heat release rate, a negative damping term appears, which is the cause of instability of the combustion process. The instability is reflected in self-excited/driven oscillations, which evolve to the limit cycles. The limit cycle amplitudes are determined by the nonlinearity of the heat release rate function. The growing self-excited/driven oscillations can be so intense as to lead to a structural damage. To prevent such consequences, the control of oscillations can be introduced by means of multiplicative control function $\Psi(y_1 + y_2)$, which is based on measurement of pressure $p = y_1 + y_2$and placed in an additional feedback branch as shown in **Figure 1b**. Multiplicative control function $\Psi(y_1 + y_2)$ is chosen in order to achieve the modulation of a fraction of the fuel influx into the combustion chamber and consequently to affect the heat release rate. Thus, by applying the control function Ψ, the right-hand side of the governing Eq. (1) is modified in the form:

http://dx.doi.org/10.5772/63220

$$\frac{\mathrm{d}^2 y_i}{\mathrm{d}t^2} + {\omega_{ni}}^2 y_i = \varepsilon \frac{\mathrm{d}}{\mathrm{d}t}\left\{\left[1+\Psi\left(y_1+y_2\right)\right]\left[\varphi_0+\varphi_1\left(y_1+y_2\right)-\tfrac{1}{3}\varphi_3\left(y_1+y_2\right)^3\right]\right\} + F\cos\omega t,\ \ (i=1,2) \qquad (2)$$

The suitable candidates of control function $\Psi(y_1 + y_2)$ are sought in the form of polynomial functions of pressure $p = y_1 + y_2$. As suggested in reference [2], the control function $\Psi(y_1 + y_2)$ is proposed in the form:

$$\Psi\left(y_1+y_2\right) = -K_1\left(y_1+y_2\right) - \frac{K_2}{\varphi_0}\left[\varphi_1\left(y_1+y_2\right)-\tfrac{1}{3}\varphi_3\left(y_1+y_2\right)^3\right], \qquad (3)$$

where K_1 denotes the amplifying factor, which is of the same sign as the constant φ_0 and K_2 is a positive constant. Besides, the constant K_2 must be greater than unity, K_2>1, as is shown later. When both $K_1 = K_2 = 0$, the system is without the control. The low pass filter, shown in **Figure 1b**, is optional. Its role is discussed in details in the paper by Pušenjak et al. [2] and will not be repeated here. Due to the low-order van der Pol model of combustion process, the implementation of the control algorithm is very fast and the active control is very effective.

The stability analysis in the scope of the active control can be applied to reduce NO_x pollution by extending the stability domain of computed pressure oscillations [9]. By applying the presented model, a realistic modeling of the flame heat release rate is quite possible, when parameters φ_0, φ_1 and φ_3, respectively, are properly adjusted by using identification methods. By such an approach, the present method can be applied to model combustion instabilities in gas turbines with lean premixed combustors and power plants.

In the next section, the EL-P method with multiple time scales [7] is applied for computation of pressure oscillations with external harmonic excitation arising in the coupled nonautonomous van der Pol oscillator. For the sake of compactness, we introduce new parameters:

$$\begin{aligned}
&\gamma_0 = \varphi_0,\ \gamma_1 = -\left[K_1\varphi_0 + \left(K_2-1\right)\varphi_1\right],\ \gamma_2 = -\left(K_1 + \frac{K_2}{\varphi_0}\varphi_1\right)\varphi_1,\\
&\gamma_3 = \frac{1}{3}\left(K_2-1\right)\varphi_3,\ \gamma_4 = \frac{1}{3}\left(K_1 + \frac{2K_2}{\varphi_0}\varphi_1\right)\varphi_3,\ \gamma_5 \equiv 0,\ \gamma_6 = -\frac{1}{9}\frac{K_2}{\varphi_0}{\varphi_3}^2
\end{aligned} \qquad (4)$$

and rewrite governing equation (2) with control function (3) in the form:

$$\frac{\mathrm{d}^2 y_i}{\mathrm{d}t^2} + {\omega_{ni}}^2 y_i = \varepsilon \frac{\mathrm{d}}{\mathrm{d}t}\left[\sum_{j=0}^{6} \gamma_j \left(y_1 + y_2\right)^j \right] + F\cos\omega t, \quad (i = 1,2) \tag{5}$$

3. Application of the extended Lindstedt-Poincare method with multiple time scales in the combustion process with asynchronous external harmonic excitation

The instability problem of the combustion process, which is posed in the form of coupled van der Pol Eq. (5) with external harmonic excitation, can be analyzed by EL-P method with multiple time scales [2]. To provide a perturbation analysis of the generalized model of instability, it is assumed at first that interaction between both resonators and external harmonic excitation does not exist. In such a case, the natural frequencies ω_{n1} and ω_{n2} are arbitrary and do not meet any of the special conditions $\omega_{n1}=\omega_{n2}$, $\omega_{n1}=3\omega_{n2}$ or $\omega_{n1}=⅓\omega_{n2}$. In addition, it is assumed, that the excitation frequency ω is far away of both natural frequencies ω_{n1} and ω_{n2}. When these conditions are met, we say that such a combustion process is driven by asynchronous external harmonic force. As we will see, the pressure oscillations developed in this case are characterized by the phenomenon of the competitive quenching. In this phenomenon, one of the resonators is excited and oscillations of the other resonator are quenched in dependence on initial conditions. On the other side, the excited oscillations under special conditions $\omega_{n1}=\omega_{n2'}=3\omega_{n2}$ or $\omega_{n1}=⅓\omega_{n2}$correspond to the several kinds of interaction between both resonators, where mutual synchronization phenomenon with close frequencies or multiple harmonics, respectively, appears. Owing to the limited space, perturbation analysis of such oscillations will not be treated.

Following the EL-P method with multiple time scales, two fast time scales $\tau_1 = \omega_1 t$ and $\tau_2 = \omega_2 t$ are introduced, where ω_1 and ω_2 are termed the nonlinear frequencies of coupled van der Pol oscillators in accordance with Eq. (12). In addition, the time scale $\tau_3 = \omega t$, which corresponds to the excitation frequency ω and a slow time scale $\tau_4 = \varepsilon t$ with a small positive expansion parameter ε are introduced. Using time scales, the time derivatives $\mathrm{d}/\mathrm{d}t$ and $\mathrm{d}^2/\mathrm{d}t^2$ are replaced by differential operators:

$$\begin{aligned}
&\frac{\mathrm{d}}{\mathrm{d}t} = \omega_1 \frac{\partial}{\partial \tau_1} + \omega_2 \frac{\partial}{\partial \tau_2} + \omega \frac{\partial}{\partial \tau_3} + \varepsilon \frac{\partial}{\partial \tau_4}, \\
&\frac{\mathrm{d}^2}{\mathrm{d}t^2} = {\omega_1}^2 \frac{\partial^2}{\partial {\tau_1}^2} + {\omega_2}^2 \frac{\partial^2}{\partial {\tau_2}^2} + \omega^2 \frac{\partial^2}{\partial {\tau_3}^2} + \varepsilon^2 \frac{\partial^2}{\partial {\tau_4}^2} + 2\omega_1\omega_2 \frac{\partial^2}{\partial \tau_1 \partial \tau_2} \\
&+2\omega_1\omega \frac{\partial^2}{\partial \tau_1 \partial \tau_3} + 2\omega_1\varepsilon \frac{\partial^2}{\partial \tau_1 \partial \tau_4} + 2\omega_2\omega \frac{\partial^2}{\partial \tau_2 \partial \tau_3} + 2\omega_2\varepsilon \frac{\partial^2}{\partial \tau_2 \partial \tau_4} + 2\omega\varepsilon \frac{\partial^2}{\partial \tau_3 \partial \tau_4}
\end{aligned} \tag{6.a,b}$$

http://dx.doi.org/10.5772/63220

Owing linear acoustics, following substitutions are proposed:

$$y_i(\tau_1,\tau_2,\tau_3,\tau_4) = x_i(\tau_1,\tau_2,\tau_4) + E_i\cos\tau_3,\ (i=1,2) \tag{7.a}$$

$$E = E_1 + E_2 \tag{7.b}$$

and by using differential operators (6a, 6b), governing equations of the coupled van der Pol oscillators [Eq. (5)] are rewritten into partial differential equations:

$$\begin{aligned}&\omega_1{}^2\frac{\partial^2 x_i}{\partial\tau_1{}^2} + 2\omega_1\omega_2\frac{\partial^2 x_i}{\partial\tau_1\partial\tau_2} + \omega_2{}^2\frac{\partial^2 x_i}{\partial\tau_2{}^2} + \omega_{ni}{}^2 x_i = \left[F + \left(\omega^2 - \omega_{ni}{}^2\right)E_i\right]\cos\tau_3\\ &-\varepsilon\left(2\sum_{k=1}^{2}\omega_k\frac{\partial^2 x_i}{\partial\tau_k\partial\tau_4} + \varepsilon\frac{\partial^2 x_i}{\partial\tau_4{}^2}\right) + \varepsilon\left(\sum_{k=1}^{2}\omega_k\frac{\partial}{\partial\tau_k} + \omega\frac{\partial}{\partial\tau_3} + \varepsilon\frac{\partial}{\partial\tau_4}\right)\\ &\left[\sum_{j=0}^{6}\gamma_j\left(x_1 + x_2 + E\cos\tau_3\right)^j\right],\ (i=1,2)\end{aligned} \tag{8}$$

After performing indicated partial derivations, one obtains:

$$\begin{aligned}&\omega_1{}^2\frac{\partial^2 x_i}{\partial\tau_1{}^2} + 2\omega_1\omega_2\frac{\partial^2 x_i}{\partial\tau_1\partial\tau_2} + \omega_2{}^2\frac{\partial^2 x_i}{\partial\tau_2{}^2} + \omega_{ni}{}^2 x_i = \left[F + \left(\omega^2 - \omega_{ni}{}^2\right)E_i\right]\cos\tau_3\\ &-\varepsilon\left(2\sum_{k=1}^{2}\omega_k\frac{\partial^2 x_i}{\partial\tau_k\partial\tau_4} + \varepsilon\frac{\partial^2 x_i}{\partial\tau_4{}^2}\right) + \varepsilon\left[\sum_{j=1}^{6} j\cdot\gamma_j\left(x_1 + x_2 + E\cos\tau_3\right)^{j-1}\right]\\ &\left[\sum_{k=1}^{2}\omega_k\frac{\partial\left(x_1 + x_2\right)}{\partial\tau_k} + \varepsilon\frac{\partial\left(x_1 + x_2\right)}{\partial\tau_4} - \omega E\sin\tau_3\right],\quad (i=1,2)\end{aligned} \tag{9}$$

When the system is not subject of control, $K_1 = K_2 = 0$, then $\gamma_0 = \phi_0$, $\gamma_1 = \phi_1$, $\gamma_2 = 0$, $\gamma_3 = -\frac{1}{3}\phi_3$, $\gamma_4 = 0$, $\gamma_5 = 0$, $\gamma_6 = 0$ and Eq. (9) is simplified in the form:

$$\begin{aligned}&\omega_1{}^2\frac{\partial^2 x_i}{\partial\tau_1{}^2} + 2\omega_1\omega_2\frac{\partial^2 x_i}{\partial\tau_1\partial\tau_2} + \omega_2{}^2\frac{\partial^2 x_i}{\partial\tau_2{}^2} + \omega_{ni}{}^2 x_i = \left[F + \left(\omega^2 - \omega_{ni}{}^2\right)E_i\right]\cos\tau_3\\ &-\varepsilon\left(2\sum_{k=1}^{2}\omega_k\frac{\partial^2 x_i}{\partial\tau_k\partial\tau_4} + \varepsilon\frac{\partial^2 x_i}{\partial\tau_4{}^2}\right) + \varepsilon\left\{\left[\varphi_1 - \varphi_3\left(x_1 + x_2 + E\cos\tau_3\right)^2\right]\right.\\ &\left.\left(\sum_{k=1}^{2}\omega_k\frac{\partial\left(x_1 + x_2\right)}{\partial\tau_k} + \varepsilon\frac{\partial\left(x_1 + x_2\right)}{\partial\tau_4} - \omega E\sin\tau_3\right)\right\},\ (i=1,2)\end{aligned} \tag{10}$$

The approximate solution of Eq. (9) in dependence on three time scales τ_1, τ_2 and τ_4 is sought in the form of power series:

$$x_i = \sum_{k=0}^{\infty} \varepsilon^k x_{ik}(\tau_1, \tau_2, \tau_4), \qquad (i = 1,2) \tag{11}$$

Similarly, the nonlinear frequencies ω_i, (i=1,2) are expressed in the form of power series about linear frequencies ω_{10} and ω_{20}, respectively:

$$\omega_i = \sum_{k=0}^{\infty} \varepsilon^k \omega_{ik}(\tau_4), \qquad (i = 1,2) \tag{12}$$

where frequencies ω_{ik}, (i=1,2) of power series (12) may be slowly varying parameters in dependence on the slow time scale τ_4. Frequencies ω_{ik}, (i=1,2) are unknown in advance and must be determined successively during the perturbation procedure. As we will see later at perturbation step of zeroth order in Eq. (9), frequencies ω_{i0}, (i=1,2) are linearly dependent on natural frequencies ω_{ni} and thus are termed linear frequencies. Frequencies ω_{ik},($k \geq 1$) are determined at perturbation step of kth order from so-called solvability conditions and may be in general nonlinear functions of slowly varied amplitudes. Therefore, frequencies ω_i, (i=1,2) are termed nonlinear on the basis of Eq. (12). By substituting the assumed solution [Eq. (11)] and the power series [Eq. (12)] into Eq. (9) and then equating terms of equal power of ε on both sides of equation, one obtains a set of PDEs, which must be successively solved as perturbation steps of ascending order:

$$\varepsilon^0 : \ \omega_{10}^2 \frac{\partial^2 x_{i0}}{\partial \tau_1^2} + 2\omega_{10}\omega_{20} \frac{\partial^2 x_{i0}}{\partial \tau_1 \partial \tau_2} + \omega_{20}^2 \frac{\partial^2 x_{i0}}{\partial \tau_2^2} + \omega_{ni}^2 x_{i0} = \left[F + \left(\omega^2 - \omega_{ni}^2 \right) E_i \right] \cos \tau_3, \tag{13}$$

$$\begin{aligned} &\omega_{10}^2 \frac{\partial^2 x_{i1}}{\partial \tau_1^2} + 2\omega_{10}\omega_{20} \frac{\partial^2 x_{i1}}{\partial \tau_1 \partial \tau_2} + \omega_{20}^2 \frac{\partial^2 x_{i1}}{\partial \tau_2^2} + \omega_{ni}^2 x_{i1} = -2 \sum_{k=1}^{2} \omega_{k0} \left(\sum_{l=1}^{2} \omega_{l1} \frac{\partial^2 x_{i0}}{\partial \tau_k \partial \tau_l} + \frac{\partial^2 x_{i0}}{\partial \tau_k \partial \tau_4} \right) \\ \varepsilon^1 : \ &+ \left[\sum_{j=1}^{6} j \cdot \gamma_j \left(x_{10} + x_{20} + E \cos \tau_3 \right)^{j-1} \right] \left[\sum_{k=1}^{2} \omega_{k0} \frac{\partial (x_{10} + x_{20})}{\partial \tau_k} - \omega E \sin \tau_3 \right] \end{aligned} \tag{14}$$

http://dx.doi.org/10.5772/63220

$$\varepsilon^2:\quad \begin{aligned}
&\omega_{10}^{\,2}\frac{\partial^2 x_{i2}}{\partial\tau_1^2}+2\omega_{10}\omega_{20}\frac{\partial^2 x_{i2}}{\partial\tau_1\partial\tau_2}+\omega_{20}^{\,2}\frac{\partial^2 x_{i2}}{\partial\tau_2^2}+\omega_{ni}^{\,2}x_{i2}=-2\sum_{k=1}^{2}\omega_{k0}\left(\sum_{l=1}^{2}\omega_{l1}\frac{\partial^2 x_{i1}}{\partial\tau_k\partial\tau_l}+\frac{\partial^2 x_{i1}}{\partial\tau_k\partial\tau_4}\right)\\
&-2\sum_{k=1}^{2}\sum_{l=1}^{2}\omega_{k0}\omega_{l2}\frac{\partial^2 x_{i0}}{\partial\tau_k\partial\tau_l}-\frac{\partial^2 x_{i0}}{\partial\tau_4^{\,2}}-\sum_{k=1}^{2}\omega_{k1}\left(\sum_{l=1}^{2}\omega_{l1}\frac{\partial^2 x_{i0}}{\partial\tau_k\partial\tau_l}+2\frac{\partial^2 x_{i0}}{\partial\tau_k\partial\tau_4}\right)\\
&+\left[\sum_{j=1}^{6}j\gamma_j\left(x_{10}+x_{20}+E\cos\tau_3\right)^{j-1}\right]\left[\sum_{k=1}^{2}\omega_{k0}\frac{\partial\left(x_{11}+x_{21}\right)}{\partial\tau_k}+\sum_{k=1}^{2}\omega_{k1}\frac{\partial\left(x_{10}+x_{20}\right)}{\partial\tau_k}+\frac{\partial\left(x_{10}+x_{20}\right)}{\partial\tau_4}\right]\\
&+\left\{\left[\sum_{j=1}^{6}\left(j-1\right)j\gamma_j\left(x_{10}+x_{20}+E\cos\tau_3\right)^{j-2}\right]\left(x_{11}+x_{21}\right)\right\}\left[\sum_{k=1}^{2}\omega_{k0}\frac{\partial\left(x_{10}+x_{20}\right)}{\partial\tau_k}-\omega E\sin\tau_3\right]
\end{aligned}\tag{15}$$

for i=1,2.

The right-hand side of Eq. (13) is only a function of time scale τ_3, while the left-hand side of Eq. (13) contains dependencies on time scales τ_1, τ_2 and τ_4. Thus, both sides of Eq. (13) are independent on each other and the right-hand side must satisfy the condition $F + (\omega^2 - \omega_{ni}^2)E_i = 0$. According to the supposition, the excitation frequency ω is far away from each of natural frequencies ω_{ni}, (i=1,2) and amplitudes E_i, (i=1,2) of solution (7a) can be determined from this condition as:

$$E_i=\frac{F}{\left(\omega_{ni}^{\,2}-\omega^2\right)},\ \left(i=1,2\right)\tag{16}$$

As mentioned earlier, in such circumstances we have deal with the asynchronous case of external excitation. When the excitation frequency is close or equal to one of the natural frequencies, the corresponding amplitude E_i cannot be uniformly determined by means of Eq. (16). In this case, we have a synchronous excitation and the corresponding solution (7a) requires setting of the amplitude E_i equal to zero. The perturbation procedure for the synchronous excitation force will be treated in details in the next section. In the sequel, the general asynchronous case is analyzed.

The general solution of zeroth order, which allows two independent natural frequencies ω_{n1} and ω_{n2}, is sought in the form:

$$x_{i0}\left(\tau_i,\tau_4\right)=A_i\left(\tau_4\right)\cos\left[\tau_i+\Phi_i\left(\tau_4\right)\right],\qquad\left(i=1,2\right)\tag{17}$$

from where it follows that the self-excited/driven oscillations of coupled autonomous van der Pol oscillator, which correspond to the zero-order solution, are foreseen as almost periodic solutions with slowly varying amplitude and phase. Inserting assumed solutions into zero-order PDE gives an important relation between linear and natural frequencies of the oscillator:

$$-\omega_{i0}^{\,2}+\omega_{ni}^{\,2}=0\quad\Rightarrow\quad\omega_{i0}=\omega_{ni}\qquad\left(i=1,2\right)\tag{18}$$

which reveals, that linear frequencies are equal to the natural frequencies of the coupled van der Pol oscillator under assumption that linear frequencies can be only positive. Consequently, it follows from Eq. (12) that nonlinear frequencies ω_1 and ω_2 are independent in this case, too. By inserting the solution (17) into first-order PDE (14), one obtains:

$$\begin{aligned}
&\omega_{10}{}^2 \frac{\partial^2 x_{i1}}{\partial \tau_1{}^2} + 2\omega_{10}\omega_{20} \frac{\partial^2 x_{i1}}{\partial \tau_1 \partial \tau_2} + \omega_{20}{}^2 \frac{\partial^2 x_{i1}}{\partial \tau_2{}^2} + \omega_{ni}{}^2 x_{i1} \\
&= 2\omega_{i0}\left\{\left[\omega_{i1} + \Phi_i'(\tau_4)\right] A_i(\tau_4)\cos\left[\tau_i + \Phi_i(\tau_4)\right] + A_i'(\tau_4)\sin\left[\tau_i + \Phi_i(\tau_4)\right]\right\} \\
&-\left\{\sum_{j=1}^{6} j\cdot\gamma_j\left(\sum_{k=1}^{2} A_k(\tau_4)\cos\left[\tau_k + \Phi_k(\tau_4)\right] + E\cos\tau_3\right)^{j-1}\right\}\left\{\sum_{l=1}^{2}\omega_{l0}A_l(\tau_4)\sin\left[\tau_l + \Phi_l(\tau_4)\right] + \omega E\sin\tau_3\right\}
\end{aligned} \tag{19}$$

Secular terms on the right-hand side appear, which causes an unbounded increase of the solution. To obtain an uniform solution, secular terms must be removed. The elimination of secular terms is achieved by assembling terms, which appear at functions $\cos[\tau_i+\Phi_i(\tau_4)]$ and $\sin[\tau_i+\Phi_i(\tau_4)]$, ($i$=1,2), respectively, and equating obtained expressions by zero. This task is accomplished by symbolic computation in Mathematica® [2] and results in solvability conditions of first order:

$$2\omega_{i0}\,A_i(\tau_4)\left[\omega_{i1} + \Phi_i'(\tau_4)\right] = 0, \tag{20}$$

$$2\omega_{i0}\left\{A_i'(\tau_4) - \frac{1}{8}A_i(\tau_4)\left[4\gamma_1 + 3\gamma_3\left[A_i(\tau_4)^2 + 2\,A_{3-i}(\tau_4)^2 + 2E^2\right]\right]\right\} = 0 \tag{21}$$

for i=1,2. If the combustion process is not externally excited, the system of governing Eq. (9) is autonomous, where $p = 0$, $E_i = 0$, (i=1,2) and $E = 0$. By inserting expressions (4) for parameters γ_j, (j=1,…,6), solvability conditions (21) can be written in the form:

$$2\omega_{i0}\left\{A_i'(\tau_4) + \frac{1}{8}A_i(\tau_4)\left[4\left[K_1\varphi_0 + (K_2-1)\varphi_1\right] - (K_2-1)\varphi_3\left[A_i(\tau_4)^2 + 2\,A_{3-i}(\tau_4)^2\right]\right]\right\} = 0 \tag{22}$$

Solvability conditions, given by means of Eqs. (20) and (22) for an autonomous case, agree perfectly with solvability conditions of first order as were derived in reference [2].

From Eq. (20) it follows that trivial solution $A_1(\tau_4) = A_2(\tau_4) = 0$ always exists. In the case of nontrivial solution $A_i(\tau_4) \neq 0$, (i=1,2) one has:

$$\omega_{i1} + \Phi_i'(\tau_4) = 0\,, \quad (i = 1,2) \tag{23}$$

http://dx.doi.org/10.5772/63220

and frequencies ω_{i1}, which appear in Eq. (23) are unknown at this stage of approximation and their computation is deferred to the second-order approximation. The nontrivial solution $A_i(\tau_4) \neq 0$, (i=1,2) can be obtained by numerical integration of Eq. (21), although the closed form of solution is obtainable in exceptional cases [2].

The solution of Eq. (21) tends to reach the asymptotic values, when $\tau_4 \to \infty$. In this case, $\lim_{\tau_4 \to \infty} A'_i(\tau_4) = 0$ and steady-state solution $A_{i_s} = \lim_{\tau_4 \to \infty} A_i(\tau_4)$ can be obtained by solving equation:

$$4\gamma_1 A_{i_s} = -3\gamma_3 A_{i_s}\left[A_{i_s}{}^2 + 2A_{(3-i)s}{}^2 + 2E^2 \right], (i = 1,2) \tag{24}$$

where following possibilities exist: (i) a trivial solution $Ai_s = 0$, (i=1,2), (ii) a nontrivial solution $A_{i_s} \neq 0 \ \ (i = 1,2), A_{1_s} = \pm A_{2_s}, \quad A_{i_s}\big|_{1,2} = \pm\frac{2}{3}\sqrt{-\frac{\gamma_1}{\gamma_3} - \frac{3}{2}E^2}$ and (iii) a nontrivial solution $A_{i_s} \neq 0, \ \ (i = 1 \ \text{ or } \ 2)$, coupled with trivial solution $A_{(3\text{-}i)s} = 0$, where $i = 1$ or 2. The solution in this case is $A_{i_s}\big|_3 = \pm\sqrt{-\frac{4\gamma_1}{3\gamma_3} - 2E^2}, \quad A_{(3-i)_s}\big|_4 = 0$. By substituting expressions for constants γ_1 and γ_3, one obtains asymptotic values in explicit form:

$$A_{i_s}\big|_{1,2} = \pm 2\sqrt{\frac{K_1\varphi_0 + (K_2 - 1)\varphi_1}{3(K_2 - 1)\varphi_3} - \frac{1}{6}E^2}, \quad A_{i_s}\big|_3 = \pm 2\sqrt{\frac{K_1\varphi_0 + (K_2 - 1)\varphi_1}{(K_2 - 1)\varphi_3} - \frac{1}{2}E^2}, \quad A_{(3-i)_s}\big|_4 = 0 \tag{25}$$

From Eq. (25) it follows that by applying the control, the parameter K_2 may not take values in the range $0 < K_2 \leq 1$ in order to prevent complex roots or the divergent behavior of asymptotic values for $K_2 = 1$, respectively. Therefore, the parameter K_2 must be greater than unity, $K_2 > 1$. If control is not applied, both constants K_1 and K_2 are equal to zero, $K_1 = K_2 = 0$, giving the steady-state (asymptotic) values:

$$A_{i_s}\big|_{1,2} = \pm 2\sqrt{\frac{\varphi_1}{3\varphi_3} - \frac{1}{6}E^2}, \quad A_{i_s}\big|_3 = \pm 2\sqrt{\frac{\varphi_1}{\varphi_3} - \frac{1}{2}E^2}, \quad A_{(3-i)_s}\big|_4 = 0 \tag{26}$$

From Eqs. (25) and (26), respectively, it follows that all nontrivial steady-state values of the combustion process with external harmonic excitation are affected to some extent, when compared by asymptotic values of self-excited oscillations [asymptotic values of self-excited oscillations can be obtained by inserting value $E = 0$ into Eq. (25) or Eq. (26), respectively].

To proceed with the perturbation procedure, generally the almost periodic solution of the first order is constructed, which contains all possible combination tones and has the form:

$$x_{i1}(\tau_1,\tau_2,\tau_4)=\sum_{k=0}^{1}\sum_{m=1}^{3-k}\left(\sum_{j=0}^{2m-k}B^{i}_{m,(2m+1)k+j}(\tau_4)\sin\left[\sum_{n=1}^{2}\left[j+(n-1)(2m-2j-k)\right](\tau_n+\Phi_n(\tau_4))\right]+\right.$$
$$\left.\sum_{j=1}^{2m-k-1}C^{i}_{m,(2m-1)k+j}(\tau_4)\sin\left[\sum_{n=1}^{2}\left[j-(n-1)(2m-k)\right](\tau_n+\Phi_n(\tau_4))\right]\right),\quad (i=1,2) \tag{27}$$

Coefficients $B^{i}_{m,(2m+1)k+j}(\tau_4)$ and $C^{i}_{m,(2m-1)k+j}(\tau_4)$, respectively, can be computed by putting the solution (27) into Eq. (19), removing secular terms from its right-hand side and equating like terms on both sides.

The second-order approximation is constructed in the same manner as the first-order approximation. To do this, one inserts solutions (17) and (27) into second-order PDE (15). The right-hand side of the obtained equation contains secular terms, which must be removed to prevent the unbounded increase of the solutions. The elimination of secular terms, which appear at functions $\cos[\tau_i+\Phi_i(\tau_4)]$, ($i$=1,2), is again achieved by assembling terms and equating obtained expressions by zero. Because this task is extensive, it is accomplished by symbolic computation in Mathematica®. The resulting solvability conditions offer a relationship between unknown nonlinear frequencies ω_{i2}, (i=1,2) and coefficients $A_i(\tau_4)$, $B^{i}_{m,(2m+1)k+j}(\tau_4)$ and $C^{i}_{m,(2m-1)k+j}(\tau_4)$, respectively. Due to the lengthy formulas, they will not be presented here. The elimination of secular terms, which appear at functions $\sin[\tau_i+\Phi_i(\tau_4)]$, ($i$=1,2), respectively, and equating obtained expressions by zero, leads to solvability conditions:

$$\left\{A_i(\tau_4)\left[4K_1\varphi_0+(K_2-1)\left[4\varphi_1-\varphi_3\left[A_i(\tau_4)^2+2\left[A_{3-i}(\tau_4)^2+E^2\right]\right]\right]\right]+8A_i'(\tau_4)\right\}$$
$$\left[\omega_{i1}+\Phi_i'(\tau_4)\right]+4A_i(\tau_4)\Phi_i''(\tau_4)=0,\quad (i=1,2) \tag{28}$$

After determination of solvability conditions of the second order, the perturbation procedure may be continued with the computation of the second-order solution $x_{i2}(\tau_1,\tau_2,\tau_4)$. Under hypothesis of the small expansion parameter $\varepsilon \ll 1$, one observes, that this task is sometimes unnecessary on the basis of the following test. By computing frequencies ω_{i2}, (i=1,2) from solvability conditions at a given instant of the slow time scale, one can check if the terms $\varepsilon^2\omega_{i2}$ of the power series (12) are sufficiently small under the prescribed tolerance. If they are so on the entire interval of the slow time scale, then the first-order perturbation analysis is adequate. Now, by considering the solvability condition of the first order (20) for the nontrivial case $A_i(\tau_4)\neq 0$, (i=1,2), that is the simplified condition $\omega_{i1}+\Phi_i'(\tau_4)=0$ in Eq. (28), one obtains:

$$\Phi_i''(\tau_4)=0 \quad\Rightarrow\quad \Phi_i'(\tau_4)=\text{const.} \tag{29}$$

By considering the above result in solvability condition (20) again, it follows:

http://dx.doi.org/10.5772/63220

$$\omega_{i1} + \Phi_i'(\tau_4) = \omega_{i1} + \Phi_i'(0) = 0 \quad \Rightarrow \quad \omega_{i1} = -\Phi_i'(0), \quad (i = 1,2) \tag{30}$$

From Eq. (30), it follows that frequencies ω_{i1} are constant. Thus, Eq. (29) can be integrated as follows:

$$\Phi_i(\tau_4) = \Phi_i(0) - \int_0^{\tau_4} \omega_{i1} \mathrm{d}\tau_4 = \Phi_i(0) - \omega_{i1}\tau_4 \tag{31}$$

From Eq. (31), one concludes that strictly speaking, phases are linear, slowly varying functions of the time scale τ_4. However, keeping in mind the definition of the slow time scale $\tau_4 = \varepsilon t$, we can approximate Eq. (31) with $\Phi_i(\tau_4) \approx \Phi_i(0)$, which implies that derivatives of phase angles are equal to zero, $\Phi'_i(\tau_4) = \Phi'_i(0) = 0$. By considering this in Eq. (30) again, we finally obtain:

$$\omega_{i1} = 0, \quad (i = 1,2) \tag{32}$$

The obtained result simply means, that nonlinear frequencies ω_i of the first order analysis of van der Pol type nonlinear system can be approximated by the zero order term of Eq. (12). Thus by considering Eq. (18), nonlinear frequencies ω_i can be approximated by the corresponding natural frequencies ω_{ni}:

$$\omega_i = \omega_{i0} = \omega_{ni}, \ (i = 1,2) \tag{33}$$

Now, the following important observation can be made. Substituting Eq. (32) into Eq. (20) and assuming $K_1 = K_2 = 0$ in Eq. (22) to consider the uncontrolled case, the solvability conditions of the first order are simplified on the form:

$$\Phi_i'(\tau_4) = 0, \tag{34}$$

$$A_i'(\tau_4) - \frac{1}{8} A_i(\tau_4) \left[4\varphi_1 - \varphi_3 \left[A_i(\tau_4)^2 + 2 A_{3-i}(\tau_4)^2 + 2E^2 \right] \right] = 0 \tag{35}$$

for i=1,2. This result is exactly the same as derived by Krilov-Bogoliubov averaging method (K-B method) in Landau et al. [8] (with $\varepsilon = 1$, so that the slow time scale $\tau_4 = \varepsilon t$ in the present method corresponds to the time t in the K-B method). Consequently, there is no difference in computed zero order amplitudes and phases of pressure oscillations, regardless of whether presented EL-P method or Krilov-Bogoliubov averaging method, respectively is applied.

4. Application of the extended Lindstedt-Poincare method with multiple time scales in the combustion process with synchronous external harmonic excitation (ω close to ω_{n2})

In this section, the combustion process with synchronous external harmonic excitation is treated. Although we will assume in the sequel, that excitation frequency ω is close to the second natural frequency, $\omega \approx \omega_{n2}$, the case with $\omega \approx \omega_{n1}$ can be treated in an analogous way. To stress the nearness of the natural frequency ω_{n2} to the excitation frequency ω, we introduce the parameter Δ by means of equation:

$$\omega_{n2}^2 = \omega^2 + \left(\omega_{n2}^2 - \omega^2\right) = \omega^2 + \varepsilon\Delta, \quad \varepsilon\Delta = \omega_{n2}^2 - \omega^2 \tag{36}$$

where ε is the same small positive expansion parameter as appears in definition of the heat release process, Eq. (1). Opposite to the asynchronous case, the second mode must be driven by the soft harmonic excitation force, which is given in the form $\varepsilon f \cos \omega t$, ($F = \varepsilon f$). For convenience, the excitation frequency ω is renamed to ω_2 in order to reduce the number of time scales. With this device, three time scales $\tau_1 = \omega_1 t$, $\tau_2 = \omega_2 t = \omega t$ and $\tau_3 = \varepsilon t$ are used in the perturbation analysis. Under these conditions, the synchronization phenomenon can be described by means of equations:

$$\begin{aligned}&\omega_1^2 \frac{\partial^2 y_1}{\partial \tau_1^2} + 2\omega_1\omega_2 \frac{\partial^2 y_1}{\partial \tau_1 \partial \tau_2} + \omega_2^2 \frac{\partial^2 y_1}{\partial \tau_2^2} + \omega_{n1}^2 y_1 = F\cos\tau_2 + \varepsilon\left\{-\left(2\sum_{k=1}^{2}\omega_k \frac{\partial^2 y_1}{\partial \tau_k \partial \tau_3} + \varepsilon \frac{\partial^2 y_1}{\partial \tau_3^2}\right)\right.\\ &\left.+ \sum_{j=0}^{6} j\gamma_j \left(y_1 + y_2\right)^{j-1}\left[\sum_{k=1}^{2}\omega_k \frac{\partial\left(y_1 + y_2\right)}{\partial \tau_k} + \varepsilon \frac{\partial\left(y_1 + y_2\right)}{\partial \tau_3}\right]\right\}\end{aligned} \tag{37.a}$$

$$\begin{aligned}&\omega_1^2 \frac{\partial^2 y_2}{\partial \tau_1^2} + 2\omega_1\omega_2 \frac{\partial^2 y_2}{\partial \tau_1 \partial \tau_2} + \omega_2^2 \frac{\partial^2 y_2}{\partial \tau_2^2} + \omega_2^2 y_2 = \varepsilon\left\{f\cos\tau_2 - \left(2\sum_{k=1}^{2}\omega_k \frac{\partial^2 y_2}{\partial \tau_k \partial \tau_3} + \varepsilon \frac{\partial^2 y_2}{\partial \tau_3^2}\right)\right.\\ &\left.+\left[\sum_{j=0}^{6} j\gamma_j \left(y_1 + y_2\right)^{j-1}\right]\left(\sum_{k=1}^{2}\omega_k \frac{\partial\left(y_1 + y_2\right)}{\partial \tau_k} + \varepsilon \frac{\partial\left(y_1 + y_2\right)}{\partial \tau_3}\right) - \Delta y_2\right\}\end{aligned} \tag{37.b}$$

Equation (7.a) for the first mode, i=1, is now rewritten in the reduced form:

http://dx.doi.org/10.5772/63220

$$y_1(\tau_1,\tau_2,\tau_3) = x_1(\tau_1,\tau_3) + E_1\cos\tau_2 \tag{38}$$

where solution of PDEs (37.a,b) is sought by means of power series:

$$x_1(\tau_1,\tau_3) = \sum_{k=0}^{\infty}\varepsilon^k x_{1k}(\tau_1,\tau_3),\ y_2(\tau_2,\tau_3) = \sum_{k=0}^{\infty}\varepsilon^k y_{2k}(\tau_2,\tau_3),\ \omega_1 = \sum_{k=0}^{\infty}\varepsilon^k\omega_{1k}(\tau_3) \tag{39}$$

Performing perturbation steps, which are presented in details in the asynchronous case and finally assembling secular terms, which appear at functions $\cos[\tau_i+\Phi_i(\tau_3)]$ and $\sin[\tau_i+\Phi_i(\tau_3)]$, ($i$=1,2), respectively, one obtains following solvability conditions of first order:

$$2\omega_{10}A_1(\tau_3)\left[\Phi_1'(\tau_3)+\omega_{11}\right] = 0 \tag{40.a}$$

$$2\omega_2 A_2(\tau_3)\Phi_2'(\tau_3) - \Delta A_2(\tau_3) + f\cos\left[\Phi_2(\tau_3)\right] = 0 \tag{40.b}$$

$$2\omega_{10}\left\{\mathrm{A}_1'(\tau_3) - \tfrac{1}{8}\mathrm{A}_1(\tau_3)\left[4\gamma_1 + 3\gamma_3\left[\mathrm{A}_1^{\,2}(\tau_3) + 2\,\mathrm{A}_2^{\,2}(\tau_3) + 2E_1^{\,2}\right]\right]\right\} = 0 \tag{40.c}$$

$$2\omega_2\left\{\mathrm{A}_2'(\tau_3) + \tfrac{f}{2\omega_2}\sin\left[\Phi_2(\tau_3)\right] - \tfrac{1}{8}A_2(\tau_3)\left[4\gamma_1 + 3\gamma_3\left[\mathrm{A}_2^{\,2}(\tau_3) + 2\,\mathrm{A}_1^{\,2}(\tau_3) + 2E_1^{\,2}\right]\right]\right\} = 0 \tag{40.d}$$

Solvability conditions (40a) and (40c) for the first mode pressure oscillation, i=1, are little changed, when compared by solvability conditions (20) and (21), respectively for asynchronous excitation. Formally, amplitude $E = E_1+E_2$ in Eq. (21) must be replaced with $E = E_1$, (E_2 = 0) in solvability conditions (40c, 40d). However, solvability conditions (40b) and (40d) for the second mode pressure oscillation, i=2, are much more changed in comparison with asynchronous case. There is a substantial difference between phase courses $\Phi_1(\tau_3)$ and $\Phi_2(\tau_3)$ provided by solvability conditions (40a) and (40b), respectively. While Eq. (40a) produces a linear dependence of phase angle $\Phi_1(\tau_3)$ on the slow time scale τ_3 [compare Eq. (31) in Section 3], Eq. (40.b) produces a variable phase angle $\Phi_2(\tau_3)$ with complicated dependence on the slow time scale, which cannot be obtained analytically.

5. Results

In this section we investigate self-excited as well as externally driven oscillations of coupled van der Pol model of combustion processes. Besides this, the effect of the control in order to suppress the nonzero amplitude of the limit cycles is analyzed. The control function is activated, when the switching time t_{on} is reached, which is defined as the time when the slowly varying amplitude approaches a steady-state value within the prescribed tolerance range. The parameter *tol* is chosen to define the allowed tolerance range and has the value $tol = 10^{-6}$ in all examples, which are analyzed bellow. Inside the time interval $0 \le t < t_{on}$, the control is not active and both parameters K_1 and K_2 are zero valued ($K_1 = K_2 = 0$), while in the time interval $t_{on} \le t \le \infty$ the control is applied with a positive valued parameter K_2 and a gain factor K_1 with the same sign as the parameter ϕ_0. In what follows, results of the analysis of the competitive quenching phenomenon by using coupled van der Pol model of combustion process are presented. Although the presented general theory is valid for a small expansion parameter , the reasonable results can be computed even for the value of the expansion parameter $\varepsilon = 1$. Nevertheless, Lindstedt-Poincare method with multiple time scales can be modified with strong nonlinearities and large expansion parameter ε [10]. The parameters of the combustion process analyzed in this section have values: $\phi_0 = 0.5, \phi_1 = 1.78 \times 10^2, \phi_3 = 1.24 \times 10^7$ and $\varepsilon = 1$. Thus, the slowly time scale $\tau_4 = \varepsilon t$ can be replaced by the time t for the sake of simplicity. By using this agreement, dependencies of all variables on the slow time variable τ_4 are denoted in **Figures 2** and **3** as dependencies on the time t.

The phenomenon of competitive quenching arises, when nonlinear frequencies ω_1 and ω_2 do not have interconnection between itself nor between first odd subharmonic or first odd superharmonic, respectively. In other words, the phenomenon of competitive quenching appears, when ω_1 is not close to ω_2 nor $3\omega_2$ or $\frac{1}{3}\omega_2$. The general theory presented in Section 3

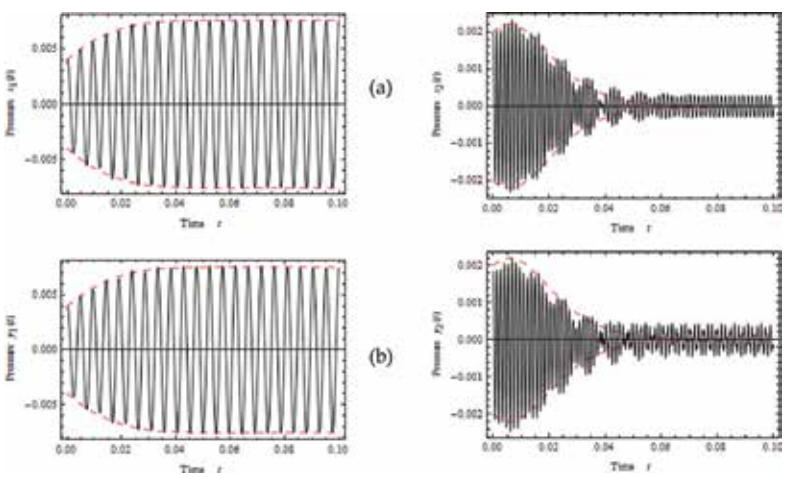

Figure 2. Comparison of pressure oscillation in the uncontrolled combustion process. (a) Pressures $x_1(t)$ and $x_2(t)$ without external excitation. (b) Pressures $y_1(t)$ and $y_2(t)$ with external harmonic excitation.— Oscillation computed by EL-P method. --- Envelope computed by EL-P method.

http://dx.doi.org/10.5772/63220

is applicable to this phenomenon on the whole, where important conclusions about the phenomenon are analyzed in details.

Characteristic for the competitive quenching phenomenon is excitation one of resonators, while oscillations of the other resonator are quenched in dependence on initial conditions. Such oscillations are analyzed in the case of natural frequencies $\omega_{n1} = 2\pi \times 210\ s^{-1}$, $\omega_{n2} = 2\pi \times 740\ s^{-1}$. The characteristic properties of the competitive quenching phenomenon at selected initial conditions $A_1(0) = 4 \times 10^{-3}$, $A_2(0) = 2 \times 10^{-3}$ are computed for the value of expansion parameter $\varepsilon = 1$ and are shown in **Figures 2** and **3**.

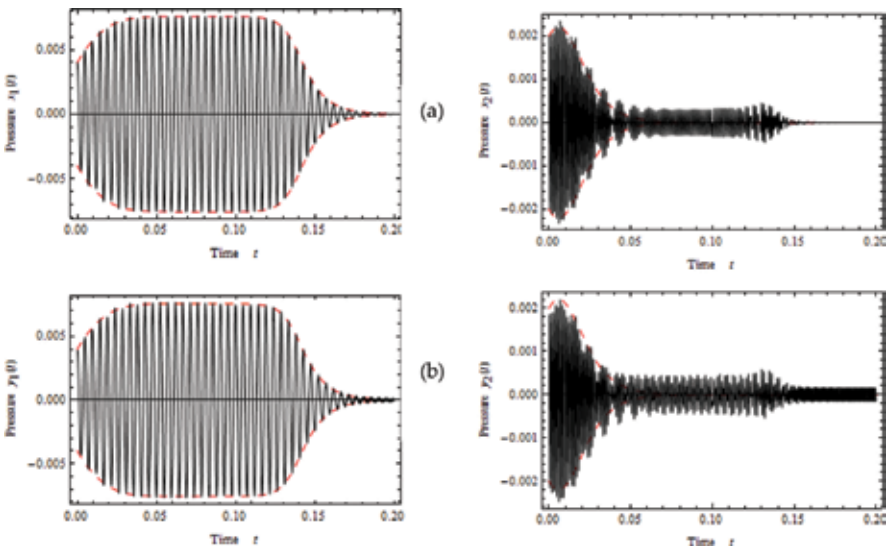

Figure 3. Comparison of pressure oscillation in the controlled combustion process. (a) Pressures $x_1(t)$ and $x_2(t)$ without external excitation. (b) Pressures $y_1(t)$ and $y_2(t)$ with external harmonic excitation. — Oscillation computed by EL-P method. --- Envelope computed by EL-P method.

The combustion process is first analyzed without applied control by setting the control parameters K_1 and K_2 to be equal to zero, $K_1 = K_2 = 0$. Computed pressure oscillations of combustion process without control are plotted in **Figure 2**. In **Figure 2a**, first- and second-mode pressure oscillations $x_1(t)$ and $x_2(t)$, respectively are shown, which are computed for the combustion process without external excitation. When external harmonic excitation is applied with excitation amplitude $f = 10^4$ and with corresponding excitation frequency $\omega = 2\omega_{n2}$, respectively, the corresponding pressure oscillations $y_1(t)$ and $y_2(t)$ look like on **Figure 2b**. Comparison of oscillations $x_1(t)$ and $y_1(t)$ shows, that external harmonic excitation has a very small impact on the first oscillation mode, so that differences are not visually observable. However, computation of steady-state amplitudes shows a small deviation. The steady-state amplitudes for the uncontrolled combustion process are computed by using Eq. (26), which determines the steady-state amplitude of harmonically excited response $y_1(t)$ by means of expression $A_{1_s}\big|_3 = \pm 2\sqrt{\varphi_1/\varphi_3 - E^2/2}$, while the steady-state amplitude of response $x_1(t)$

without the external excitation is obtained by the expression $A_{1_s}|_3 = \pm 2\sqrt{(\varphi_1/\varphi_3)}$. When harmonic excitation is not applied, $E = 0$, the steady-state amplitude is $A_{1_s}|_3 = \pm 0.007578$and with the applied harmonic excitation, the steady-state amplitude is $A_{1_s}|_3 = \pm 0.007568$. We can see, that the difference between steady-state values is very small, but the computed values can be approximately checked on **Figure 2**.

On the contrary, comparison of second mode oscillations $x_2(t)$ and $y_2(t)$ reveals significant differences. Steady-state amplitudes of both responses are in accordance with Eq. (26) equal to zero, $A_{2_s}|_4 = 0$. Zeroed steady-state amplitudes of second-mode oscillation can be seen in **Figure 2** by dashed curve, which presents the envelope of zero-order solution (17).

Combining zero-order solutions $x_{i0}(\tau_i, \tau_4)$ by using Eq. (17) and first-order solutions $x_{i1}(\tau_1,\tau_2,\tau_4)$ by Eq. (27), respectively, in power series (11), one obtains corresponding courses of self-excited oscillations $x_i(\tau_1,\tau_2,\tau_4) \approx x_{i0}(\tau_i, \tau_4)+\varepsilon\ x_{i1}(\tau_1,\tau_2,\tau_4)$, ($i$=1,2) for the combustion process without external excitation taking $E = 0$ into account. Self-excited time responses are plotted by continuous lines in **Figure 2a**.

On contrary, harmonically excited counterparts are computed by means of Eqs. (7a, 7b), where Eq. (11) is considered in approximation $x_i(\tau_1,\tau_2,\tau_4) \approx x_{i0}(\tau_i, \tau_4)+\varepsilon\ x_{i1}(\tau_1,\tau_2,\tau_4)$, ($i$=1,2). The corresponding time responses are plotted by continuous lines in **Figure 2b**. The most important difference occurs between second-mode time responses $x_2(t)$ and $y_2(t)$, respectively, after the passage of the transient phenomenon.

While transient self-excited oscillation $x_2(t)$ without external harmonic excitation expires in a sinusoidal oscillation with corresponding limit cycle, transient oscillation $y_2(t)$ with external harmonic excitation expires in a composite oscillation of aperiodic nature.

As is clearly seen from **Figure 2**, the amplitudes of oscillations x_i and y_i, respectively, slightly differ from the zero-order amplitudes $A_1(\tau_4)$, $A_2(\tau_4)$ due to the first-order contributions $x_{i1}(\tau_1,\tau_2,\tau_4)$, ($i$=1,2) added to the zero-order solutions $x_{i0}(\tau_i, \tau_4)$. Thus, the first-order contributions are of the moderate size than the zero-order solutions, and it can be expected that the contributions of the second-order solutions $x_{i2}(\tau_1,\tau_2,\tau_4)$, ($i$=1,2) are still smaller and thus can be neglected. From this reason, it follows that the first-order EL-P analysis is sufficient even if the expansion parameter takes the value $\varepsilon = 1$.

The characteristic properties of the competitive quenching phenomenon depicted in **Figure 3** indicate the effect of the applied fuel influx control on the combustion process. The control is activated in the switching time t_{on}, which is computed by means of the numerical integration of solvability conditions (22) until amplitudes $A_1(\tau_4)$, $A_2(\tau_4)$ approach the steady-state values, $A_{1_s}|_3 = \pm 2\sqrt{\varphi_1/\varphi_3 - E^2/2}$ $A_{(3\text{-}i)s}|_4 = 0$ within the tolerance range $tol = 10^{-6}$. By activating the control function in the switching time $t_{on} = 0.1$, which is determined in a way as is described, the values of control parameters are changed to $K_1 = 0.5$, $K_2 = 2$.

http://dx.doi.org/10.5772/63220

Figure 3 shows the courses of slowly varying amplitudes $A_1(\tau_4)$, $A_2(\tau_4)$, drawn by dashed lines, while the corresponding pressure oscillations $x_i(\tau_1,\tau_2,\tau_4) \approx x_{i0}(\tau_i,\tau_4)+\varepsilon\, x_{i1}(\tau_1,\tau_2,\tau_4)$, ($i$=1,2) without external excitation and responses y_i with external harmonic excitation, respectively, are drawn by continuous lines.

From **Figure 3a**, it follows that pressure oscillations x_i(t) without external excitation are successfully quenched to zero after the activation of the control in the switching time t_{on} = 0.1.

On contrary, **Figure 3b** reveals that quenching of pressure oscillations $y_i(t)$ after the activation of the control is not perfect, because a small composite oscillation of aperiodic nature remains due to the constantly present external harmonic excitation. However, the remaining oscillation with very small amplitude is acceptable.

6. Validation of the van der Pol model of combustion processes

In the combustion chamber, theoretically an infinite number of acoustic modes of pressure wave propagation can exist. However, experimental researches of combustion processes, done by Sterling [4] and Dunstan [3], indicate the existence of two dominant longitudinal acoustic modes with corresponding natural frequencies. This fact validates the choice of 2-DOF van der Pol model of combustion processes, proposed in this chapter. Another experimentally verified feature of acoustic modes is occurrence of incommensurate natural frequencies [8]. Considering this feature in the proposed van der Pol model leads to the multiple time scales concept. Due to the strong nonlinear coupling, various combination tones emanate in addition to dominant natural frequencies. As mentioned in Section 3, first-order solution in Eq. (27) contains all possible combination tones with 21 corresponding Fourier coefficients $B^i_{m,\,(2m+1)k+j}(\tau_4)$ and 11 Fourier coefficients $C^i_{m,\,(2m-1)k+j}(\tau_4)$, respectively, for both modes (i=1,2), which must be determined. Computation of Fourier coefficients using EL-P method is validated by comparison with K-B method [2]. By considering all combination tones of Eq. (27) in K-B method, an exact agreement of computed coefficients in both methods is found.

The choice of the van der Pol model of combustion processes is justified especially due to the existence of limit cycles. Limit cycles in combustion process arise as a result of heat release saturation. This feature of the van der Pol model is particularly valuable because it allows to predict the highest level of the acoustic pressures by means of the calculation of the steady-state values, see Eq. (25). The static characteristic of the heat release process is described by means of the generalized nonlinearity of van der Pol type, which includes the saturation term. The generalized static characteristic of heat release rate contains three parameters φ_0, $\varphi_1$and φ_3, respectively, which must be determined by identification methods so as to provide the best matching with a real heat release process.

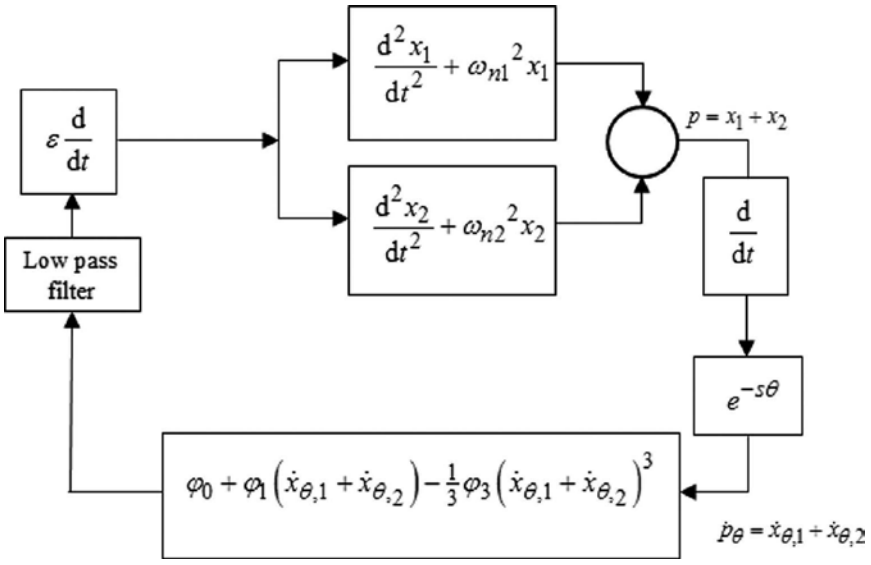

Figure 4. Van der Pol model of the combustion process with transport time delay θ.

A further validation can be obtained by modification of van der Pol model to consider a transport time delay θ from nozzle to flame surface of combustion processes. For this purpose, the time delay, differentiator block and low pass filter are included in the feedback path of a modified van der Pol model as is depicted in **Figure 4**. To show the effect of the time delay on self-excited pressure oscillations and to determine the steady-state values, external excitation is omitted, because we know now, that its influence is small. On the other side, the computational effort in such an analysis is much smaller.

In accordance with the proposed structure, the van der Pol model in **Figure 4** is described by governing equations:

$$\frac{d^2x_i}{dt^2} + \omega_{ni}{}^2 x_i = \varepsilon \frac{d}{dt} LPF\left[\varphi_0 + \varphi_1\left(\dot{x}_{\theta,1} + \dot{x}_{\theta,2}\right) - \frac{1}{3}\varphi_3\left(\dot{x}_{\theta,1} + \dot{x}_{\theta,2}\right)^3\right], \quad (i = 1,2) \tag{41}$$

where $\dot{p}_\theta = \dot{x}_{\theta,1} + \dot{x}_{\theta,2}$ is the time derivative of pressure $p = x_1 + x_2$ at the burning plane, which is delayed for a time delay θ and *LPF* denotes the action of the low pass operator on the heat release process.

By performing the EL-P procedure as described in Section 3, one obtains the following set of PDEs:

$$\varepsilon^0 : \omega_{10}{}^2 \frac{\partial^2 x_{i0}}{\partial \tau_1{}^2} + 2\omega_{10}\omega_{20} \frac{\partial^2 x_{i0}}{\partial \tau_1 \partial \tau_2} + \omega_{20}{}^2 \frac{\partial^2 x_{i0}}{\partial \tau_2{}^2} + \omega_{ni}{}^2 x_{i0} = 0 \tag{42}$$

http://dx.doi.org/10.5772/63220

$$\varepsilon^1: \quad \begin{aligned} &\omega_{10}{}^2 \frac{\partial^2 x_{i1}}{\partial \tau_1{}^2} + 2\omega_{10}\omega_{20} \frac{\partial^2 x_{i1}}{\partial \tau_1 \partial \tau_2} + \omega_{20}{}^2 \frac{\partial^2 x_{i1}}{\partial \tau_2{}^2} + \omega_{ni}{}^2 x_{i1} = -2\sum_{k=1}^{2} \omega_{k0} \left(\sum_{l=1}^{2} \omega_{l1} \frac{\partial^2 x_{i0}}{\partial \tau_k \partial \tau_l} + \frac{\partial^2 x_{i0}}{\partial \tau_k \partial \tau_4} \right) \\ &+ \sum_{k=1}^{2} \omega_{k0} \frac{\partial}{\partial \tau_k} \left\{ LPF\left[\varphi_0 + \varphi_1 \left(\sum_{k=1}^{2} \omega_{k0} \frac{\partial \left(x_{\theta,10} + x_{\theta,20} \right)}{\partial \tau_k} \right) - \frac{1}{3} \varphi_3 \left(\sum_{k=1}^{2} \omega_{k0} \frac{\partial \left(x_{\theta,10} + x_{\theta,20} \right)}{\partial \tau_k} \right)^3 \right] \right\} \end{aligned} \quad \vdots\vdots \quad (43)$$

Low pass filter is linear and the filter dynamics is assumed to be much faster than the slowly varying amplitudes and phases in dependence on the slow time scale τ_4 (the index $_4$ in τ_4 is retained here for convenience). Because the time delay θ can be assumed small, amplitudes and phases are considered independent of delay (that is $A_{\theta,i}(\tau_4) = A_i(\tau_4)$ and $\Phi_{\theta,i}(\tau_4) = \Phi_i(\tau_4)$). Under this assumption, the zero-order solution of Eq. (42) reads:

$$x_{i0}(\tau_i, \tau_4) = A_i(\tau_4)\cos\left[\tau_i + \Phi_i(\tau_4)\right], \quad x_{\theta,i0}(\tau_i, \tau_4) = A_i(\tau_4)\cos\left[\tau_i + \Phi_i(\tau_4) - \omega_{i0}\theta\right], \quad (i = 1,2) \quad (44)$$

The low pass filter produces The gain $G(\omega)$ and the phase shift $\phi(\omega)$ at the phase shift at the specified frequency ω and affects the input signal in accordance with the following relationship:

$$\begin{aligned} &LPF\left[x_{i0}(\omega)\right] = G(\omega) A_i(\tau_4)\cos\left[\tau_i + \Phi_i(\tau_4) - \phi(\omega)\right], \\ &LPF\left[x_{\theta,i0}(\omega)\right] = G(\omega) A_i(\tau_4)\cos\left[\tau_i + \Phi_i(\tau_4) - \omega_{i0}\theta - \phi(\omega)\right] \end{aligned} \quad (45a,b)$$

By means of zero-order solutions (44), one deduces the following solvability conditions for elimination of secular terms in Eq. (43):

$$\begin{aligned} 2\omega_{i0} \mathrm{A}_i(\tau_4)\left[\omega_{i1} + \Phi_i'(\tau_4)\right] = G(\omega_{i0})\omega_{i0}{}^2 A_i(\tau_4)\cos\left[\omega_{i0}\theta + \phi(\omega_{i0})\right] \\ \times\left[\varphi_1 - \tfrac{1}{4}\varphi_3\left[\omega_{i0}{}^2 A_i{}^2(\tau_4) + 2\omega_{(3-i,0)}^2 A_{(3-i)}^2(\tau_4)\right]\right], \end{aligned} \quad (46)$$

$$\begin{aligned} 2\omega_{i0}\Bigg\{ \mathrm{A}_i'(\tau_4) - \frac{1}{8} G(\omega_{i0})\omega_{i0}^2 \mathrm{A}_i(\tau_4)\sin\left[\omega_{i0}\theta + \phi(\omega_{i0})\right] \\ \times\left[4\varphi_1 - \varphi_3\left[\omega_{i0}^2 \mathrm{A}_i(\tau_4)^2 + 2\omega_{(3-i,0)}^2 \mathrm{A}_{(3-i)}^2(\tau_4)\right]\right]\Bigg\} = 0 \end{aligned} \quad (47)$$

Equations (46) and (47) determine the evolution of slowly varying amplitudes $A_i(\tau_4)$ and phases $\Phi_i(\tau_4)$, respectively. By comparing solvability conditions in Eqs. (20) and (22) (with $K_1 = K_2 = 0$!), one can conclude that evolution of amplitudes and phases, respectively, is strongly influenced by the transport time delay θ as well as by the transfer function of the low pass

filter. This influence is reflected in the change of nontrivial steady-state values. Besides trivial steady-state values $A_{1_S} = A_{2_S} = 0$ the following nontrivial steady-state values are obtained from Eq. (47):

$$(a) \quad A_{1_s} = \frac{2}{\omega_{10}}\sqrt{\frac{\varphi_1}{3\varphi_3}}, \quad A_{2_s} = \frac{2}{\omega_{20}}\sqrt{\frac{\varphi_1}{3\varphi_3}} \tag{48}$$

$$(b) \quad A_{i_S} = \frac{2}{\omega_{i0}}\sqrt{\frac{\varphi_1}{\varphi_3}}, \quad A_{(3-i)_S} = 0, \quad (i = 1,2) \tag{49}$$

The obtained results show that steady-state values of first- and second-mode pressure oscillations depend inversely on the values of natural frequencies $\omega_{ni} = \omega_{i0}$[see Eq. (33)]. This outcome is extremely valuable in prediction of the highest level of the acoustic pressures and is in accordance with experimental observations [8].

7. Implementation of the van der Pol model of combustion processes

To eliminate growing combustion oscillations, the coupling between acoustic waves and the unsteady heat release must be interrupted by applying the control. To reach this goal, passive and active control methods are enforced. The passive control is effective in a limited range of operating conditions and design changes are usually expensive and time consuming. Earlier concepts of active control of combustion instabilities used loudspeakers to increase surface losses in a combustor [1]. The lack of loudspeaker actuators is insufficient robustness for use in industrial applications and prohibitive power requirements at large-scale combustion systems. The recent development of active control seeks to achieve a stable operation regime of a full-scale combustion system. The proposed van der Pol model of combustion processes applies a recent concept of an active feedback control of the heat release by controlling the fuel flow rate. The control function is multiplicative and is realized with the modulation of the injection of the fuel flow. The properties of a good actuation can be reached by the use of fuel valve with a linear response characteristic, large bandwidth and operating range to achieve the effective control of two oscillation modes and to affect limit cycle oscillation. In addition, the fuel valve should have a fast response time, good robustness and durability; however, it should not have hysteresis behavior.

Sensors are generally provided to measure the dynamic quantities, which are related to the combustion oscillations. In the present model, the pressure of the acoustic wave and the fuel flow are measured quantities, which are acquired by means of the pressure transducers and sensors, which measure the light emission of some chemicals in the flame or by chemiluminescence sensors, respectively. The use of pressure transducers is advantageous, because they can be installed outside the area of high temperatures at the burning plane on account of

http://dx.doi.org/10.5772/63220

acoustic wave propagation across the entire combustion chamber. Pressure transducers have large bandwidth and a good robustness. The placement of pressure transducers is important, because the location of the possible pressure node must be avoided and on other side, the signal-to-noise ratio must be maximized.

Recent development in the heat release sensing offers the use of diode lasers. Earlier, they had been used for temperature measurements, but recently they can directly measure fuel concentrations. A comprehensive review of this topic is given in [9].

The proposed van der Pol model of combustion processes is based on the grey-box principle. This means that the controller must be designed on system measurements. The instability of the combustion process may have severe consequences, which makes measurement a difficult task. Due to existence of two oscillation modes, which span over a wide frequency range, the controller must be able to control both modes. The combustion process almost always involves time delays caused by fuel convection and acoustic wave propagation. When such a delay becomes larger than an oscillation period, assumptions made in Section 6 are violated and provide a great challenge to the controller design [11].

8. Conclusions

In this chapter, the EL-P method with multiple time scales is successfully applied to the analysis of instability problem in the combustion process with external harmonic excitation, which is modeled by means of coupled van der Pol oscillator. By applying the control of the fuel influx, the asphyxiation of pressure oscillations is reached and studied in the phenomenon of the competitive quenching.

The solvability conditions of the first order in EL-P method are derived, which determines slowly varying amplitudes and phases as well as steady-state values. With external harmonic excitation, both limit cycle oscillations and compound oscillations can be successfully suppressed to the acceptable level by using the multiplicative feedback control.

Author details

Rudolf R. Pušenjak[1*] and Igor Tičar[2]

*Address all correspondence to: rudolf.pusenjak@fini-unm.si

1 Faculty of Industrial Engineering Novo mesto, Novo Mesto, Slovenia

2 University of Maribor, Faculty of Electrical Engineering and Computer Science, Maribor, Slovenia

References

[1] Dowling A. P., Morgans A. S. "Feedback control of combustion oscillations." *Annu. Rev. Fluid Mech*. 37: 151-182, 2005.

[2] Pušenjak R. R., Tičar I., Oblak M. M. "Self-excited oscillations and fuel control of a combustion process in a Rijke tube." *Int. J. Nonlin. Sci. Num*. 15(2): 87-106, 2014.

[3] Dunstan W. J. System Identification of Nonlinear Resonant Systems. PhD thesis, University of California, San Diego, 2003.

[4] Sterling J. D. "Nonlinear analysis and modelling of combustion instabilities in a laboratory combustor." *Combust. Sci. Tech*. 89: 167-179, 1993.

[5] Peracchio A. A., Proscia W. M. "Nonlinear heat-release/acoustic model for thermoacoustic instability in lean premixed combustors." *ASME J. Eng. Gas Turbines Power*. 121(3): 415-421, 1999.

[6] Murray R. M., Jacobson C. A., Casas R., Khibnik A. I., Johnson C. R. Jr., Bitmead R., Perachio A. A., Proscia W. M. "System identification for limit cycling systems: a case study for combustion instabilities." *American Control Conference Proceedings*, 1998.

[7] Pušenjak R. R. "Extended Lindstedt-Poincare method for non-stationary resonances of dynamical systems with cubic non-linearities." *J. Sound Vib*. 314(1-2): 194-216, 2008.

[8] Landau I. D., Bouziani F., Bitmead R. R., Voda-Besançon A. "Analysis of control relevant coupled nonlinear oscillatory systems." *Eur J. Control*. 14(4): 263-282, 2008.

[9] Docquier N., Candel N. "Combustion control and sensors: a review." *Prog. Energy. Combust. Sci* . 28: 107-150, 2002.

[10] Pušenjak R. R., Oblak M. M., Tičar I. "Modified Lindstedt-Poincare method with multiple time scales for combination resonance of damped dynamical systems with strong non-linearities." *Int. J. Nonlin. Sci. Num*. 11(3): 173-201, 2010.

[11] Cohen J. M., Banaszuk A. "Factors effecting the control of unstable combustors." *J. Prop. Power*. 19(5): 811-821, 2003.

Chapter 15

Solution Combustion Synthesis: Applications in Oxide Electronics

Rita Branquinho, Ana Santa, Emanuel Carlos,
Daniela Salgueiro, Pedro Barquinha,
Rodrigo Martins and Elvira Fortunato

Additional information is available at the end of the chapter

http://dx.doi.org/10.5772/64761

Abstract

Oxide-based electronics have been well established as an alternative to silicon technology; however, typical processing requires complex, high-vacuum equipment, which is a major drawback, particularly when targeting low-cost applications. The possibility to deposit the materials by low-cost techniques such as inkjet printing has drawn tremendous interest in solution processible materials for electronic applications; however, high processing temperatures still required. To overcome this issue, solution combustion synthesis has been recently pursued. Taking advantage of the exothermic nature of the reaction as a source of energy for localized heating, the precursor solutions can be converted into oxides at lower process temperatures. Theoretically, this can be applied to any metal ions to produce the desired oxide, opening unlimited possibilities to materials' composition and combinations. Solution combustion synthesis has been applied for the production of semiconductor thin films based on ZnO, In_2O_3, SnO_2 and combinations of these oxides, and also for high κ dielectrics (Al_2O_3). All of which are required for numerous electronic devices and applications such as fully oxide-based thin-film transistors (TFTs). The properties of produced thin films are highly dependent on the precursor solution characteristics; hence, the influence of several processing parameters; organic fuel, solvent and annealing temperature was studied. Although precursor solution degradation/oxide formation mechanisms are not yet fully understood, particularly for thin films, we demonstrate that high-performance devices are obtained with combustion solution-based metal oxide thin films. The results clearly show that solution combustion synthesis is becoming one of the most promising methods for low-temperature flexible electronics.

Keywords: solution processing, combustion synthesis, environmentally friendly, metal oxide materials, thin-film transistors, semiconductor oxides, dielectric oxides

INTECH
open science | open minds

© 2016 The Author(s). Licensee InTech. This chapter is distributed under the terms of the Creative Commons Attribution License (http://creativecommons.org/licenses/by/3.0), which permits unrestricted use, distribution, and reproduction in any medium, provided the original work is properly cited. CC BY

1. Introduction

1.1. Solution combustion synthesis

Solution combustion synthesis (SCS) is a popular method for the preparation of a wide variety of materials due to its simplicity, broad range of applicability and the possibility of easily obtaining products in the desired composition. This method has been widely used for the development of oxide powder materials; including perovskites, spinels, ferrites; for diverse applications, such as catalysis and solid oxide fuel cells [1–3] and is becoming one of the most convenient methods for the preparation of simple and multicomponent oxides for electronic applications [4].

SCS is based on a redox system that requires a solution that upon heating to moderate temperatures leads to the development of a strongly exothermic redox reaction, which generally provides the energy for the metal oxide formation. The ignition temperature of the exothermic reaction is significantly lower than the final combustion temperature which results in the material formation; thus allowing the conversion of solution precursors into oxides at lower process temperatures [1–3].

The precursor solution for combustion synthesis is typically constituted by metal nitrates, which are employed simultaneously as metal source and oxidizing agents, and an organic fuel that acts as a reducing agent. However when using metal chlorides, as a metal ion source, a combustion aid is required to provide the oxidizing nitrate ions; in this case, ammonium nitrate is typically used. The most frequently applied fuels are urea, acetylacetone and glycine, amongst others, since these can form stable complexes with metal ions to increase solubility and prevent selective precipitation of the metal ions in solution. This process produces oxide materials of good compositional homogeneity, which is especially important in the synthesis of multicomponent oxides. Historically, water is the most widely used solvent for the combustion synthesis of powder materials [1–3]. Recently, the pursuit of environmental friendly solvents for electronic applications, such as ethanol and water, is growing [5–7]; however, organic solvents, including 2-methoxyethanol and acetonitrile, are currently the most widely used for the production of oxide thin films for electronic applications purposes [5].

The resulting solution is then heated to evaporate the solvent and when ignition temperature is reached the exothermic reaction takes place. During the combustion reaction, the fuel is oxidized by the nitrate ions. The precursor materials are converted into the metal oxide, and gaseous H_2O, CO_2 and N_2 are the remaining products formed in the combustion reaction. This process can in theory be applied to any desired metal ion.

The solution combustion synthesis of a metal oxide can be represented by the combination of metal nitrate decomposition reaction and fuel oxidation reaction. As an example, respective equations for the combustion synthesis of Al_2O_3 from aluminium nitrate and using urea as fuel are given as follows [Eq. (1) and (2)] [6].

http://dx.doi.org/10.5772/64761

$$2Al\left(NO_3\right)_3.9H_2O \rightarrow Al_2O_3 + 18H_2O + 3N_2 + \left(\frac{15}{2}\right)O_2 \quad (1)$$

$$5CO\left(NH_2\right)_2 + \left(\frac{15}{2}\right)O_2 \rightarrow 10H_2O + 5CO_2 + 5N_2 \quad (2)$$

The overall combustion reaction can thus be written as Eq. (3)

$$2Al\left(NO_3\right)_3.9H_2O + 5CO\left(NH_2\right)_2 \rightarrow Al_2O_3 + 10H_2O + 5CO_2 + 8N_2 \quad (3)$$

Note that these are theoretical reaction equations that do not consider possible secondary reactions such as nitrates decomposition, urea hydrolysis, thermal decomposition and also fuel-oxidizer adducts; however, the overall reaction allows the calculation of a stoichiometric condition that can be used as a reference [3, 6].

There are many essential variables in solution combustion synthesis, including metal ion, metal precursor type and concentration, content of organic fuel, combustion aid and oxidizer/fuel proportion; which is determinant for the thermodynamics of the oxide formation [2].

A concept for determining the stoichiometric proportion of oxidizer and fuel for SCS was adopted from the Jain method [8], which is based on propellant chemistry and allows the calculation of the reducing/oxidizing valences (OV/RV) of a redox mixture. In this method, oxygen and nitrogen are considered oxidizers with the respective valence of −2 and 0. On the other hand, carbon, hydrogen and metal ions are considered as reducing elements with their final valences of +4 and +1 and the corresponding metal valence, respectively. Consequently, urea has a reducing valence of +6 (RV = 4 + 4 × 1 + 2 × 0 − 2) whilst aluminium nitrate has an oxidizing valence of −15 (OV = 3 + 2 × 0 − 3 × 6), resulting in a 15/6 (or 5/2) reducing/oxidizing valences for an optimal stoichiometric redox mixture of urea-aluminium nitrate.

The relation between the redox stoichiometry and the molar ratio of reagents can be determined by the reducing/oxidizing valences (RV/OV) of the reagents and is given by Eq. (4)

$$\Phi = \frac{RV}{OV}n \quad (4)$$

The oxygen consumption or production is controlled by the fuel/oxidizer ratio (Φ) which also depends on n; the number of moles of fuel per mole of oxidizer [1–3]. The optimal stoichiometry composition of the redox mixture is obtained for $\Phi = 1$ that corresponds to a condition in which the reaction does not require any molecular oxygen to occur. For the given example of urea-aluminium nitrate redox mixture, 5 moles of urea are required per 2 moles of aluminium nitrate to assure redox stoichiometry of the aluminium oxide formation reaction, as depicted in Eq. (3) [6].

A fuel-lean condition is obtained when $\Phi < 1$ and upon reaction molecular oxygen is produced; whereas when $\Phi > 1$ molecular oxygen is required to fully convert the fuel and the redox mixture is in a fuel-rich regime [3].

1.2. Solution-based oxide electronics

The evolution from rigid silicon-based electronics to flexible electronics requires the use of new materials with novel functionalities that allow non-conventional, low-cost and environmental friendly processing technologies [9, 10]. Metal oxide-based electronics have been well established as an alternative to silicon technology, demonstrating exceptional electronic performance as active semiconductor components, which can be tuned for the applications, where high transparency/electrical conductivity is demanded [11, 12]. The major investment of several high-profile companies: SHARP, SAMSUNG, LG, BOE has led to the commercialization of oxide-based display backplanes in a very short period of time, and the global market is expected to increase [9, 10]. The current typical processing techniques require complex high-vacuum equipment which is a major drawback, particularly when targeting low-cost applications.

Recently, the demands for low-cost flexible electronics has led to a remarkable development of solution-based production methods and solution-processed inorganic metal oxide semiconductor materials for high-performance thin-film transistors (TFTs), and such devices have demonstrated competitive results when compared with materials obtained by physical techniques [4, 13].

Several solution-based chemical synthetic routes have been exploited for the preparation of these oxides because of their simplicity, versatility, and scale-up capability; however, the application of solution combustion synthesis to the production of thin films for TFT applications was first reported in 2011 [4]. Since then, significant research efforts have been put on the development of semiconductor materials such as indium oxide and indium, zinc tin and gallium-based multicomponent oxides [13–16] and more recently of dielectric materials [5, 6, 17]. However, most of the research as focussed on the use of toxic solvents (2-methoxyethanol) and scarce materials (indium), which can be a major drawback in the upscaling of this technology. Consequently, the challenge remains to unveil the combination of solution combustion synthesis processing parameters that allow an environmentally friendly production of high-quality insulator and semiconductor thin films at low temperature and their combination in fully combustion solution-processed TFTs.

In this work, we focus on the environmentally friendly solution combustion synthesis of oxide-based materials for electronic applications, including insulator and semiconductor thin films by studying the influence of synthetic and processing parameters, such as fuel type; solvent and annealing temperature, on their electrical properties. Fully combustion solution-processed indium-free AlO_x/ZTO TFTs using ethanol as solvent were successfully produced demonstrating extremely promising performance for electronic applications.

http://dx.doi.org/10.5772/64761

2. Experimental details

2.1. Precursor solution preparation and characterization

The preparation of all precursor solutions was performed in a similar manner. Typically, the metal salts were dissolved in 25 mL of solvent, either 2-methoxyethanol (2-ME, $C_3H_8O_2$, Fluka, 99%), ethanol (C_2H_6O, Merck, 99.5%) or deionized water, to yield solutions with the desired metal ion concentration. Then, the fuel (urea; $CO(NH_2)_2$, Sigma, 98%) and ,if required, the combustion aid (ammonium nitrate; NH_4NO_3, Roth, 98%) were added to the prepared solutions which were maintained under constant stirring until complete dissolution. The urea to metal nitrate molar proportion was determined by the Jain method, as described in Section 1.1, to guarantee the redox stoichiometry of the reaction for each material; namely 1.6:1 for Zn^{2+} metal ions and 2.5:1 for In^{3+} and Al^{3+} metal ions. In the case of metal chloride precursors, a combustion aid is required and the molar proportion of metal ion:NH_4NO_3:urea used was 1:1:1 for tin chloride solutions.

Semiconductor ZTO precursor solutions were prepared by mixing zinc oxide and tin oxide precursor solutions in a 2:1 proportion. Zinc oxide precursor solution was prepared as described earlier in 2-methoxyethanol or ethanol to yield solutions with 0.05 M concentration. Tin oxide precursor solutions were prepared by mixing tin chloride ($SnCl_2 \cdot 2H_2O$, Sigma, 98%), urea and ammonium nitrate to yield solutions with 0.05 M concentration. Individual solutions were magnetically stirred for 12 h before ZTO solution preparation.

Dielectric aluminium oxide precursor solutions were prepared by dissolving aluminium nitrate nonahydrate ($Al(NO_3)_3 \cdot 9H_2O$, Fluka, 98%) and urea in 2-methoxyethanol, ethanol or water, to yield solutions with 0.1 M concentration. Prior to their use, all solutions where magnetically stirred for at least 15 min and filtrated through a 0.45 μm hydrophilic filter. All reagents were used without further purification.

Thermal characterization of precursor solutions was performed by thermogravimetry and differential scanning calorimetry (TG-DSC). TG-DSC analyses were performed on precursors dried for 12 h at 80°C under air atmosphere up to 550°C with a 10°C/min heating rate in an aluminium crucible using a Simultaneous Thermal Analyzer, Netzsch (TGA-DSC—STA 449 F3 Jupiter).

2.2. Thin-film deposition and characterization

Prior to deposition all substrates (silicon wafer and soda-lime glass) were cleaned in an ultrasonic bath at 60°C in acetone for 15 min, then in 2-isopropanol for 15 min. and dried under N_2; followed by a 30 min. UV/Ozone surface activation step using a PSD-UV Novascan system. Thin films were deposited by spin coating the precursor solutions at 2000 rpm for 35 s (Laurell Technologies) followed by an immediate hotplate annealing in ambient conditions; this procedure was repeated to obtain the desired thickness.

The films' structure was assessed by glancing angle X-ray diffraction (GAXRD) performed by an X'Pert PRO PANalytical powder diffractometer using with Cu Kα line radiation

(λ = 1.540598 Å) with angle of incidence of the X-ray beam fixed at 0.9°. The surface morphology was investigated by atomic force microscopy (AFM, Asylum MFP3D) and scanning electron microscopy (SEM-FIB, Zeiss Auriga Crossbeam microscope). Cross section of produced films and devices was performed by focussed ion beam (FIB). In FIB milling experiments, Ga^+ ions were accelerated to 30 kV at 5 pA and the etching depth was around 250 nm. Spectroscopic ellipsometry measurements of thin films deposited on silicon substrates were made over an energy range of 1.5–6.0 eV with an incident angle of 70° using a Jobin Yvon Uvisel system to determine film thickness.

2.3. Electronic device fabrication and characterization

Metal-insulator-semiconductor (MIS) capacitors were produced by AlO_x thin-film deposition onto p-type silicon substrates (1–10 Ω cm) as described earlier (see section 2.2). Aluminium gate electrodes (100 nm thick) with an area of 8.7×10^{-3} cm^2 were deposited by thermal evaporation via shadow mask. A 100-nm-thick aluminium film was also deposited on the back of the silicon wafer to improve electrical contact. Electrical characterization was performed measuring both the capacitance-voltage and capacitance-frequency characteristics in the range off 10 kHz to 1 MHz of the devices using a semiconductor characterization system (Keithley 4200SCS).

Thin-film transistors (TFTs) were produced in a staggered bottom-gate, top-contact structure by depositing AlO_x thin films onto p-type silicon substrates (1–10 Ω cm) as described earlier. The semiconductor layer was deposited by sequentially spin coating four layers of semiconductor precursor solution 0.05 M onto the AlO_x thin films and annealed in air at 350°C for 30 min after each layer deposition. For comparison, AlO_x/IGZO TFTs were also produced with sputtered IGZO thin films. IGZO thin films were fabricated in a AJA ATC-1300F sputtering system using a IGZO target with 2:1:1 composition (in In_2O_3:Ga_2O_3:ZnO molar ratio). Deposition was carried out in Ar+O_2 atmosphere at a pressure of 2.3 mTorr and r.f. power of 100 W, to obtain a 30 nm thick film. Post-processing annealing was performed in air on a hotplate at 180°C for 1 h. Finally, source and drain aluminium electrodes (100 nm thick) were deposited by e-beam evaporation via shadow mask onto annealed films, defining a channel width (W) and length (L) of 1400 μm and 10 μm, respectively (W/L = 14). Electrical characterization was performed by the measurement of current-voltage characteristics of the devices using a semiconductor parameter analyser (Agilent 4155C) attached to a microprobe station (Cascade M150) inside a dark box, at room temperature. The saturation mobility (μ_{SAT}) was determined from the following equation: [18]

$$I_D = \left(\frac{C_i W \mu_{SAT}}{2L} \right) (V_G - V_T)^2 \tag{5}$$

where C_i is the gate dielectric capacitance per unit area, W and L are the channel width and length, V_G is the gate voltage and V_T is the threshold voltage, which was determined in the saturation region by linear fitting of a $I_D^{1/2}$ *vs.* V_G plot.

http://dx.doi.org/10.5772/64761

3. Results

The core of oxide-based electronics for displays applications are thin-film transistors (TFTs). **Figure 1** shows a schematic representation of a TFT structure and respective transfer plot. TFTs are three terminal field-effect devices, whose working principle relies on the modulation of the current flowing in a semiconductor placed between two electrodes (source and drain). A dielectric layer is inserted between the semiconductor and a transversal electrode (gate), being the current modulation achieved by the capacitive injection of carriers close to the dielectric/semiconductor interface, known as field effect [12].

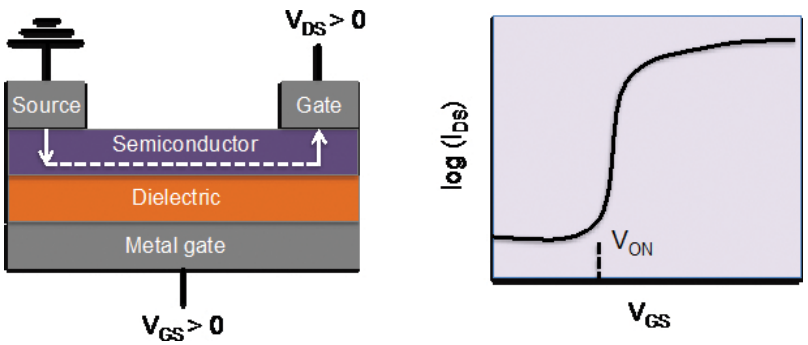

Figure 1. Schematic representation of a bottom-gate TFT structure and typical field effect electrical characteristics plot.

The semiconductor and gate insulator are equally important material components in field-effect transistors; consequently, the development of both materials by solution techniques is essential [6].

3.1. Amorphous semiconductor oxides

Amorphous oxide semiconductors (AOSs) have drawn significant attention in the field of flat panel displays during the last decade, due to their high carrier mobility when compared to amorphous silicon (a-Si). Indium-gallium-zinc oxide (IGZO) is the most explored semiconductor due to its superior field effect mobility and enhanced electrical performance [11, 12]. However, alternative semiconductor materials that rely on abundant and non-toxic elements are required due to environmental demands. Zinc-tin-oxide (ZTO) is a promising indium and gallium-free alternative and impressive results have already been obtained in TFTs applications [19, 20].

Several solution-processed ZTO-based TFTs have been reported; however, processing temperature above 400°C and a toxic organic solvent, such as acetonitrile, 2-ethoxyethanol or 2-methoxyethanol are usually required [5]. The use of non-toxic solvents has been pursued and ethanol [5] and water [7] based ZTO TFTs have already been reported.

The decomposition of urea [Eq. (2)] and zinc nitrate [Eq. (6)] is represented as follows.

$$Zn\left(NO_3\right)_2.6H_2O \rightarrow ZnO + 6H_2O + N_2 + \left(\frac{5}{2}\right)O_2 \tag{6}$$

$$CO\left(NH_2\right)_2 + \left(\frac{3}{2}\right)O_2 \rightarrow 2H_2O + CO_2 + N_2 \tag{2}$$

The overall ZnO formation reaction can thus be written as follows Eq. (7).

$$\begin{aligned} &3Zn\left(NO_3\right)_2 \cdot 6H_2O + 5CO\left(NH_2\right)_2 \rightarrow \\ &3ZnO + 28H_2O + 8N_2 + 5CO_2 \end{aligned} \tag{7}$$

Using the Jain method, the reducing valence of urea is +6 and the oxidizing valence of zinc nitrate is –10. In order to assure the redox stoichiometry 5/3 (or 1.6), moles of urea are required per mole of zinc nitrate.

The tin oxide formation can be represented by the following equation:

$$\begin{aligned} &SnCl_2 + \frac{1}{3}CO\left(NH_2\right)_2 + NH_4NO_3 + \frac{1}{2}O_2 \rightarrow \\ &SnO_2 + 2HCl + \frac{5}{3}H_2O + \frac{4}{3}N_2 + \frac{1}{3}CO_2 \end{aligned} \tag{8}$$

In the combustion synthesis of tin oxide, a combustion aid, ammonium nitrate, was added to the precursor solution as commonly performed for chlorine-based metal salts. According to Jain's method, the oxidizer valence of ammonium nitrate (NH_4NO_3) is −2 and to achieve $\Phi = 1$ 0.3 mol of urea per mole of ammonium nitrate are required. In this case, a fuel-rich condition, $\Phi > 1$, was used to ensure the full oxidation of the metal precursor.

ZTO precursor solution was prepared after mixing individual of zinc and tin oxide precursor solutions of 0.05 M concentration in a 2:1 proportion, respectively. Thermal analysis of ZTO precursor solutions was performed to investigate the influence of solvent on their decomposition behaviour. TG-DSC measurements were performed on precursors dried for 12 h at 80°C. **Figure 2** shows the DSC results for ZTO precursors up to 350°C as above this temperature no further events were observed.

The combustion reaction of the organic fuel with the metal nitrates typically leads to an intense exothermic peak with corresponding abrupt mass loss. For ZTO precursors, these were observed at 125°C and 108°C for 2-ME and ethanol-based solutions, respectively. A smaller peak is observed at 275°C which can be related to secondary reactions [3, 4] that can occur during thermal decomposition of the reagents.

http://dx.doi.org/10.5772/64761

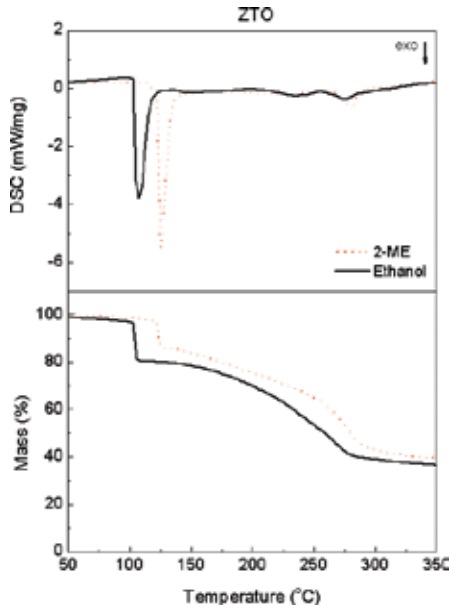

Figure 2. TG-DSC analysis of ZTO-based precursor solutions using 2-methoxyethanol (2-ME) and ethanol as solvent. Adapted from [5].

The precursor solution degradation mechanism is expected to be different in bulk and thin-film form which explains the need for higher thin-film processing temperature than the one determined by thermal analysis. Devices annealed at temperatures below 350°C did not show effective gate modulation as such, the processing temperature was fixed at this temperature although the minimum temperature required for full degradation of the precursors is 275°C.

Structural characterization of the films (**Figure 3a**) indicates that amorphous films are obtained up to 350°C for both precursor solution solvents, as no diffraction peaks were observed. Morphological surface analysis show that smooth and uniform films are obtained regardless

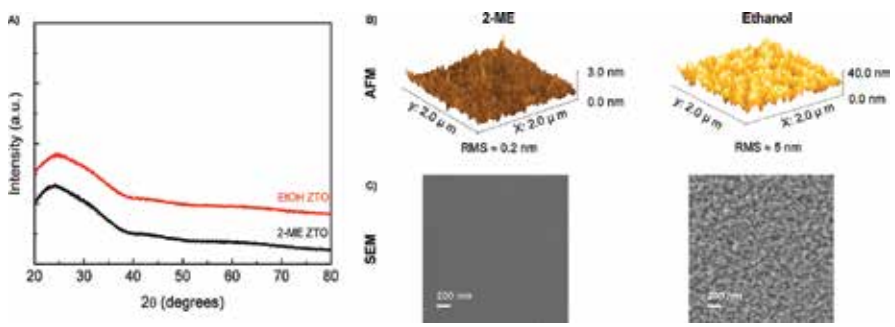

Figure 3. Structural and morphological analysis of 2-methoxyethanol (2-ME) and ethanol-based ZTO thin films produced at 350°C: a) XRD, b) AFM, c) SEM.

of solvent; however, 2-ME-based ZTO films demonstrate a lower surface roughness, 0.2 nm, when compared to ethanol-based films; 5 nm.

Combustion solution-based ZTO TFTs were produced by spin-coating precursor solutions onto commercial Si/SiO_2 substrates. Electrical characterization of TFTs was performed by measuring the transfer and output characteristics of the devices in ambient conditions in the dark. **Figure 4** shows a cross section SEM image of ZTO TFTs produced on Si/SiO_2, with Al source-drain electrodes, obtained after FIB milling and electrical characterization of 2-ME and ethanol-based ZTO TFTs.

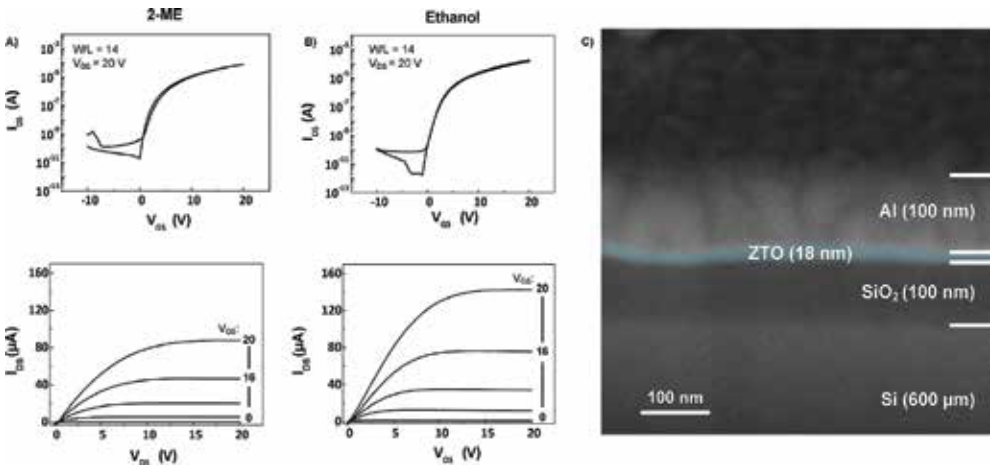

Figure 4. Electrical and morphological characterization of ZTO/SiO_2 TFTs produced at 350°C: transfer and output characteristics of a) 2-methoxyethanol (2-ME) and b) ethanol-based ZTO/SiO_2 TFTs. c) SEM-FIB cross section of a ZTO/SiO_2 TFT.

The analysis of the electrical characteristics reveals that ZTO TFTs show an I_{on}/I_{off} above 10^6, saturation mobility of 2 $cm^2/V \cdot s$, low subthreshold swing and low hysteresis. Output characteristics exhibit saturation suggesting a low background carrier concentration and anticipate the absence of transconductance degradation as V_{GS} increases, revealing good dielectric/semiconductor interface properties and no significant carrier injection problems. These devices exhibit high operational stability under positive gate bias stress [21]. Combustion synthesis-based ZTO thin films thus demonstrate high potential for alternative and environmental friendly solution-based electronic applications, allowing their use as reliable switching elements in active matrices.

3.2. Dielectric oxides

Insulator materials suitable for TFT gate dielectric applications must fulfil some criteria, namely i) high bang gap, with favourable conduction band offset to avoid high gate leakage; ii) high dielectric constant (high-κ) the added capacitance can compensate interface traps, thus

http://dx.doi.org/10.5772/64761

improving the transistor performance and allow low operating voltage; iii) good interface properties, which can be achieved using amorphous dielectrics [11, 22, 23].

Solution-based high-κ dielectrics, such as Al_2O_3, HfO_2, ZrO_2, have demonstrated high performance and suitability for the application in metal oxide semiconductor-based TFTs [5, 6, 17, 24–28]. Amongst these, aluminium oxide is one of the most developed materials from solution synthesis since several aluminium precursors salts are readily availability at low cost. The influence of processing parameters on the solution combustion synthesis of aluminium oxide was studied.

The decomposition reactions for aluminium, urea and the overall aluminium oxide formation reaction are already represented by Eq. (1), (2) and (3), respectively. According to Jain's method and to ensure redox stoichiometry, 2.5 mol of urea per mole of aluminium nitrate were used to prepare aluminium oxide precursor solutions with 0.1 M concentration. The influence of several processing parameters such as fuel, solvent and annealing temperature on the properties of dielectric AlO_x thin films was studied.

Thermal analysis of AlO_x precursor solutions was performed to investigate the influence of solvent on their decomposition behaviour. **Figure 5** shows the DSC results for AlO_x precursors prepared with 2-methoxethanol, ethanol and water.

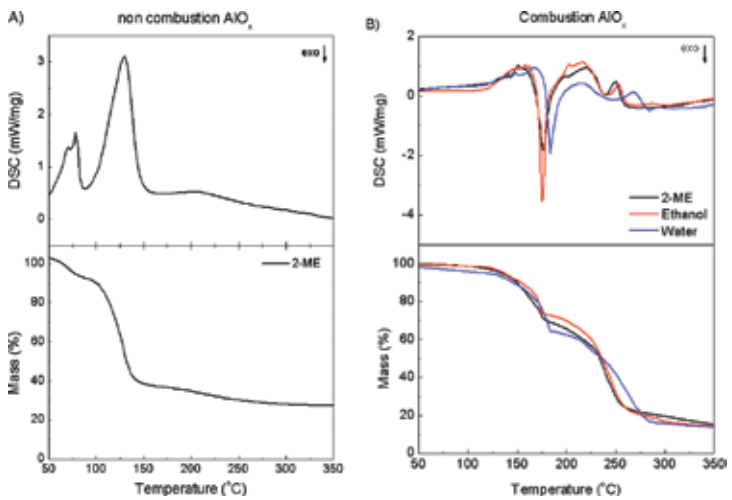

Figure 5. TG-DSC analysis of AlO_x-based precursor solutions: a) non-combustion AlO_x precursor using 2-methoxyethanol (2-ME) and b) combustion AlO_x precursor using 2-ME, ethanol and water as solvent.

Thermal behaviour of AlO_x precursor solutions is strongly affected by the presence of urea, which acts as fuel; when no fuel is added only endothermic peaks corresponding to solvent evaporation (water at 95°C and 2-methoxyethanol at 125°C) which is the main component of the solution with a corresponding 60% mass loss and subsequent organics decomposition (235°C) are observed, meaning that additional energy must be supplied to promote oxide formation. On the other hand, when urea is added in a stoichiometric proportion an intense

exothermic peak with corresponding abrupt mass loss at about 180°C is observed. This exothermic event is attributed to the combustion reaction of the organic fuel with the metal nitrates; a smaller peak at 250°C is also observed and can be related to the degradation of residual organics. Thermal behaviour of combustion AlO_x precursor solutions does not shown significant variations when using different solvents. The influence of solvent in the oxide formation reaction is apparently more significant for multicomponent oxides, such as ZTO (**Figure 2**).

Thin films of AlO_x were produced by spin-coating precursor solution onto a substrate (either soda-lime glass or Si) and annealing on a hotplate for 30 min. The influence of several processing parameters on the structural and morphological properties of dielectric AlO_x thin films obtained from 0.1 M concentration solutions was studied. XRD, SEM and AFM characterization of the AlO_x thin films was performed and **Figure 6** shows typical data obtained for AlO_x thin films produced at 350°C from 2-methoxyethanol, ethanol and water-based precursor solutions.

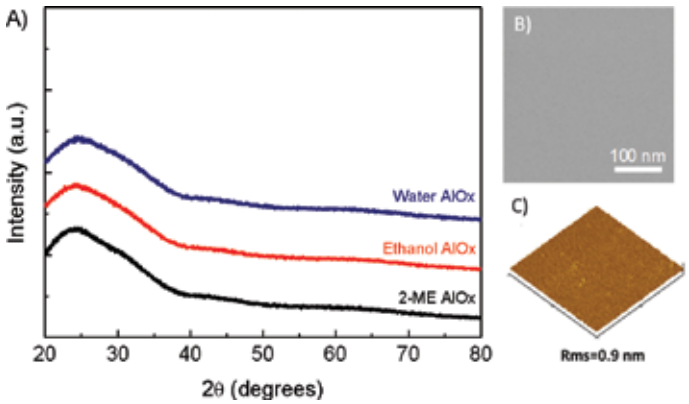

Figure 6. Structural and morphological analysis of combustion solution AlO_x thin films produced at 350°C: a) XRD, b) SEM and c) AFM of water-based films. Inset show gate current density.

Generally, structural and morphological properties of AlO_x thin films did not vary significantly regardless of processing parameters within the studied range. The variation of precursor solution's solvent does not influence the structural properties of the films, which is in agreement with that observed for DSC measurements. Morphological properties are slightly influenced by the solvent used with rms film roughness increasing from 0.3 nm when using 2ME or ethanol to 0.9 nm for water-based films. Fuel content and annealing temperature also do not affect structural and morphological properties as amorphous, highly uniform and smooth AlO_x thin films with rms roughness of below 1 nm were consistently obtained at 350°C. The properties demonstrated by these aluminium oxide thin films produced from solution synthesis are highly desirable for electronic applications as low surface roughness leads to enhanced interface properties.

http://dx.doi.org/10.5772/64761

The effect of processing parameters on the electrical properties of these films was studied by assessing the electrical performance of capacitors and thin-film transistors comprising the solution-based AlO_x films.

Solution-based AlO_x capacitors were produced by spin-coating AlO_x precursor solutions onto commercial Si substrates followed by aluminium gate contact deposition by thermal evaporation. The effect of processing parameters on the electrical performance of these devices was studied and **Figure 7** shows capacitance-voltage measurements for different fuel, using either urea, citric acid or no fuel; and annealing temperature, 350, 250 and 200°C. The effect of precursor solution solvent variation has already been reported elsewhere [6].

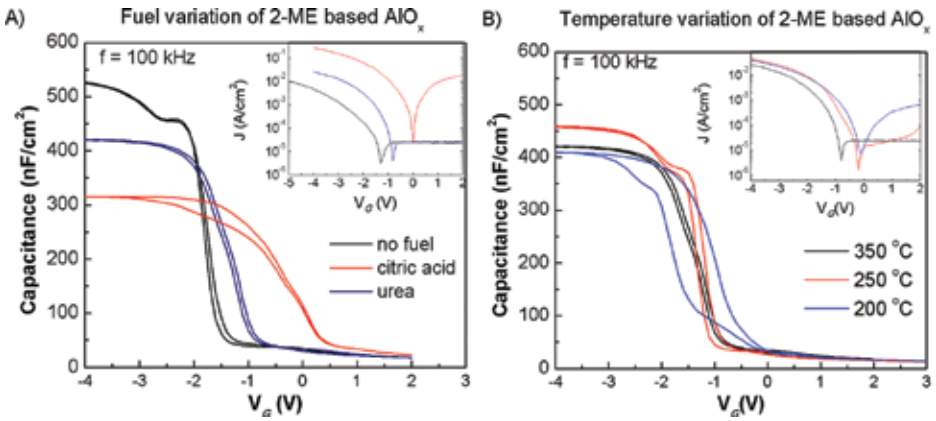

Figure 7. Electrical characterization of AlO_x capacitors produced with different parameters: a) fuel variation in 2-ME; b) temperature variation for 2-methoxyethanol-based films. Inset show gate current density.

The electrical characteristics of AlO_x capacitors produced with no fuel show a non-uniform capacitance variation at −3 to −2 V indicating the presence of organic residues within the film such as nitrate groups; these ions favour water adsorption leading to higher capacitance due to the high dielectric constant of water, as previously observed [6, 29]. To improve film properties, when a non-combustion synthesis route is applied, either higher temperature or UV-assisted annealing is currently being used [26, 30]. When citric acid is added as fuel low capacitance and high current density is observed, this is consistent with more porous AlO_x films and in fact their application as gate dielectric in TFTs was not successful as only short-circuited devices were obtained. Urea leads to consistent one domain capacitance characteristics and low current density within TFT operating voltage range as required for gate dielectric applications. The film properties are highly affected by processing temperature due to inefficient organics removal; at 250°C a two domain system is obtained, similar to that observed for non-combustion synthesis route, and at 200°C large hysteresis indicates an increase in charge defects concentration consistent with organic impurities within the film. Although from DSC analysis, the ignition temperature of AlO_x combustion reaction was determined to be 180°C, still higher temperature is required to obtain thin films with desirable dielectric properties. This inconsistency between thermal analysis and electrical properties obtained at

low temperature is attributed to the difference between bulk and film decomposition processes.

IGZO TFTs comprising combustion solution-based AlO_x gate dielectric were produced by sputtering IGZO semiconductor layer onto annealed AlO_x thin films and finally evaporating aluminium source/drain contacts. The use of a standard sputtered semiconductor allowed the assessment of the TFTs performance variation solely due to the dielectric layer's processing parameters influence. Electrical characterization of TFTs was performed by measuring the electrical characteristics of the devices in ambient conditions in the dark (**Figure 8**).

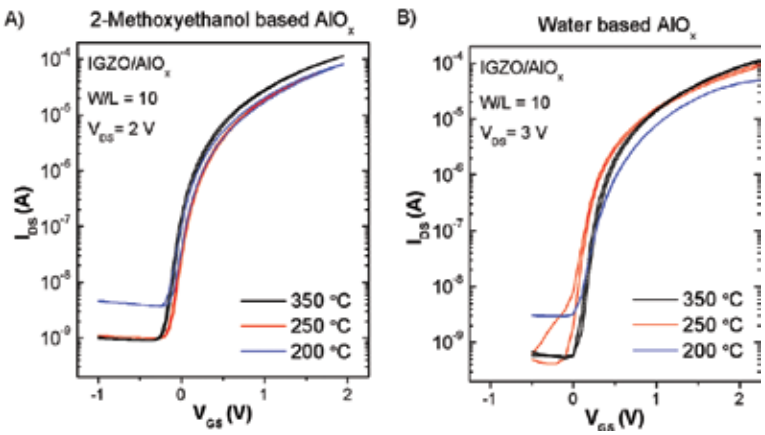

Figure 8. Electrical characterization of IGZO/AlO_x TFTs produced at different temperatures using a) 2-methoxyethanol and b) water as solvent.

TFT performance is assessed trough the analysis of the turn-on voltage (V_{ON}), the threshold voltage (V_T), drain current on-off ratio (I_{ON}/I_{OFF}), subthreshold slope (S) and saturation mobility (μ_{SAT}), which was calculated using AlO_x capacitance at the 10 kHz in order to minimize overestimation. Electrical characteristics of these devices are presented in **Table 1**.

AlO_x solvent	Temperature (°C)	V_{ON} (V)	I_{ON}/I_{OFF}	μ_{SAT} cm²/Vs
2-ME	350	−0.36	1×10^5	17.3
	250	−0.30	8×10^4	9.6
	200	−0.25	2×10^4	13.5
Water	350	0	5×10^5	9.2
	250	−0.10	5×10^5	6.9
	200	0	7×10^3	12.9

Table 1. Electrical characteristics of solution-based IGZO/AlO_x TFTs.

Despite the non-ideal capacitance-voltage characteristics obtained for low-temperature AlO_x thin films, IGZO/AlO_x TFTs were successfully produced. Similarly to what is obtained for

capacitors the TFTs performance is highly dependent on annealing temperature. For both solvents used, 2-methoxyethanol and water, enhanced properties are obtained for 350°C and similar trend with temperature variation is observed which is in agreement with DSC-TG analysis. For lower temperatures, a hysteresis increase and on/off current ratio decrease is observed, being more significant for 200°C, due to oxide charge defects within the dielectric as a consequence of incomplete organic residues removal. Nevertheless, successful gate modulation at low operation voltage, due to the higher capacitance achieved with very thin AlO_x films, was obtained for all devices which demonstrated close to zero V_{ON}, high I_{ON}, high saturation mobility and low subthreshold swing as required for electronic applications.

3.3. Fully solution-based oxide TFTs

The realization of printed electronics requires all solution-based devices; consequently, semiconductor and dielectric materials must be combined in TFTs. Fully combustion-solution-based TFTs comprising the developed dielectric and semiconductor materials have been successfully fabricated. **Figure 9** shows transfer characteristics of these devices [5, 6].

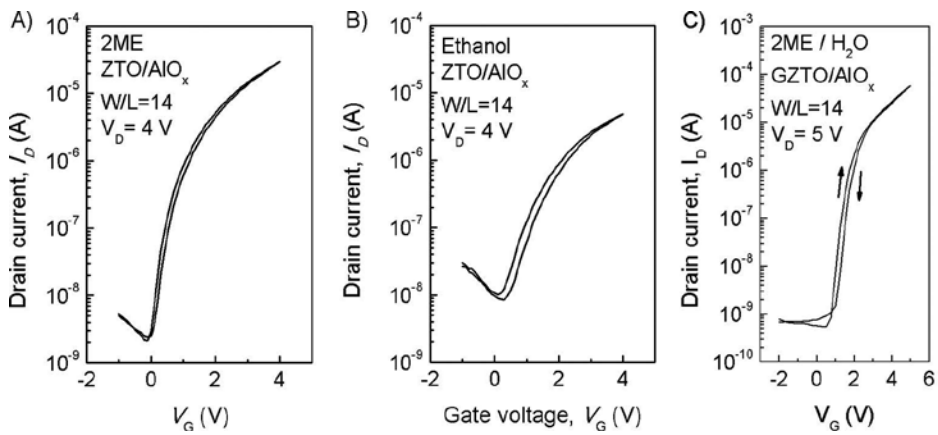

Figure 9. Transfer characteristics of fully combustion solution-based bottom gate TFTs produced at 350°C on highly doped p-Si (gate) with a) 2ME-based ZTO and AlO_x, b) ethanol-based ZTO and AlO_x, and c) 2ME-based GZTO and water-based AlO_x. Adapted from [5, 6].

The combination of solution-processed dielectric and semiconductors yielded TFTs with a good overall performance, demonstrating very low clockwise hysteresis, close to zero V_{ON} and I_{ON}/I_{OFF} above 10^4. Generally, 2ME-based devices show better performance when compared to more environmental friendly ethanol; saturation mobility increases from 0.8 $cm^2/V \cdot s$ to 2.3 $cm^2/V \cdot s$ for ZTO/AlO_x TFTs, also 2ME GZTO shows μ_{SAT} of 1.3 $cm^2/V \cdot s$ when combined with water-based AlO_x. These differences in device performance are attributed to trapped charges at the semiconductor-insulator interface as consequence of the semiconductor films' composition and rougher morphology of ethanol-based films [5, 6]. The high I_{OFF} observed mainly arises from the use of non-patterned semiconductor layers which can be improved by implementing patterning techniques. The combination of AlO_x dielectrics and ZTO-based

semiconductors yielded very promising results for application in fully solution-processed electronics; however, the processing temperature required for good TFT performance was 350°C which is still too high for flexible substrates. Nevertheless, these results are within the state-of-the-art for solution-processed ZTO TFTs using different solvents (**Table 2**).

Ref	Solvent	Gate dielectric	T (°C)	Mobility ($cm^2 V^{-1} s^{-1}$)	I_{ON}/I_{OFF}	V_{ON} (V)
[32]	Acetonitrile	HfO_y/AlO_x	400	3.84	10^5	~ −0.2
[31]	Acetonitrile	ZrO_2	500	~ ▪ 10	10^9	~ −0.3
[33]	Acetonitrile	SiO_2	350	0.30	10^4	~ 5
[20]	Acetonitrile	Si_3N_4	500	7.7	10^8	~ −8
[4]	2-methoxyethanol	SiO_2	225	0.32	10^4	~ −30
			250	1.76	10^7	~ 10
[34]	2-methoxyethanol	SiO_2	450	1.95	10^7	~ −19
[35]	2-methoxyethanol	SiO_2	550	17.02	10^7	~ −4
[5]	2-methoxyethanol	AlO_x	350	2.6	10^4	~ 0
	Ethanol	AlO_x	350	0.8	10^2	~ 0.1
[7]	Water	SiO_2	250	0.12	10^5	~ 5
			300	3.03	10^7	~ −3

Table 2. Selected processing details for reported solution-based ZTO TFTs.

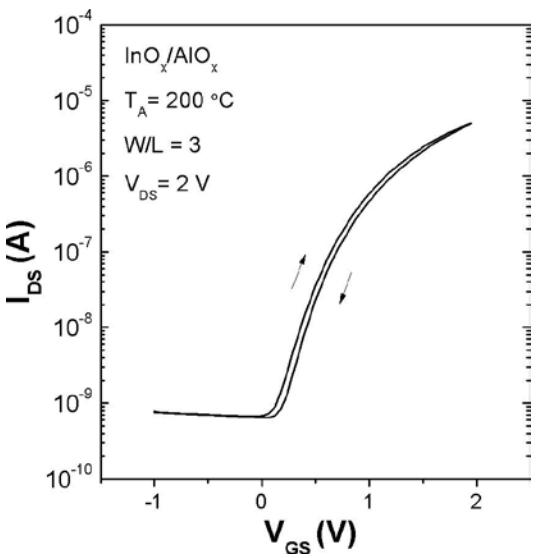

Figure 10. Transfer characteristics of fully combustion-solution-based InO_x/AlO_x TFTs produced from 2ME precursors using a maximum processing temperature of 200°C.

The use of indium-free semiconductor materials, such as ZTO and GZTO, although environmentally relevant somehow lead to a compromise of solution-processed TFTs performance both in saturation mobility and processing temperature.

Fully solution-based TFTs were obtained at maximum processing temperature of 200°C when combining the developed 2-methoxyethanol-based AlO_x dielectric with solution-based indium oxide semiconductor produced using UV-assisted low-temperature annealing as reported in [36]. Transfer characteristics of low-temperature InO_x/AlO_x TFTs are depicted in **Figure 10**.

In O_x/AlO_x TFTs showed higher saturation mobility (μ_{SAT} = 5.6 $cm^2 V^{-1} s^{-1}$) when compared to indium-free devices processed at higher temperatures and otherwise similar electrical performance whilst at the same time being compatible with polymeric substrates for flexible electronics applications.

4. Conclusions

The application of solution combustion synthesis to prepare oxide materials for electronic devices was successfully achieved for dielectric and semiconductor thin films using varied processing parameters. We have clearly demonstrated that dielectric AlO_x thin films can be obtained using green solvents such as ethanol and water and successfully combined with ethanol-based ZTO semiconductor layers to yield fully combustion solution-based TFTs. Although electrical properties of these solution-processed TFTs are still far for what is required in AMTFT displays applications, successful preparation and combination of dielectric and semiconductor oxides films by a relatively low-temperature solution process represents a significant achievement and an advancement towards environmentally friendly production process. The facile applicability of SCS to other metal precursors opens numerous possibilities for low temperature synthesis of oxides materials and thin films required for the development of all solution-based devices. The mechanisms behind precursor degradation/oxide formation process are not yet fully understood so the challenge remains to unravel the ideal combination of solvent, oxidizer and organic fuel to obtain high-quality materials and properties. Nevertheless, this versatile synthesis method combined with innovative low-temperature annealing processes will continue to play a major role in the future development flexible electronics.

Acknowledgements

This work was partly funded by FEDER funds through the COMPETE 2020 Programme and National Funds through FCT—Portuguese Foundation for Science and Technology under the projects POCI-01-0145-FEDER-007688, Reference UID/CTM/50025 and EXCL/CTM-NAN/0201/2012; European Community FP7 2007-2013 project i-FLEXIS Grant Agreement n. 611070. D. Salgueiro acknowledges FCT-MEC for doctoral grant SFRH/BD/110427/2015. Authors would like to acknowledge J. V. Pinto for XRD, D. Nunes for SEM-FIB and T. Sequeira for AFM measurements.

Author details

Rita Branquinho*, Ana Santa, Emanuel Carlos, Daniela Salgueiro, Pedro Barquinha, Rodrigo Martins and Elvira Fortunato

*Address all correspondence to: ritasba@fct.unl.pt

i3N/CENIMAT, Department of Materials Science, Faculty of Science and Technology, NOVA University of Lisbon and CEMOP/UNINOVA, Caparica, Portugal

References

[1] M. Epifani, E. Melissano, G. Pace, and M. Schioppa, "Precursors for the combustion synthesis of metal oxides from the sol-gel processing of metal complexes," J. Eur. Ceram. Soc., vol. 27, no. 1, pp. 115–123, 2007.

[2] Z. Shao, W. Zhou, and Z. Zhu, "Advanced synthesis of materials for intermediate-temperature solid oxide fuel cells," Prog. Mater. Sci., vol. 57, no. 4, pp. 804–874, 2012.

[3] S. L. Gonzalez-Cortes and F. E. Imbert, "Fundamentals, properties and applications of solid catalysts prepared by solution combustion synthesis (SCS)," Appl. Catal. A Gen., vol. 452, pp. 117–131, 2013.

[4] M.-G. Kim, M. G. Kanatzidis, A. Facchetti, and T. J. Marks, "Low-temperature fabrication of high-performance metal oxide thin-film electronics via combustion processing," Nat. Mater., vol. 10, no. 5, pp. 382–388, 2011.

[5] R. Branquinho, D. Salgueiro, A. Santa, and A. Kiazadeh, "Towards environmental friendly solution-based ZTO/AlO x TFTs," Semicond. Sci. Technol., vol. 30, no. 2, p. 24007, 2015.

[6] R. Branquinho, D. Salgueiro, L. Santos, P. Barquinha, L. Pereira, R. F. D. P. Martins, and E. Fortunato, "Aqueous combustion synthesis of aluminium oxide thin films and application as gate dielectric in GZTO solution-based TFTs," ACS Appl. Mater. Interfaces, vol. 6, pp. 195592–195599, 2014.

[7] J. H. Park, W. J. Choi, J. Y. Oh, S. S. Chae, W. S. Jang, S. J. Lee, K. M. Song, and H. K. Baik, "Low-temperature, aqueous-solution-processed zinc tin oxide thin film transistor," Jpn. J. Appl. Phys., vol. 50, no. 7, p. 070201, 2011.

[8] S. R. Jain, K. C. Adiga, and V. R. Pai Verneker, "A new approach to thermochemical calculations of condensed fuel-oxidizer mixtures," Combust. Flame, vol. 40, pp. 71–79, 1981.

[9] E. Fortunato, P. Barquinha, R. Branquinho, D. Salgueiro, E. Carlos, A. Liu, F. K. Shan, and R. Martins, "Is the new oxide electronics (r)evolution solution based?," J. Phys. D Appl. Phys., 2016, in press.

[10] J. F. Wager, "Oxide TFTs: A Progress Report," Inf. Disp. (1975), vol. 32, no. 1, pp. 16–21, 2016.

[11] P. Barquinha, L. Pereira, R. Martins, and E. Fortunato, Transparent Electronics: From Materials to Devices. John Wiley & Sons, Inc., Hoboken, New Jersey, 2012.

[12] E. Fortunato, P. Barquinha, and R. Martins, "Oxide semiconductor thin-film transistors: a review of recent advances," Adv. Mater., vol. 24, no. 22, pp. 2945–2986, 2012.

[13] B. Du Ahn, H.-J. Jeon, J. Sheng, J. Park, and J.-S. Park, "A review on the recent developments of solution processes for oxide thin film transistors," Semicond. Sci. Technol., vol. 30, no. 6, p. 064001, 2015.

[14] Y. H. Kang, S. Jeong, J. M. Ko, J.-Y. Lee, Y. Choi, C. Lee, and S. Y. Cho, "Two-component solution processing of oxide semiconductors for thin-film transistors via self-combustion reaction," J. Mater. Chem. C, vol. 2, no. 21, p. 4247, 2014.

[15] J. W. Hennek, M.-G. Kim, M. G. Kanatzidis, A. Facchetti, and T. J. Marks, "Exploratory combustion synthesis: amorphous indium yttrium oxide for thin-film transistors," J. Am. Chem. Soc., vol. 134, no. 23, pp. 9593–9596, 2012.

[16] J. W. Hennek, J. Smith, A. Yan, M.-G. Kim, W. Zhao, V. P. Dravid, A. Facchetti, and T. J. Marks, "Oxygen getter" effects on microstructure and carrier transport in low temperature combustion-processed a-InXZnO (X = Ga, Sc, Y, La) transistors," J. Am. Chem. Soc., vol. 135, no. 29, pp. 10729–10741, 2013.

[17] E. J. Bae, Y. H. Kang, M. Han, C. Lee, and S. Y. Cho, "Soluble oxide gate dielectrics prepared using the self-combustion reaction for high-performance thin-film transistors," J. Mater. Chem. C, vol. 2, no. 28, pp. 5695–5703, 2014.

[18] D. K. Schroder, Semiconductor Material and Device Characterization, 3rd ed. John Wiley & Sons, Inc., Hoboken, New Jersey, 2006.

[19] J. S. Lee, Y.-J. Kwack, W.-S. Choi, and C. Woon-Seop, "Low-temperature solution-processed zinc-tin-oxide thin-film transistor and its stability," J. Korean Phys. Soc., vol. 59, no. 5, p. 3055, 2011.

[20] R. D. Chandra, M. Rao, K. Zhang, R. R. Prabhakar, C. Shi, J. Zhang, S. G. Mhaisalkar, and N. Mathews, "Tuning electrical properties in amorphous zinc tin oxide thin films for solution processed electronics.," ACS Appl. Mater. Interfaces, vol. 6, no. 2, pp. 773–7, 2014.

[21] A. Kiazadeh, D. Salgueiro, R. Branquinho, J. Pinto, H. L. Gomes, P. Barquinha, R. Martins, and E. Fortunato, "Operational stability of solution based zinc tin oxide/SiO2 thin film transistors under gate bias stress," APL Mater., vol. 3, no. 6, p. 062804, 2015.

[22] L. Pereira, P. Barquinha, E. Fortunato, R. Martins, D. Kang, C. J. Kim, H. Lim, I. Song, and Y. Park, "High k dielectrics for low temperature electronics," Thin Solid Films, vol. 516, no. 7, pp. 1544–1548, 2008.

[23] P. Barquinha, L. Pereira, G. Gonçalves, R. Martins, E. Fortunato, D. Kuscer, M. Kosec, A. Vilà, A. Olziersky, and J. R. Morante, "Low-temperature sputtered mixtures of high κ and high bandgap dielectrics for GIZO TFTs," J. Soc. Inf. Disp., vol. 18, no. 10, pp. 762–772, 2010.

[24] Y. B. Yoo, J. H. Park, K. H. Lee, H. W. Lee, K. M. Song, S. J. Lee, and H. K. Baik, "Solution-processed high-k HfO2 gate dielectric processed under softening temperature of polymer substrates," J. Mater. Chem. C, vol. 1, no. 8, p. 1651, 2013.

[25] J. Ko, J. Kim, S. Y. Park, E. Lee, K. Kim, K.-H. Lim, and Y. S. Kim, "Solution-processed amorphous hafnium-lanthanum oxide gate insulator for oxide thin-film transistors," J. Mater. Chem. C, vol. 2, no. 6, pp. 1050–1056, 2014.

[26] S. Park, K.-H. Kim, J.-W. Jo, S. Sung, K.-T. Kim, W.-J. Lee, J. Kim, H. J. Kim, G.-R. Yi, Y.-H. Kim, M.-H. Yoon, and S. K. Park, "In-depth studies on rapid photochemical activation of various sol-gel metal oxide films for flexible transparent electronics," Adv. Funct. Mater., vol. 25, pp. 2807–2815, 2015.

[27] C. Avis and J. Jang, "High-performance solution processed oxide TFT with aluminum oxide gate dielectric fabricated by a sol-gel method," J. Mater. Chem., vol. 21, no. 29, pp. 10649–10652, 2011.

[28] C. Avis, Y. G. Kim, and J. Jang, "Solution processed hafnium oxide as a gate insulator for low-voltage oxide thin-film transistors," J. Mater. Chem., vol. 22, no. 34, p. 17415, 2012.

[29] J. H. Park, K. Kim, Y. B. Yoo, S. Y. Park, K.-H. Lim, K. H. Lee, H. K. Baik, and Y. S. Kim, "Water adsorption effects of nitrate ion coordinated Al2O3 dielectric for high performance metal-oxide thin-film transistor," J. Mater. Chem. C, vol. 1, no. 43, pp. 7166–7174, 2013.

[30] Y.-H. Kim, J.-S. Heo, T.-H. Kim, S. K. Park, M.-H. Yoon, J. Kim, M. S. Oh, G.-R. Yi, Y.-Y. Noh, and S. K. Park, "Flexible metal-oxide devices made by room-temperature photochemical activation of sol-gel films," Nature, vol. 489, no. 7414, pp. 128–132, 2012.

[31] T.-J. Ha and A. Dodabalapur, "Photo stability of solution-processed low-voltage high mobility zinc-tin-oxide/ZrO2 thin-film transistors for transparent display applications," Appl. Phys. Lett., vol. 102, no. 12, p. 123506, 2013.

[32] Y. G. Kim, C. Avis, and J. Jang, "Low voltage driven, stable solution-processed zinc-tin-oxide TFT with HfOy and AlOx stack gate dielectric," ECS Solid State Lett., vol. 1, no. 2, pp. Q23–Q25, 2012.

[33] J.-S. Lee, S.-M. Song, D.-W. Kang, Y.-H. Kim, J.-Y. Kwon, and M.-K. Han, "Effects of ultra-violet treatment on electrical characteristics of solution-processed oxide thin-film transistors," ECS Trans., vol. 50, no. 8, pp. 121–127, 2013.

[34] W. Hu and R. L. Peterson, "Charge transport in solution-processed zinc tin oxide thin film transistors," J. Mater. Res., vol. 27, no. 17, pp. 2286–2292, 2012.

[35] C. Kim, N.-H. Lee, Y.-K. Kwon, and B. Kang, "Effects of film thickness and Sn concentration on electrical properties of solution-processed zinc tin oxide thin film transistors," Thin Solid Films, vol. 544, pp. 129–133, 2013.

[36] J. Leppäniemi, H. Majumdar, K. Ojanperä, T. Kololuoma, J. Dahl, M. Tuominen, P. Laukkanen, and A. Alastalo, "Rapid low-temperature processing of metal-oxide thin film transistors with combined far ultraviolet and thermal annealing," Appl. Phys. Lett., vol. 113514, pp. 1–10, 2014.

Edited by Konstantinos G. Kyprianidis and Jan Skvaril

Over the past few decades, exciting developments have taken place in the field of combustion technology. The present edited volume intends to cover recent developments and provide a broad perspective of the key challenges that characterize the field. The target audience for this book includes engineers involved in combustion system design, operational planning and maintenance. Manufacturers and combustion technology researchers will also benefit from the timely and accurate information provided in this work.

The volume is organized into five main sections comprising 15 chapters overall:

- Coal and Biofuel Combustion
- Waste Combustion
- Combustion and Biofuels in Reciprocating Engines
- Chemical Looping and Catalysis
- Fundamental and Emerging Topics in Combustion Technology

ISBN 978-953-51-5781-6

Photo by grafoto / iStock

IntechOpen